The Dynamic Modelling and Development of a Controller for a General Purpose Remotely Operated Underwater Vehicle

Dissertation

Presented to the Department of Mechanical Engineering

University of Cape Town

In fulfilment of the Requirement for the Degree

Master of Science in Engineering

by

Maximillian Finbow

March 2016

Supervisor: Associate Professor Hennie Mouton

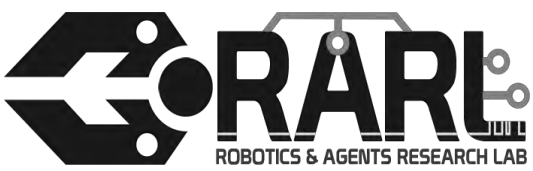

The financial assistance of the National Research Foundation (NRF) towards this research is hereby acknowledged. Opinions expressed and conclusions arrived at, are those of the author and are not necessarily to be attributed to the NRF.

This dissertation was formatted to be read in book format in colour. It is therefore recommended that the document is printed double sided and in colour.

If viewing this dissertation in electronic format, it is recommended that two page view is selected.

Research Proposal

The UCT *SEAHOG* Remotely operated underwater vehicle (ROV) will be used for underwater observation, equipment recovery and obtaining samples of marine organisms up to 300 m deep in the ocean. The *SEAHOG* uses a vectored thruster propeller arrangement to generate its control forces. These forces need to be automatically balanced between the four horizontal thrusters for ease of operation in response to desired operator inputs. Therefore a controller that can perform automatic control functions would be advantageous.

While there are controllers that exist that can successfully control an ROV "model-free", a dynamic model of the ROV is desirable to carry out other control research using simulation techniques such as vision based control. Therefore, a mathematical dynamic model of the *SEAHOG* should be developed.

The model will aid in the design of controllers for a variety of functions such as automatic depth and orientation holding and ultimately position holding and autopilot. It will also aid in improving the ease of control of the ROV by allowing thrust balancing for simple user inputs such as forward, reverse and sideways movements.

It is proposed that a dynamic mathematical model for the *SEAHOG* will be developed as part of this project along with the design of a controller to aid in thrust balancing for simple user inputs such as forward and sideways motions; along with functions such as automatic depth and heading holding.

As part of the ongoing development of the *SEAHOG* ROV, this project will include various design elements that contribute to the mechanical and electrical structure of the ROV as a result of recommendations from previous projects. These tasks include redesigning the Junction Box, connecting the tether, upgrading the power pod cooling systems and overhauling the graphical user interface and user control software of the ROV.

Abstract

A preliminary mathematical model for the UCT *SEAHOG* Remotely operated underwater vehicle (ROV) is developed, including estimation of the rigid body, hydrodynamic and hydrostatic properties of the robot. A single state thruster model is developed and verified according to real life test data. A closed-loop speed controller is developed for the thruster module using a standard PI scheme and is implemented on an MSP430 microcontroller using software fixed-point algorithms. The complete ROV system is simulated in Simulink® in an open-loop configuration to gain insight into the expected motion from the vehicle. Controllers for depth and heading holding are designed using standard PID linearized control methods with gain scheduling and are then assessed within the complete system in a simulation environment.

In addition, upgrades and maintenance are performed on the Power Pod, light and camera modules. Redesign, manufacture and testing of the *SEAHOG* junction box is performed, including a design solution to connect the tether power and fibre-optic lines at the surface and on the ROV. An extensive overhaul of the *SEAHOG* GUI is performed, utilising multicore processing architecture in LabVIEW and resulting in a user-orientated interface capable of controlling and monitoring all existing system data from the robot.

Summary

Introduction to the *SEAHOG* ROV

The *SEAHOG* remotely operated underwater vehicle (ROV) is a general class ROV that has a mass of approximately 80 kg, dimensions of 910 mm x 510 mm x 655 mm and was commissioned for the purposes of marine research. The platform includes a forward and rear camera, lighting and available space for navigational and environmental sensors. An exploded view of the *SEAHOG* is given following in Figure A.

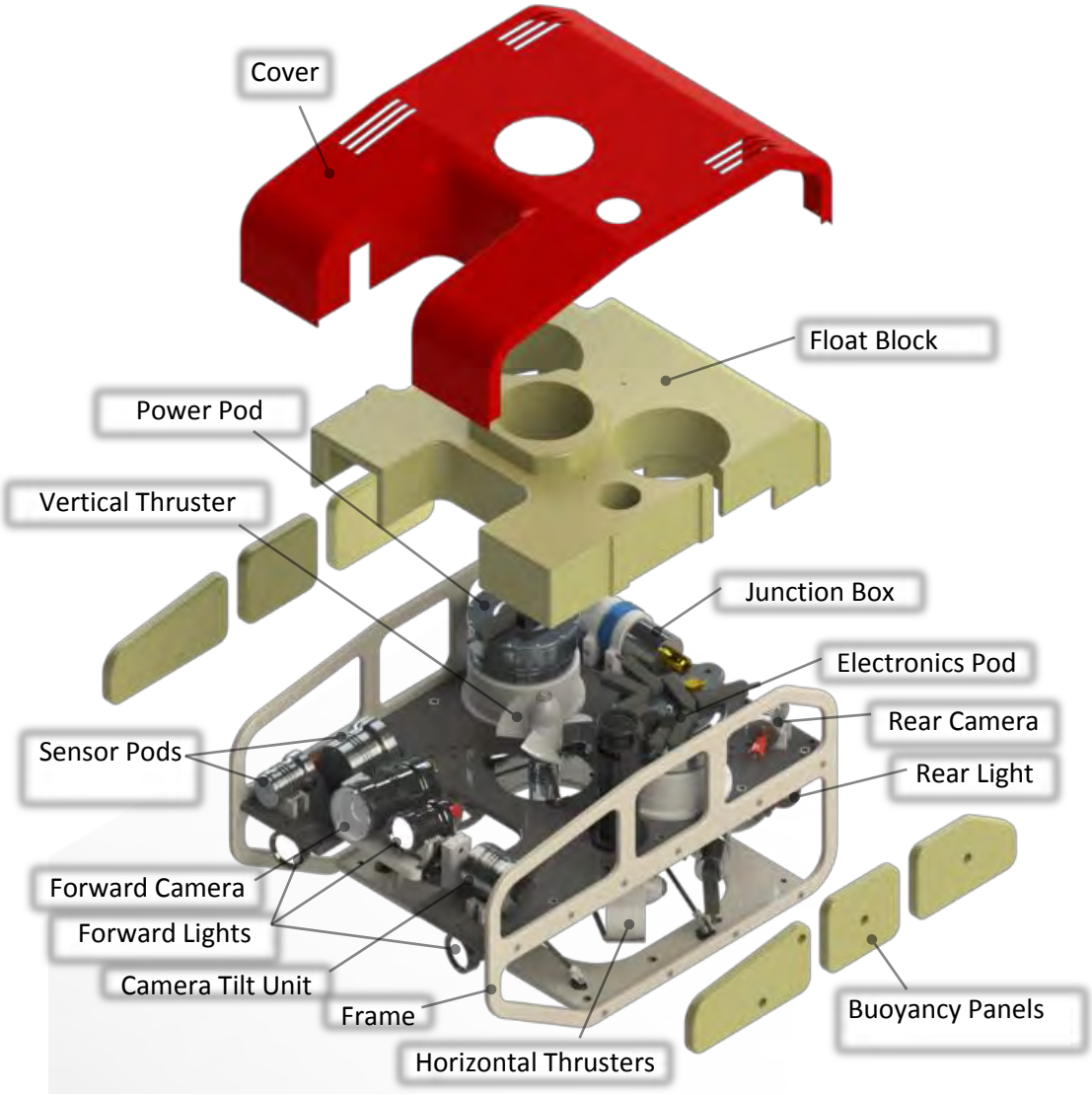

Figure A – Exploded view of the *SEAHOG* ROV with labelled modules and components

The *SEAHOG* has five thruster modules: one vertically orientated and four horizontally orientated in a vectored thrust arrangement. The *SEAHOG* is capable of executing translational motion along all three axes, as well as rotational motion about its vertical axis.

Project Introduction

In order to aid in navigation, dynamic positioning and precision ROV operations, a degree of autonomy is desirable from the *SEAHOG*. This project was the first step towards equipping the *SEAHOG* with automatic control functionality.

The purpose of this project was to model the *SEAHOG* ROV dynamic system and create a basic simulation framework on which could be improved in the future and that could be used to investigate underwater control and robotics problems using the *SEAHOG* ROV platform. Modelled elements of the overall ROV system included the following:

- Thruster Model
    - Propeller thrust
    - Motor and drive train
    - Control electronics
    - Software propeller speed controller
- ROV Model
    - Rigid body mass and inertia
    - Added mass and inertia
    - Hydrodynamic damping forces
    - Hydrostatic restoring forces
    - Thrust mapping
    - Provision for externally applied forces such as currents
- Control Electronics and Sensors
    - Proposal of control computation hardware
    - Pressure transducer
        - Sensor model
        - Mapping of sensor position to actual sensed depth
        - Estimation of actual depth according to sensed depth
    - Proposal of AHRS
- Controllers
    - Classical linear PD structure with adaptive elements for heading holding
    - Classical linear PID structure with adaptive elements for depth holding

The incomplete structural state of the *SEAHOG* at the time of this project prevented the verification of several model aspects, however, advanced CAD techniques were employed to provide as accurate an approximation of the real system as possible. The resulting model was well poised for verification and future improvements.

SEAHOG Dynamic Model

The general dynamic equation governing the motion of an ROV is given as:

$$\boldsymbol{M\dot{\nu} + C(\nu)\nu + D(\nu)\nu + g(\eta) = \tau + w}$$

with:

$\boldsymbol{M}$ - System mass and inertia matrix including added mass and inertia terms

$\boldsymbol{C(\nu)}$ - Coriolis centripetal matrix included added mass and inertia terms

$\boldsymbol{D(\nu)}$ - Damping matrix

$\boldsymbol{g(\eta)}$ - Restoring forces (gravitational/buoyancy forces and moments)

$\boldsymbol{\tau}$ - Control inputs

$\boldsymbol{w}$ - Wind, waves and currents environmental disturbances

The way in which each of the above elements were determined for the *SEAHOG* in this project are given following.

Mass and Inertia Properties:

The mass and inertia of an ROV comprises of a rigid-body component and an added mass component. The rigid-body component is related to the physical mass of the ROV and the added mass is a means to describe the pressure induced forces that are related to a body accelerating a fluid as it moves through it.

Solidworks CAD tools were used to estimate the rigid-body mass and inertia of the ROV.

Advanced computational tools were not available for determining the added mass and inertia properties, therefore a series of approximations using empirical data needed to be used. The *SEAHOG* hull was approximated as a rectangular prism and the average of several empirical data methods were used to determine the added mass components. It was necessary to use an average of several empirical methods due to how each method was somewhat ill-suited to the *SEAHOG* geometry. The added inertia was approximated using empirical data and by enforcing slender-body theory on the *SEAHOG*. Once again, an average was taken due to how the approximation methods were somewhat ill-suited to the geometry of the *SEAHOG* hull.

Hydrodynamic Damping Properties:

The hydrodynamic damping of an ROV body is typically comprised of a linear and a quadratic damping matrix, with the former dominating at low speeds and the latter dominating at high speeds. Solidworks Flow Simulation software was used to obtain approximations of the damping characteristics of the ROV. A thorough investigation into the CFD software was conducted so as to obtain an idea of the possible

shortfalls and inaccuracies that could occur due to the software. It was concluded however, that the software was sufficient to provide a preliminary baseline for the damping properties of the *SEAHOG*.

Due to the non-symmetrical *SEAHOG* hull, the damping properties were applied as a single matrix with varying elements instead of separate linear and quadratic damping coefficients. The damping matrix that was implemented consisted of varying elements that derived their values according to fit curves that were created from the drag simulation results.

Restoring Moments (Gravitational and Buoyancy Forces):

The restoring forces and moments on an ROV body serve to maintain the body's hydrostatic stability and are related to the magnitude of the gravity and buoyancy forces acting on the body and the centres through which they act. The *SEAHOG* employs a passive buoyancy system whereby the hydrostatic design serves to passively minimise angles of pitch and roll.

The gravity force acting on the *SEAHOG* was determined using Solidworks, using the mass properties of the CAD model. The buoyancy force was also found using Solidworks by manipulating the CAD model to represent the volume of water that was displaced by the ROV. In addition, the centre of gravity and centre of buoyancy were both found using Solidworks.

Environmental Disturbances:

Environmental disturbances were not tackled as part of this project but their inclusion as part of future work was catered for in the model.

Control Inputs:

The control inputs came from five rigidly mounted thrusters on the *SEAHOG*. The mapping from individual axial thrust forces to the body-fixed thrust was derived using the geometric layout of the thrusters. In addition, a thrust allocation scheme was derived, whereby each thruster speed input was determined according to the desired thrust force and moment vector.

The force in the body-fixed x and y directions was defined by an operator input and the thrust force and moment for the z and yaw directions were defined according to controller outputs.

Thruster Model and Propeller Speed Controller

The thrusters on the *SEAHOG* consist of a propeller that is magnetically coupled to a brushless DC motor housed within an air filled pressure housing. The brushless motor is controlled by a Maxon motor controller board, which receives signals from a custom designed electronics board. Modelling of the thruster subsystem was a significant part of the project as it was fully verified by experimental results. The elements that form part of the thruster module and that were subsequently modelled are: the propeller, the motor and drivetrain, the Maxon motor controller and the control electronics. Each of these elements is shown following in Figure B.

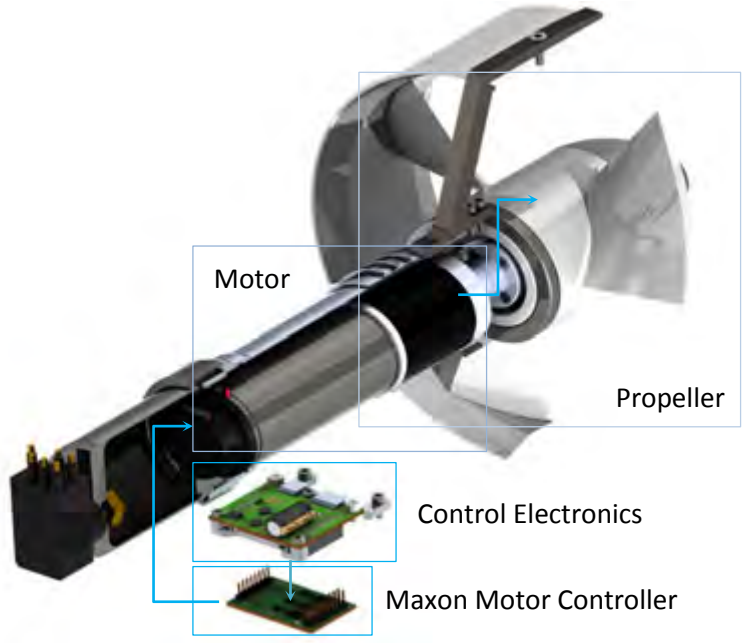

Figure B – Sectioned thruster module, with modelled elements shown

Propeller Model:

The propeller model was chosen as a one state thruster model, whereby the state equations are described as:

$$\dot{\Omega} = \beta\tau - \alpha\Omega|\Omega|$$

$$T = C_t\Omega|\Omega|$$

Thruster constants β, α and C_t were experimentally determined in tank tests by logging the torque input (τ) and the propeller speed (Ω). It is well known that a single state propeller model is only adequate at describing the thrust output from a stationary thruster running the propeller in steady state conditions, due to the effect of the advance speed on the thrust output. However, since it was possible to fully verify the single state model, it was deemed to be a sufficient starting point in the thruster model's development.

Motor and Drivetrain:

The Maxon brushless motor used to actuate the propeller was modelled according to data provided with the motor. Motor friction characteristics were derived mathematically according to given load and current characteristics in the motor datasheet. A constant efficiency factor was used for the motor gearbox and the magnetic coupling efficiency was determined using experimental data.

Maxon Motor Controller:

The Maxon power amplifier handles the hardware level control of the brushless motor as well as applying software algorithms to control the speed of the motor. The controller receives an analogue voltage and converts it to a desired motor speed.

There was limited information on the digital control algorithms implemented on the controller, making it a challenging component to model. It was approximated as a linear PI controller with different gains for accelerating and decelerating the motor. In addition, it was established that the controller limited the acceleration of the motor so as to prevent damage to components.

Finally, the Maxon controller was observed to not accurately represent the desired speed sent to it from the custom control electronics board. There were various reasons identified for this, however the speed offset was modelled as a non-unity sensor gain.

The thruster system was evaluated so that the similarity between the model and real life response was deemed to be sufficient. Figure C following shows the simulated and real life speed response of the thruster to a sequence of step inputs.

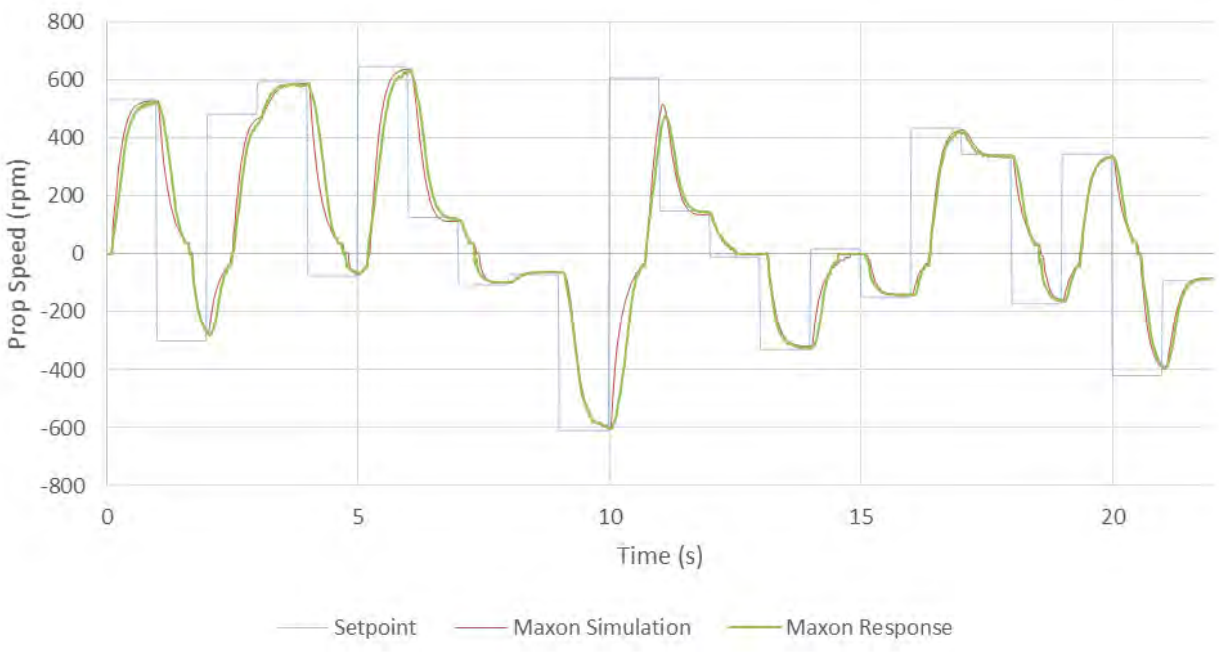

Figure C – Thruster real life and simulated response to series of step inputs

Propeller Speed Controller:

The MSP430 microcontrollers on the custom designed electronics board were utilised to correct the steady state speed offset observed when using the Maxon motor controller. A classical linear PI controller was implemented digitally on the MSP430. Implementing the digital control algorithms on a microcontroller using software defined fixed-point arithmetic proved to be challenging and hence the simple PI control design was deemed sufficient.

The controller succeeded at drastically reducing the speed offset of the Maxon controller but sacrificed the response speed slightly and introduced slightly more apparent noise into the system. The simulation and real life propeller speed responses were seen to differ more significantly than before in just the Maxon controller case. It was suspected that the data manipulation in the microcontroller was responsible for the model and real life response discrepancies.

The controller was deemed to have successfully met its design criteria due to its successful setpoint tracking behaviour and since the small drop in controller speed did not seem significant in the context of the greater ROV system. Figure D following shows the simulated and real life speed response of the thruster under the influence of the designed software controller to a sequence of step inputs.

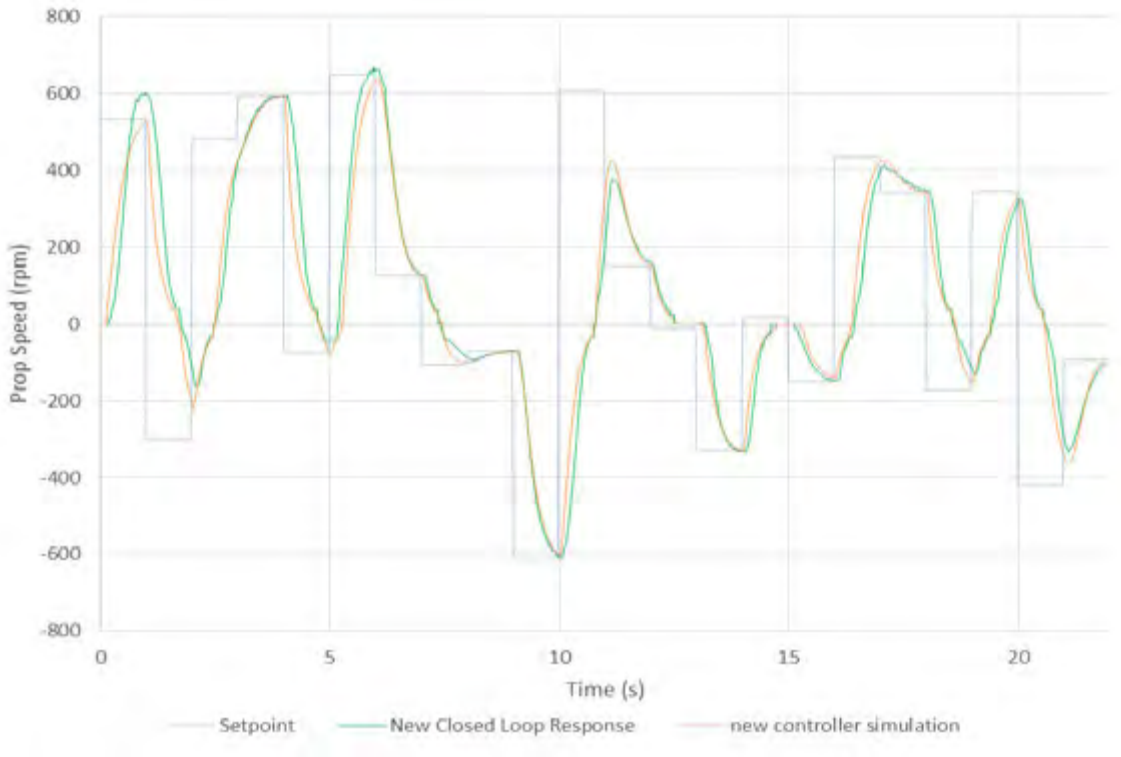

Figure D – Thruster real life and simulated response to series of step inputs under influence of designed software controller

ROV Heading and Depth Controller Designs

This project, while having a focus on system modelling, provided a baseline heading and depth controller for the *SEAHOG*. It was envisaged that future controllers could improve upon the work completed in this project, with an understanding that the control methodologies chosen in this project are not well suited to the underwater environment.

Open-loop simulations were conducted to establish that motion purely in heave and yaw did not affect other motion on the ROV significantly and was therefore considered decoupled for the purpose of designing a depth and heading controller. The controllers were therefore designed in their respective decoupled single degree of freedom dynamic systems.

Depth Controller:

The depth controller was designed using a classical linear PID structure. The controller also had adaptive elements such as gain scheduling and feed forward compensation and was designed to condition each input as a step that had a predetermined gain associated with it. The feed forward and integrator element in the controller was necessary due to the bias inherent in the ROV plant due to the non-zero buoyancy force.

The resulting controller response was reasonably uniform across different step sizes. In addition, continuous inputs such as sine waves were tracked successfully, however no controller gain adaptation was applied during the tracking of continuous inputs, limiting its capabilities.

Heading Controller:

The heading controller was designed using a classical PD structure in the form of a controller gain and dominant lead compensator. Once a stable design had been achieved, gain scheduling was employed to achieve a uniform response across different step sizes.

A reasonably linear response for different step sizes was achieved with successful tracking of continuous inputs like sine waves. A discontinuous control law was required due to the speed deadband of the thrusters. The discontinuous control law was designed so that the ROV would settle within 0.2˚ of the setpoint.

Both controller designs were shown to perform effectively in their decoupled and isolated dynamic models. A reasonably consistent response was achieved by both of them regardless of the nonlinear dynamics present in the system. It was necessary however to test them within the complete dynamic ROV system and assess them according to some typical ROV manoeuvres.

Complete System Simulation Evaluation

Both controllers performed as designed within the whole ROV system simulation. Figure E following shows the ROV executing depth and heading holding manoeuvres in the absence of other inputs and external disturbances.

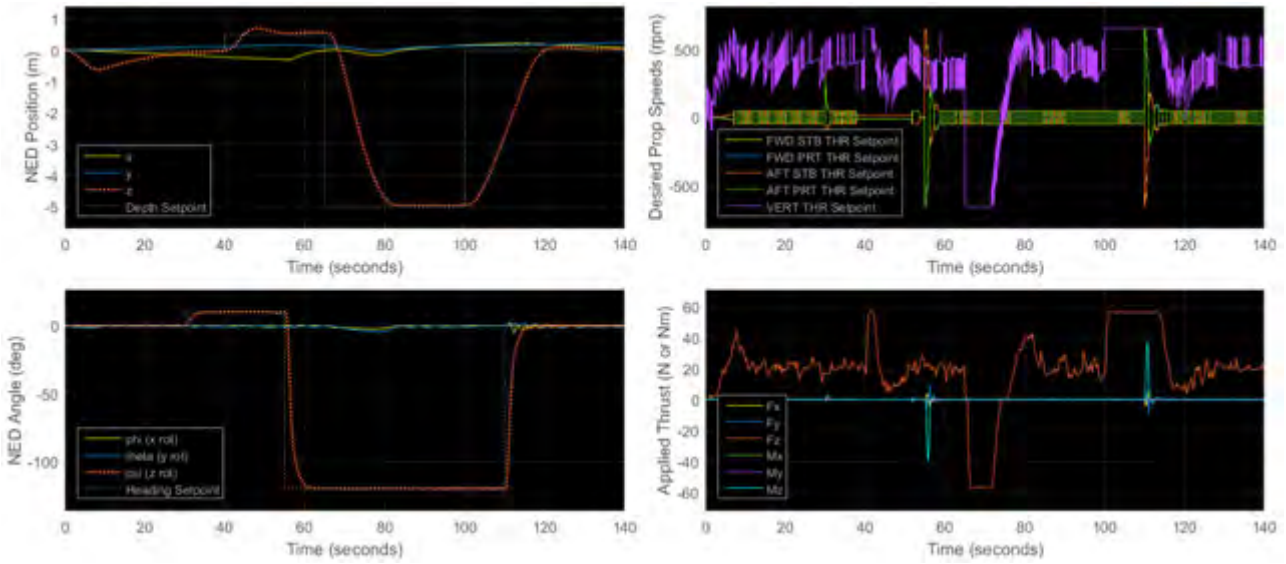

Figure E – *SEAHOG* executing depth and heading holding manoeuvres only

In general, the controllers' performances were degraded in the presence of horizontal user input thrusts in surge and sway. In addition, the attitude of the ROV had a significant effect on the performance of the controllers. As seen following in Figure F, oscillations of the pitch and roll of the ROV (induced due to the thrust in surge, shown in the bottom right of the figure as Fx) result in the depth controller and heading controller oscillating about their setpoints.

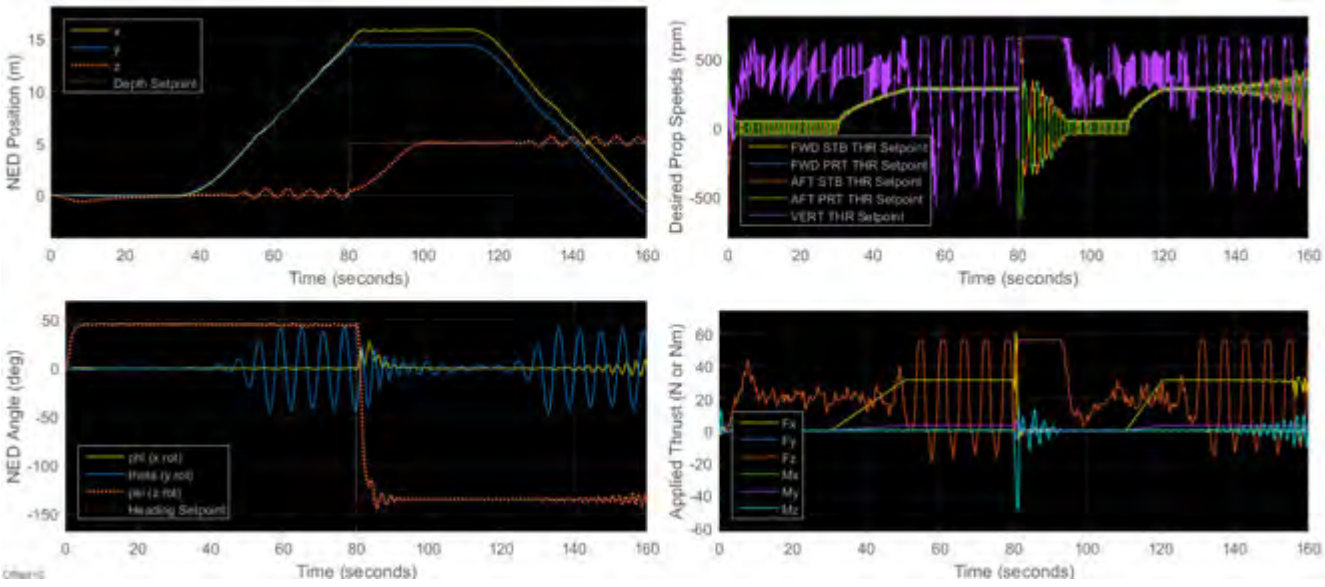

Figure F – *SEAHOG* executing depth and heading holding manoeuvres in the presence of thrust in surge

It was concluded that the attitude of the ROV had the largest effect on degrading the depth controller's performance and that torques induced from motion coupling had the largest effect on degrading the heading controller's performance.

Conclusions and Recommendations

Depth and Heading Controllers:

The controllers did not display unstable behaviour throughout a variety of operating scenarios. Their performance was adequate in the absence of disturbances or horizontal operator thrust inputs. The attitude of the ROV and torques induced by motion coupling were shown to significantly degrade the performance of the controllers. It was deemed however, that a sufficient heading and depth controller design had been created as a baseline on which future work could improve.

SEAHOG Model:

Advanced CAD techniques were used where possible to approximate different aspects of the *SEAHOG* due to the incomplete state of the robot. Very little verification was performed on the ROV properties due to its incomplete state, however, care was taken using CAD tools to provide a baseline for verification and improvements to the model in the future.

Thruster Model and Speed Controller:

The thruster model was adequately approximated with some discrepancy between the model and the real life response. The discrepancies were attributed to the limited data handling capabilities of the control microcontroller. However, it was deemed that the controller was sufficient since it provided good setpoint tracking. The reduced speed of the response after implementing the software controller design was found to not be a significant factor due to the significantly slower dynamics of the *SEAHOG* itself.

Recommendations:

Various verification recommendations were made, especially for verification of the added mass and hydrodynamic damping properties of the robot as these were found to have a significant effect on the simulated behaviour of the ROV.

It was recommended that a more advanced thruster model should be developed and that verification should be performed on the transient conditions of propeller speed vs. thrust produced, since only the steady state thrust vs. propeller speed was verified in this report.

An obvious recommendation was for the continued development of the *SEAHOG* itself and the installation of control computing hardware on-board the robot. It was shown that increasing the righting moment arm of the ROV would serve to provide greater stability and aid in ROV manoeuvrability. However it was recommended that better approximations to the model parameters should be made before mechanical modifications are made to the mechanical ROV structure.

Finally, it was concluded that a sufficient initial model had been created for the *SEAHOG* ROV that could be improved upon in the future – both in the model parameters and the controllers designed for it.

Plagiarism Declaration

I, Maximillian Finbow, hereby declare that the work on which this Dissertation is based is my original work (except where acknowledgments indicate otherwise) and that neither the whole work nor part of it has been, is being, or is to be submitted for another degree in this or any other university. I authorise the University to reproduce for the purpose of research either the whole or any portion of the contents in any manner whatsoever.

All significant contributions and contributions in this document that are sourced from the work, or works, of other people has been attributed, cited and referenced using the IEEE 2006 Reference standard.

Maximillian Finbow,

University of Cape Town, 23 March 2016

Acknowledgements

While the completion of this dissertation was greatly enriching personally, professionally and technically, I acknowledge the privileged position I was in for it to be possible. I am humbled by the fact that a variety of circumstances prevent many who desire to undertake post-graduate studies from being able to pursue them. As a white male I am particularly humbled by the support I have received that could well have been appropriated to someone less advantaged than myself. Therefore I would like to sincerely acknowledge and thank the following parties for granting and assisting me in this unique opportunity:

The University of Cape Town through the Reino Stegen Scholarship for contributing to funding my studies in my first year.

The National Research Foundation (NRF) for financial assistance in my second year of studies through the Scarce Skills Master's Scholarship.

My supervisor, Hennie Mouton, who has graciously supported me throughout my project and provided me with valuable inputs.

My family, especially my parents, for their unwavering and continued support and belief in me, without which I would have had to forgo many of the opportunities granted to me.

Timothy Hope, for providing hours of entertainment and experienced engineering advice. It was a pleasure serving on the *SEAHOG* team with you!

The rest of the RARL team, for cricket breaks and a thoroughly enjoyable two years in the lab.

Pierre Smith in the workshop, whom I have always enjoyed working with and have appreciated the experience he offers and his advice on all of my mechanical designs.

My girlfriend Faye, for her instrumental support throughout my project, keeping me grounded and enjoying life outside of academics with me.

Table of Contents

Table of Figures

List of Tables

List of Symbols

General Symbols

η - Efficiency
ρ - Density of fresh water
g - Gravitational acceleration constant

Thruster Model

Ω - Propeller velocity
T - Thrust
τ - Input torque to propeller
C_t , β , α - Thruster model constants

Controller Designs

K_i - Integral controller gain
K_p - Proportional controller gain
K_d - Derivative controller gain
$u(s)$ - Controller output
$e(s)$ - Error between setpoint and feedback

Sensor Modelling

z - Depth
P - Pressure
$\boldsymbol{r_{Od}}$ - Vector from origin to sensor position

ROV Model

$\boldsymbol{p}^i = \begin{bmatrix} x \\ y \\ z \end{bmatrix} \epsilon \mathbb{R}^3$ - Inertial position

$\boldsymbol{\Theta} = \begin{bmatrix} \phi \\ \theta \\ \psi \end{bmatrix} \epsilon \mathbb{R}^3$ - Attitude (Euler angles)

$\boldsymbol{v}_O^b = \begin{bmatrix} u \\ v \\ w \end{bmatrix} \epsilon \mathbb{R}^3$ - Body-fixed linear vel.

$\boldsymbol{\omega}_{ib}^b = \begin{bmatrix} p \\ q \\ r \end{bmatrix} \epsilon \mathbb{R}^3$ - Body-fixed angular vel.

$\boldsymbol{f}_O^b = \begin{bmatrix} X \\ Y \\ Z \end{bmatrix} \epsilon \mathbb{R}^3$ - Body-fixed forces

$\mathbf{m}_O^b = \begin{bmatrix} K \\ M \\ N \end{bmatrix} \epsilon \mathbb{R}^3$ - Body-fixed moments

$\boldsymbol{\eta} = \begin{bmatrix} \boldsymbol{p}^i \\ \boldsymbol{\Theta} \end{bmatrix} \epsilon \mathbb{R}^6$ - Global position

$\boldsymbol{\nu} = \begin{bmatrix} \boldsymbol{v}_O^b \\ \boldsymbol{\omega}_{ib}^b \end{bmatrix} \epsilon \mathbb{R}^6$ - Body-fixed velocity

$\boldsymbol{\tau} = \begin{bmatrix} \boldsymbol{f}_O^b \\ \boldsymbol{m}_O^b \end{bmatrix} \epsilon \mathbb{R}^6$ - Body-fixed applied forces and moments

$\boldsymbol{r_g}$, $\boldsymbol{r_b}$ - Vector from origin to centre of gravity / centre of buoyancy

H , B , L - Height, breadth and length of the *SEAHOG*

$\boldsymbol{B}$ - Thrust mapping matrix
$\boldsymbol{M}$ - Mass and Inertia Matrix
$\boldsymbol{C(\nu)}$ - Coriolis matrix
$\boldsymbol{D(\nu)}$ - Damping matrix
$\boldsymbol{g(\eta)}$ - Restoring forces and moments

Glossary

BLDC	Brushless Direct Current (Motor)
BODY	Body-Fixed Reference Frame
CAD	Computer Aided Design
CB	Centre of Buoyancy
CFD	Computational Fluid Dynamics
CG	Centre of Gravity
DAC	Digital to Analogue Converter
DAQ	Data Acquisition
EKF	Extended Kalman Filter
FPU	Floating Point Unit
GUI	Graphical User Interface
MEMS	Micro Electro-Mechanical System
NED	North-East-Down Co-ordinate System
NEU	North-East-Up Co-ordinate System
O	Origin
PI	Proportional Integral
PWM	Pulse-Width Modulation
RANS	Reynolds-Averaged Navier-Stokes
RARL	Robotics and Agents Research Laboratory
ROV	Remotely Operated Vehicle
RS485	Recommended Standard 485
SMC	Sliding Mode Control
SNAME	Society of Naval Architects and Marine Engineers
SPI	Serial Peripheral Interface
SST	Shear-Stress-Transport
UCT	University of Cape Town

Chapter 1 - Introduction

1.1 Remotely Operated Underwater Vehicles

A Remotely Operated underwater Vehicle (ROV) system typically consists of a submersible that is attached via a cable, called a tether, to a human-operated control console located at the surface. Figure 1 below depicts these main elements, which are found in all ROV systems, for clarity.

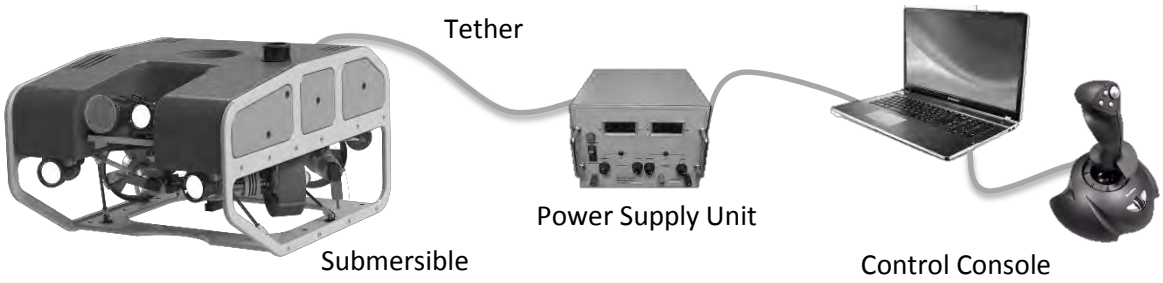

Figure 1 - Essential ROV system elements

The tether supplies the submersible with power and communication signals and can contain multiple copper and fibre-optic cores.

ROVs are versatile platforms that span a range of applications and sizes. Some of the areas in which ROVs are used are [1]:

- The oil and gas industry for locating hydro-carbon fuels in ocean beds as well as the inspection and maintenance of oil rigs and equipment.
- The mining industry for underwater mining operations.
- The military in retrieving weapons, ships and aircraft lost to the ocean floor.
- Scientists and historians in acquiring valuable data and material from which studies can be conducted to establish the earth's history, existence and future.
- Marine biologists for sample collection at depth and for observation of underwater rehabilitation sites.

Observation class ROVs are usually the simplest ROVs and contain lighting and cameras for underwater observation. These ROVs typically have a mass below 75 kg and have depth ratings of less than 300 m [2].

General class ROVs are slightly bigger than observation class ROVs and may be able to carry small manipulator arms or mapping tools. They typically have a maximum working depth of less than 1000 m [3]. Work class and Heavy Work class ROVs are the largest of the ROVs and can be used for underwater mining or trenching and cable laying on the ocean floor at up to 3000 m [4]. Figure 2 below depicts a heavy work class, a general class and an observation class ROV at approximate sizes relative to each other to demonstrate the scale and variation of ROVs.

Figure 2 - The CBT800 trencher ROV from SMD designed to dig trenches and bury cables at depths of up to 3000 m [4] with the UCT *SEAHOG* and the VideoRay Pro observation class ROV pictured at the bottom left

Now that the concepts and applications of ROVs have been introduced, the UCT *SEAHOG* ROV can be detailed specifically.

1.2 The UCT *SEAHOG* ROV

The *SEAHOG* was commissioned by the department of Biological Sciences at the University of Cape Town (UCT) in 2009. The department desired an underwater robot to be developed that could assist them in a number of tasks such as the observation of underwater mining rehabilitation zones, equipment recovery and biological sample taking.

Currently the *SEAHOG* is the 3rd generation of General class ROVs developed at the Robotics and Agents Research Laboratory (RARL) at UCT and is a culmination of the experienced gained from two previous ROV iterations. More information on the development of ROVs at RARL can be found in [5]. A rendering of the *SEAHOG* is shown below in Figure 3.

Figure 3 - Rendering of the *SEAHOG* ROV

Current characteristics and components of the *SEAHOG* are:

- Mass of approximately 80 kg
- Dimensions: length 910 mm x height 510 mm x width 655 mm
- 300 m designed operational depth (tested to 450 m)
- 4 Vectored horizontal thrusters (propellers) for movement in the horizontal plane
- 1 vertical thruster
- Forward facing camera for live video feedback
- Tilt mechanism to control camera pitch
- Rear facing camera for live video feedback and tether monitoring
- Sonar unit
- Three forward and one rear facing variable brightness lights

- Available space for environmental and motion sensors

During this report, the dynamic modelling of the *SEAHOG* will be undertaken and thus more detail of its various subsystems will be given and discussed later on. To give an overview of the subsystems and names of modules on the robot however, a labelled exploded view is given following in Figure 4 below. Names of subsystems used throughout this report will be kept consistent with the figure.

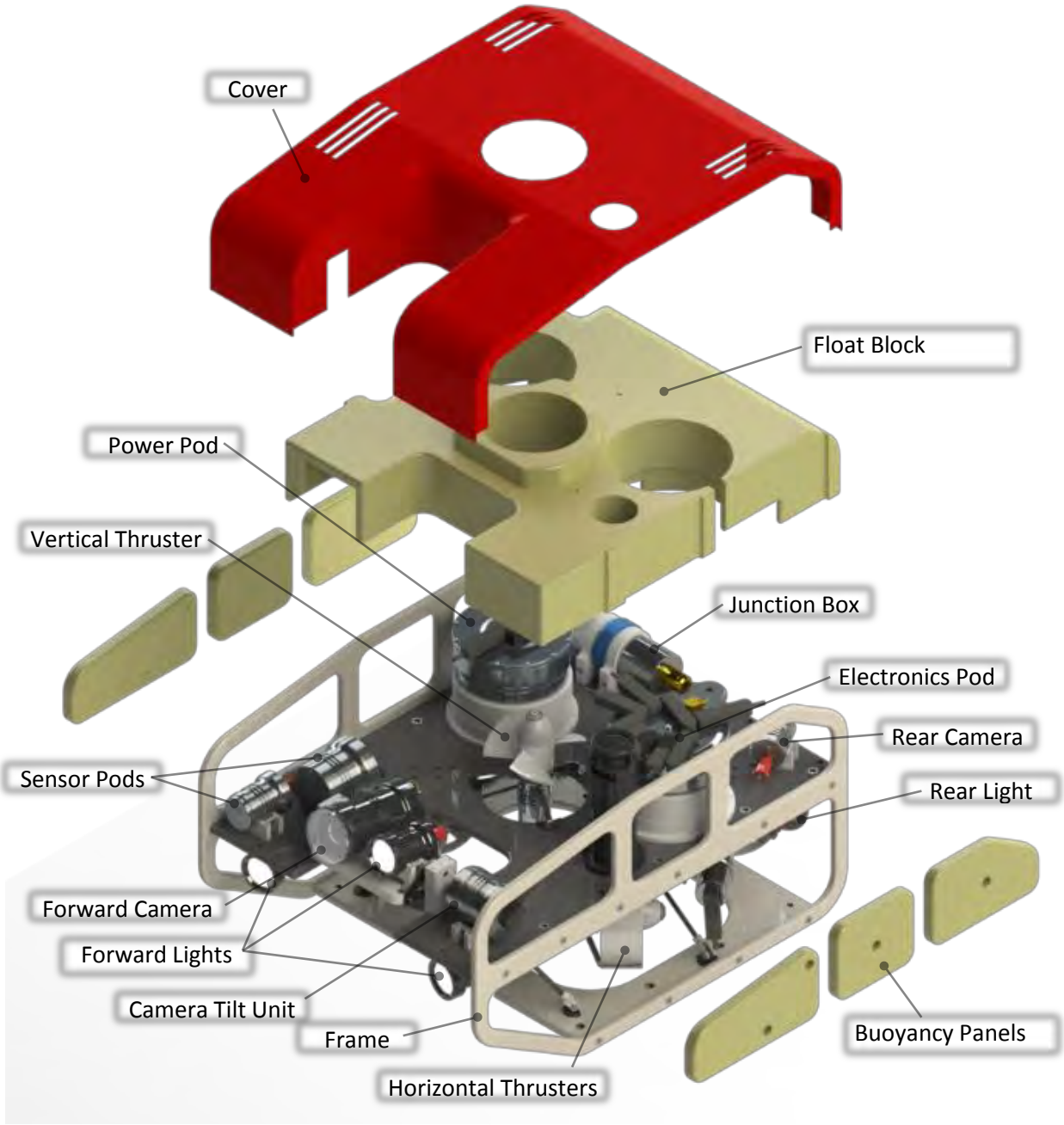

Figure 4 - Exploded view of the *SEAHOG* with major components labelled

The *SEAHOG* is an under-actuated system that uses a total of five thrusters to control a total of four degrees of freedom (DOFs): three translational axes and one rotational axis. This will be expanded upon later in this report. The orientations of the five thrusters and the directions of thrust that are achievable from them are shown following in Figure 5.

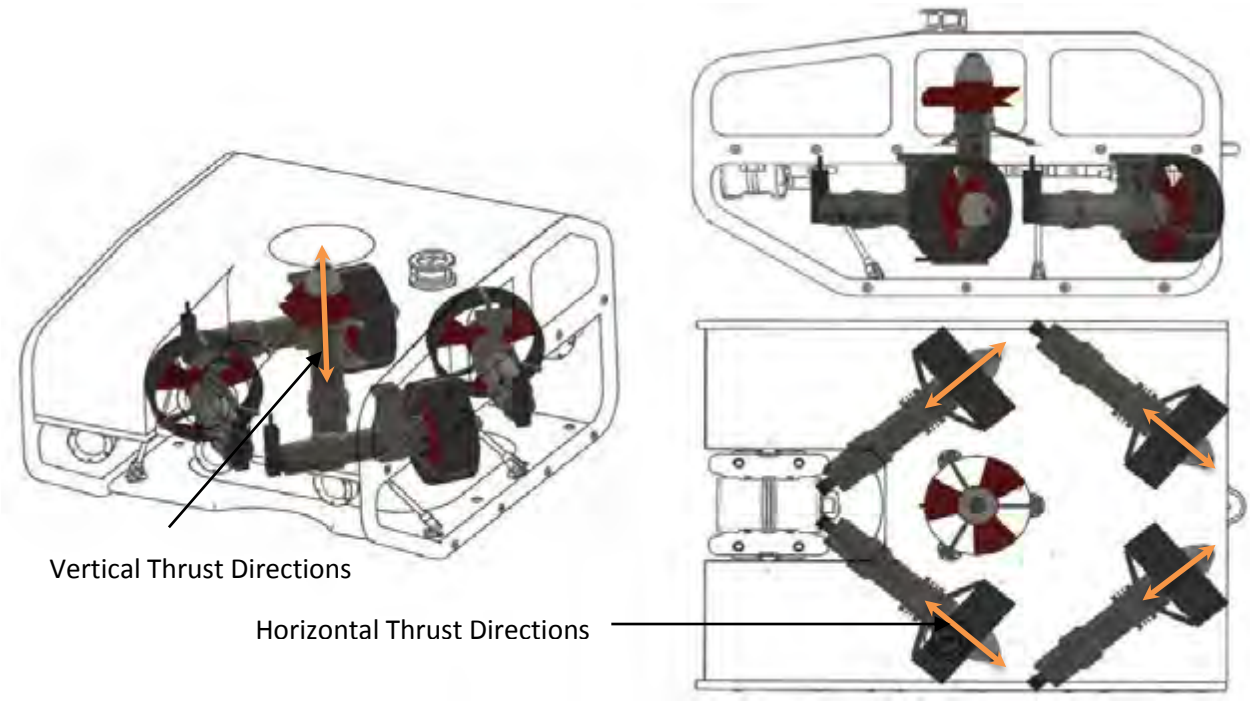

Figure 5 - Thruster module layout with achievable thrust directions shown

Now that the *SEAHOG* ROV has been introduced, this project can be put into the context of the ongoing development of the *SEAHOG* and highlight aspects that motivate its undertaking.

1.3 Motivation and Background for Project

Three previous Master's projects on the *SEAHOG* had provided a robust and reliable mechanical and electrical backbone for the ROV at the time of this project's inception. The ROV was mostly complete apart from a few subsystems, namely: the float block and buoyancy panels, the camera tilt unit and the ROV cover. These were expected to be completed as part of an existing Master's project and thus the next phase of *SEAHOG* development was naturally the communications and control aspects of the robot.

Standard data communication protocols had been established early in the *SEAHOG*'s development, which allowed subsystems and modules with their own intelligence to be developed independently of the master control system of the robot. This meant that most of the systems that were prerequisite to installing a controller (such as the power and communications network and system monitoring sensors) were already present. While each subsystem in turn had been tested and holistically developed, little work had been given to the control of the whole robot and no software had been developed for it for more than testing purposes. There was thus a need for this stage of development to be tackled in a Master's project.

In addition, it was envisaged that a dynamic mathematical model of the system would serve to benefit future control research conducted on the ROV. Thus, development of a dynamic mathematical model became a focal point of the project.

1.4 Project Scope and Plan of Development

Due to this project being a small part of the larger ongoing *SEAHOG* project, the scope of this project encompassed aspects outside of the control and system modelling focus of the project. However, focus will be given to the aspects that were mentioned specifically in the project's motivation in the min section of the report. A list of deliverables and outcomes that have been identified as the primary goals for this project are given below:

- Dynamic mathematical model of the *SEAHOG* ROV including:
    - Thruster characterisation
    - Buoyancy and mass characterisation
    - Drag characterisation
    - Provision for underwater current effects
    - Orientation and depth sensor models
- Thrust allocation scheme for operator inputs and basic control designs for:
    - Forward, sideways and rotation thrust balancing between vectored thrusters
    - Heading holding
    - Depth holding

The control design above will be designed and assessed in the form of simulations and will serve to provide a baseline upon which future projects can test the *SEAHOG* when it has been structurally completed.

It is inevitable that in a large scale project such as the *SEAHOG*, aspects that have not been covered in previous projects but are essential to the completion of the ROV have been overlooked. Thus, some tasks that are not a primary output of the project but are essential to the ongoing development of the *SEAHOG* have been added as appendices to this report. Tasks provided in the appendices serve mostly as a reference for those continuing the development of the *SEAHOG* but nonetheless form part of the work completed in this project. The tasks and deliverables completed as auxiliary work in this project are:

- Design, manufacture and testing of a new Junction Box
- Upgrades to Power Pod cooling systems
- Upgrades to light and camera modules
- Development of a graphical user interface (GUI) for user control and operation of the ROV

Details of the auxiliary tasks completed in this project are detailed in Appendix B – ROV Upgrades and Maintenance.

Background research that supplements the work conducted in this report will be presented as part of each section where necessary. However, in-depth background research was undertaken so as to supplement

some sections in this report. Work and theory presented in the main section of this report has been deemed the most pertinent of a larger body of research conducted and presented in Appendix A – Literature Review. The literature review should be consulted to gain a broader understanding of the information presented in this report and, where applicable, gain insight into design decisions made in this report.

With an overview of the field of ROVs, the specific ROV platform and the goals of this project given, the report will go on to describing the development of the *SEAHOG* dynamic mathematical model. The kinematics and dynamics of underwater vehicles in general will firstly be described. The thruster dynamic model will then be focussed on, after which the complete model of the ROV will be developed. Once this is complete, control schemes and simulations will be developed and the results presented from complete system simulations will be presented. The report will conclude with recommendations for future work in areas such as model, hardware and controller development.

Chapter 2 - Kinematics and Dynamics of Underwater Vehicles

2.1 Introduction

Kinematics refers to a description of the motion of a body and dynamics refers to the effect of forces on that body. This chapter will serve to describe the kinematics and dynamics of underwater vehicles. The equations and relationships developed in this chapter will be used later in the report when the *SEAHOG* dynamic model is being developed. The nomenclature for describing the motion of marine vehicles was defined by the Society of Naval Architects and Marine Engineers (SNAME) [6] and will be used throughout this report.

2.2 Axes Definitions and Reference Frames

Motions in each of the six degrees of freedom, in the context of marine vehicles, are known as the following: surge, sway, heave, roll, pitch and yaw [6]. These are described below in Figure 6 according to their definitions in the body bound reference frame (BODY or b-frame).

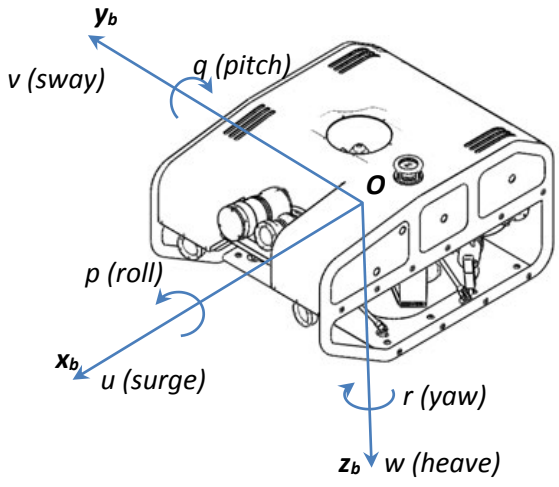

Figure 6 - Definition of motion in six axes for a marine vessel [6]

Nomenclature for the associated positions, velocities and forces acting on a body along a certain axis are presented below in Table 1.

Table 1 - SNAME notation of forces, velocities and positions for marine vessels [6]

DOF	associated body-fixed axis	forces and moments	linear and angular velocities	positions and euler angles
1	x_b – linear	X	u	x
2	y_b – linear	Y	v	y
3	z_b – linear	Z	w	z
4	x_b – rotational	K	p	Φ
5	y_b – rotational	M	q	Θ
6	z_b – rotational	N	r	ψ

In this report, the kinematics associated with the body-fixed ROV reference frame described previously in Figure 6 will be evaluated relative to the inertial North-East-Down co-ordinate system. The North-East-Down co-ordinate system (NED or n-frame) is denoted as: $[x_n, y_n, z_n]^T$ and is defined relative to the Earth's reference ellipsoid [7]. It is usually defined as the tangent plane on the surface of the Earth moving with the vessel, with the x-axis pointing towards true North, the y-axis pointing towards East and the z-axis pointing downwards normal to the Earth's surface [8]. Shown alongside in Figure 7 is the North-East-Up (NEU) co-ordinate system, which is the same as NED just with the down axis reversed. In addition, the figure shows how NED is related to lines of latitude and longitude through angles φ and λ respectively. For marine vessels operating in a local area - with approximately constant longitude and latitude - an Earth-fixed tangent plane on the surface is used for navigation and can be assumed to be inertial such that Newton's laws still apply [8]. Therefore, references to the n-frame, for simplicity sake, will be denoted as inertial using the co-ordinates: $[x_i, y_i, z_i]^T$ and have a local, arbitrarily defined origin with a globally defined orientation.

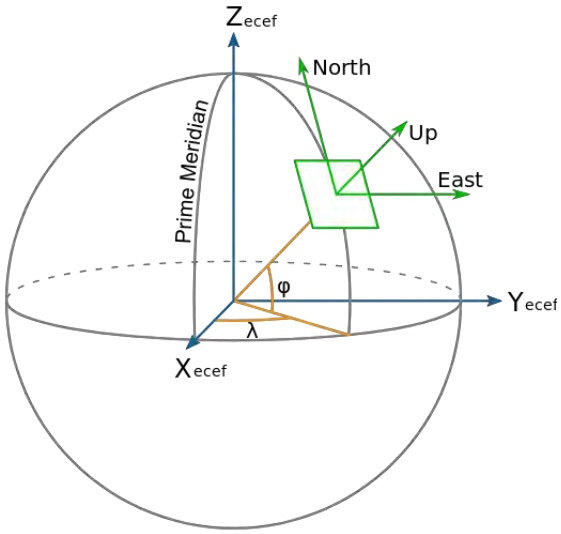

Figure 7 - Depiction of the North-East-Up (NEU) co-ordinate system

To describe the position, velocity and forces of the six DOF underwater system, six vectors of dimension three are required. Each individual vector is defined as follows:

Inertial position: $\boldsymbol{p}^i = \begin{bmatrix} x \\ y \\ z \end{bmatrix} \epsilon \mathbb{R}^3$ Attitude (Euler angles): $\boldsymbol{\Theta} = \begin{bmatrix} \phi \\ \theta \\ \psi \end{bmatrix} \epsilon \mathbb{R}^3$

Body-fixed linear velocity: $\boldsymbol{v}_O^b = \begin{bmatrix} u \\ v \\ w \end{bmatrix} \epsilon \mathbb{R}^3$ Body-fixed angular velocity: $\boldsymbol{\omega}_{ib}^b = \begin{bmatrix} p \\ q \\ r \end{bmatrix} \epsilon \mathbb{R}^3$

Body-fixed force: $\boldsymbol{f}_O^b = \begin{bmatrix} X \\ Y \\ Z \end{bmatrix} \epsilon \mathbb{R}^3$ Body-fixed moment: $\mathbf{m}_O^b = \begin{bmatrix} K \\ M \\ N \end{bmatrix} \epsilon \mathbb{R}^3$

where the notation $\boldsymbol{\omega}_{ib}^b$ represents the quantity **ω** of frame *b* relative to frame *i* (subscript) decomposed in frame *b* (superscript) and the notation $\boldsymbol{f}_O^b$ represents the quantity $\boldsymbol{f}$ of point *O* decomposed in frame *b*. For clarity, the above vectors can be compared to Table 1 shown previously to see how the vector quantities and parameters fit into the context of an underwater body, as defined in the table.

In summary then, we can describe the general motion of an underwater vehicle in six DOFs with respect to its n-frame position, b-frame velocity and b-frame force by the following vectors [8]:

$$\boldsymbol{\eta} = \begin{bmatrix} \boldsymbol{p}^i \\ \boldsymbol{\Theta} \end{bmatrix} \epsilon \mathbb{R}^6, \quad \boldsymbol{\nu} = \begin{bmatrix} \boldsymbol{v}_O^b \\ \boldsymbol{\omega}_{ib}^b \end{bmatrix} \epsilon \mathbb{R}^6, \quad \boldsymbol{\tau} = \begin{bmatrix} \boldsymbol{f}_O^b \\ \boldsymbol{m}_O^b \end{bmatrix} \epsilon \mathbb{R}^6 \qquad \{2.1\}$$

This completes the definition of the reference frames and their related nomenclature that will be used in this report. It is now possible to define the transformation between the body fixed and inertial reference frames.

2.3 Body-Fixed to Inertial Transformations

To assess the performance of any ROV position or attitude controller, it will be necessary to track how the body fixed orientation of the ROV coincides with the inertial frame. However, the ROV thrusters are rigidly fixed to its body and will thus provide a body-fixed thrust orientation. Therefore it is necessary to transform the body-fixed ROV frame into the inertial frame. This section will detail and define these transformations.

Velocity in the inertial frame ($\dot{\boldsymbol{\eta}}$) can be found by taking the body-bound velocity ($\boldsymbol{\nu}$) and transforming it through the rotation matrix as shown below [8]:

$$\dot{\boldsymbol{\eta}} = \boldsymbol{J}(\boldsymbol{\eta})\boldsymbol{\nu}$$
$$\Updownarrow$$
$$\begin{bmatrix} \dot{\boldsymbol{p}}^i \\ \dot{\boldsymbol{\Theta}} \end{bmatrix} = \begin{bmatrix} \boldsymbol{R}_b^i(\boldsymbol{\Theta}) & \mathbf{0}_{3\times3} \\ \mathbf{0}_{3\times3} & \boldsymbol{T}_\Theta(\boldsymbol{\Theta}) \end{bmatrix} \begin{bmatrix} \boldsymbol{v}_O^b \\ \boldsymbol{\omega}_{ib}^b \end{bmatrix} \qquad \{2.2\}$$

where $\boldsymbol{\eta}, \boldsymbol{\nu} \epsilon \mathbb{R}^6$.

The rotation matrix $\boldsymbol{R}_b^i(\boldsymbol{\Theta})$ shown in equation 2.2 above is derived by rotating the linear inertial frame through angles ψ, θ and ϕ about axes z, y and x respectively, until they align with the body fixed linear axes of the vehicle. Using vector geometry, this yields the matrix:

$$\boldsymbol{R}_b^i(\boldsymbol{\Theta}) = \begin{bmatrix} c\psi c\theta & c\psi s\theta s\phi - s\psi c\phi & c\psi s\theta c\phi + s\psi s\phi \\ s\psi c\theta & s\psi s\theta s\phi + c\psi c\phi & s\psi s\theta c\phi - c\psi s\phi \\ -s\theta & c\theta s\phi & c\theta c\phi \end{bmatrix} \quad \{2.3\}$$

where, s · = sin (·), c · = cos (·), t · = tan (·).

The rotation matrix $\boldsymbol{T}_\Theta(\boldsymbol{\Theta})$ shown previously in equation 2.2 is derived by rotating the inertial rotational frame through angles ψ, θ and ϕ about axes z, y and x respectively, until they align with the body fixed rotational axes of the vehicle. It should be noted that changes of angles in the body-fixed frame require a North fixed reference to be meaningful in the inertial frame. This is why the NED co-ordinate system was chosen as the inertial frame in which to define the ROV's motion. Applying conservation of angular momentum through each rotation yields the matrix:

$$\boldsymbol{T}_\Theta(\boldsymbol{\Theta}) = \begin{bmatrix} 1 & t\theta s\phi & t\theta c\phi \\ 0 & c\phi & -s\phi \\ 0 & s\phi/c\theta & c\phi/c\theta \end{bmatrix} \quad \{2.4\}$$

If we now solve equation 2.2 we gain expressions for the individual linear components of $\dot{\boldsymbol{\eta}}$:

$$\begin{aligned} \dot{x} = {} & u\cos\psi\cos\theta + v(\cos\psi\sin\theta\sin\phi - \sin\psi\cos\phi) \\ & + w(\sin\psi\sin\phi + \cos\psi\cos\phi\sin\theta) \end{aligned} \quad \{2.5\}$$

$$\begin{aligned} \dot{y} = {} & u\sin\psi\cos\theta + v(\cos\psi\cos\phi + \sin\phi\sin\theta\sin\psi) \\ & + w(\sin\theta\sin\psi\cos\phi - \cos\psi\sin\phi) \end{aligned} \quad \{2.6\}$$

$$\dot{z} = -u\sin\theta + v\cos\theta\sin\phi + w\cos\theta\cos\phi \quad \{2.7\}$$

And rotational components of $\dot{\boldsymbol{\eta}}$:

$$\dot{\phi} = p + q\sin\phi\tan\theta + r\cos\phi\tan\theta \quad \{2.8\}$$

$$\dot{\theta} = q\cos\phi - r\sin\phi \quad \{2.9\}$$

$$\dot{\psi} = q\frac{\sin\phi}{\cos\theta} + r\frac{\cos\phi}{\cos\theta}, \ \theta \neq \pm 90^\circ \quad \{2.10\}$$

It can be clearly seen from equation 2.10 above that the system is undefined at pitch angles of ±90˚.

As was shown previously on page 5 in Figure 5, the *SEAHOG* is an under-actuated system where the pitch and roll degrees of freedom are not controllable. To minimise this disadvantage, the ROV has been designed to be hydro-dynamically stable, with a lower centre of gravity than its centre of buoyancy, which will tend to passively minimise angles of pitch and roll. It is predicted that under normal operation the *SEAHOG* will never experience pitch angles of close to ±90˚ and thus the above system will never become undefined and is assumed to be sufficient for this project.

This completes a description of six DOF kinematics, showing that they can be described by a total of six differential equations, listed above. It is now possible to explore how forces affect an underwater body through its dynamics.

2.4 Underwater Dynamics

2.4.1 Introduction

This section will describe the interaction of an underwater vehicle and the static and dynamic effects that act on it due to the underwater environment. It will show that the six DOF dynamics of an underwater vehicle can be expressed as [8]:

$$\boldsymbol{M\dot{\nu} + C(\nu)\nu + D(\nu)\nu + g(\eta) = \tau + g_O + w} \quad \{2.11\}$$

where the above symbols represent the following quantities:

$\boldsymbol{M}$ - System mass and inertia matrix (including added mass and inertia)

$\boldsymbol{C(\nu)}$ - Coriolis-centripetal matrix (including added mass and inertia)

$\boldsymbol{D(\nu)}$ - Damping matrix

$\boldsymbol{g(\eta)}$ - Gravitational/buoyancy forces and moments

$\boldsymbol{\tau}$ - Control inputs

$\boldsymbol{g_O}$ - Vector used for pre-trimming (ballast control)

$\boldsymbol{w}$ - Wind, waves and currents environmental disturbances

The *SEAHOG* ROV employs passive buoyancy control through a float block that has been designed to hold the ROV in a horizontal orientation whilst stationary. Ballast control is sometimes referred to as active buoyancy control and is not present on the *SEAHOG*. Therefore this report will treat $\boldsymbol{g_O}$ from equation 2.11 above as 0, making the six DOF dynamic system:

$$\boldsymbol{M\dot{\nu} + C(\nu)\nu + D(\nu)\nu + g(\eta) = \tau + w} \quad \{2.12\}$$

2.4.2 Rigid Body Dynamics

During the derivations of the following equations of motion, the following assumptions were made:

- The vessel is rigid.
- Forces due to a slowly rotating NED frame are negligible, resulting in treating the NED frame as inertial [8].

Figure 8 below shows the vectors and elements used in the following equations to describe the rigid body dynamics for an underwater vehicle. The general form is given, where the origin (O) is not chosen on the centre of gravity (CG). The position of the origin will be chosen and motivated later in the report, when a greater understanding of how it will affect the overall system has been gained.

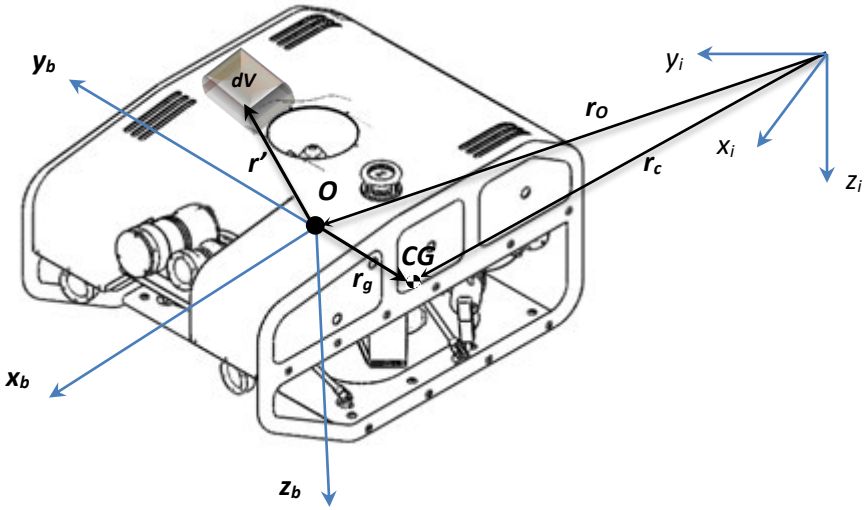

Figure 8 - Vectors used in the rigid body dynamics for an underwater vehicle

The translational motion of the origin of a body is related to the translational motion of the CG through the vector $\boldsymbol{r_g}$. It is derived from Euler's first axiom, that states that the applied force on a body is proportional to its rate of change of momentum [8] or:

$$\dot{\boldsymbol{p}}_{CG} = \boldsymbol{f}_{CG} \qquad \{2.13\}$$

From this we get, when combined with Newton's second law:

$$m\dot{\boldsymbol{v}}^i_{CG} = \boldsymbol{f}^i_{CG} \qquad \{2.14\}$$

This makes it possible to derive the translational motion of a body about its origin as a result of body-fixed forces. The translational motion of a body can be described as [8]:

$$m\left[\dot{\boldsymbol{v}}^b_O + \dot{\boldsymbol{\omega}}^b_{ib} \times \boldsymbol{r}^b_g + \boldsymbol{\omega}^b_{ib} \times \boldsymbol{v}^b_O + \boldsymbol{\omega}^b_{ib} \times \left(\boldsymbol{\omega}^b_{ib} \times \boldsymbol{r}^b_g\right)\right] = \boldsymbol{f}^b_O \qquad \{2.15\}$$

where:

m - mass of rigid body

$\boldsymbol{v}_O$ - translational velocity of the body at its origin

$\boldsymbol{\omega}_{ib}$ - rotational velocity of the body in the inertial frame relative to the body-fixed frame

$\boldsymbol{r}_g$ - is the vector $[x_g, y_g, z_g]^T$ from the origin to the centre of gravity of the body

$\boldsymbol{f}_O$ - is the body-fixed applied force vector $[X, Y, Z]^T$

Euler's second axiom states that the rate of change of angular momentum of a body is proportional to the moment applied on that body or:

$$\dot{\boldsymbol{h}}_{CG} = \boldsymbol{m}_{CG} \quad \{2.16\}$$

This implies that:

$$\dot{\boldsymbol{h}}_{CG} = \boldsymbol{I}_{CG}\dot{\boldsymbol{\omega}}_{ib} \quad \{2.17\}$$

The angular momentum about O is defined as:

$$\boldsymbol{h}_O = \int_V (\boldsymbol{r}' \times \boldsymbol{v}_p)\rho_m dV \quad \{2.18\}$$

where v_p is the velocity of the volume element dV and ρ_m is the density of the element.

It is now possible to derive the rotational motion of a body about its origin as a result of body-fixed moments applied to the body. The rotational motion of a body can be described as [8]:

$$\boldsymbol{I}_O\dot{\boldsymbol{\omega}}_{ib}^b + \boldsymbol{\omega}_{ib}^b \times \boldsymbol{I}_O\boldsymbol{\omega}_{ib}^b + m\boldsymbol{r}_g^b \times \left(\dot{\boldsymbol{v}}_O^b + \boldsymbol{\omega}_{ib}^b \times \boldsymbol{v}_O^b\right) = \boldsymbol{m}_O \quad \{2.19\}$$

where:

$\boldsymbol{I}_O$ - Inertia tensor defined at the origin of the body-fixed axes

$\boldsymbol{m}_O$ - is the body-fixed applied moment vector $[K, M, N]^T$

The inertia tensor is defined as:

$$\boldsymbol{I}_O \coloneqq \begin{bmatrix} I_x & -I_{xy} & -I_{xz} \\ -I_{yx} & I_y & -I_{yz} \\ -I_{zx} & -I_{zy} & I_z \end{bmatrix}, \qquad \boldsymbol{I}_O = \boldsymbol{I}_O{}^T > 0 \quad \{2.20\}$$

Using notation defined by SNAME and presented previously in Table 1 on page 9, it is possible derive the individual elements of the vector $\boldsymbol{f}_O$ using equation 2.15 [8]:

$$X = m\left[\dot{u} - vr + wq - x_g(q^2 + r^2) + y_g(pq - \dot{r}) + z_g(pr + \dot{q})\right] \quad \{2.21\}$$

$$Y = m\left[\dot{v} - wp + ur - y_g(r^2 + p^2) + z_g(qr - \dot{p}) + x_g(qp + \dot{r})\right] \quad \{2.22\}$$

$$Z = m\left[\dot{w} - uq + vp - z_g(p^2 + q^2) + x_g(rp - \dot{q}) + y_g(rq + \dot{p})\right] \quad \{2.23\}$$

Similarly, this process can be carried out for the elements of the moment vector $\boldsymbol{m}_O$ using equation 2.19 [8]:

$$\begin{aligned} K = {} & I_x\dot{p} + \left(I_z - I_y\right)qr - (\dot{r} + pq)I_{xz} + (r^2 - q^2)I_{yz} + (pr - \dot{q})I_{xy} \\ & + m\left[y_g(\dot{w} - uq + vp) - z_g(\dot{v} - wp + ur)\right] \end{aligned} \quad \{2.24\}$$

$$M = I_y\dot{q} + (I_x - I_z)rp - (\dot{p} + qr)I_{xy} + (p^2 - r^2)I_{zx} + (qp - \dot{r})I_{yz} + m\big[z_g(\dot{u} - vr + wq) - x_g(\dot{w} - uq + vp)\big] \quad \{2.25\}$$

$$N = I_z\dot{r} + \big(I_y - I_x\big)pq - (\dot{q} + rp)I_{yz} + (q^2 - p^2)I_{xy} + (rq - \dot{p})I_{zx} + m\big[x_g(\dot{v} - wp + ur) - y_g(\dot{u} - vr + wq)\big] \quad \{2.26\}$$

It is now possible to express the rigid body (RB) dynamics as of the system in terms of a rigid body control input, $\boldsymbol{\tau}_{RB}$. This yields the matrix equation:

$$\boldsymbol{M}_{RB}\dot{\boldsymbol{\nu}} + \boldsymbol{C}_{RB}(\boldsymbol{\nu})\boldsymbol{\nu} = \boldsymbol{\tau}_{RB} \quad \{2.27\}$$

where:

$$\boldsymbol{M}_{RB} = \begin{bmatrix} m & 0 & 0 & 0 & mz_g & -my_g \\ 0 & m & 0 & -mz_g & 0 & mx_g \\ 0 & 0 & m & my_g & -mx_g & 0 \\ 0 & -mz_g & my_g & I_x & -I_{xy} & -I_{xz} \\ mz_g & 0 & -mx_g & -I_{xy} & I_y & -I_{yz} \\ -my_g & mx_g & 0 & -I_{xz} & -I_{yz} & I_z \end{bmatrix} \quad \{2.28\}$$

and

$$\boldsymbol{C}_{RB}(\boldsymbol{\nu}) = \begin{bmatrix} 0 & 0 & 0 \\ 0 & 0 & 0 \\ 0 & 0 & 0 \\ -m\big(y_g q + z_g r\big) & m(y_g p + w) & m(z_g p - v) \\ m(x_g q - w) & -m\big(x_g p + z_g r\big) & m(z_g q + u) \\ m(x_g r + v) & m(y_g r - u) & -m\big(x_g p + y_g q\big) \end{bmatrix}$$

$$\begin{bmatrix} m\big(y_g q + z_g r\big) & -m\big(x_g q - w\big) & -m\big(x_g r + v\big) \\ -m\big(y_g p + w\big) & m\big(x_g p + z_g r\big) & -m\big(y_g r - u\big) \\ -m\big(z_g p - v\big) & -m\big(z_g q + u\big) & m\big(x_g p + y_g q\big) \\ 0 & -I_{xz}p - I_{yz}q + I_z r & I_{xy}p + I_{yz}r - I_y q \\ I_{xz}p + I_{yz}q - I_z r & 0 & -I_{xy}q - I_{xz}r + I_x p \\ -I_{xy}p - I_{yz}r + I_y q & I_{xy}q + I_{xz}r - I_x p & 0 \end{bmatrix} \quad \{2.29\}$$

This completes the description of the rigid-body dynamics of an underwater vehicle. It is now necessary to describe and derive the various force components that act upon the vehicle during motion in the form of the vector $\boldsymbol{\tau}_{RB}$ shown above in equation 2.27.

2.4.3 Hydrodynamic Effects

The hydrodynamic effects acting on a submerged body can be classified into radiation-induced forces, environmental effects and restoring forces.

Radiation-Induced Forces

Radiation-Induced forces and moments are defined as forces on a body when the body is forced to oscillate with the wave excitation frequency and there are no incident waves [9]. These forces and moments are made up of the following components [8]:

- Added mass due to the inertia of the surrounding fluid
- Potential damping due to energy transferred to generated surface waves

Contributions from different hydrodynamic effects on a body can be assumed to be linearly superimposed [9]. Therefore, the contribution of radiation-induced hydrodynamic forces can be expressed as:

$$\boldsymbol{\tau}_R = \underbrace{-\boldsymbol{M}_A\dot{\boldsymbol{\nu}} - \boldsymbol{C}_A(\boldsymbol{\nu})\boldsymbol{\nu}}_{\text{added mass}} - \underbrace{\boldsymbol{D}_P(\boldsymbol{\nu})\boldsymbol{\nu}}_{\substack{\text{potential}\\ \text{damping}}} \quad \{2.30\}$$

Other effects included in radiation-induced damping are damping due to skin friction, wave drift damping and damping due to vortex shedding [8]. These are expressed as [8]:

$$\boldsymbol{\tau}_D = -\underbrace{\boldsymbol{D}_S(\boldsymbol{\nu})\boldsymbol{\nu}}_{\text{skin friction}} - \underbrace{\boldsymbol{D}_W(\boldsymbol{\nu})\boldsymbol{\nu}}_{\substack{\text{wave drift}\\ \text{damping}}} - \underbrace{\boldsymbol{D}_M(\boldsymbol{\nu})\boldsymbol{\nu}}_{\substack{\text{damping due to}\\ \text{vortex shedding}}} \quad \{2.31\}$$

In the context of submerged underwater vehicles, the effects of potential damping and wave drift damping are negligible compared to other damping terms and will thus be taken as 0 [8]. The total hydrodynamic damping matrix can therefore be expressed as:

$$\boldsymbol{D}(\boldsymbol{\nu}) \coloneqq \boldsymbol{D}_S(\boldsymbol{\nu}) + \boldsymbol{D}_M(\boldsymbol{\nu}) \quad \{2.32\}$$

which allows the sum of hydrodynamic damping forces and moments to be written as:

$$\boldsymbol{\tau}_H = \boldsymbol{\tau}_R + \boldsymbol{\tau}_D = -\boldsymbol{M}_A\dot{\boldsymbol{\nu}} - \boldsymbol{C}_A(\boldsymbol{\nu})\boldsymbol{\nu} - \boldsymbol{D}(\boldsymbol{\nu})\boldsymbol{\nu} \quad \{2.33\}$$

Environmental Disturbances

Wind, waves and currents will subject a marine vessel to external forces. For an underwater vehicle specifically, the distance of the body beneath the free surface will determine the effect of wave motion on the body. The further away it is, the less the effect will be [10]. The controller developed in this report will not factor in the effects of environmental disturbances but it will make provision for their inclusion in later projects. The vector of environmental disturbances is denoted as $\boldsymbol{w}$.

Restoring Forces

Restoring forces are static effects due to the mass and buoyancy of the vehicle through Archimedes' principle. Restoring effects are denoted by the vector $\boldsymbol{g}(\boldsymbol{\eta})$. These include ballast control effects but, as described earlier, these will be ignored due to the passive buoyancy control present on the *SEAHOG*.

Summary

The rigid body force vector can now be expressed in terms of the hydrodynamic effects discussed in this section as follows:

$$\boldsymbol{\tau}_{RB} = \boldsymbol{\tau}_H + \boldsymbol{w} - \boldsymbol{g}(\boldsymbol{\eta}) + \boldsymbol{\tau} \quad \{2.34\}$$

where $\boldsymbol{\tau}$ represents control forces from propulsion, such as forces from the thrusters.

The resulting model can now be expressed by recalling equation 2.12:

$$\boldsymbol{M}\dot{\boldsymbol{\nu}} + \boldsymbol{C}(\boldsymbol{\nu})\boldsymbol{\nu} + \boldsymbol{D}(\boldsymbol{\nu})\boldsymbol{\nu} + \boldsymbol{g}(\boldsymbol{\eta}) = \boldsymbol{\tau} + \boldsymbol{w}$$

With the mass and Coriolis matrices being a combination of rigid body mass and added mass:

$$\boldsymbol{M} = \boldsymbol{M}_{RB} + \boldsymbol{M}_A$$
$$\boldsymbol{C}(\boldsymbol{\nu}) = \boldsymbol{C}_{RB}(\boldsymbol{\nu}) + \boldsymbol{C}_A(\boldsymbol{\nu})$$

Each of these hydrodynamic effects can now be developed in more detail individually.

2.4.4 Added Mass

When a rigid body moves through a fluid, fluid particles are accelerated due to the motion of the body. This acceleration requires a force – which is provided by the submersed vehicle. The concept of added mass is not a fixed quantity of water that moves with the body and increases its mass by a constant amount [11]. Added or virtual mass can also be understood as pressure-induced forces and moments due to a forced harmonic excitation of a body proportional to its acceleration [8]. As a result, the added mass forces will be opposite in direction to the forced harmonic motion of an underwater body [8].

It is convenient to derive the added mass quantities through Lagrangian Mechanics. The kinetic energy of the fluid [12]:

$$T_A = \frac{1}{2}\boldsymbol{\nu}^T\boldsymbol{M}_A\boldsymbol{\nu} \quad \{2.35\}$$

can be related to the forces and moments imparted onto the underwater vehicle by equations of the form [12]:

$$\frac{d}{dt}\left(\frac{\delta T}{\delta \boldsymbol{\nu}_O^b}\right) + \boldsymbol{\omega}_{ib}^b \times \frac{\delta T}{\delta \boldsymbol{\nu}_O^b} = \boldsymbol{f}_O^b \quad \{2.36\}$$

$$\frac{d}{dt}\left(\frac{\delta T}{\delta \boldsymbol{\omega}_{ib}^b}\right) + \boldsymbol{\omega}_{ib}^b \times \frac{\delta T}{\delta \boldsymbol{\omega}_{ib}^b} + \boldsymbol{\nu}_O^b \times \frac{\delta T}{\delta \boldsymbol{\nu}_O^b} = \mathbf{m}_O^b \quad \{2.37\}$$

If we express $\boldsymbol{M}_A$ as:

$$\boldsymbol{M}_A = -\begin{bmatrix} X_{\dot{u}} & X_{\dot{v}} & X_{\dot{w}} & X_{\dot{p}} & X_{\dot{q}} & X_{\dot{r}} \\ Y_{\dot{u}} & Y_{\dot{v}} & Y_{\dot{w}} & Y_{\dot{p}} & Y_{\dot{q}} & Y_{\dot{r}} \\ Z_{\dot{u}} & Z_{\dot{v}} & Z_{\dot{w}} & Z_{\dot{p}} & Z_{\dot{q}} & Z_{\dot{r}} \\ K_{\dot{u}} & K_{\dot{v}} & K_{\dot{w}} & K_{\dot{p}} & K_{\dot{q}} & K_{\dot{r}} \\ M_{\dot{u}} & M_{\dot{v}} & M_{\dot{w}} & M_{\dot{p}} & M_{\dot{q}} & M_{\dot{r}} \\ N_{\dot{u}} & N_{\dot{v}} & N_{\dot{w}} & N_{\dot{p}} & N_{\dot{q}} & N_{\dot{r}} \end{bmatrix} \quad \{2.38\}$$

where the above notation convention denotes, as an example denoted below, an added mass force X for an acceleration $\dot{w}$ in the z_b direction [6]:

$$X = -X_{\dot{w}}\dot{w} \quad \{2.39\}$$

with:

$$X_{\dot{w}} \coloneqq \frac{\delta X}{\delta \dot{w}} \quad \{2.40\}$$

It was shown that ideal theory gives good approximations for added mass terms for an underwater body, hence it follows that $\boldsymbol{M}_A = \boldsymbol{M}_A^T$ for an underwater body [13]. The symmetry of the added mass matrix implies that for an unsymmetrical body, the added mass matrix will consist of 21 distinct terms. If the energy equation 2.35 is now expanded, assuming that $\boldsymbol{M}_A = \boldsymbol{M}_A^T$, we obtain the following:

$$\begin{aligned} T_A = \frac{1}{2}\,[&-X_{\dot{u}}u^2 - Y_{\dot{v}}v^2 - Z_{\dot{w}}w^2 - 2Y_{\dot{w}}vw - 2X_{\dot{w}}wu - 2X_{\dot{v}}uv \\ &- K_{\dot{p}}p^2 - M_{\dot{q}}q^2 - N_{\dot{r}}r^2 - 2M_{\dot{r}}qr - 2K_{\dot{r}}rp - 2K_{\dot{p}} \\ &- 2p\left(X_{\dot{p}}u + Y_{\dot{p}}v + Z_{\dot{p}}w\right) \\ &- 2q\left(X_{\dot{q}}u + Y_{\dot{q}}v + Z_{\dot{q}}w\right) \\ &- 2r(X_{\dot{r}}u + Y_{\dot{r}}v + Z_{\dot{r}}w)] \end{aligned} \quad \{2.41\}$$

It is now possible to substitute equation 2.41 into equations 2.36 and 2.37 to obtain expressions for the added mass forces for each of the six elements of the added mass force vector $\boldsymbol{\tau}_A$. These equations are extensive and will not be listed here but can be found in [8] and [14]. It is possible to derive the added mass and inertia tensors from these equations, however, the presence of symmetry in a body allows for significant simplification to these terms. The added mass matrix is symmetrical and therefore, from equation 2.38 previously, there are a possible 21 distinct terms that comprise the added mass equations of a body immersed in a fluid. Due to the large amount of distinct terms, for convenience sake, the added mass and inertia tensors will be presented during the development of the *SEAHOG* model in their simplified form, after the symmetry of the vehicle has been assessed.

Now that the added mass and inertia tensors have been described, the hydrodynamic damping of the system can be analysed and described.

2.4.5 Hydrodynamic Damping

Each of the elements of $\boldsymbol{D}(\boldsymbol{\nu})$, the hydrodynamic damping matrix, will be discussed in turn in this section.

Skin Friction

Damping due to skin friction is as a result of friction between a fluid and the "skin" of the object moving through it and is thus related to the surface roughness of the object. It becomes an important factor when considering the low frequency motion of a vessel [8]. Boundary layer theory results in linearly dependant skin friction damping for laminar flow, while turbulent flow results in quadratic damping [15].

Damping due to Vortex Shedding

As an object moves through a fluid, it is possible that the interaction of the body and the fluid creates a low pressure zone downstream of the body. The body will tend to move towards this low pressure zone, thereby effectively increasing the drag on the object. This concept is known as damping due to vortex shedding. The viscous damping force due to vortex shedding forms part of *Morison's equation* [16] and is modelled as:

$$f(U) = -\frac{1}{2}\rho C_D(R_n) A|U|U \qquad \{2.42\}$$

where ρ is the fluid density, A is the projected cross-sectional area, $C_D(R_n)$ is the drag coefficient as a function of the Reynolds number and U is the fluid velocity relative to the vehicle.

For convenience, the damping effects on a submerged body are often separated into linear and quadratic effects as follows:

$$\boldsymbol{D}(\boldsymbol{\nu}) = \boldsymbol{D} + \boldsymbol{D}_n(\boldsymbol{\nu}) \qquad \{2.43\}$$

For the sake of simplicity, an example of the damping matrix will be shown from a slow moving underwater vehicle that is executing a non-coupled motion. This would result in the diagonal damping matrix [8]:

$$\boldsymbol{D}(\boldsymbol{\nu}) = -\left[X_u, Y_v, Z_w, K_p, M_q, N_r\right]^D - \left[X_{|u|u}|u|, Y_{|v|v}|v|, Z_{|w|w}|w|, K_{|p|p}|p|, M_{|q|q}|q|, N_{|r|r}|r|\right]^D \qquad \{2.44\}$$

where the above notation is defined as, for the linear term as an example, X_u being the linear coefficient for a force in the x_b direction as a result of a velocity (u) in the x_b direction and, for the quadratic term as an example, $Y_{|v|v}$ being the quadratic coefficient for a force in the y_b direction as a result of a velocity (v) in the y_b direction, denoted as $Y_{|v|v}|v|$ in position 2, 2 of the quadratic damping matrix.

Once again, as with the added mass and inertia tensors, the geometric properties and thus the symmetry of a body lends itself to significant simplification of the damping matrices. However the way in which this can be implemented will be analysed further during the *SEAHOG* model development. This completes the damping matrix description and thus leaves only the restoring forces and moments to be described in this section.

2.4.6 Restoring Forces and Moments

The vector for restoring forces and moments consists of both the gravitational force and the buoyancy force that acts on a body through Archimedes' principle. The definition and nomenclature associated with these quantities is shown below in Figure 9.

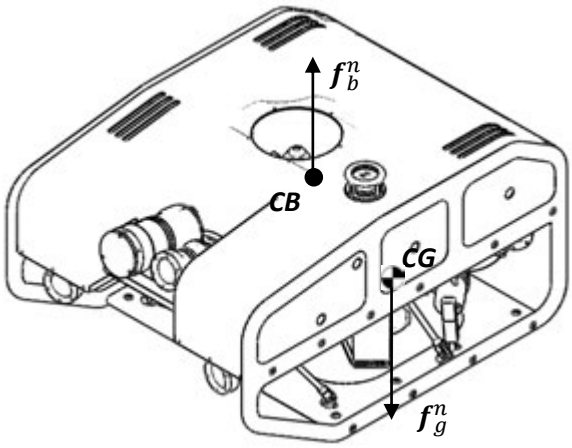

Figure 9 - Buoyancy force acting through the centre of buoyancy and gravity force acting through the centre of gravity

The buoyancy force will always be directed towards the lowest pressure zone which is typically the surface and can be thus defined to have the direction of $-z$ in the global frame. This force acts through the centre of buoyancy. The gravity force will act through the centre of gravity and will typically be directed towards the centre of the Earth or $+z$ in the inertial frame.

The vector from the b-frame Origin to the centre of buoyancy and gravity is respectively defined as $\boldsymbol{r}_b^b = [x_b, y_b, z_b]^T$ and $\boldsymbol{r}_g^b = [x_g, y_g, z_g]^T$. If m is the mass of the body, ∇ is the volume of the fluid displaced by the body, g is the gravitational acceleration constant and ρ is the density of the fluid that the body is submerged in, then according to SNAME notation, the gravity and buoyancy forces on the body are defined as [6]:

$$W = mg, \qquad B = \rho g \nabla \tag{2.45}$$

and hence:

$$\boldsymbol{f}_b^n = -\begin{bmatrix} 0 \\ 0 \\ B \end{bmatrix}, \qquad \boldsymbol{f}_g^n = \begin{bmatrix} 0 \\ 0 \\ W \end{bmatrix} \tag{2.46}$$

These forces can be transformed into the body-fixed frame by applying the inverse of the rotation matrix defined in equation 2.3 on page 11 previously. The results of these transformations can be combined to form the total restoring forces and moments vector $\boldsymbol{g}(\boldsymbol{\eta})$. This vector is defined as [8]:

$$\boldsymbol{g}(\boldsymbol{\eta}) = \begin{bmatrix} (W-B)\sin\theta \\ -(W-B)\cos\theta\sin\phi \\ -(W-B)\cos\theta\cos\phi \\ -\left(y_g W - y_b B\right)\cos\theta\cos\phi + \left(z_g W - z_b B\right)\cos\theta\sin\phi \\ \left(z_g W - z_b B\right)\sin\theta + \left(x_g W - x_b B\right)\cos\theta\cos\phi \\ -\left(x_g W - x_b B\right)\cos\theta\sin\phi - \left(y_g W - y_b B\right)\sin\theta \end{bmatrix} \quad \{2.47\}$$

This completes the description of the hydrodynamic forces acting on an underwater body and thus each term of the equation of motion for an underwater body has now been described and derived.

2.5 Summary

This chapter has shown how the body-fixed reference frame and the NED reference frame is used to describe the kinematics and dynamics of an underwater body. It has shown that the equation of motion for an underwater vehicle can be described as:

$$\boldsymbol{M\dot{\nu}} + \boldsymbol{C(\nu)\nu} + \boldsymbol{D(\nu)\nu} + \boldsymbol{g(\eta)} = \boldsymbol{\tau} + \boldsymbol{w}$$

in the body-fixed frame, which can be used to find the velocity of the vehicle in the inertial frame through the transformation:

$$\boldsymbol{\dot{\eta}} = \boldsymbol{J(\eta)\nu}$$

The velocity in the inertial frame can be integrated to obtain the absolute position of the ROV, allowing the performance of any simulated controller to be assessed. Each of the elements in the above equations have been described and derived, where appropriate, to give an overview of the physical interaction of an underwater vehicle with its surrounding environment. Assumptions that have been made in the derivation of these expressions include the following:

- The area of interest of motion in the NED frame is sufficiently localised to treat the frame as inertial
- The ROV will never reach pitch angles of ±90˚ allowing the orientation of the ROV to be described by Euler angles
- The vehicle is rigid
- Potential damping and wave drift damping are negligible in the area of interest for the ROV model
- The model will not include the effects of environmental disturbances
- Hydrodynamic effects can be linearly superimposed [9]

This completes the description of the kinematics and dynamics of an underwater vehicle within the context of the scope of this report. An aspect that has not been dealt with in this section is the control input $\boldsymbol{\tau}$ into the system by vehicle actuators such as thrusters. It has been shown however, that the dynamics of the thrusters on an underwater vehicle greatly influences its overall dynamics and thus must be taken into account in the vehicle model [17]. Therefore, the next chapter will detail the development, implementation and verification of a thruster model that can be integrated into the rest of the *SEAHOG* ROV dynamic model.

Chapter 3 - Thruster System Dynamic Model Identification

3.1 Thruster Model Introduction

The general dynamics and kinematics of an underwater vehicle have been described in the previous chapter. The dynamics of the actuators of the vehicle, however, were excluded from the description. Thrusters are implemented as actuators on underwater vehicles and typically consist of a propeller that is driven by some power source. As will be explained in the following section, the thruster dynamics are very important and have a significant effect on the dynamics of the overall system. Therefore this chapter will detail the development and verification of a thruster model for the *SEAHOG* thrusters.

The thruster model is dependent on the physical mechanical and electrical systems that it consists of. Each separate system will be described and defined in this chapter. The separate components that constitute the thruster system and that must subsequently be modelled are shown below in Figure 10.

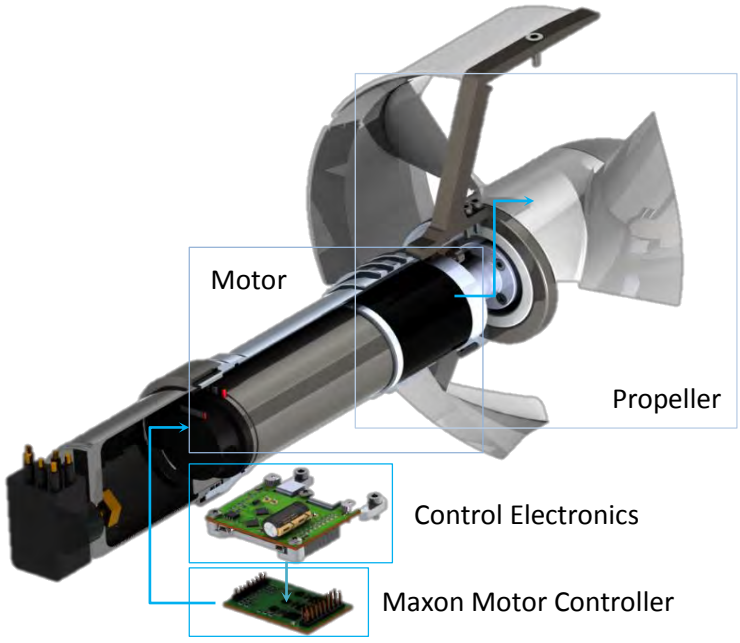

Figure 10 - Cross-section of a *SEAHOG* thruster showing subsystems to be modelled

Figure 11 below shows the Simulink® block diagram created for the *SEAHOG* thrusters. Each sub-diagram will be individually developed throughout the chapter, giving insight to the individual parts that constitute the overall system.

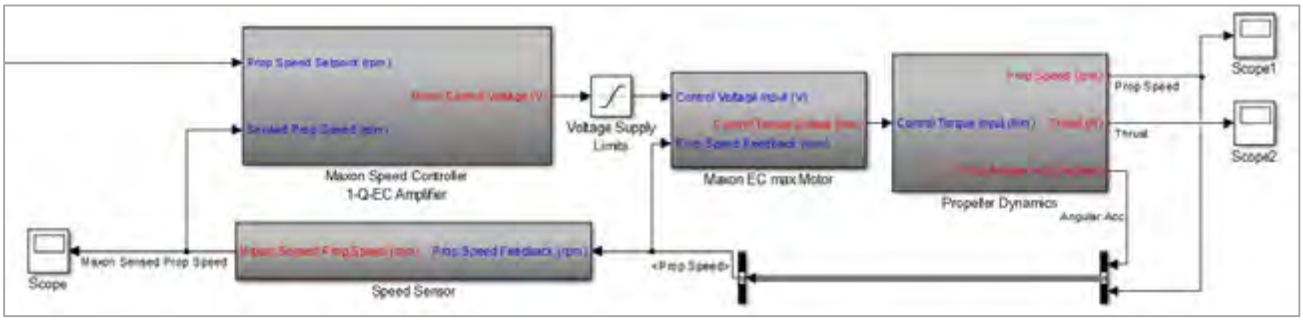

Figure 11 - SEAHOG thruster Simulink® block diagram

With an overview of the *SEAHOG* thruster system given, an investigation into the mathematics governing the thruster dynamics can be carried out.

3.2 Introduction to Thruster Modelling

It has been shown that the dynamics of the thrusters on an underwater vehicle dominate the vehicle behaviour by restricting the maximum closed loop bandwidth and creating a limit cycle for station keeping or dynamic positioning operations [17]. The limit cycle is formed as part of the non-linear dynamics of the thruster purely and has been shown not to be rooted in other non-linear effects such as stiction or deadband [17]. In addition, the effect of the relative motion of the water in terms of angle of attack on the propeller blades has a significant effect on the thrust produced by it. This means that thrust losses are expected as a result of currents, the motion of the underwater vehicle and flows generated by other thrusters [18]. Consequently, developing an accurate model of the thrust generated by a thruster is a non-trivial endeavour.

The thrust output of a thruster is defined in [19] as the axial force of the propeller and is a two state function that is dependent on the propeller velocity ($\boldsymbol{n}$) and the velocity of the vehicle itself ($\boldsymbol{\nu}$):

$$\boldsymbol{\tau} = \boldsymbol{b}(\boldsymbol{\nu}, \boldsymbol{n}) \qquad \{3.48\}$$

where, recalling from equation 2.12, $\boldsymbol{\tau}$ is the thruster control vector.

The thrust generated by a single screw propeller has been approximated by the first order, non-linear function below [20]:

$$T = \rho D^4 K_T(J_0)|n|n \quad \{3.49\}$$

where:

T - Thrust generated

ρ - Density of seawater

D - Propeller diameter

$K_T(J_0)$ - Thrust coefficient as a function of the advance number

n - Propeller angular velocity

and the advance number is defined as: $J_0 = V_a/(nD)$ with V_a as the advance velocity. The advance velocity is the velocity of the water flowing into the propeller and it has been shown that the thrust of a propeller generally decreases as it advances through the water [21]. The thrust producing behaviour of thrusters is generally classified into four states or quadrants that each depend on the sign of the propeller angular velocity vs. the sign of the advance velocity. Figure 12 following shows the relationship between the thrust coefficient and the advance number for all four quadrants of thruster control.

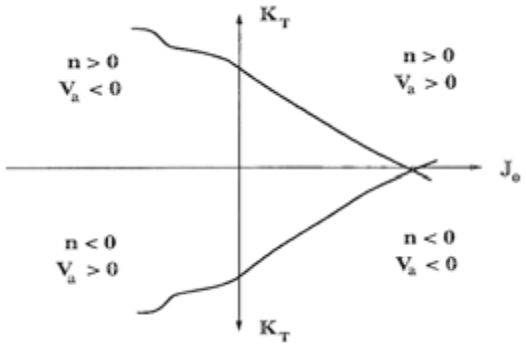

Figure 12 - Relationship between thruster coefficient and advance coefficient according to propeller vs. vehicle velocity [19]

From the figure above, it can be deduced that there is a linear reduction in thrust when the vehicle is moving in the same direction as water being passed through the thruster. When the water is being passed through the thruster propeller in the opposite direction to the propeller's motion however, a non-linear thrust behaviour is observed [22]. Due to the linear behaviour in the positive J_0 axis, K_T can be approximated as [19]:

$$K_T = \alpha_1 + \alpha_2 \frac{V_a}{nD} \quad \{3.50\}$$

with α_1 and α_2 constants related to the thruster propeller dimensions. The thruster force can therefore be written as [19]:

$$T(n, V_a) = T_{|n|n}|n|n + T_{|n|V_a}|n|V_a \quad \{3.51\}$$

where $T_{|n|n} > 0$ and $T_{|n|V_a} < 0$; both being constants related to the thruster dimensions.

An introduction to the behaviour of underwater thrusters has now been given along with a generalised thruster model and it is possible to select and develop a model to implement as the thruster contribution to the overall *SEAHOG* model.

3.3 Thruster Model Selection

3.3.1 Introduction

In selecting the thruster model for the *SEAHOG*, it was important to consider the facilities available for the model's verification and the methods in which it would be verified. It can be seen from equation 3.51 previously that the greater the advance speed, the lower the thrust output from the thruster. The coefficients governing this behaviour are usually obtained by moving the thruster through the water at fixed rates and orientations in a tow tank such as in [18]. The development of a rig capable of this would be extensive, as the rig would have to be highly instrumented; resulting in significant monetary and time expense. Room for the development of this kind of rig did not fit into the scope or budget of this project and thus it was decided to allow for the development of more advanced models in the future. In addition, determining the advance speed is a complicated task due to the wide range of factors that can influence it. For this project, it was decided that a simplified model would be developed for the *SEAHOG* thrusters.

A single state lumped parameter model was developed in [17] to show that the thruster dynamics in an ROV model play a significant role overall. This model was chosen as the basis of the *SEAHOG* thruster model developed in this report and will be detailed in the next section.

3.3.2 Single State Thruster Model

The lumped parameter model developed in [17] demonstrated the square law relationship between thrust and propeller speed and that there is a time lag between motor control torque and produced thrust. The time lag is very prominent at low propeller speeds – in operations such as station keeping and dynamic positioning. For clarity, station keeping is an automatically controlled ROV manoeuvre for holding a number of degrees of freedom constant and is similar to the concept of dynamic positioning.

In [17], a single state thruster model was developed by considering a shrouded propeller with a blade pitch (p) that develops a thrust (T) driven by a torque source (τ) at angular velocity (Ω). The thruster shroud has a cross-sectional area (A) which is related to its diameter (D) and encloses a volume of fluid (V). The ambient fluid has a density (ρ) and a volumetric flowrate within the shroud (Q). A graphical representation of these parameters is given following in Figure 13.

The model has been simplified under the following assumptions [17]:

1. The energy stored is due solely to the kinetic energy of the fluid in the shroud.
2. The kinetic energy of the external ambient fluid is negligible.
3. Friction losses are negligible.
4. Ambient fluid is incompressible.
5. Fluid flow at the thruster intake and exhaust is parallel, one dimensional, and at ambient pressure.
6. Rotational flow effects are ignored.
7. Gravity effects are negligible.
8. The thruster is completely symmetric with respect to the flow direction.

A cross-section of the shroud or Kort nozzle of a *SEAHOG* thruster is given following in Figure 13. The components and parameters used in the thruster model are labelled.

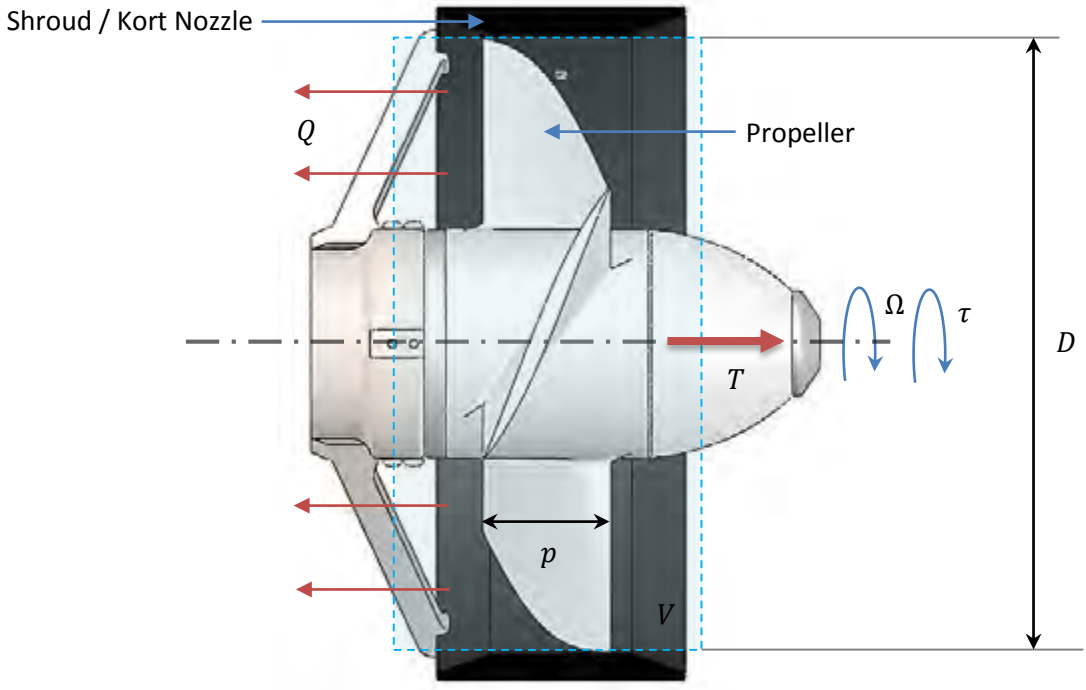

Figure 13 - Schematic of a *SEAHOG* thruster, showing components and model variables

It has already been established that assumptions 2 and 5 given previously are not accurate when the vehicle is in motion, and will lead to reduced thrust in real life. It should be noted that assumption 8 is accurate for a *SEAHOG* thruster, as the propeller has been designed to be symmetrical and output the same thrust in either axial direction.

Using the parameters detailed previously and from Figure 13 above, the model developed in [17] can be expressed as:

$$\dot{\Omega} = \beta\tau - \alpha\Omega|\Omega| \qquad \{3.52\}$$

$$T = C_t\Omega|\Omega| \qquad \{3.53\}$$

with:

$$\beta = \frac{1}{\eta^2 p^2 \rho V}, \quad \alpha = \frac{\eta p A}{2V}, \quad C_t = A\rho\eta^2 p^2 \qquad \{3.54\}$$

and η is the efficiency of the propeller.

This completes the description of the thruster model that will be used in this report. However, due to its known shortcomings, it should be compared to more recent models for future reference and so that the consequences of choosing a simplified model can be noted.

3.3.3 Advantages and Disadvantages of the 1 DOF Model

As has been discussed previously, the simplified thruster model has been shown to produce more thrust than in more comprehensive models when the vehicle is advancing through the water. Table 2 below compares three thruster models of different complexity, to assess each one's strengths and weaknesses.

Table 2 - Comparison of advantages and disadvantages for different thruster models

Model Type	**Advantages**	**Disadvantages**
1 state: propeller speed [17]	• Simple to verify and develop thruster parameters • Forms part of more intricate models	• Only accurate in steady state conditions • Only accurate when vehicle is stationary • Only applies to the two linear quadrants of thruster operation
2 states: propeller speed, water velocity [21]	• Accurate for transient thruster conditions • Applies to all four quadrants of thruster operation • Explains thrust overshoot that is not observed in the 1 DOF model	• Loss of accuracy when vehicle is moving through water • More difficult to obtain model parameters – requires measurement of water speed into thruster
3 states: propeller speed, vessel speed relative to water, shroud inflow velocity [23]	• Valid for all four quadrants of operation • Accurate under non-static vessel conditions	• Requires accurate knowledge of flow around the thruster and vehicle to fully realise its benefits

From Table 2 above, it is clear to see what can be expected from the model that will be developed for the *SEAHOG* in this chapter. While there are shortcomings to this model however, the single state model forms the steady state part of more advanced models and will thus still be useful for future work. In addition, the model will be fully verifiable and will thus contribute real, useful data to the *SEAHOG* model.

3.3.4 Summary

This section has motivated and detailed the selection of a single state thruster model that can be expressed as:

$$\dot{\Omega} = \beta\tau - \alpha\Omega|\Omega|$$
$$T = C_t\Omega|\Omega|$$

to be used as the basis of the *SEAHOG* thruster model. It is known that this model is only accurate under constant propeller speed conditions and thus leaves room for more advanced thruster models to be developed in the future. This being said, the model will be fully verifiable, contributing useful data to the overall *SEAHOG* model.

Now that a thruster model has been selected and described, it can be developed specifically for the *SEAHOG* using data from the *SEAHOG* thrusters.

3.4 The *SEAHOG* Thrusters

3.4.1 Introduction

With a thruster model chosen and understood, it is now possible to apply that model to the *SEAHOG* thrusters. The next sections will develop each aspect of the thruster model to be used in this report, including: the physical model of the propeller in the water, the motor and the control electronics. This process of development and verification will result in it being possible to develop the low level propeller speed control of the thruster module in the following chapter. However, it is essential for the SEAHOG thrusters themselves to be well understood for the system identification and model development to be possible, therefore, the following section will give a detailed description of the thrusters and the methods used to verify model parameters. For more information on the design and development of the thruster modules, see [24].

3.4.2 *SEAHOG* Thrusters, Test Rig and Data Capture Details

The *SEAHOG* thrusters were designed and developed at RARL at UCT. Details of the thruster module are given below in Table 3 and a *SEAHOG* thruster rendering is depicted following in Figure 14.

Table 3 - *SEAHOG* thruster details and design aspects

Housing Type	Atmospheric air-filled stainless steel pressure vessel
Propeller Type	Three blade, symmetrical
Method of Power Transmission to Propeller	Radial, two pole pair magnetic coupling
Motor	Maxon EC-max 40 120W, 48V brushless DC motor
Gearbox Reduction Ratio	1:12
Motor Power Amplifier	Maxon DEC Module 50/5 digital 1-Q-EC amplifier
Control and Communication Electronics	Two MSP430 microcontrollers

Figure 14 - Rendering of a *SEAHOG* thruster

A cross-section of the thruster is given below in Figure 15 to show the electronic control hardware and the propeller drive train located within the housing.

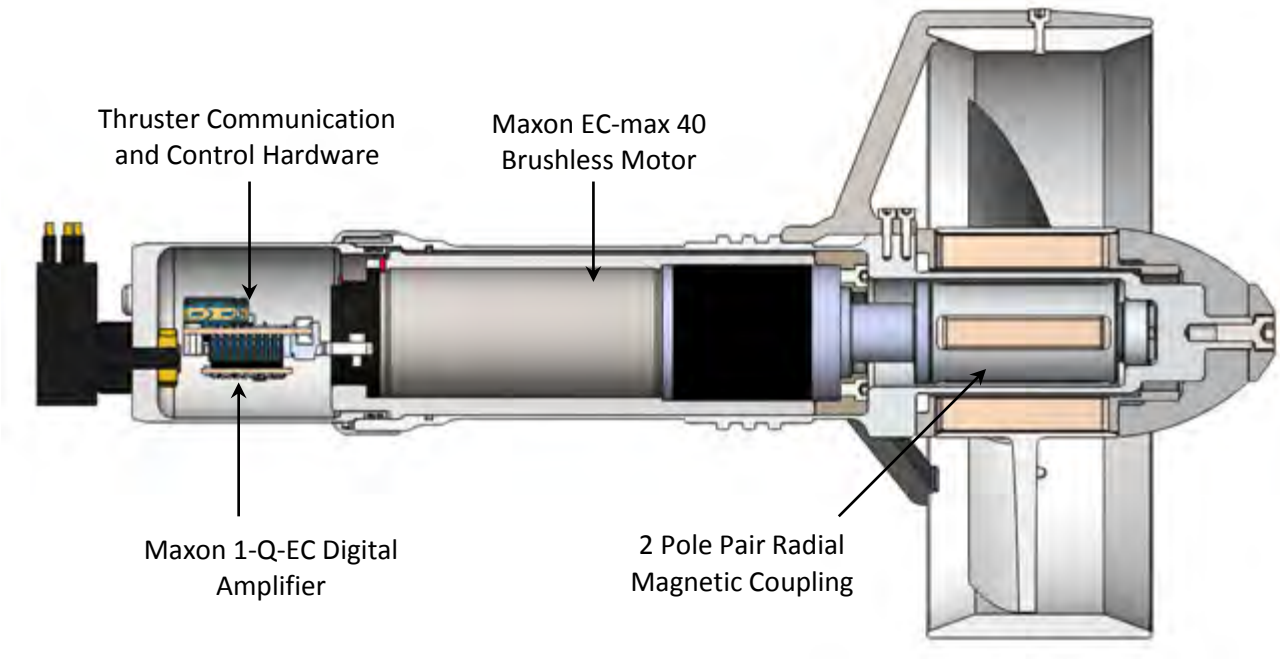

Figure 15 - Cross-section of a *SEAHOG* thruster with interior components revealed

The *SEAHOG* thruster communication structure works as follows:

- One microcontroller is allocated to communicate on the ROV Recommended Standard 485 (RS485) network and receive desired speed set-points from a central control unit.
- Another microcontroller is responsible for the low level speed control of the thruster - receiving speed set-points from the communications microcontroller via Serial Peripheral Interface (SPI) and sending values to the Digital to Analogue Converter (DAC) via SPI.
- An analogue voltage is then sent from the DAC to an input pin on the Maxon Digital Amplifier. The analogue voltage level represents the speed that is desired of the motor.
- The Maxon Digital Amplifier executes its own closed-loop control behaviour to bring the speed of the motor to the desired speed, which is related to an analogue voltage through an equation given in the datasheet. The amplifier handles both the brushless control of the motor, such as exciting the correct coils at the correct times, in addition to applying closed loop speed control to the motor. An effective DC voltage is applied across the coils using Pulse-Width Modulation (PWM).

The communication network between an operator console and the electronics of a *SEAHOG* thruster is shown following in Figure 16. The operator console shown in the figure was used in testing but is for illustration and could be readily replaced with a centralised controller, communicating with all five of the *SEAHOG* thrusters.

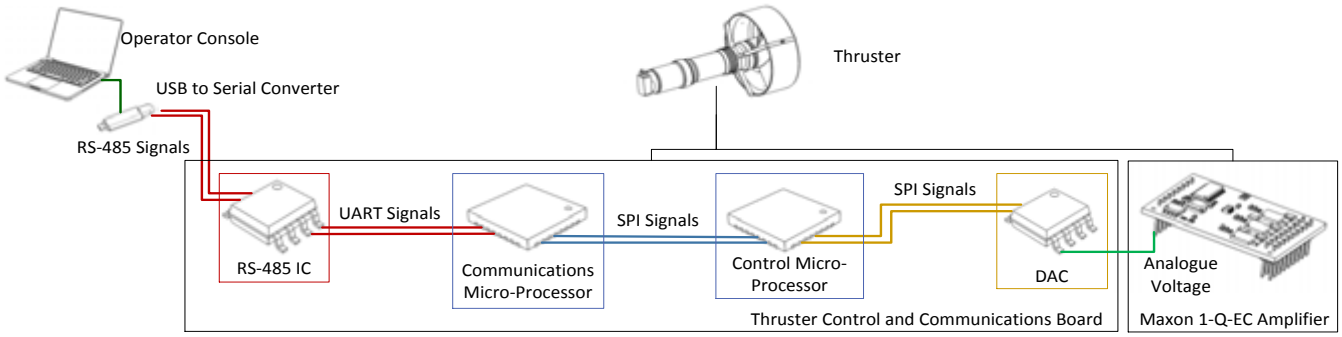

Figure 16 - Low level communication network of the *SEAHOG* thruster

Testing of the thrusters for parameter identification was conducted in a freshwater-filled tank of dimensions 1m deep x 1m wide x 3m long. The thruster was attached to an aluminium frame, as shown following in Figure 17, which was fastened to the tank rigidly so that the thruster would not move during operation.

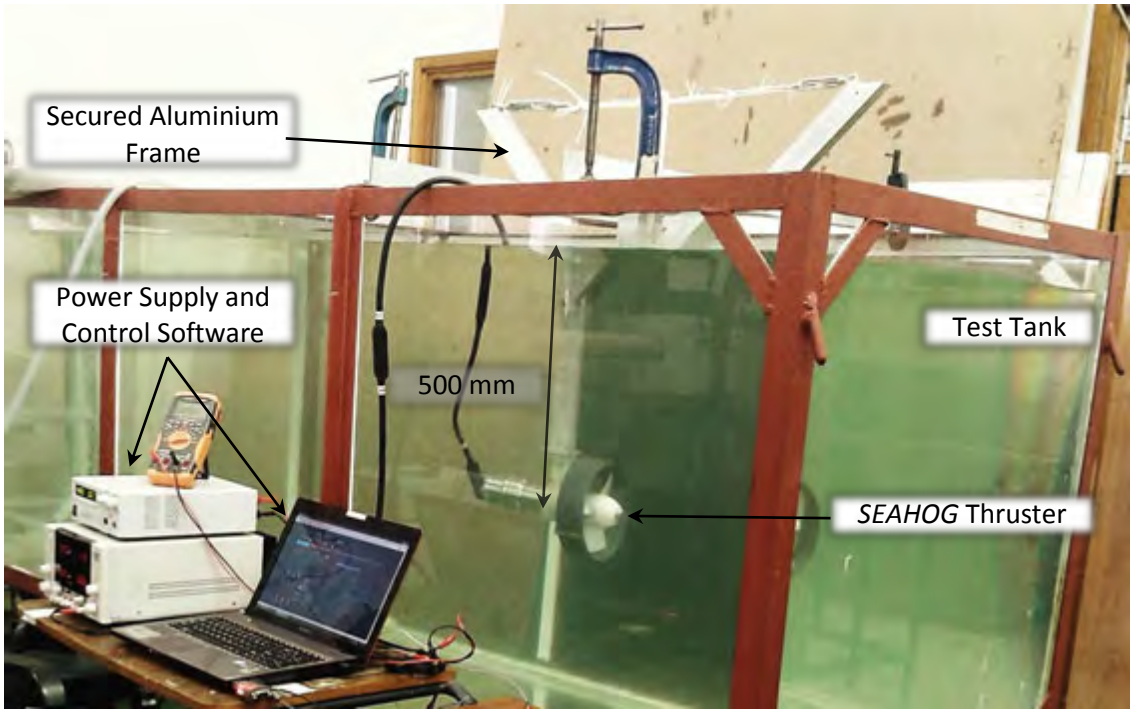

Figure 17 - Test tank used for thruster testing and parameter identification

The thruster subsystem was tested independently of the rest of the ROV using custom designed LabVIEW data logging software. The communication setup closely mimicked that of the ROV itself, with the laptop communicating to the thruster via a virtual serial port on an RS485 network. The system network architecture for the communications between a controller and the thrusters had not been defined at the time of this project and thus it was assumed that any extra media conversion latency that would take place on the actual ROV network would be negligible for the purposes of developing this thruster model.

Now that an overview of the *SEAHOG* thruster, drive train, communication network, testing methods and data capture methods have been given, detailed system identification can begin on individual parts of the thruster. The next section will focus on creating a model of the Maxon Brushless DC (BLDC) motor.

3.5 Maxon EC-max Brushless Motor Model

3.5.1 Introduction

This section will develop the model for the BLDC motor used to actuate the *SEAHOG* thruster's propeller. Figure 18 below shows the motor sub-diagram within the greater scheme of the thruster model.

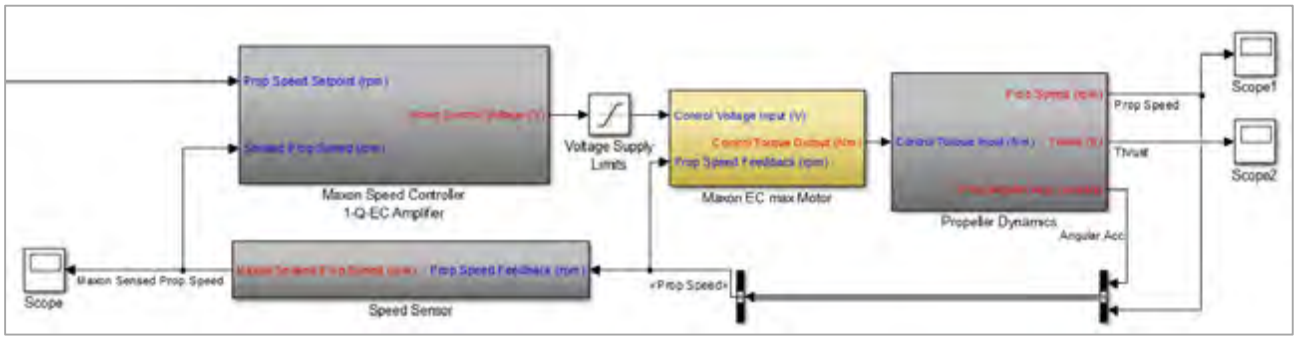

Figure 18 - Thruster model sub-diagram of interest for motor model development in yellow

This section will develop the highlighted sub-diagram, resulting in a fully defined motor model for the thrusters.

3.5.2 Introduction to BLDC Motors

BLDC motors are typically modelled as a brushed motor, with the resistance and inductance values being twice the value of one of the motor windings as shown below in Figure 19 [25].

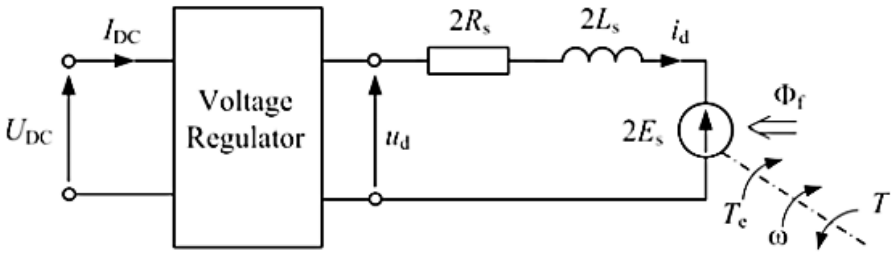

Figure 19 - Approximation of a BLDC motor as a special case of a DC motor [25]

The reason that values of $2R_s$ and $2L_s$ are used above is due to the construction and winding of a BLDC motor. When the motor is wound in a "Wye" configuration, common in BLDC motors, current flows through two coils every excitation cycle. This is clarified following in Figure 20: as the rotor rotates through positions 101 to 001, the three coils: a, b and c, will be polarised in different ways. The left hand side of Figure 20 following shows the levels of signals from the different Hall Effect sensors and the voltages

applied to each corresponding coil as the rotor rotates. The right hand side of the diagram shows the physical motor, its coils and how current flows through them for each excitation cycle, 1 to 6.

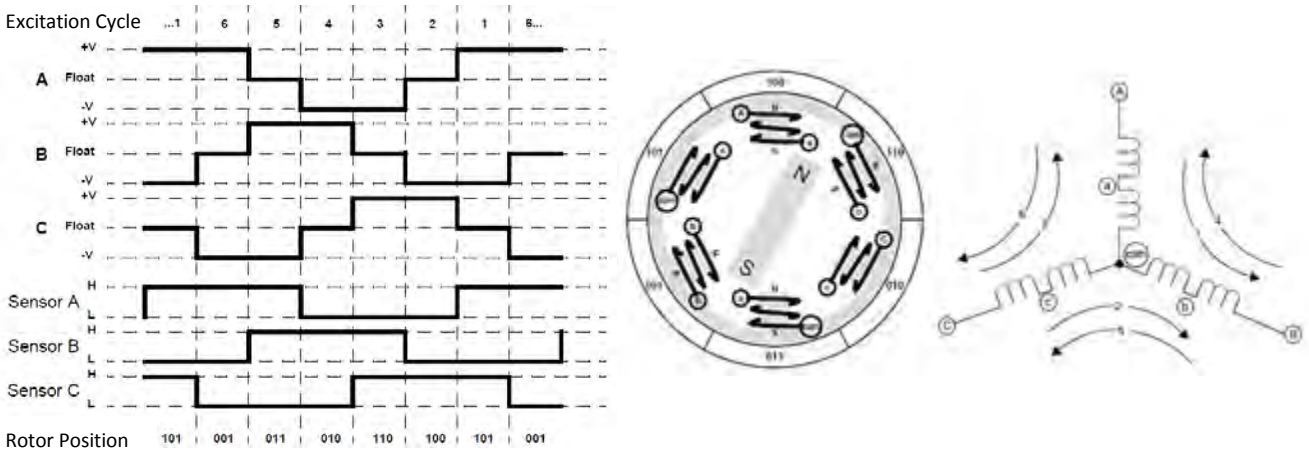

Figure 20 - BLDC motor operation cycle for one revolution [26]

When studied in detail, Figure 20 gives a very comprehensive and clear demonstration of the workings of a BLDC motor. This completes the general introduction of BLDC motors and allows the Maxon EC-max motor to be described specifically in the next section.

3.5.3 Maxon EC-max 40 Motor Characteristics

Important characteristics taken from the Maxon motor datasheet are presented in Table 4 below along with the symbols used to describe the quantity.

Table 4 - Maxon EC-max 40 motor characteristics

Nominal Supply Voltage	V_{nom}	48 V
Continuous Power Rating	P_c	120 W
No Load Speed	n_{nl}	10100 ±1010 rpm
No Load Current	I_{nl}	0.16 to 0.31 A
Nominal Speed	n_{nom}	9250 rpm
Nominal Current	I_{nom}	4.06 A
Nominal Torque	T_{nom}	0.17 Nm
Torque Constant	k_t	44.8 mNm/A
Speed Constant	k_s	1/213 V/rpm
Terminal Resistance, Phase to Phase	R	1.03 Ω
Terminal Inductance, Phase to Phase	L	0.204 mH
Stall Torque	T_s	2.09 Nm
Starting Current	I_s	46.6 A
Gearbox Reduction Ratio	N	12
Maximum Motor Efficiency	$\eta_{m\,max}$	85%
Maximum Gearbox Efficiency	η_{gb}	83%

The symbols presented in Table 4 will be used in the following section during the model development and serve as a reference for future work that references parameters related to the Maxon motor.

3.5.4 Motor Model and Transfer

The equations that govern the operation of a BLDC motor are derived from the circuit diagram presented previously in Figure 19. The torque generated by the motor is a function of the current in the motor coils and is related to the torque constant, k_t through:

$$\tau_{motor}(t) = k_t i(t) \quad \{3.55\}$$

where $i(t)$ is the current flowing in the motor coil. The current is a function of the voltage over the coil which can be expressed as:

$$i(t) = \frac{V_m(t)}{Z(t)}$$
$$V_m(t) = V_a(t) - e(t) \quad \{3.56\}$$
$$Z(t) = R + L\frac{di}{dt}$$

with:

V_m - Voltage over motor coil impedance

V_a - Applied voltage to terminals

e - Back EMF

Z - Impedance of the motor coil

It should be noted that while, as shown in Figure 19 previously, current passes through two motor coils per excitation cycle, the values given in Table 4 for resistance and inductance represent terminal to terminal values – meaning that they do not need to be multiplied by two as this effect has already been accounted for in the way that the values were obtained.

The back EMF is related to the rotational speed of the motor shaft and the speed constant, k_s through:

$$e(t) = k_s n_m(t) \quad \{3.57\}$$

where n_m is the motor shaft speed.

Equations 3.55, 3.56 and 3.57 can be combined to give the torque generated by the motor as:

$$\tau_{motor}(t) = k_t\big(V_a(t) - k_s n_m(t)\big) \times \frac{1}{R + L\frac{di}{dt}} \quad \{3.58\}$$

Taking the Laplace transformation of equation 3.58 gives us the transform for the Maxon motor in the s plane:

$$\tau_{motor}(s) = k_t\big(V_a(s) - k_s n_m(s)\big) \times \frac{1}{R + Ls} \quad \{3.59\}$$

where the values for constants in the above equation can be found in Table 4, given previously.

A Note on Efficiency and Friction: It should be noted that the efficiency of the motor, the gearbox and the magnetic coupling will play a role in reducing the torque that reaches the propeller from the motor. The values given previously in Table 4 for efficiency of the gearbox and motor are the maximum efficiencies

that are achievable according to the datasheet. This means that the effects such as wear, friction and operating temperature will have an effect on the efficiency, possibly causing it to deviate from the given values. The gearbox efficiency can be assumed to be fairly constant over the operational speed range of the motor due to the efficiency factor of the gearbox being related largely to the angle of contact of the gear teeth. The motor however will have frictional effects that will result in a varying efficiency depending on the speed of the motor. Quantified data was not available for the effects of friction in the motor and therefore it was necessary to derive an expression for the motor friction using the given motor data. In addition, the efficiency of the magnetic coupling needed to be experimentally determined. The following two subsections will derive expressions for the motor frictional effects and the magnetic coupling efficiency.

3.5.5 Derivation of Motor Friction and Efficiency

Aim: To quantify the frictional effects within the motor and the motor efficiency as a function of the motor speed using given motor data.

Background and Theory: It is expected that the frictional effects in a motor will be modelled as a constant "stiction" value, combined with a linear friction that is related to the speed of the motor such that:

$$T_f = A + k_{fr}\omega \qquad \{3.60\}$$

According to the motor datasheet, the maximum efficiency factor of the motor is 85%.

Isolating the motor allows it to be modelled as follows in Figure 21.

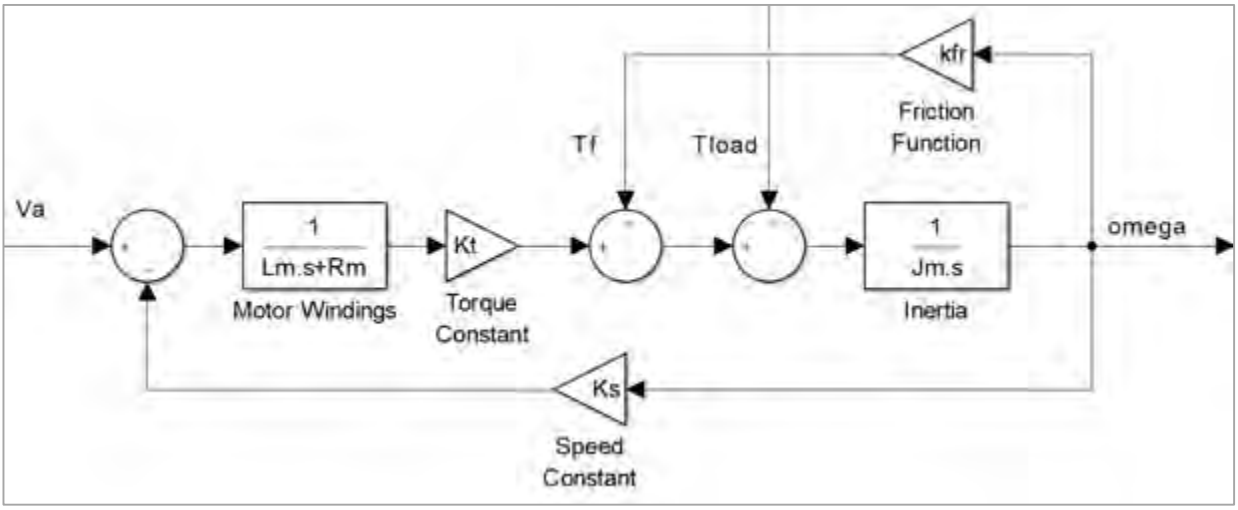

Figure 21 - Generic block diagram of a DC motor

This subsection will focus on defining the torque input Tf as shown above in the figure.

Using the stall characteristics of the motor (when ω = 0), the static friction can be determined. With the static friction determined, the no-load characteristics of the motor (when Tload = 0) can be used to define the linear friction coefficient.

Method: Due to tolerances in the given data for the motor, it is important to determine values that correlate with each other mathematically for the purposes of defining the friction torque. This is necessary because it is unclear from the datasheet which values were measured while including the motor efficiency and what the motor efficiency is for that particular operating scenario. For example, the start-up or stall current is given as 46.7 A in the datasheet. As a check:

$$I_s = \frac{V_a}{R_m} = \frac{48}{1.03} = 46.6\ A \approx 46.7\ A \quad \{3.61\}$$

Therefore, the start-up current correlates well to the value given in the datasheet and will therefore be used in the calculations following.

At stall conditions, $\omega = 0, T_{net} = 0$ and $T_{load} = T_s$, therefore, using the stall conditions of the motor:

$$T_{net} = T_m - T_f - T_{load} = Ik_t - T_f - T_s = 46.7 \times 0.0448 - T_f - 2.09 = 0$$
$$T_f = 0.002\ Nm \quad \{3.62\}$$

The above T_f value is at zero motor speed and therefore, using equation 3.60, $A = 0.002$.

Once again, to check that the given data correlates mathematically, the actual no-load speed is found by assuming the no-load current reading is accurate:

$$n_{nl} = \frac{V_a - I_{nl} \times R_m}{k_t} = \frac{48 - 0.31 \times 1.03}{0.0448} = 1064\ rad/s = 10163\ rpm \quad \{3.63\}$$

10163 rpm falls within the tolerance of the no-load speed specification from Table 4 and can therefore be used as the no-load speed in the following calculations.

At no-load motor conditions, $T_{load} = 0$ and $T_{net} = 0$ therefore:

$$T_{net} = T_m - T_f - T_{load} = 0.31 \times 0.0448 - T_f - 0 = 0$$
$$T_f = 0.0139\ Nm \quad \{3.64\}$$

Using equation 3.60 to solve for k_{fr} gives $k_{fr} = 1.12 \times 10^{-5} Nm/(rad/s)$.

As a check, the nominal motor characteristics can be used to see if they correlate with the derived model of friction. Checking the nominal motor speed by assuming that the motor efficiency is not included in the operating scenario gives a nominal speed of:

$$n_{nom} = \frac{V_a - I_{nom} \times R_m}{k_t} = \frac{48 - 4.06 \times 1.03}{0.0448} = 978\ rad/s = 9340\ rpm \quad \{3.65\}$$

Using a motor speed of 9340 rpm, the friction torque can be determined for nominal motor conditions as:

$$T_{net} = T_m - T_f - T_{load} = 4.06 \times 0.0448 - T_f - 0.17 = 0$$
$$T_f = 0.0119\ Nm \quad \{3.66\}$$

Solving for k_{fr} gives $k_{fr} = 1.01 \times 10^{-5} Nm/(rad/s)$, which is within 10% of the value determined under no-load conditions previously.

Therefore, taking an average of the two k_{fr} values, the friction within the motor can be modelled as:

$$T_f = 0.002 + 1.07 \times 10^{-5}\omega\ [Nm] = 0.002 + 1.12 \times 10^{-6} n\ [Nm] \quad \{3.67\}$$

Analysis and Conclusion: The speed at which maximum motor efficiency is achieved was not given on the datasheet. It would therefore be useful to find a curve of motor efficiency vs. motor speed. The motor efficiency is generically defined as:

$$\eta = \frac{P_{out}}{P_{in}} = \frac{\omega \times T_{load}}{V_m \times I} = \frac{\omega \times T_{load}}{V_m \times \frac{V_a - k_s\omega}{R_m}} \quad \{3.68\}$$

where, under no acceleration:

$$T_{net} = \underbrace{\frac{V_a - k_s\omega}{R_m} k_t}_{T_m} - \underbrace{(0.002 + 1.07 \times 10^{-5}\omega)}_{T_f} - T_{load} = 0$$

$$T_{load} = \frac{V_a - k_s\omega}{R_m} k_t - (0.002 + 1.07 \times 10^{-5}\omega) \quad \{3.69\}$$

Combining the above two equations and substituting in different motor speed values yields the curve shown following in Figure 22.

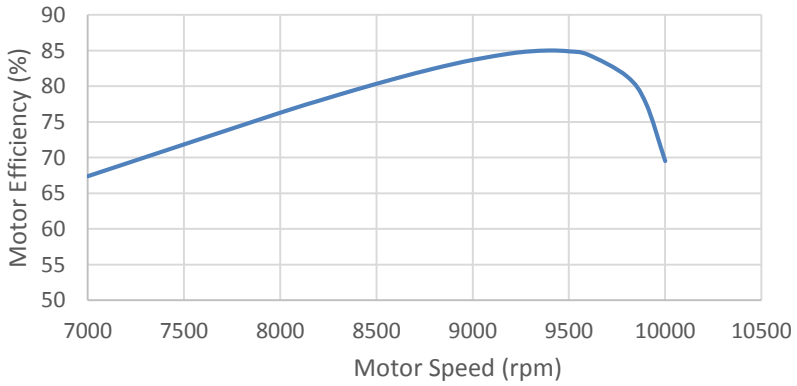

Figure 22 - Efficiency for Maxon EC-max 40 motor vs. motor speed

The graph correlates very well with the maximum efficiency value given by the datasheet of 85%. The maximum efficiency obtained was 85.03% at 9400 rpm motor speed.

This completes the derivation of an expression for the friction torque contribution in the motor, along with its efficiency characteristics. The following section will derive an expression for the efficiency of the magnetic coupling.

3.5.6 Magnetic Coupling Efficiency Test

Aim: To find the efficiency of the thruster magnetic coupling in water as a function of the propeller speed.

Background and Theory: Stainless Steel 316 forms the membrane between the outer and inner rotor of the thruster magnetic coupling. This material was chosen due to its low magnetic conductivity and thus its resistance to the formation of eddy currents in the membrane. Cold working that occurred during manufacture of the membrane however, is known to make stainless steel more susceptible to induced eddy currents. Eddy currents result in a magnetic braking effect, resisting the movement of the magnets around the membrane. The currents induced are proportional to the speed of rotation of the coupling, and thus a dynamic efficiency is expected from the coupling. It is expected that the power dissipated by the coupling will be quadratically related to the speed of the coupling rotation [27].

If the motor current draw is measured under the influence of only the motor and gearbox efficiency and then with the magnetic coupling attached, the efficiency of the magnetic coupling can be calculated as:

$$\eta_{coupling} = 1 - \frac{I_{with\ coupling} - I_{without\ coupling}}{I_{with\ coupling}} \quad \{3.70\}$$

Method: The motor was driven at different constant speeds in a horizontal orientation outside of the housing with the magnetic coupling removed and the current draw of the motor was measured. The thruster was then assembled with the magnetic coupling attached and the propeller removed. It was an assumption that the smooth outer surface of the magnetic coupling would not exert a significant load on the motor due to the water resistance in a steady state condition. The motor was then driven at different constant speeds in water and the current draw was measured using the procedure outlined in section 3.6.4.

Results: Equation 3.70 was applied to the current readings to give a coupling efficiency shown following in Figure 23.

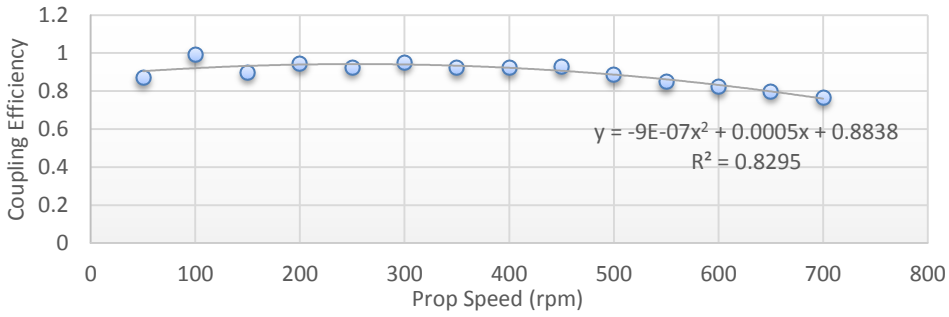

Figure 23 - Efficiency of *SEAHOG* thruster magnetic coupling vs. prop speed

A quadratic trend line was added due to the expected quadratic correlation of the data. The value expected at 0 rpm represents the efficiency of the coupling due to its friction alone, with the eddy current power dissipation component being zero.

Analysis: The local maximum is not centred over 0 rpm. This is expected however, since the dynamic friction of the Vesconite bearings will be lower than their static friction, resulting in slightly decreased friction at greater speeds. It can be seen that at approximately 300 rpm the effect of eddy current braking overcomes the reduced friction of the bearings, decreasing the overall coupling efficiency.

Conclusion: A describing function for the dynamic efficiency of the magnetic coupling can be expressed as:

$$\eta_{coupling} = -9 \times 10^{-7} n_{prop}^2 + 0.0005 n_{prop} + 0.8838 \quad \{3.71\}$$

Eddy current braking results in an efficiency loss of about 10% when measured from the maximum friction contribution to the efficiency factor, to the maximum eddy current braking contribution

3.5.7 Summary and Motor Block Diagram

Combining equations 3.59, 3.67 and 3.71, and taking into account the gearbox reduction ratio of 12, gives the overall transfer for the torque input to the propeller as a function of the voltage input to the motor:

$$\tau_{prop}(s) = 12\eta_{coupling}\eta_{gearbox}\left[k_t\left(V_a(s) - k_s n_m(s)\right) \times \frac{1}{R + Ls} - \left(0.002 + 1.12 \times 10^{-6} \times 12 n_{prop}\right)\right] \quad \{3.72\}$$

The Simulink® block diagram that was created for the Maxon motor is given following in Figure 24 with inputs in blue and outputs in red. Note that N1 and N represent the gearbox ratio effect of reducing speed and increasing torque. A 10 A current limit is applied as this is the maximum output current by the Maxon motor controller. Finally, the "Friction Signal Conditioning" sub-diagram ensures that the stiction contribution to the friction function does not exert a torque so as to accelerate the motor from rest in the opposite direction to the applied torque.

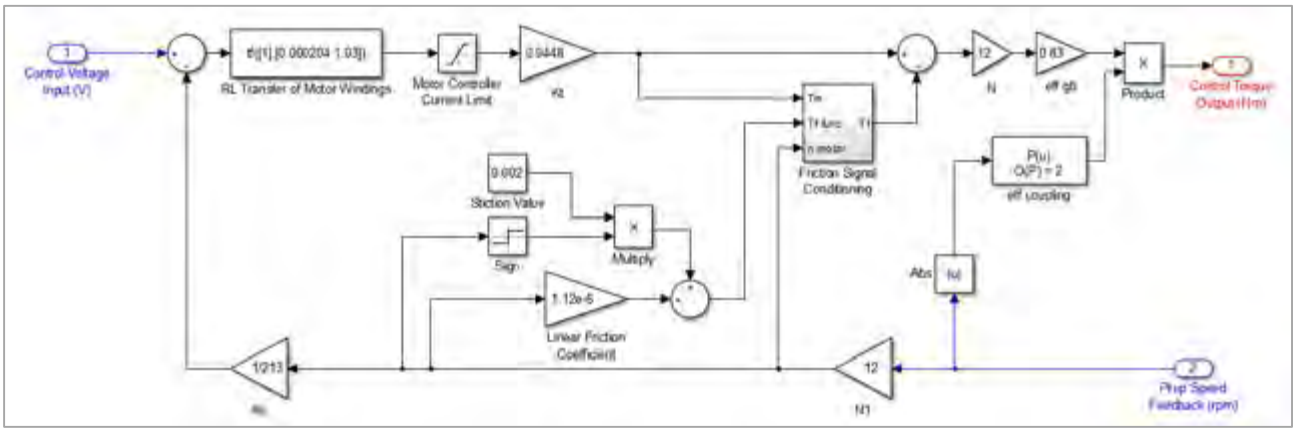

Figure 24 - Simulink® model of the Maxon EC-max 40 BLDC motor

This completes the description and development of the Maxon motor model, allowing it to be integrated into the rest of the model. With the torque output from the motor defined, the propeller model can now be developed so that the thrust output from the thruster can be determined.

3.6 System Identification – Single State Propeller Model

3.6.1 Introduction

With the input torque to the propeller approximated, it is possible to develop the chosen one-DOF propeller model for the *SEAHOG* propeller. Figure 25 below shows the sub-diagram of interest for this section highlighted in yellow within the overall thruster model. Complete sub-diagrams are shown in green.

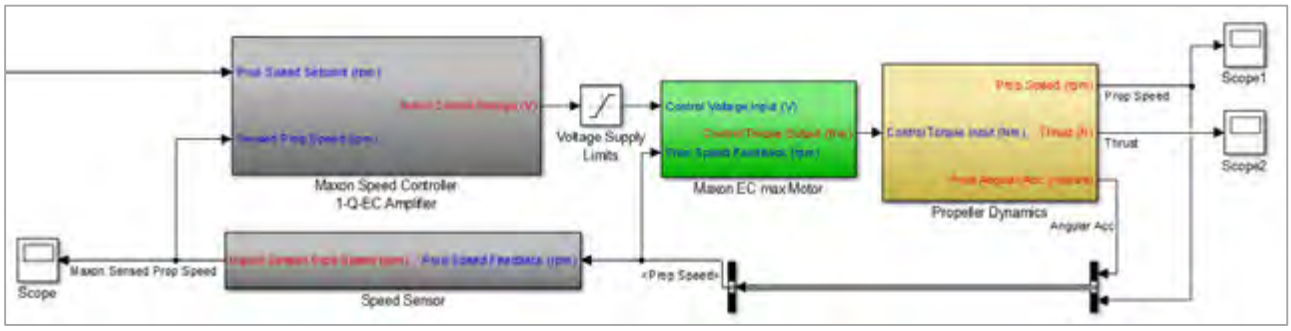

Figure 25 - Thruster model sub-diagram of interest for propeller model development in yellow

Recall that the thruster model to be used in this section has been defined previously in this report and is expressed as equations 3.52 and 3.53:

$$\dot{\Omega} = \beta\tau - \alpha\Omega|\Omega|$$

$$T = C_t\Omega|\Omega|$$

with:

$$\beta = \frac{1}{\eta^2 p^2 \rho V}, \quad \alpha = \frac{\eta p A}{2V}, \quad C_t = A\rho\eta^2 p^2$$

Some of the data presented in this section (such as the propeller thrust vs. speed results) was obtained and presented in [24] to better characterise the development carried out on the *SEAHOG* thruster in that project. If more insight is desired into the development of the thruster module and the methods in which the data was obtained, see [24].

The following constants presented in Table 5 were known before testing took place, due to them corresponding directly to the physical thruster system and environment.

Table 5 - Known thruster model constants pre testing

Constant	Value
Density of Fresh Water	1000 kg/m^3
Propeller Blade Pitch	0.036 m
Propeller Duct Area	0.0241 m^2

The *SEAHOG* is designed to operate in the ocean but, as previously mentioned, testing was carried out in a freshwater tank – hence the density of freshwater is used for the purposes of obtaining values in this testing.

The previous section derived the torque transmitted to the propeller by the motor as a function of the control voltage applied to it and the propeller speed. The purpose of this section is to determine numerical values for the constants β, α and C_t and then to verify the constants. An approach was taken that is similar to the original paper that developed the thruster model [17]. This section will use experimental data to obtain values for the thruster model's unknown constants, detailing the process used to obtain them.

3.6.2 Thrust vs Prop Speed Squared to Obtain C_t

The squared relationship between thrust (T) and prop speed squared ($\Omega|\Omega|$) is linear and proportional to C_t. The thrust generated by a *SEAHOG* thruster in the forward and reverse direction is given following in Figure 26. It can be seen that there is a slight difference in thrust in either direction, despite the thruster's symmetrical propeller.

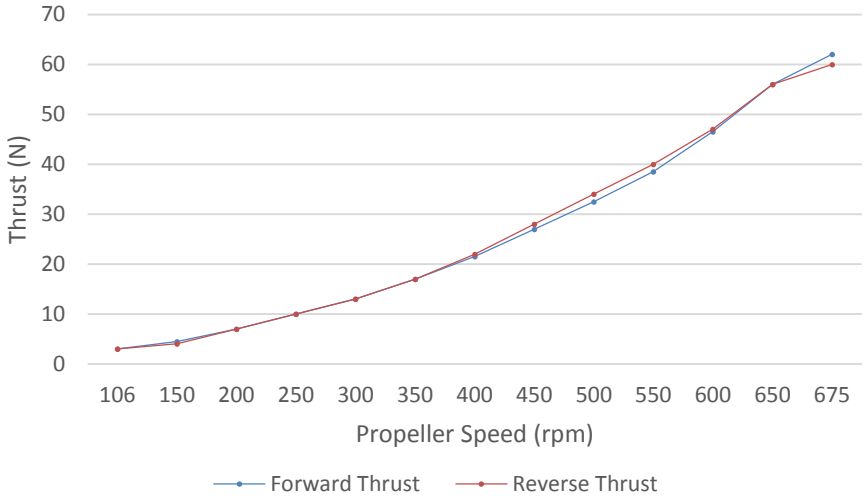

Figure 26 - Thrust generated by a *SEAHOG* thruster in the forward and reverse directions according to propeller speed

It should be noted that the thrust values used in Figure 26 are the average values of a series of tests that were carried out. Using the thrust values, the propeller speed squared could be plotted against the thrust produced, yielding the following results in Figure 27.

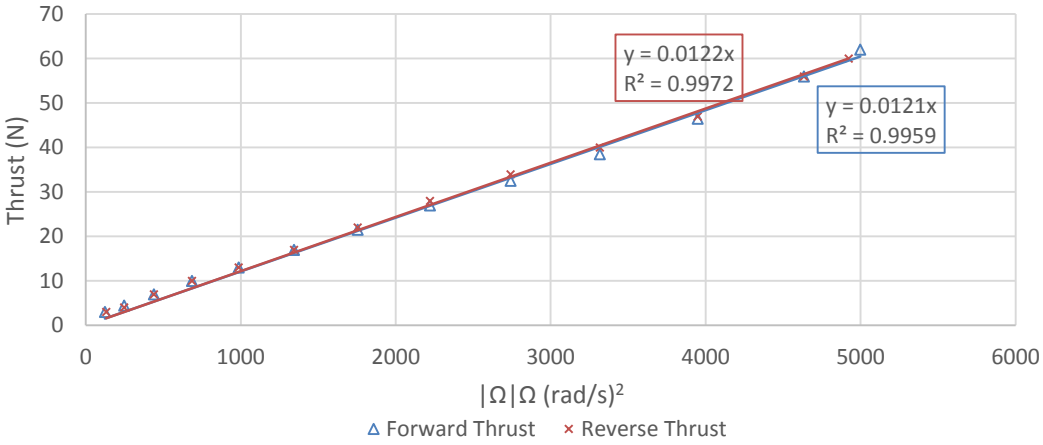

Figure 27 - Graph of thrust vs. propeller speed squared for forward and reverse directions

As expected, there is a great correlation of the data with a very similar trend for both the forward and reverse directions. The gradients of the lines are used directly as the C_t values – 0.0121 for the forward direction and 0.0122 for reverse.

Using the definition for C_t:

$$C_t = A\rho\eta^2 p^2$$

it was possible to solve for the propeller efficiency. The propeller yielded an efficiency of 62% in both directions. This efficiency is impressive but certainly achievable for a propeller of this type [28].

3.6.3 Steady State Response to estimate β/α Ratio

It is possible to obtain a ratio for β/α from constant propeller speeds. Recall from equation 3.52:

$$\dot{\Omega} = \beta\tau - \alpha\Omega|\Omega|$$

but with constant propeller speeds, $\dot{\Omega} = 0$ and thus the equation can be arranged to give:

$$|\Omega|\Omega = \frac{\beta}{\alpha}\tau \qquad \{3.73\}$$

This equation can be used to later verify the constants β and α when they are individually derived from dynamic sequences of data i.e. when $\dot{\Omega} \neq 0$. The torque input to the propeller was found using the previously developed motor model:

$$\tau = 12\eta_{gearbox}\eta_{coupling}[k_t \times I_{motor} - T_f] \qquad \{3.74\}$$

Figure 28 following shows the β/α ratio for the forward and reverse directions in the form of the trend line gradient. A value of 3782.3 $N^{-1}s^{-2}$ and 3921.0 $N^{-1}s^{-2}$ was obtained for the forward and reverse propeller directions respectively.

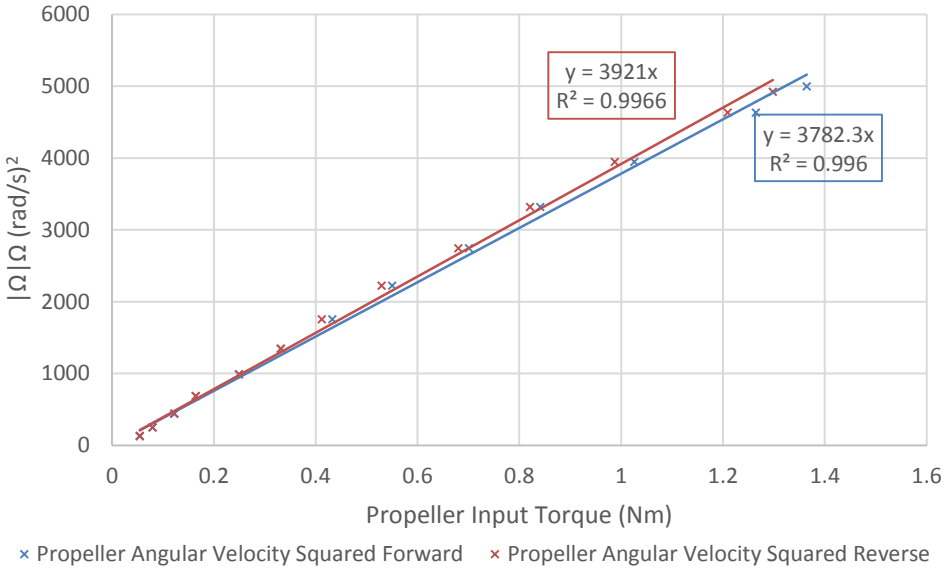

Figure 28 - Graph of propeller velocity squared vs. propeller input torque

Figure 28 gives a ratio for the constants but they cannot be individually determined without dynamic data. While it appears that the definitions of α and β:

$$\beta = \frac{1}{\eta^2 p^2 \rho V}, \quad \alpha = \frac{\eta p A}{2V}$$

can be used to determine their values now that the propeller efficiency is known, substituting the volume enclosed by the propeller duct for V would be incorrect. This is because the effective involved volume of water that is used in the energy balance derivation of the model may differ from the volume enclosed by the duct. Therefore the volume is still an unknown quantity and a dynamic data sequence was necessary to determine the individual constant values. The following section will present a dynamic sequence that will allow numerical values of β and α to be obtained.

3.6.4 Dynamic Response to determine α and β

Method:

A least squares linear regression can be performed on the thruster model:

$$\dot{\Omega} = \beta\tau - \alpha\Omega|\Omega|$$

if a sequence of values corresponding to a dynamic thruster response is obtained. If the propeller speed (Ω) and propeller input torque (τ) are known for each time step then the regression can be used to determine α and β.

It was necessary to have a function that estimated the applied torque to the propeller to perform the regression. Torque inputted to the propeller is related to the current in the motor coils and estimated by equation 3.74. Therefore the current in the motor coils along with the propeller speed was measured and logged during the dynamic test sequence with a National Instruments 9201 ADC Data Acquisition (DAQ) unit. Both the propeller speed and the current draw were logged simultaneously, giving enough data to plot and analyse sets of $\dot{\Omega}$, τ and $\Omega|\Omega|$ against the propeller speed state equation.

Current Measurement:

The simplest method to measure the current in a motor coil is to measure the voltage across a shunt resistor placed in series with the motor coil. The resistance of the shunt resistor must be much smaller than that of the coils so as to influence the behaviour of the motor as little as possible. A differential amplifier was used to amplify the voltage over the resistor and condition it for the correct range of inputs into the National Instruments DAQ unit. The sensing circuit is given following in Figure 29, with its corresponding circuit component values given in Table 6 following.

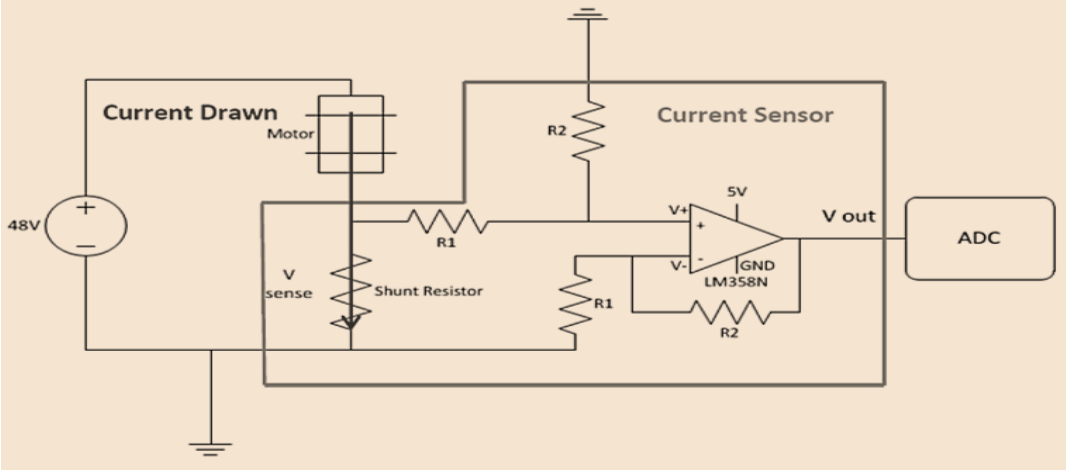

Figure 29 - Current sensing circuit used to measure current draw vs prop speed

Table 6 - Current sensing circuit values

Motor Winding Resistance	1.03 Ω
Max Motor Current	4 A
Shunt Resistance	0.1 Ω
R1	1 kΩ
R2	10 kΩ

To compensate for the operational current draw of the motor controller circuitry, the current was calibrated with an ammeter in series with the motor coil. The ammeter readings were compared to the ADC readings to yield the following linear relationship:

$$I_{motor} = 1.0135\, V_{ADC} - 0.0245 \quad \{3.75\}$$

Each current reading could now be transformed into an approximate propeller input torque value using the torque constant of the motor and the efficiencies of the drivetrain substituting equations 3.71 and 3.75 into equation 3.74:

$$\begin{aligned} \tau &= 12\eta_{gearbox}\eta_{coupling}\left[k_t \times I_{motor} - T_f\right] \\ &= 12 \times 0.83 \times \left(-9 \times 10^{-7} n_{prop}^2 + 0.0005 n_{prop} + 0.8838\right)\left[0.0448\right. \\ &\qquad \left. \times \left(1.0135 V_{ADC} - 0.0245\right) - \left(0.002 + 1.12 \times 10^{-6} \times 12 n_{prop}\right)\right] \end{aligned} \quad \{3.76\}$$

Experimental Setup:

Throughout this report, the following dynamic sequence of numbers is used for all thruster propeller speed evaluations that only rotate the propeller in a single direction. The sequence consists of 22 randomly generated steps of different levels inputted at a frequency of 1 Hz. The thruster propeller speed and current draw data was captured at a rate of 40 Hz, providing sets of 880 data points. The setpoint and thruster speed response is shown following in Figure 30. It can be seen that the forward and reverse responses are very similar and thus the constants α and β are expected to be similar regardless of rotation direction.

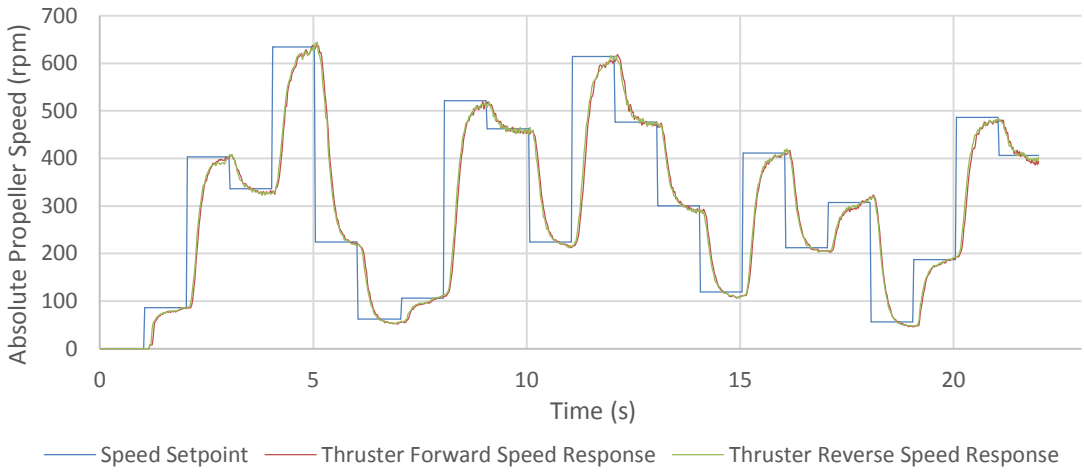

Figure 30 - Graph showing the set-point and thruster speed response over time for the dynamic single direction test sequence

It was necessary in this test, however, to filter the current readings due to the large amount of noise inherent in them. In order to prevent the filter from changing the nature of the system response, both the current and the speed readings (input and output) were taken after being filtered in the same manner by filters that did not form part of the loop itself. This effectively cancelled the effect of the filtering and allowed a true representation of the system to be obtained. Moving average filters were applied to the readings. Tests were run four times for both reverse and forward directions with varying amounts of elements in the moving average array. Figure 31 following demonstrates how filtering affects the readings obtained by showing the filtered and unfiltered outputs and inputs to the system.

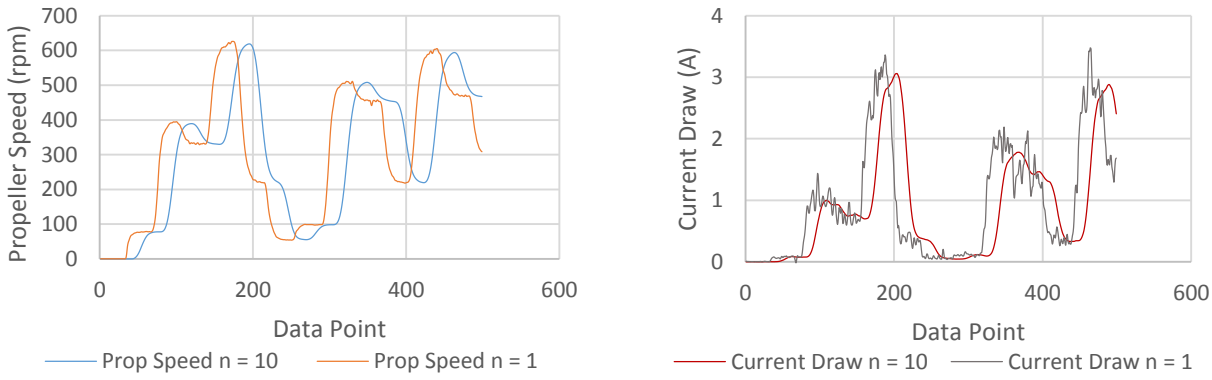

Figure 31 - Filtered and unfiltered speed and current values with a moving average filter

Figure 31 shows the speed and current draw of a test sequence with 10 elements and 1 element in the moving average array respectively. It can be clearly seen that the unfiltered current readings are very noisy, especially at higher speeds. The phase lag introduced by the filter can be clearly seen in both the speed and current data, demonstrating the necessity for filtering both the speed and current readings to mitigate this effect.

The dynamic test sequence was carried out for filter values of 20, 10, 5 and 1 to gain an understanding of how the filter was effecting the data values and correlations. This provided enough data to run linear regressions in Microsoft Excel and obtain values for β and α.

Results:

Least squares regression was applied to the forward and reverse thruster speed profiles in Microsoft Excel to obtain values for constants β and α. The results of the linear regression mapping is shown below in Table 7.

Table 7 - Thruster model coefficients from dynamic tests

Forward Direction		Reverse Direction	
β/α – Static Case	3782	β/α – Static Case	3921
β/α – Dynamic Case	4073	β/α – Dynamic Case	3928
% Difference	7.69	% Difference	0.18
β	64.5 $N^{-1}s^{-2}$	β	80.6 $N^{-1}s^{-2}$
α	0.016	α	0.021

In addition to the above results, the unknown system constants defined in equation 3.54 that are part of β, α and C_t could now be found. The only remaining unknown constant was the involved fluid volume of the system (V). This was found to be 0.0169 m^3 and 0.0143 m^3 for the forward and reverse directions respectively.

With all the constants obtained for the thruster model it was possible to analyse the results to verify if they were realistic.

3.6.5 Analysis and Verification of Constants

The ratio β/α could be verified by comparing the static to the dynamic result. As presented in Table 7 previously, there is a 7.14% and a 0.18% difference in the static and dynamic cases for forward and reverse respectively. These are both close results, especially in the reverse direction. They were deemed acceptable because there could have been some model discrepancy due to assumptions made in how the data was obtained – namely, how the propeller input torques were estimated from the current measurements. In addition, the actual efficiency of the gearbox and the motor could have varied from the given and derived cases. In addition, the water flow over the thruster housing will be different for either direction of thrust, which could have affected the dynamic behaviour of the propeller.

To demonstrate the effect of a small change in efficiency on the β/α ratio, the gearbox efficiency of 0.83 was decreased to 0.73 and a new set of dynamic results were derived, which resulted in a 12% increase in the β/α value obtained. This demonstrated the significant effect that a small discrepancy in unknown values could have on the experimentally determined constants.

It was possible to verify that the actual magnitudes of β and α were in the correct range by solving for the involved fluid volume constant V and comparing it to the volume of the thruster duct. It was found in [17], when this model was tested for the first time, that the involved fluid volume was twice that of the volume enclosed by the thruster duct. It is therefore expected that the involved fluid volume may be larger than the thruster duct itself. The results for the *SEAHOG* thruster are shown below in Table 8.

Table 8 - Involved fluid volume difference between thruster duct and dynamically derived cases

Forward Direction		**Reverse Direction**	
SEAHOG thruster - volume enclosed by duct = 0.00192 m^3			
Involved fluid volume V	0.017 m^3	Involved fluid volume V	0.014 m^3
Difference factor	8.68	Difference factor	6.64

Table 8 shows that the value of V is larger than expected, being about eight times larger than the volume enclosed by the thruster duct.

Due to the larger than expected volume discrepancy, a series of simulations were performed on the partially complete system model to further verify the constants. The simulated current draw in the motor was used as an indication of the correctness of the constants due to the following - consider the thruster model:

$$\dot{\Omega} = \beta\tau - \alpha\Omega|\Omega|$$

The greater the α term is, the greater the input torque τ must be and thus the greater the current draw of the motor will be. Therefore, if a steady state condition of a certain speed is simulated, the simulated current draw can be compared to actual current draw readings. This will verify α and since the ratio β/α is known from experimental results, β will also be verified. Results for the verification experiment in the forward thrust direction are given following in Table 9.

Table 9 - Simulated motor current vs. actual motor current draw for different propeller speeds

Prop. Speed (rpm)	**Actual Current Draw (A)**	**Simulated Current Draw (A)**	**% Diff. ($(I_a - I_s)/ I_a$)**
300	0.60	0.66	-10.0
400	1.05	1.16	-10.5
500	1.75	1.83	-4.6
600	2.70	2.5	-0.7

The results from Table 9 are reasonable, given that the actual current draw results were taken from [24] and may have reduced accuracy and the influence of noise inherent in them. The general result of the

simulated and actual current draws being within about 10% of each other was deemed sufficient verification of constants α and β.

The constant C_t for this model was considered verified due to its simple relationship to propeller speed squared. The propeller efficiency is related to the constant C_t and therefore a way that the constant could be checked was by comparing the efficiency value to the efficiencies of similar propellers. It was verified in [28] that an efficiency of 62%, while being impressive, is achievable by this type of propeller.

3.6.6 Summary and Propeller Block Diagram

A summary of all the chosen thruster model constants and parameters and results derived from them are given below in Table 10.

Table 10 - Summary of determined constants and results for the *SEAHOG* propeller model

Forward Direction		**Reverse Direction**	
β	64.5 $N^{-1}s^{-2}$	β	80.6 $N^{-1}s^{-2}$
α	0.016	α	0.021
C_t	0.0121 kg m	C_t	0.0122 kg m
Propeller Efficiency η	0.62	Propeller Efficiency η	0.62
Involved Fluid Volume V	0.017 m^3	Involved Fluid Volume V	0.014 m^3
Propeller Blade Pitch p	0.036 m		
Propeller Duct Area A	0.0241 m^2		
Volume Enclosed by Duct V	0.00192 m^3		

This completes the mathematical description of the physical thruster propeller model. The Simulink® block diagram used in the model is given below in Figure 32 with inputs in blue and outputs in red.

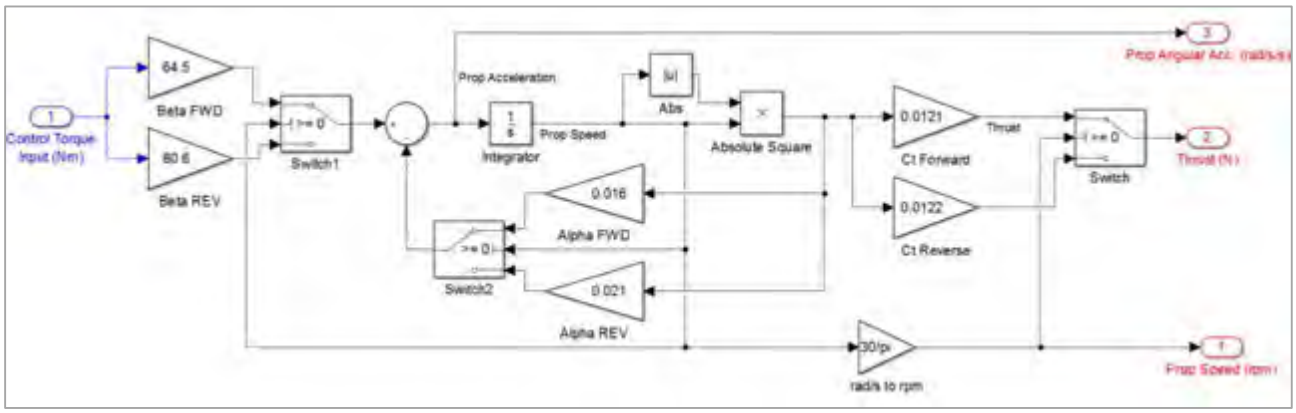

Figure 32 - Simulink® model of a *SEAHOG* thruster propeller

Now that the motor and propeller models have been derived, an investigation into the Maxon digital amplifier can be undertaken in order to approximate its behaviour.

3.7 System Identification – Maxon 1-Q-EC Digital Amplifier

3.7.1 Introduction

Now that the propeller and motor in the *SEAHOG* thruster have been defined and modelled, it is possible to analyse the electronic speed controller that handles part of the closed loop control of the propeller speed. The sub-diagrams to be tackled in this section are highlighted in yellow below in Figure 33. Both of these sub-diagrams form part of the Maxon amplifier and therefore both will be determined in this section. Completed subsystems are shown in green.

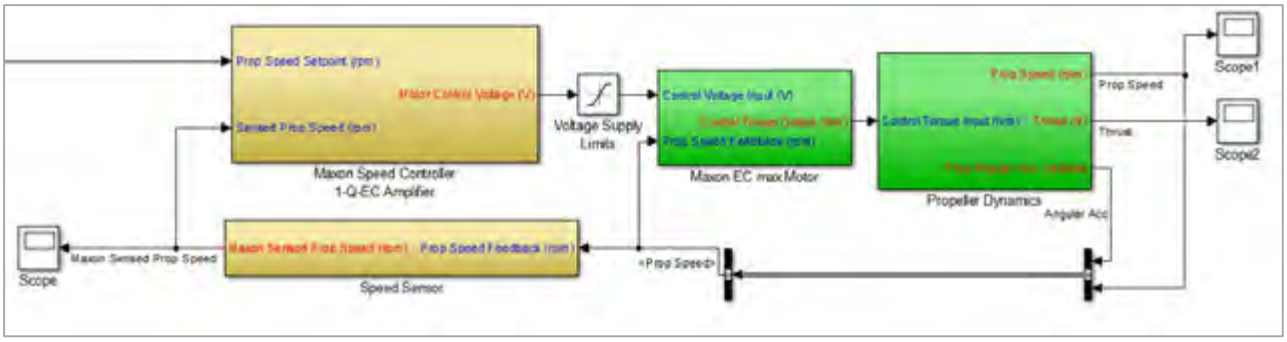

Figure 33 - Thruster model sub-diagram of interest for motor controller model development in yellow

The one quadrant electronically commutated (1-Q-EC) digital amplifier by Maxon Motor was chosen to control the operation of the *SEAHOG* thruster's BLDC motor. More insight is given into the physical and hardware aspects of this controller and how it was integrated into the *SEAHOG* thruster system in [24], if desired. The motor controller implements hardware control of the motor in the form of processing Hall Effect sensor signals and switching motor coil voltage levels at the correct instances. It senses the speed of the motor by monitoring the time between Hall Effect signals and has the ability to implement closed loop speed control in software by varying the PWM duty cycle that is applied to the motor coils, effectively changing the DC control voltage to the motor.

This section will detail the model developed for the Maxon motor controller and verify it under different conditions. Using step functions, the basic control structure will be developed. Once this is satisfactory, dynamic sequences will be used to verify all modes of motor operation are accurate according to the model. The assumptions that were made in the model development will also be noted.

3.7.2 Motor Controller System Setup

The controller receives an analogue voltage between 0-5 V and interprets it as a desired speed through the following equation:

$$n_{des} = \left[\frac{V_{set} - 0.1}{4.9} \times (n_{max} - n_{min})\right] + n_{min}$$
$$V_{set} = \left(\frac{n_{des} - n_{min}}{n_{max} - n_{min}} \times 4.9\right) + 0.1 \quad \{3.77\}$$

where:

n_{des} - Desired motor speed

V_{set} - Analogue setpoint voltage

n_{max} - Maximum control voltage limit

n_{min} - Minimum control voltage limit

The constants n_{max} and n_{min} are set by digital inputs and are 20000 rpm and 500 rpm respectively for the *SEAHOG* thruster. A disadvantage with this is that the no load speed for the chosen BLDC motor is 10100 rpm – meaning that only about half the full control input voltage range of 0-5 V can be utilised, which will decrease the resolution of possible speed setpoints.

The controller outputs the motor speed in the form of a square wave that has a frequency that is related to the motor speed via the equation:

$$f_{Monitor\,n} = \frac{n \times z_{pol}}{20} \qquad \{3.78\}$$

with $f_{Monitor\,n}$ as the square wave frequency and z_{pol} the number of pole pairs of the motor. The *SEAHOG* BLDC motor has one pole pair.

Calibrations and work carried out in [24] ensured and verified that the speed value from the Maxon controller read by the MSP430 control board was a close enough estimate to be deemed as the true propeller speed. It should be noted that the calibrations that were required to obtain correct speed readings on the MSP430 control board imply that there is a possibility the Maxon controller speed sensor that generates the square wave described by equation 3.78 may be inaccurate, for whatever reason. This will be described following in section 3.7.6.

3.7.3 Data Scaling and Conversion

As was shown in Figure 16 previously on page 32, the Maxon controller is supplied an analogue voltage from a ten bit DAC controlled by a Texas Instruments MSP430 microcontroller. Certain limitations on the hardware capabilities of the MSP430 required some simplifications to how the Maxon controller was interfaced with, however. An example of this was how the speed equation 3.77 was implemented. The MSP430 does not have floating point unit (FPU) hardware capability. The extent of the data operations capabilities of the microcontroller are performing fixed-point operations manually through the use of software algorithms.

Due to the data handling limitations of the MSP430 chip, a simplification of equation 3.77 was implemented to convert the desired prop speed command into a value to be sent to the DAC and hence be converted to an analogue voltage for the Maxon controller. The actual values of equation 3.77 are as follows:

$$V_{set} = 0.003015 n_{des} - 0.02564 \quad \{3.79\}$$

For simplification, the constant value of 0.02564 was ignored so that the microcontroller could merely scale the propeller speed reading without an offset. With a 5 V supply and a 10 bit DAC, the scaling value to convert the desired prop speed to a DAC value was determined by equating it to the desired speed coefficient from equation 3.79:

$$\begin{gathered} Scale\ Value \times \frac{5}{1024} = 0.003015 \\ Scale\ Value = 0.6174 \end{gathered} \quad \{3.80\}$$

A value of 0.6172 can be achieved if the desired speed is multiplied by 79 and then bit shifted right seven times. Multiplication and bit shift operations are easily executed by the MSP430, which makes this approximation ideal for speed of execution by the microcontroller. Therefore, the final conversion between desired propeller speed and the corresponding DAC value is:

$$N_{DAC} = \frac{79}{2^7}\, n_{setpoint} = 0.6172\, n_{setpoint} \quad \{3.81\}$$

resulting in an analogue voltage setpoint of:

$$V_{set} = 0.6172 \times \frac{5}{1024}\, n_{setpoint} = 0.003014\, n_{setpoint} \quad \{3.82\}$$

which is close to the original equation, 3.79. It should be noted that the desired propeller speed needs to be multiplied by the gearbox ratio of 12 to obtain the speed setpoint used in equation 3.82 above.

This completes the description of how the input prop speed setpoint is converted to the required analogue voltage input for the Maxon motor controller.

3.7.4 Speed Sensing – Quantisation and Variable Sampling Time

As previously mentioned, the Maxon controller uses the different Hall Effect sensor signals to generate a square wave that is proportional to the speed of the motor as shown previously by equation 3.78. The control MSP430 microcontroller reads in the square wave from the Maxon controller, generating an interrupt on every edge and then calculating the difference in time between the edges and converting it to a motor speed reading. It was assumed that the Maxon controller also exhibits similar sensing methods to the one chosen for the MSP430, since the Maxon controller was modelled in this way in [29]. It should be noted however that calibrations were necessary in [24] to ensure that the speed measurement calculated by the microcontroller was accurate enough to be taken as the actual speed of the motor. Therefore, it is possible that the Maxon controller speed sensor is not completely accurate, for whatever reason. For simplicity, the same sensor approximation was created for both the MSP430 and the Maxon controller and applied in the Simulink® model. Any effects that would result in the Maxon controller not representing the correct speed were applied in the Maxon controller sub-diagram itself in the Simulink® model. More discussion on the Maxon controller's speed sensor is given in section 3.7.6 following.

A similar system to the *SEAHOG* thrusters (a Maxon motor controller and motor) was modelled in [29], where the delays in the system were identified and analysed. It was stated that while sampling delays in electronics are typically negligible compared to the slow mechanical response of a system, small, high speed motors may have mechanical time constants that are in the same order of magnitude as the sampling delays. Table 11 following gives a summary of the relevant time constants in the *SEAHOG* thruster system, showing that both the electrical and mechanical constants are of a similar magnitude.

Table 11 - Time constants in the *SEAHOG* thruster system

Time Constant	Value
Maxon Controller Sampling Rate/Period	250 Hz / 4 ms
Motor Mechanical Time Constant	5.17 ms
Sensor Update Period at deadband limit $n_{prop} = 41.6$ rpm	40.0 ms
Sensor Update Period at $n_{prop} = 700$ rpm	2.38 ms

It should be noted from the above table that there will be a range of sensing update periods from the speed sensor due to how the motor speed directly influences how quickly interrupts are generated in the microcontrollers and hence how quickly speed readings are generated.

Practically, the mechanical time constant of the system will be greater than given in Table 11 due to the table value being for the motor purely, without a gearbox and propeller attached. However it may still be significantly close to the electronics delays due to the range of speed sensing sampling times. The delays in the system due to the control software were identified in [29] as shown below in Figure 34.

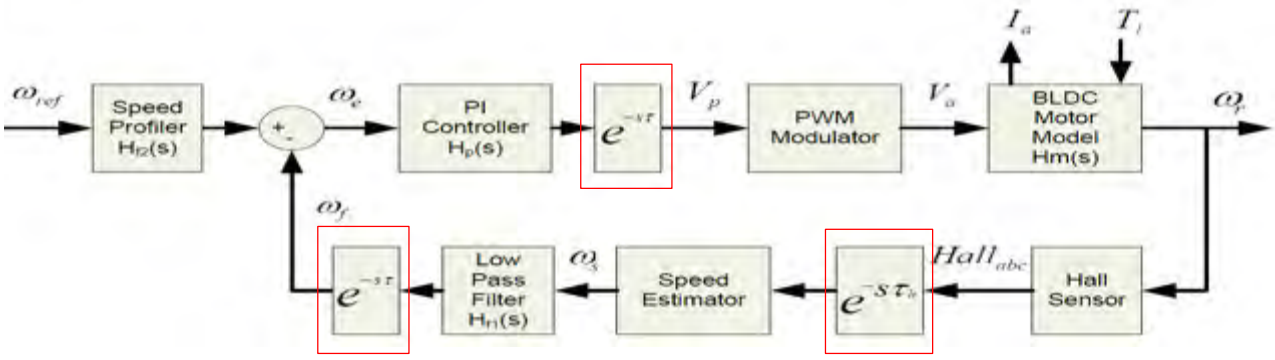

Figure 34 - Control block diagram of a Maxon controller and motor with loop delays present

The resulting Simulink® block diagram that was created for the speed sensor shown previously in Figure 33 is shown following in Figure 35. Due to the decreasing sample time as the motor slows down, a cut-off of ±5 rpm was given as a sensing deadband where the speed reading would be set as zero.

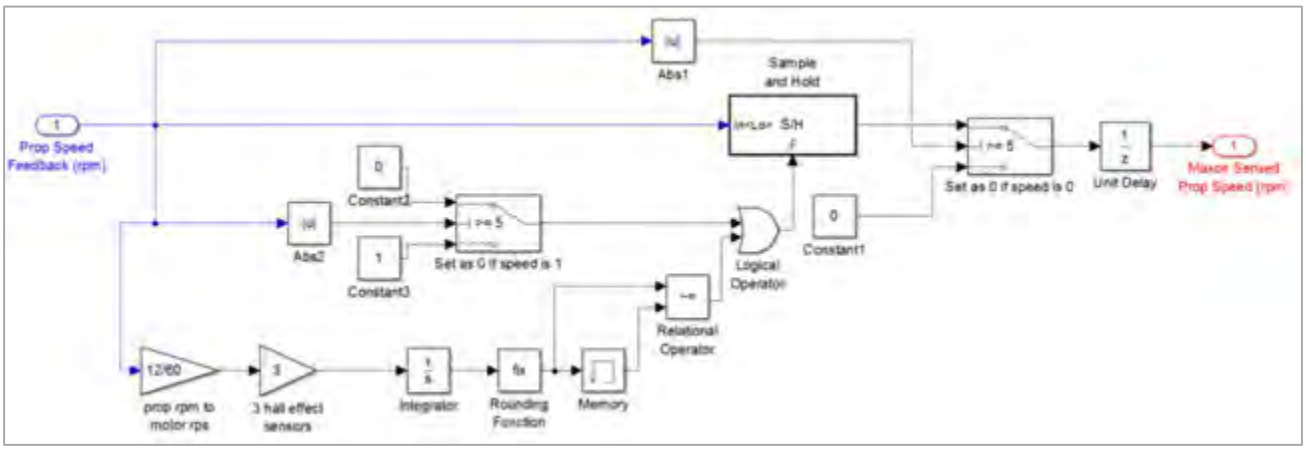

Figure 35 - Speed sensor Simulink® block diagram

The logic of the block diagram is shown following in Figure 36. The principle of the sensor is that for every Hall Effect signal, the speed reading is updated.

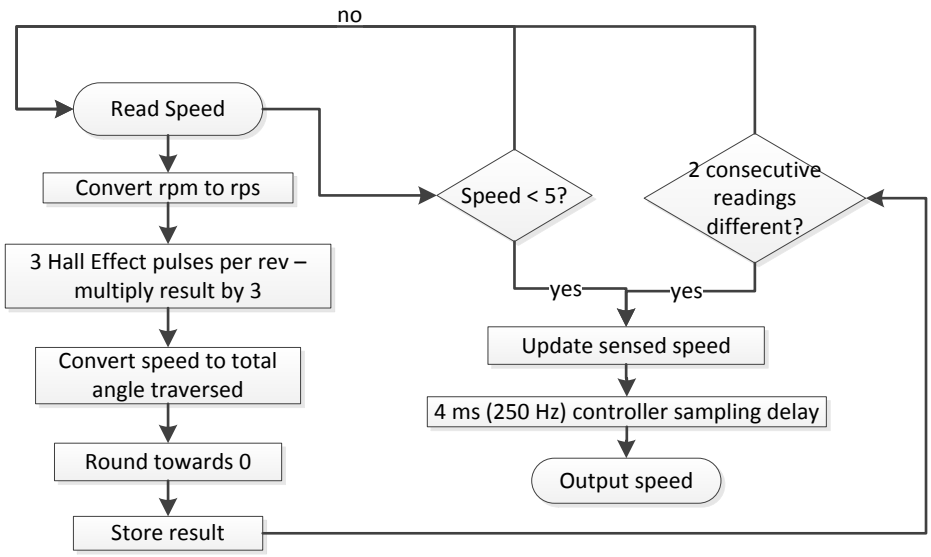

Figure 36 - Speed sensor execution logic

This completes the description of the sampling delays and data quantisation effects present in the thruster system. With the electronic system delays implemented in the model it was possible to apply a simple controller and continue the system identification process.

In the following data set results, it should be noted that the data passed to the user interface testing console is captured one sample delayed to the present time reading, effectively making each sample delayed by 25 ms – which was the rate of communication between the testing operator console and the thruster.

3.7.5 Basic Control Structure and Preliminary Investigations

Maxon would not disclose any information regarding the control scheme used in the controller due to it being proprietary information. It was therefore a challenge identifying this particular part of the thruster system. The only insight given by the controller datasheet was that the closed loop control was of a proportional-integral (PI) scheme. Therefore, with the motor, propeller and speed sensor modelled, a simple PI controller was added to the simulation to control the voltage input into the motor based on propeller setpoints that were scaled as given previously in 3.7.3.

Due to the nonlinear nature of the thruster plant and the possible effects of saturations in the system, step tests spanning the whole operating speed range of the thruster were performed. The integral and proportional gains were tuned to give the correct damping and response. The results of these preliminary step tests are shown following in Figure 37. The actual response is shown in blue and the simulated response is shown in yellow.

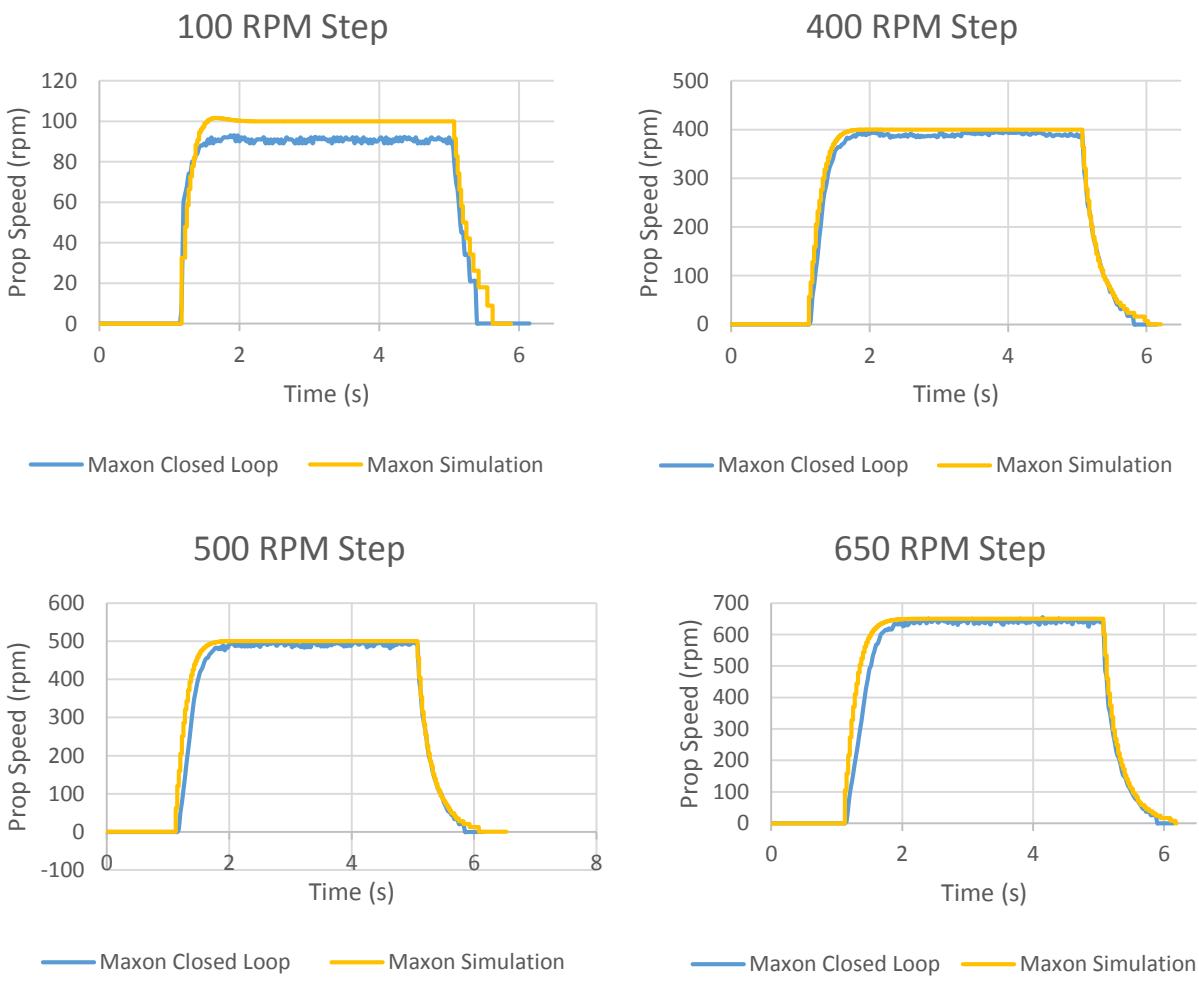

Figure 37 - Preliminary simulated and actual step responses to obtain correct damping and response shape

Figure 37 shows the sampling effects of the speed sensor quite clearly in both the real life case and the simulation, especially in the 100 rpm step. The responses were achieved using an integrator and gain of the

form K_i/s. It was observed that a different gain was required for acceleration and deceleration, representing the differing ways in which the Maxon controller accelerates and applies braking to the motor shaft.

As a preliminary investigation into how the Maxon controller works, Figure 37 gives a lot of insight into deviations of the Maxon controller from a basic digital integral controller. The effects that need to be tackled are given below:

1. Steady state offset – it can be seen from each step (especially 100 rpm) that the controller deviates from the desired setpoint.
2. Acceleration rate limiting – it is suspected that the Maxon controller limits the acceleration rate of the shaft so as to not over-current the motor. This can be seen as a deviation in the acceleration slope between the simulation and actual response, especially for greater step values.

A clear idea of the next steps of development for simulating the Maxon controller have been gained from these preliminary tests and will be tackled in the next sections.

3.7.6 Maxon Controller Speed Sensor Gain

In a pure integral controller, a possible reason that setpoint tracking would not be achieved becomes apparent when considering the steady state response of the system. Consider the system below in Figure 38.

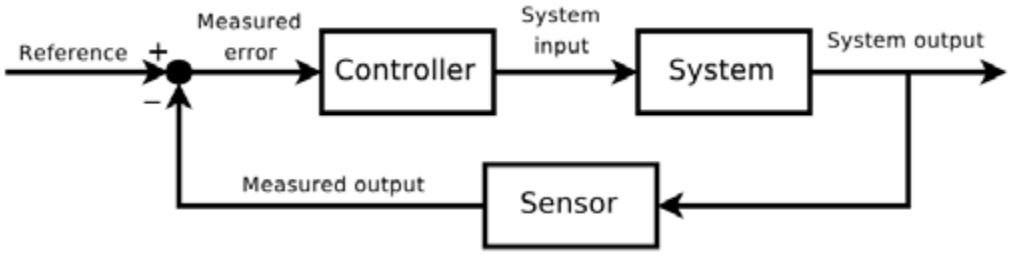

Figure 38 - General control system structure

If the controller is of the form K_i/s, using final value theorem the steady state response of the system can be derived to be:

$$\frac{System\ Output}{Reference} = \frac{1}{Sensor} \qquad \{3.83\}$$

This shows clearly that if the sensor does not have a unity gain, there will be an offset between the desired setpoint and the actual settling value.

In the Maxon controller, non-setpoint tracking behaviour could be present for numerous reasons such as slight voltage offsets in control and DAC circuitry and the simplification of the setpoint equation that was applied in the MSP430 control microcontroller. It was decided to model these effects as a non-unity sensor gain. It should be noted that, as previously mentioned, the speed readings taken by the MSP430 were

calibrated so as to be close enough estimations of the real speed to be considered accurate and the effects of non-unity sensor gain as modelled in this section were added to the feedback path of the Maxon controller's sub-diagram.

The speed offset was analysed at different prop speeds and converted to a factor to be used as the sensor gain. The resulting curve is shown below in Figure 39.

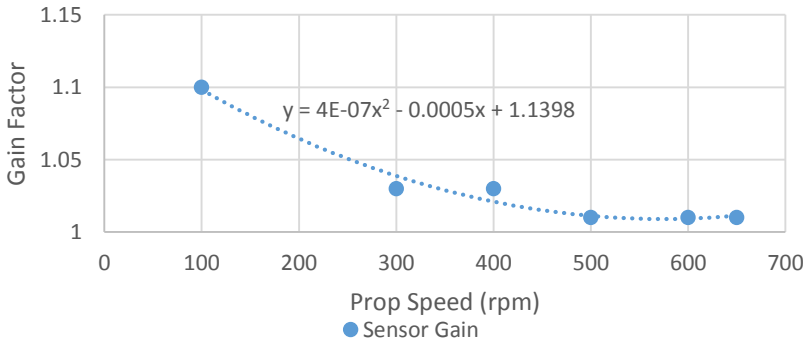

Figure 39 - Sensor gain factor vs. propeller speed with fit curve

With the sensor gain effect added, the simulated responses accurately mimicked the real life offset in steady state speeds as shown below in Figure 40.

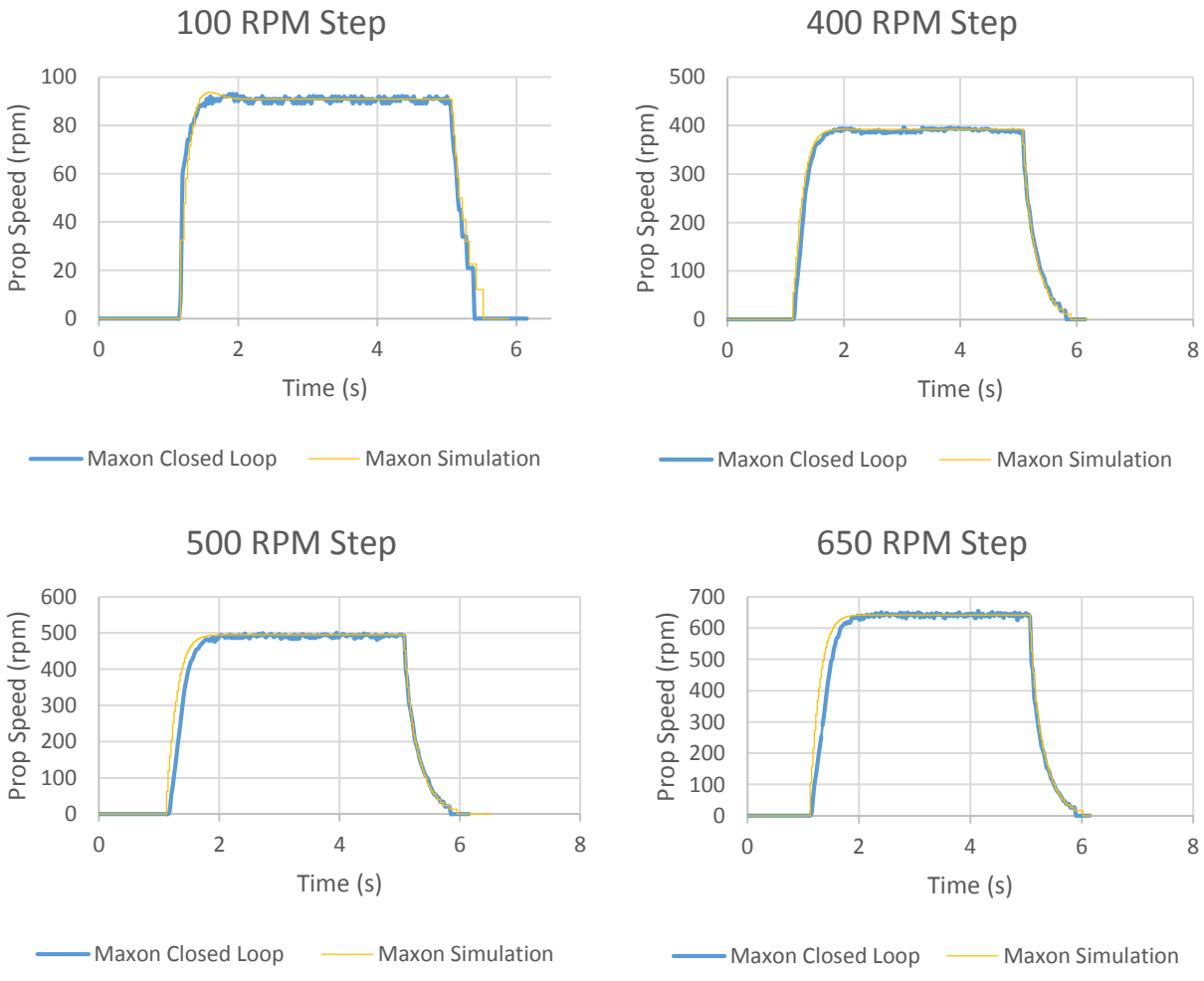

Figure 40 - Simulated and actual step responses with sensor gain applied

As can be seen from Figure 40, the setpoint offset is now accurately portrayed. For greater step values however, the simulated response is still faster than the actual response. Limiting the acceleration rate will be investigated in the next section.

3.7.7 Acceleration Rate Limiting

Applying acceleration rate limiting to the Maxon controller's input was necessary to slow the response of the controller. An acceleration rate limit of 2400 rpm/s was applied to the controller's input. A deceleration limit was not necessary due to the simulated response being adequate from just applying a different integral gain to the deceleration part of the simulation as can be seen previously in Figure 40.

Another option that could have replaced the acceleration rate limit to achieve similar responses would have been to schedule controller gains depending on the magnitude of the step. This however seemed less likely and more complicated than acceleration limiting. Commercial controllers of BLDC motors are known to implement acceleration limiting and thus this method was chosen to slow the response of the controller.

To verify the plausibility of acceleration rate limiting in the Maxon controller, a step was applied when the thruster was in water and in air as shown following in Figure 41. If there was no acceleration rate limiting, the smaller propeller load in the air would allow the propeller to accelerate faster however, according to the figure the acceleration rates are almost identical.

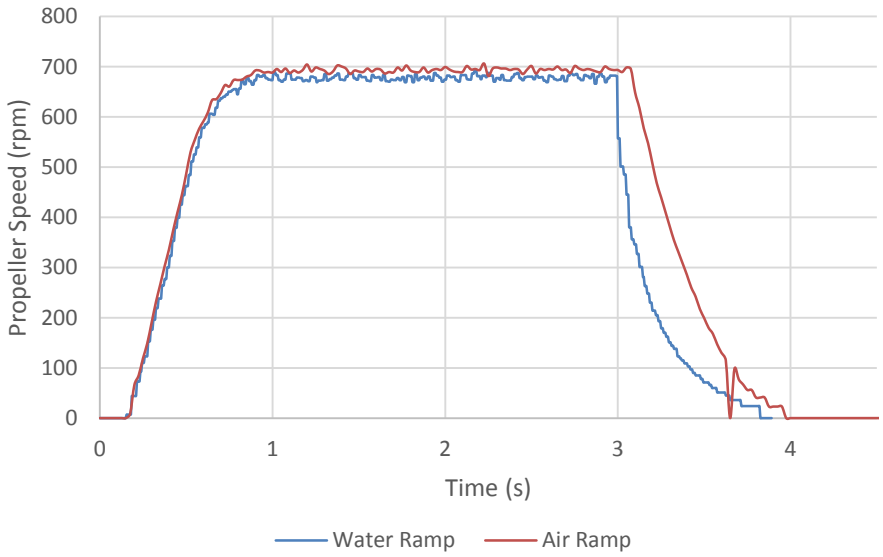

Figure 41 - Response to a 700 rpm step applied to the Maxon controller thruster system in water and in air

In addition, a test was performed in water that passed two different DAC values directly to the Maxon controller – a maximum DAC value that was, when converted to a speed setpoint using equation 3.77, above the operational range of the motor and a DAC value towards the upper operational speed range of the motor. The resulting speed data is shown following in Figure 42.

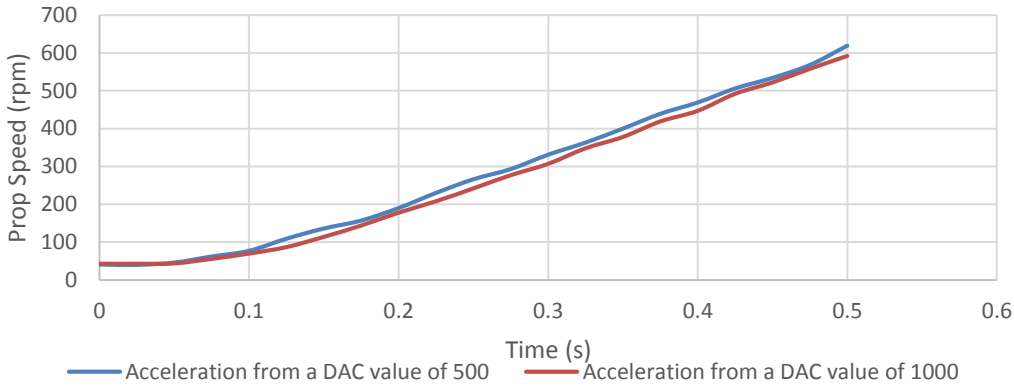

Figure 42 - Motor speed curves showing acceleration according to different DAC inputs

As can be seen from the graph, there is very little difference in the acceleration rate of the motor, with the higher DAC input actually accelerating the motor slightly slower than the lower one; although this is insignificant and can be attributed to experimental uncertainty.

As a result of the two tests performed, it was concluded that it is likely that there is an acceleration rate limit applied to the motor.

As can be seen following in Figure 43, acceleration limiting allows for slower responses at greater step inputs without significantly jeopardising the response speed of smaller steps.

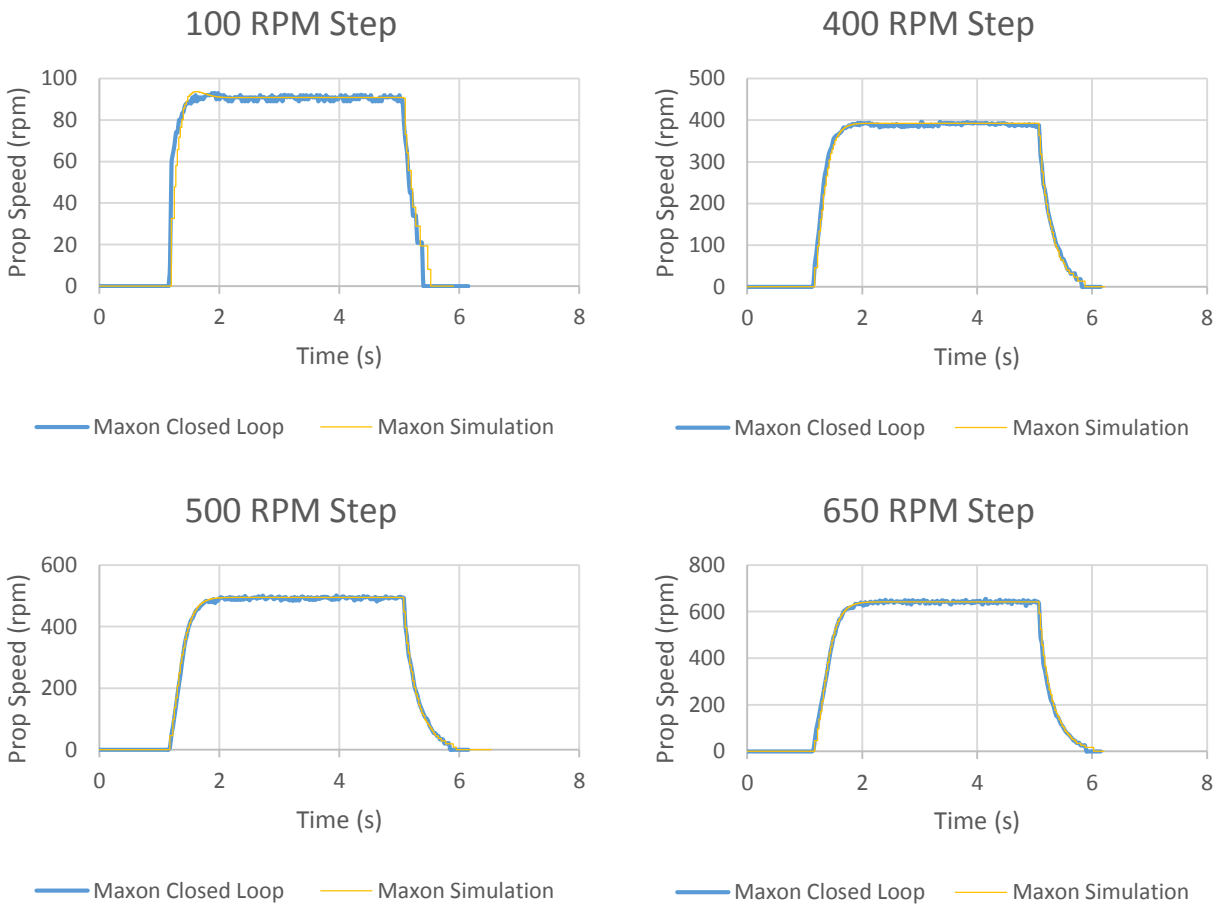

Figure 43 - Simulated and actual responses with acceleration limiting added

This completes the basic control structure of the Maxon controller. To verify the similarity of the model to the actual response, the dynamic sequence described previously in section 3.6.4 was simulated and compared to the actual response as shown following in Figure 44.

In general the similarity is very good between the simulation and actual responses, with the simulated response leading or lagging the actual response slightly during the time intervals 11-12 s and 16-17 s, for example. Due to the Maxon controller being an unknown digitally implemented controller, there could be any number of factors that influence how the controller responds. For instance the current draw of the motor could be monitored, and play a role in limiting the acceleration of the motor. Due to these possible unknown factors, the similarity between responses was deemed sufficient for speed setpoints in one direction only. An aspect that still had to be addressed however, was the response of the system to bi-directional speed inputs. This will be discussed in the next section.

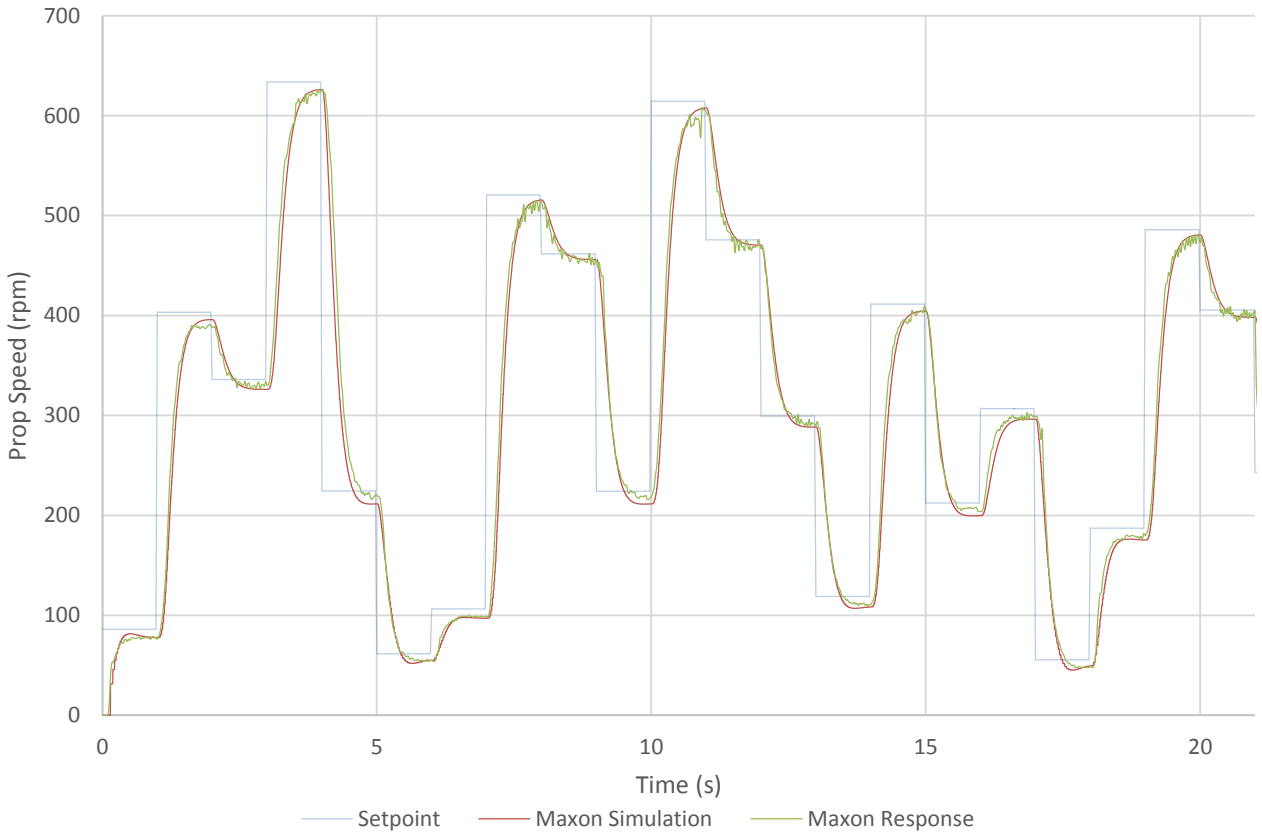

Figure 44 - Single direction dynamic motor sequence with Maxon actual and simulated responses

3.7.8 Bi-Directional Response, Nonlinearities and Signal Conditioning

The Maxon speed controller has a deadband between 0-500 rpm of motor speed. From testing, it was found that this was in fact the most challenging aspect to model, due to the largely unknown behaviour of the Maxon controller while traversing the deadband and since the speed reading rate decreases the slower the motor turns. Nevertheless, it was not sufficient to have an accurate simulation for single directions only, given that ROV manoeuvres such as station keeping will require reasonably rapid alternating thrust directions – meaning that the motor will traverse the deadband region frequently.

To account for this behaviour, an input signal conditioning subsystem was added before the Maxon feedback comparator. The logic of this subsystem was incorporated into the effects of the previously discussed acceleration rate limiter. By analysing a bi-directional dynamic response of the motor, it was possible to approximate that the motor controller would slow the motor down until the deadband region was reached after which it would rapidly switch the rotational direction and begin to accelerate the shaft in the opposite direction. The logic applied in the signal conditioning subsystem is given following in Figure 45.

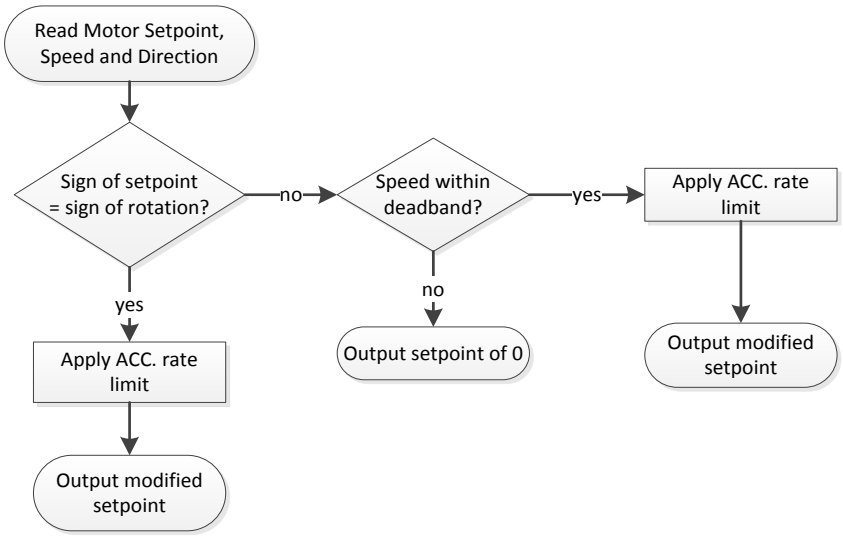

Figure 45 – Maxon controller input conditioning block diagram logic

The simulated and actual response to a dynamic sequence with bi-directional inputs is shown following in Figure 46.

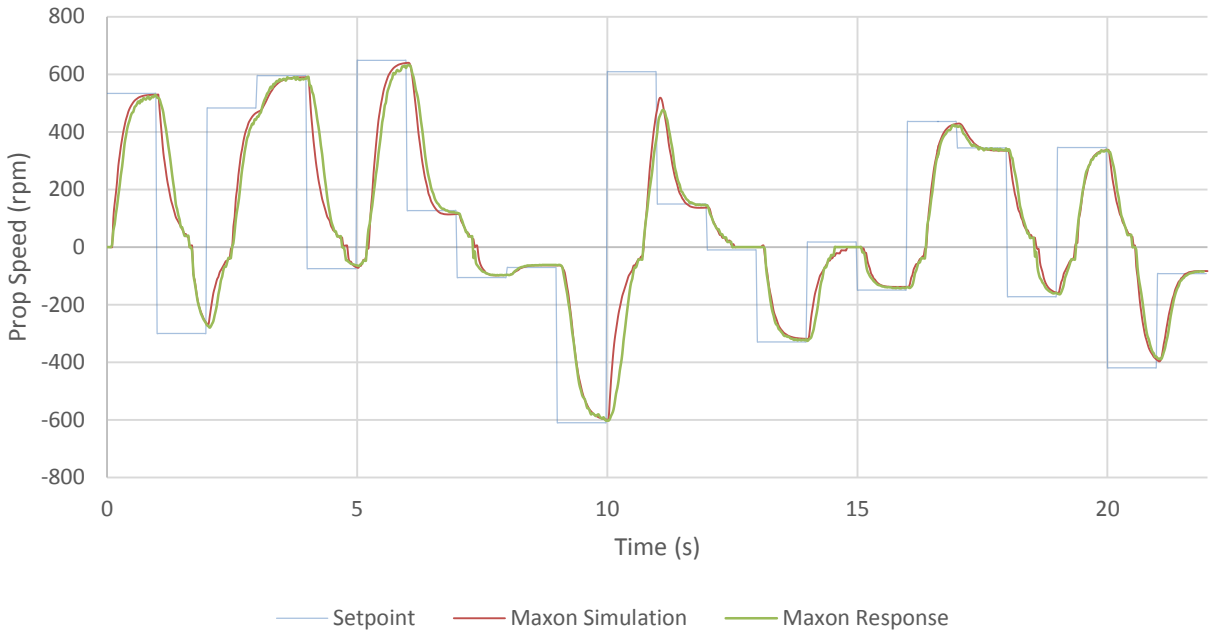

Figure 46 - Maxon controller simulated and actual response to a series of bi-directional inputs

Figure 46 shows that once again there are slight differences between the actual and simulated responses, such as the simulation leading or lagging the actual response. It is expected however, that the most variation between the model and real life case will be in an operating scenario similar to the one shown in Figure 46, where the propeller changes direction and there is the largest variation of water flow into and around the propeller. Therefore the variations in Figure 46 are expected to be attributable to aspects of the system that were not modelled in this project, such as the water velocity into the propeller.

The speed around the deadband matches the real life case quite well, which is important since station keeping operations will require frequent change of direction of the propeller. The deadband effect can also be seen between times 12-13 s and 14-15 s where the motor does not respond to setpoint commands within the deadband region.

The Maxon controller was concluded to be sufficiently approximated at this stage, with an accurate response traversing the entire operating range of the thruster.

3.7.9 Maxon Controller Summary

The Maxon motor controller was approximated as an Integral only controller that runs at 250 Hz. An integral gain of 95 is applied for acceleration, and if it is desired that the motor be slowed down, a gain of 60 is applied during deceleration.

To represent the offset seen between the desired setpoint and actual steady state value observed, a sensor gain is added to the controller's speed feedback path.

The controller input is conditioned by applying an acceleration rate limiter if both the motor direction and setpoint direction is the same. If they are different, the controller input is set to zero until the motor slows down to the deadband, at which point normal control is resumed in the opposite direction.

The final Simulink® block diagram for the Maxon motor controller is shown below in Figure 47.

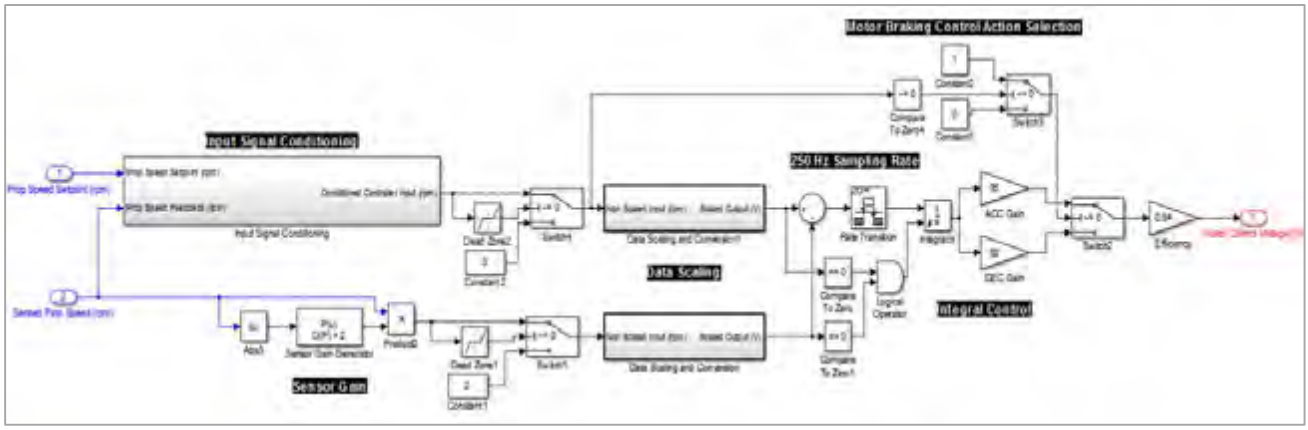

Figure 47 - Final Maxon motor controller Simulink® block diagram

The speed sensor was modelled so as to approximate the speed under the assumption that a speed update was supplied every Hall Effect sensor pulse. This resulted in a varying sensor rate of 25-420 Hz depending on the speed of the motor.

This completes the Maxon motor controller model and thus the final subsystem in the thruster model is completed. With the entire system modelled, the simulation accuracy can be analysed and system specifications can be developed in the following section.

3.8 Thruster Model Analysis and System Characteristic Specifications

3.8.1 Introduction

All subsystems that comprise the thruster system have been modelled, with acceptable looking responses for operations over the entire thruster speed and direction range. Thruster model parameters - such as the Maxon controller gains - were tweaked until a response that matched closest to the actual response was obtained for step inputs. It is now possible to analyse the simulation accuracy to provide a benchmark upon which can be improved in the future. In addition to this, the system characteristics can be defined.

This section will analyse the simulated and actual thruster responses, identify sources of error in a basic analysis and quantify the errors. With a sufficient response obtained, a brief investigation into the frequency response characteristics of the system will then be undertaken and finally characteristics for the thruster system will be formulated.

3.8.2 Model Error Basic Analysis

This section will compare the difference in model and actual responses under certain conditions.

Steady State Response: Using the step functions generated, the simulation and actual responses were compared during the steady state portion of the graph to give the following results listed in Table 12.

Table 12 - Difference between model and actual Maxon response and difference between the actual settling value and setpoint

Step Size (rpm)	Average Discrepancy between Model and Actual Response Under Steady State Conditions (%)	Discrepancy Between Real Life Settling Value and Setpoint (%)
100	-0.33	9.37
300	0.95	2.71
400	-0.77	2.63
500	-0.70	1.68
600	-0.11	1.09
650	-0.05	1.33

As can be seen from the above table, the simulation very closely matches the real life under constant propeller speeds. In addition, there is a 1-9 % discrepancy between the desired setpoint and the settling value of the response which has an increasing trend as the speed setpoint decreases.

Single Direction Dynamic Sequence: The difference between corresponding readings of the simulation and the actual response were taken for the single direction dynamic thruster sequence and are shown following in Figure 48. The results of the analysis are given following in Table 13.

Table 13 - Error analysis of single direction dynamic sequence

Average Error Over Entire Sequence	6.07 rpm
Maximum Error	73.75 rpm
Minimum Error	-28.71 rpm

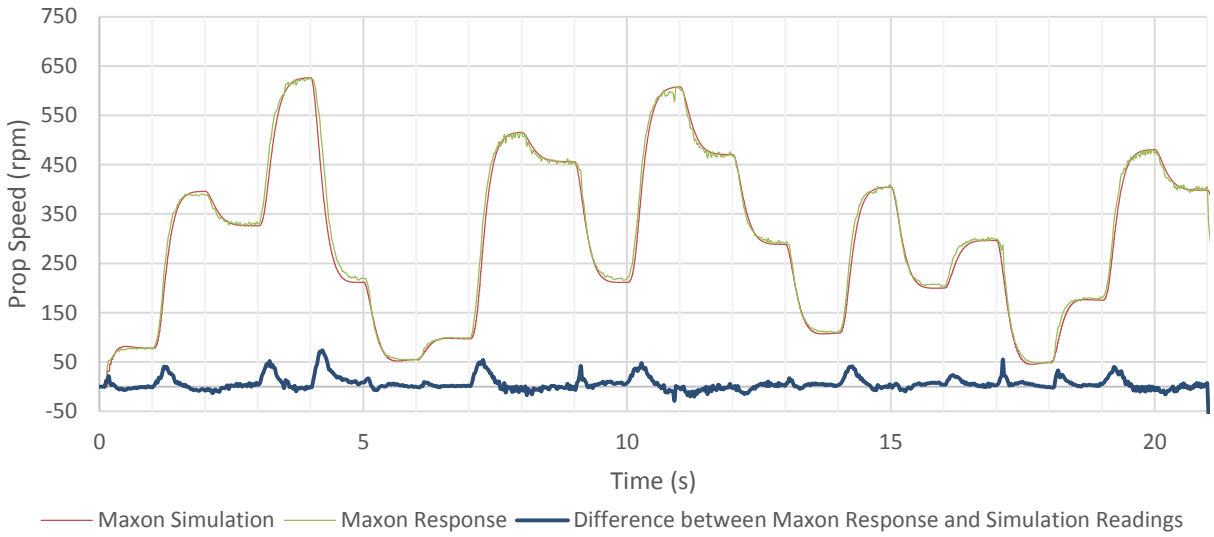

Figure 48 - Plot of Maxon simulation, actual response and difference between simulation and actual readings for single direction dynamic sequence

In general, the greatest sources of error occur during the transition from one setpoint to another – which is to be expected, given the accurate steady state results presented previously.

Bi-Directional Dynamic Sequence: The same analysis for the single direction dynamic sequence was performed for the bi-directional dynamic sequence. The results of the analysis are presented below in Table 14 and a graph showing the responses and the error between them is given following in Figure 49.

Table 14 - Error analysis of bi-directional dynamic sequence

Average Error Over Entire Sequence	-6.53 rpm
Maximum Error	184.87 rpm
Minimum Error	-232.93 rpm

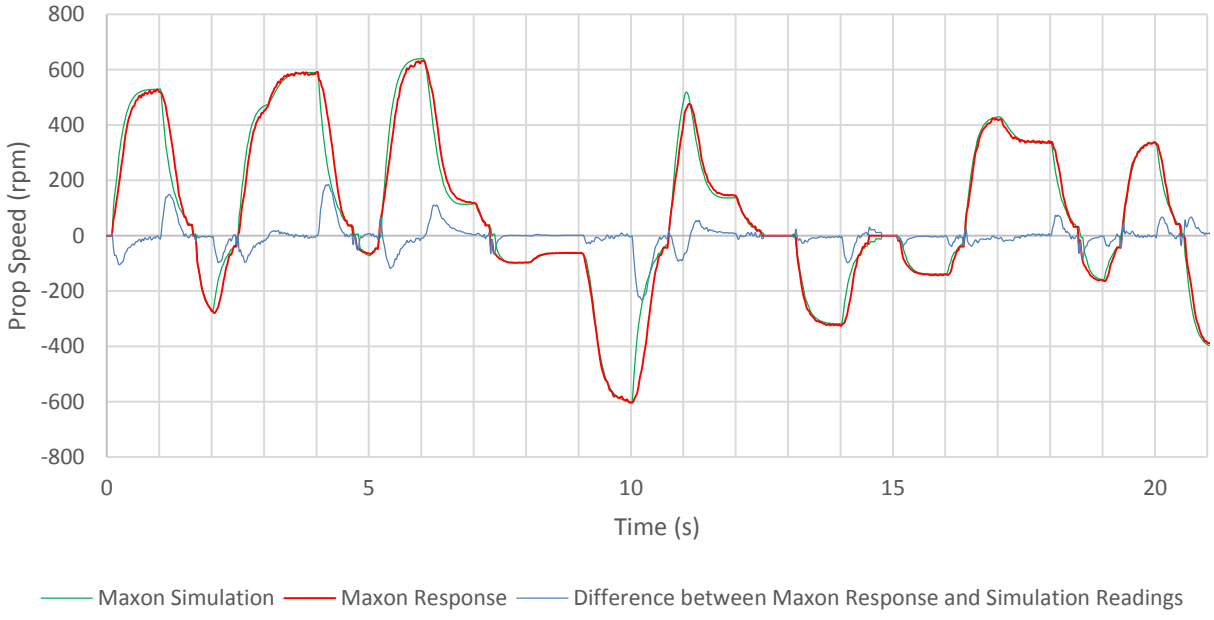

Figure 49 - Plot of Maxon simulation, actual response and difference between simulation and actual readings for bi-directional dynamic sequence

Again, as can be seen from Figure 49, the error magnitude increases during the transition between setpoints. It can also be seen that these errors in transient conditions tend to exceed the error magnitude for motion within the deadband region.

Analysis: The model is very accurate for steady state conditions, with the greatest source of error, naturally, being presented in transient states. The model is quite accurate for different speeds in a single direction and less accurate when bi-directionality is applied. When analysing Figure 49, it can be seen that the magnitude of the errors increase even when changing between two different speeds in the same direction. This is not expected and implies that other effects that are not included in the model, such as water flow velocity, may be affecting the results. It makes sense then that there are greater errors presented in the bi-directional case, since the propeller will disturb the water more.

In addition, it is possible that the controller might rely on parameters that are difficult to deduce without more information about the controller and thus may behave slightly differently under seemingly the same conditions. To verify this suspicion, the single and bi-directional sequences were run three times in a row and the variation of the results was calculated. The results are given below in Table 15.

Table 15 - Varinace between readings of consecutive Maxon controlled dynamic thruster sequences

Single Direction Sequence		Bi-Directional Sequence	
Maximum Variation	32 rpm	Maximum Variation	92 rpm
Average Variation	3.80 rpm	Average Variation	6.98 rpm

Sections from the dynamic sequences are given following in Figure 50 to show the variation in response between consecutive runs.

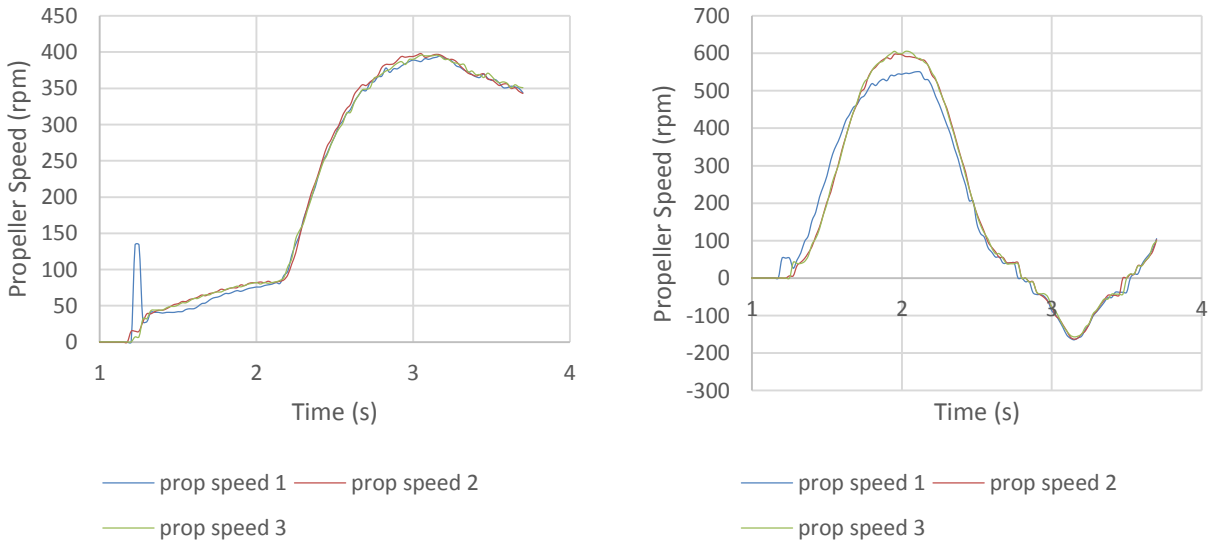

Figure 50 - Sections from the single [left] and bi-directional [right] dynamic sequences, showing behavioural variations in different consecutive runs

It should be noted that some effects – such as the peaks just after the one second mark, are not due to the Maxon controller but are errors in the readings. Erroneous readings are infrequent however, and a clear variation in readings for both the single and bi-directional cases can be seen.

Conclusions of Analysis: The Maxon controller itself can respond slightly differently under seemingly the same conditions. This could be due to unknown factors within the Maxon controller itself. Therefore, the model created for this controller can only approximate its behaviour, leading naturally to some variation between the model and the real case.

The simulation was tuned so that the settling value of the simulation and the actual response after a step input were within 1% of each other. In a dynamic response, a maximum error of 214 rpm occurred with the average error over the entire sequence being approximately 7 rpm. The average error reading however will decrease as more time is spent by the thruster in a steady state condition and thus it is not a very true reflection of the model accuracy.

Regardless of the model error however, due to there being a maximum variation of about 92 rpm between consecutive runs of the Maxon controller alone, the accuracy of the model was deemed sufficient to serve as a preliminary thruster model for the *SEAHOG* ROV.

3.8.3 System Frequency Response

With a sufficient representation of the system obtained, the frequency response of the thruster system could be investigated. Due to the non-linear plant model and the variable sampling effects of the speed sensor, the plant was linearized using Simulink® about propeller speeds of 50 rpm, 300 rpm and 650 rpm. Linearization about these points would account for the increasing effect of the thrust vs. propeller speed squared relationship. The Tustin method of linearization was used in Simulink®.

To account for variable rates in the loop, the sampling rate of the loop was set at the lowest rate experienced at each linearization point for a worst case scenario representation for each system linearization. This would take into account the limited sensor bandwidth at low speeds. An effect that was not included in the linearization however, is the effect of the acceleration rate limiter in the Maxon controller. Effectively, the acceleration rate limiter will serve to decrease the system bandwidth and its effects on the behaviour of the system will be discussed in the following chapter.

The open-loop response was calculated between the Maxon controller comparator output and the Maxon speed sensor output for the open-loop Bode Plot to obtain approximate system stability margins. The closed loop frequency response was calculated between the propeller speed input and the Maxon speed sensor output to obtain approximate measures of the system bandwidth.

Figure 51 following shows the open-loop Bode Plot for the thruster system. It can also been seen that the limited bandwidth of the speed sensor at low speeds causes a large signal attenuation at about 15 Hz. This behaviour was also exhibited for the 300 rpm and 650 rpm steps at higher frequencies. In all of these cases however, the limitations of the sensor bandwidth is not very significant for the operating frequency range of interest, as can be seen in Figure 51 following. The gain and phase margins extracted from the figure are given following in Table 16. As expected, the system is stable with large gain and phase margins.

Table 16 - Thruster system approximate stability margins

Speed Around Which Linearization was Applied	Gain Margin	At Frequency	Phase Margin	At Frequency
50 rpm	34.6 dB	7.26 Hz	71.7˚	0.68 Hz
300 rpm	35.1 dB	9.42 Hz	74.0˚	0.65 Hz
650 rpm	36.3 dB	9.46 Hz	75.7˚	0.58 Hz

In Figure 51 following, each data series is listed with the point around which the system was linearized, and the limiting discrete rate of the system in seconds, for example: *OL 50rpm 0.033* is the data series linearized around a point represented at a propeller speed of 50 rpm, where the slowest rate in the system is 0.033 s.

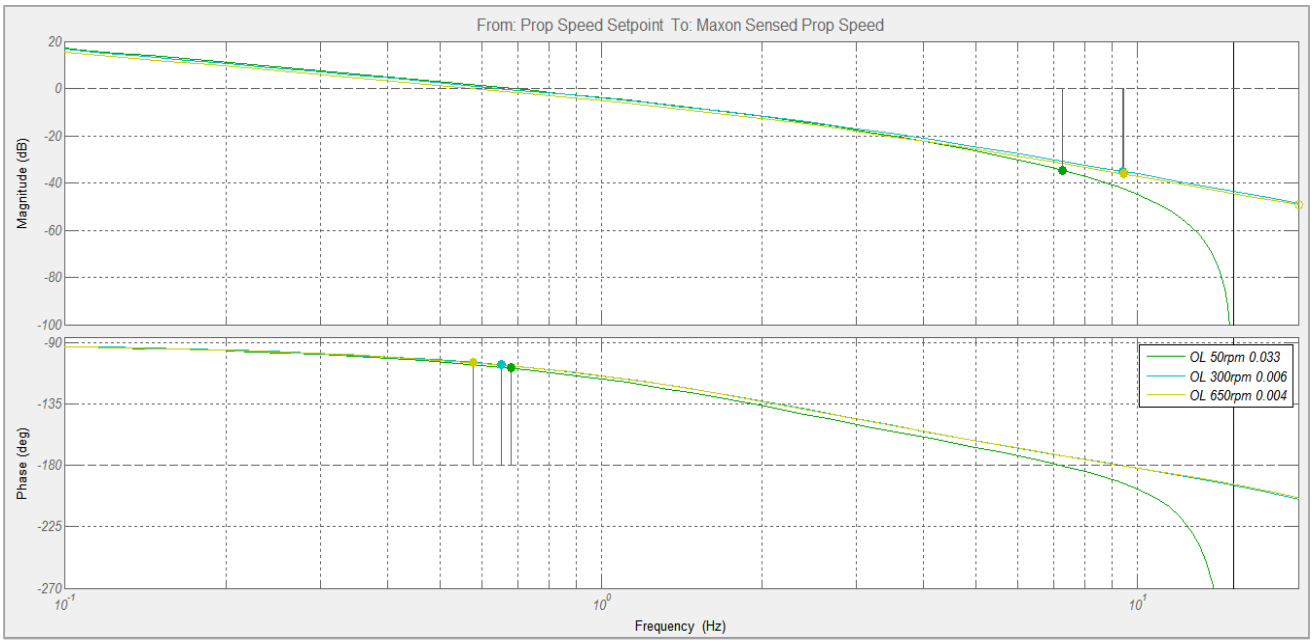

Figure 51 - Open-loop Bode Plot of the thruster system showing stability margins

The closed loop Bode Plot is given following in Figure 52 with the bandwidth for each linearization listed following in Table 17. The absence of resonant peaks point to the largely damped responses of the thruster.

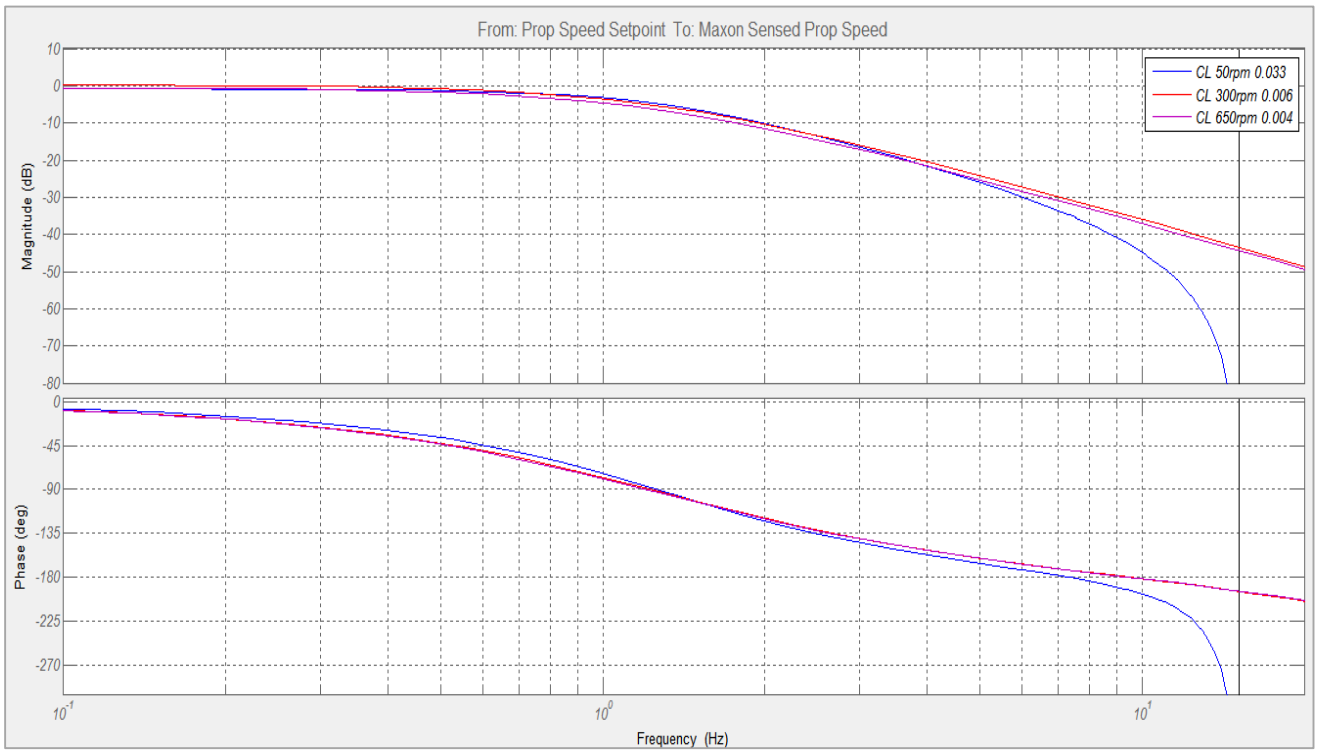

Figure 52 - Closed loop Bode Plot for the thruster system

Table 17 – Bandwidth approximation for thruster system linearized around different points

Speed Around Which Linearization was Applied	Bandwidth (Frequency at -3 dB Point)
50 rpm	0.954 Hz
300 rpm	0.911 Hz
650 rpm	0.746 Hz

From Table 17, the effect of the squared relationship in the plant model can be seen by the decreasing bandwidth of the system when linearized around higher propeller speeds.

Frequency response analysis was performed on the forward plant model only, assuming that due to the similarity in the forward and reverse plant models, the frequency responses would be largely the same. This completes the frequency analysis of the thruster system and thus concludes the thruster system analysis, allowing for specifications to be drawn that will serve to characterise the *SEAHOG* thruster system.

3.8.4 Thruster System Specifications

Linearizing the thruster model using Simulink® allowed an approximate transfer function of the closed loop system to be obtained. Due to the 650 rpm linearization point giving the most limited bandwidth, it is assumed as a worst case scenario and therefore its transfer will be given. An approximate transfer for the thruster system is therefore:

$$G(z) = \frac{n_{prop}(z)}{n_{prop\ des}(z)} = \frac{0.0002z^3 + 0.0006\,z^2 + 0.0006\,z + 0.0002}{z^4 - 1.121\,z^3 - 0.6488\,z^2 + 0.7717\,z + 0.0002} \quad \{3.84\}$$

with a sampling time of 0.004 s.

The bandwidth of the system as a worst case scenario is approximately 0.746 Hz. This value however does not take into account the effect of the acceleration rate limiter on the system.

The effect of the acceleration rate limiter and the nonlinear plant model will result in different response characteristics depending on the speed that the thruster is operating at and the size of the step input. Therefore, to give more insight than merely the bandwidth of the system, the 95% rise time is given for different step sizes below in Table 18. The rise time was measured from actual data and from the simulation but the simulation results are cited due to the slower, 40 Hz data capture rate of the actual response limiting the resolution of the results. Additionally, the time is calculated from the initial acceleration of the motor and does not account for the dead time effects in the system between the motor acceleration and the input command.

Table 18 - Approximate 95% rise time for different steps under the Maxon controlled thruster system

Step Size (rpm)	95% Rise Time Actual Response (s)	95% Rise Time Simulation Response (s)
100	0.100 to 0.250	0.233
300	0.250 to 0.500	0.511
400	0.500 to 0.525	0.518
500	0.550 to 0.575	0.556
600	0.575 to 0.600	0.571
650	0.575 to 0.600	0.594

With deadband effects, the maximum rate of change in propeller speed that can be achieved is 946 rpm/s. The thruster system was approximated as a second order linear continuous system with a closed loop transfer of:

$$G(s) = \frac{\omega_n^2}{s^2 + 2\zeta\omega_n s + \omega_n^2} \quad \{3.85\}$$

with ω_n = 7.45 rad/s and ζ = 1.

The approximation is accurate within the frequency range of interest, up to approximately 3 Hz, as shown by the following closed loop Bode Plot in Figure 53. The thruster model that has been linearized about various operating points is given in green with the approximation given in blue. If a more accurate approximation is desired, a lag term can be multiplied to the current approximation, with a time constant related to a frequency of approximately 100 Hz. The extra lag will tend to decrease the phase, pulling the green line down towards the blue line.

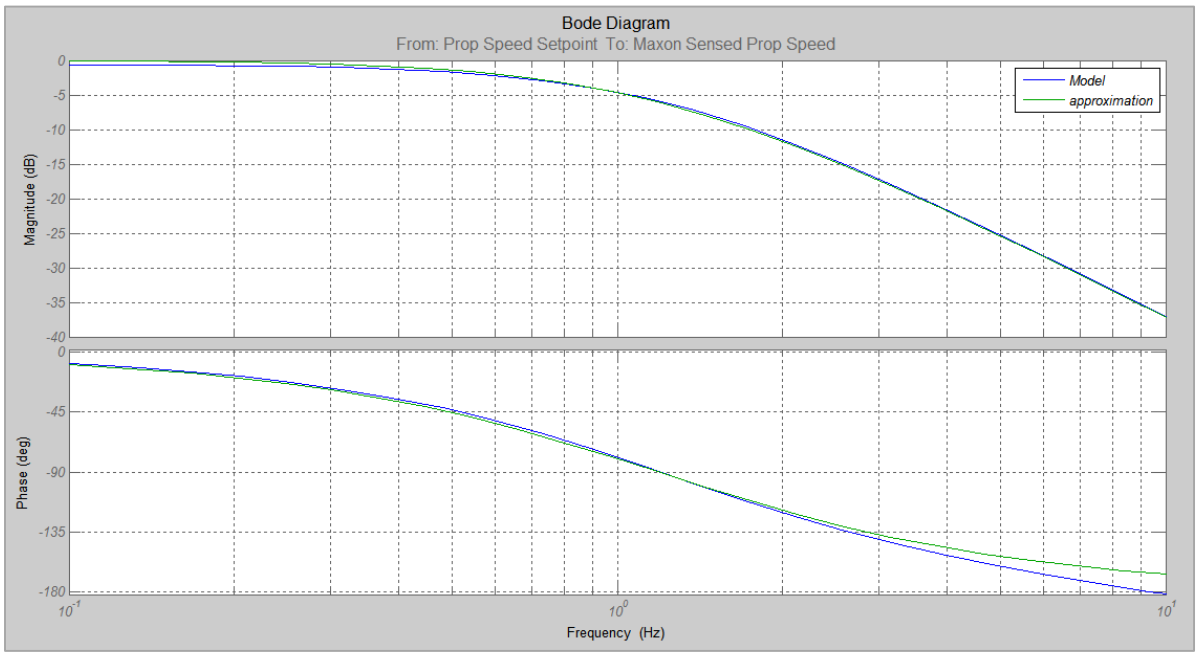

Figure 53 - Bode plot of closed loop thruster response vs. 2nd order system approximation

The approximation of the system allows the damping factor and natural undamped frequency of the system to be approximated as 1 and 7.45 rad/s respectively.

Characteristics for the thruster system under the influence of the Maxon controller have now been formulated, completing the development of the thruster system model identification, allowing the chapter to be summarised in the next section.

3.9 Thruster Model Summary

The *SEAHOG* thrusters consist of a three blade symmetrical propeller with an efficiency of 62%. The propeller is driven by a two pole pair radial magnetic coupling with an efficiency that is related to the speed of the propeller due to eddy current braking effects. A Maxon BLDC motor coupled to a 12:1 reduction gearbox drives the propeller and is powered and controlled by a Maxon 1-Q-EC digital amplifier.

The propeller was modelled using a single state model developed in [17] that uses propeller speed as the system state. There are known shortcomings of this model however, which have been explained using more complex models in more recent literature. However, due to the limited available testing and verification facilities a more advanced model was not chosen. We can expect there to be lower thrusts produced in real life than from the model due to the model not taking into account the thrust reducing effect of advance speed.

While the thrust is then an estimation in the present model, the propeller speed was modelled to an acceptable degree of accuracy. The thruster model was verified against real responses from the thruster in both rotational directions over the entire thruster operating range.

The Maxon controller was estimated as an integral controller with a non-unity speed sensing gain – accounting for its offset setpoint tracking behaviour. The speed sensor was approximated by assuming it would supply a speed update every Hall Effect signal as the motor rotates – which accounted for the observed quantisation effects in the thruster responses. Acceleration rate limiting was applied and verified, which serves to limit the closed loop bandwidth of the system. While the Maxon controller does the have the option to be an open-loop controller, for safety reasons - such as to prevent damage to other systems - its closed loop functionality was chosen. The controller has a control deadband of 500 rpm motor speed or 42 rpm propeller speed, after the gearbox.

The model underwent final verification through a series of basic error analyses. It was shown that while there is error in the transient actual and modelled responses of the thruster, there is also a variation between consecutive test runs of the thruster itself. For that reason the model was deemed to be accurate enough, allowing its frequency response to be characterised and characteristics of the system to be formulated.

The thruster portrays largely damped behaviour with a closed loop bandwidth of 0.746 Hz, a maximum operating range of ±650 rpm and a maximum rate of change of speed of about 1000 rpm/s when traversing the deadband. The system is overdamped with a damping factor of 1, when approximated as a second order linear continuous system.

This completes the extensive *SEAHOG* thruster model development and verification chapter. Characteristics of the system are now available and can be used to develop new specifications for any extra software implemented speed control on the thruster's control MSP430 microcontroller. The following chapter will detail the digital speed control that was modelled and then implemented on the thruster's control microcontroller – and the considerations that were necessary for its successful implementation.

Chapter 4 - Thruster System Low Level Control Design

4.1 Introduction

All aspects of the thruster system that needed to be identified and modelled have been successfully identified and verified. The model that was created in the previous chapter incudes all of the subsystems within the thruster system that could not be designed - only identified. The MSP430 microcontroller that calculates the speed of the propeller and sends analogue voltages to the Maxon controller via the DAC can also be programmed to implement digital control algorithms.

Some work went into successfully improving the steady state speed error to within 1 % of the setpoint speed in [24]. However, the way in which this was achieved relied on extensive parameter tuning and was aimed mainly at correcting steady state propeller speed errors. The way in which the previous control scheme was applied will be discussed in the following section.

It was decided to correct the speed offset of the Maxon controller using another control loop, executed by the control MSP430 on the thruster electronics board that would modify the Maxon controller's control input voltage. This forms part of the Simulink® model as shown below in Figure 54 with the completed sub-diagrams in green and the new controller in yellow.

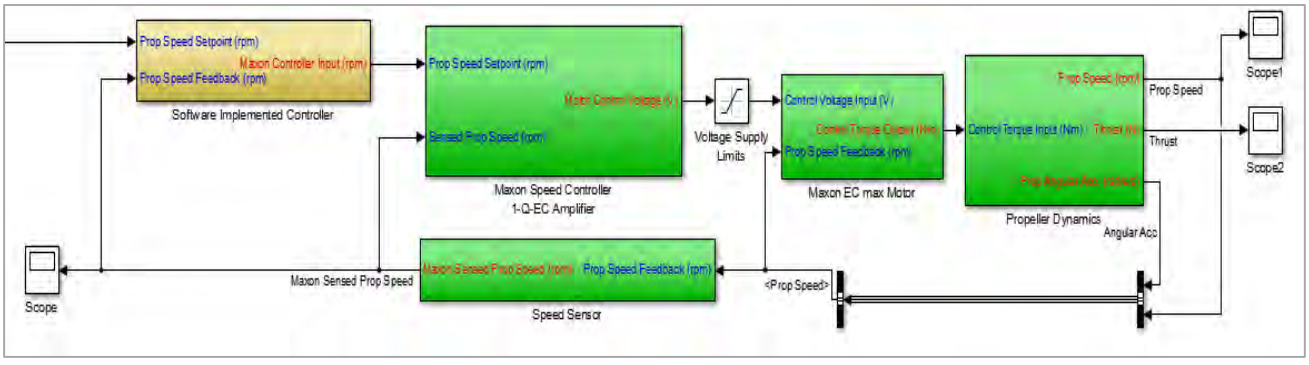

Figure 54 - Simulink® block diagram with completed sub-diagrams in green and new controller block in yellow

The motivation for designing a speed setpoint tracking controller is that it distributes the processing power on the ROV, allowing a central controller that is in charge of controlling all five thrusters to sample at lower rates, and have confidence that the setpoint it sends to the thrusters will be the exact settling speed value. This will be advantageous if the processing power for the central control unit and the communication bandwidth is limited.

This chapter will first describe the previously implemented speed control scheme and motivate the necessity for a new control algorithm to be implemented. It will then discuss and detail the design of the new controller using the thruster model developed in the previous chapter. The new controller will then be implemented and compared to the real response. This chapter will also detail the practical considerations that were necessary to successfully implement the control, due to the MSP430's limited data processing capabilities.

4.2 Previous Closed Loop Control Structure

It was decided in [24] to implement a closed loop control scheme to ensure that the steady state speed offset present in the Maxon controller's closed loop speed control was reduced. This was achieved using a reasonably arbitrary arrangement of filtering via moving average arrays, which was applied only once the propeller speed was within a certain proximity of the setpoint. The band in which the control started to be applied and the size of the averaging arrays were variable and arbitrarily determined, depending on the speed setpoint.

The control law that was applied resembled a feed forward proportional controller with low pass filtering of the sensed speed. The control was only applied within a certain speed band relative to the setpoint. Figure 55 below shows the basic control architecture applied previously in the thruster. The filters are not included in the figure.

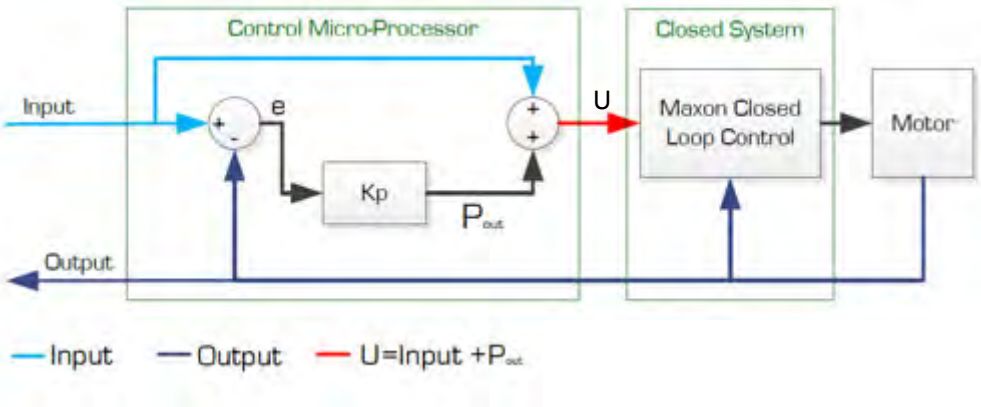

Figure 55 - Basic representation of the control structure applied previously on the thruster [24]

Another disadvantage of the implementation of the previous control scheme was that if a new setpoint was supplied at the input of the controller, the moving average arrays would be deliberately re-initialised and the control would reset until the motor was close enough in speed to the setpoint once again. Therefore, a master controller that communicates quickly with each of the thruster modules would keep resetting the closed loop control on the microcontroller, effectively negating its effects.

The extensive data averaging calculations in the algorithms resulted in a computationally intensive load on the microcontroller. This resulted in a slow response of the controller as the microcontroller populated its moving average arrays. Figure 56 below shows where the control action of the microcontroller takes over from the Maxon control in the green circles.

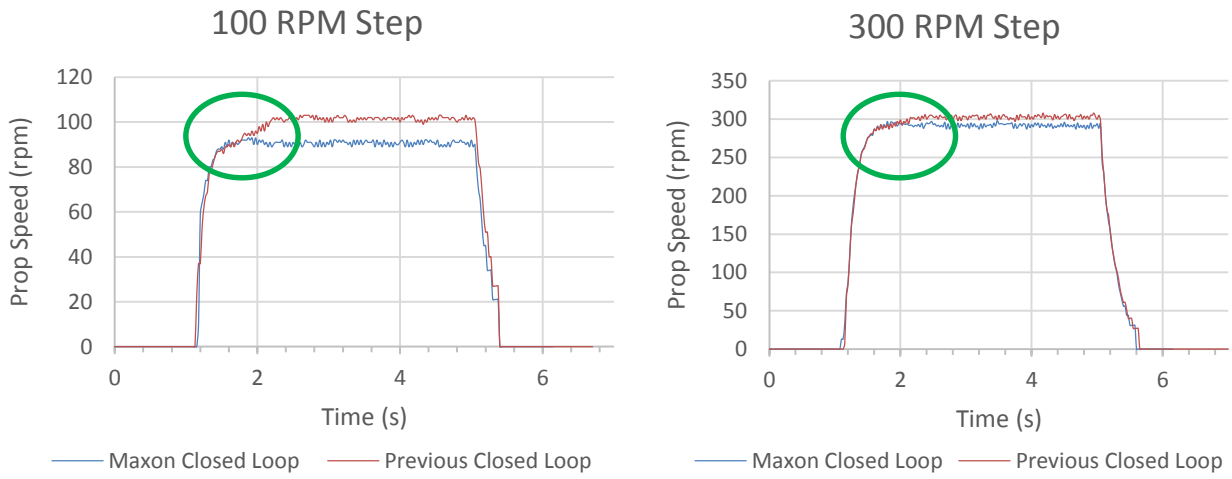

Figure 56 - Response to step inputs by the previous control structure

While it can be clearly seen that the controller significantly decreases the steady state error, it requires about 1 s to settle after it has reached the speed band in which it is applied, making the overall response slower. An advantage however is that due to the controller utilising the Maxon control until a certain speed, the initial motor acceleration is not slowed by the controller.

Due to the extensive number of experimentally determined factors in the control method and the disadvantages discussed in this section, it was decided to replace the previous control scheme with a standard design, such as a PI controller. With a motivation for a new controller given, a controller design could be formulated and will be detailed in the next section.

4.3 Thruster Speed Controller Design

4.3.1 Introduction

The controller to be designed in this section determines speed in the same way as the Maxon motor controller as described in section 3.7.4 previously. The objective of the controller is to provide perfect setpoint tracking while sacrificing the speed of the Maxon controller as little as possible.

The control law will initially be designed in the continuous domain and then converted via the bilinear transform to be implemented in the digital domain. The bilinear transform transforms the s domain into the z domain via the approximation:

$$s = \frac{2}{T_{samp}} \frac{1 - z^{-1}}{1 + z^{-1}} \quad \{4.86\}$$

Effects of sampling rates will be assessed as part of an iterative design process. As will be shown, the hardware limitations of the MSP430 result in the implementation of the control loop being difficult. These aspects will be presented and discussed in this chapter alongside the design process.

4.3.2 Control Design Specifications

A list of design specifications for the new thruster controller design is given below in Table 19.

Table 19 - New software controller specifications

Specification #	Description	Criteria
S1	95% rise time for a 650 rpm step	≤ 0.66 s
S2	Bandwidth	≥ 0.67 Hz
S3	Maximum Overshoot as % of Step	≤ 10 %
S4	Phase Margin	≥ 30˚
S5	Gain Margin	≥ 7 dB

An explanation and motivation of the specifications presented above is given following.

S1. Due to the nonlinearities in the plant and effects such as the acceleration rate limiter, a specification that will be given priority over system bandwidth is the 95% rise time for a step of 650 rpm. The rise time obtained for a 650 rpm step in the previous chapter was approximately 0.6 s, and thus the new system shall have a rise time within 10% greater than this. The rise time is defined in this case from the initial acceleration instance of the motor to when the motor reaches 95% of the setpoint speed. It does not include dead time effects between the input signal and the motor acceleration.

S2. Due to the acceleration rate limiter present in the Maxon controller, it is not expected for the controller to improve the actual bandwidth of the system significantly. Therefore an approximate bandwidth specification that is 10% less than the old system will be aimed for. The bandwidth of the system under the influence of the Maxon controller only, was limiting at 0.746 Hz. Since this value was obtained without

accounting for the acceleration rate limiter, the rise time of the system will be prioritised over the system bandwidth, as it can be measured more truthfully.

S3. It is not entirely necessary that the system remains overdamped, however, for the sake of minimising control action, the system overshoot shall be limited to less than 10% of the step size.

S4 & S5. While there is not necessarily a direct relationship between damping and stability margins, as a rule of thumb the gain and phase margins shall be ≥7 dB and ≥30˚ respectively.

4.3.3 Practical Considerations and Hardware Limitations

The MSP430 microcontroller that is used in the *SEAHOG* thruster can only perform software fixed-point operations. The way in which the fixed-point numbers are defined in the MSP430 fixed-point library are by using a 16 bit signed integer (x_i) that is allocated a precision, Qn with $n \epsilon [1:15]$ to give a fixed-point number (x_q) through the formula:

$$Qn(x_q) = x_i \times 2^{-n} \quad \{4.87\}$$

The advantage of fixed-point is that it is possible to achieve a greater numerical accuracy than with integers but, as shown following in Figure 57, it can be seen that precision has to be traded off for number range. Every time the resolution is doubled, the range is halved.

Type	Bits		Range		Resolution
	Integer	Fractional	Min	Max	
_q15	1	15	-1	0.999 970	0.000 030
_q14	2	14	-2	1.999 940	0.000 061
_q13	3	13	-4	3.999 830	0.000 122
_q12	4	12	-8	7.999 760	0.000 244
_q11	5	11	-16	15.999 510	0.000 488
_q10	6	10	-32	31.999 020	0.000 976
_q9	7	9	-64	63.998 050	0.001 953
_q8	8	8	-128	127.996 090	0.003 906
_q7	9	7	-256	255.992 190	0.007 812
_q6	10	6	-512	511.984 380	0.015 625
_q5	11	5	-1,024	1,023.968 750	0.031 250
_q4	12	4	-2,048	2047.937 500	0.062 500
_q3	13	3	-4,096	4,095.875 000	0.125 000
_q2	14	2	-8,192	8,191.750 000	0.250 000
_q1	15	1	-16,384	16,383.500 000	0.500 000

Figure 57 - Fixed-point number allocation, showing number ranges and resolutions

As an example, a PI control scheme will be used to illustrate the complications that will arise while using fixed-point arithmetic.

Consider a PI continuous controller of the form:

$$u = e\left(K_p + \frac{K_i}{s}\right) \quad \{4.88\}$$

where u is the controller output, e is the error signal, K_p is the proportional gain and K_i is the integral gain. Equation 4.88 can be transformed using the bilinear transform to give the difference equation:

$$u_n = \frac{1}{2}\left[2u_{n-1} + e_{n-1}\left(K_i\, T_{samp} - 2\, K_p\right) + e_n\left(2\, K_p + K_i\, T_{samp}\right)\right] \quad \{4.89\}$$

It is this equation that must be successfully executed by the microcontroller using fixed-point operations to obtain a controller output for each time step.

From equation 4.89, it can clearly be seen that the sampling rate T_{samp} will affect the magnitude of some of the variables in the difference equation. The order of magnitude required for the control output u_n is related to the maximum propeller speed, 700 rpm. However, due to the possibility of a control output that overshoots the maximum propeller speed, the possible range of u_n must be in the region of 0 - 1400 rpm. This is important, because if the range is exceeded, the number will overflow and an incorrect value will be obtained.

As T_{samp} decreases, it becomes increasingly difficult to convert each product in the difference equation to a fixed-point number with a large enough range without losing a significant amount of resolution. When converting to larger range numbers, any part of the number beyond its resolution is lost. This means that, in an extreme case, if the product of $T_{samp}\ K_i$ is too small, the result will be truncated every time-step and in effect the integral part of the controller will be negated. Alternatively, there is a possibility that the resolution of the final control output is too low, which will result in the possibility of a speed offset in the final settling value, as the resolution of the number will result in it constantly being rounded off to a value that just below or above the true setpoint. In addition, the limited data resolution will appear as noise that is introduced into the system.

These practical considerations outweigh the small drop in performance that may result from merely applying a simple controller on the MSP430. A fine balance was required between choosing a sampling rate for the controller (and hence fixed-point precisions for the difference equation variables) and its resulting performance.

With the practical design limitations of the MSP430 clearly understood, it is possible to formulate a controller design that will serve to control the input into the Maxon controller.

4.3.4 Continuous Domain Controller Design

It was decided that due to the low frequency range of interest for the operation of the thruster and considering the implementation challenges that would be faced, a simple PI controller scheme would be tuned and implemented on the control MSP430 microcontroller. This being said, it was necessary to check the stability of the loop when another pole was added in the form of an extra integrator.

Firstly, using the thruster model that was developed in the previous chapter, simulations were performed to tune the proportional and integral gains of the new controller. An effect that was very prevalent in the design procedure was the acceleration rate limiter and the non-linear propeller plant. It can be seen following in Figure 58 that these nonlinearities play a significant role in altering the system behaviour

across the entire operating range of the thruster. The graphs show responses to different step inputs when a PI controller is applied that was tuned to have a slightly underdamped response at the given operating speed.

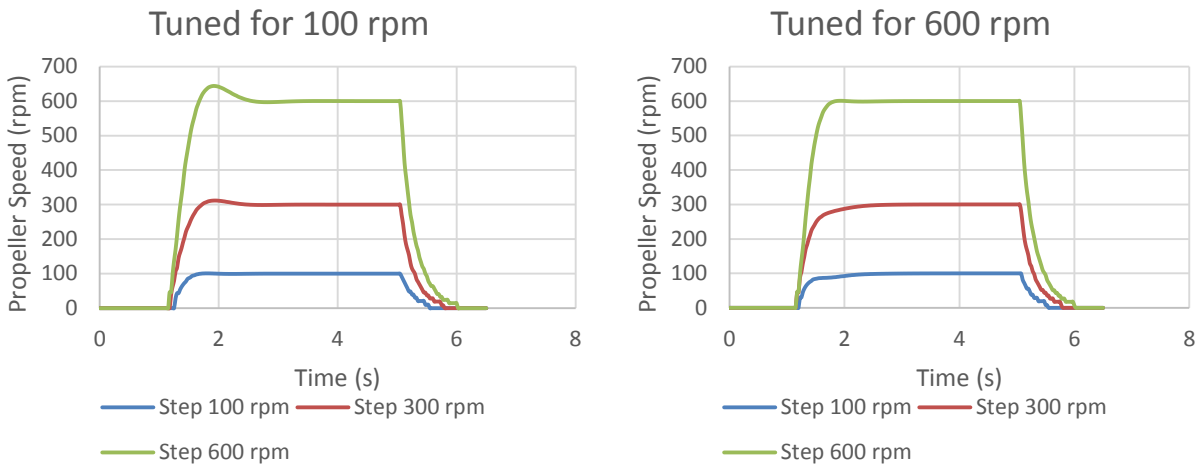

Figure 58 - Step responses for PI gains tuned at different operating points

It can be seen from Figure 58 that if a standard PI controller is implemented, a uniform response over the entire thruster operating range is not expected. However, given that the close to worst-case scenarios are shown above, it is expected that the range of responses will be acceptable within the context of the greater ROV control system if a PI controller is tuned at an intermediate operating point, such as 300 rpm.

In general, the nonlinearities in the system will serve to increase the damping for smaller step sizes. Therefore, a balanced approach was taken whereby near overdamped tuning was performed midway in the thruster's operating range, at 300 rpm. This provided a balance of reducing overshoot at higher steps while not jeopardising controller speed at lower steps. Figure 59 following shows the simulated step responses of a controller tuned for 300 rpm.

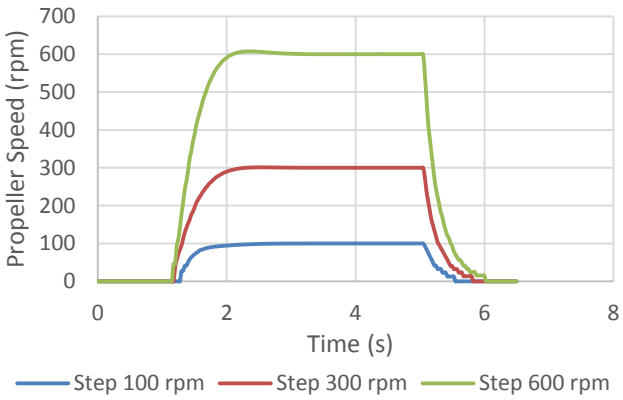

Figure 59 - Thruster system simulated step responses with a PI controller tuned for 300 rpm

With an acceptable looking response across the entire thruster operating range, the gains were adjusted so as to meet specification S1. The resulting tuned gains were: $K_p = 0.27$ and $K_i = 2.6$, resulting in a 95% rise time for a 650 rpm step of 0.61 s.

With a desired response gained by tuning step functions, the open-loop stability of the loop was assessed using a Bode Plot, with the results given following in Table 20 and Figure 60. The Tustin method was used for all Simulink® linearizations in this chapter.

Table 20 - Gain and Phase Margins for new system with added PI controller

Linearization Speed (rpm)	Gain Margin (dB)	at Frequency (Hz)	Phase Margin (˚)	at Frequency (Hz)
50	30.6	3.28	72.6	0.37
300	33.7	4.05	66.5	0.40
650	34.5	3.97	67.6	0.36

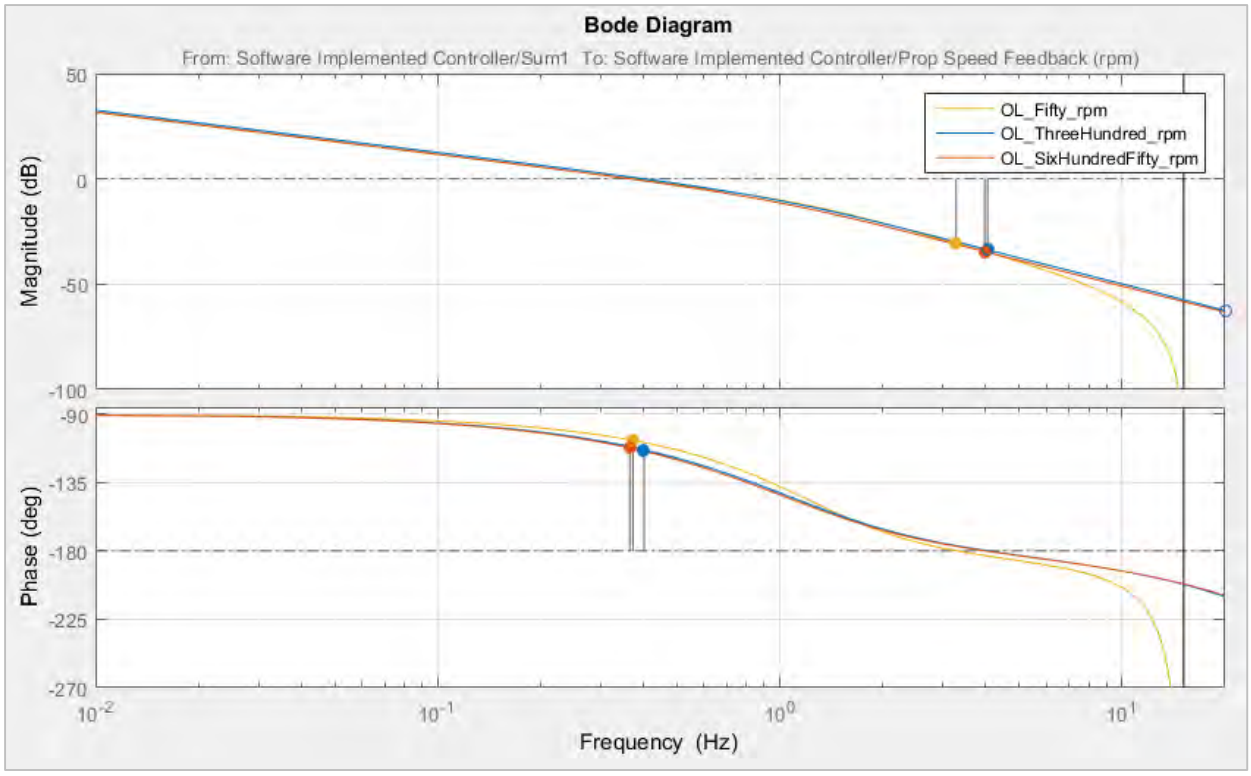

Figure 60 - Bode Plot for stability margins of the new system linearized about different speeds

Once again, the loop has large gain and phase margins, pointing towards its higher damping and inherent plant stability.

When compared to the previous system, when the new software controller was not implemented, it can be seen from Figure 61 following that both systems exhibit similar stability characteristics. However, it can be seen that in the new system, increasing the gain of the system will have a more dramatic effect on decreasing the damping of the system.

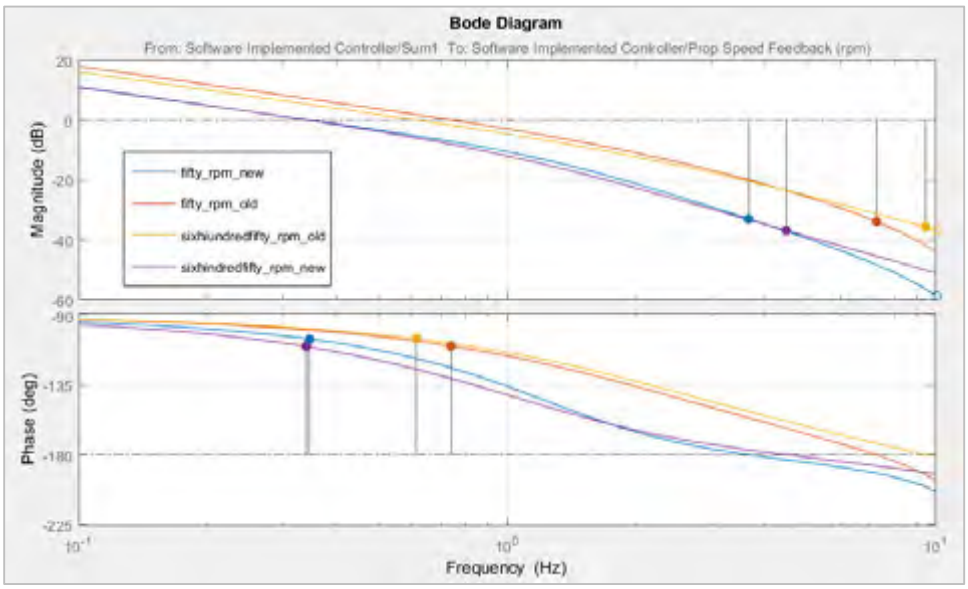

Figure 61 - Bode Plot for comparison between Maxon controlled system and new system with an additional software controller

Referring to Figure 62 below, the open-loop transfer was measured between points 1 and 3 for the new controller and 2 and 3 for the Maxon controller. For closed loop transfers, points 4 and 3 were used, with the new controller and first comparator being bypassed for the Maxon closed loop transfer.

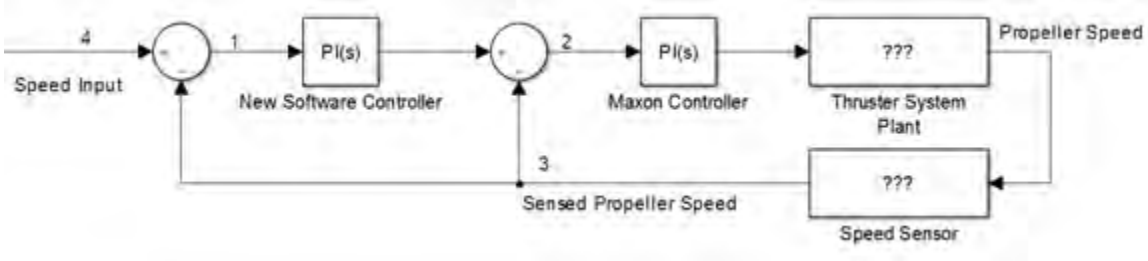

Figure 62 - Thruster system general control structure, showing points used for frequency analyses

While the introduction of an additional pole into the system at s = 0 has been shown to not significantly influence the stability of the system, it will serve to decrease the bandwidth of the system if the damping factor is to remain the same. Increasing the controller gain will increase the bandwidth, however the damping of the system will then decrease.

A comparison of the Maxon controlled and software controlled closed loop responses are shown following in Table 21 and Figure 63 following.

Table 21 - Comparison of bandwidths for Maxon controlled and new system

Linearized System	Worst Case Bandwidth (frequency at -3 dB)
Maxon Controlled	0.746 Hz
Software Controlled	0.572 Hz

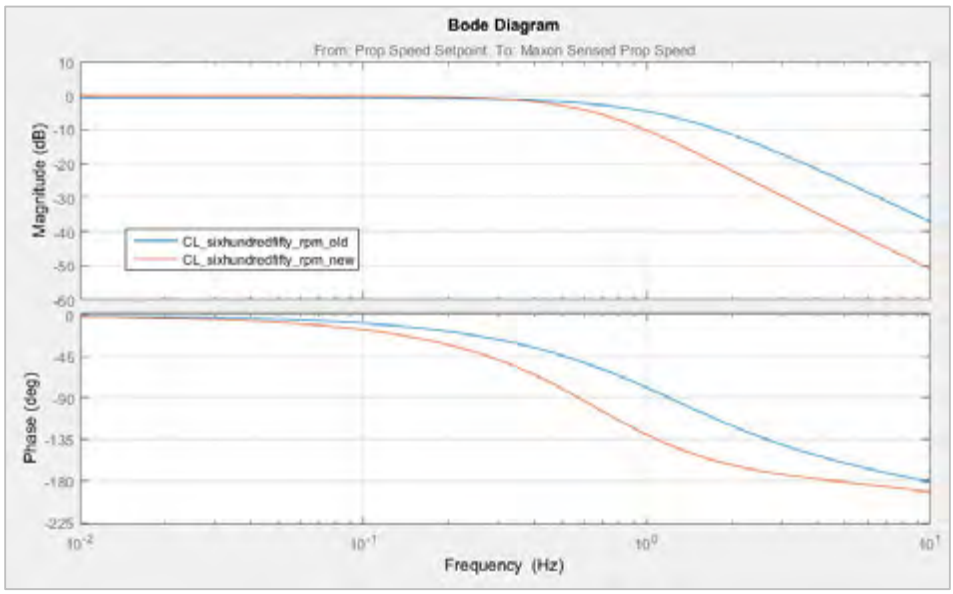

Figure 63 - Closed loop frequency responses showing the worst case bandwidth scenarios for the Maxon controller (old), and software controlled (new) systems

It can be clearly seen that the bandwidth of the new system is lower than the old system. The bandwidth could be increased by increasing the gain and implementing a dominant lead compensator at a frequency of greater than 2 Hz. However, due to ease of implementation, this was not attempted on the microcontroller. It was assumed that in the greater scheme of the whole ROV system, the thruster bandwidth and response time would be sufficient with just a PI controller. Both the phase and gain characteristics for the new system are assumed to be sufficient, however a more extensive control design could be attempted in the future if a more capable microcontroller was employed on the thruster electronics board.

Now that it has been established that the system is stable with sufficient phase, gain and bandwidth characteristics and with an initial continuous controller design proposed, the effects of digitising the controller and the effects of the digital sampling rate can be investigated in the next section.

4.3.5 Digitisation of Controller

A linearization of the system was performed at a 650 rpm plant operating speed - as this proved to give the lowest bandwidth for the system in the previous chapter - for the controller sampling rates of 10 Hz, 50Hz, 200 Hz and continuous to observe the effects of different sampling rates. A Bode Plot for the system open and closed loop responses is given following in Figure 64 and Figure 65 respectively.

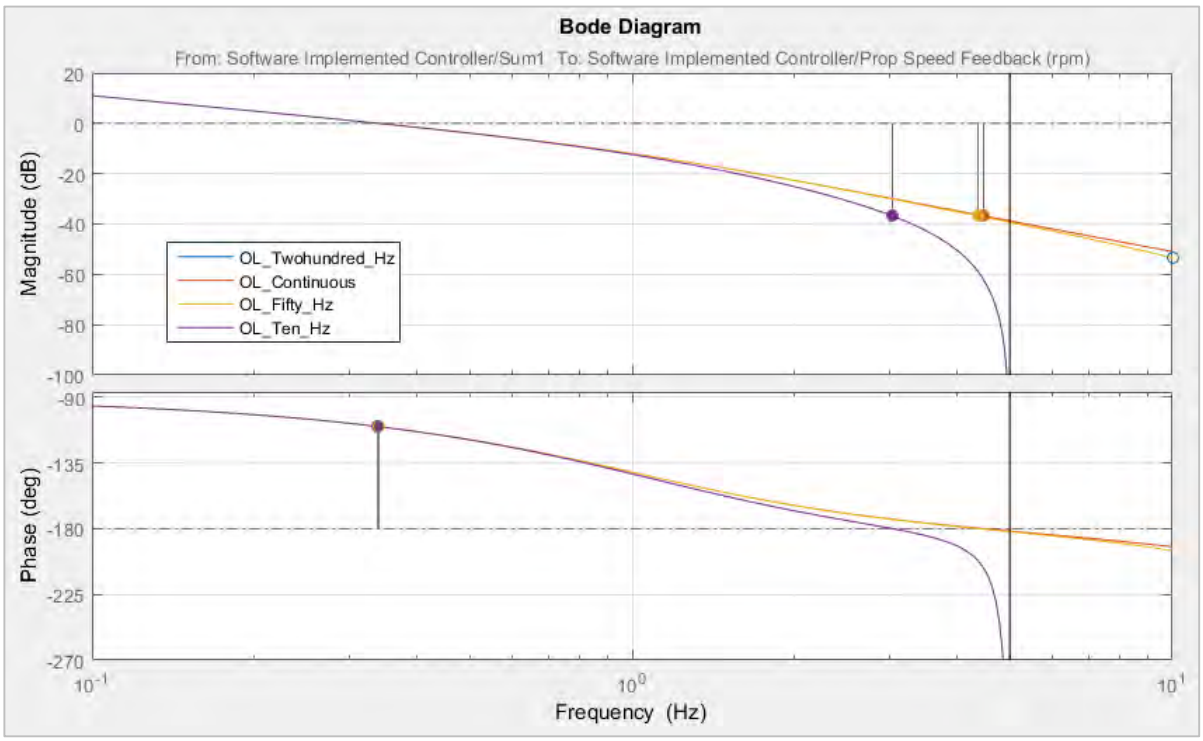

Figure 64 - Open-loop Bode Plot for the new system at different sampling rates

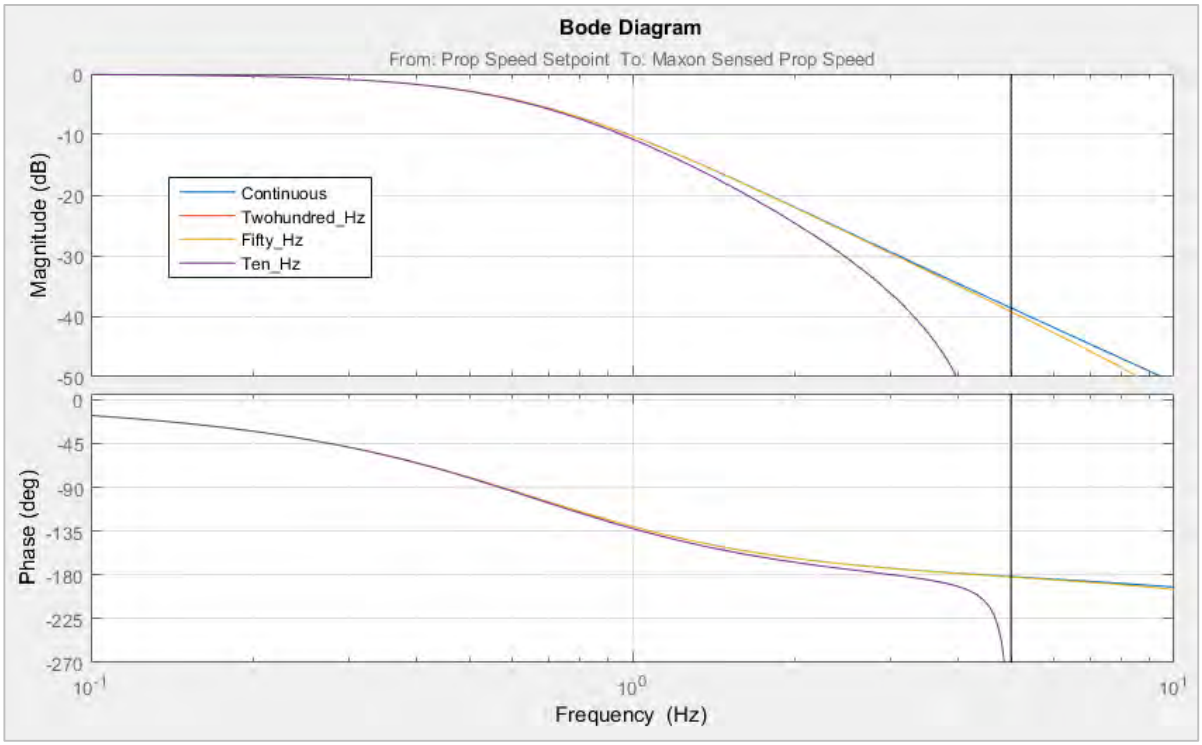

Figure 65 – Closed loop frequency response for new system at different sampling rates

Figure 64 shows that decreasing the sampling rate does not significantly affect the system stability if the system characteristics are kept constant. While there will be a point when the system becomes unstable as a result of a low controller sampling rate, it will be less than 10 Hz, which is an impractically low rate and would not typically be chosen.

Figure 65 shows that within the frequency region of interest for the thruster, the different sampling rates do not affect the bandwidth of the system significantly. This is useful for practical implementation of the control. As explained previously in section 4.3.3, the sampling rate has an inherent effect in the control difference equation to be executed by the microcontroller. If the sampling period is greater, it will be easier to convert the smallest products in the difference equation up to the range required at the controller output. This will result in less data and precision loss and hence serve to introduce less apparent noise into the system and provide better setpoint tracking.

Therefore, as a result of the sampling rate analysis it can be concluded that a sampling rate can be chosen that is advantageous for practical implementation on the microcontroller but should ideally be faster than a rate of 10 Hz. A rate of 200 Hz is fast enough to be approximated as continuous, but 50 Hz is a more appropriate rate, as it will introduce less apparent noise into the system and does not risk executing too quickly for the microcontroller to complete the control algorithm.

With the effects of the controller sampling rate understood, all important aspects of the controller have been covered and a summary of the digital controller design can be given in the next section.

4.3.6 Speed Controller Design Summary

A PI control scheme was designed to be implemented on the MSP430 at a rate of 50 Hz. The proportional gain was set at 0.27 and the integral gain was set at 2.6. The gain values were chosen by tuning the controller at 300 rpm for a slightly underdamped response and then increasing the gain slightly so that the rise time specification was met. Due to the acceleration rate limiter and non-linear plant model, the higher the step input into the system, the lower the damping of the system became. Tuning at 300 rpm was a trade-off between minimising control action for higher steps while minimising the loss of controller speed for lower step values.

The expected bandwidth of the system, not taking into account the effects of the acceleration rate limiter, is 0.572 Hz, with a similar damping factor and stability margins to the previous system. A more extensive design was not attempted due to the difficulties of implementing it on the microcontroller, however the current design is expected to be sufficient in the scheme of the greater ROV system.

With the controller design complete, the next section will present verification tests that were performed to evaluate the controller and once again validate the theoretical model compared to real life.

The implemented Simulink® block diagram representation of the controller is given following in Figure 66.

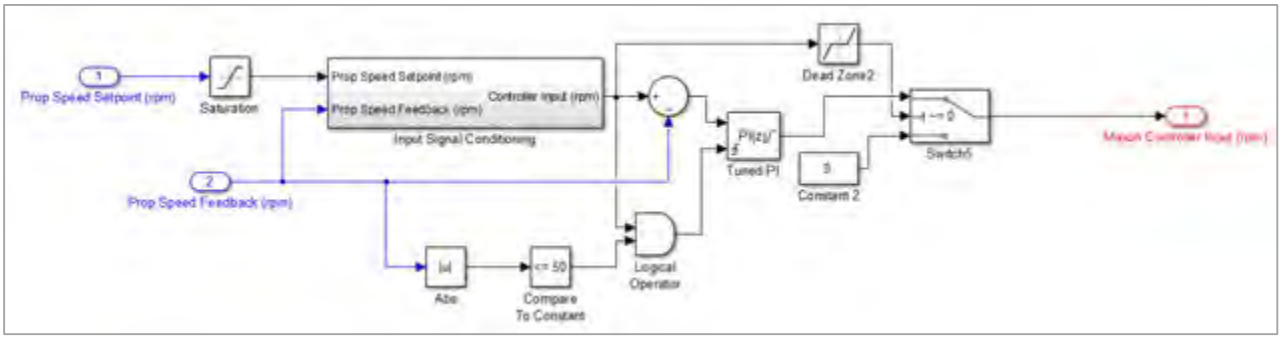

Figure 66 - Software controller Simulink® block diagram

4.4 Controller and Model Verification and Validation

4.4.1 Introduction

With a simple digital PI controller design specified, it was necessary to implement and verify the control scheme on the microcontroller, comparing the real life response to the simulation so as to account for any effects that are not included in the simulation. As mentioned previously, the fixed-point arithmetic on the microcontroller was a challenge to successfully implement and thus any possible data precision losses were accounted for. This section will give a description of how the controller difference equation was implemented on the microcontroller, present verification tests performed using the new control scheme and finally as a summary, detail the resulting controller design in full.

4.4.2 Data Manipulation and Implementation of Control Algorithm

Recall from section 4.3.3 previously, the difference equation to be implemented by the microcontroller:

$$u_n = \frac{1}{2}\left[2u_{n-1} + e_{n-1}\left(K_i\, T_{samp} - 2\, K_p\right) + e_n\left(2\, K_p + K_i\, T_{samp}\right)\right]$$

With chosen gains of $K_p = 0.27$ and $K_i = 2.6$ and a sampling period of $T_{samp} = 0.02$ s, the difference equation could be broken up into separate products that could be individually combined and converted so as to give a final setpoint output u_n.

The difference equation was broken up into the following constants:

$$\begin{aligned} A &= K_i * T_{samp} = 2.6 * 0.02 = 0.052 \\ B &= 2K_p = 2 * 0.2 = 0.4 \\ D &= A - B = -0.348 \\ E &= A + B = 0.452 \end{aligned} \quad \{4.90\}$$

The constants were used in the following algorithm, representing the difference equation that must be executed:

$$\begin{aligned} F &= e_{n-1} * D = -0.348e_{n-1} \\ G &= e_n * E = 0.452e_n \\ u_n &= 0.5(2u_{n-1} + F + G) \\ e_{n-1} &= e_n \\ u_{n-1} &= u_n \end{aligned} \quad \{4.91\}$$

In all of the above expressions, an appropriate fixed-point number with sufficient resolution and range had to be chosen for each constant and variable.

Saturation of the output was applied at a 700 rpm output and a similar control input conditioner to the one applied to the Maxon controller was applied to the input into the comparator. The signal conditioner logic

was shown previously in Figure 45 on page 61. The only difference is that the acceleration rate limiter in the Maxon controller was not applied to the new software controller.

With the digital algorithm defined, implementation and testing of the new controller was possible. This was achieved by assessing a range of step inputs and dynamic sequences in the same way that the Maxon controller was assessed in the previous chapter.

4.4.3 Step Test Verification

A series of step inputs were applied to the controller to compare the simulation to the real life case and assess any discrepancies between them.

An initial observation that was made, as displayed in Figure 67 following, is that when the same gains were applied to the simulation and the microcontroller, the response from the microcontroller was slower than in the simulation.

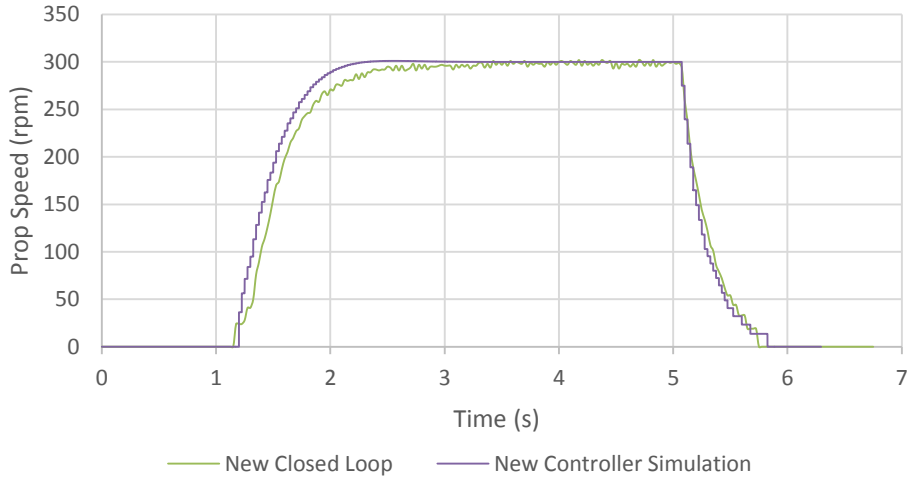

Figure 67 - 300 rpm step response of the new controller, where microcontroller and simulation gains are the same

It was assumed that the reason for this slower response was that if precision is lost in the microcontroller operations, the value will be truncated. The truncation can be propagated throughout the algorithm, resulting in a significantly slower response.

In addition, a noteable discrepancy between the model and the actual response is the initial lead of the controller as it begins to accelerate, and then a lag of the actual response to the simulation. This behaviour is expected to be due to internal Maxon controller factors that are difficult to determine. It is possible that the Maxon controller provides a higher gain initially to accelerate the motor past the deadband from stationary. If this were the case, the designed software controller would appear to lag after this initial acceleration, due to the actual control action being initially faster than the designed control action.

It was therefore decided to tune the controller in real life to match the simulation as closely as possible. The gains were increased in real life from $K_p = 0.27$ and $K_i = 2.6$ to $K_p = 0.27$ and $K_i = 3.2$ and the following results were obtained, shown in Figure 68.

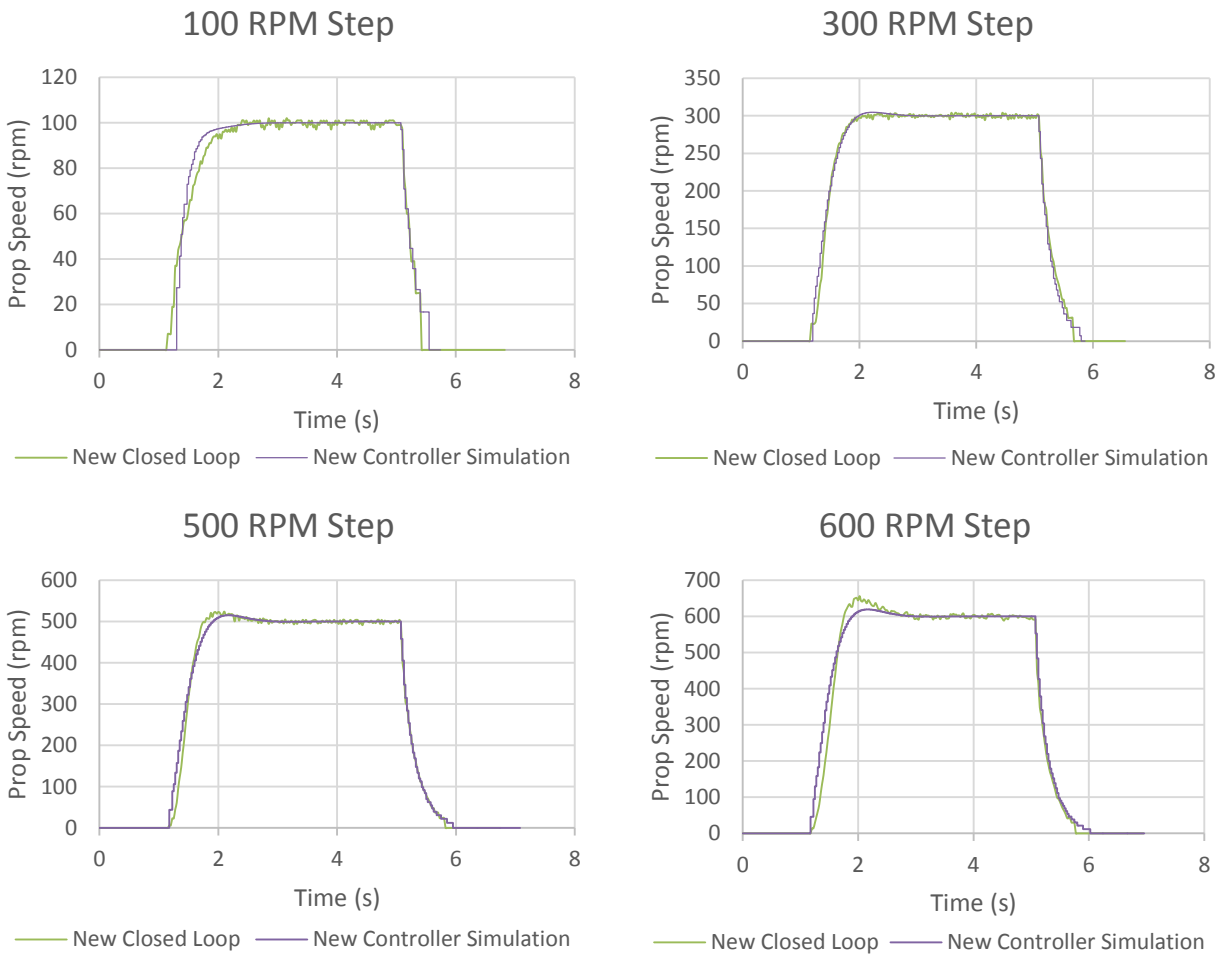

Figure 68 - Simulated and actual step responses for the new controller with increased gains

The increased damping in lower steps can be clearly seen, with the setpoint being tracked quite well. It should be noted that the overshoot in higher steps is greater in the actual response than in the simulation. This will be discussed more in the following section. In addition, while the speed of the actual response is improved, there is still a small lag in the actual response initially, when compared to the simulation.

Now that a good impression of the controller has been gained, with adjusted gains that more truthfully mimic the simulation behaviour as an approximation of unknown factors in the system, the system can be analysed for dynamic responses as given in the following section.

4.4.4 Dynamic Sequence Verification

A single direction and bi-directional simulation was applied to the system and the response was recorded. The simulations were performed under the same conditions as the dynamic tests in the previous chapter. The results of the simulated vs. the actual responses are shown following in Figure 69 and Figure 70.

Presentation of the dynamic responses of the thruster system along with the step responses given in the previous section has provided sufficient information to analyse the new controller and determine its performance, which will be undertaken in the following section.

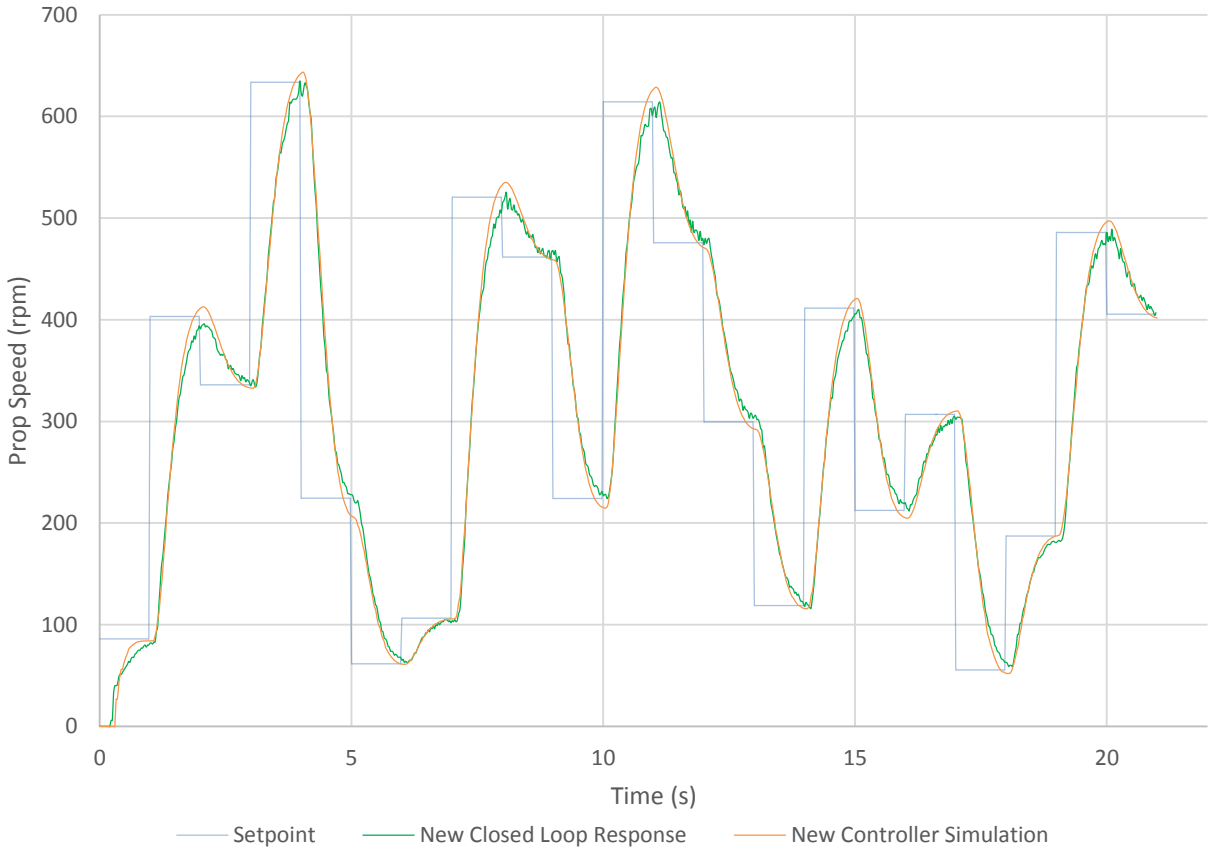

Figure 69 - Simulated and actual response for single direction dynamic sequence

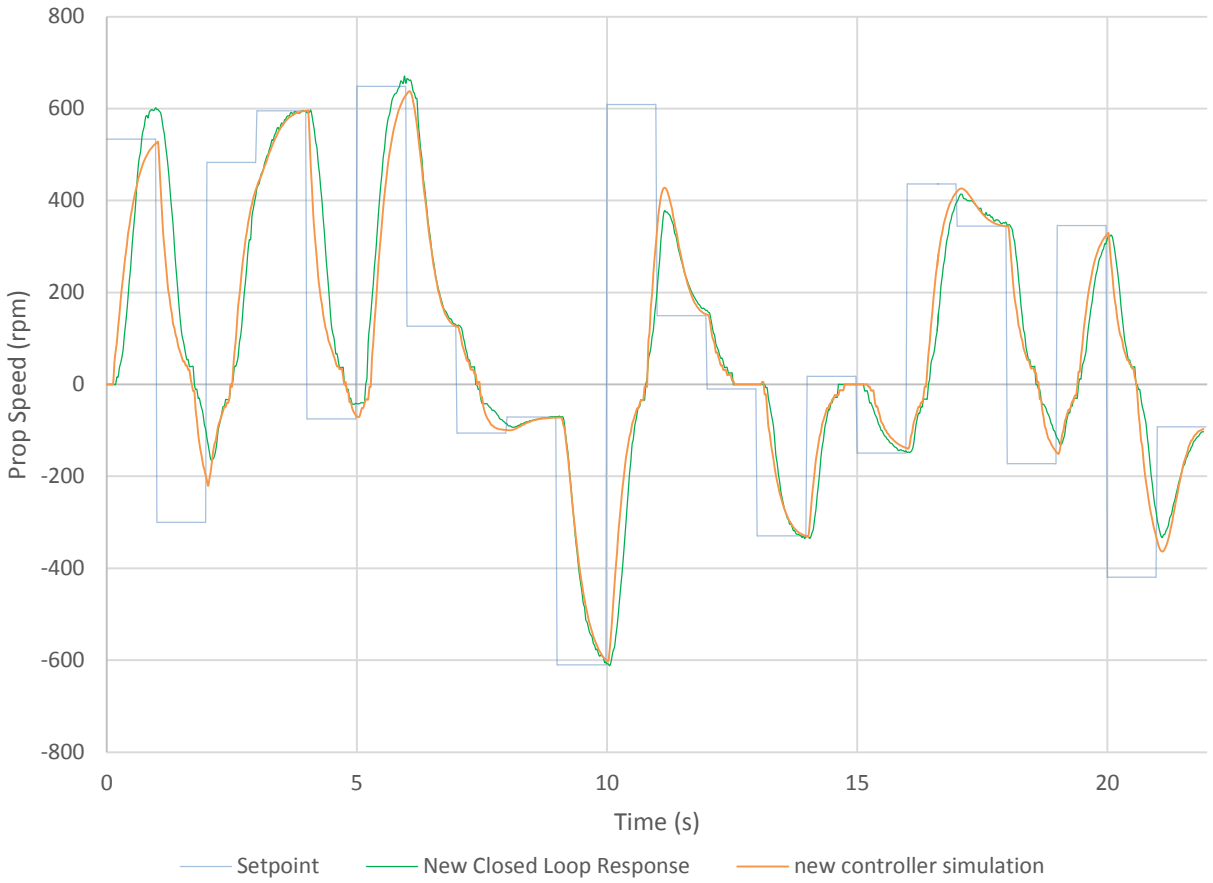

Figure 70 - Simulated and actual responses for bi-directional dynamic sequence

4.4.5 Performance Analysis

This section will analyse the steady state response of the new controller, specifying its characteristics. In addition, commentary will be given on the dynamic response using the results presented in the previous section.

Table 22 following gives characteristics of the controller responding to step functions to establish a measure of the setpoint tracking ability, speed and damping of the controller. Due to the uncertainty in the 40 Hz data capture rate, the rise time is given as an interval.

Table 22 - Analysis of step characteristics and controller steady state conditions

Step Size (rpm)	Average Speed (rpm)	% Speed Offset	% Overshoot	95% Rise Time (s)
100	99.9	0.13	2.0	0.800 to 0.825
300	299.8	0.07	1.3	0.575 to 0.600
400	400.9	0.21	4.5	0.500 to 0.525
500	499.3	0.14	4.8	0.500 to 0.525
600	599.5	0.09	9.3	0.500 to 0.525
650	650.0	0.00	4.8	0.625 to 0.650

Table 23 following gives characteristics of the apparent noise introduced into the system in steady state conditions.

Table 23 - Analysis of noise characteristics at steady state conditions

Step Size (rpm)	Speed Std. Dev. (rpm)	Maximum Speed Variation (rpm)	Noise Amplitude as % of Step
100	1.17	5	5.00
300	2.21	10	3.33
400	3.86	19	4.75
500	3.44	14	2.80
600	4.42	20	3.33
650	5.73	33	5.08

The following is observed from the above tables:

1. Setpoint tracking is very good.
2. As expected, the overshoot increases as the step increases. Although, due to the controller output saturation at 700 rpm, the maximum overshoot peak occurs at 600 rpm. At lower speeds, the overshoot is comparable to the noise amplitude and is thus actually close to 0% overshoot.
3. There is a trend of increasing rise time as the step size decreases, however, the trend is not very strong and the rise time appears to change somewhat irregularly according to step size.
4. At higher speeds in general, the amplitude of the noise increases relative to the size of the step, as shown by the speed standard deviation values.

From the dynamic sequences it can be seen that in general the response in real life is slower than in the simulation. It is interesting that in the single direction dynamic sequence, there is a trend of the actual response not reaching the same speed peaks as the simulation, even with the increased real life gains. This could be due to a loss of precision in the microcontroller as the error signal decreases, resulting in truncation of values close to the setpoint and ultimately a slowing response as the error decreases.

For the bi-directional dynamic sequence, the simulation and actual response match quite well, apart from in the first few seconds of the test, when a large speed overshoot is observed in the real life case. Importantly, the behaviour around the deadband region is quite well approximated.

In general, the similarity between the different tests and their respective simulations is sufficient - with a notable observation being the slower actual response in the single direction dynamic sequence. With an analysis of the new controller complete, it is possible to define specifications of the controller in the following section.

4.4.6 Controller Specifications

Desired specifications for the new controller were presented in Table 19 previously in section 4.3.2. The design specifications for the new controller can now be determined from real life values. A summary of the design criteria and obtained specification values is given following in Table 24.

Table 24 - Software controller thruster system vs. design specifications

Specification #	Description	Criteria	Actual Value	Specification Met?
S1	95% rise time for a 650 rpm step	≤ 0.66 s	0.65 s	Yes
S2	Bandwidth	≥ 0.67 Hz	0.59 Hz	No
S3	Maximum Overshoot as % of Step	≤ 10%	9.3%	Yes
S4	Phase Margin	≥ 30˚	66.5˚	Yes
S5	Gain Margin	≥ 7 dB	30.6 dB	Yes

As can be seen from the table, the desired bandwidth was not achieved when the controller model was linearized. However, this was expected and it was decided previously that the rise time would take priority over the bandwidth, due to the non-uniform response of a PI controller across the whole thruster operating range. Since the rise time was achieved, it was decided that the bandwidth that was achieved was acceptable, due to the difficulty with implementing a more complex control design on the given hardware.

In addition to the design specifications, real life data from the new controller analysis in the previous section allowed typical and worst case scenario characteristics to be given for the thruster system, as given following in Table 25. The typical values were calculated using an average of the presented data in Table 22 and Table 23.

Table 25 - Software controller thruster system worst case scenario and typical characteristics

Description	Worst Case	Typical
95% rise time	0.83 s	0.60 s
Steady state noise as % of running speed	5.08%	4.05%
Setpoint tracking error as % of speed	0.21%	0.11%
Maximum Thruster Output Speed	700 rpm	700 rpm

This completes the specifications of the new “software controller” controlled thruster system. Finally, to determine how closely the control design performed according to its original goals presented at the beginning of this chapter, a comparison between the new “software controller” controlled system and the previous “Maxon controller only” controlled system will be given in the following section.

4.5 Comparison of New Software Controller and Maxon Controller

It was the aim of the new software controller to provide perfect setpoint tracking while minimising the loss of controller speed that would be inherent in the system after introducing another control loop. This section will analyse the speed offset, the rise times and the steady state speed variation of the Maxon and the new controller systems. The results are presented below in Table 26, Table 27 and Table 28.

The "% Improvement" column was calculated by comparing the two values obtained for the Maxon and Software controlled systems as follows:

$$\%\ Improvement = \frac{Maximum\ Value - Minimum\ Value}{Minimum\ Value} \quad \{4.92\}$$

If the minimum value is from the Maxon controller column, the % Improvement value was given as negative, representing a decrease in performance by the Software controller.

Table 26 - Comparison of steady state speed offset as a percentage of the speed setpoint

Step Size (rpm)	Maxon Controller %	Software Controller %	% Improvement
100	9.37	0.13	711
300	2.71	0.07	377
400	2.63	0.21	115
500	1.68	0.14	110
600	1.09	0.09	111
650	1.33	0.00	≈332

Table 27 - Comparison of the 95% rise time for different input steps

Step Size (rpm)	Maxon Controller (s)	Software Controller (s)	% Improvement
100	0.250	0.825	-230
300	0.500	0.600	-20.0
400	0.525	0.525	-0.0
500	0.575	0.525	9.5
600	0.600	0.525	14.3
650	0.600	0.650	-8.3

Table 28 - Comparison of steady state noise as a percentage of the running speed

Step Size (rpm)	Maxon Controller %	Software Controller %	% Improvement
100	3.00	5.00	-66.6
300	3.67	3.33	10.2
400	2.75	4.75	-72.7
500	4.00	2.80	42.9
600	3.50	3.33	5.1
650	4.62	5.08	-10.0

A comparison between the new and old control responses are shown following in Figure 71. It can be seen that, given that there is some irregular behaviour, in general the software controller is slower than the Maxon controller for smaller steps but is similar in speed to the Maxon controller for larger steps. The

improved setpoint tracking capability is not observed in the figure however, due to the frequency of setpoint inputs.

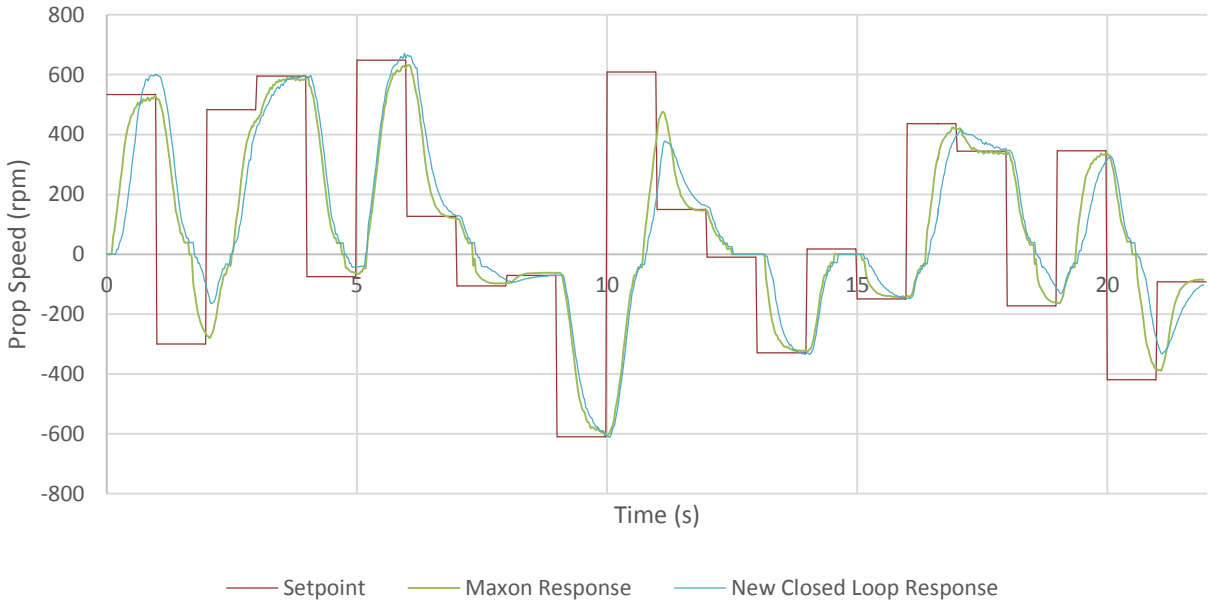

Figure 71 - Dynamic thruster response under influence of new and old control schemes

It can be concluded from Table 26 previously that there is a dramatic improvement in setpoint tracking with the new controller.

As expected, the response speed of the controller is slower than previously at lower speeds, with little improvement at higher speeds. The lack of improvement was expected due to the acceleration rate limiter in the Maxon controller. The previous maximum speed swing achievable was 946 rpm/s, it is now lower at 759 rpm/s. It is assumed however, that this will be sufficient within the greater scheme of the ROV control.

It appears that while the difference in noise amplitude for both control systems is irregular, there is a general trend, as expected, of the new controller introducing slightly more apparent noise into the system.

It can be concluded that the new controller design achieved its goals by dramatically decreasing the steady state offset while only reducing the controller speed a small amount, apart from on the lower operational extreme where the response is quite overdamped. This was deemed acceptable however, within the greater context of the ROV system.

The implementation of the control using software fixed-point algorithms did increase the amplitude of the steady state noise in general, but not significantly and a loss of precision served to slow the controller response as it neared the setpoint.

With the new controller design completed, implemented and analysed, the development of the new controller is complete and a summary of its development can be given in the following section.

4.6 Software Speed Controller Summary

To improve the inherent steady state speed offset present in the Maxon controlled thruster system, a new software implemented controller was designed to provide a modified input into the Maxon controller. The aim of the controller was to provide perfect setpoint tracking without jeopardising the speed of the Maxon controller to a large extent.

Implementing the control on an MSP430 microcontroller that was only capable of software fixed-point arithmetic made the control complicated to achieve. This was due to how fixed-point numbers halve their range if their resolution is doubled. With constants in the region of 0.4 needing to be scaled up to an output range of 0 to 1400 rpm, data manipulation became arduous to implement. This was a motivating factor to merely implement a simple PI control scheme.

A preliminary design simulation showed that there would not be a uniform response from the controller over the thruster's entire operating range, but the controller could provide a fast enough response for large steps, without introducing too much overshoot, whilst providing a slower but acceptable response speed for smaller step values.

Linearization of the system model allowed the frequency response of the system to be analysed, showing that it's large stability margins remained intact, but how increasing the gain would have a more dramatic effect than before at decreasing the system damping without the addition of compensators. In addition, the bandwidth of the system decreased due to introduced integrator in the software controller.

The sampling effects did not serve to decrease the stability or bandwidth of the loop before an impractically slow sampling rate limit was reached.

The controller was implemented at a sampling rate of 50 Hz and higher gains in real life were necessary to achieve the same response of the simulation. This was attributed to the truncation of values during a loss of numerical resolution in the microcontroller combined with internal factors in the Maxon controller. The gains of the implemented controller were $K_p = 0.27$ and $K_i = 3.2$, which represented gains in the simulation of $K_p = 0.27$ and $K_i = 2.6$.

An analysis showed that the new controller significantly decreased the steady state offset while only slowing the response at lower speeds a small amount. The slower responses were deemed to be permissible, and the noise introduced into the system using fixed-point arithmetic was not deemed to be significantly more than the noise present in the Maxon controlled system.

This completed the design, implementation and verification of a software controller on the thruster to provide perfect setpoint tracking. The thruster system has now been completely defined at a subsystem level, allowing modelling of the rest of the *SEAHOG* ROV to commence.

Chapter 5 - Dynamic Model of the *SEAHOG*

5.1 Introduction to the *SEAHOG* Dynamic Model

The previous two chapters have successfully developed a model for the actuators of the *SEAHOG* ROV providing a thrust force input into the general ROV equation of motion, recalled from equation 2.12 in Chapter 2 as:

$$\boldsymbol{M\dot{\nu}} + \boldsymbol{C(\nu)\nu} + \boldsymbol{D(\nu)\nu} + \boldsymbol{g(\eta)} = \boldsymbol{\tau} + \boldsymbol{w}$$

With a detailed and sufficiently accurate dynamic model developed for the thrusters, the identification for all of the remaining system parameters could be undertaken in this chapter so as to apply the generalised equation of motion directly to the *SEAHOG* ROV. Parameters that needed to be identified consisted of the following:

$\boldsymbol{M}$ - System mass and inertia matrix including added mass and inertia terms

$\boldsymbol{C(\nu)}$ - Coriolis centripetal matrix included added mass terms

$\boldsymbol{D(\nu)}$ - Damping matrix

$\boldsymbol{g(\eta)}$ - Gravitational/buoyancy forces and moments

$\boldsymbol{B}$ - Transformation from localised axial thrust forces to ROV body-fixed thrust vectors

The manufacturing of the *SEAHOG* was not completed at the time of this report and so, unfortunately, it was impossible to experimentally determine or verify many of the above factors. However, due to the capabilities of advanced modelling techniques and Computer Aided Design (CAD) tools, almost all of the physical parameters could be approximated to some level of accuracy.

This chapter will describe the processes used to identify the remaining system parameters, the values obtained for them and any simplifications or assumptions that were made. This chapter will begin by defining physical properties of the *SEAHOG* such as its origin, centre of mass and centre of buoyancy, after which the parameter identification and model development will proceed.

5.2 *SEAHOG* BODY Coordinate Origin and Restoring Forces

5.2.1 Introduction

It is important to define the body-fixed coordinate frame on the *SEAHOG* so that the rest of the model has a clearly defined reference. This section will firstly define the origin to be used in the BODY reference frame on the robot, after which the centre of gravity and buoyancy will be defined and finally the restoring forces term $\boldsymbol{g}(\boldsymbol{\eta})$ in the general ROV equation of motion will be defined.

5.2.2 Body-Fixed Coordinate frame Position of Origin

The *SEAHOG* body-fixed reference frame is defined as detailed previously in section 2.2. The origin of the *SEAHOG* body-fixed frame is coincident with the intersection of the bottom face of the frame base plate and the axis of the vertical thruster. The exact location of the origin and orientation of the body fixed axes is shown following in Figure 72.

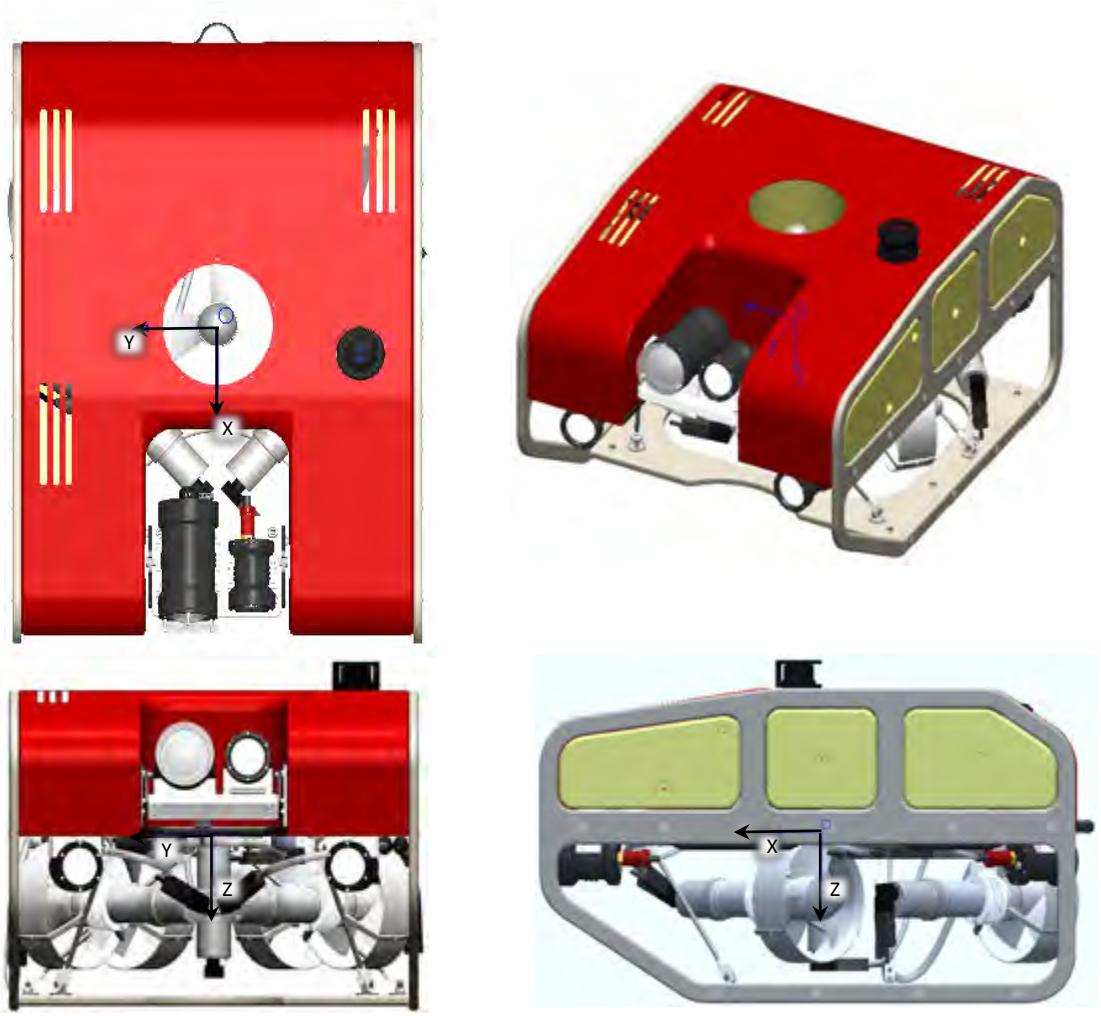

Figure 72 - Body-Fixed coordinate origin position defined on the *SEAHOG*

The origin of the reference frame was chosen so that the partial symmetry of the ROV structure could be taken advantage of. If the origin is chosen so that it is coincident with the centre of gravity, the Coriolis and

Inertia tensors are simplified significantly. However, due to the computational power of Solidworks, this data was freely available from the CAD model and was thus simple to implement. A more challenging task however, was the drag and added mass matrix identification, both of which can be simplified significantly if the co-ordinate system is symmetrically positioned within the body. Therefore, it was decided that it was more advantageous from a model parameter identification point of view to position the origin to take advantage of the ROV's symmetry.

This completes a description and motivation for the location of the *SEAHOG*'s body-fixed reference frame, allowing the centre of mass and gravity to be defined relative to it.

5.2.3 Centre of Mass and Centre of Buoyancy

The centre of mass was determined using the Solidworks CAD model of the ROV. The material properties of every component was checked, and all the interior components were added to the sub-system modules with masses assigned to irregular components such as the circuit boards. The mass of every component was measured and then compared to its corresponding mass in the model. This task was performed with care so that in aggregate the mass of the modelled individual sub-systems was within 0.1 kg of the equivalent real mass. An estimation of the mass of the subsea cables connecting each sub-system were also included in the calculations.

There were some unknown factors that were significant and had to be estimated and factored into the design. One of these factors was the epoxy and protective coatings that would be applied in future to the float block material. The extra mass was estimated by determining the float block material surface area and multiplying it by a 0.5 mm thick layer, giving the volume of epoxy to be applied. After which, the volume was multiplied by the mixed epoxy density, giving an estimated extra mass. Obviously, the extra volume of the epoxy would result in increased buoyancy as well. The nett estimated effect for the added epoxy was calculated as 0.22 kg, meaning that the ROV weight in the Solidworks model would need to be the equivalent of 0.22 kg less than the buoyancy force to be neutrally buoyant.

The buoyancy force is derived by Archimedes' principle and is equivalent to the mass of seawater displaced by the ROV. The centre of buoyancy is the centroid of the volume of water that is displaced by the ROV. The buoyancy force and centre of buoyancy were both calculated using Solidworks as described following:

- The volume of material that makes up a part in Solidworks is calculated automatically by the software - only the material volume however, not the volume enclosed by a vessel, for example.
- It was necessary to find the volume of water displaced by each module and thus the CAD model of each subsystem housing was emptied and the cavity inside was filled with a solid part.
- The completely solid and filled vessel resulted in Solidworks effectively calculating the volume of the entire module, including its interior space.

- Applying water for the material properties of each part subsequently gave the mass of water displaced by each part.
- With the mass properties of the whole ROV set as water, the centre of mass function on Solidworks was then used to find the centre of mass of the assembly.
- Since the centre of mass was showing the centroid of the volume of water that the ROV was displacing, it represented the centre of buoyancy.
- The mass of the entire assembly multiplied by gravity after the density of seawater was applied gave the magnitude of the buoyancy force.

The buoyancy of the ROV is designed to be slightly positive so that if communication is lost to it permanently, it will resurface passively. It was decided that the buoyancy would be trimmed by adding small masses and extra buoyancy blocks so that the difference in buoyancy and mass is approximately 20 N. The nett buoyancy force must not be too great in magnitude, since the vertical thruster will have to constantly produce this force to keep the ROV at a constant depth.

To meet the nett 20 N buoyancy force criteria, the mass of the ROV needed to be increased slightly. It was assumed that small, high density mass pieces will be added to the ROV so as to increase the weight without significantly increasing the buoyancy or CG position. The design procedure for the passive buoyancy module (float block) on the *SEAHOG* is described in [24]. Ideally, for the ROV to naturally rest in a horizontal orientation and to have positive buoyancy, the CG and CB must be as close to coaxial as possible in the vertical direction, with the buoyancy force being slightly greater in magnitude than the weight. The resulting centre of buoyancy and centre of gravity and their magnitudes, according to the Solidworks CAD data, are given below in Table 29.

Table 29 - CG and CB properties on the *SEAHOG*

	CG	CB	Difference (CG – CB)
x position (mm)	-43.6	-43.1	-0.5
y position (mm)	-6.4	-5.9	-0.5
z position (mm)	-17.8	-60.9	43.1
Magnitude (N)	804.0	824.0	-20

It should be noted that there is a minor difference between the X and Y position of the CG and CB. The offset will result in the ROV naturally resting in a horizontal position with non-zero pitch and roll values, however, the pitch and roll angles are expected to be negligibly small. From the above table, we can define the vectors $\boldsymbol{r}_b^b$ and $\boldsymbol{r}_g^b$, as described previously in section 2.4.6 as:

$$\boldsymbol{r}_g^b = \begin{bmatrix} -0.044 \\ -0.006 \\ -0.018 \end{bmatrix} \text{m}; \boldsymbol{r}_b^b = \begin{bmatrix} -0.043 \\ -0.006 \\ -0.061 \end{bmatrix} \text{m} \quad \{5.93\}$$

With the magnitudes and positions of the CG and CB defined, with the buoyancy force, B = -824.0 N and the weight, W = 804.0 N defined, the restoring moments and forces can be defined.

5.2.4 Restoring Forces and Moments

With CG, CB, W and B defined, the restoring forces and moments vector can be constructed from equation 2.47 as:

$$\boldsymbol{g}(\boldsymbol{\eta}) = \begin{bmatrix} -20sin\theta \\ 20cos\theta sin\phi \\ 20cos\theta cos\phi \\ 0.28cos\theta cos\phi + 35.87cos\theta sin\phi \\ 35.87sin\theta + 0.46cos\theta cos\phi \\ -0.46cos\theta sin\phi + 0.28sin\theta \end{bmatrix} \quad \{5.94\}$$

Notice that the sign has been changed for the terms given above due to the way in which the general ROV equation of motion was poised. When the $\boldsymbol{g}(\boldsymbol{\eta})$ term is taken to the same side of the equation as the input thrust vector, $\boldsymbol{\tau}$, the positive buoyancy of the ROV can be seen to exert a -20 N force, which is correct given that the NED frame is positive down.

With the derivation of the restoring forces in the *SEAHOG* system defined, the mass and Coriolis tensors can be derived in the following section.

5.3 Rigid-Body Mass and Coriolis Terms

5.3.1 Introduction

The Mass and Coriolis terms, $\boldsymbol{M}$ and $\boldsymbol{C}(\boldsymbol{\nu})$ are split into a rigid body term and an added mass term such that:

$$\boldsymbol{M} = \boldsymbol{M}_{RB} + \boldsymbol{M}_{A}$$
$$\boldsymbol{C}(\boldsymbol{\nu}) = \boldsymbol{C}_{RB}(\boldsymbol{\nu}) + \boldsymbol{C}_{A}(\boldsymbol{\nu})$$

In addition, it should be noted that the mass matrices $\boldsymbol{M}_{RB}$ and $\boldsymbol{M}_{A}$ are of dimension 6x6 and thus contain mass terms for the translational axes and inertia terms for the rotational axes. For convenience, they will be referred to as mass matrices. The rigid body term ($\boldsymbol{M}_{RB}$) is related to the physical properties of the *SEAHOG* directly, whereas the added mass terms are related to the interaction of the ROV with the surrounding fluid. This section will use the expressions for the Coriolis and mass terms derived in Chapter 2 and obtain the numerical expressions for the rigid-body terms in the context of the *SEAHOG*.

5.3.2 Rigid-Body Mass and Coriolis

As derived and defined previously in section 2.4.2 the rigid body mass and Coriolis matrix terms, $\boldsymbol{M}_{RB}$ and $\boldsymbol{C}_{RB}(\boldsymbol{\nu})$ are defined by equations 2.28 and 2.29.

Using Solidworks CAD data, the inertia, mass and CG position, as shown below, could be combined to produce the rigid-body mass and Coriolis matrices.

$$m = 81.96\,\text{kg}\,;\ \boldsymbol{r}_g^b = \begin{bmatrix} -0.044 \\ -0.006 \\ -0.018 \end{bmatrix}\text{m}\,;\ I_O = \begin{bmatrix} 3.19 & 0.15 & -0.06 \\ 0.15 & 4.21 & 0.00 \\ -0.06 & 0.00 & 5.79 \end{bmatrix}\text{kgm}^2$$

It should be noted that although the BODY frame origin was not picked to be coincident with the CG, the off diagonal elements of the inertia tensor shown above are very small in magnitude compared to the diagonal elements. This is expected, due to the Origin's close proximity to the CG.

The rigid body mass and Coriolis matrices are given below:

$$\boldsymbol{M}_{RB} = \begin{bmatrix} 81.96 & 0 & 0 & 0 & -1.46 & 0.52 \\ 0 & 81.96 & 0 & 1.46 & 0 & -3.57 \\ 0 & 0 & 81.96 & -0.52 & 3.57 & 0 \\ 0 & 1.46 & -0.52 & 3.19 & 0.15 & -0.06 \\ -1.46 & 0 & 3.57 & 0.15 & 4.21 & 0.00 \\ 0.52 & -3.57 & 0 & -0.06 & 0.00 & 5.79 \end{bmatrix} \quad \{5.95\}$$

$$\boldsymbol{C}_{RB}(\boldsymbol{\nu}) =$$

$$\begin{bmatrix} 0 & 0 & 0 \\ 0 & 0 & 0 \\ 0 & 0 & 0 \\ -81.96(-0.006q - 0.018r) & 81.96(-0.006p + w) & 81.96(-0.018p - v) \\ 81.96(-0.044q - w) & -81.96(-0.044p - 0.018r) & 81.96(-0.018q + u) \\ 81.96(-0.044r + v) & 81.96(-0.006r - u) & -81.96(-0.044p - 0.006q) \end{bmatrix} \quad \{5.96\}$$

$$\begin{bmatrix} 81.96(-0.006q - 0.018r) & -81.96(-0.044q - w) & -81.96(-0.044r + v) \\ -81.96(-0.006p + w) & 81.96(-0.044p - 0.018r) & -81.96(-0.006r - u) \\ -81.96(-0.018p - v) & -81.96(-0.018q + u) & 81.96(-0.044p - 0.006q) \\ 0 & 0.06p + 5.79r & 0.15p - 4.21q \\ -0.06p - 5.79r & 0 & -0.15q + 0.06r + 3.19p \\ -0.15p + 4.21q & 0.15q - 0.06r - 3.19p & 0 \end{bmatrix}$$

With the rigid-body mass and Coriolis matrices listed, the added mass terms can be determined.

5.4 Added Mass and Coriolis Terms

5.4.1 Introduction

Recall that the mass and Coriolis terms, $\boldsymbol{M}$ and $\boldsymbol{C}(\boldsymbol{\nu})$ are split into a rigid body term and an added mass term such that:

$$\boldsymbol{M} = \boldsymbol{M}_{RB} + \boldsymbol{M}_{A}$$
$$\boldsymbol{C}(\boldsymbol{\nu}) = \boldsymbol{C}_{RB}(\boldsymbol{\nu}) + \boldsymbol{C}_{A}(\boldsymbol{\nu})$$

The rigid body terms were defined in the previous section. This section will discuss how the added mass terms were approximated for use in the *SEAHOG* dynamic model.

The added mass matrix is extensive and it is often difficult to experimentally determine all of its elements. Therefore it is common practise to use a simplified added mass matrix in an ROV model, listing only the parameters that can be experimentally determined with a reasonable degree of accuracy. In addition, due to added mass being only a function of the vehicle geometry and the fluid density, assumptions of symmetry are often used to simplify the matrix.

A body with three planes of symmetry, such as a rectangular prism, will have a diagonal added mass matrix. This section will proceed by assessing the symmetrical properties of the *SEAHOG* and discussing how the added mass matrix can be simplified. It will then discuss the available resources for determining the added mass terms and how they were used to define added mass terms for the *SEAHOG*. Finally, the added mass and Coriolis matrices will be presented with the approximated added mass values.

5.4.2 *SEAHOG* Symmetrical Properties

Added mass is a phenomenon of pressure induced forces that result from the motion of a body increasing the kinetic energy of a fluid. As a result, large volumes and surface areas of an underwater vehicle will have the greatest effect on the vehicle's added mass. Therefore, the added mass effects on the *SEAHOG* will be largely due to the hull of the vehicle (all modules covered by the red ROV cover). Due to the complex geometry and flow conditions of the thrusters, they were removed for the purposes of defining the added mass of the *SEAHOG*.

Using the knowledge that the ROV hull is of most interest for the purposes of added mass, a simplification can be made, whereby the hull of the ROV only is considered for defining the vehicle's added mass. Simplification of added mass expressions will be necessary in the absence of advanced computational tools that can accurately give the added mass properties of the ROV.

A body with two planes of symmetry will have an added mass matrix with seven non-zero independent terms, which is a significant simplification from the 21 non-zero independent terms required if there is no

body symmetry. While there is not always body symmetry in three planes, due to the difficulty of experimentally verifying the off diagonal elements of an added mass matrix, three plane symmetry is often assumed [30], [31]. Considering only the hull of the *SEAHOG* (shown by the red cover) in Figure 73 following, symmetry exists in the X-Z plane (front view). For the hull specifically, there is partial symmetry in the X-Y plane (side view) as shown by the dotted line. There is little symmetry in the Y-Z plane (top view).

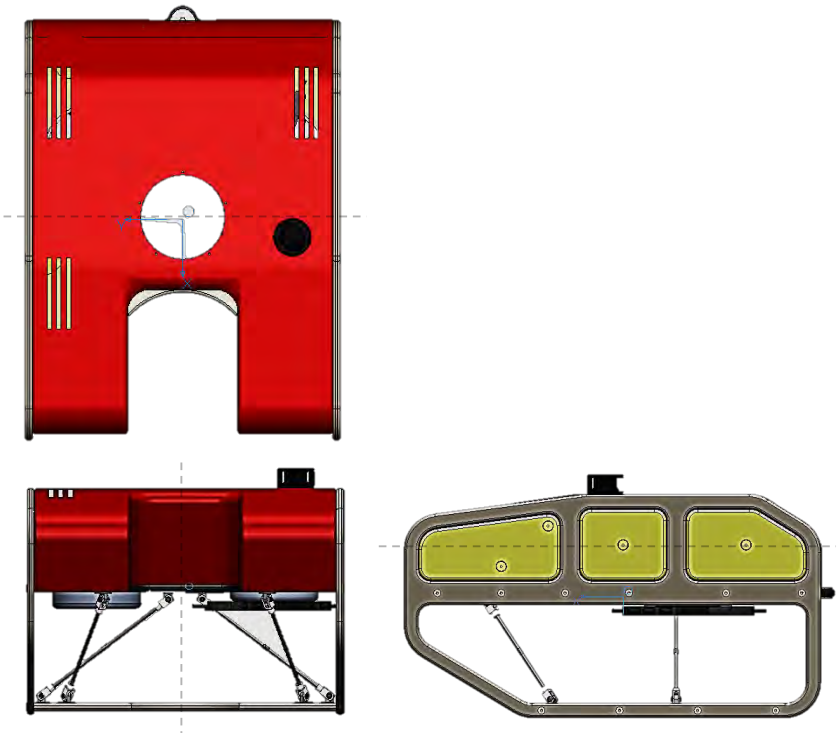

Figure 73 - 3rd angle projection of the SEAHOG hull and frame to demonstrate hull symmetry

Due to the largely prismatic shape of the *SEAHOG* hull, for the purposes of this report the assumption of three plane symmetry will be enforced. As previously noted, this is common practise in the initial stages of ROV model development, especially where the vehicle will only be moving at low speeds [19]. It is noted however, that the assumption of symmetry should be verified at a later date when the ROV construction is complete.

With the assumption of three planes of symmetry, the added mass and coriolis matrices simplify to:

$$\boldsymbol{M}_A = \left[X_{\dot{u}}, Y_{\dot{v}}, Z_{\dot{w}}, K_{\dot{p}}, M_{\dot{q}}, N_{\dot{r}}\right]^D \quad \{5.97\}$$

$$\boldsymbol{C}_A(\nu) = \begin{bmatrix} 0 & 0 & 0 & 0 & -Z_{\dot{w}}w & Y_{\dot{v}}v \\ 0 & 0 & 0 & Z_{\dot{w}}w & 0 & -X_{\dot{u}}u \\ 0 & 0 & 0 & -Y_{\dot{v}}v & X_{\dot{u}}u & 0 \\ 0 & -Z_{\dot{w}}w & Y_{\dot{v}}v & 0 & -N_{\dot{r}}r & M_{\dot{q}}q \\ Z_{\dot{w}}w & 0 & -X_{\dot{u}}u & N_{\dot{r}}r & 0 & -K_{\dot{p}}p \\ -Y_{\dot{v}}v & X_{\dot{u}}u & 0 & -M_{\dot{q}}q & K_{\dot{p}}p & 0 \end{bmatrix} \quad \{5.98\}$$

Therefore, it is necessary to determine only six distinct added mass terms.

With the symmetrical properties of the *SEAHOG* well understood, along with the three planes of symmetry assumption, the six distinct added mass terms can be approximated.

5.4.3 Formulation of Added Mass Terms

There are various ways in which the added mass can be found. Computer software such as WADAM or WAMIT is capable of finding the entire added mass matrix for a body. The software however was not available for use in this project. In addition, due to the incomplete state of the *SEAHOG*, experimental procedures could not be performed to determine the added mass. It was deemed beyond the scope of this project to create a simplified scale model and rig to capture added mass data and scale it using dimensional analyses, which meant that the only remaining feasible option to estimate the *SEAHOG*'s added mass properties was to use empirical data methods.

A method had to therefore be proposed, in which empirical data was used to approximate the added mass properties of the *SEAHOG*. A procedure was outlined in [30], whereby empirical data was used to estimate the added mass of five different ROVs. The results were compared to WADAM software calculations and proved to have a general accuracy of about ±10% [30]. Therefore, as an initial estimate to use in the *SEAHOG*'s dynamic model, empirical methods were deemed sufficient. This section will detail the method in which the added mass terms were found for the *SEAHOG*.

The added mass coefficient (k) is defined as the ratio of added mass of a body to the displaced fluid mass of that body. Empirical data exists for added mass coefficients of parallelepipeds with equivalent width and height, 2D rectangular cross sections for beams of infinite length, and flat plates. Empirical data for these three cases is given following in Table 30.

Table 30 - Empirical data for added mass coefficients of different shapes [32]

Type of Analysis	Direction of Motion	a/b	k	Reference Area/Volume
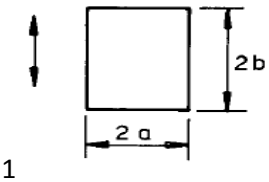 1	Vertical	0.1	2.23	$A_R = \pi a^2$
		0.2	1.98	
		0.5	1.70	
		1	1.51	
		2	1.36	
		5	1.21	
Rectangular plates 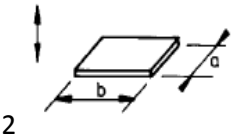 2	Vertical	0.40	0.801	$V_R = \frac{\pi}{4} a^2 b$
		0.50	0.757	
		0.63	0.704	
		0.67	0.690	
		0.80	0.642	
		1.00	0.579	
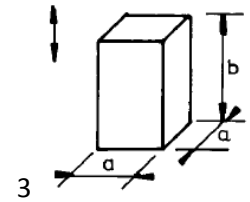 3	Vertical	0.17	0.13	$V_R = a^2 b$
		0.20	0.15	
		0.25	0.19	
		0.33	0.24	
		0.50	0.36	
		1.00	0.68	

It should be noted that the reference area and volume is an empirically derived quantity related to the type of analysis. It does not represent the area or volume of the shape in the analysis necessarily.

In all cases of added mass in this project, it is assumed that the motion of the vehicle is responsible for accelerating a stationary fluid. This is important, as added mass differs in the case that a stationary object is accelerated by a moving fluid.

The three linear added mass terms can be calculated using the data from Table 30 directly using [32]:

$$M_{A_{ij}} = \rho k A_R L \quad \{5.99\}$$

$$M_{A_{ij}} = \rho k V_R \quad \{5.100\}$$

Where ρ is the fluid density and L is the length of the rectangular prism.

To determine the added inertia terms, empirical data was found for flat plates rotating about their central axis as shown following in Figure 74, where kI_1' represents the added mass per unit length.

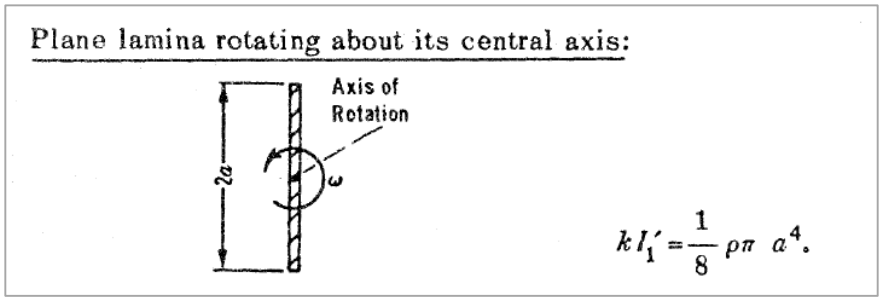

Figure 74 - Added mass for flat plate rotating about its central axis [33]

In addition, if slender body theory is assumed, the linear added mass terms can be related directly to the added inertia terms. This assumption is not necessarily accurate for the *SEAHOG*, as slender bodies have a large length to width ratio (only 1.34 for the *SEAHOG*). It should therefore be noted that the added inertia terms should be verified by experiment at a later stage when the *SEAHOG* is structurally complete. Using slender body theory, the added inertia terms can be related to the linear added mass terms by the following [19]:

$$A_{44} = \int_{-L/2}^{L/2} A_{44}^{(2D)} dx \triangleq \int_{-B/2}^{B/2} y^2 A_{33}^{(2D)} dy + \int_{-H/2}^{H/2} z^2 A_{22}^{(2D)} dz \quad \{5.101\}$$

Which simplifies to:

$$A_{44} = \frac{1}{12}\left(A_{33}^{(2D)} B^3 + A_{22}^{(2D)} H^3\right) \quad \{5.102\}$$

where L, B and H represent the length, breadth and height of the vehicle and A_{44} represents the term $K_{\dot{p}}$ from equation 5.97 previously. The same form of the equation is held for A_{55} and A_{66} and so they are not listed here.

While it is now possible to find an estimate for each of the six necessary added mass and inertia terms that comprise the added mass and Coriolis matrices, there are some important observations that must be made about each of the linear added mass analysis types in Table 30 previously and the added inertia analysis techniques:

1. Linear analysis type 1 allows the added mass coefficient to be found per unit length using equation 5.99. This is a form of strip theory, whereby the added mass for individual "strips" is calculated and then summed over the length of a body. Added mass is computed like this by software programs such as WAMIT. The data presented for this method in Table 30 however, is for beams of infinite length. Therefore, the shorter the beam length is, the more inaccurate this method will become.
2. Linear analysis type 2 is specifically for flat plates, where the height of the plate is negligible compared to the other dimensions. Therefore, the more significant the height dimension is of the body, the more inaccurate this method will become.
3. Linear analysis type 3 is for parallelepipeds of specific dimension aspect ratios. However, the data given only covers the domain where the height of the block exceeds the other dimensions. It would therefore be inaccurate to extrapolate the data to the domain where the height is smaller than the other body dimensions.
4. The empirical data for rotating plates assumes that the thickness of the plate is negligible compared to its other dimensions. The more significant the thickness of the plate is, the less accurate this method will become.
5. Using slender body theory to relate the linear added mass terms to the added inertia terms assumes a large length to width ratio. The smaller this ratio is, the less accurate this method will become.

Now that enough information is available to estimate the added mass terms for the *SEAHOG*, with the shortcomings of each empirical data method understood, the added mass for the *SEAHOG* can be derived.

5.4.4 *SEAHOG* Added Mass

The *SEAHOG* hull was approximated as a rectangular prism with dimensions 0.660 x 0.870 x 0.215 m as shown following in Figure 75.

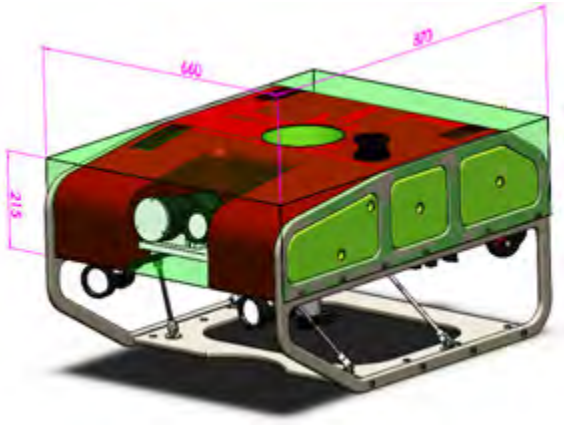

Figure 75 - Added mass domain approximation for the *SEAHOG* hull

Figure 75 shows that the *SEAHOG* hull approximation is reasonably ill-suited to the available added mass analysis techniques given previously. It was therefore decided that an average approximation using several analysis techniques would be used for each added mass term. Table 31 following shows the analysis types that were used to determine the linear DOF added mass terms.

Table 31 - Method used to determine added mass terms for the *SEAHOG*

Added Mass Term	Analysis Technique from Table 30 to Find Added Mass
$\boldsymbol{X_{\dot{u}}}$	Average of 2D strip theory (Anal. 1) and a 3D parallelepiped (Anal. 3) with $a = \sqrt{HB}$*.
$\boldsymbol{Y_{\dot{v}}}$	Average of 2D strip theory (Anal. 1) and a 3D parallelepiped (Anal. 3) with $a = \sqrt{HL}$.
$\boldsymbol{Z_{\dot{w}}}$	Average of 2D strip theory (Anal. 1) and of two flat plate (Anal. 2) analyses, where the longer ROV side is assigned first to "a" and then to "b".

*A value of $\sqrt{HB}$ was used so that the original area of the face is maintained. According to analysis type 3, the length and breadth of the parallelepiped must be equal. The actual area of the *SEAHOG* face in this particular analysis is HB, representing the product of the height and length of the ROV. If the value of a, shown in the above table, is used, it can be seen that the analysis area will remain the same as with the unmodified *SEAHOG* dimensions.

To determine the added mass terms, equation 5.99 was used for the strip theory method and equation 5.100 was used for the 3D methods. A water density of 1000 kg/m^3 was chosen, due to the uncertainty of what testing environment will be available in the future for model verification. The reference volume or area can be found using formulae in Table 30 and the geometry of the approximated added mass domain is shown previously in Figure 75. The "a/b" ratio determines the added mass coefficient "k", which was found in each case by using the given data to create a fit curve in MS Excel that relates the "a/b" ratio to a value of "k". The specific value of "k" could then be found by using the fit curve equation.

Combining the methods described in Table 31 and Table 30, the linear added mass terms could be found. The variables used in the added mass calculations, along with the calculated results, are given following in Table 32.

Table 32 - Input variables and results to added mass calculations for linear DOF added mass terms

Added Mass Matrix Term	2D Analysis		3D Analysis		Average Added Mass (kg)
	Input Variables (m)	Outputs (kg)	Input Variables (m)	Outputs (kg)	$\frac{M_{h1} + M_{h2}(+M_{h3})}{2\ (3)}$
$\boldsymbol{X_{\dot{u}}}$	a = 0.108 ; b = 0.435 L = 0.660	M_{h1} = 45.7	a = 0.438 b = 0.870	M_{h2} = 38.5	42.1
$\boldsymbol{Y_{\dot{v}}}$	a = 0.108 ; b = 0.330 L = 0.870	M_{h1} = 57.8	a = 0.543 b = 0.660	M_{h2} = 56.7	57.2
$\boldsymbol{Z_{\dot{w}}}$	a = 0.330 ; b = 0.108 L = 0.870	M_{h1} = 389.7	a_1 = 0.870 b_1 = 0.660 a_2 = 0.660 b_2 = 0.870	M_{h2} = 392.3 M_{h3} = 297.6	359.9

With the linear added mass terms approximated, the form of equation 5.102 could be used to determine the added inertia terms using slender body theory. In addition, data was used from Figure 74 to obtain the added inertia terms. The results from the two methods were averaged and are presented following in Table 33.

Table 33 - Added mass terms for rotational DOFs

Added Mass Matrix Term	Added Inertia Value (kgm^2)
$\boldsymbol{K_{\dot{p}}}$	7.0
$\boldsymbol{M_{\dot{q}}}$	16.0
$\boldsymbol{N_{\dot{r}}}$	4.1

With all six added mass terms defined, the added mass and Coriolis matrices can be given in the next section as a summary.

5.4.5 Summary - Added Mass and Coriolis Matrices

The use of extensive added mass computational software was not available for use in this project. Due to the unfeasibility of experimental determination in this project, the added mass terms had to be approximated using empirical data methods. Extensive simplification of the *SEAHOG* was necessary to obtain empirical estimates of the added mass terms. Therefore, the *SEAHOG* hull was determined to be the most significant contributor to added mass and was treated as a rectangular prism. The assumption of three plane symmetry was then enforced, so as to simplify the added mass matrix to be diagonal.

The average of 2D strip theory and empirical 3D methods were used to obtain estimates of the linear added mass terms. Enforcing the assumption of slender body theory allowed the added inertia terms to be found according to the linear terms. The slender body results were then averaged with empirical data so as to give approximate added inertia terms.

It was noted that both the symmetry and slender body theory assumptions are not strictly accurate for the *SEAHOG* hull and thus it will be recommended that experimental and more extensive computational methods are used in the future to verify the estimated added mass terms. However, for the purposes of this report, the presented method was deemed sufficient to provide values as a starting point in the *SEAHOG* dynamic model.

Finally, the added mass and Coriolis matrices are presented following:

$$\boldsymbol{M}_A = [42.1\,, 57.2\,, 359.9\,, 7.0\,, 16.0\,, 4.1]^D \quad \{5.103\}$$

$$\boldsymbol{C}_A(v) = \begin{bmatrix} 0 & 0 & 0 & 0 & -359.9w & 57.2v \\ 0 & 0 & 0 & 359.9w & 0 & -42.1u \\ 0 & 0 & 0 & -57.2v & 42.1u & 0 \\ 0 & -359.9w & 57.2v & 0 & -4.1r & 16.0q \\ 359.9w & 0 & -42.1u & 4.1r & 0 & -7.0p \\ -57.2v & 42.1u & 0 & -16.0q & 7.0p & 0 \end{bmatrix} \quad \{5.104\}$$

With the added mass properties of the *SEAHOG* sufficiently estimated, the hydrodynamic damping and drag properties can be defined in the following section.

5.5 Hydrodynamic Damping Matrix

5.5.1 Introduction

Recalling from section 2.4.5, the hydrodynamic damping on a submerged body will consist of a linear and a quadratic term, as stated in equation 2.43:

$$\boldsymbol{D}(\boldsymbol{v}) = \boldsymbol{D} + \boldsymbol{D}_n(\boldsymbol{v})$$

Simulation and CAD techniques were used to determine the damping coefficients of the *SEAHOG* due to the structurally incomplete state of the robot. Solidworks Flow Simulation was employed due to its availability and user-friendly and accessible nature for a non-expert in Computational Fluid Dynamics (CFD). It was decided that a general idea of the damping terms should be obtained from simulations as an initial estimate of the damping factors of the robot. In the future, a more detailed analysis can be executed if necessary.

This section will state some of the important factors of utilising a flow simulation software package and how the capabilities of the software can affect the computational results. It will then describe how the damping terms for the *SEAHOG* were obtained and finally list and analyse the damping characteristics of the ROV.

5.5.2 CFD and Simulation Software

It should be noted that while CFD software packages can be used to rapidly accelerate engineering analysis and design, detailed understanding of the simulation package and the scenario that is being simulated is necessary to obtain accurate results. In addition, an understanding of the driving equations behind fluid dynamics is required to inform correct decisions when setting up the simulation. CFD computation packages iteratively solve the Reynolds-Averaged Navier-Stokes (RANS) equation to obtain solutions for a certain flow scenario. An example of a formulation of the RANS equation is given below [34]:

$$\begin{aligned} \rho(\boldsymbol{U}\cdot\nabla\boldsymbol{U}) + \nabla\cdot\left(\mu_T(\nabla\boldsymbol{U} + (\nabla\boldsymbol{U})^T) - \frac{2}{3}\mu_T(\nabla\cdot\boldsymbol{U})\boldsymbol{I}\right) \\ = -\nabla P + \nabla\cdot\left(\mu(\nabla\boldsymbol{U} + (\nabla\boldsymbol{U})^T) - \frac{2}{3}\mu(\nabla\cdot\boldsymbol{U})\boldsymbol{I}\right) + \boldsymbol{F} \\ \nabla\cdot(\rho\boldsymbol{U}) = 0 \end{aligned} \quad \{5.105\}$$

with $\boldsymbol{U}$ and P being the fluid time-averaged velocity and pressure respectively and μ_T being the turbulent viscosity.

Some of the most important considerations involved in a CFD analysis will be discussed following so as to better understand their implications in this project.

Meshing:

Iterative simulation problems are executed by solving throughout nodes in a mesh of solid and fluid domains. If the mesh is not created correctly, it can have a significant effect in decreasing the accuracy of the simulation results. Soldiworks Flow Simulation has an advantage of automatically creating a mesh, however, the disadvantage of this is that there is limited control over how the mesh is created.

Due to the large scope of this project, it was decided that the automatic meshing function of Solidworks would be sufficient to obtain an initial estimate of the ROV's drag characteristics, however, it is noted that for accurate results an expert analysis using a specialist fluid simulation program should be used.

Computational Domain:

The size of the domain in which the CFD analysis is executed can have an effect on the results of the computation. This is due to how the fluid interaction with a solid body could result in flow effects that decay only far away from the body. The disadvantage with a larger computational domain however, is that the simulation will require more time to solve.

An approach was taken in [35], whereby the computational domain was increased to a point where variations in the results beyond that point were negligible. This approach is recommended, however due to the limited time available for fluid simulations, a smaller domain size was chosen for this project. The chosen computational domain size will be explained following in section 5.5.4.

Boundary Conditions:

The in and out flows from the computational domain will have a significant influence on the computational results and therefore it is important to clearly define the operating environment in which the ROV is being simulated. Once the operating scenario is defined, it is important to correctly define the boundary conditions of the computational domain so as to mimic the operating environment.

The *SEAHOG* will be simulated in an unbound body of water, representing testing manoeuvres that will be executed sufficiently far from the water surface and the boundaries of the test environment. This type of computational domain will require a free slip boundary condition on all of the computational domain's walls. A free slip condition represents zero shear stress in the fluid at the computational boundary, representing a large, unconstrained body of water.

Turbulence Modelling:

Scenarios with simple flow conditions exhibit laminar flows that often have definite solutions using the RANS equation. For more complex flow conditions however, numerical methods are required to come to a

solution. While laminar flows are simple to model and solve, flow obstructions, such as the body of an ROV, can cause flow separations and lead to turbulent flow conditions.

The Reynolds number is a good indicator of the likelihood of turbulence in a flow scenario. It is dimensionless and represents the ratio of inertial to viscous forces in a fluid. It is defined as:

$$Re = \frac{\rho \boldsymbol{v} L}{\mu} \qquad \{5.106\}$$

with $\boldsymbol{v}$ as the relative velocity between the body and the fluid, L as the characteristic linear dimension of the surface that is interacting with the flow and μ as the dynamic viscosity of the fluid.

Typically, higher Reynolds numbers result in turbulent flows. However, complex geometries like an ROV hull could create turbulence at low Reynolds numbers in localised areas.

Turbulence is characterised by chaotic, three dimensional flows including intensive mixing and vortices. The turbulent viscosity (μ_T) can be seen previously in equation 5.105. Different models exist to determine the turbulent viscosity. The $k-\epsilon$ turbulence model is commonly used in industry due to it being computationally inexpensive and robust. Other turbulence models exist, such as the Shear-Stress-Transport (SST) model, which gives highly accurate predictions of flow separation and has been used in ROV drag characterisation previously [35]. Unfortunately, there is no option to choose a turbulence model in Solidworks and thus the $k-\epsilon$ model was used in the flow simulations in this project.

Summary:

From the investigation in this section, it can be seen that the results of flow simulations conducted in this project will have limited accuracy due to the automatic meshing function and predetermined turbulence model of Solidworks Flow Simulation. This being said, Solidworks Flow Simulation has been used to determine the drag characteristics of several ROVs to a reasonable degree of accuracy in [30]. It is therefore accepted that the simulations in this report will supply a sufficient baseline on which an ROV model can be constructed. Regardless, due to the incomplete state of the *SEAHOG*, verification of the drag characteristics cannot be performed as part of this project. Therefore, more detailed and specialised CFD analyses will be beneficial at a future point when the *SEAHOG* is complete and the simulation results can be verified by experiments.

With a clear and detailed understanding gained of the aspects of software CFD analyses, it is now possible to conduct simulations as accurately as possible to obtain estimates of the drag characteristics of the robot.

5.5.3 Maximum Speed Estimation

Introduction:

It is important to carry out drag simulations over the whole range of ROV operational speeds and hence it is important to have an estimation of the maximum achievable speed of the ROV. This will allow simulation speed points to be optimally placed so as to capture the linear and quadratic damping speed regions of the ROV. This section will serve to propose an estimation of the maximum speeds achievable by the *SEAHOG* in each degree of freedom.

Method:

Due to the availability of the CAD model for the *SEAHOG*, it was possible to carry out flow simulations at certain speeds. The simulations could be used to find the opposing drag force on the ROV at a certain relative fluid velocity. In addition, due to the comprehensive characterisation of the *SEAHOG* thrusters, the maximum force imparted to the ROV could be found. Therefore, using the geometric layout of the thrusters, it was possible to find the maximum force that could be imparted for a certain degree of freedom. The thruster geometric layout is given in section 5.6 following.

An estimated speed could therefore be found by using drag simulations, where the drag force in the DOF of interest was equivalent to the maximum thrust in that direction. In reality there will not only be drag forces and thrust forces acting on the robot however, and therefore the maximum simulated speed for drag was chosen as slightly greater than the maximum ROV speed in each direction.

Results:

Using the proposed method and a maximum axial thrust of 60 N per thruster, the following limits, given in Table 34 following were found using simulations as an estimation of the maximum speeds reachable by the ROV in each direction.

Table 34 - Estimated maximum speeds for the *SEAHOG* in each degree of freedom

DOF	Maximum Thrust Force	Corresponding Maximum Speed Estimate
Surge	176.8 N	1.5 m/s
Sway	162.0 N	0.8 m/s
Heave	60.0 N	0.4 m/s
Roll	16.2 Nm	1.4 rad/s
Pitch	17.7 Nm	1.0 rad/s
Yaw	63.7 Nm	2.6 rad/s

With an estimate obtained for the maximum speed obtainable in each ROV DOF, it was possible to carry out CFD simulations in Solidworks Flow Simulation over the entire range of motion for the ROV. The simulation setup will be given in the following section.

5.5.4 Simulation Setup

To fully characterise the drag characteristics of the *SEAHOG*, three translational and three rotational axes needed to be simulated for. This section will describe all the aspects of the simulation, including the simulation settings and how the simulation was set up before computing the drag results.

CAD Model Setup:

In order for Solidworks to be able to mesh the ROV successfully, the *SEAHOG* CAD model had to be simplified somewhat. Modules such as the Sensor and IMU pod were removed as they are shielded from external flows by the ROV cover and are not expected to contribute to the drag characteristics of the robot.

The thrusters would have their own complex flow conditions which would be difficult to model and therefore modelling the effects of the thrusters on the drag characteristics of the *SEAHOG* is beyond the scope of this project. As a result, the horizontal thrusters were removed from the CAD model. The housing of the vertical thruster was expected to contribute to drag in the horizontal plane and thus it was left in. The propeller of the vertical thruster was removed however, so as to not induce any unrealistic torques created from flows over the propeller when simulating in the heave DOF. Figure 76 following shows the modified *SEAHOG* CAD model that was used in the Solidworks CFD simulations.

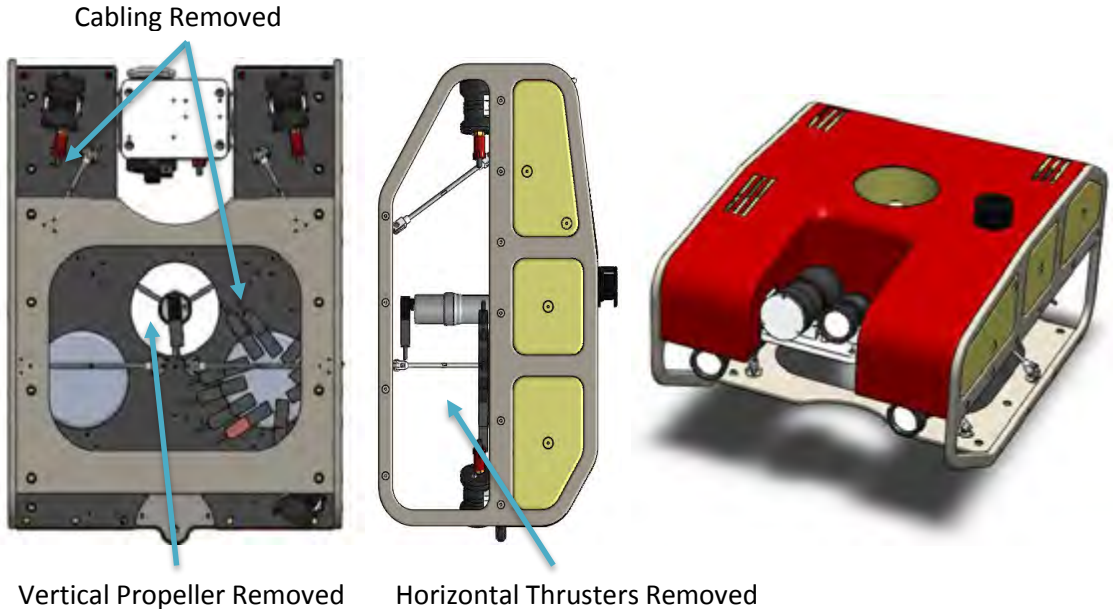

Figure 76 - Modified CAD model of the SEAHOG for drag simulations. Showing bottom, side and isometric views

Surface Roughness and Viscous Drag:

At low speeds, the Reynolds number is low, representing dominant viscous damping forces over inertial damping forces. Surface roughness can contribute significantly to viscous drag, however due to the structurally incomplete state of the ROV, the surface roughness properties were unknown and therefore surface roughness values were set as zero.

Meshing:

Solidworks gives the option to choose how refined the initial created mesh is. This represents the factor that different mesh elements can differ in size by. The maximum number of eight was chosen for all the simulations, meaning that two adjacent cells could be a maximum of eight times smaller or larger than each other.

Simulation Domain Size:

The simulation domain size was recommended at 20 times the length of the corresponding ROV side in [35]. It was found that when the domain size was increased beyond this point, there were no significant differences in the computational results. Due to limited time available for simulations however, the computational domain size was set at 10 times the corresponding ROV side length for all of the drag simulations in this project.

To gauge the effects of this smaller domain size on the calculated results, simulations were carried out at the maximum simulated velocity, in each of the linear dimensions for the larger and smaller computational domain. This allowed the domain size difference on the results to be quantified and analysed. The computed drag forces for linear motion through the water in the recommended domain size and the implemented domain size are shown following in Table 35. The equation used to compute the difference in results is given following:

$$\%\ Diff. = \left(\frac{Large\ Domain\ Result}{Small\ Domain\ Result} - 1\right) \times 100 \qquad \{5.107\}$$

Table 35 - Difference in computed drag forces for recommended and implemented domain sizes

Water Direction	Water Velocity (m/s)	Domain Size (m)	X (N)	% Diff.	Y (N)	% Diff.	Z (N)	% Diff.
x	1.75	17.6x13.1x9.26	204.7	*5.6*	-6.7	0	-17.5	-1.7
		8.8x6.55x4.63	193.9		-6.7		-17.8	
y	1.00	17.6x13.1x9.26	-1.0	-9.1	118.8	*-4.4*	10.5	54.4
		8.8x6.55x4.63	-1.1		124.3		6.8	
z	0.60	17.6x13.1x9.26	-1.0	-16.7	2.5	-19.4	84.5	*-5.6*
		8.8x6.55x4.63	-1.2		3.1		89.5	

While there is certainly significant variation for some of the results, the results of interest are the force in the same direction as the water velocity. These results can be seen as the italicised elements in the above table. The results are all below 6%, which was deemed sufficiently small for the purposes of this project.

In conclusion, a computational domain size of 8.80 x 6.55 x 4.63 m was chosen, representing a cube with sides that are ten times the length of the corresponding ROV side. Figure 77 following shows the *SEAHOG* inside the computational domain.

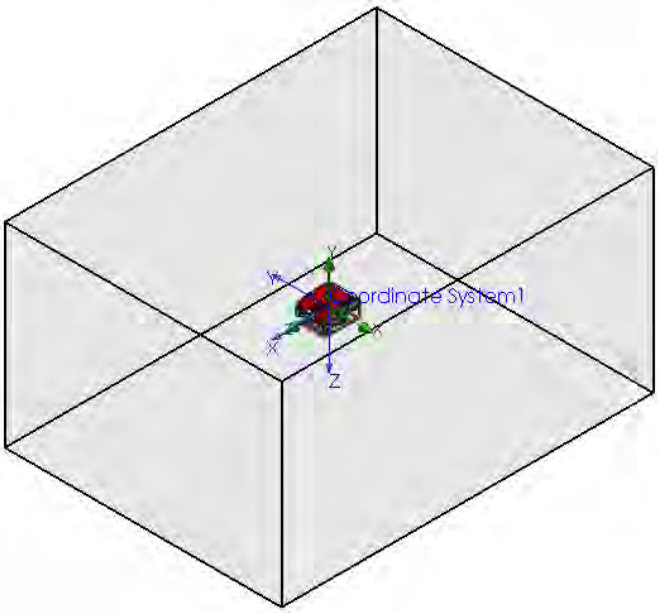

Figure 77 - The *SEAHOG* and computational domain for drag simulations

Turbulence and Boundary Conditions:

As previously noted, the ROV will be simulated for a scenario of operating in a free unbound body of water far enough from the boundaries of its environment so that they do not have a significant effect on the damping of the ROV. This requires the boundary conditions of the computational domain to be free slip conditions, with zero fluid shear stress between the computational boundary and the simulated fluid. Solidworks applies these conditions automatically if no boundary conditions are specified.

Turbulence intensity is the percentage of a flow that is unsteady or "turbulent" – for example, a completely laminar flow with no rapid fluctuations in fluid speed or direction will have a turbulence intensity of 0%. The turbulence intensity around a slow moving ROV body is generally accepted as well below 1% [35] and therefore the turbulence intensity in the ROV drag simulations was set to 0.1%.

General Settings:

It is unknown whether the testing environment for the *SEAHOG* will be seawater or freshwater. There is typically approximately 2% difference in the density of seawater and freshwater and it was therefore assumed to not be a significant factor in affecting the computation results. Therefore, the fluid medium was chosen as freshwater with a density of 1000 kg/m^3.

Forces and moments in all six DOFs were set as goals for convergence in each simulation. If all six goals did not converge, a maximum of 300 solving iterations was set as the limit.

For the linear DOFs, water was passed over the ROV body for a range of linear speeds with the ROV stationary. This approach is acceptable since the drag on a body is related to the relative motion of the fluid and the body.

For the rotational DOFs, Solidworks has the capability of defining a rotating mesh. This is achieved by creating a boss that encompasses the solid body that will rotate and then setting the speed at which it will rotate. Three different bosses were created so as to capture each rotational axis and are shown following in Figure 78.

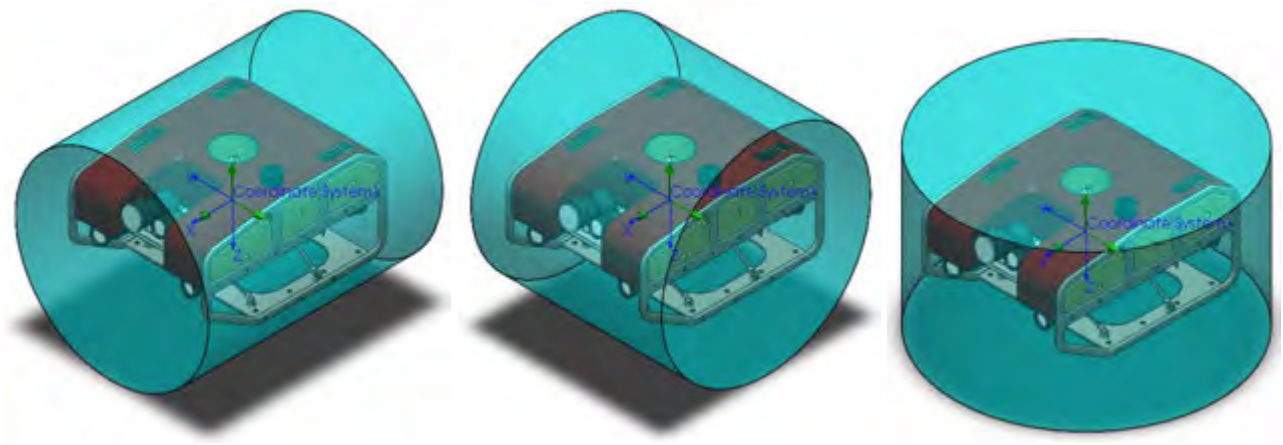

Figure 78 - The *SEAHOG* in rotational mesh domains of roll, pitch and yaw respectively

The boss sizes used for the rotating mesh domain are given following in Table 36.

Table 36 - Boss size for rotating mesh domain

Rotational Axis	Boss Diameter (mm)	Boss Length (mm)
x_b	933	1130
y_b	1009	919
z_b	1260	754

Finally, the range of speeds that were simulated for are given following in Table 37.

Table 37 - Drag simulation speed ranges for each DOF

BODY Axis	Simulated Speed Range	Drag Force (N)	Drag Torque (Nm)
x	±1.75 m/s	X	
y	±1.00 m/s	Y	
z	±0.60 m/s	Z	
ϕ	±1.50 rad/s		K
θ	±1.20 rad/s		M
ψ	±2.75 rad/s		N

This completes a detailed description of the Simulation setup, allowing the results to be listed in the following section.

5.5.5 Drag Simulation Results

72 Solidworks flow simulations were conducted to gather six data points for each direction of water flow in each DOF. Two batches of simulations were run for each degree of freedom, one in each direction. This was necessary due to the non-symmetrical nature of the *SEAHOG*'s hull. Three low speed simulations were conducted for each direction in each degree of freedom to investigate the linear damping region due to viscous forces. Three simulations at higher speeds were conducted so as to capture the inertial damping effects of the water and to capture the quadratic damping region.

The simulation results are presented following in Figure 79 to Figure 84. Least squares regression was used to fit 3rd order polynomials to results that were significantly above zero. As can be seen by the variance values (R^2), all results display very good correlation.

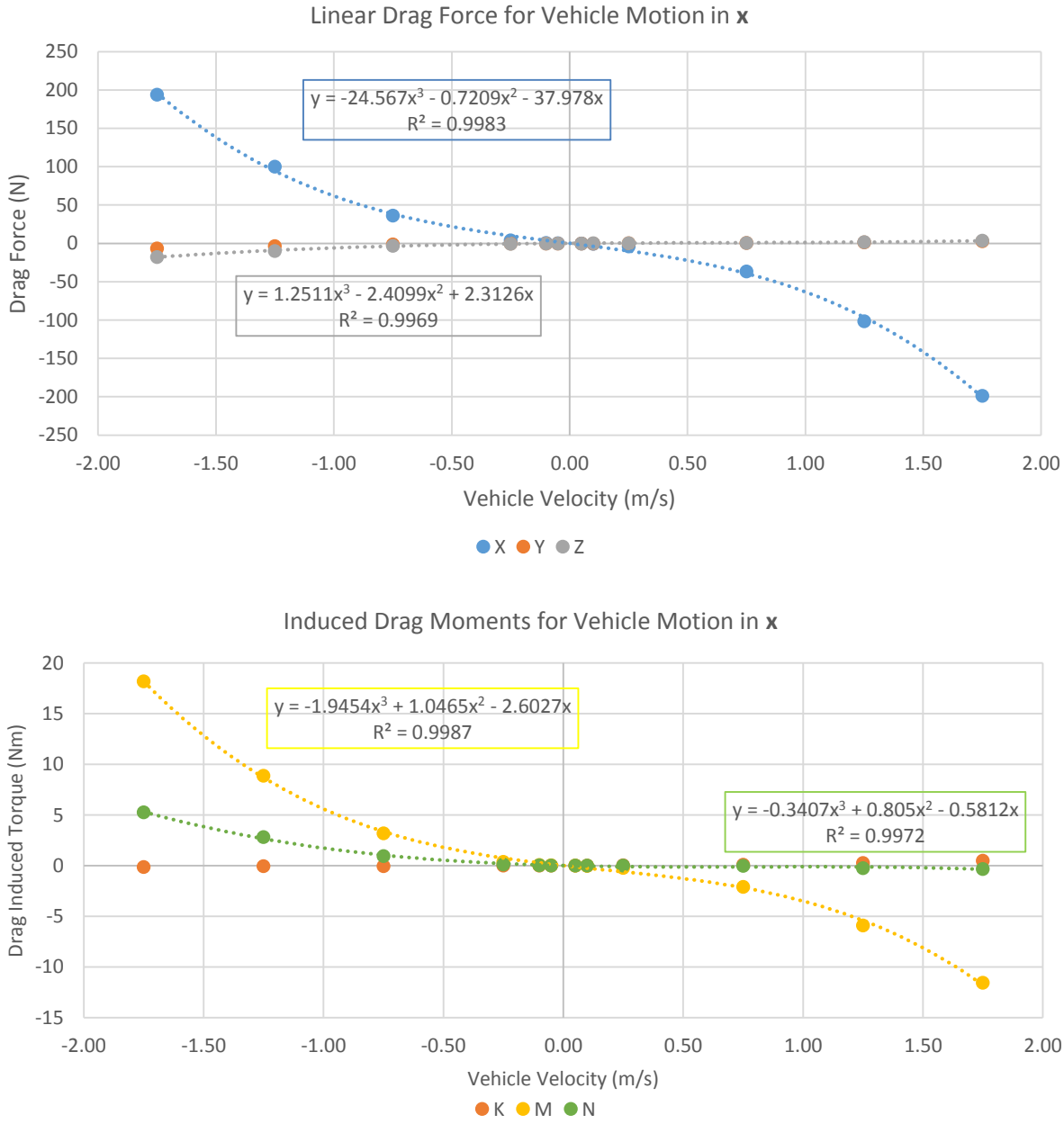

Figure 79 - Linear drag forces [top] and induced moments [bottom] due to vehicle motion in x

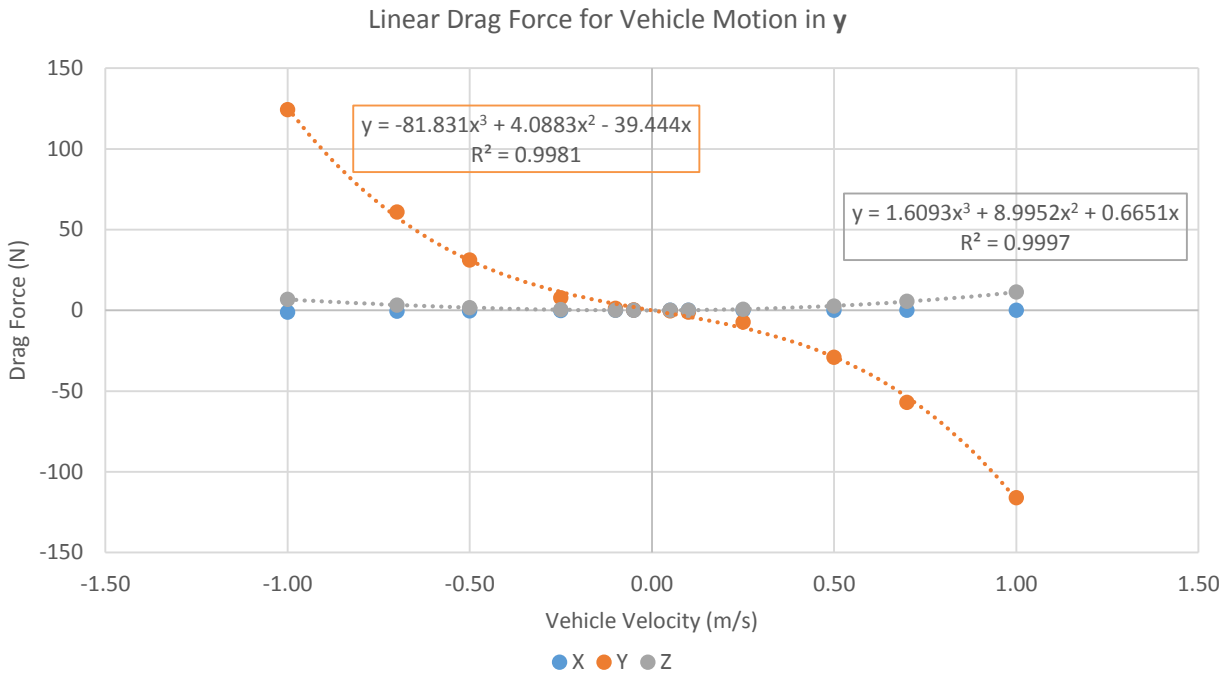

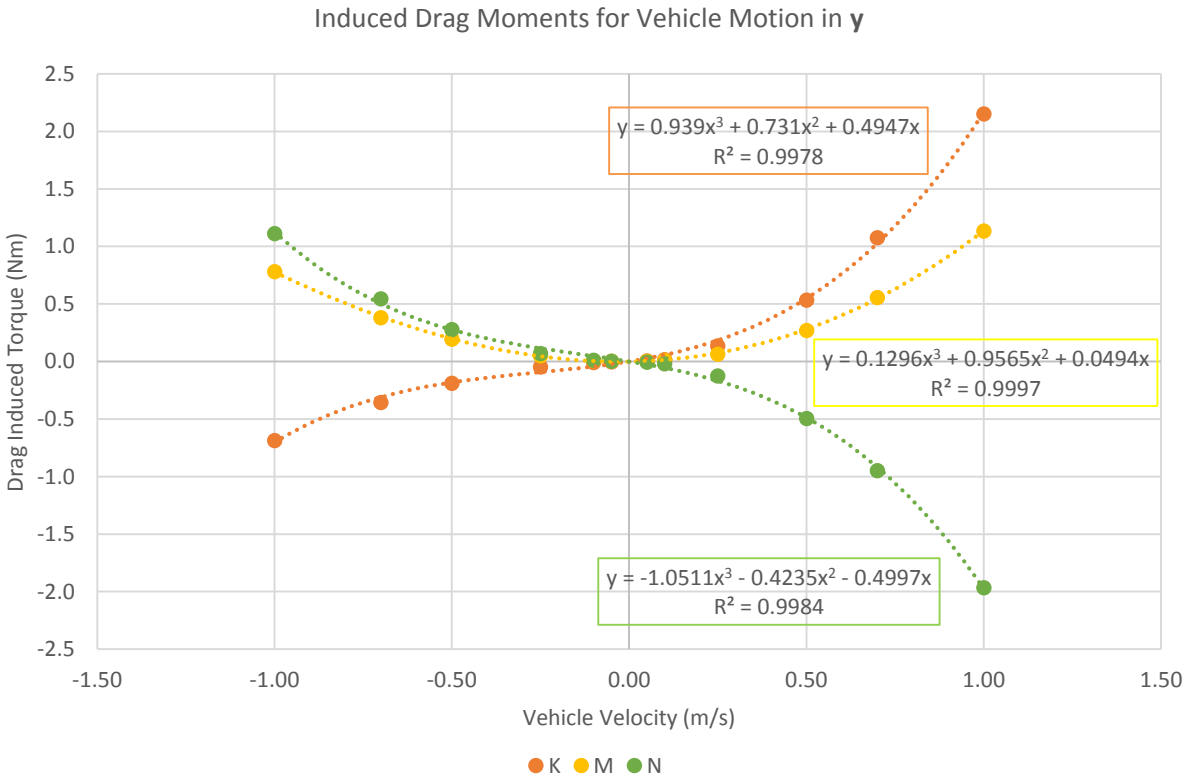

Figure 80 - Linear drag forces [top] and induced moments [bottom] due to vehicle motion in y

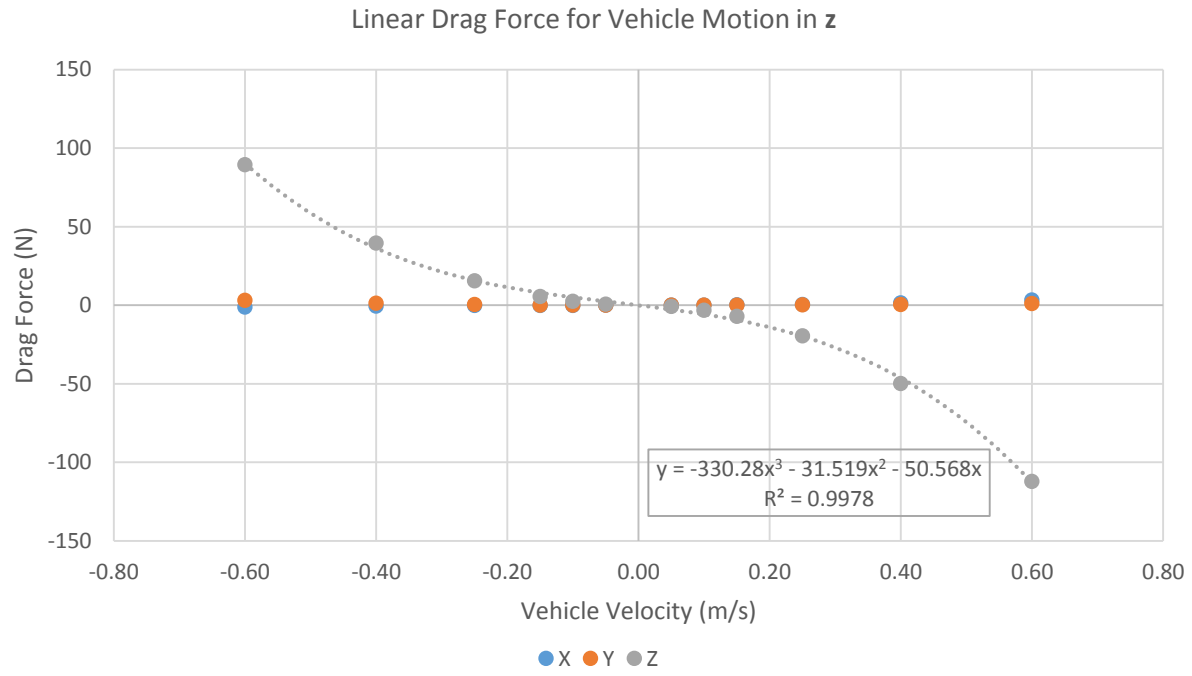

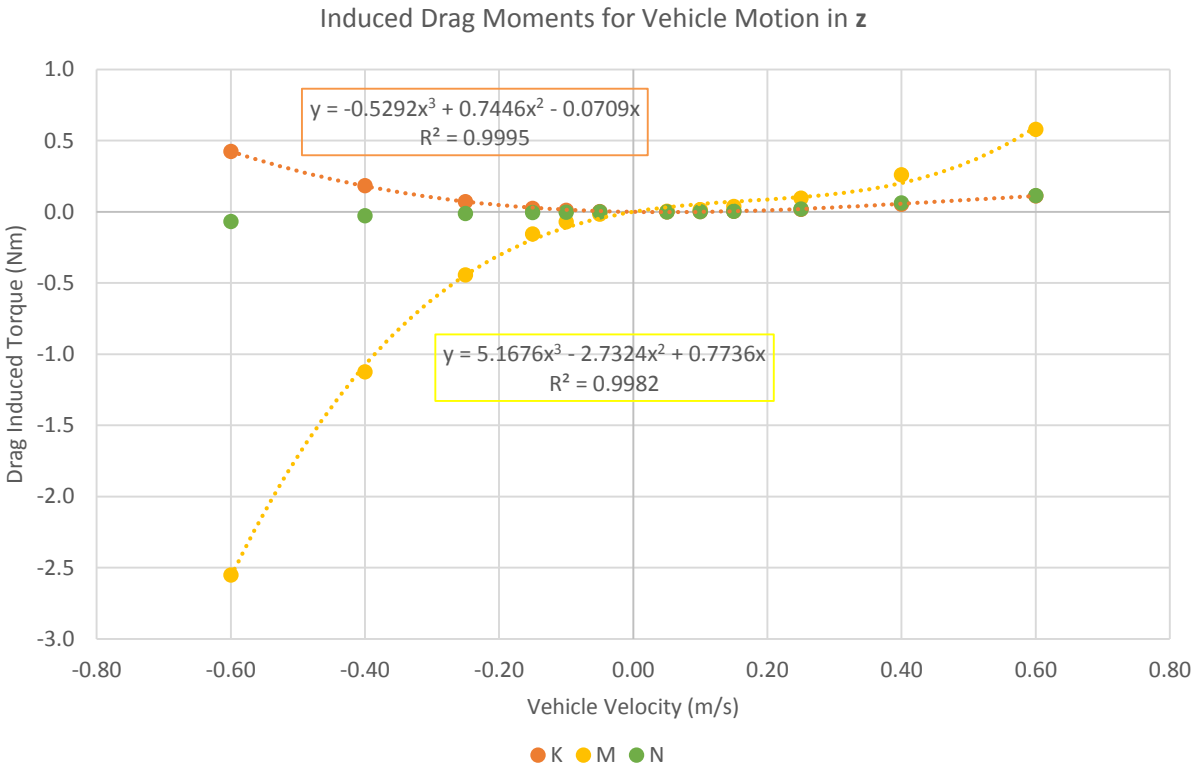

Figure 81 - Linear drag forces [top] and induced moments [bottom] due to vehicle motion in z

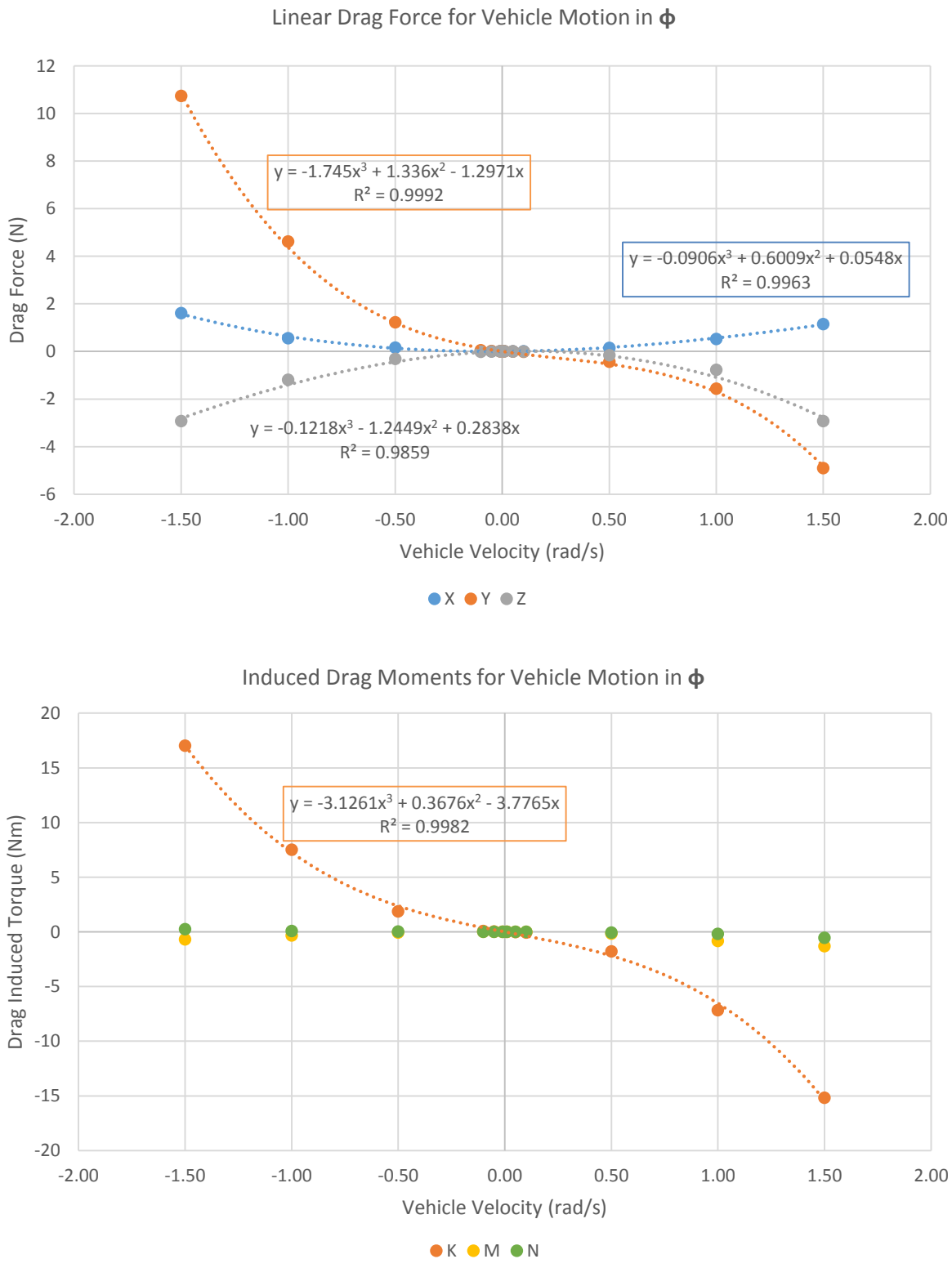

Figure 82 - Linear drag forces [top] and induced moments [bottom] due to vehicle motion in ϕ

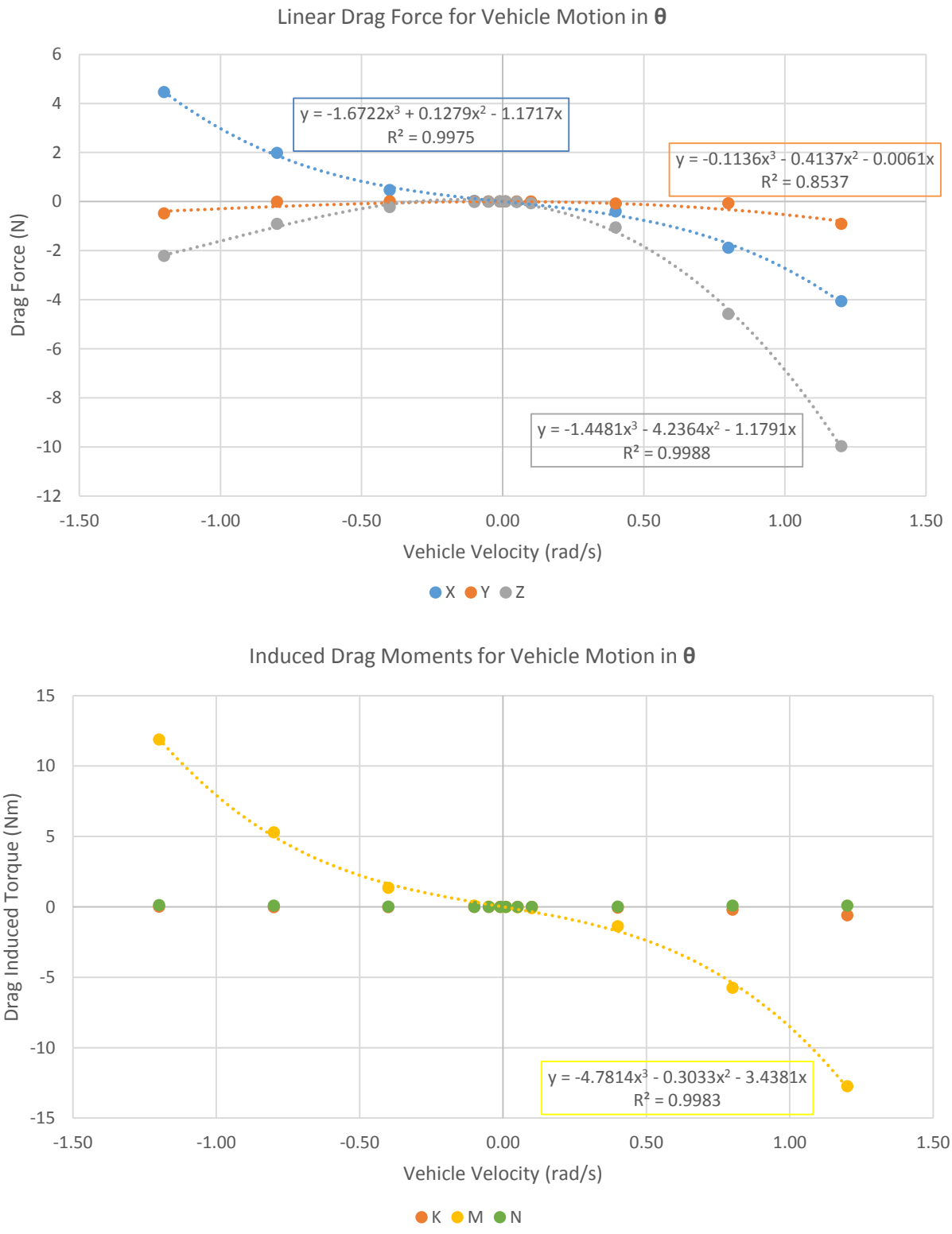

Figure 83 - Linear drag forces [top] and induced moments [bottom] due to vehicle motion in θ

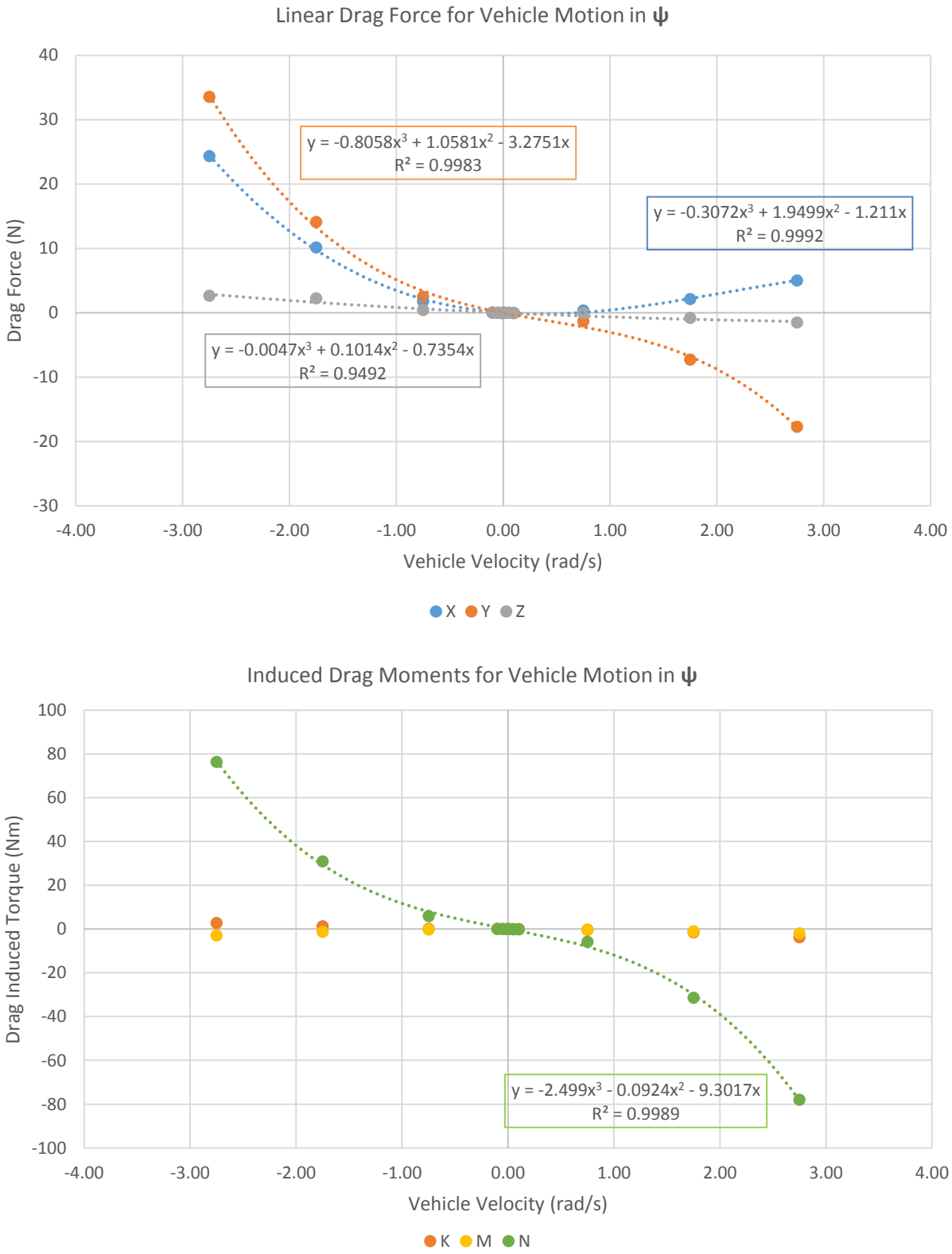

Figure 84 - Linear drag forces [top] and induced moments [bottom] due to vehicle motion in ψ

5.5.6 Analysis of Flow Simulation Results

Introduction:

Drag forces act so as to oppose the direction of motion of a body, which can be seen in the simulation results as a negative close-to anti-symmetric curve that corresponds to the force in the direction of motion. If the hull of the ROV was symmetrical, the damping for both directions of water flow in a certain DOF would be equal in magnitude and opposite in direction. However, this is not the case on the *SEAHOG* and thus curves are not completely anti-symmetrical. In all cases, the linear damping region can be seen at slow speeds with the quadratic damping becoming dominant at higher speeds.

Before the ROV system is simulated in a model, some insights can be drawn as to the nature of motion that can be expected from the *SEAHOG* during operation. This section will give an analysis of the flow simulation results so as to draw more insight into how the ROV will react during certain manoeuvres.

Horizontal Linear Motion:

When analysing the **x** and **y** direction results (Figure 79 and Figure 80 previously), it can be seen that the drag is largely decoupled in the horizontal plane, with minimal lift forces being generated. However, motion in **x** creates pitching and yawing moments due to unsymmetrical aspects of the body like the sonar tower and the tilt tray modules. It can be expected then that the drag will cause the ROV to pitch down as it moves forward. In addition, the yaw moment will serve to pull the ROV off its heading if a constant thrust is supplied by the thrusters. Motion in the **y** direction will create yaw pitch and roll moments. It is therefore important to assess the passive stabilisation of the ROV in the completed ROV model, so as to determine if the ROV will be sufficiently stable to use as an operational platform. This will be investigated in the following chapter.

Vertical Linear Motion:

It can be seen from Figure 81, that motion in the **z** direction will cause a pitching and rolling moment. Due to the fact that the pitch and the roll of the ROV are not independently controllable with the current thruster layout, the extent to which the drag of the ROV will contribute to it not ascending and descending in a straight line will be assessed in the following chapter.

Rotational Motion in Yaw:

It can be seen from Figure 84 previously that yaw rotation manoeuvres on the *SEAHOG* can be expected to induce horizontal linear drag forces, resulting in the *SEAHOG* being unable to pivot exactly on the spot. This is not expected to be a significant problem but is mostly an insight into the expected yaw rotational motion of the *SEAHOG*.

Conclusion:

With an understanding of the flow simulation results given, the application of the results in the model can be given with a summary of the damping matrix section.

5.5.7 Summary and Conclusion

Recall that flow simulations were executed on the *SEAHOG* hull so as to populate a damping matrix such that:

$$\boldsymbol{D}(\boldsymbol{v}) = \boldsymbol{D} + \boldsymbol{D}_n(\boldsymbol{v})$$

Due to the non-symmetrical ROV hull however, the above damping matrices would need to be discontinuous and separate for either direction of motion of the ROV. It was therefore decided that implementing the fit curves generated in Figure 79 to Figure 84 would be easier than populating separate linear and quadratic damping matrices. Therefore, the damping of the ROV was implemented as a single matrix with varying elements, deriving their values from the 3rd order polynomial curves given in the flow results.

In this section, Solidworks Flow Simulation software was used to conduct flow simulations and obtain the drag characteristics of the *SEAHOG*. It was noted that the automatic meshing function and predetermined turbulence model in Solidworks may contribute to less accurate results. However it was deemed sufficient enough to provide a preliminary insight into the drag characteristics of the ROV to be used in the *SEAHOG* dynamic model.

With the damping matrix fully defined, the next section will derive the thrust transformation matrix so as to transform axial thrusts from individual thrusters to a body-fixed thrust vector.

5.6 Thrust Transformation Matrix

Previously in this report a detailed model was developed for the thruster dynamics, resulting in an axial thrust output for a *SEAHOG* thruster. Due to the simple thruster model that was chosen, the effects of flows created by other thrusters and ambient conditions are not taken into consideration. It is therefore possible to simply transform the axial thrusts generated by each of the five *SEAHOG* thrusters into a BODY thrust orientation such that:

$$\boldsymbol{\tau} = \boldsymbol{B}\boldsymbol{\tau}_i \qquad \{5.108\}$$

where $\boldsymbol{\tau}_i$ is the individual axial thrust force vector from the thrusters, $\boldsymbol{\tau}$ is the BODY thrust representation and $\boldsymbol{B}$ is a transformation matrix related to the geometric thruster layout.

The thruster number allocation is given following in Table 38 with a depiction of the thruster positions, along with the nomenclature used to derive the transformation $\boldsymbol{B}$, given following in Figure 85.

Table 38 - Names and numbering of *SEAHOG* thrusters

Forward Starboard	1	Aft Port	4
Forward Port	2	Vertical	5
Aft Starboard	3		

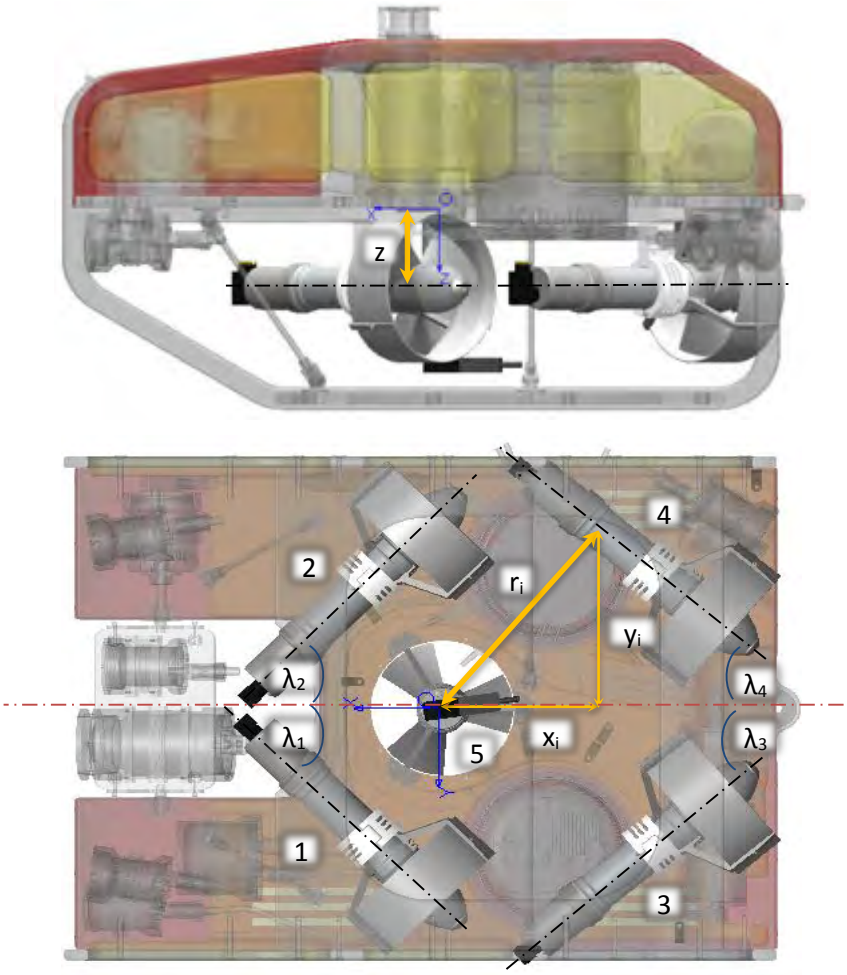

Figure 85 – *SEAHOG* side and bottom views, showing thruster layout, nomenclature and allocated thruster numbers

The positions of angles λ_i were chosen due to the ease of determining them and the simplification that they offer in the thrust transformation matrix. A positive thrust force is defined as thrust towards the thruster housing end cap, where the black subsea Birns connector is mounted.

Using the geometry presented in Figure 85, it is possible to derive expressions for the thrust in each of the BODY degrees of freedom, as defined previously in Table 1 on page 9, with T_i being the thrust produced by the i^{th} thruster:

$$\begin{aligned} X &= T_1 cos\lambda_1 + T_2 cos\lambda_2 + T_3 cos\lambda_3 + T_4 cos\lambda_4 \\ Y &= -T_1 sin\lambda_1 + T_2 sin\lambda_2 + T_3 sin\lambda_3 - T_4 sin\lambda_4 \\ Z &= T_5 \\ K &= z(T_1 sin\lambda_1 - T_2 sin\lambda_2 - T_3 sin\lambda_3 + T_4 sin\lambda_4) \\ M &= z(T_1 cos\lambda_1 + T_2 cos\lambda_2 + T_3 cos\lambda_3 + T_4 cos\lambda_4) \\ N &= -r_1 T_1 + r_2 T_2 - r_3 T_3 + r_4 T_4 \end{aligned} \quad \{5.109\}$$

On the *SEAHOG*, values of λ_1 and λ_2 have been previously defined as 45˚, and values of λ_3 and λ_4 have been previously defined as 40˚. The distances $r_1 = r_2 = 0.209$ m, $r_3 = r_4 = 0.322$ m and $z = 0.1$ m.

This yields the expression for the thrust transformation as:

$$\boldsymbol{\tau} = \begin{bmatrix} \cos 45 & \cos 45 & \cos 40 & \cos 40 & 0 \\ -\sin 45 & \sin 45 & \sin 40 & -\sin 40 & 0 \\ 0 & 0 & 0 & 0 & 1 \\ 0.1\sin 45 & -0.1\sin 45 & -0.1\sin 40 & 0.1\sin 40 & 0 \\ 0.1\cos 45 & 0.1\cos 45 & 0.1\cos 40 & 0.1\cos 40 & 0 \\ -0.209 & 0.209 & -0.322 & 0.322 & 0 \end{bmatrix} \begin{bmatrix} T_1 \\ T_2 \\ T_3 \\ T_4 \\ T_5 \end{bmatrix} \quad \{5.110\}$$

It can now be seen that thrust in pitch and roll is linearly dependant on the x and y thrust, resulting in the pitch and roll not being independently controllable. As a result, it is clear that a pitching or rolling moment will be induced if thrust is applied in the x or y direction.

This completes the derivation and identification of the thrust transformation matrix, providing the body-fixed thrust as a function of thrust inputs from each of the five *SEAHOG* thrusters. Within the scope of this project, all aspects of the *SEAHOG* dynamic model are now complete.

5.7 Summary of the *SEAHOG* Dynamic Model

This chapter has detailed and defined the dynamic equations that govern the motion of the *SEAHOG* ROV. The model development has comprised of identifying the essential components of the equations of motion of an underwater vehicle given as:

$$\boldsymbol{M\dot{\nu} + C(\nu)\nu + D(\nu)\nu + g(\eta) = \tau}$$

The rigid body inertial properties have been defined using advanced and detailed CAD techniques in Solidworks. The added mass properties were estimated using several assumptions and empirical data. The damping properties were defined using CFD techniques in Solidworks Flow Simulation software. The gravity and buoyancy vector was determined using Solidworks CAD techniques. In addition, the transformation from axial thrusts to a BODY input thrust vector was defined using the thruster geometric layout.

The model was developed under the following assumptions:

1. The ROV will be performing operations significantly far enough away from boundaries and free surfaces within the operational environment.
2. The assumption of three planes of symmetry was enforced for defining the added mass of the vehicle.
3. The assumption of slender body theory was enforced to define the rotational DOF added mass terms.
4. Ambient flows and currents are negligible.
5. All *SEAHOG* surfaces are smooth.
6. For the purposes of added mass, the *SEAHOG* body will accelerate an otherwise stationary fluid with its motion.

There are some known simplifications and aspects that have been neglected in the developed model due to their complexity. Aspects of the model developed in this report that may be significant but have been neglected due to their complexity, or just due to them lying outside of the project scope, are:

1. Damping effects and added mass from the thrusters housings.
2. Damping effects from thruster flow trajectories and the interaction with them and the *SEAHOG* body.
3. Forces from the tether.
4. Propeller gyroscopically induced torques and reaction torques from propeller rotational motion.

Some aspects of the model have been developed with more confidence in their accuracy than others but unfortunately, due to the incomplete state of the *SEAHOG* mechanical and electronic systems, most of the aspects of the *SEAHOG* model developed in this chapter could not be verified. Verification will certainly be recommended for future projects, however.

With the *SEAHOG* dynamic model sufficiently complete, open-loop simulations were conducted and are presented in the following chapter so as to characterise the motion of the *SEAHOG*.

Chapter 6 - Open-loop Response and Motion Characterisation

6.1 Introduction

With the *SEAHOG* dynamic model complete for the purposes of this report, it was possible to run some open-loop simulations on the system to give an initial estimation of the vehicle's characteristics and to inform future design improvements and recommendations. This chapter will present a list of simulations that were run on the *SEAHOG* model and thereafter provide an analysis of the results, informed by aspects of the model that have been omitted from the scope of this project. A description and general characterisation of the vehicle's motion while executing different manoeuvres will be provided along with vehicle motion characteristics.

Before the simulations are presented, a list of desired objectives and outputs from this chapter will be presented following.

6.2 Chapter Objectives and Desired Outputs

It is desired that through basic simulations of the *SEAHOG* dynamic system (including the thruster model developed in this report), a better understanding will be gained of the motion that can be expected from the *SEAHOG*. Specifically, it is desired that the following are determined in this chapter:

1. A thrust allocation scheme for control inputs.
2. Characteristics of maximum vehicle velocity and acceleration in controllable DOFs – specifically: surge, sway, heave (ascending and descending) and yaw.
3. Description of the vehicle attitude under maximum vehicle acceleration in different DOFs.
4. Characteristics of maximum vehicle acceleration in surge, heave and yaw.
5. Description of motion coupling.
6. Assessment of vehicle stability.

7. Analysis of results when considering future inclusion of omitted factors from the model.

Now that a clear idea of the objectives of this chapter has been given, before simulations are conducted a standard scheme should be defined in which user inputs allocate thrust to individual thrusters according to the desired motion.

6.3 Thrust Allocation According to Control Inputs

The *SEAHOG* will be controlled by an operator using a joystick-type device. In open-loop mode, the Joystick will be moved to a certain position that will correspond to a desired thrust level that corresponds to the 2D joystick vector. The x and y components of the horizontal thrust vector can therefore be derived using the following equation:

$$T_{x\,des} = \frac{Joystick_x}{Max\ Joystick_x} \times Max\ Thrust_x \qquad \{6.111\}$$

The joystick values will be defined according to the actual joystick data output and therefore, for the purposes of this report the joystick scale will be -1 to 1 for convenience. Therefore, control inputs (whether they are from an operator or from a controller) will represent a scale from maximum negative to maximum positive thrust, represented by a number range of -1 to 1.

To ensure that the ratio of individual thrust vector inputs are accurately translated into the resulting thrust vector applied by the thrusters, the inverse of equation 5.110 can be used. Recall that the applied body-fixed thrust is related to individual thruster inputs via:

$$\boldsymbol{\tau} = \boldsymbol{B}\boldsymbol{\tau}_i$$

And hence the individual thrusts required for a certain desired body-fixed thrust can be found using:

$$\boldsymbol{\tau}_i = \boldsymbol{B}^{-1}\boldsymbol{\tau}_{\boldsymbol{des}} \qquad \{6.112\}$$

It should be noted however, that matrix $\boldsymbol{B}$ has dimensions 6x5 and thus a generalised or "pseudoinverse" must be found for it. It is possible to solve for a unique solution to equation 6.112 by finding the pseudoinverse of $\boldsymbol{B}$. Simulink can calculate the pseudoinverse, where $\boldsymbol{B}^+$ is the Moore-Penrose pseudoinverse and satisfies the following four criteria:

- $\boldsymbol{B}^+\boldsymbol{B}\boldsymbol{B}^+ = \boldsymbol{B}^+$
- $\boldsymbol{B}\boldsymbol{B}^+\boldsymbol{B} = \boldsymbol{B}$
- $\boldsymbol{B}\boldsymbol{B}^+$ and $\boldsymbol{B}^+\boldsymbol{B}$ are Hermitian.

The solutions to equation **5.110** are therefore described by [36]:

$$\boldsymbol{\tau}_i = \boldsymbol{B}^+\boldsymbol{\tau}_{\boldsymbol{des}} + (\boldsymbol{I} - \boldsymbol{B}^+\boldsymbol{B})\boldsymbol{w} \quad \{6.113\}$$

where $\boldsymbol{w}$ is an arbitrary vector. Due to the linearly dependant columns of $\boldsymbol{B}$, the product $\boldsymbol{B}^+\boldsymbol{B} \neq \boldsymbol{I}$ and hence there are multiple solutions to equation 6.113. A vector exists for $\boldsymbol{w}$ such that $(\boldsymbol{I} - \boldsymbol{B}^+\boldsymbol{B})\boldsymbol{w} = 0$, and hence, for convenience, it is possible to describe the solutions to equation **5.110** by the following:

$$\boldsymbol{\tau}_i = \boldsymbol{B}^+\boldsymbol{\tau}_{\boldsymbol{des}} \quad \{6.114\}$$

It is possible to further simplify equation 6.114 by removing the pitch and roll DOFs, as these are not independently controllable and do not form part of the control interest of this project. In addition, the vertical thrust is orthogonal and decoupled from the horizontal thrust and can therefore be treated separately. The resulting matrix will have dimensions 4x3 and be denoted as $\boldsymbol{B}'$. The final thrust allocation set of equations is given following as:

$$\boldsymbol{\tau}_i = \boldsymbol{B}'^+\boldsymbol{\tau}_{\boldsymbol{des}}$$

$$\begin{bmatrix} T_1 \\ T_2 \\ T_3 \\ T_4 \end{bmatrix} = \begin{bmatrix} 0.325 & -0.445 & -0.888 \\ 0.325 & 0.445 & 0.888 \\ 0.352 & 0.289 & -0.977 \\ 0.352 & -0.289 & 0.977 \end{bmatrix} \begin{bmatrix} X_{des} \\ Y_{des} \\ N_{des} \end{bmatrix} \quad \{6.115\}$$

$$T_5 = Z_{des}$$

The above system will ensure that the ratio of thrusts desired by the operator will be correctly allocated to the individual thrusters. It is possible however, that a combination of user inputs will result in a desired thrust that is greater than the maximum possible thrust output from an individual thruster. Since the output of equation 6.115 will result in the individual components of the thrust vector being in the correct ratio, it is possible to scale the resulting thrust values sent to each thruster.

The thrust scaling was implemented by finding the maximum element of $\boldsymbol{\tau}_i$ and if it was greater than the maximum thrust achievable (55 N), the vector was scaled as follows:

$$\boldsymbol{\tau}_{iScaled} = \boldsymbol{\tau}_i \times \frac{55}{T_{max}} \quad \{6.116\}$$

Finally, since thrust inputs were defined to be inputted on a scale from -1 to 1, it is necessary to scale each thrust command to match the actual desired thrust force. The scaling was applied as a gain that was equivalent to the maximum thrust achievable in a particular direction. The maximum thrust in each controllable DOF is presented following in Table 39.

Table 39 - Maximum thrust possible in individual DOFs

Controllable BODY DOF (Thrust force)	Maximum Thrust (N or Nm)
x_b (X)	156.4
y_b (Y)	123.8
z_b (Z)	55.0
$z_{rot\ b}$ (N)	56.4

Now that the thrust allocation scheme is defined, the final step is to relate the desired thrusts to a propeller speed, which can be estimated using the propeller thrust equation 3.53. Hence, the propeller speed is allocated to each thruster by:

$$\Omega_i = \pm\sqrt{\frac{T_{iScaled}}{C_t}} \qquad \{6.117\}$$

The final resulting thrust allocation block diagram in Simulink® is given following in Figure 86.

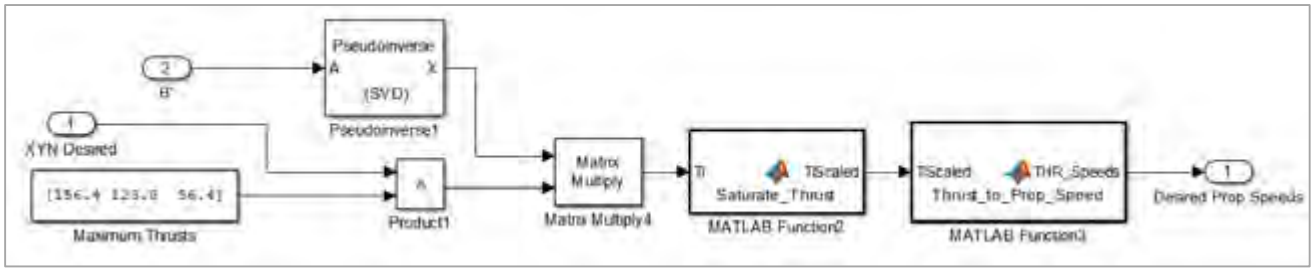

Figure 86 - Prop speed allocation scheme according to thrust inputs

With the thrust allocation scheme defined, open-loop simulations could be performed so as to help to characterise the motion of the *SEAHOG* ROV and achieve the objectives as stipulated in the previous section.

6.4 Open-Loop Simulations

6.4.1 Introduction

The simulations were performed in an open-loop configuration: that is to say, speed inputs were applied to the closed loop thruster models which then in turn applied thrust inputs to the ROV dynamic system. A schematic of the open-loop setup is given following in Figure 87 for clarity.

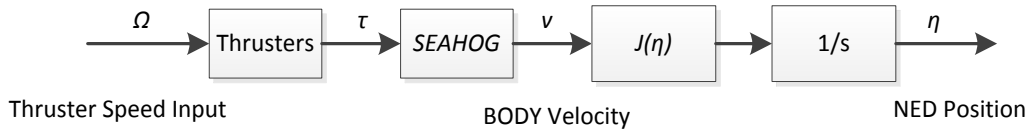

Figure 87 - Open-loop simulation setup for motion characterisation

Now that the simulation setup is known, simulation results can be presented that define the *SEAHOG* speed characteristics.

6.4.2 Maximum Speed Characteristics

Using the thrust allocation scheme developed in this chapter, a step input of maximum thrust was applied to each controllable DOF in turn. The resulting propeller speeds were then applied as a step into the *SEAHOG* dynamic model and the maximum velocity was noted in that DOF. For horizontal motion simulations, the vertical thruster was bypassed and a 20 N force was applied directly to the vertical DOF to simulate neutral buoyancy. The results are presented following in Table 40.

Table 40 - Maximum speed characteristics for the *SEAHOG* ROV

Characteristic	DOF/Velocity	Velocity	Thruster Inputs (rpm)
Maximum Surge +	x_b / u	1.56 m/s	1 = 619; 2 = 619; 3 = 644; 4 = 644; 5 = NA
Maximum Sway +/-	y_b / v	1.00 m/s	1 = -644; 2 = 644; 3 = 519; 4 = -519; 5 = NA
Maximum Heave -	z_b / w	0.56 m/s	1 = 0; 2 = 0; 3 = 0; 4 = 0; 5 = -650
Maximum Heave +	z_b / w	0.35 m/s	1 = 0; 2 = 0; 3 = 0; 4 = 0; 5 = 650
Maximum Yaw +/-	ψ_b / r	2.35 rad/s	1 = -614; 2 = 614; 3 = -644; 4 = 644; 5 = NA
Passive Ascension Rate	z_b / w	0.28 m/s	0 for all

With the maximum speed characteristics known, a description of the vehicle's attitude as a result of maximum thrust inputs can be given.

6.4.3 Motion Description and Characterisation under Maximum Acceleration

It is important to have an understanding of the attitude experienced by the vehicle under maximum accelerations. This is because the rate of acceleration and thrust characteristics may have a significant influence on the stability of the vehicle. This section will present the results of the simulations conducted in the previous section and provide an analysis of the motion with regards to the attitude of the vehicle. From

previous experimental simulation results, it was deemed necessary to run each simulation for 30 seconds so that the transient and steady state motion conditions of the vehicle could be observed.

For each of the presented data sets, the thruster inputs can be found for the corresponding simulation in Table 40, shown previously.

Surge:

Figure 88 following shows the motion for a full surge input.

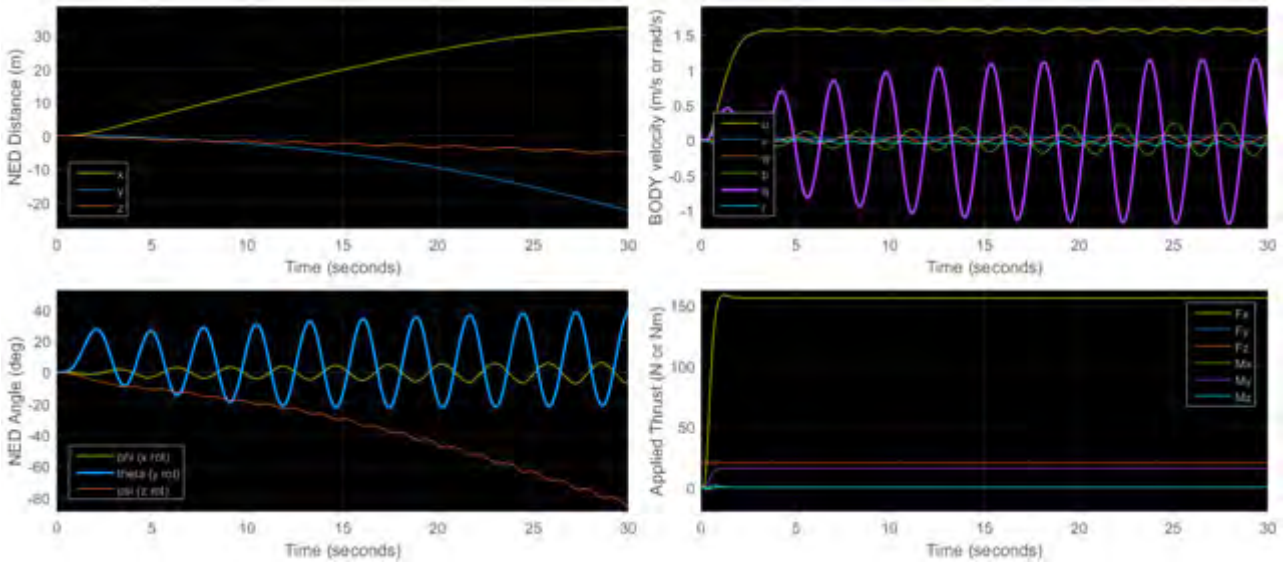

Figure 88 - Full surge open-loop motion characteristics

It can be seen that the pitch is very oscillatory for a maximum surge input. The system is not unstable however, with the pitch reaching a steady state of oscillating between -22˚ and 38˚. In addition, the roll is affected to a lesser extent, oscillating between -7˚ and 6˚. Coupling can be seen between the surge and yaw DOFs, demonstrated by a gradual decrease in yaw. Due to the oscillatory nature of the pitch, it is possible that the acceleration of the vehicle in this direction should be limited to prevent oscillations. The effect of limiting acceleration in surge will be investigated later in this chapter.

It was suspected that the actual body oscillation in real life would be less than in the simulation. This was due to other factors that have not been included in the model in this project that provide greater damping to the system. The momentum of water flowing through the thrusters, in addition to the thruster bodies themselves, will serve to increase the overall drag and stabilise the ROV to a greater extent. Additionally, the location of the tether cable will provide a stabilising moment in the pitch DOF due to its own drag and momentum. To better visualise the effect of the tether, Figure 89 following shows how the tether will oppose the motion of the *SEAHOG* in the pitch DOF due to its location.

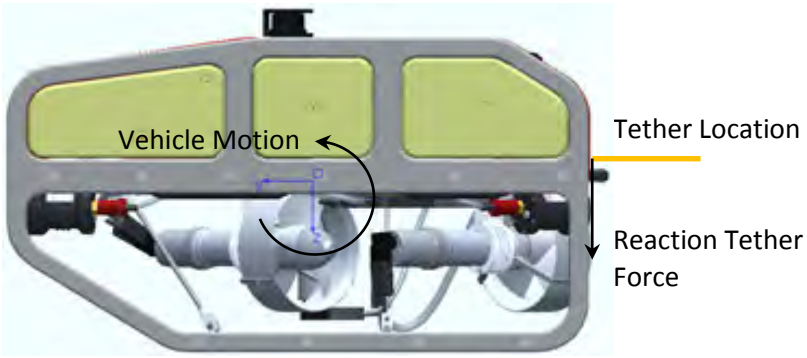

Figure 89 - Stabilising reaction force from tether

To demonstrate the effect of greater damping on the system, the drag was increased and the full surge simulation was rerun with the resulting motion shown following in Figure 90.

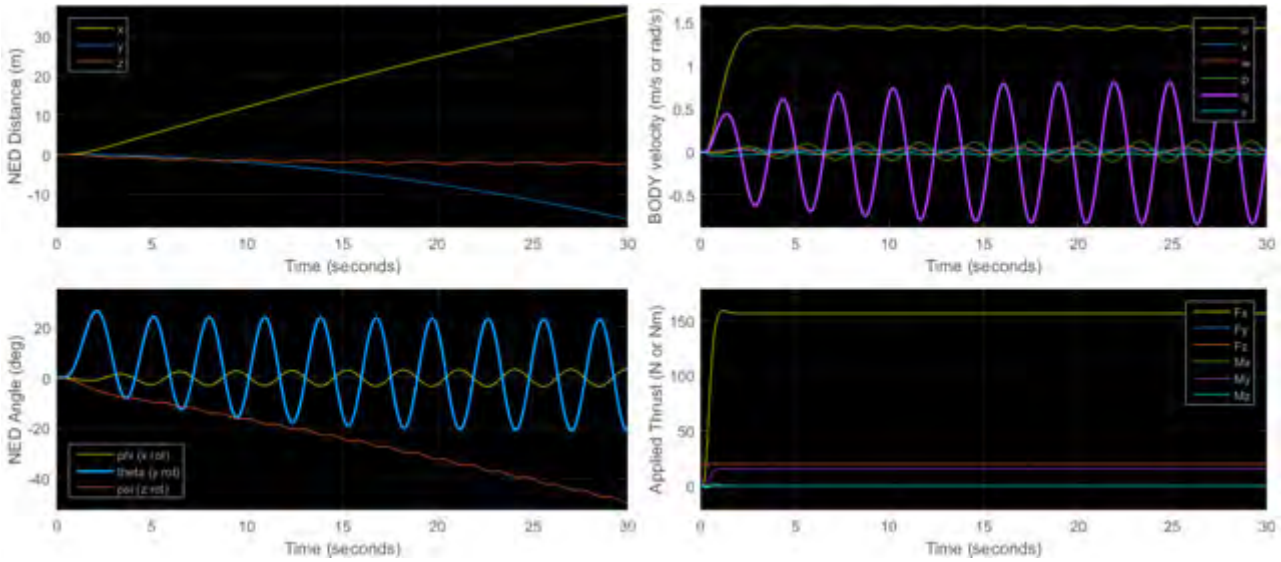

Figure 90 - Full surge open-loop motion characteristics with increased drag

As can be seen, the motion is still oscillatory with approximately the same period, however the amplitudes are now reduced. The pitch is shown to oscillate between -22˚ and 24˚ and the roll is shown to oscillate between -4˚ and 3˚. It was expected that the oscillations of the body would be reduced under the influence of greater damping, which could imply that future work and model improvements will result in the *SEAHOG* demonstrating more stable behaviour.

Sway:

Figure 91 following shows the motion for a full sway input.

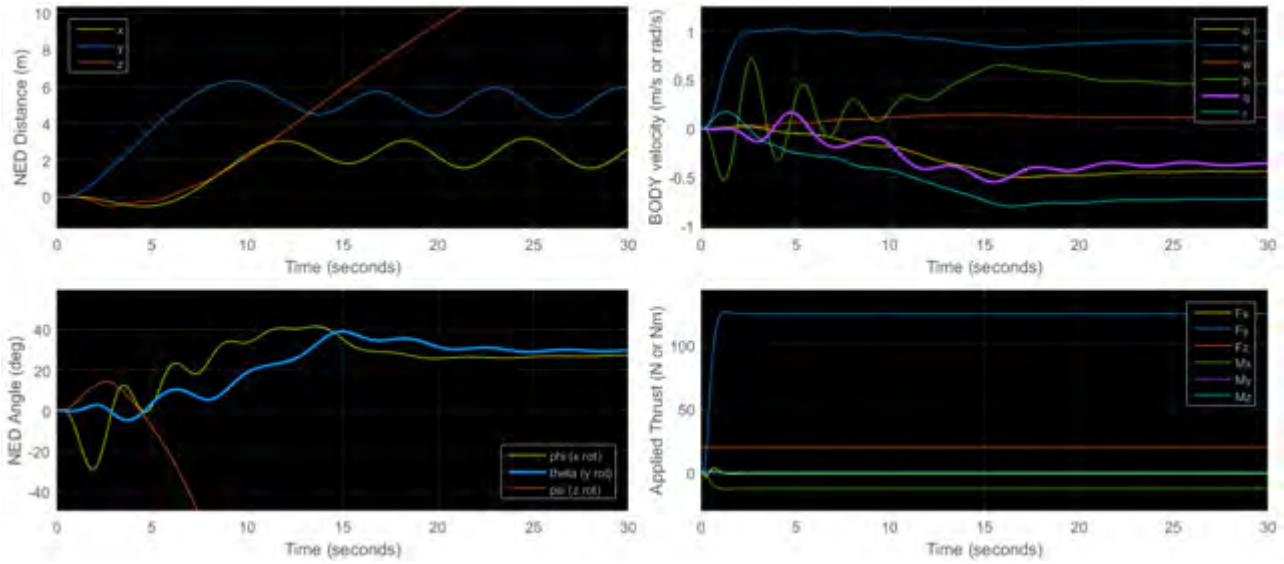

Figure 91 - Full sway open-loop motion characteristics

Motion in the sway direction can be seen to affect the stability of the vehicle to a lesser extent than motion in the surge direction. The initial thrust input causes a maximum roll of -29˚ which then slowly stabilises. It can be seen that the roll and pitch reach equilibrium points at 26˚ and 30˚ respectively.

A large amount of motion coupling can be seen in this manoeuvre to the heading of the ROV. The x and y NED position is seen to oscillate, showing that the ROV ends up rotating too fast for translation along the y axis to occur. For motion in the sway DOF however, transient behaviour is of most interest since typically a user operating the ROV in this DOF will only be making small adjustments to position and not travelling long distances. It is therefore assumed that the strong motion coupling to the heading motion will not be a significant detriment to the human operator executing a sway manoeuvre.

Heave:

Figure 92 following shows the motion for a full heave input in the descending direction.

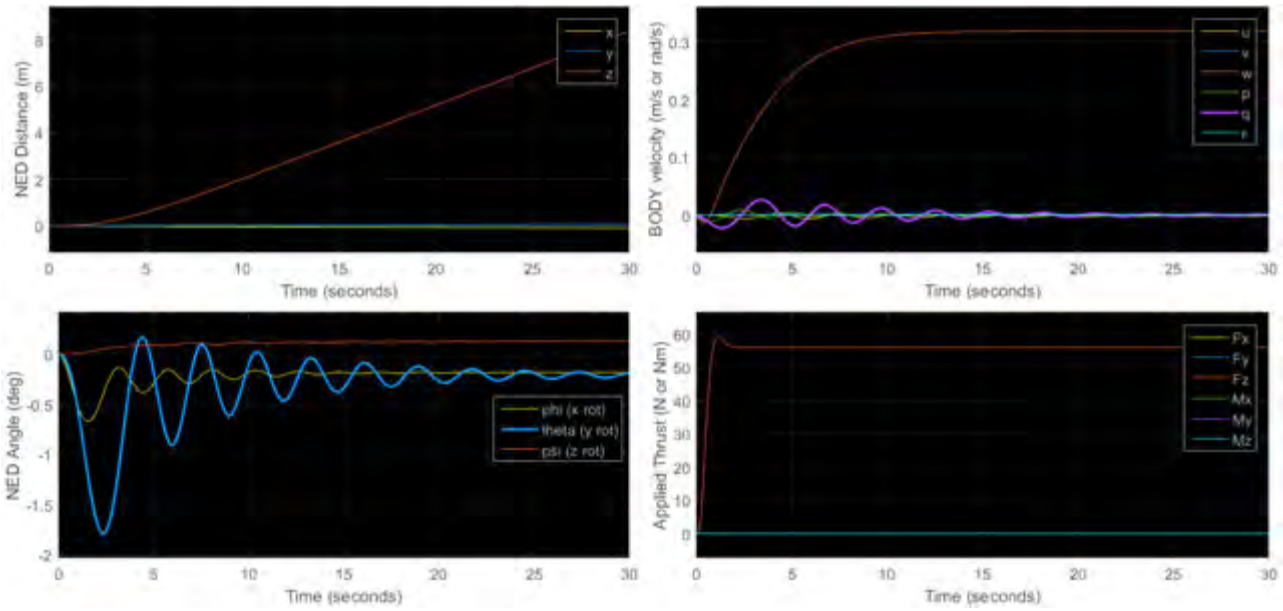

Figure 92 - Full heave descending open-loop motion characteristics

It can be seen that descending in the heave direction causes very little disturbance to the vehicle in other DOFs. In addition, very little motion coupling exists between DOFs for this manoeuvre. It should be noted however, that in the thruster and *SEAHOG* models, the effects of rotational flows and their resulting torques were ignored. Therefore it is possible that in reality, descending or ascending manoeuvres will impart a torque that will cause the ROV to rotate in the yaw direction. Once again however, forces from the tether are expected to counteract any rotations induced to some extent.

Another consideration that will possibly have a large effect on descending in the heave direction is the extra drag and flows from the horizontal thrusters. However, as mentioned in the previous chapter, analysing how the flows from the thrusters affect the overall system is a complex problem and will not be dealt with in this report.

Figure 93 following shows that a significantly different behaviour can be expected if the ROV is ascending.

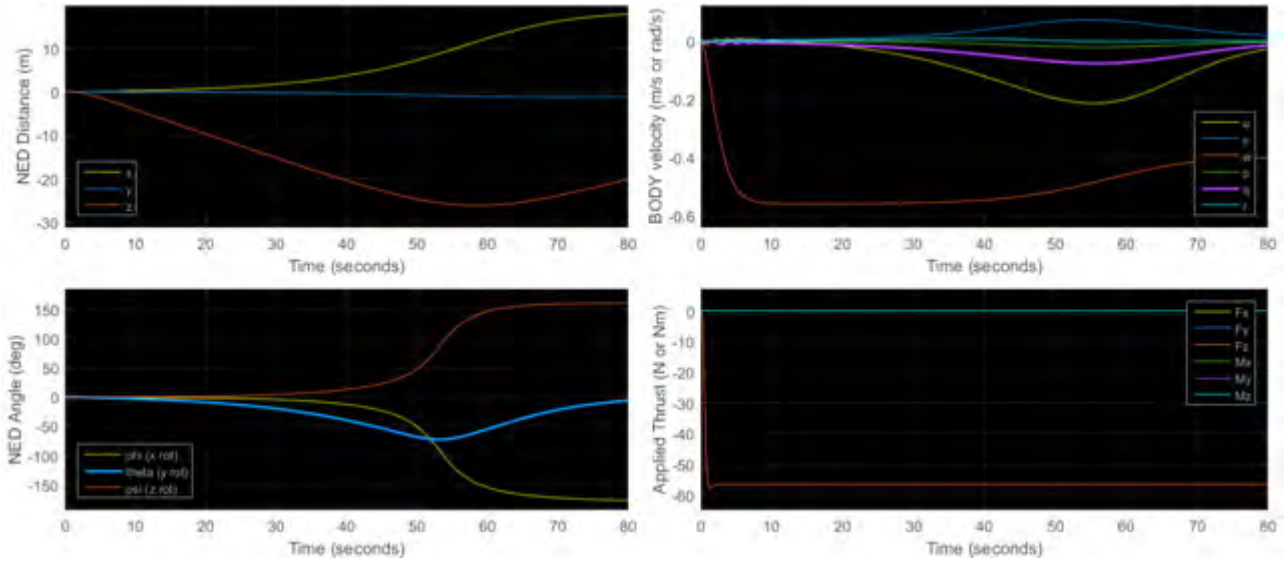

Figure 93 - Full heave ascending open-loop motion characteristics

The simulation shown in Figure 93 was run for over 80 seconds to see if the ROV continues to roll. As can be seen, no stabilisation occurs which causes the ROV to roll to an angle less than -90˚, effectively transferring the vertical thrust vector into a horizontal one. This seems unlikely to happen in real life, however it demonstrates a lack of righting moment supplied by the buoyancy and weight of the robot for this particular manoeuvre.

Fortunately, the motion coupling for this manoeuvre happens slowly. The simulation shows that a significant change in attitude can only be expected after about 40 seconds of ascending. As a result, another simulation was run to assess whether the ROV could be stabilised by reversing the thrust periodically. The results are shown following in Figure 94. As can be seen by the green circle, reversing the thrust does tend to stabilise the ROV, mostly in pitch but also somewhat in roll.

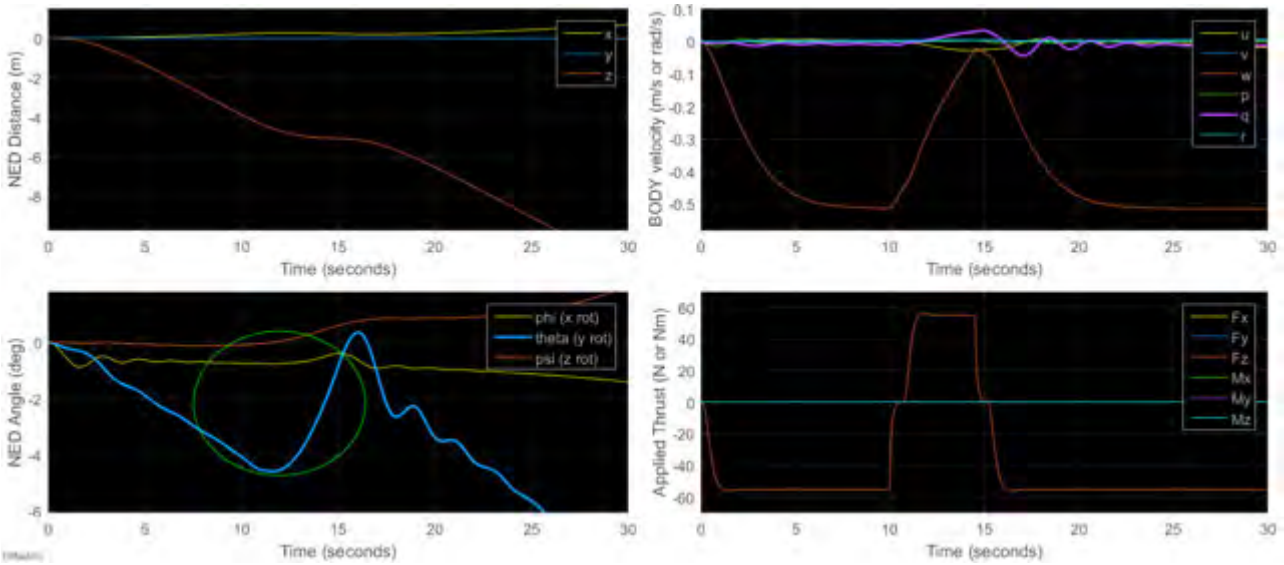

Figure 94 - Motion for alternating thrust control in an open-loop heave ascending manoeuvre

The results from Figure 94 are promising and suggest that controlled ascension will be possible but an optimal thrust pattern should be established on how to achieve it. However, section 6.4.6 following will provide an investigation into the reason for this behaviour so as to get insight into how the problem can be mitigated in the future.

For a worst case scenario, the ROV has been designed to passively resurface. A simulation was conducted with zero thrust inputs from the thrusters to analyse the passive resurfacing characteristics of the *SEAHOG*. The results are shown following in Figure 95.

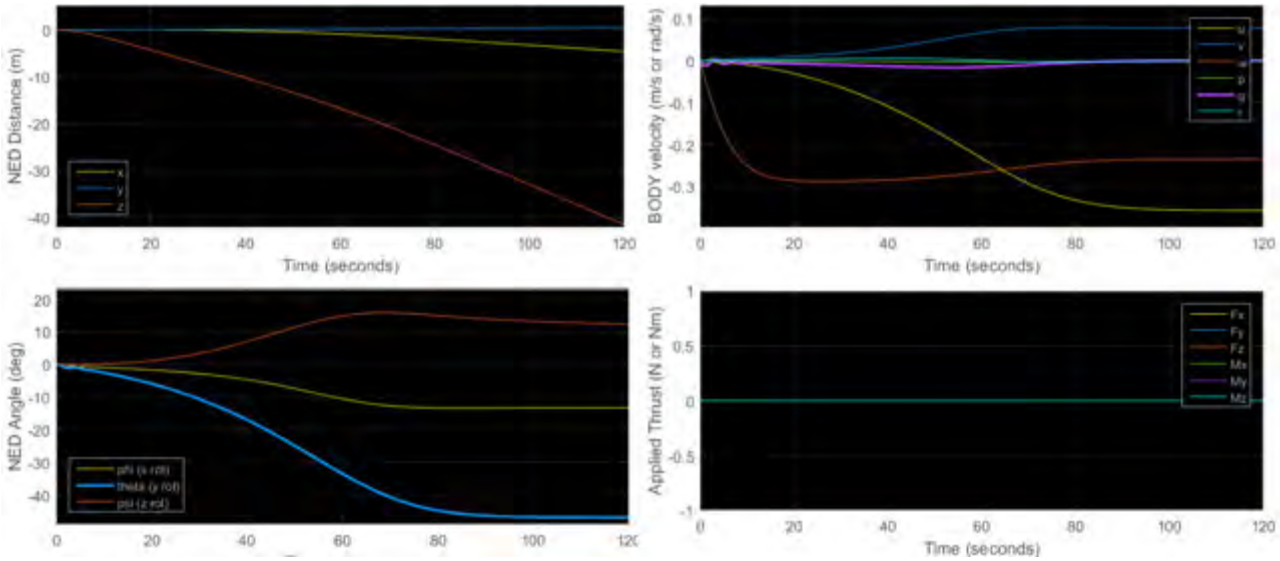

Figure 95 - Passive heave ascension motion characteristics

As expected, passive ascension of the ROV does not cause an unacceptable amount of pitching or rolling and, as given previously in Table 40, a maximum ascension rate of approximately 0.28 m/s is expected. Therefore, ascending by virtue of the ROV's buoyancy alone is a valid solution as a worst case scenario.

Yaw:

Figure 96 following shows the motion for a full yaw input.

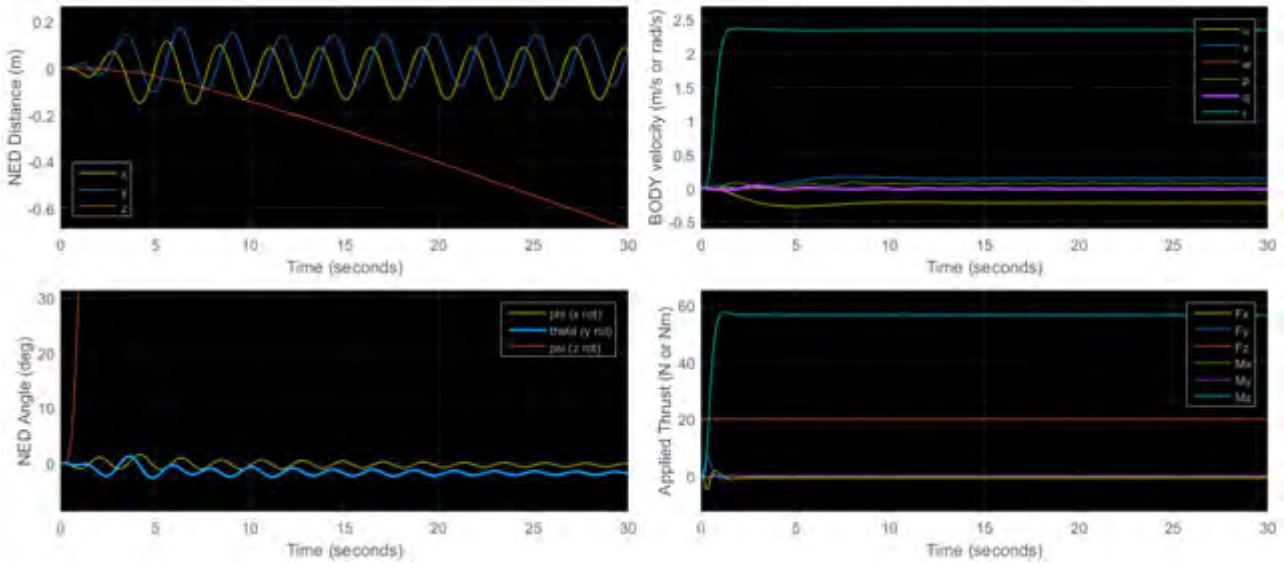

Figure 96 - Full yaw open-loop motion characteristics

Motion in the yaw DOF can be seen to be very stable, with very little motion coupling. Effects from the tether may serve to limit the yaw rate to a greater extent than shown in the simulation. Again, the transient conditions for the yaw simulation are of most interest since yaw manoeuvres will mostly be small corrections to heading and practically a maximum of 180˚ rotation, when motion in the opposite direction is desired.

Summary:

In general, the motion of the *SEAHOG* is stable enough for controllers to be designed for the purpose of controlling certain DOFs.

Full acceleration is possible in all DOFs except surge, in which oscillatory motion will result in the pitch and roll of the robot.

Coupling exists between DOFs under surge and under sway. However, motion in heave and yaw can be considered decoupled for depth holding and heading holding operations respectively.

A description of the open-loop motion characteristics has been given for all controllable DOFs giving a good idea of what can be expected from the *SEAHOG* when conducting different manoeuvres. It has been established that maximum acceleration is not possible in surge without causing oscillatory motion in the pitch and roll DOFs. In addition, an ascending heave manoeuvre will cause a constant roll of the ROV until the vertical thrust vector is effectively translated to a horizontal vector. Therefore, the next section will briefly investigate what maximum acceleration rate is possible in surge and, following that, an investigation into the cause of the roll in an ascending heave manoeuvre will be investigated.

6.4.4 Maximum Acceleration Rate in Surge

From Figure 90 previously, it was shown that a step input into the thrusters for a surge manoeuvre will cause an oscillatory limit cycle in the pitch and roll DOFs. The acceleration rate of 0.64 m/s^2 demonstrated in the simulation is therefore not practically possible. This section will investigate the maximum acceleration achievable for a surge operation without inducing a limit cycle to the system.

It was important to establish if the shape of the *SEAHOG* itself induced the oscillatory motion, or if it was the rapid application of thrust. Therefore, two simulations were conducted where a thrust speed ramp was applied over 5 s and 10 s respectively. The results are shown following in Figure 97 and Figure 98.

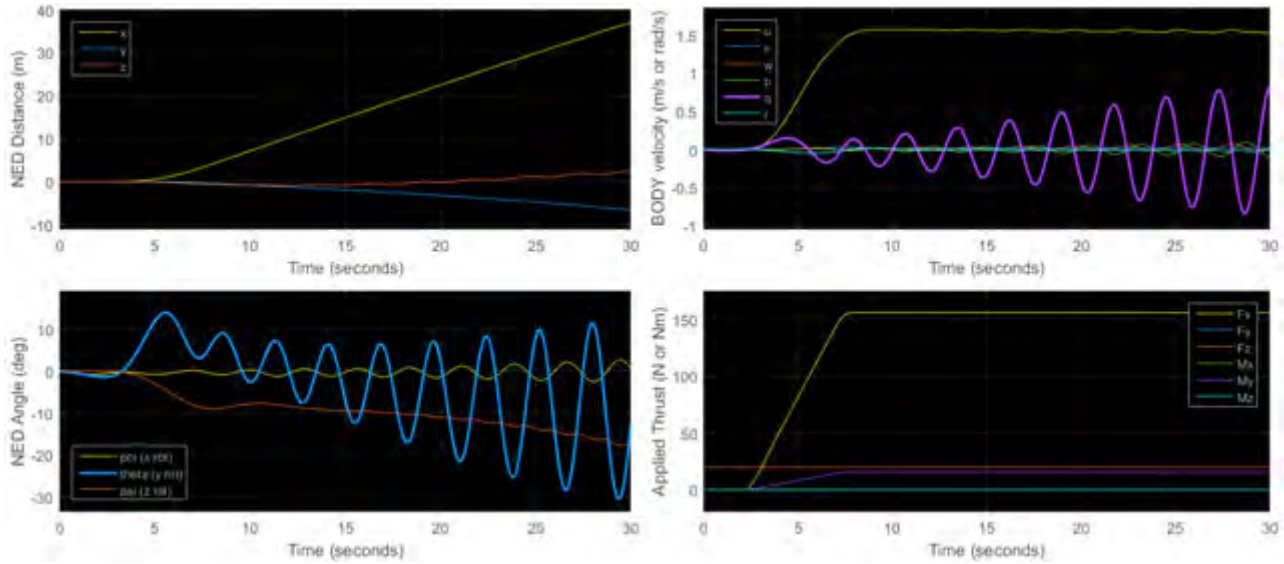

Figure 97 - Surge manoeuvre applying thrust speed ramp over 5 s

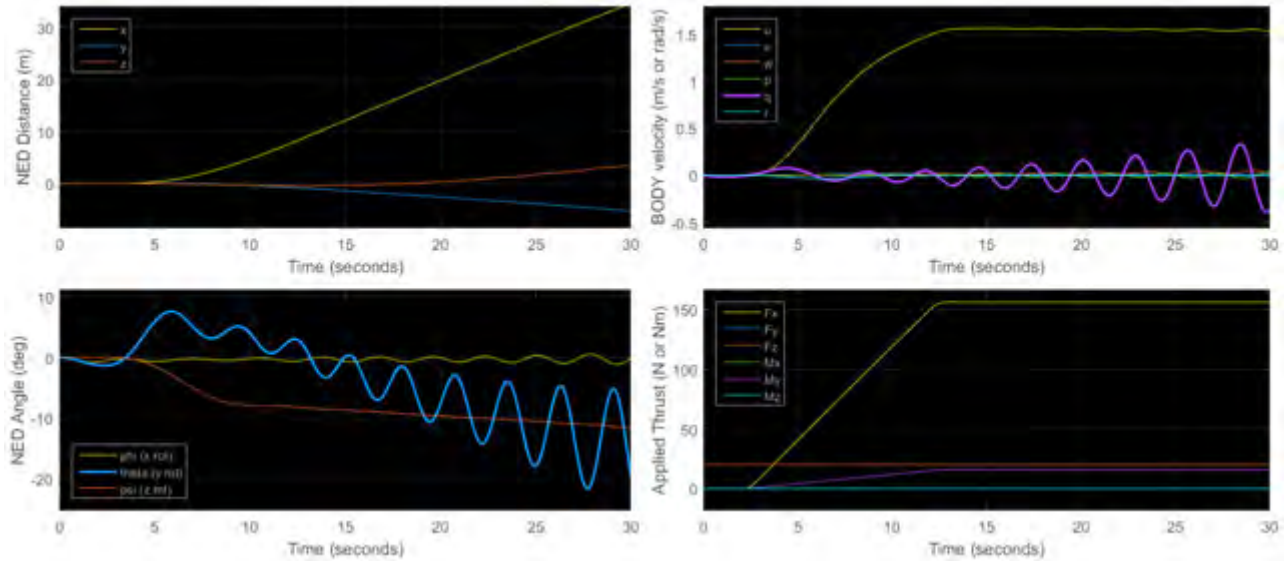

Figure 98 - Surge manoeuvre applying thrust speed ramp over 10 s

The results show immediately that the amplitude of oscillation in pitch and roll is greatly reduced when applying a speed ramp. However, it can be seen from Figure 98 that the hull of the *SEAHOG* itself induces a

growing oscillation if a constant maximum thrust is applied. This is easily counteracted by decreasing the thrust however and is thus not considered a significant issue for an operator controlling the *SEAHOG*.

Due to the still largely oscillatory nature of the pitch in Figure 97, the practical maximum acceleration for ease of use will be cited as an average of the acceleration between Figure 97 and Figure 98. The value obtained is 0.34 m/s^2 approximately, which is close to half the acceleration achievable if a step input is applied.

Increasing the vertical distance between the CG and the CB can also serve in the future to be a solution that allows the *SEAHOG* to accelerate at a greater rate. Figure 99 following shows the simulated results for a full surge input where the righting moment has been doubled.

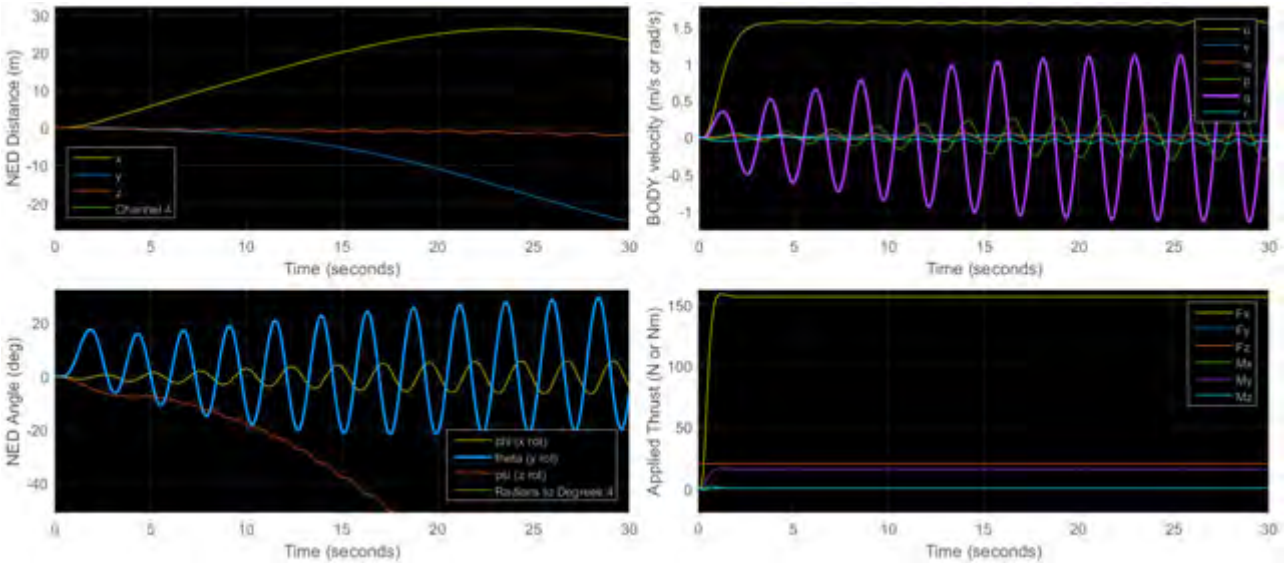

Figure 99 - Full surge manoeuvre with double the righting moment

The pitch is seen to oscillate between -21˚ and 28˚ and the roll is seen to oscillate between -6˚ and 6˚. The amplitudes of the oscillations are both decreased from the original righting moment properties which were a pitch oscillation of -22˚ to 38˚ and a roll oscillation of -7˚ to 6˚. It would appear that the shape of the ROV body is conducive to this limit cycle behaviour, however it is not conducive that the drag of the ROV is in fact the primary contributor to the oscillations set up in the body. However, it can be seen nevertheless that increasing the righting moment helps to decrease the oscillations in the body somewhat, making it more stable.

Now that a measure of the practical limit to acceleration in the surge direction has been obtained for the current system design, the acceleration characteristics for the *SEAHOG* can be listed in the following section.

6.4.5 Maximum Acceleration Characteristics

With all of the maximum accelerations in each controllable DOF established, the *SEAHOG* acceleration characteristics are listed following in Table 41.

Table 41 - Characteristics of maximum acceleration for *SEAHOG* manoeuvres

Characteristic	DOF/Acceleration	Max. Acceleration	Thruster Inputs (rpm)
Maximum Surge +	x_b / $\dot{u}$	0.34 m/s^2	1 = 619; 2 = 619; 3 = 644; 4 = 644; 5 = NA
Maximum Sway +/-	y_b / $\dot{v}$	0.45 m/s^2	1 = -644; 2 = 644; 3 = 519; 4 = -519; 5 = NA
Maximum Heave -	z_b / $\dot{w}$	0.10 m/s^2	1 = 0; 2 = 0; 3 = 0; 4 = 0; 5 = -650
Maximum Heave +	z_b / $\dot{w}$	0.04 m/s^2	1 = 0; 2 = 0; 3 = 0; 4 = 0; 5 = 650
Maximum Yaw +/-	ψ_b / $\dot{r}$	1.60 rad/s^2	1 = -614; 2 = 614; 3 = -644; 4 = 644; 5 = NA

Finally, an investigation into the motion of the ROV in an ascending heave manoeuvre will be investigated in the following section so as to give an indication of possible reasons for the vehicle's motion behaviour observed in this manoeuvre.

6.4.6 Ascending Heave Manoeuvre - Motion Investigation

An investigation was conducted into the ascending heave manoeuvre to gain insight into the mechanism responsible for the continued rolling motion of the ROV without any passive stabilisation being observed.

Firstly, cross coupling drag effects were removed in the simulation. All terms that contributed to forces in a different DOF than that of the motion in that DOF were removed, with the simulation results shown following in Figure 100.

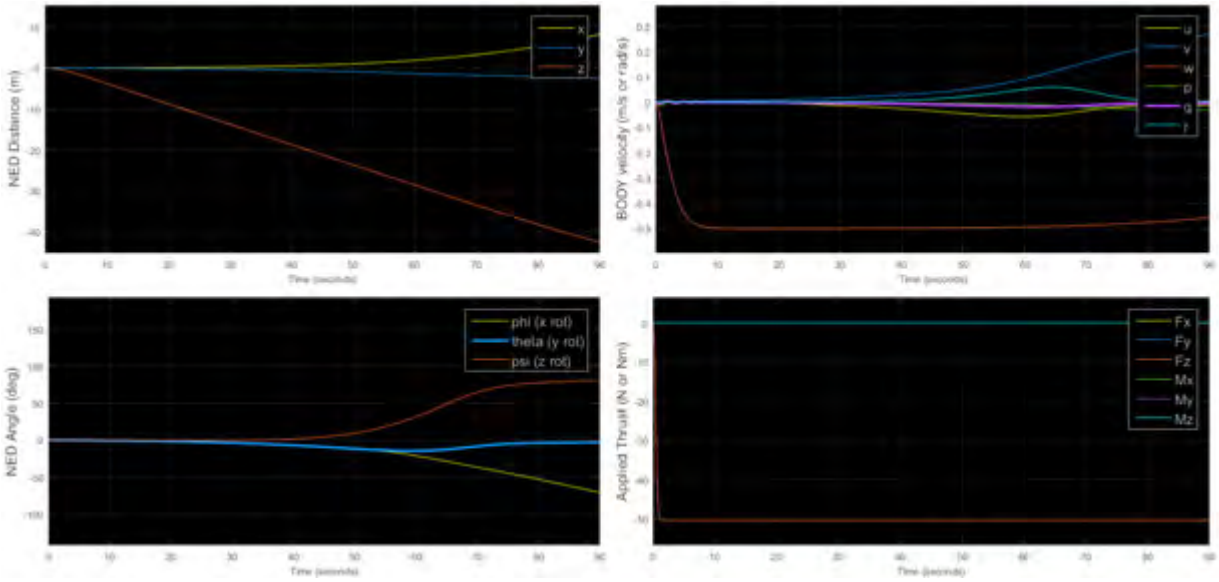

Figure 100 - Full thrust ascending heave manoeuvre with cross-coupling drag effects removed

It can be seen from the figure that the roll still increased but at a reduced rate. Another aspect identified that could contribute to the roll was the unsymmetrical rigid body properties of the *SEAHOG*. Therefore, the off diagonal elements of the rigid body matrix were removed, and their contributions in the rigid body Coriolis matrix were also removed. Also, as another simulation verification measure, the ROV was initialised at a depth of 50 m and a heading of -180˚.

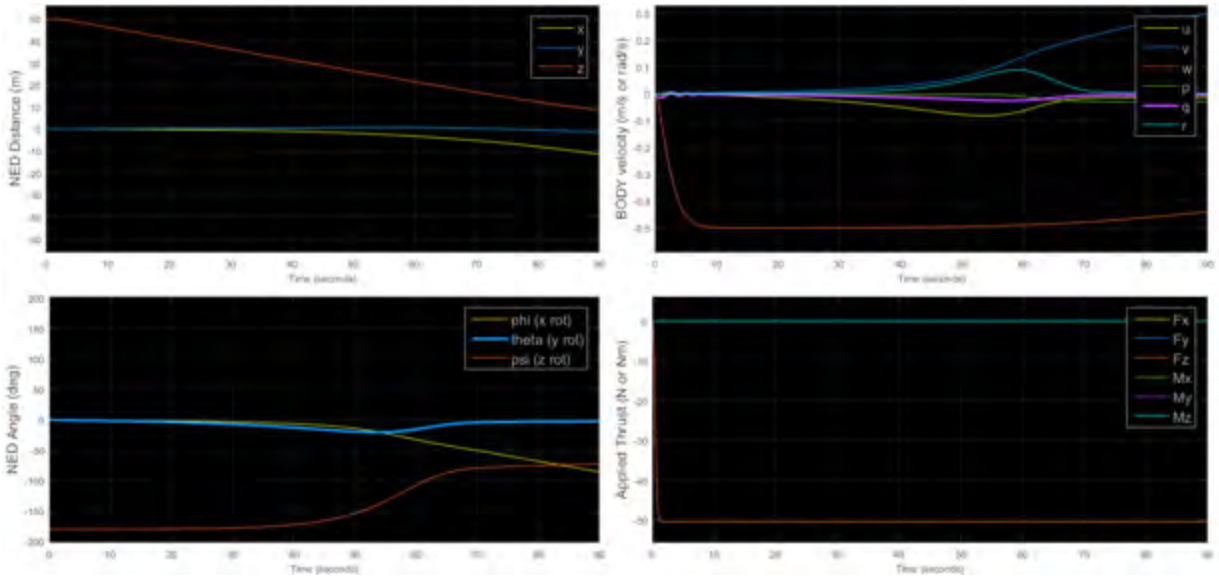

Figure 101 - Full thrust ascending heave manoeuvre without drag cross-coupling and non-symmetrical mass elements

Figure 101 shows that removing non-symmetrical rigid body elements did not prevent the gradual increase in roll. The initialisation of the *SEAHOG*'s position and heading shows that the simulation transformations are working correctly, with the ROV rotating in yaw in the same direction as previously, as expected. In addition, the ROV moved in the negative x direction due to its heading initialisation, which was also expected.

The effect of the horizontal position of the CG relative to the CB was investigated, whereby the horizontal positions of the CG and CB were moved to be coincident. Given that Figure 100 and Figure 101 showed previously that the roll was not caused by drag cross-coupling or the unsymmetrical properties of the *SEAHOG* hull, it was expected that the cause of the continued roll was related to the inertial properties of the ROV. It was expected that moving the CG position relative to the CB would have an effect on the direction of roll. Figure 102 following shows that the roll direction was positive instead of negative after changing the CG and CB position.

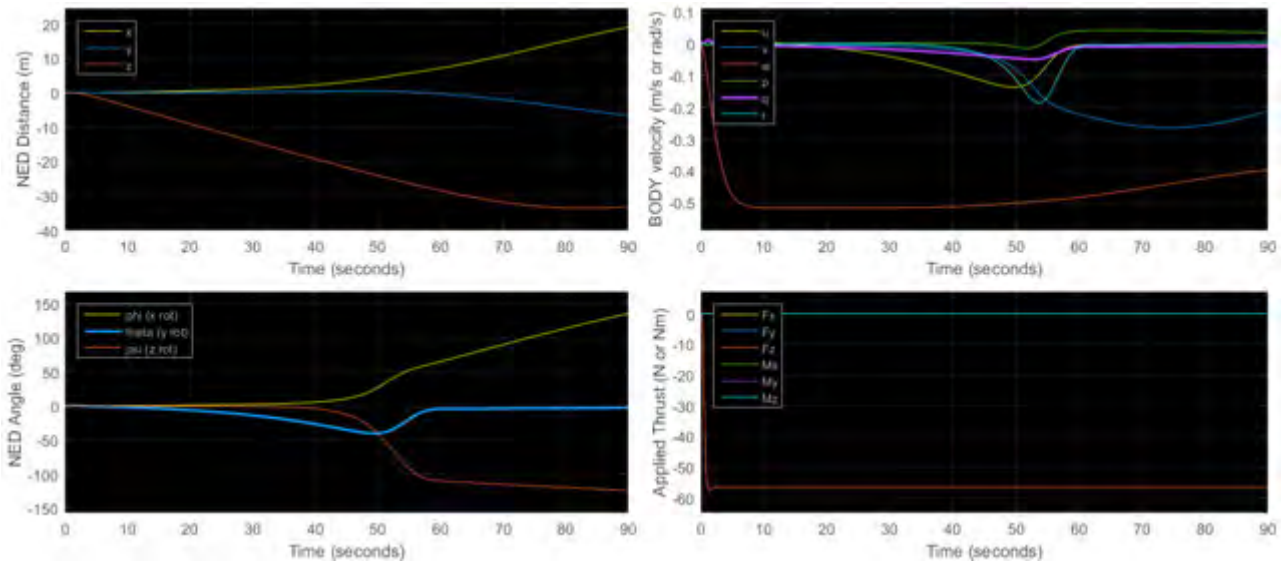

Figure 102 - Full ascending heave manoeuvre with coincident CG and CB horizontal position

Results from Figure 102 showed that the position of the CG and CB did have an effect on the motion of the body in this manoeuvre, seen by the ROV rolling in the opposite direction to before. Since moving the CG and CB position affected the motion of the body but did not solve the problem, it was suggested that the body's inertial properties might have been driving the anomalous motion observed in the ascending heave manoeuvre.

The anomalous behaviour of the *SEAHOG* observed in the ascending heave manoeuvre was finally identified to be linked directly to the added mass term associated with the vertical motion of the ROV ($Z_{\dot{w}}$). Recalling from chapter 5, the added mass for ROV motion in the vertical direction was approximated as 359.9 kg, which is more than four times the mass of the *SEAHOG* itself. The added mass term was

decreased in the added mass Coriolis matrix ($\boldsymbol{C_A(\nu)}$) by a factor of four, and the results are shown following in Figure 103.

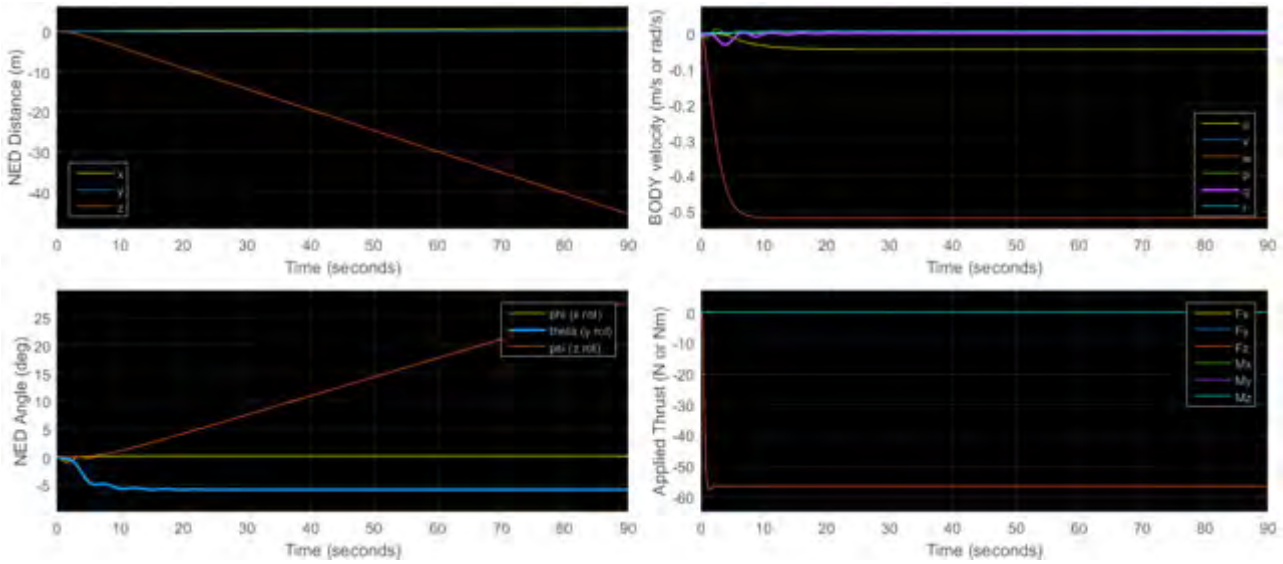

Figure 103 - Full ascending heave manoeuvre with vertical added mass Coriolis elements decreased by a factor of 4

Figure 103 shows clearly that the ROV ascended in a stable orientation. Evidently, the added mass properties of the ROV can have a significant effect on the motion of the vehicle and it will therefore be recommended that future work is conducted to more accurately approximate the added mass terms of the ROV.

It is clear that the added mass of the ROV has a significant effect on its behaviour, as has been illuminated by the ascending heave manoeuvre. While it is expected that the approximated added mass values in this project are not cannot achieve a high level of accuracy, a solution to the observed rolling of the ROV should still be proposed. If it is assumed that the approximated added mass values are correct, it can be seen that the righting moment of the ROV is not sufficient to stabilise the ROV in the ascending heave manoeuvre. A final simulation was run with the original *SEAHOG* model and two times the righting moment arm, which is shown following in Figure 104.

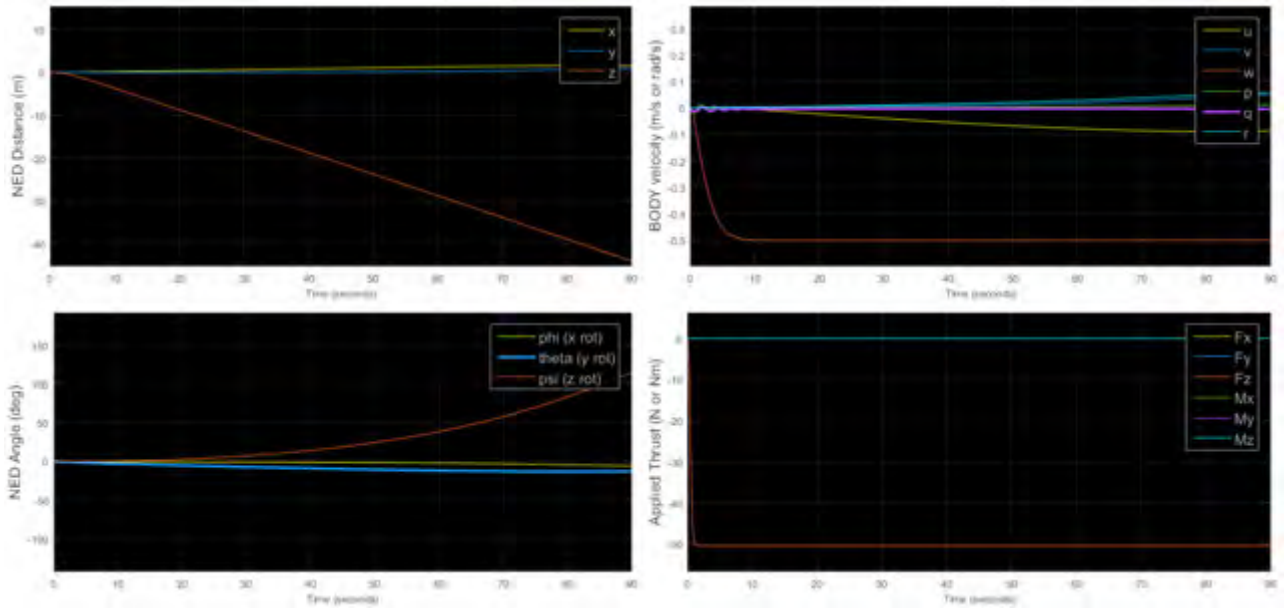

Figure 104 - Full thrust ascending heave manoeuvre with double the righting moment arm

Figure 104 shows that increasing the moment arm will succinctly solve the problem of a gradually increasing roll and effectively stabilise the ROV in this manoeuvre, regardless of the added mass values.

This completes the investigation into the ascending heave manoeuvre, allowing a summary of the open-loop simulation data to be given.

6.4.7 Summary

Simulations were conducted in an open-loop configuration, whereby speed inputs were applied to the thrusters so as to establish the maximum velocity and acceleration achievable by the *SEAHOG* in controllable DOFs. Simulation results were analysed so as to give an understanding of the characteristics of motion experienced by the *SEAHOG*.

In general, all the simulated manoeuvres exhibited stable behaviour apart from under maximum acceleration in surge and ascending in heave. Oscillations in pitch and roll occurred if step inputs were applied to accelerate the vehicle in surge. However, if a ramp thrust was applied to accelerate the vehicle, it was possible to mitigate oscillatory behaviour. It was shown that increasing the righting moment arm decreased the oscillations somewhat, although significant oscillation was still observed in the pitch of the ROV. It was therefore suspected that the shape of the ROV hull and its related drag properties could be conducive to producing limit-cycle type behaviour in the ROV's pitch during motion in the surge direction. It will be recommended that an investigation into the drag effects of the *SEAHOG* hull on its motion is conducted in the future.

Ascending in the heave direction at full thrust resulted in a gradual roll so that the vertical thrust vector ended up being horizontally orientated which was found to be directly linked to the added mass term associated with vertical ROV motion. While the continued rolling of the ROV seems unlikely in real life, it was shown that by reversing the thrust periodically, it was possible to ascend and periodically stabilise the roll DOF in the simulation. Alternatively, increasing the righting moment is an effective solution for increasing the stability of the vehicle in all ROV manoeuvres.

With a good idea of the expected motion from the *SEAHOG*, the possible effects on the motion from assumptions in the current model can be discussed. In addition, the effect on the motion from future improvements to the model can be discussed.

6.5 Effect of Future Model Improvements and Current Model Assumptions on Motion

This project deals with creating a preliminary model to be used for the simulation of the *SEAHOG* ROV's motion. It will, as a result, not encapsulate all significant aspects of the real life system. Therefore, insight into the effects of the assumptions of the current model and the possible effects from future improvements to the model will be valuable for the purposes of model verification. This section will provide insight into how current assumptions and future model improvements are expected to affect the dynamic system of the *SEAHOG*.

It should be noted that in reality a greater deal of motion coupling may exist in the system. This is due to the following assumptions in the formulation of the *SEAHOG* model:

- Three plane symmetry in the formulation of the added mass matrix – in reality there may be cross coupling between added mass elements.
- Neglecting rotational flow effects and gyroscopic torques from thrusters.
- Neglecting reaction torques on the *SEAHOG* frame induced by propeller rotations.

In addition, the assumption that all *SEAHOG* surfaces are smooth in the model will lead to lower drag at low speeds than in reality. As can be recalled from section 5.5.2, viscous damping is dominant at low Reynold's numbers which is in turn related to surface roughness. This will have an effect on the acceleration of the vehicle and its controllability at low speeds.

A significant aspect of the model to be included in the future is that of the tether cable. The tether, due to the position of its anchorage on the *SEAHOG* body will serve to stabilise the vehicle in pitch and yaw by providing reaction moments to induced movement. However, it will also provide disturbances to the system due to its own drag and momentum.

The aspects mentioned in this section can be used as a reference for future work whereby a comparison can be made between the real observed motion of the vehicle and its discrepancies to the model. This completes a description of the effects expected from current model assumptions and future model improvements, allowing the open-loop motion of the *SEAHOG* to be summarised in the following section with regards to the control aspects of this project.

6.6 Open-Loop Motion Characterisation Summary

The objectives of this chapter were to obtain maximum velocity and acceleration specifications for the *SEAHOG* and to characterise its motion by simulating different open-loop manoeuvres. All of the objectives were achieved and the source of any anomalous behaviour was identified. The model itself was deemed to be correctly constructed, due to the wide variety of operating scenarios that were simulated without anomalous behaviour arising from aspects of the simulation that were not related to the model parameters directly.

As a result of the open-loop characterisation of the *SEAHOG*'s motion, it was possible to make important control design decisions based on the simulations in this chapter. Some of the main results of the chapter, for the purpose of future control system modelling, are:

1. Motion in heave can be decoupled from other motion.
2. Motion in yaw can be decoupled from other motion.

In addition, general insights as to the ease of operation of the *SEAHOG* by a human operator, according to the simulation results, are:

- Ascension in the heave direction may cause roll and therefore horizontal translation. This can be counteracted by reversing the vertical thrust direction periodically.
- Motion in the surge direction will tend to set up an oscillating limit cycle in the vehicle. This will most likely only happen after the desired manoeuvre is completed, but can be counteracted if necessary by a decrease in speed.

Sufficient insight has been gained as to the motion of the *SEAHOG*, allowing control objectives and specifications to be formulated. However, the position and orientation sensors will be an important aspect of the system and must therefore first be modelled in the following chapter.

Chapter 7 - Hardware and Sensors

7.1 Introduction

Up until this point, the motion of the *SEAHOG* has been measured directly from the real life motion of the body according to the simulation. However, an important fact to consider is that if closed loop control is desired in real life, the system states have to be measured physically by some means. Localisation is the term that is associated with determining the position and orientation of a body in space and presents numerous significant challenges for underwater systems. The Literature Review in Appendix A should be consulted for a detailed investigation of underwater localisation and sensors. This chapter will serve to propose hardware components that can be used for localisation on the *SEAHOG* and describe and model them to be used in simulations in this report.

Appendix B contains detailed information about the communications network on the *SEAHOG* and will provide insight into some of the motivations for design decisions presented in this chapter. Since this report does not encapsulate the installation of control hardware on the *SEAHOG*, sensor and hardware choices in this report will serve mostly as an informed suggestion for future projects.

The scope of this project includes designing controllers for automatic heading and depth holding functions, therefore sensors must be specified that have the ability to measure the attitude and depth of the *SEAHOG*. This chapter will specify and describe the available sensors for sensing the motion of the *SEAHOG* in the required manner and will then model the sensors so as to provide a theoretical sensory system to be used in simulations.

For the sake of context, the modules designated to house scientific and localisation sensors on the *SEAHOG* are highlighted in blue, following in Figure 105.

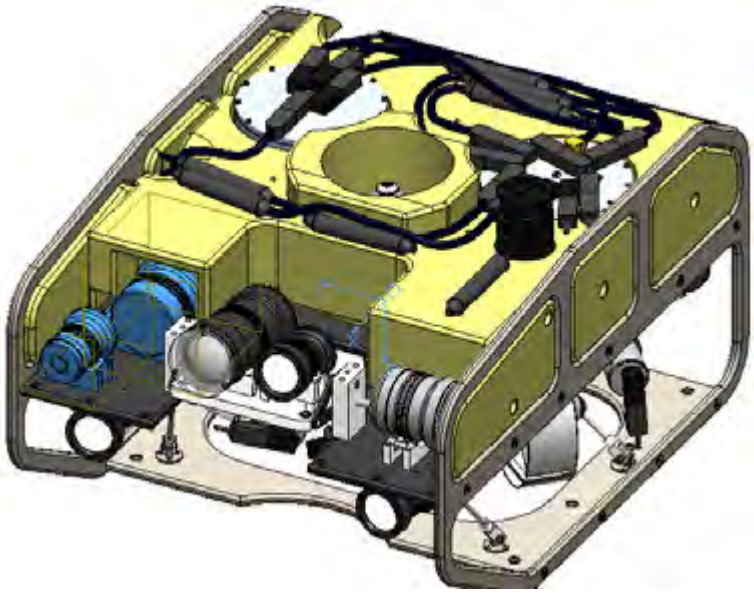

Figure 105 - Designated modules on the *SEAHOG* for housing sensors shown in blue

7.2 Attitude Sensing

An iNEMO, STEVALMKI062V2 inertial module evaluation board was purchased previously for use on the *SEAHOG* and thus it was decided that it would be modelled in this project for the purposes of attitude determination. The iNEMO evaluation board is shown alongside in Figure 106.

Features and components of the iNEMO include [37]:

- LSM303DLH 6 axis Micro Electro-Mechanical System (MEMS) accelerometer and magnetometer
- LY330ALH MEMS Yaw gyroscope
- LPR430AL MEMS Pitch and Roll gyroscope
- STM32F103RET7 32-bit microcontroller (includes 3 12 bit ADC channels)
- STLM75DS2F digital temperature sensor
- USB and RS232 external communication busses

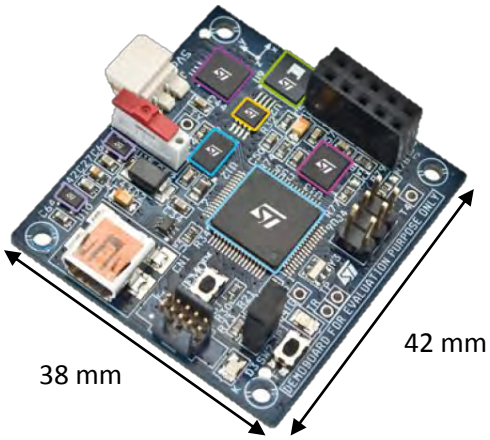

Figure 106 - iNEMO inertial module evaluation board

One of the most attractive aspects of the iNEMO device is the embedded software functions that have been developed to provide accurate and drift free attitude readings using a seven state Extended Kalman Filter (EKF) algorithm. The algorithm fuses data from the several available sensors on the device. A brief description of Kalman filtering and sensor fusion is provided in the Literature Review found in Appendix A of this report.

The iNEMO can be commanded to output data in raw format, Euler angles, attitude, or quaternions. Conveniently, the embedded EKF algorithms serve to give the iNEMO the functionality of an Attitude and Heading Reference System (AHRS). A description of different inertial navigational devices, such as AHRS systems, is provided in Appendix A.

The iNEMO can therefore provide a highly stable attitude reading at a rate of 50 Hz. Since the attitude of the ROV is independent of the mounting position of the attitude sensors, provided that they are aligned parallel to the BODY reference frame, the iNEMO device can be modelled simply as a sensor that provides accurate body attitude information at a rate of 50 Hz. This simple model of the AHRS sensor was deemed sufficient for this project.

Greater investigation into the accuracy and noise characteristics of the iNEMO sensor would require experimentation using real data and does not fall within the scope of this project. The convenience of using externally developed data processing algorithms has a trade-off of increasing the complexity of evaluating the sensor system itself. It was therefore decided that evaluation of the performance of the sensor should be reserved for a future project, where the sensor can be integrated and assessed directly from within the real life *SEAHOG* system.

This completes a description of a simple and robust solution to determining the attitude of the *SEAHOG*. The final state that must be sensed on the *SEAHOG* within the context of this project is the depth, which will be discussed in the following section.

7.3 Depth Sensing

7.3.1 Sensor Data and Description

A PBT Pressure Transmitter from "SICK Sensor Intelligence" with part number 6042443 was procured for the *SEAHOG* before the inception of this project and thus it was decided to model this sensor for determining the depth of the ROV. The sensor is of industrial grade and presents numerous advantages due to its excellent price to performance ratio and maintenance and corrosion free design. Characteristics of the sensor are presented following in Table 42 [38].

Table 42 - PBT pressure transmitter characteristics

Characteristics Type	Datasheet Value	Interpreted Value
Pressure Range	0 – 40 Bar Gauge	0 – 4000 KPa
Output Signal	Analogue Voltage: 0 – 10 V	
Non-Linearity	≤ ±0.5% of span	≤ ±20 KPa
Zero Offset	≤ 0.8% of span	≤ 32 KPa
Signal Noise	≤ 0.3% of span	≤ 30 mV (≤ 12 KPa)
Error from Temperature	≤ 2.5% of span	≤ 100 KPa

The sensor will be sampled from an available ADC channel on the iNEMO AHRS system as described in the previous section. The input voltage range of the ADC pin on the iNEMO is 0 - 5 V, therefore the analogue output from the pressure transmitter must be scaled down by half. This can be achieved by a simple resistor divider circuit. The iNEMO has 12 bit ADC modules, giving a resolution of 4095 steps over 5 V. The actual achievable resolution is therefore 1.22 mV, which corresponds to 976.8 Pa or 99.6 mm. For convenience, it will be assumed that a pressure reading is sampled at 50 Hz, at the same time as the attitude data update. The ADC on the STM32F1 can supply ADC readings far in excess of 50 Hz and therefore it is assumed that it will be achievable to sample the pressure at 50 Hz. Extensive testing will be necessary however for future work to confirm the assumptions made in this report about the hardware capability.

It was assumed that error from temperature fluctuations can be calibrated out, as the *SEAHOG* will be operating outside the ocean thermocline region, as shown following in Figure 107 [39].

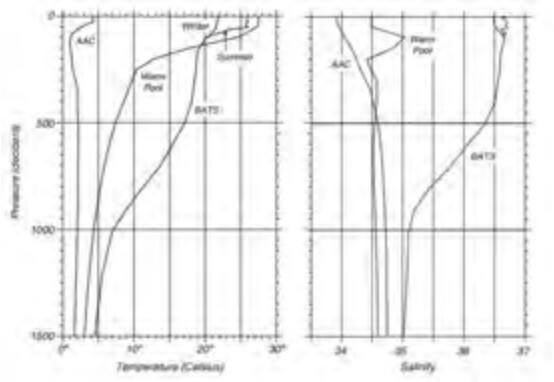

Figure 107 – Typical temperature and salinity profiles in the open ocean at different global locations

Figure 107 shows three curves with increasingly tropical latitudes from left to right. The BATS curve represents data taken at a latitude of 31.8˚ N, which is similar in proximity to the equator to Cape Town's latitude of 33.9˚ S. It can therefore be reasonably assumed that the *SEAHOG* will experience fluctuations in temperature of only approximately 4˚ C, which is only 5% of the entire temperature range of the pressure transmitter. Thus, sensor error from temperature was not included in the sensor model.

The non-linearity of the sensor was modelled using real test data that was conducted by the manufacturer and supplied with the sensor. The supplied test data is given following in Table 43.

Table 43 - Manufacturer sensor test data for PBT Pressure Transmitter

Pressure (bar)	Pressure (Pa)	Signal (V)	Error (%)
0.000	0.000	0.027	0.27
20.000	2000000	5.032	0.32
40.000	4000000	9.992	-0.08

It was assumed that the zero offset error will be calibrated out automatically at the surface. Therefore, data from Table 43 was used to define a fit curve to approximate the nonlinear error of the sensor as shown following in Figure 108.

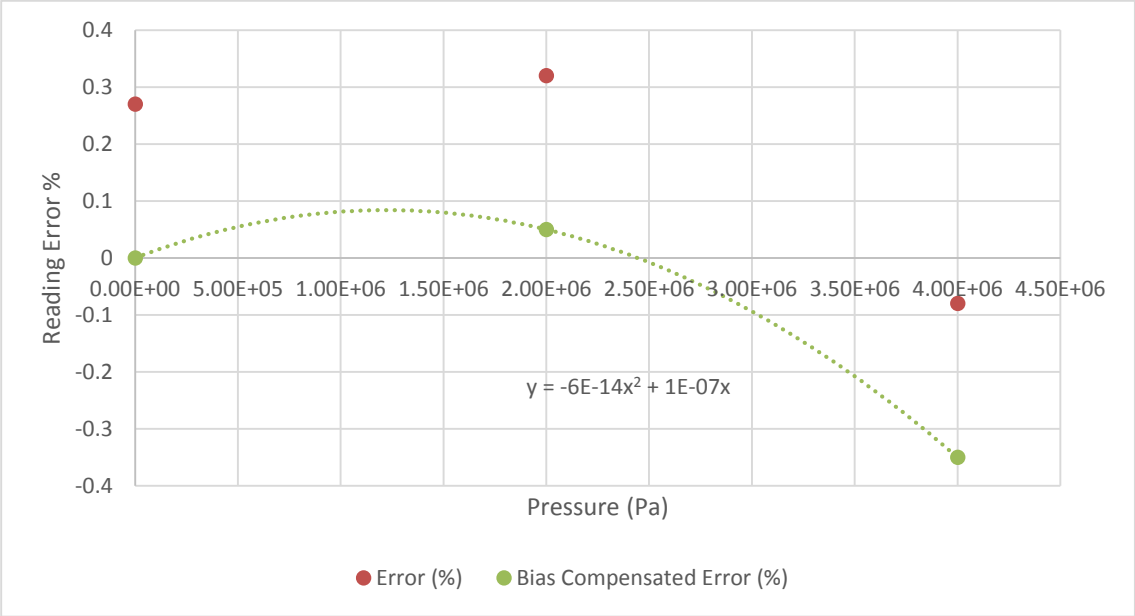

Figure 108 - Nonlinearity for PBT pressure transmitter described by error data

The sensor signal noise was modelled as band limited white noise in the pressure domain for convenience, with an amplitude of 12 KPa.

7.3.2 Sensor Model

Depth in a fluid is related to the static pressure via the following formula:

$$z = \frac{P}{\rho g} \quad \{7.118\}$$

where P is the pressure and ρ is the density of freshwater in this case. A motivation for why freshwater density was used is given in section 5.5.4 previously.

The depth sensor, as described in the previous subsection, can be modelled through the following formula:

$$P_{sense} = \left(P + \underbrace{(-0.0006P^2 + 0.0138P)\frac{P}{100}}_{Non-Linearity} + \underbrace{\mathcal{N}(0, 12 \times 10^3)}_{\substack{Band\ Limited \\ White\ Noise}} \right) \text{[Pa]} \quad \{7.119\}$$

The sensed pressure corresponds to an analogue voltage through the following formula:

$$V_{sense} = P_{sense} \times \frac{10}{P_{max\ sense}} = \frac{1}{4 \times 10^5} P_{sense} \text{ [V]} \quad \{7.120\}$$

The sensed analogue voltage is scaled by half so that it is an acceptable level for the iNEMO ADC input pins, which results in an ADC reading of:

$$ADC = \left\lfloor \frac{V_{sense} \times (2^{12} - 1)}{2 \times 5} \right\rfloor = \lfloor 409.5 V_{sense} \rfloor \quad \{7.121\}$$

The ADC scale corresponds linearly to the depth range and therefore the depth can be found using:

$$z_{sense} = ADC \times \frac{4 \times 10^6}{2^{12} - 1} \times \frac{1}{\rho g} = 0.0996 ADC \text{ [m]} \quad \{7.122\}$$

The Simulink® model of the sensor was created so as to assess whether any filtering was necessary on the sensor output voltage. Figure 109 following shows the unfiltered depth measurements from the sensor.

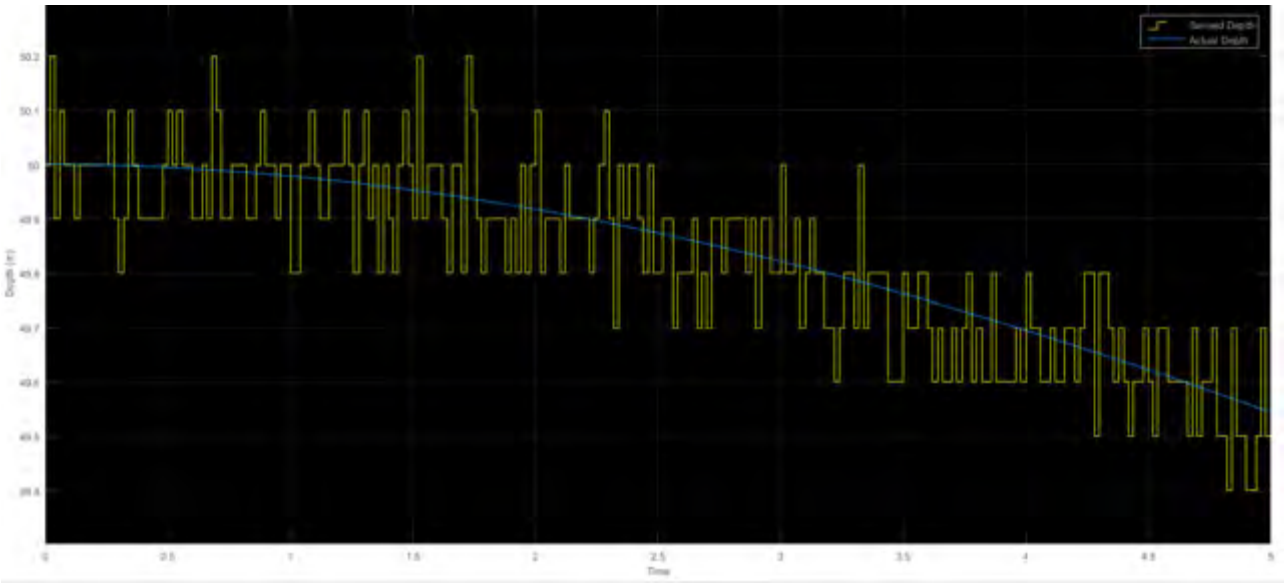

Figure 109 - Actual depth vs. unfiltered sensed depth

Figure 109 shows that the noise, combined with quantisation effects in the ADC, causes a noisy response that should be filtered. It was decided that a passive 1st order low pass filter with a cut-off frequency of 10 Hz should be implemented on the sensor output. Figure 110 following shows the less noisy filtered response.

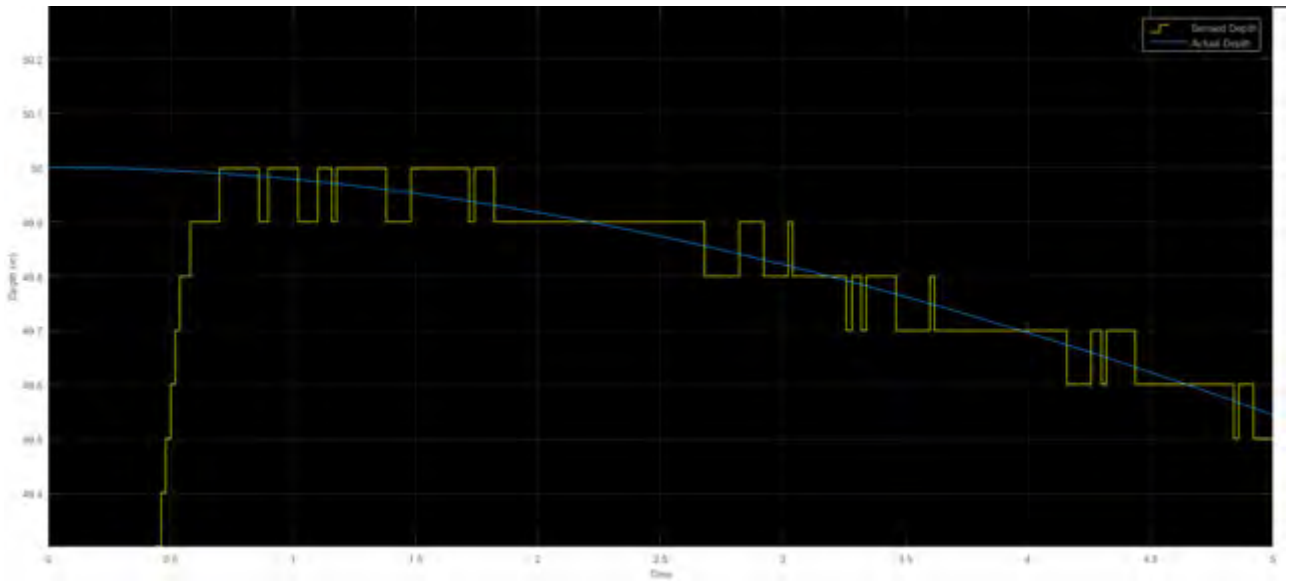

Figure 110 - Filtered depth measurement

It should be noted that due to the capacitors in the low pass filter needing to charge up, the sensed depth starts at 0 m and increases until it reaches the actual depth in the above figure. In real life the ROV will have to descend from the water surface and therefore the transient behaviour of the filter in the simulation is not a concern.

Finally, it should be noted that readings will be taken at a rate of 50 Hz, alongside attitude readings from the iNEMO AHRS.

The pressure transmitter is not mounted coincident with the origin of the *SEAHOG*. Since the sensor is rigidly mounted to the *SEAHOG* body, the attitude of the *SEAHOG* will result in the sensor reading not being coincident with the depth of the *SEAHOG*'s origin at all times. Therefore, a transformation must be provided that maps the position of the sensor on the *SEAHOG* to the origin with respect to the attitude of the ROV. The transformation will be derived in the following section.

7.3.3 Sensor Position Mapping

The depth sensor is positioned relative to the *SEAHOG* origin according to Figure 111 following.

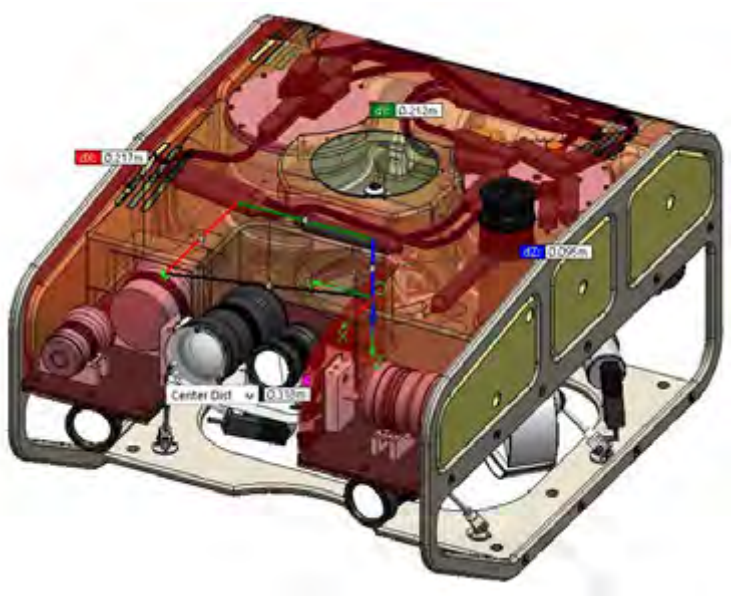

Figure 111 - Position of pressure transmitter relative to *SEAHOG* origin

The vector from the origin to the sensor is described as:

$$\boldsymbol{r_{Od}} = \begin{bmatrix} x_d \\ y_d \\ z_d \end{bmatrix} = \begin{bmatrix} 0.217 \\ 0.212 \\ -0.095 \end{bmatrix} \text{m} \qquad \{7.123\}$$

If a global attitude reading is obtained from the iNEMO AHRS system, then the pitch and roll angles of the ROV will have an effect on the sensed depth by the pressure transmitter. The yaw angle will not have an effect however, as this is the horizontal plane heading of the ROV.

The transformation from sensed to actual estimated depth can be found using the transformation from body fixed to global orientation, as described previously by equation 2.3. The general form of finding the origin position relative to the sensed position can be derived as:

$$\begin{aligned} \boldsymbol{p}_O^i &= \boldsymbol{p}_{sense}^i - \boldsymbol{R}_b^i(\boldsymbol{\Theta})\boldsymbol{r_{Od}} \\ &= \boldsymbol{p}_{sense}^i - \begin{bmatrix} c\psi c\theta & c\psi s\theta s\phi - s\psi c\phi & c\psi s\theta c\phi + s\psi s\phi \\ s\psi c\theta & s\psi s\theta s\phi + c\psi c\phi & s\psi s\theta c\phi - c\psi s\phi \\ -s\theta & c\theta s\phi & c\theta c\phi \end{bmatrix} \begin{bmatrix} 0.217 \\ 0.212 \\ -0.095 \end{bmatrix} \end{aligned} \qquad \{7.124\}$$

Since the pressure transmitter only supplies a measure of the depth, we are only interested in the z component of the above equation. Therefore:

$$\hat{z}_O = z_{sense} - (-0.217 \sin\theta + 0.212 \cos\theta \sin\phi - 0.095 \cos\theta \cos\phi) \qquad \{7.125\}$$

where the notation $\hat{z}$ represents an estimate of z.

This completes a description of the sensors required to detect the required states of the *SEAHOG* for the purposes of this project. A general description of possible control computing hardware will be suggested in the following section.

7.4 Controller Hardware

This section will provide some aspects of the controller hardware that will be necessary for constructing a controller model in this project. Due to this project not including testing and installation of the hardware however, specifications for control hardware presented in this report will serve only as a suggestion for future work.

Despite the incomplete state of the *SEAHOG* at the time of this project, one of the main contributing factors to excluding a hardware aspect from the project was the necessity to test and possibly restructure the communications network architecture of the *SEAHOG*. Appendix B contains detailed information on the network architecture of the *SEAHOG* and should be consulted for a more in depth understanding of the issues tackled in this section. The existing network architecture is shown following in Figure 112.

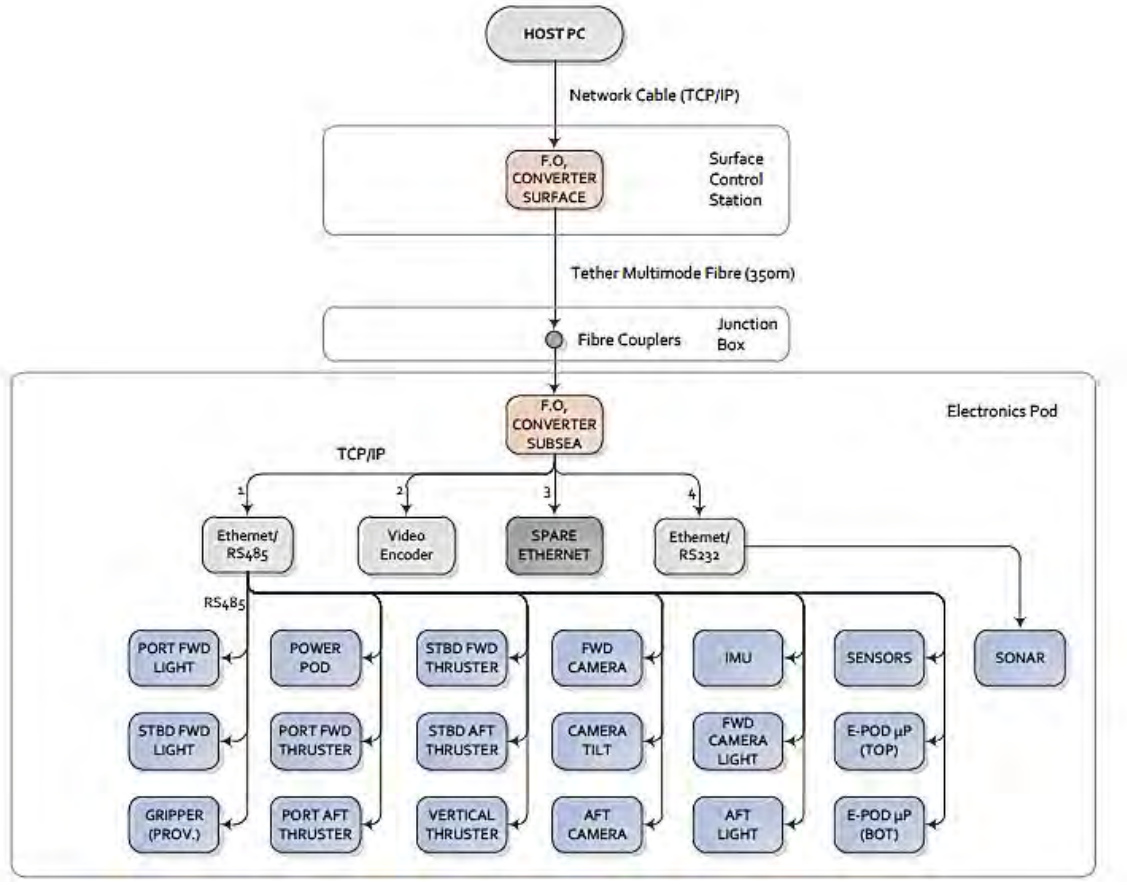

Figure 112 - Current *SEAHOG* network architecture

Figure 112 shows that all of the *SEAHOG* modules are on the same RS485 line. Therefore, the surface-located host PC must handle all functions of control and monitoring of the entire *SEAHOG* system. It is predicted that this will be too processor intensive, introducing latency into the system. In addition, it is desirable to allocate the sensor and control subsystems a high bandwidth. In keeping with the *SEAHOG* design philosophy therefore, distributed processing power is desired for the communications network,

where automatic control functions can be executed independently of the host PC control station and user inputs.

Therefore, a preliminary idea for the network architecture of the *SEAHOG* when sensors and control computing power are installed is as shown following in Figure 113.

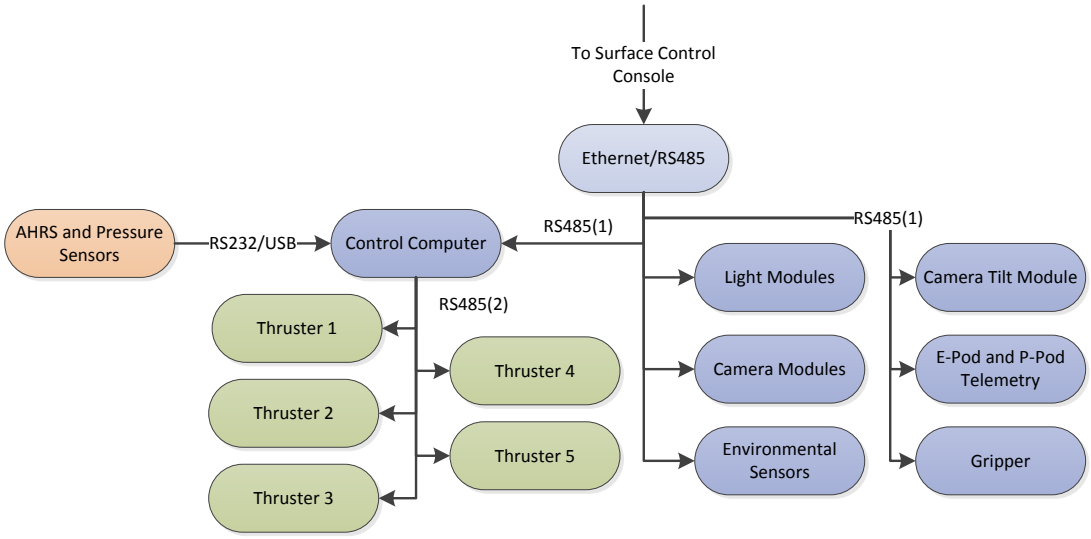

Figure 113 - Proposed network architecture with control computer included

It is proposed that system monitoring and non-critical modules for control are connected on the primary RS485 network. The installed control computer will act as a device on the primary RS485 network and will relay telemetry and system statuses to the host PC at the surface. The control computer will be connected via the spare RS485 network to essential control sensors and actuators such as the thrusters and AHRS and pressure sensors.

It was determined during a previous project that with the designated packet structure and communications setup, the exchange of information between a control computer and a thruster module will take approximately 1.6 ms [24]. This means that the fastest rate at which commands can be sent to all five *SEAHOG* thrusters is 125 Hz. If the thrusters were installed with all the other ROV modules on a single RS485 network, a worst case scenario would be when the thrusters could only be communicated to after all of the other modules had been communicated to. Some modules must send multiple data packets to relay all of their data and other modules might not have a communication cycle as fast as 1.6 ms. If it is assumed that the communication cycles for the other modules is also 1.6 ms however, the communication rate for all thrusters drops, as a worst case scenario, to approximately 28 Hz.

The sensor update rate is 50 Hz, therefore it is desirable to have a communication cycle of greater than 50 Hz to all of the thrusters. As a result, it would be prudent to separate the thrusters from the rest of the ROV modules, as shown previously in Figure 113. Any control computing hardware should be capable of

executing control algorithms to determine thruster speed updates at a rate of minimum 50 Hz, which corresponds to a period of maximum 20 ms.

If the network architecture in Figure 113 is implemented along with the two sensors described in the previous sections, it is proposed that the control computer has the following basic capabilities and specifications as given in Table 44.

Table 44 - Proposed specifications and capabilities of control computing hardware

Specification Type	Description and Value
External Communication Busses	At least 2 serial and 1 USB or at least 3 serial
Attitude Sensor Read Rate	Capable of at least 50 Hz
Control Algorithm Execution Rate	Maximum period of 20 ms (rate of 50 Hz)

It should be noted that Table 44 is not an exhaustive list of specifications and it is highly recommended that the long term development and goals of the *SEAHOG* project are assessed so as to holistically encapsulate possible future requirements before specifying and procuring the control hardware.

This completes the general description and provision of specifications for the control computing hardware within the context of this project. The following section will provide a summary and overview of the sensing and computing system comprised of the individual subsystems described in this chapter.

7.5 Hardware Model and Summary

This chapter has described the sensors and control hardware that is necessary to provide the sensory data and compute control algorithms so that controllers can be designed in the following chapter of this project. Enough information was provided so that a model of each hardware aspect could be created. A pressure transmitter was modelled for the purpose of determining ROV depth and the iNEMO inertial navigation system was described and modelled for the purpose of determining vehicle attitude.

An overview of the theoretical proposed hardware setup, which will be implemented in simulations in this project, is given following in Figure 114.

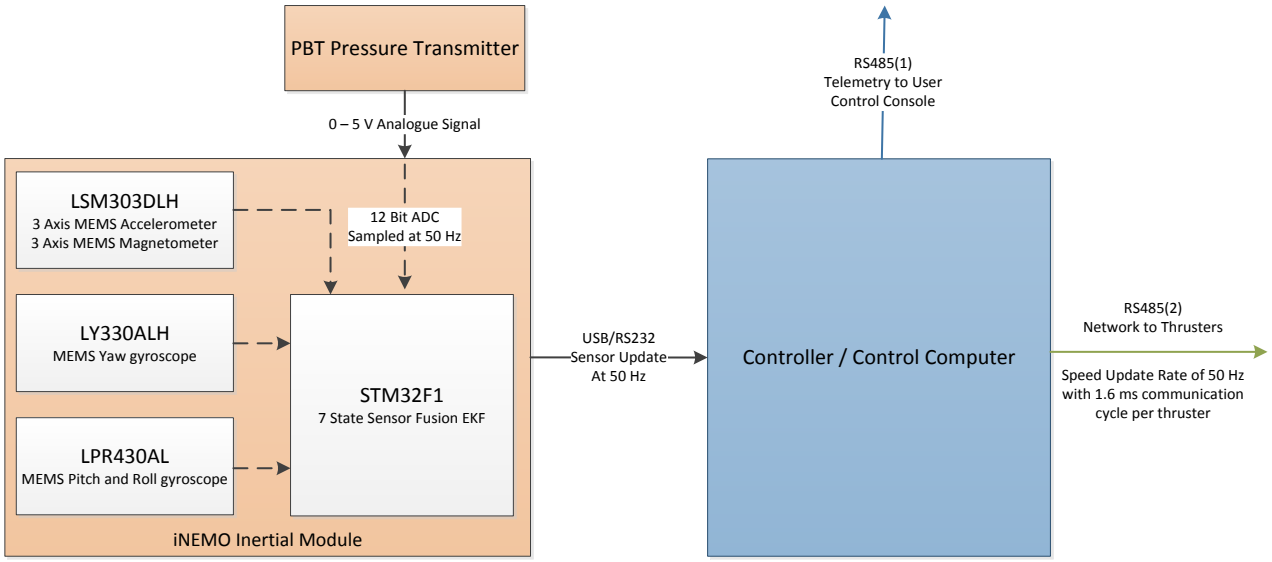

Figure 114 - Hardware schematic overview for sensors and control computational hardware in this project

This completes the modelling of the sensors and hardware required to sense the necessary states of the *SEAHOG* and subsequently apply control algorithms.

With the ROV model, thruster model and sensor and hardware models complete, the project has reached a stage where control designs can be formulated. The following chapter will detail the design process for the controllers developed in this project and formulate controller specifications based on the results of test simulations.

Chapter 8 - Control Systems Design

8.1 Introduction

The dynamic model of the *SEAHOG* and its thrusters has been completed. In addition, a proposal for the sensors and hardware that will be used on the robot, along with their respective models, has been given. Subsequently, it is now possible to design controllers to achieve the objectives of depth and heading holding.

This chapter will detail the design process for a depth controller and a heading controller for the *SEAHOG*. Research was conducted in the literature review, found in appendix A, where a broad investigation into different underwater control techniques was conducted. As a result of information presented in the review, it was decided that controllers would be designed in this project using simple PID techniques so as to give a baseline from which future controllers can be compared. Therefore, controllers developed in this chapter will adopt a classical adaptive PID structure, whereby linearization techniques will be used to tune appropriate controller gains at different operating points.

By linearizing the dynamic system about different operating points and designing controllers for the local operating region, it is possible to obtain a stable system with uniform controller performance across the full operating range of the ROV. Correct design can ensure a bumpless transfer between operating points and different controller parameters [40]. Therefore, due to the well understood characteristics of PID control, one of the biggest challenges that will be faced in the control designs of this project will be the scheduling of controller gains and the algorithms used to switch between different controller operating parameters.

The following section will describe in detail the design of the depth controller, after which the heading controller design will be described. Finally a summary and assessment of the different controllers will be given, discussing the expected consequences of the chosen controller design techniques.

8.2 Depth Holding Controller

8.2.1 Introduction

As was found in chapter 6, motion in the heave direction on the *SEAHOG* is sufficiently decoupled to separate and analyse on its own. Hence, an automatic depth controller will be developed in this section by isolating the heave motion parameters and creating a decoupled model that can be linearized at different operating points.

Before the control design is undertaken, it is important to establish the objectives of the controller that will be designed in this section. Given that this is the first controller to be designed for the *SEAHOG*, broad objectives will be given rather than exact specifications. As a result, controller performance can then be used as a benchmark for improvement in the future. A list of objectives for the depth holding controller developed in this section is given following:

$O_{dc}1$. Provide depth holding to within a tolerance of ±100 mm, as per the resolution of the depth sensor, for a variety of different step sizes.

$O_{dc}2$. Provide reasonable setpoint tracking for a variety of sine waves that encapsulate and span the operational speed range of the ROV.

Assumptions for the operating conditions and environment of the ROV include all previously listed assumptions from the ROV and thruster model derivations. Specifically, notable assumptions and performance limitations for the depth controller are:

$A_{dc}1$. The controller will be designed in the absence of currents and external disturbances.

$A_{dc}2$. The ROV will maintain close to horizontal orientation throughout its motion.

$A_{dc}3$. Due to the known shortcomings of PID controllers in an underwater environment, robustness to model uncertainties will not be a design consideration of the controller.

$A_{dc}4$. The controller will execute control algorithms and supply a speed setpoint update to the thruster at a rate of 50 Hz.

The design approach for the depth controller will first establish the decoupled dynamic model for the system. Then an investigation into the stability of the system will be undertaken, resulting in greater insight into the type of controller that will be necessary in the design. Finally, the controller will be designed and any adaptive controller qualities will be described.

With the objectives and assumptions for the controller design clearly understood, the dynamic model for motion in heave can be derived in the following section.

8.2.2 Decoupled Dynamic Model for Heave

Recall the general dynamic equation of motion for the *SEAHOG*:

$$\boldsymbol{M\dot{\nu}} + \boldsymbol{C}(\boldsymbol{\nu})\boldsymbol{\nu} + \boldsymbol{D}(\boldsymbol{\nu})\boldsymbol{\nu} + \boldsymbol{g}(\boldsymbol{\eta}) = \boldsymbol{\tau}$$

which can be represented as follows if motion in the heave direction only is considered:

$$(m_{rb} + m_a)\dot{w} + 0 + \left(Z_w w + Z_{|w|w}|w|\right) + 20 = \tau_5 \qquad \{8.126\}$$

In the above model, off diagonal mass elements have been ignored and cross-coupling drag effects have been ignored, which is a reasonable assumption for the design of this controller - as was discovered previously in chapter 6 through open-loop simulations. Specifically, when data from the actual *SEAHOG* model is substituted into equation 8.126, the model obtained is:

$$(81.69 + 359.9)\dot{w} + (330.28w^2 + 31.52w + 50.57)w + 20 = \tau_5$$

$$\dot{w} = \frac{1}{441.59}\left(\tau_5 - 20 - w(330.28w^2 + 31.52w + 50.57)\right) \qquad \{8.127\}$$

and the thrust input is modelled as:

$$\tau_5 = |\Omega|\Omega C_t \qquad \{8.128\}$$

where the propeller speed is governed by the thruster model developed previously in this report and where $C_t = 0.0121$.

Since the vertical thruster is aligned with the vertical axis of the NED frame and according to assumption $A_{dc}2$ - the ROV is expected to maintain close-to horizontal attitude throughout depth holding operations - equation 8.127 above can be used as a direct mapping from the body-fixed z axis of the ROV to the global z axis. It should be noted however, that the performance of the controller will be directly influenced by the orientation of the ROV.

The Simulink® block diagram of the decoupled thruster and ROV system is given following in Figure 115.

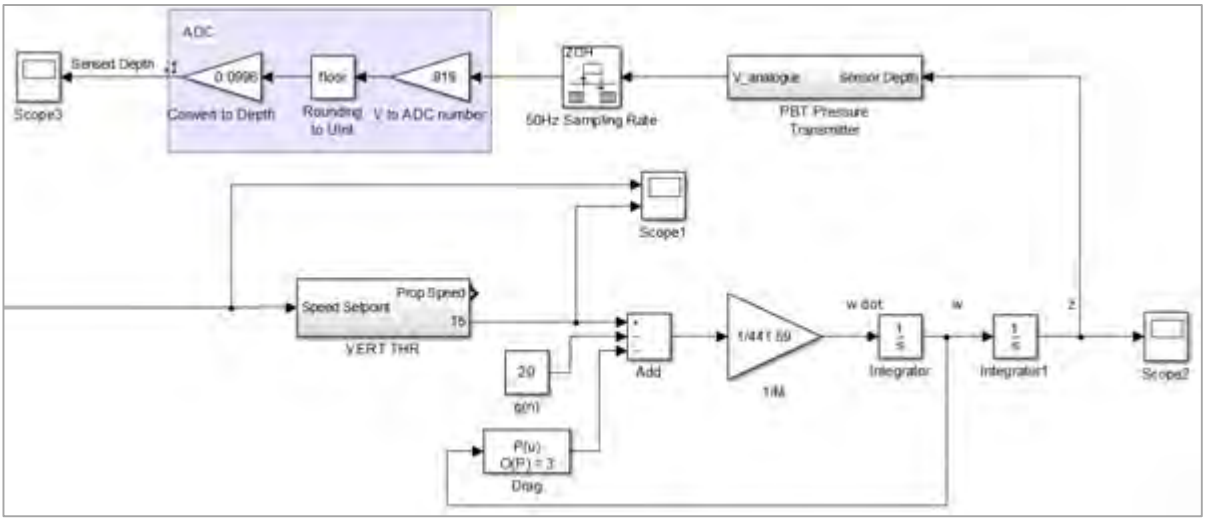

Figure 115 - Decoupled *SEAHOG* model for vertical motion

With the decoupled dynamic model described, the control design procedure can begin in the following section with an investigation into the stability of the system.

8.2.3 Investigation of Controller Stability and Linearizations

The controller output for the depth controller took the form of a desired propeller speed. The positive 20 N buoyancy force in the ROV plant would require a non-zero propeller speed to hold the ROV at a constant depth and therefore an integrator was a necessary part of the depth holding controller. A standard PID structure with gain scheduling and logical controller parameter switching was chosen to achieve the controller goals stipulated in the introduction to this section. Figure 116 following shows the general control structure necessary for the depth controller design. Control elements are highlighted in light blue. In addition, signals have been assigned numbers so as to aid in describing the frequency response plots presented following in this section.

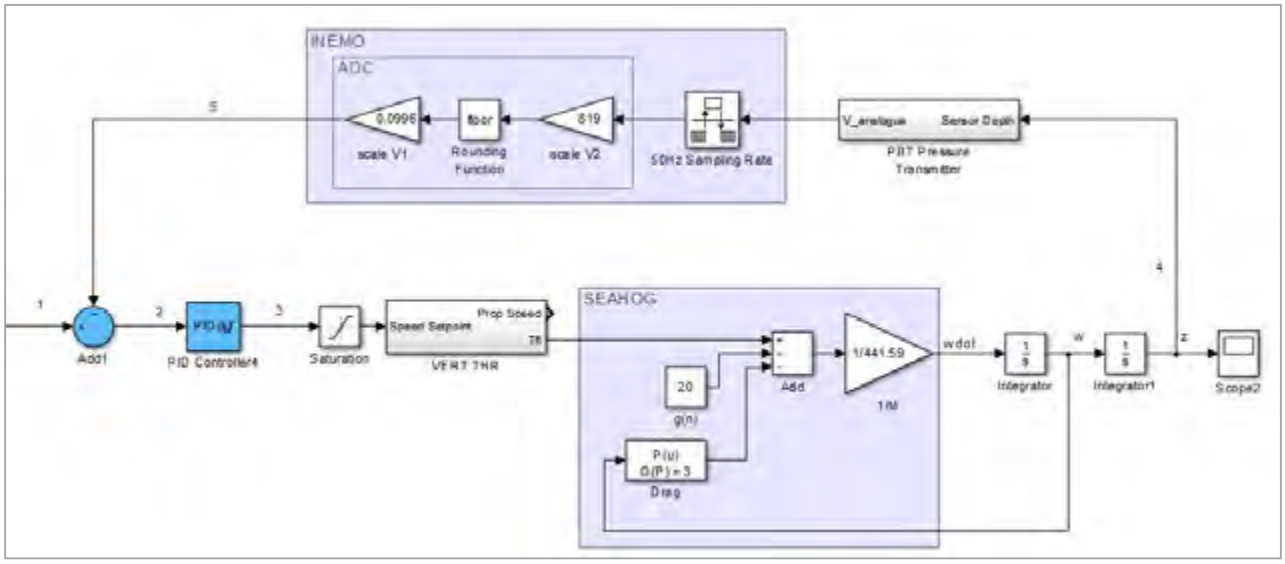

Figure 116 - Generalised control structure for the depth controller

An investigation into the open-loop dynamics of the system was conducted so as to illuminate the effects of the nonlinear dynamics of both the ROV and the thruster and hence inform the design procedure.

To analyse the system, linearization tasks were performed in Simulink® using the Tustin rate conversion method and a sampling time of 0.02 s (50 Hz). To capture the full range of dynamics available from the system, linearizations needed to be conducted under the following conditions:

L_i1. Slow ROV speed and low thrust.

L_i2. Fast ROV speed and low thrust.

L_i3. Slow ROV speed and high thrust.

L_i4. Fast ROV speed and high thrust.

Conditions L_i1 to L_i4 would give a good representation of the response of the system at different extremes of the nonlinear dynamics present in the system – namely: the propeller speed squared relationship vs. thrust and the nonlinear fluid damping function. To achieve the desired linearization conditions, a preliminary PI controller was applied in the position of the PID controller so as to provide a gradual change in thrust over time. The thrust and vehicle velocity values obtained from the simulation were roughly normalised for convenience and are shown following in Figure 117, along with appropriate linearization points L_i1 – L_i4.

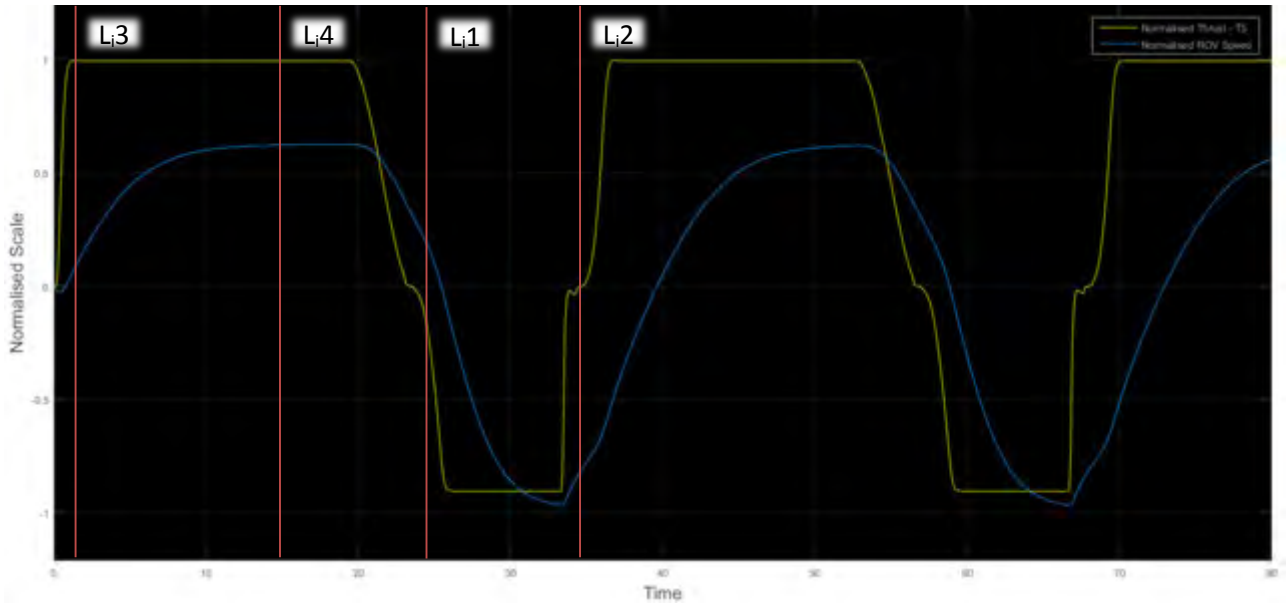

Figure 117 - Linearization points for heave open-loop system stability investigation

Conducting Bode Plot frequency analyses at the simulation times shown in Figure 117 allowed the open-loop response of the plant to be calculated between points 3 and 5 shown previously in Figure 116. The resulting frequency response is shown following in Figure 118.

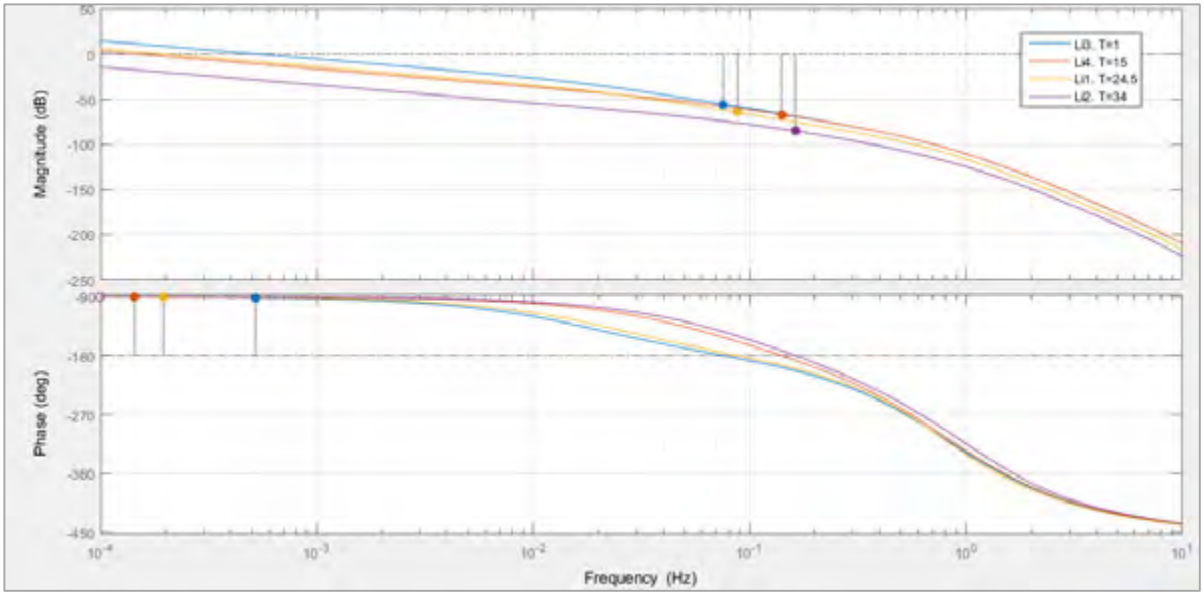

Figure 118 - Open-loop Bode Plot analysis for the ROV decoupled model for motion in heave

Figure 118 shows that the plant is stable with large gain and phase margins, which is expected due to the viscous and inertial damping provided by the water. Figure 118 also highlights how the frequency response of the plant varies significantly according to the speed and thrust level of the ROV.

The control input into the system for the depth controller is propeller speed. A zero error condition can only be maintained at a non-zero propeller speed since the thruster will constantly have to counteract the 20 N buoyancy force in the ROV plant. Therefore, an integrator element in the controller was necessary to achieve perfect setpoint tracking. Consequently, the effects of the integrator in the PI controller that was implemented to produce Figure 117 previously were investigated. Using a Bode Plot response that included the PI controller (between points 2 and 5 in Figure 116) the frequency response of the system is given following in Figure 119.

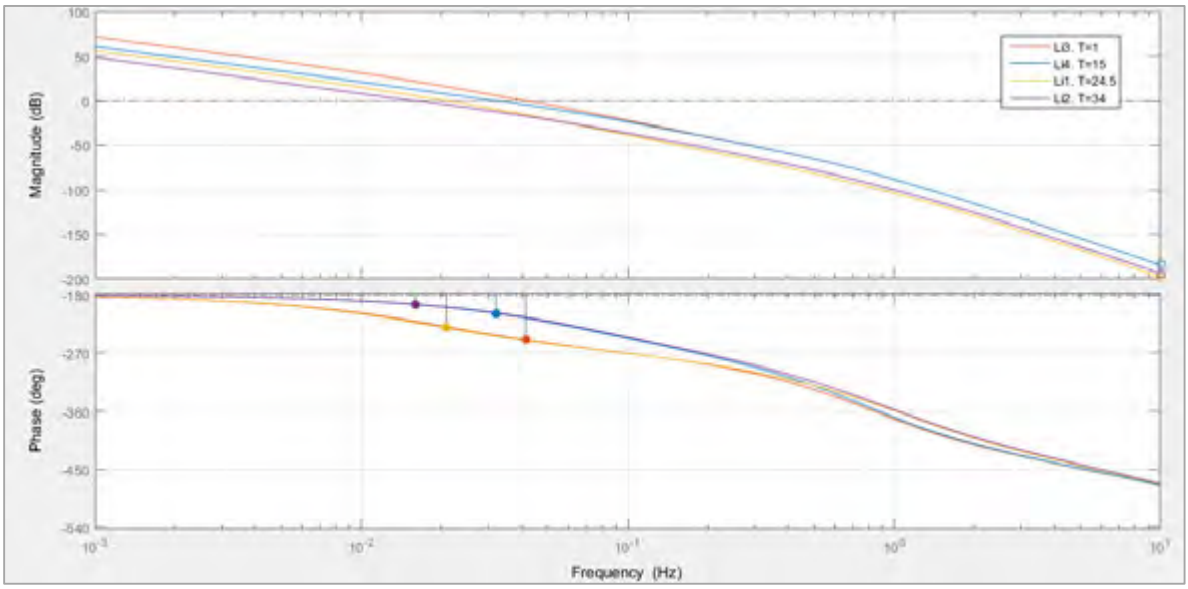

Figure 119 - Open-loop Bode Plot analysis with added integrator for the ROV decoupled heave model

As expected, Figure 119 shows very clearly that the additional phase lag provided by the controller integrator causes the system to become unstable. At low ROV speeds (Li1. and Li3. in Figure 119), it can be seen that the phase drops more rapidly than at high ROV speeds.

By increasing the proportional gain in the PI controller, a small amount of phase can be added to the system, as shown following in Figure 120.

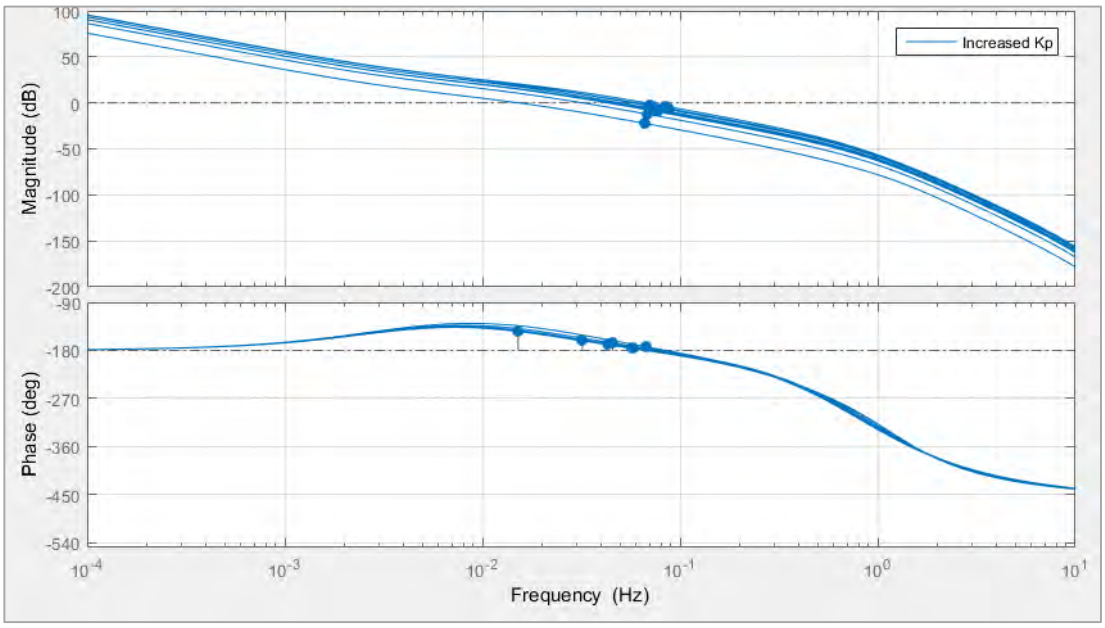

Figure 120 - Open-loop frequency response to PI depth controller with increased Kp

However, this results in an ill-tuned response to step inputs due to various nonlinear effects in the system such as saturations on the thruster speed. To obtain the desired response, it is necessary to decrease the proportional gain, which in turn reduces the amount of phase in the system, resulting in the response returning towards the response shown previously in Figure 119.

It has been shown in [17] that the nonlinear dynamics of the thrusters results in movement of the slow thruster pole, forcing the system's effective closed loop poles into the right hand plane on a root locus plot. The resulting instability increases the thrust, pulling the closed loop poles back to the imaginary axis and forming a pure oscillator. Figure 121 following shows this concept on the s plane for clarity [17].

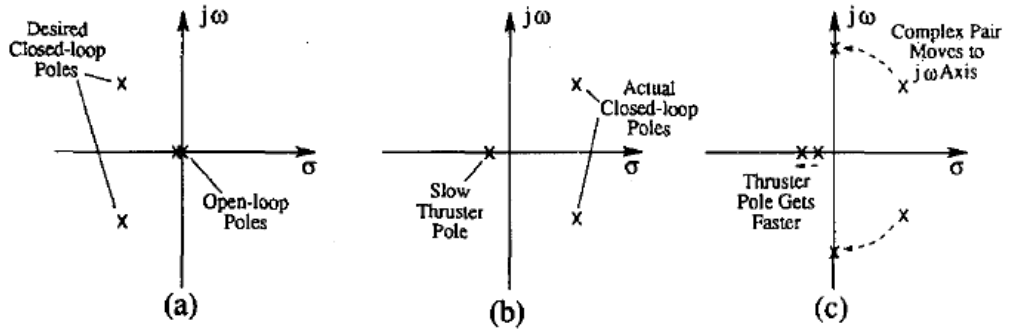

Figure 121 - (a) If no thruster dynamics are present, the open-loop poles are easily placed to produce the desired closed-loop response. (b) The unacknowledged presence of the slow thruster pole results in the actual closed-loop poles moving into the right half plane. (c) The resulting instability causes the thrust level to increase, which speeds up the thruster pole. The thruster pole frequency increases until the pole pair reaches the jω axis to form a pure oscillator.

In the *SEAHOG* system however, the thruster pole movement can be shown to not be the dominating factor for instability in the depth controller. The effect of the thruster on the ROV system can be obtained by analysing the thruster frequency response between the propeller speed input into the thruster and the

thrust output (between point 3 and thruster output T5 previously in Figure 116). The results of the analysis are shown following in Figure 122.

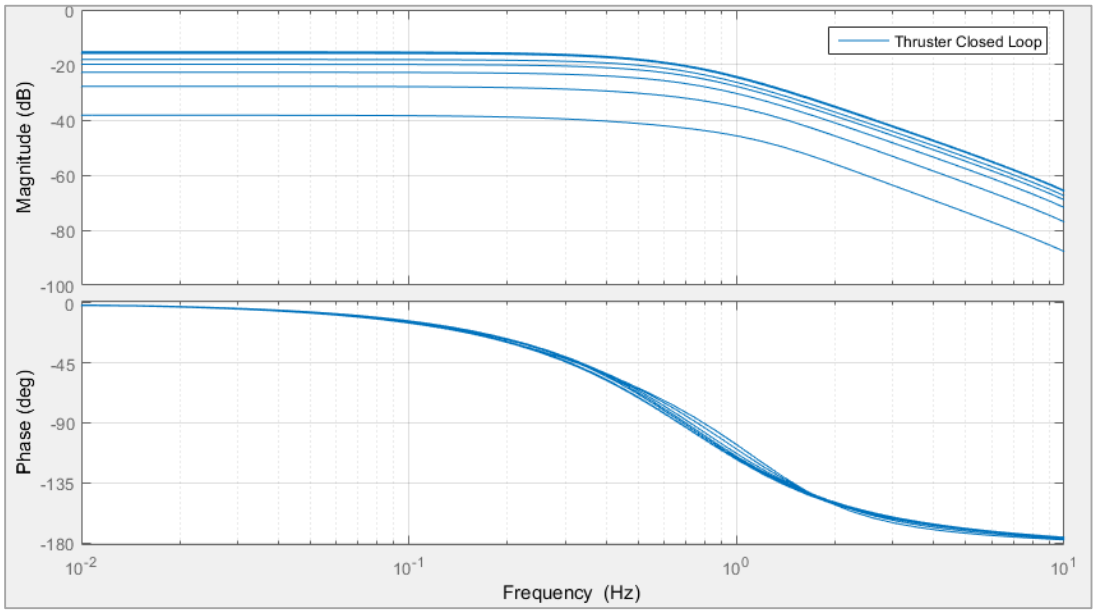

Figure 122 - Closed loop frequency response of the *SEAHOG* thrusters

When compared to Figure 119 previously, it can be seen from Figure 122 that the largest differences in phase due to different dynamic states in the thruster, occur at a higher frequency to that of the decoupled ROV model. Therefore it can be concluded that the thruster dynamics are fast enough to not have a significant effect on the ROV and that the cause of limit-cycle behaviour in the depth controller is due to the nonlinear ROV dynamics.

A time plot simulation was run using the system shown by the Bode Plot of Figure 119. The limit cycle can be clearly seen following in Figure 123.

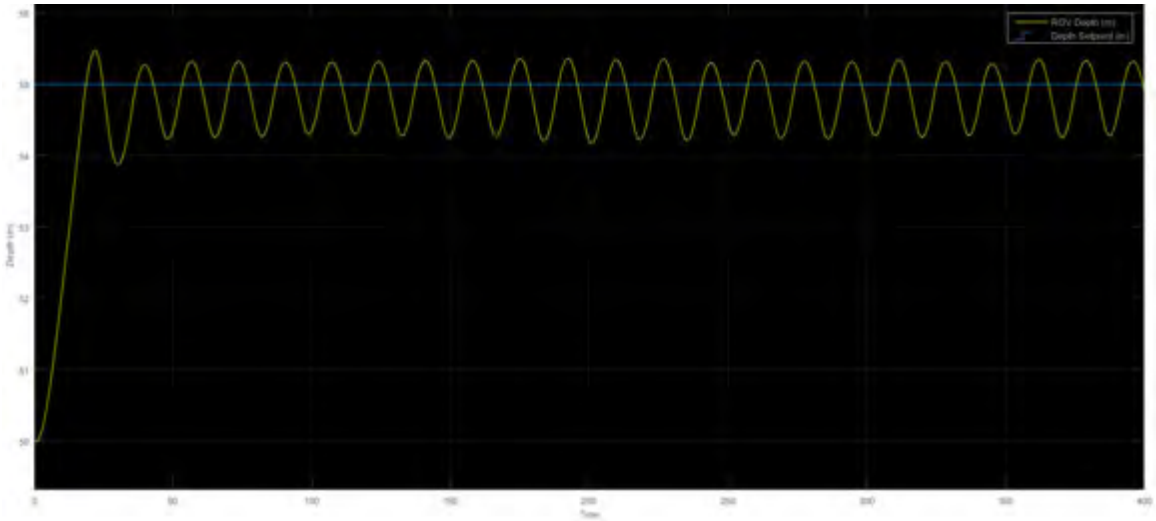

Figure 123 - Time response to a step input of the integrator controlled system

This section has shown that the presence of the nonlinear ROV dynamics in the decoupled model will contribute to forming a limit cycle due to a dominating phase lag at low speeds. Therefore, in the following section, compensation elements will be added to the control structure so as to counteract the phase lag.

8.2.4 Lead Compensation and Derivative Control Elements

The derivative part of a PID controller can be seen as a lead compensator and is therefore an appropriate measure to increase phase of the system and hence increase the bandwidth. The form of a PID controller in Simulink® is shown following:

$$u(s) = e(s)\left(K_p + \frac{K_i}{s} + K_d \frac{s}{\frac{1}{\tau_n}s + 1}\right) \quad \{8.129\}$$

A PID controller was tuned to be close to under-damped for a 5 m step input. The corresponding controller parameters were: $K_p = 550, K_i = 55, K_d = 1300, \tau_n = 1.2$ and the resulting position, controller input and thrust response is shown following in Figure 124.

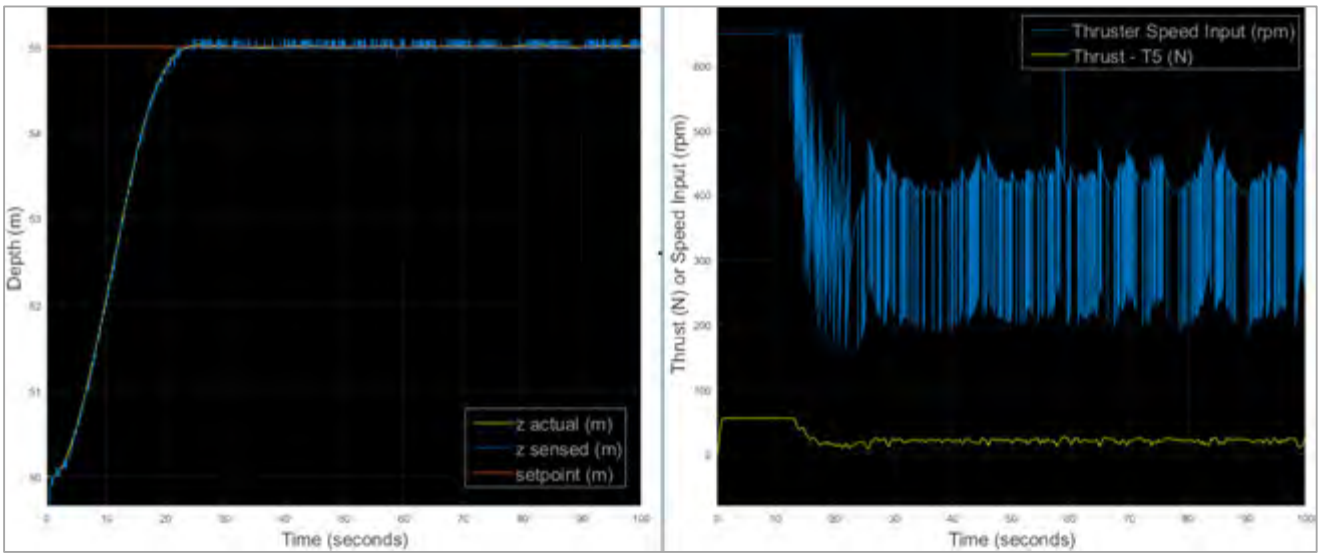

Figure 124 - PID tuned response to a step input for depth controller

The actual depth response from Figure 124 can be seen to settle within the resolution band of sensed depth, making it sufficient.

The resulting loop stability can be assessed between points 2 and 5 from Figure 116 for linearization points L_i1 – L_i4 as described in the previous section. The linearization point and corresponding simulation time is shown following in Figure 125.

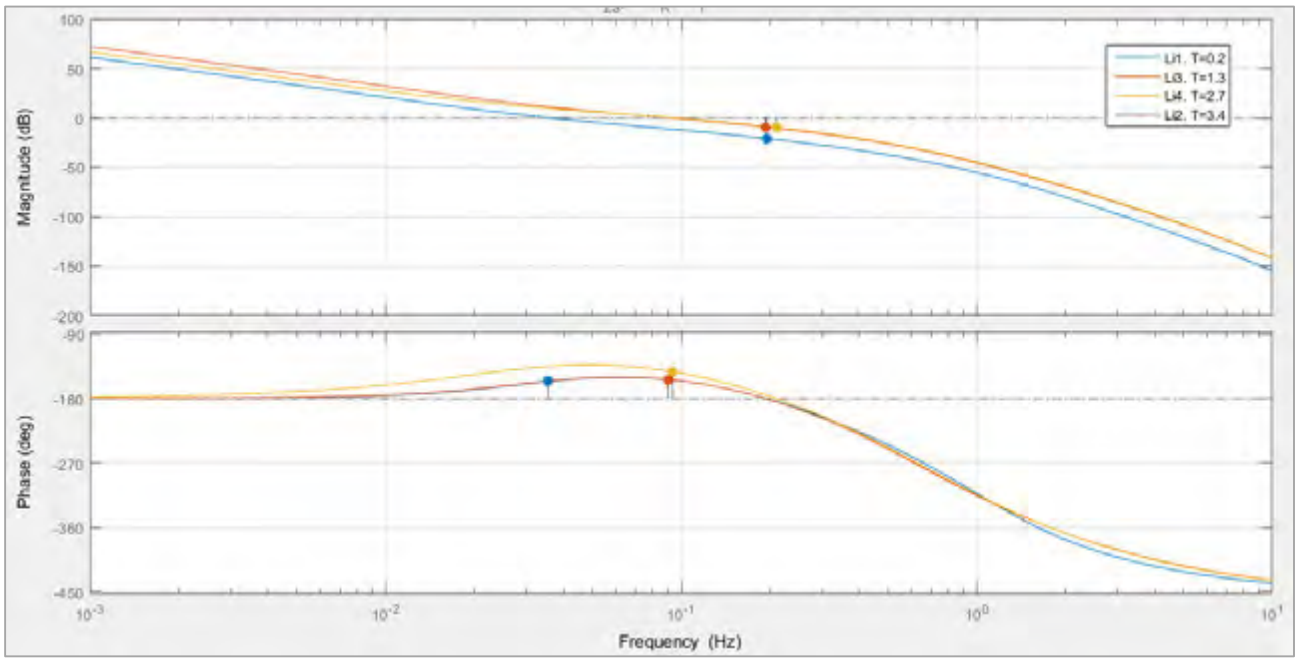

Figure 125 - Open-loop Bode Plot with added derivative element to PID controller

The added phase from the derivative element of the controller is clearly visible as all the responses are seen to increase above -180˚ phase at about 0.1 Hz. The system is now stable for all linearization points, enabling setpoint tracking to be possible as seen previously in Figure 124.

Generally, a good minimum phase and gain margin is 30˚ and 7 dB respectively. The minimum phase and gain margin obtained from Figure 125 was 23.9˚ and 9.5 dB. The phase margin is slightly smaller than ideal, however due to the reasonably damped response obtained in Figure 124 previously, it was decided that the controller gains were sufficient.

At this point, a preliminary stable controller had been designed, however it was predicted that the controller's performance would vary depending on the states of the ROV. Figure 126 following shows the controller's response to a 5 m and a 3 m step input respectively. The difference of the responses can be clearly seen by the overshoot experienced in the smaller step.

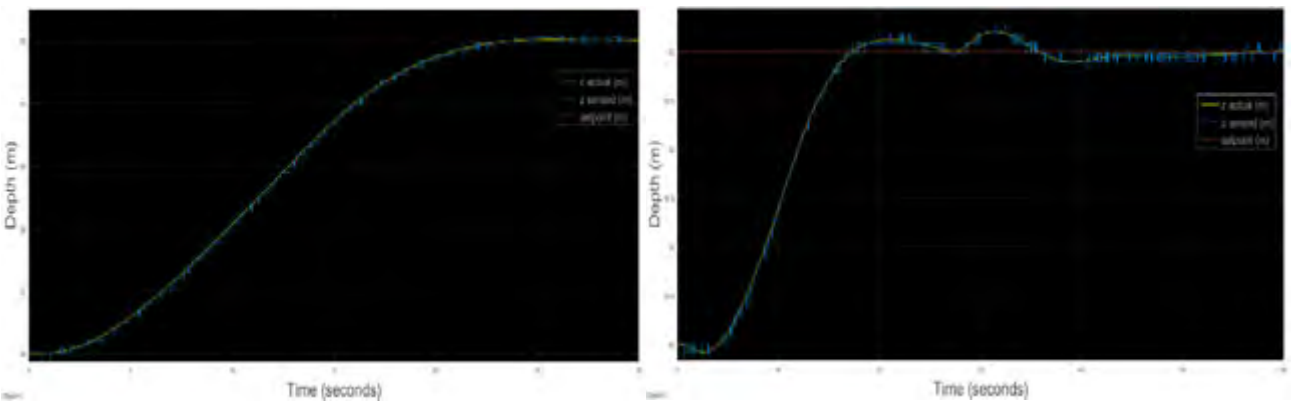

Figure 126 - PID tuned depth controller response to 5 m [left] and 3 m [right] step inputs

Gain scheduling was applied so as to obtain a uniform response across all step sizes and system states. The following section will describe the adaptive structure adopted for this controller and will investigate how gain scheduling can be implemented to provide a more consistent performance for different step sizes.

8.2.5 Gain Scheduling

As has been established in this report, the nonlinear dynamics of the thruster and the ROV itself lead to degraded controller performance if classic PID control methods are used, where the controller performance varies as the vehicle states move away from the linearization points used for designing the controller. This section will serve to determine an adaptive controller structure that makes use of gain scheduling to ensure a uniform response from the ROV for all operational states.

It should first be established however, which of the proportional, integral and derivative gains in the PID controller should be tuned to provide a uniform response across different system states.

To investigate the predicted behaviour of the ROV at different speeds and thrust levels, a 10 m step was applied to the system under the PID controller described previously by equation 8.129. The ROV velocity and thrust profiles are shown following in Figure 127.

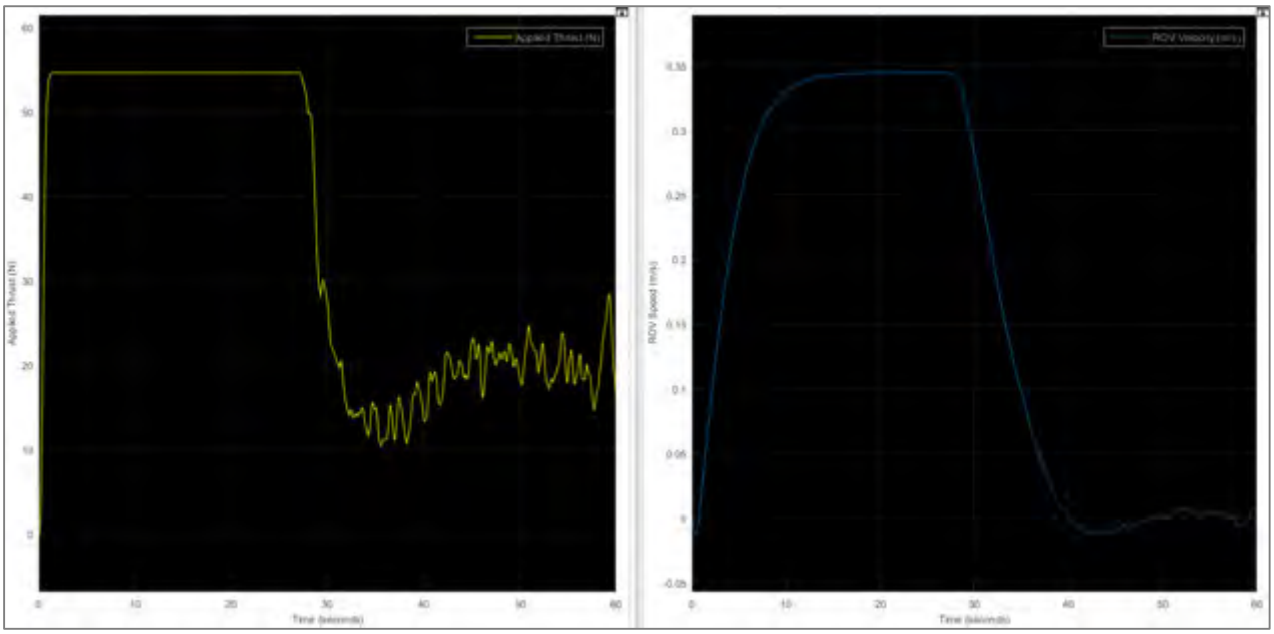

Figure 127 - Thrust and velocity for a 10 m step input under simple PID controlled system

The corresponding open-loop frequency response is shown following in Figure 128.

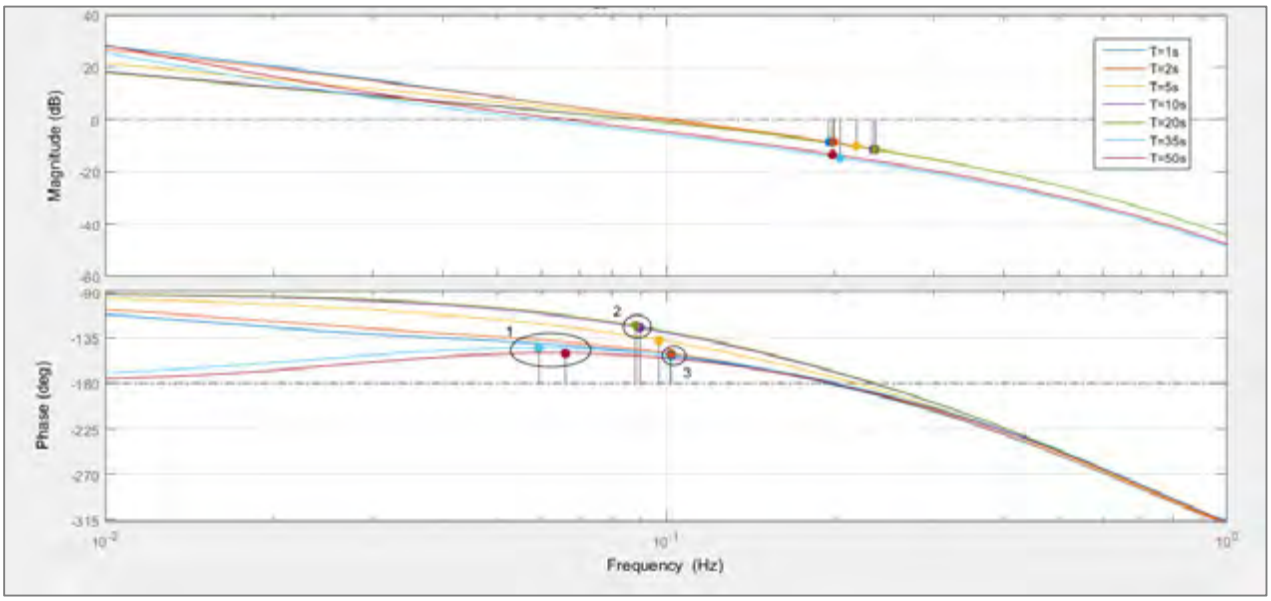

Figure 128 - Open-loop frequency response for PID controlled system at different linearization times

Using Figure 127 and Figure 128, insight could be drawn into the nature of how the ROV system would respond. As shown by ellipse 3 in Figure 128, at times of 1 s and 2 s the speed of the ROV is low and the phase margin is lower than the linearizations shown in ellipse 2. From the relative positions of ellipse 1 and 2 it can be seen that higher damping exists at higher ROV speeds but the gain of the system is decreased. As shown by ellipse 1 however, as the thrust level decreases, the gain and damping is decreased. It can therefore be assumed that for small steps, greater gains will be required at the cost of less damping to maintain a similar rise time. By varying the gain of the system, it is be possible to move the 0 dB crossover point until the phase of the system is similar and a similar system response is obtained regardless of the system state.

Now that it has been established that an effective way of ensuring a uniform response from the system for different system states would be to vary the system gain, the way in which this could be achieved was investigated.

Equation 8.129 can be rewritten in the following form:

$$u(s) = e(s)\left(\frac{K_p s^2 + \left(K_i + \tau_n\left(K_d + K_p\right)\right)s + K_i\tau_n}{(s+\tau_n)s}\right) \quad \{8.130\}$$

A PID controller can also be represented as a PI controller multiplied by a lead-lag compensator resulting in the following form of the controller:

$$u(s) = e(s)\left(K\frac{ps+1}{s} \times \frac{\tau_1 s + 1}{\tau_2 s + 1}\right) \quad \{8.131\}$$

It is advantageous to analyse the controller in the form of equation 8.131 since the effects of K, p, τ_1 and τ_2 have a direct and identifiable effect on the system response. Whereas in equation 8.130, the gain constants are less isolated and it is difficult to identify how varying a constant will affect the overall system.

Therefore, equation 8.130 was manipulated to represent K_p, K_i and K_d in terms of the constants in equation 8.131 with the results shown following:

$$K = K_i$$

$$\tau_2 = \frac{1}{\tau_n}$$

$$p = \frac{K_i + \tau_n(K_d + K_p) + \sqrt{K_i^2 + 2\tau_n K_i(K_d - K_p) + \tau_n^2(K_p + K_d)^2}}{2\tau_n K_i} \quad \{8.132\}$$

$$\tau_1 = \frac{2K_p}{K_i + \tau_n(K_d + K_p) + \sqrt{K_i^2 + 2\tau_n K_i(K_d - K_p) + \tau_n^2(K_p + K_d)^2}}$$

If equation 8.131 is consulted, it can be seen that constant K is directly related to the gain in the system. Therefore, when consulting the relationships shown in equation 8.132, it can be seen that K_i is a suitable candidate to be tuned and hence control the gain of the system. However, since K_i forms part of the expressions for τ_1 and p, the effect of changing K_i on them should be kept to a minimum.

For a rapid response to a changing setpoint, it is typically desired that K_p is high. To maintain stability, as previously discovered, with a high K_p value, a high K_d is also required [40]. If we can enforce the following relationship:

$$K_i \ll K_p, K_d \quad \{8.133\}$$

then the effect of K_i on τ_1 and p can be kept to a minimum. To illustrate this, values of $K_p = 520; K_d = 1400;\ \tau_n = 1.2$ were used in equation 8.132 previously with different values of K_i. The resulting controller constants are shown following in Table 45.

Table 45 - Resulting equivalent controller constants, derived from Simulink controller gains

	$K_i = 1$	$K_i = 10$	$K_i = 30$
K	1	10	30
τ_2	0.83	0.83	0.83
τ_1	0.226	0.225	0.224
p	1920.6	192.6	64.6

Table 45 shows that the compensator time constants τ_1 and τ_2 remain fairly constant for a wide range of gains, allowing the phase characteristics of the controller's lead-lag compensator to remain fairly constant. In addition, due to the direct relationship of $K = K_i$, the gain of the system is directly modified using K_i. The greatest change observed by modifying the K_i gain is seen in p. The effect of varying p will change the position at which phase is added by the controller's $ps + 1$ term (in equation 8.131 previously). As K_i increases, the frequency at which phase is added by the $ps + 1$ term increases.

If the position that the phase is added by the $ps + 1$ part of the controller is at too high a frequency then it may negate the extra phase added by the compensator part of the controller. It is therefore necessary to

check that for all possible values of K_i, there is enough phase in the system for it to remain stable. To verify that there is enough phase provided by the controller for different values of K_i, an open-loop frequency response of the controller with the form of equation 8.130 and controller gain values given previously above Table 45 is shown following as a Bode Plot in Figure 129.

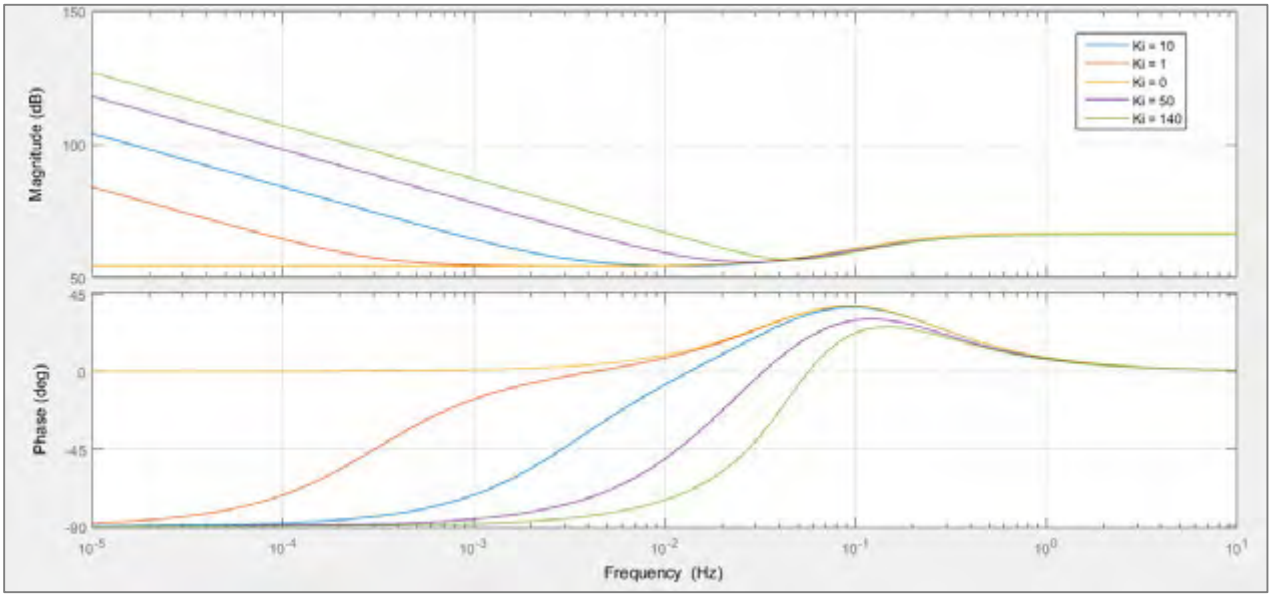

Figure 129 - Bode Plot for a PID controller with different integral gains

Figure 129 shows that there is enough phase available around the critical frequency of 0.1 Hz for K_i values ranging from 0 to 140 and therefore It is expected that enough phase will be available from the controller to allow for a consistent response across different step sizes whilst maintaining stability. It was therefore concluded that the K_i controller gain should be chosen as the scheduled gain to ensure uniform responses for varying system states.

Gains were chosen by tuning the gain for a close-to critically damped response to different steps. The values obtained for optimal gains according to the input step size is given following in Figure 130.

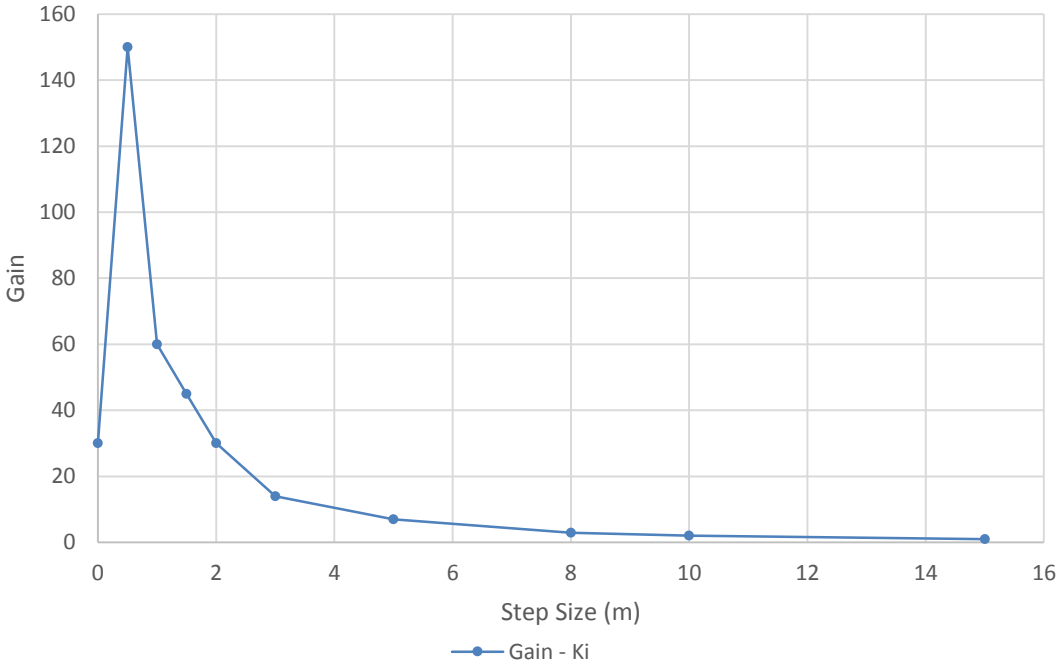

Figure 130 - Ki gain values according to input step size

With the gain scheduling aspects of the controller well understood, motivated and defined, the adaptation logic of the controller, including the logic used for gain scheduling, will be discussed in the following section.

8.2.6 Controller Adaptation

It has been established previously in this chapter that a PI controller can be tuned to be stable when linearized for conditions L_i1 – L_i4 with the addition of a derivative element to the controller. Bode Plot analyses have been presented for linearizations occurring under the conditions of a step input and show that stability is maintained for all operating conditions. In addition, it has been established that the integral gain can be varied without significantly reducing the added phase provided by the derivative controller element. Therefore, the following controller structure and procedure for its design is proposed:

- The controller will condition operator inputs (depth setpoints) to be handled as step inputs that are tuned for a uniform response regardless of the size of the step.
- The derivative and proportional gains will be held constant and the integrator gain will be scheduled to provide, as much as possible, a uniform response across all step sizes.
- A uniform response requires that the integrator initial state is the same for all conditions directly preceding a step input. Therefore the integrator will be reset to 0 for each new setpoint received so as to replicate the initial controller state used to derive the scheduled gains.
    - Additionally, the ROV has been designed with a positive 20 N buoyancy force. This will play a significant role in the response of the controller. For the controller to achieve the first point above, the controller will implement a feed forward element so as to compensate for the higher effective gain of the plant in the ascending heave direction.
    - A note should be made at this point that for rapidly changing operator inputs, such as a ramp or sine wave depth reference, the integrator will constantly be reset, resulting in a steady state offset. Therefore, an adaptation deadband will be implemented whereby the integrator will not be reset if corresponding inputs are small in magnitude. The adaptation deadband also serves to prevent switching the feed forward controller element and applying a large gain unnecessarily if the controller is applying sufficient setpoint tracking.

The adaptation deadband was determined by simulating a variety of setpoints and modifying the deadband to obtain the best setpoint tracking response, prioritising step inputs over continuous inputs. A deadband of 0.51 m was applied.

The control input into the thrusters takes the form of a propeller speed and therefore the feed forward element was determined using the thrust vs. propeller speed graph shown previously in Figure 26. The approximate propeller speed that corresponds to a thrust of 20 N is 375 rpm.

Figure 131 following shows in a logical flow diagram how the above strategies were applied.

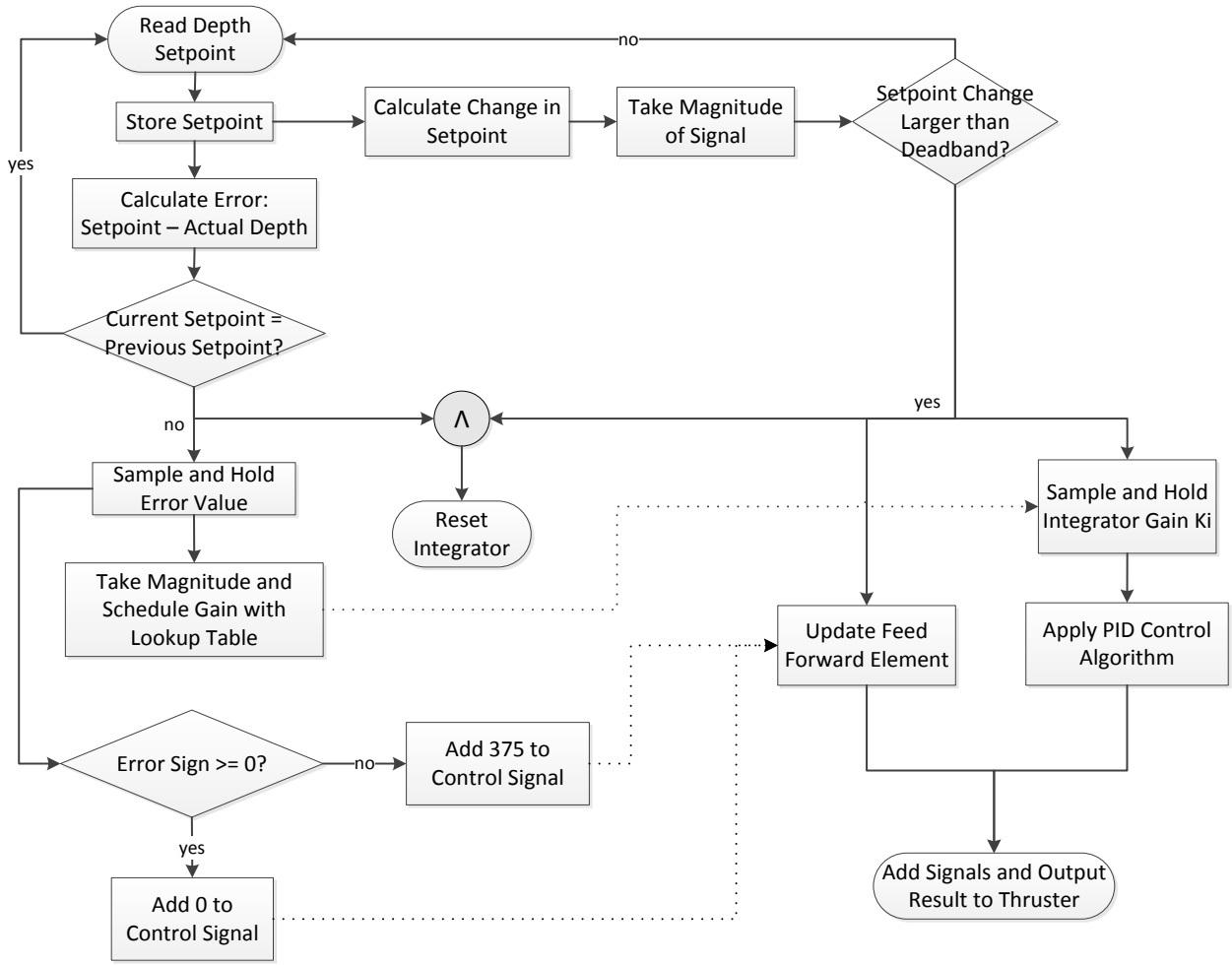

Figure 131 - Flow diagram of depth controller logic for gain scheduling and integrator reset

The controller has now been designed and described and it is possible to assess it under a variety of input commands in the following section.

8.2.7 Depth Controller Test Simulations and Performance Evaluation

To determine the effectiveness of the controller it was necessary to simulate the following scenarios:

Sc1. Small and large input steps for descending motion.

Sc2. Small and large input steps for ascending motion.

Sc3. Several input steps, ascending and descending, in a sequence to assess the effectiveness of the integrator reset function.

Sc4. Continuous inputs such as sine waves:

a. With small amplitudes.

b. With large amplitudes.

Sc5. Combination of continuous and step inputs.

From research conducted in the literature review and presented in part earlier in this chapter, the expected known shortcomings of a PID controller scheme are expected to be seen to some extent in the simulations. The adaptation algorithm will be assessed according to how well the shortcomings are mitigated. While most of the shortcomings of a classical control structure in an underwater environment are realised in real life testing, it is expected that a non-uniform response is expected in a simulation environment.

Scenarios 1 - 3: Step Input Responses

Figure 132 and Figure 133 following show simulated responses to different step sizes in the ascending and descending directions. Each step is applied after 30 s allowing the ROV to stabilise itself at 50 m depth initially.

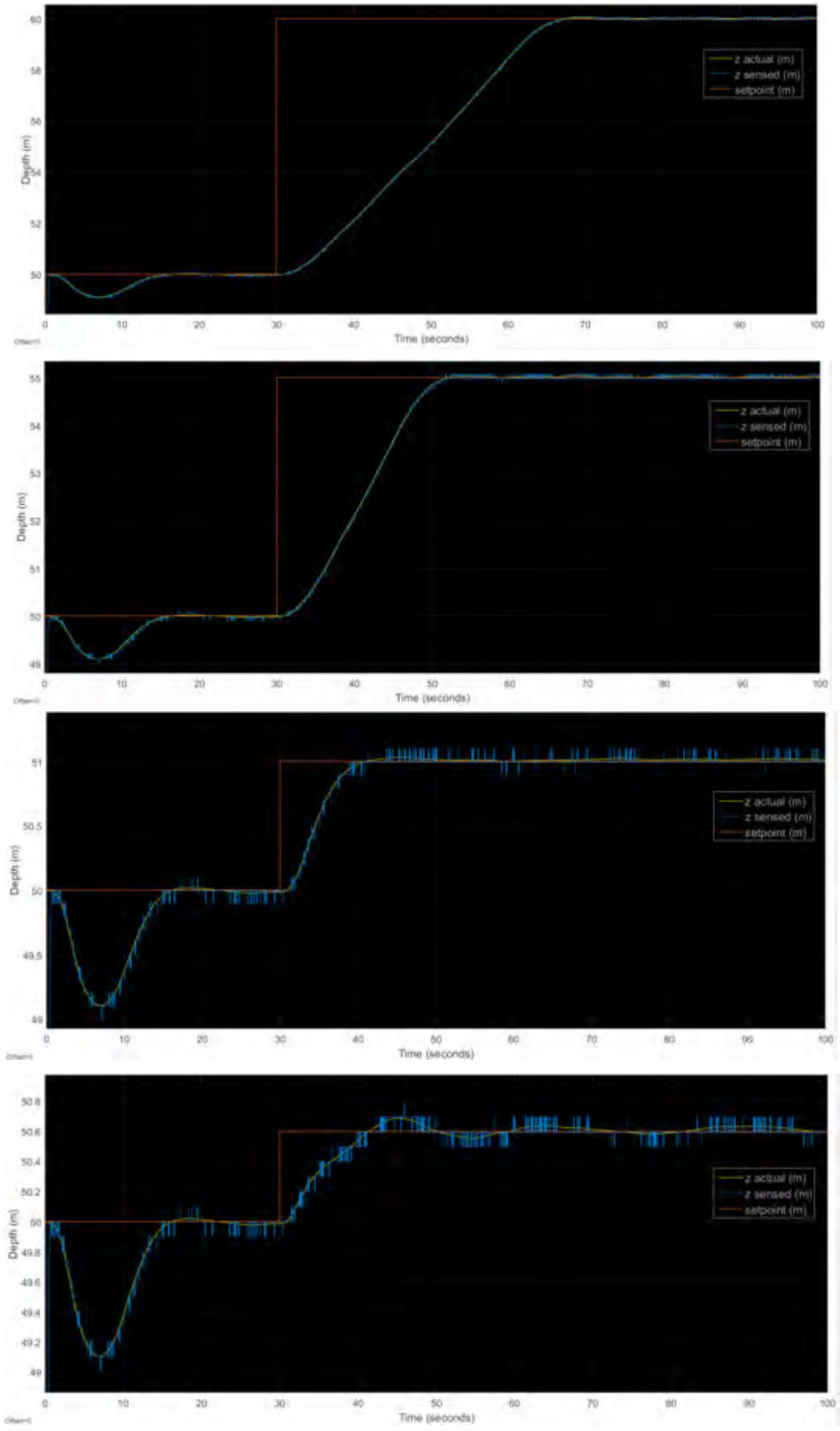

Figure 132 - Sc1. Response to descending direction step inputs of 10 m, 5 m, 1 m and 0.6 m top to bottom

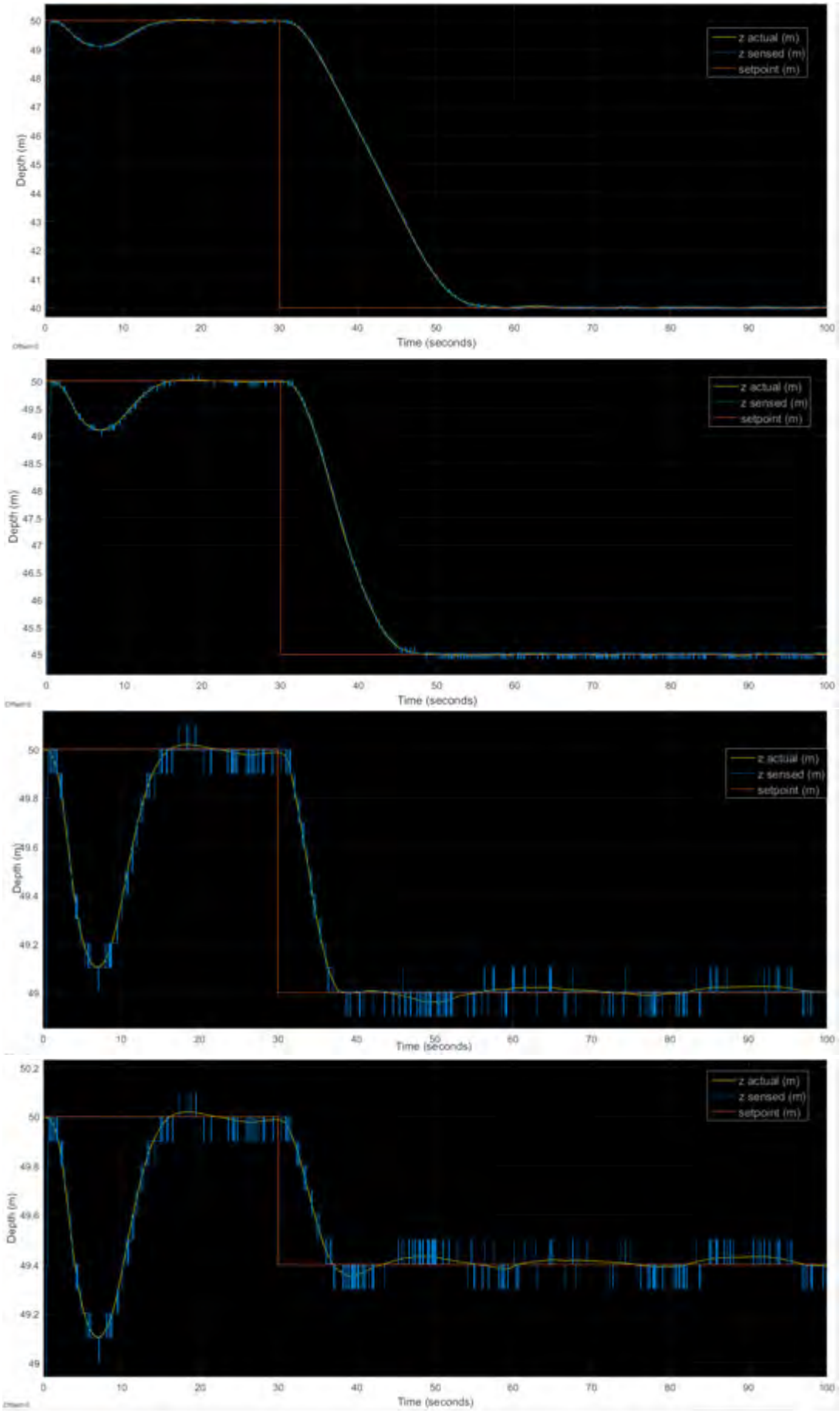

Figure 133 - Sc2. Response to ascending direction step inputs of 10 m, 5 m, 1 m and 0.6 m top to bottom

Figure 132 and Figure 133 show that in both the ascending and descending direction, over a variety of step sizes, a reasonably uniform response is obtained. The response is seen to slow down as the deadband region of 0.5 m is approached. This was expected, due to how the higher applied integrator gains for steps less than 1 m significantly influence the nature of the controller as shown previously in Figure 129.

Within the deadband region, the integrator gain is held at its current value. Therefore a variety of responses are expected for different step sizes within the deadband region. Figure 134 and Figure 135 following show the range of responses to step inputs within the deadband region for ascending and descending manoeuvres respectively.

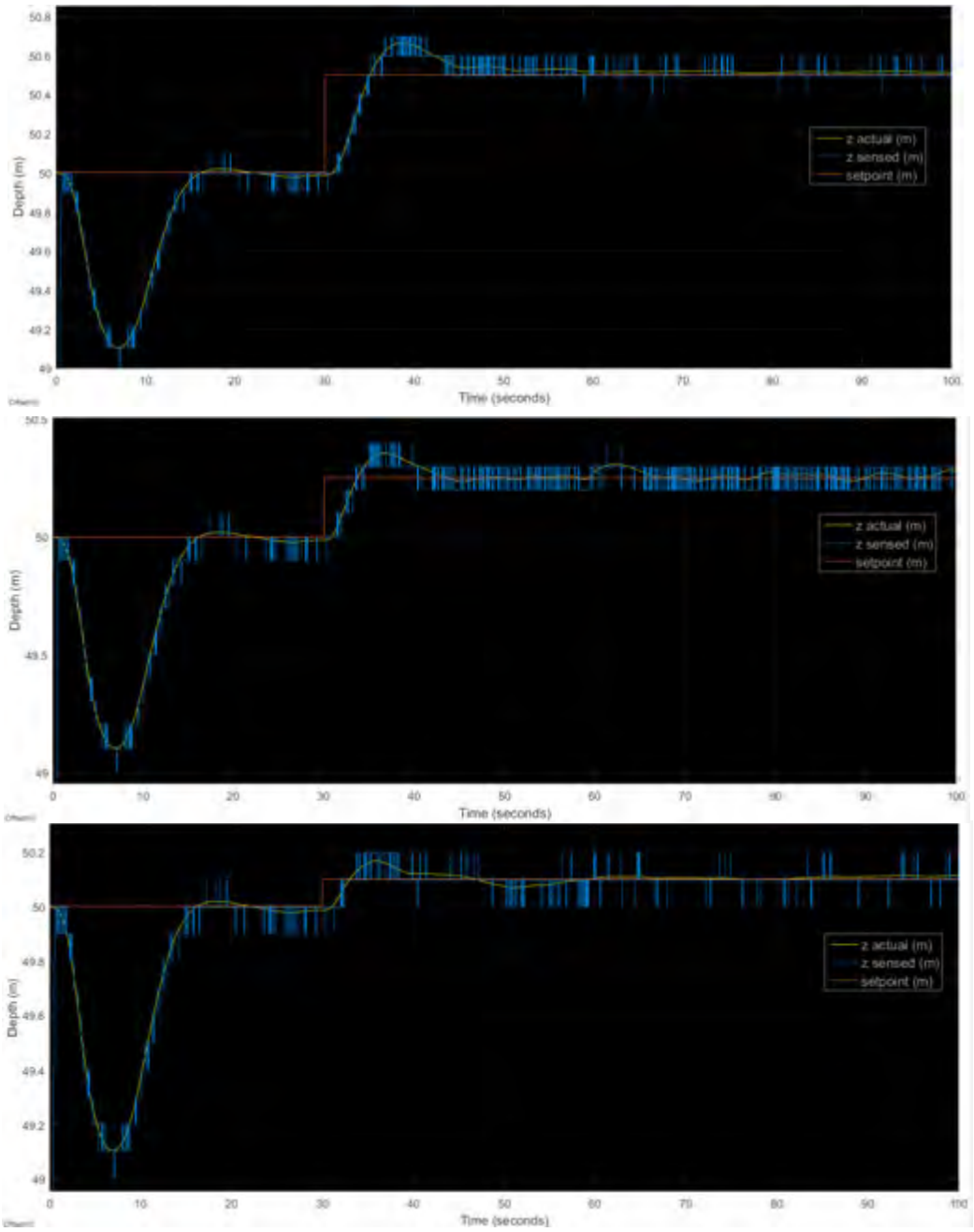

Figure 134 - Sc1. Steps within the deadband in the descending direction: 0.5 m, 0.25 m and 0.1 m top to bottom

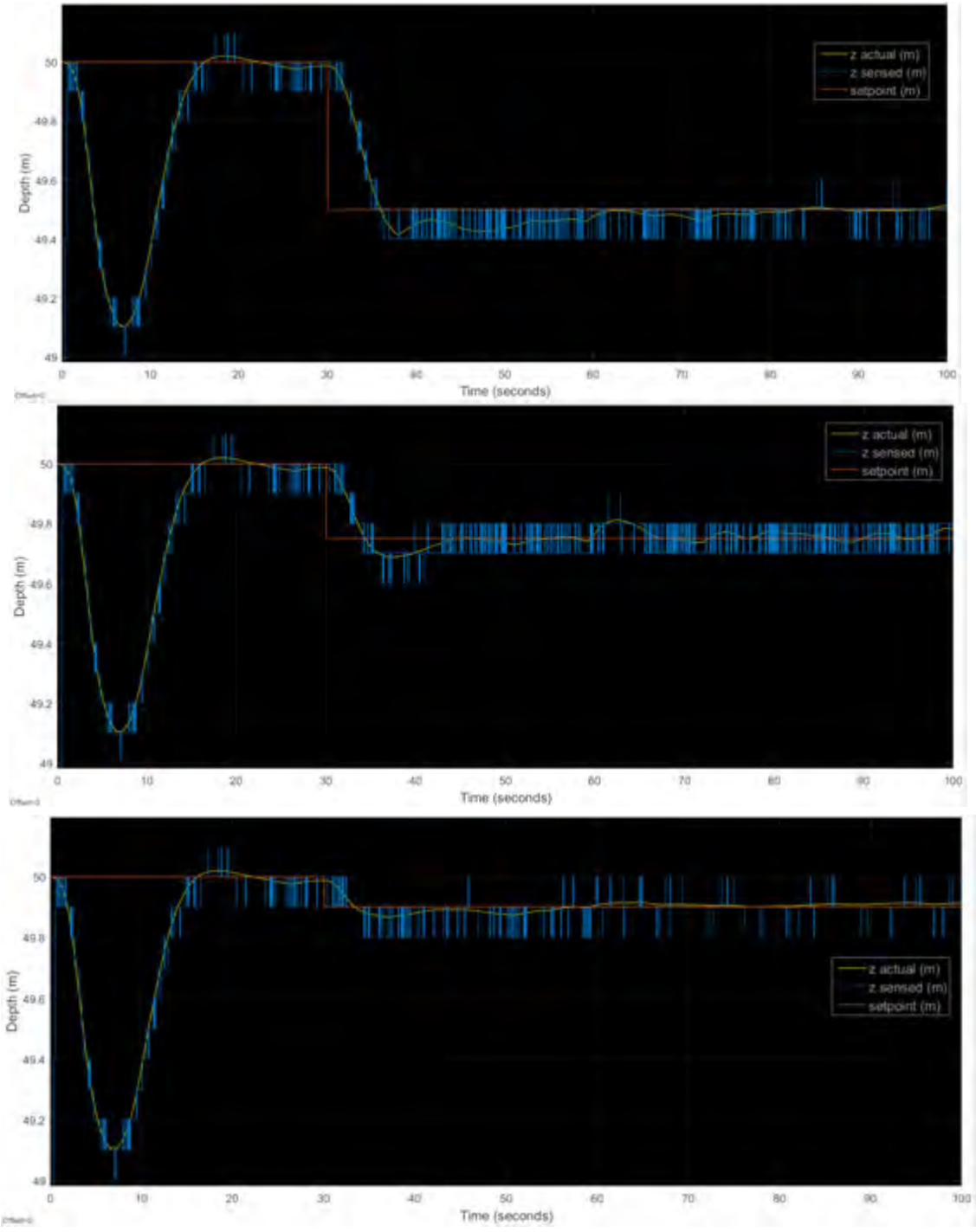

Figure 135 - Sc2. Steps within the deadband in the ascending direction: 0.5 m, 0.25 m and 0.1 m top to bottom

Figure 134 and Figure 135 show that the damping decreases towards the upper limit of the deadband. However, the responses all settle within about 15 s and track the setpoint to within the resolution of the sensor.

To verify the integrator reset function, a random step sequence was input with a period of 50 s per step as shown following in Figure 136.

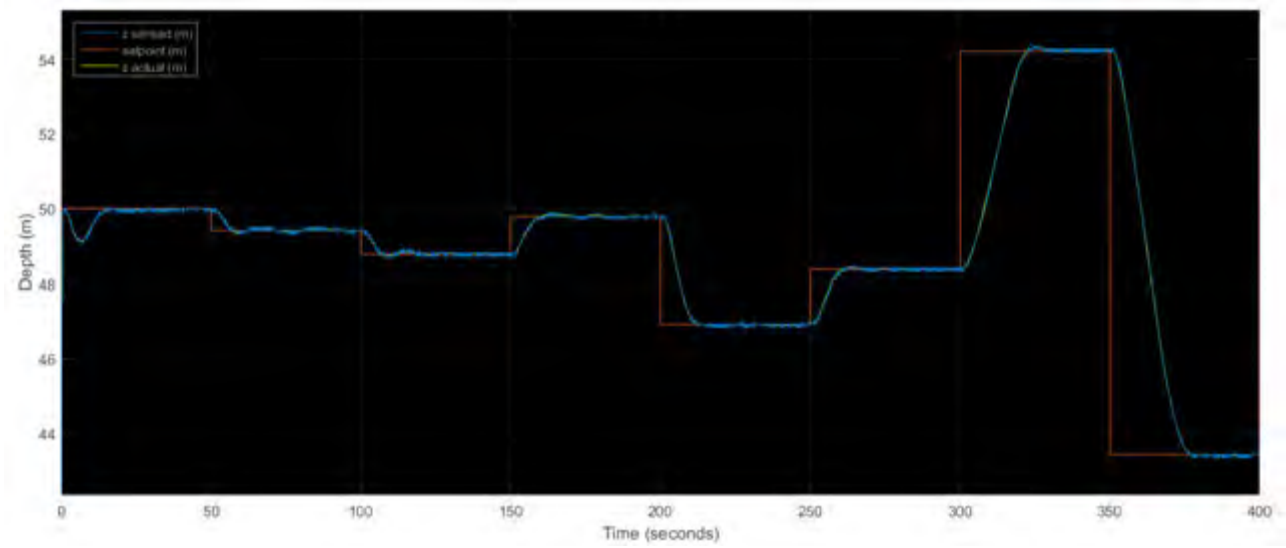

Figure 136 - Sc3. System response to randomly sized depth step inputs

A simulation was conducted to compare the adaptive control structure with a standard non-adaptive controller. A sensible K_i value was chosen according to a tuned step size of 3 m. The chosen K_i value was 14 and the response from the controller, excluding the gain scheduling, deadband and integrator reset functionality is shown following in Figure 137.

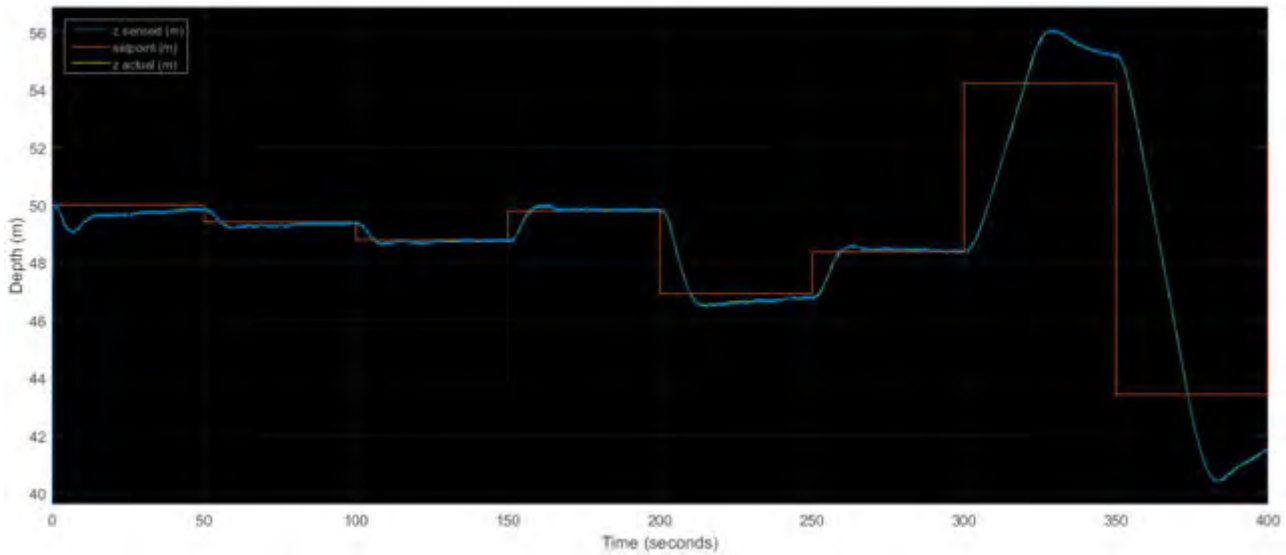

Figure 137 - System response to random step inputs from non-adaptive PID depth controller

Scenarios 1 to 3 defined at the beginning of this subsection have now been assessed in simulations, showing that the adaptive depth controller exhibits sufficient setpoint tracking capabilities for steps of different sizes in the ascending and descending directions and that the adaptive control structure is superior to a standard non-adaptive PID control structure.

Scenario 4 - 5: Continuous Input Tracking

It should be noted that the logic used in the controller as described previously in Figure 131 does not result in adaptation of the integrator gain for continuous inputs. This is because the relative input step size must be greater than the adaptation deadband for the integrator gain to be updated. It was deemed that more advanced control techniques should be employed in the future to provide a more robust adaptation law. In this project the controller will be assessed to provide a benchmark for continuous setpoint tracking upon which can be improved in the future.

Due to the adaptive nature of the controller, it is expected that a variety of closed-loop frequency response characteristics will be observed from the controller. A variety of step and sine waves were input into the system and the system was linearized about a variety of operating points so as to obtain as much as possible a complete picture of the variation of closed-loop response characteristics from the system. The resulting response is given following in Figure 138.

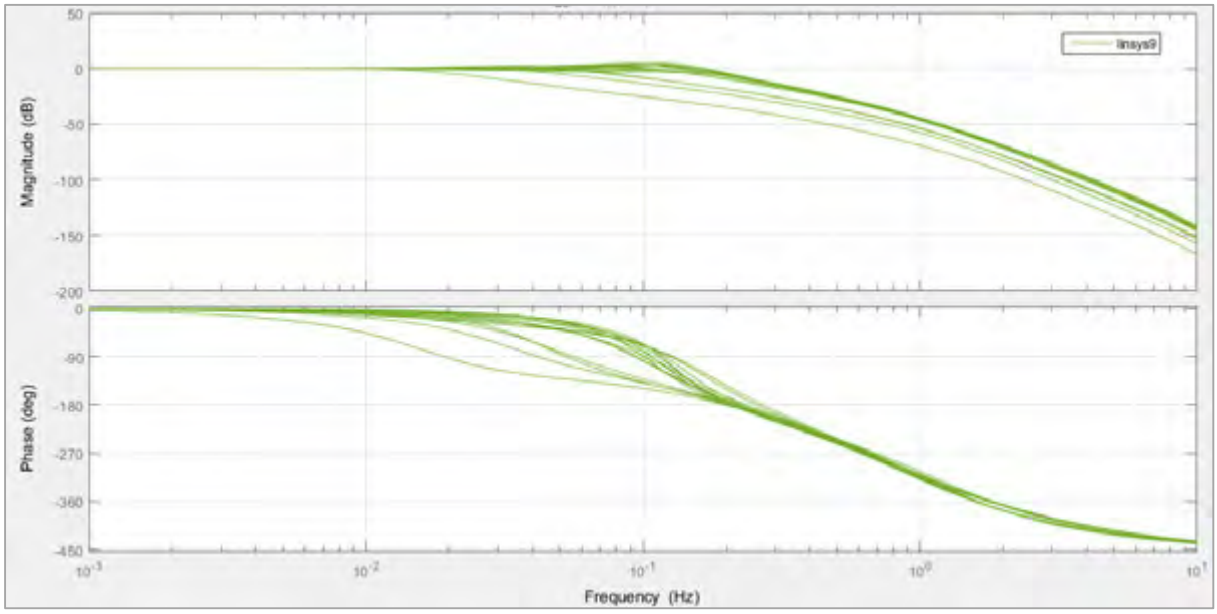

Figure 138 - Closed-loop frequency response for depth controller

The bandwidth and resonance properties of the depth controller are given following in Table 46. The typical values were obtained by taking an average of data from Figure 45.

Table 46 - Depth controller closed-loop characteristics

	Worst Case	Typical
Bandwidth (-3 dB point)	0.018 Hz	0.133 Hz
Resonant Peak (dB)	4.80 dB	3.80 dB

Tracking of continuous inputs was assessed by inputting sine waves of different amplitudes. The frequency of the wave was increased until the controller was deemed to be unable to sufficiently track the setpoint. Sufficient setpoint tracking was not determined using a standard criteria, due to the fact that the resolution

of the depth sensor would have a greater effect on the response overshoot and phase lag at lower amplitudes.

The results of the continuous input simulations is given following in Table 47.

Table 47 - Sine wave tracking characteristics of depth controller

Input Amplitude (m)	Maximum Input Frequency (Hz)	Gain (dB)	Phase (deg.)
0.1	0.048	3.52	-16.5
0.5	0.024	1.58	-8.3
1	0.019	1.29	-2.6
5	0.009	0.57	-0
10	0.006	0.34	1.5

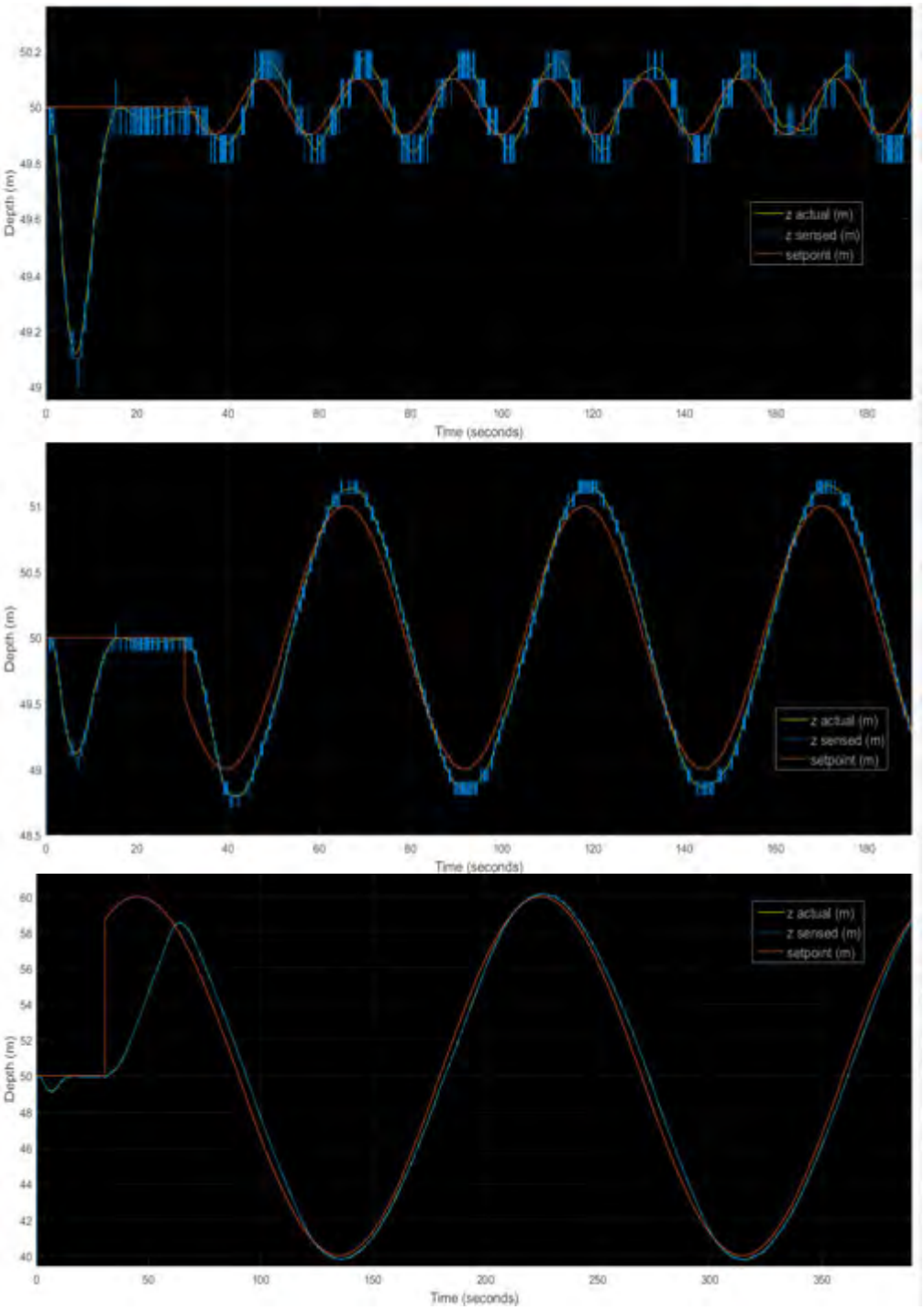

Figure 139 - Depth controller response to sine waves of amplitude 0.1 m, 1 m and 10 m from top to bottom

Figure 139 illustrates how for smaller input amplitudes the sensor resolution becomes more significant in the overshoot and phase lag. While it can be seen that there is definitely room for improvement of the controller in the future, Figure 139 illustrates how the current controller is capable of tracking continuous inputs to some extent. For practical ROV observation operations, depth holding is envisaged to be of most importance, which is why the controller was designed with a depth holding focus.

All evaluation scenarios have now been assessed, allowing the controller to be summarised in the following section.

8.2.8 Depth Controller Summary

An investigation into the stability of the decoupled ROV system was undertaken, showing that a PI controller would be insufficient to stabilise the system and that a derivative element of the controller was required to add phase to the system.

A depth tracking controller was designed using a continuous PID control scheme, digitized using the bilinear transform and executed at a rate of 50 Hz with a scheduled integrator gain, according to the step size desired. The controller logic was designed to condition every input to respond as if a step had been inputted, therefore, the integrator was reset when a new step input was received. To prevent a steady state offset when continuous inputs were received, an adaptation deadband was applied to the difference in consecutive inputs, within which the integrator would not be reset. Additionally, a feed-forward control element was added to the thruster input to account for the additional 20 N buoyancy force inherent in the ROV plant model.

The controller successfully met objectives $O_{dc}1$ and $O_{dc}2$, with the controller successfully tracking constant setpoints to within a tolerance of ±100 mm and capable of tracking a sine waves of a variety of amplitudes and frequencies.

Figure 140 following shows two examples of the depth controller tracking a variety of inputs.

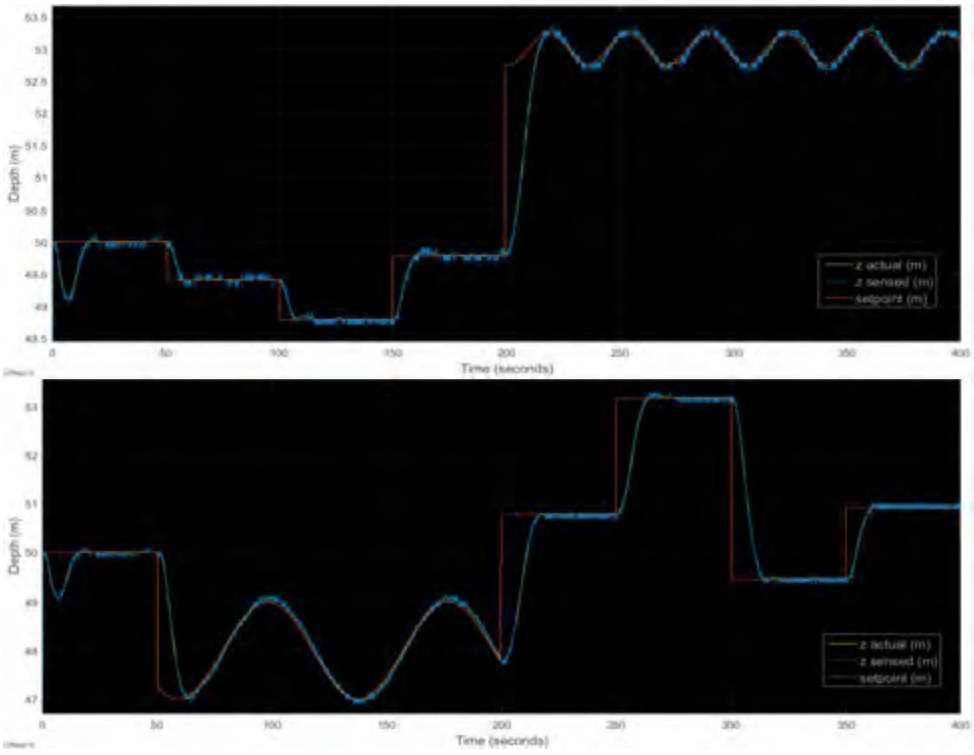

Figure 140 - Depth controller responses for varied inputs

This completes the depth controller design, allowing the heading controller to be designed in the following section. Critiques and shortfalls of the depth controller will be discussed following in this chapter.

8.3 Heading Holding Controller

8.3.1 Introduction

Open-loop simulations in chapter 6 showed that the motion of the *SEAHOG* is sufficiently decoupled to allow for yaw manoeuvres to be isolated and analysed as a separate system. Therefore, this section will develop a heading holding controller that will be based on the decoupled yaw motion of the ROV.

Once again, objectives shall be established for the capabilities of the heading holding controller rather than in-depth specifications. Greater investigation into the hardware capabilities of the chosen iNEMO AHRS is necessary before a sufficient understanding of the achievable specifications for the heading controller will have been gained. Therefore, once again the controller developed in this report for heading holding will serve as a benchmark for future work to improve on. A list of objectives for the heading holding controller is given following:

$O_{hc}1$. Provide heading holding to within a tolerance of ±0.2˚ for different step sizes starting from stationary.

$O_{hc}2$. Provide reasonable heading setpoint tracking for variety of sine waves that have an amplitude spanning the operational speed range of the ROV.

Assumptions for the operating conditions and environment of the ROV include all previously listed assumptions from the ROV and thruster model derivations. Specifically, notable assumptions and performance limits for the heading controller are:

$A_{hc}1$. The controller will be designed in the absence of currents and external disturbances.

$A_{hc}2$. The ROV will maintain close to horizontal orientation throughout its motion.

$A_{hc}3$. Due to the known shortcomings of PID controllers in an underwater environment, robustness to model uncertainties will not be a design consideration of the controller.

$A_{hc}4$. The controller will execute control algorithms and supply a speed setpoint update to the thrusters at a rate of 50 Hz.

$A_{hc}5$. The maximum required step size will be 180˚.

A similar approach will be taken in the design of the heading controller that was taken for the depth controller. However, notable differences between the two designs are that four thrusters are providing the thrust input into the system instead of one. In addition, there are no unsymmetrical effects in the heading motion plant, such as the 20 N buoyancy force in the vertical DOF. Whilst this may remove the necessity of feed-forward control elements and an integrator, the deadband speed region of the thrusters is predicted to be significant now. These differences will warrant small modifications to the control strategy, however

the overall design approach for the depth controller is predicted to be sufficient for the heading controller as well.

With the objectives and assumptions for the controller design clearly understood, the dynamic model for motion in yaw can be derived in the following section.

8.3.2 Decoupled Dynamic Model for Yaw

Recall the general dynamic equation of motion for the *SEAHOG*:

$$\boldsymbol{M\dot{\nu}} + \boldsymbol{C}(\boldsymbol{\nu})\boldsymbol{\nu} + \boldsymbol{D}(\boldsymbol{\nu})\boldsymbol{\nu} + \boldsymbol{g}(\boldsymbol{\eta}) = \boldsymbol{\tau}$$

which can be represented as follows if motion in the yaw direction only is considered:

$$(I_{rb} + I_a)\dot{r} + 0 + \left(K_r r + K_{|r|r}|r|\right) + 0 = m_\psi \qquad \{8.134\}$$

In the above model, off diagonal mass elements have been ignored and cross-coupling drag effects have been ignored, which is a reasonable assumption for the design of this controller - as was discovered previously in chapter 6 through open-loop simulations. Specifically, when data from the actual *SEAHOG* model is substituted into equation 8.134, the model obtained is:

$$\begin{gathered}(5.79 + 4.1)\dot{r} + (2.499r^2 + 0.0924r + 9.3017)r = m_\psi \\ \dot{r} = \frac{1}{9.89}\left(m_\psi - r(2.499r^2 + 0.0924r + 9.3017)\right)\end{gathered} \qquad \{8.135\}$$

The control input into the system is a moment (N_{des}) provided by thrusts from four vectored thrusters. The desired level of thrust is determined by a percentage of the maximum thrust available per thruster:

$$T_{i\,des} = Thrust\ Level \times 55 \qquad \{8.136\}$$

The thrust allocation for each thruster in a yaw manoeuvre was defined previously in equation 6.115 in chapter 6 as:

$$T_{1\,des} = -T_{2\,des} = -0.89N_{des}\ ;\ T_{3\,des} = -T_{4\,des} = -0.98N_{des} \qquad \{8.137\}$$

and the propeller speed corresponding to the desired thrust is determined by equation 6.117:

$$\Omega_i = \pm\sqrt{\frac{T_{i\,des}}{C_t}}$$

It is not strictly true that the ROV will maintain close-to horizontal orientation throughout operations, however this has been given as an assumption shown previously by $A_{hc}2$ for the purposes of designing the heading holding controller. It is assumed that the ROV will be controlled by the operator in such a way that the ROV will remain close to horizontal. Therefore, with assumption $A_{hc}2$, the BODY yaw orientation can be directly mapped to the NED heading.

The Simulink® block diagram of the decoupled thruster and ROV system is given following in Figure 141. Note that communication cycle delays have been implemented with a time value of 4 ms, given that the controller has been specified to communicate with all five thrusters at 50 Hz.

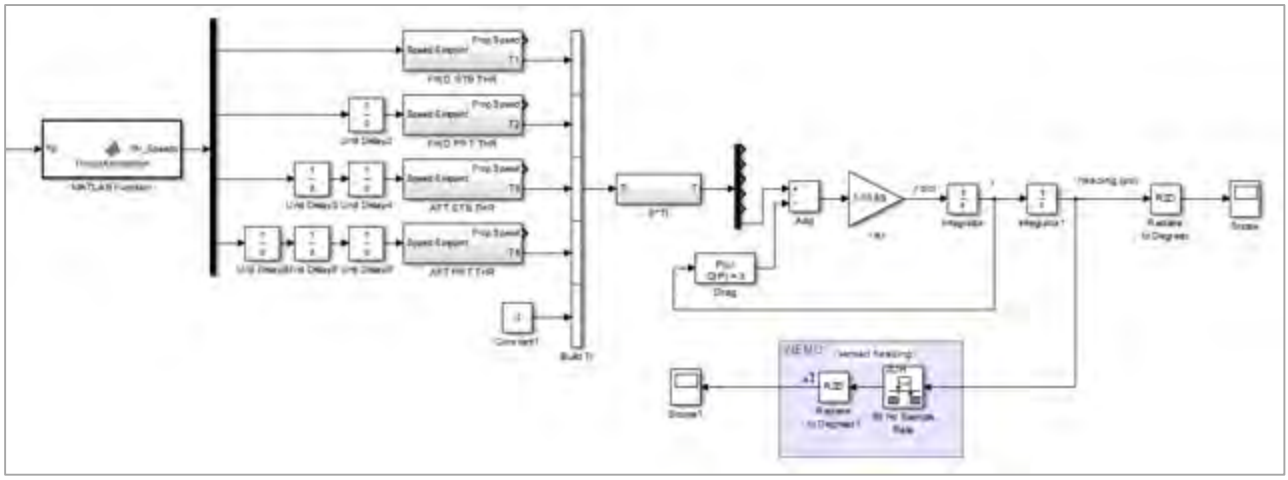

Figure 141 - Decoupled Simulink® plant model for heading controller

The *SEAHOG* plant for decoupled yaw motion has now been described and it is possible to begin the design procedure in the following section with an investigation into the system stability.

8.3.3 Yaw Motion Plant Stability

Linearizations were conducted on the plant in a similar manner as for the depth holding controller. Once again, the four combinations of fast and slow ROV speed and high and low thrust had to be assessed. The control elements were chosen as a gain and a compensator, as these elements would allow the phase and gain of the system to be directly manipulated. Figure 142 following shows the general control structure expected for the heading controller with control elements in light blue.

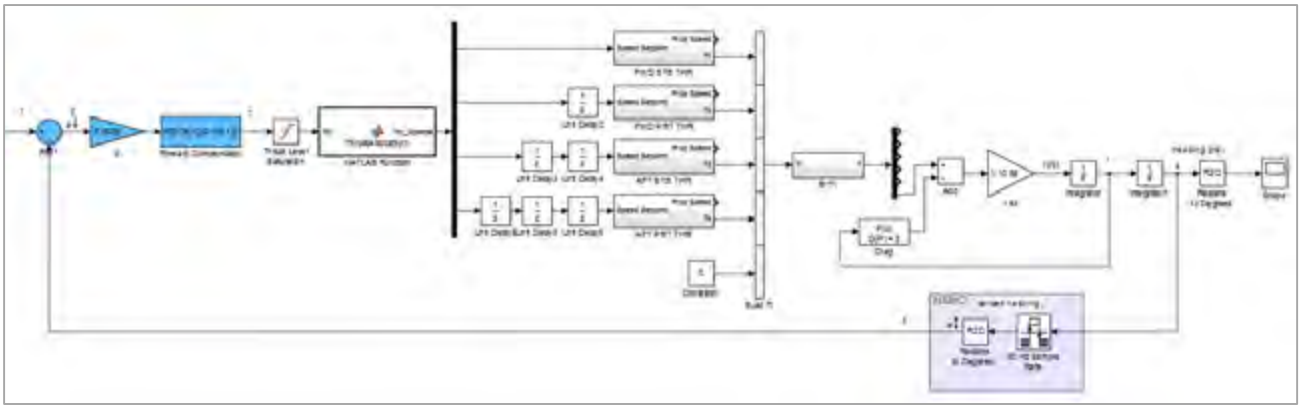

Figure 142 - Decoupled Heading controller Simulink® model

Figure 143 following shows an open loop frequency response plotted between points 3 and 5 and between points 2 and 5 from Figure 142. The compensator was removed and a gain of 0.0094 was applied. The low controller gain is necessary to scale the input such that the system was not saturating. Once the input is decreased so that saturations on the propeller speeds are not predominant, a more truthful response from the system can be obtained from the Bode Plot. Figure 143 following shows the -180˚ and 0 dB crossover points as dots, representing the phase and gain margin positions for the systems shown in the figure.

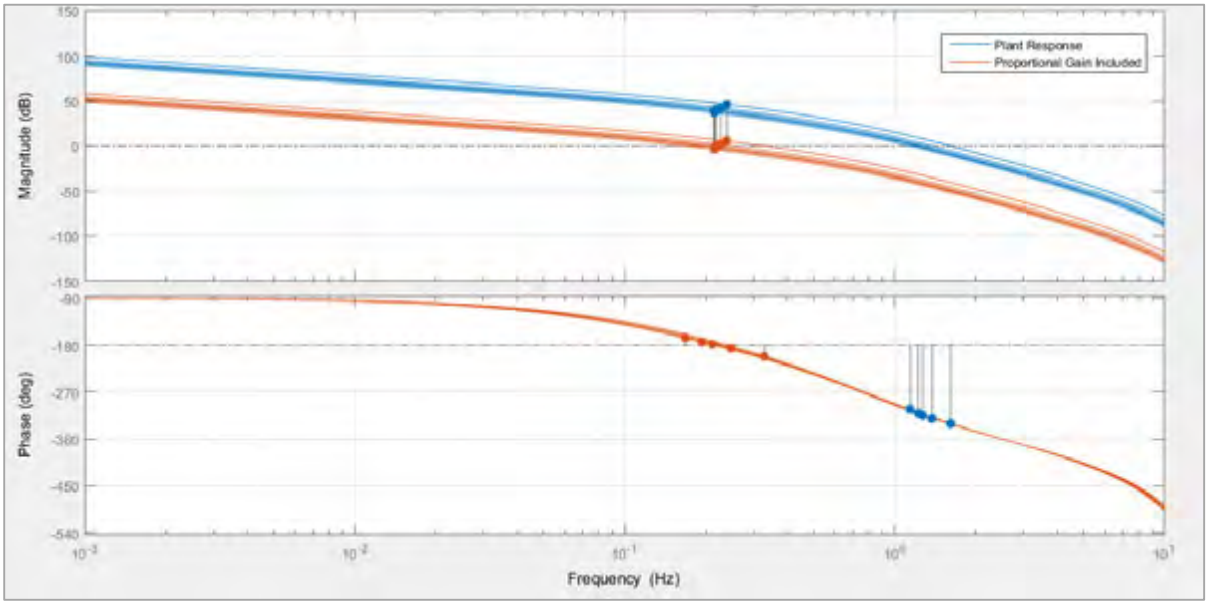

Figure 143 - Decoupled yaw motion ROV plant open-loop frequency response with and without proportional gain

Figure 143 shows that the plant itself has a high gain. It was therefore necessary to implement the low proportional gain of 0.0094 so as to avoid saturations in the thrusters. It can be seen then that a desirable response can be obtained from merely a proportional controller at the expense of limited bandwidth. It is therefore desirable to add phase in the form of a dominant lead compensator at a design frequency of about 0.5 Hz to improve the system bandwidth.

It has been established in this subsection that it will be easy to design a stable controller for heading holding operations. The following section will describe the design process of adding phase to the system so as to improve the bandwidth.

8.3.4 Lead Compensation

To increase the system bandwidth, a dominant lead compensator was designed with a maximum phase point of 0.47 Hz and a lag frequency 10 times the lead frequency. The implemented compensator is shown following:

$$G(s)_{fwd\ comp} = \frac{1.06s + 1}{0.11s + 1} \qquad \{8.138\}$$

The resulting frequency response was calculated between points 2 and 5 from Figure 142 previously and is shown following in Figure 144.

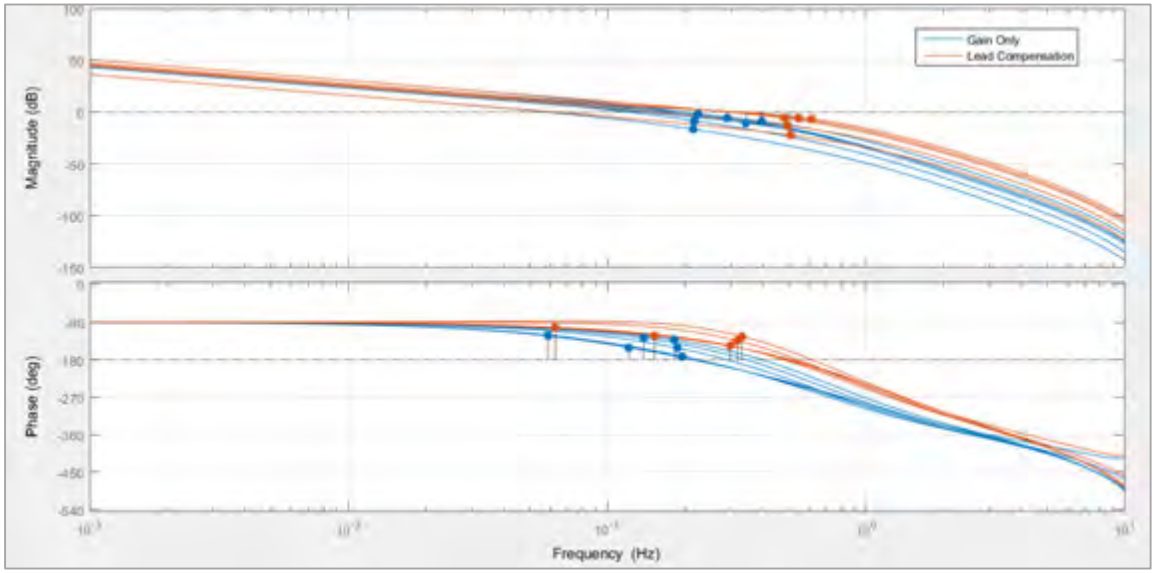

Figure 144 - Bode Plot showing the decoupled heading controller system with a dominant lead compensator added

The added phase of the compensator allowed the gain of the system to be increased and hence a greater bandwidth was obtained. With a basic stable controller designed, it was possible to tune the proportional gain to find an optimal controller response according to step size. Final adaptive and nonlinear controller elements can now be described in the following section.

8.3.5 Gain Scheduling and Deadband Control

The controller was tuned to have a close-to critically damped response for varying step sizes, resulting in the gains shown following in Figure 145.

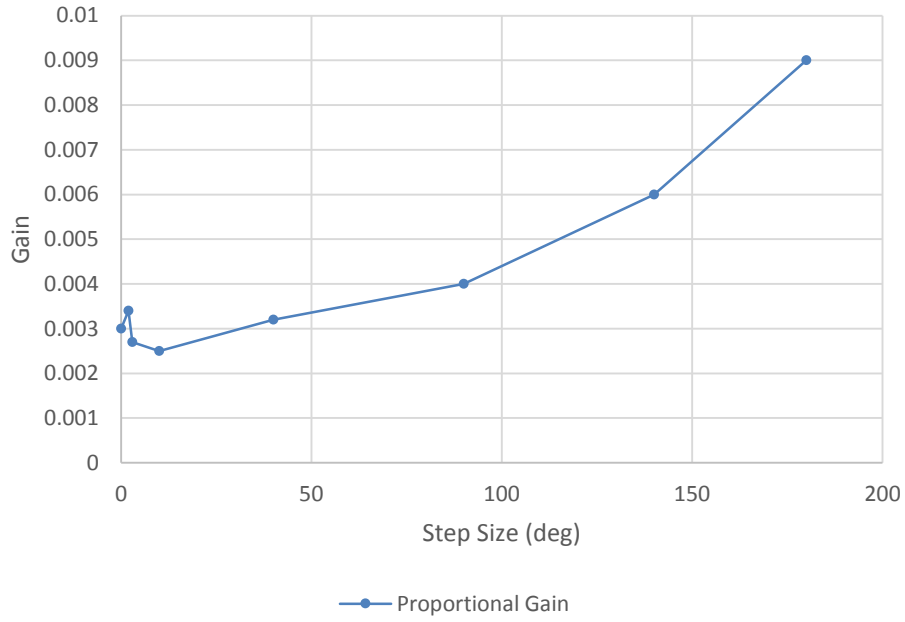

Figure 145 - Proportional gains for heading controller according to step size

The gains were implemented in a lookup table with linear interpolation between points. The proportional gain was scheduled in the same way as in the depth controller, taking the magnitude of the relative step size and applying a gain according to Figure 145. Unlike the depth controller however, the heading controller does not implement an integrator. Therefore complications with integrator resetting and adaptation dead-bands were not necessary to implement. The scheduling logic therefore was designed to detect a change in setpoint and schedule a gain according to the difference between the current heading and the desired heading.

An issue that became significant for the heading controller was the speed deadband region of ±46 rpm in the thrusters. As the error decreases under the control action of the designed heading controller, the desired propeller speed that is outputted from the controller decreases. Once the deadband of the thrusters was reached, the thrusters would output 0 rpm propeller speed and therefore the heading was prone to settling with an offset from the desired setpoint. Figure 146 following shows how a 10˚ step input results in the system settling greater than 1˚ from the setpoint due to control signals lying within the thruster deadband region.

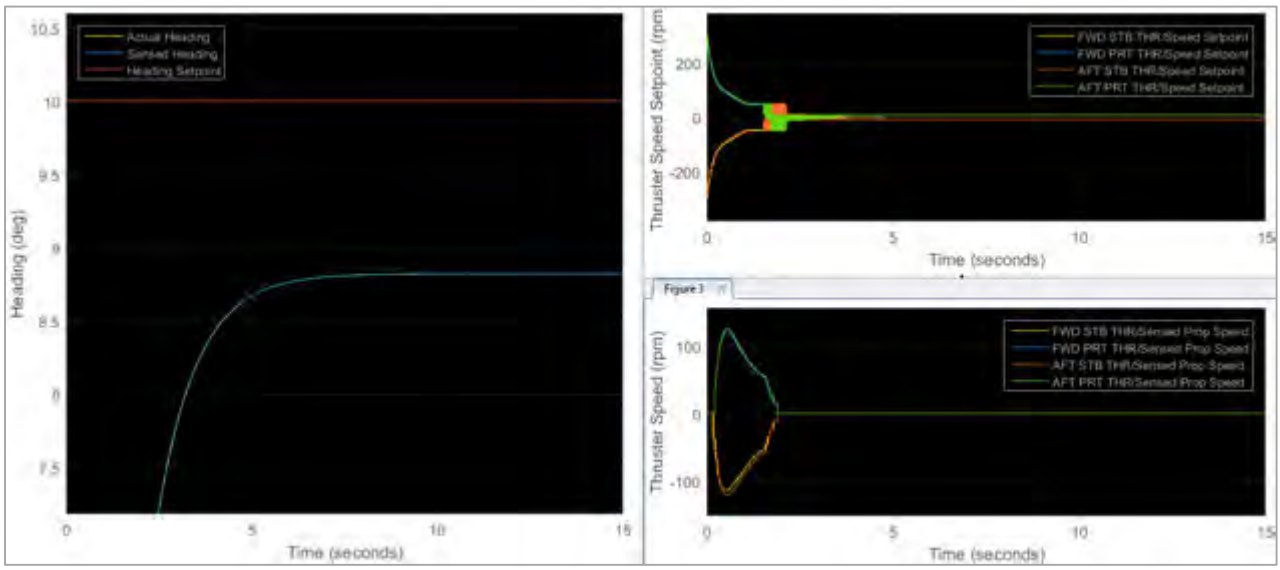

Figure 146 – Effect of thruster speed deadband on heading control

As a result, a nonlinear control law was applied to the propeller speed for small errors as shown following:

$$u(s) = \begin{cases} 47, & 0 < s < 46 \\ -47, & -46 < s < 0 \end{cases} \quad \{8.139\}$$

where $u(s)$ is the modified speed control input into the thrusters and s is the unmodified control input. As shown following in Figure 147, the discontinuous control law results in chattering about the setpoint and large amounts of switching from the actuators.

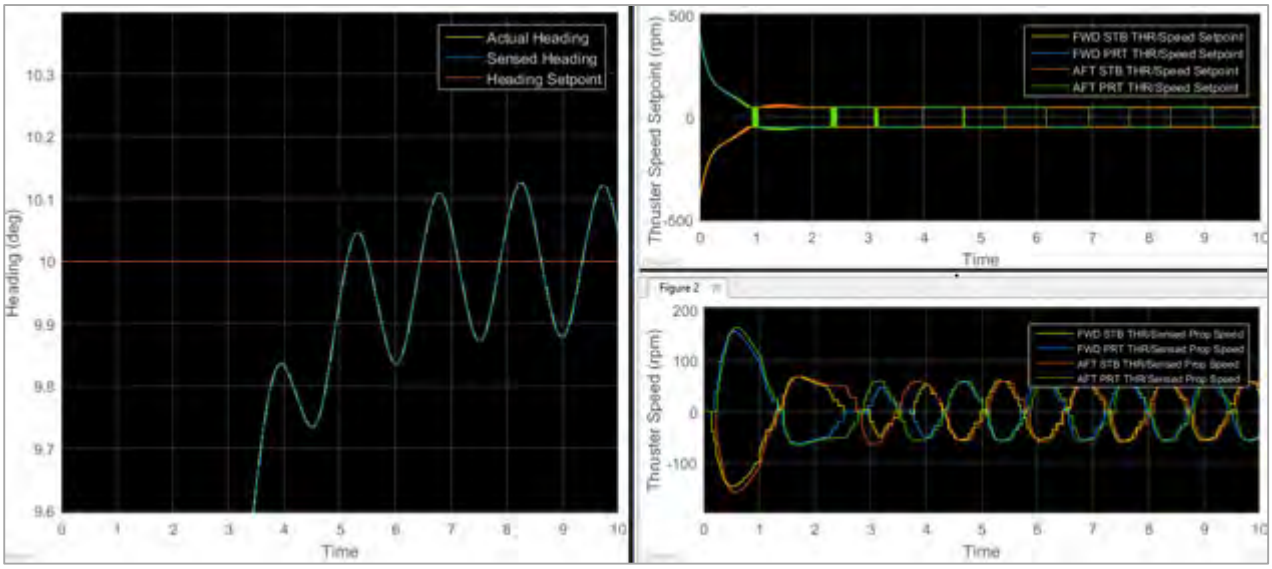

Figure 147 - Chattering due to discontinuous deadband control

To counteract chattering, the discontinuous control law was modified as follows:

$$u(s) = \begin{cases} 47, & 14 < s < 46 \\ -47, & -46 < s < -14 \end{cases} \quad \{8.140\}$$

The modification effectively decreases the size of the deadband and allows the propellers to be at 0 rpm if the current position is close enough to the setpoint. As a result, chattering in the system is reduced as shown following in Figure 148.

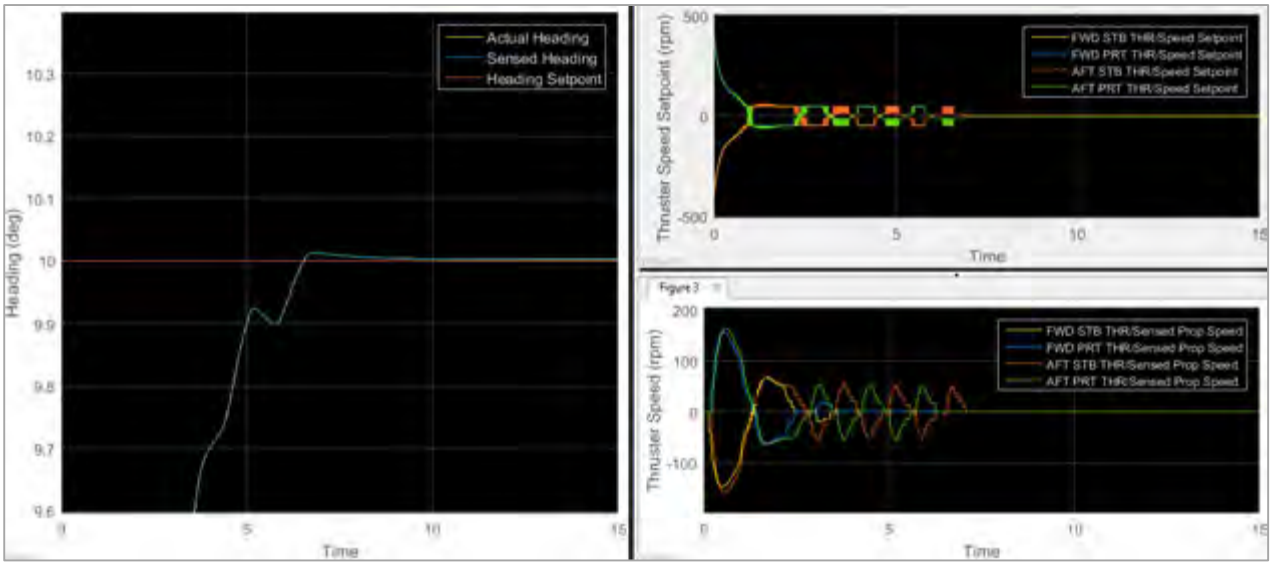

Figure 148 - Modified discontinuous control law to reduce chattering

With gain scheduling included, the resulting open loop frequency response, calculated between points 2 and 5 from Figure 142 previously was obtained as shown following in Figure 149.

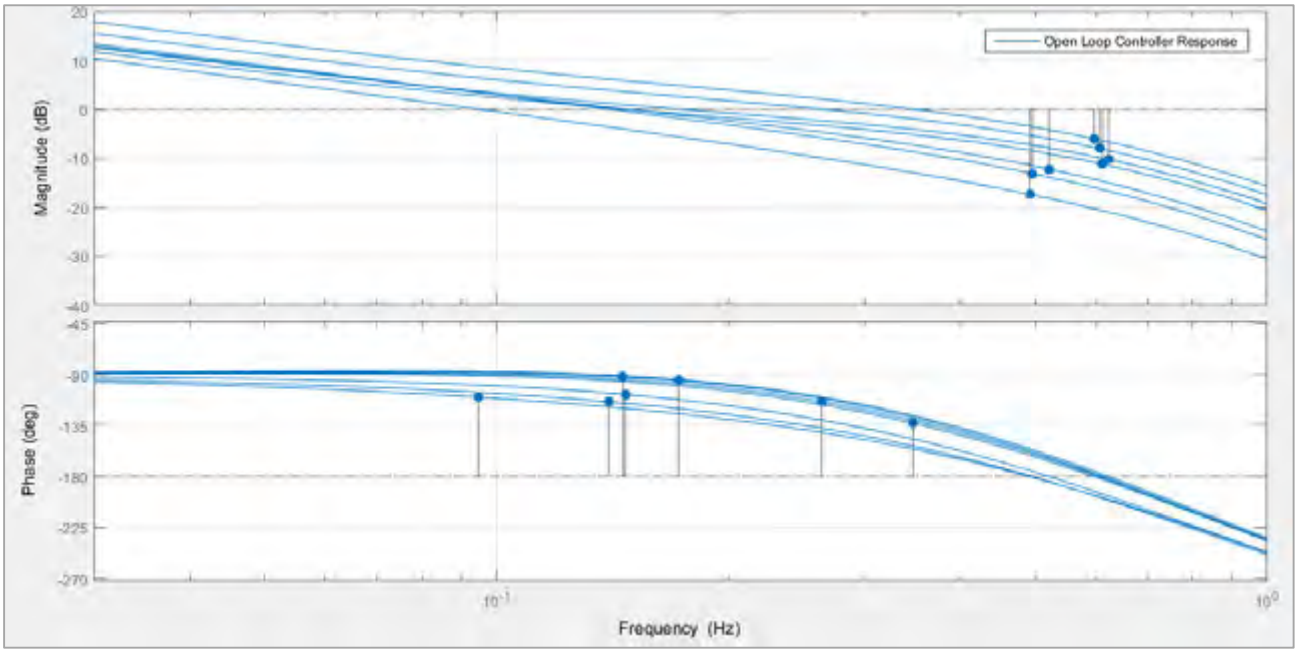

Figure 149 - Bode Plot for the complete heading controller with gain scheduling included

It was deemed that the heading holding controller was now sufficiently designed and its performance could be evaluated in the following section.

8.3.6 Heading Controller Test Simulations and Performance Evaluation

To evaluate the heading holding controller, a variety of step inputs were analysed, allowing the rise time and damping characteristics of the system to be analysed. The closed loop system was then linearized to obtain a measure of the available bandwidth in the system. This was then investigated using continuous sine wave inputs to assess the capability of the controller to track continuous inputs.

Shown following in Figure 150 are responses by the controller to different sized step inputs. The effect of the thruster speed deadband can be seen more prominently at low speeds, where there is a slight offset between the settling heading and the setpoint. The deadband was adjusted to meet $O_{hc}1$, so that the settling heading was within 0.2˚ of the setpoint.

It can be seen that across the range of step sizes, a very similar response is obtained. Therefore, assessment of standard controller parameters such as damping and rise time could be carried out following.

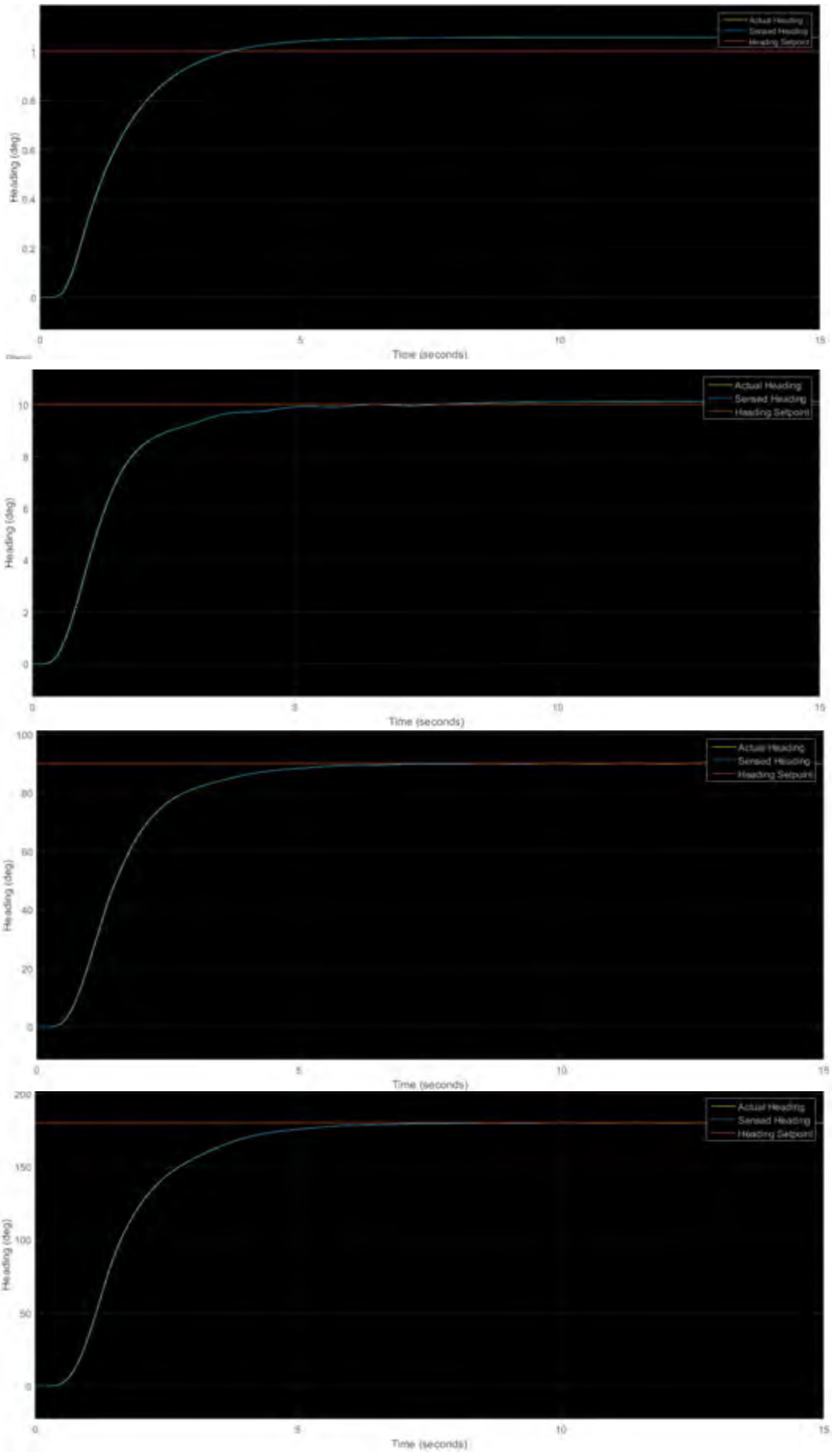

Figure 150 - Response to heading step inputs by the heading controller

Table 48 following lists characteristics of rise time and settling value for the heading controller over different step sizes. The 95% rise time was calculated as the time from the beginning of the simulation to the time when the response has risen to 95% of the settling value.

Table 48 - Characteristics of rise time and settling value for heading controller

Step Size (deg.)	95% Rise Time (s)	Settling Value Range (deg.)
1	3.55	0.90 – 0.90
10	3.41	10.1 – 10.1
90	3.71	89.9 – 90.1
180	4.79	179.8 – 180.1

It can be seen that over the entire range of step sizes, the rise time remains within close proximity, with a maximum variation of 1.24 s. The settling value is within ±0.2˚ for all step sizes.

The system model was linearized in a closed-loop configuration between points 1 and 5 shown previously in Figure 142. The resulting response is shown following in Figure 151.

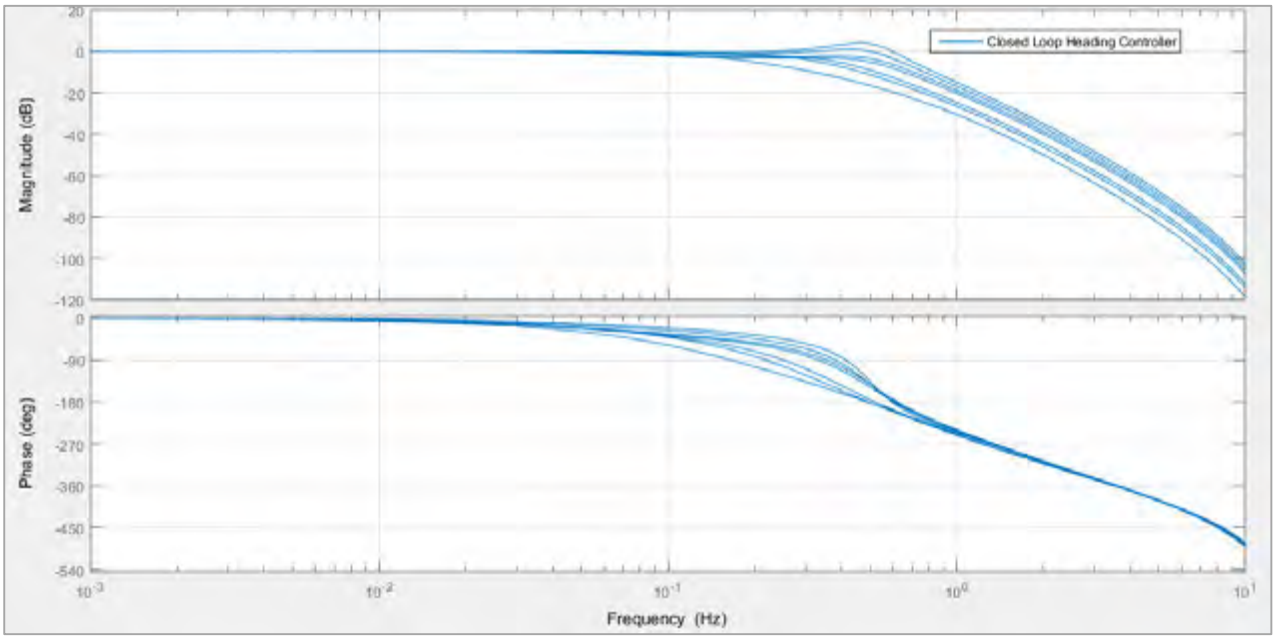

Figure 151 - Closed-loop frequency response for heading controller

The worst case bandwidth specification is taken at the -3 dB point and was found from Figure 151 to be 0.53 Hz. The system can be seen to have a resonant peak of 4.01 dB at 0.45 Hz.

To assess continuous tracking capabilities of the controller over the whole speed range of the ROV, a frequency was selected from Figure 151, whereby a gain range of -1.35 dB to -0.53 dB and a range of -57.8˚ to -21.4˚ phase was expected. The frequency chosen was 0.095 Hz and sine waves of a variety of amplitudes were inputted into the system at this frequency. The results are shown following in Figure 152.

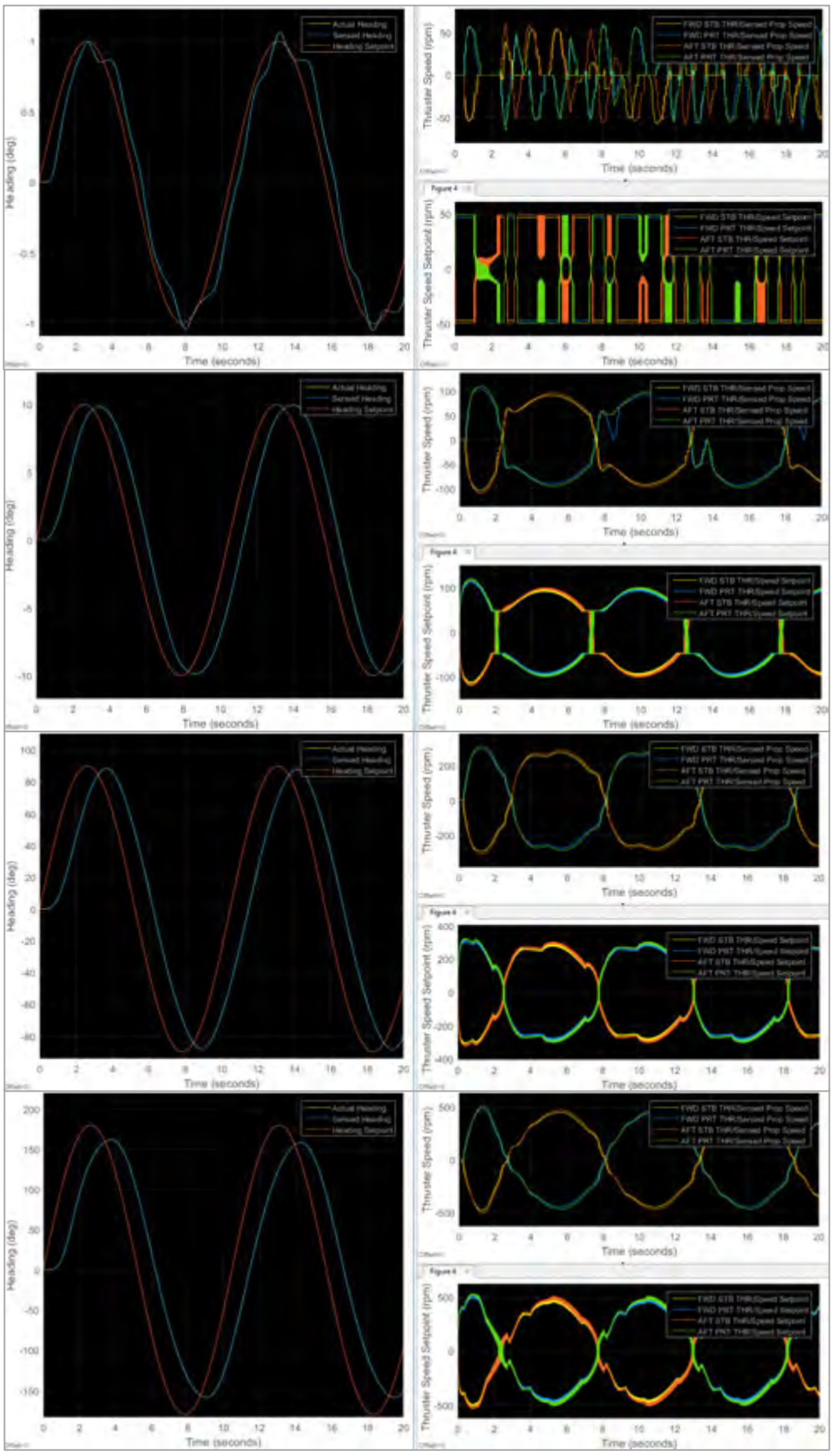

Figure 152 - Heading controller response to different amplitude input sine waves

The gain and phase was calculated from each of the simulations shown in Figure 152 previously. The results are given following in Table 49.

Table 49 - Manually calculated gain and phase for heading controller response to different amplitude sine waves

Frequency	Amplitude (deg.)	Gain (dB)	Phase (deg.)	Expected Gain (dB)	Expected Phase (deg.)
0.095	1	0.51	-3.8	-1.35 to -0.53	-57.8 to -21.4
	10	-0.03	-30.6		
	90	-0.21	-36.8		
	180	-1.13	-43.0		

It can be seen that the results correlate with the expected results from the closed loop response of Figure 151 quite well. In general the gain is higher than expected however and the results from the 1˚ amplitude wave do not correlate very well. However, due to the close proximity of the control action to the deadband for small amplitude actuation, the results are expected to show some variation to the case that excludes nonlinear effects such as deadband. The effect of the deadband control action on the results can be seen previously in the top graph of Figure 152.

This completes an analysis of the controller across different operational scenarios, showing sufficient compliance with controller objectives and allowing the controller to be summarised in the following section.

8.3.7 Heading Controller Summary and Specification Characteristics

A heading controller was designed for the *SEAHOG* whereby the controller would control a desired level of thrust which would in turn be converted to a propeller speed and allocated to each of the four horizontal thrusters.

For the heading controller it was assumed that the ROV would remain close to horizontal throughout operation and therefore the ROV plant did not include unsymmetrical aspects like the 20 N buoyancy force present in the decoupled depth controller model. Therefore, an integrator was not necessary and the heading controller was designed using a proportional gain and a dominant lead compensator. This provided enough phase so that the gain could be scheduled so as to obtain a consistent response from the controller regardless of step size and maintain stability.

Due to the deadband of the thruster speeds, a discontinuous control law was applied so as to bring the setpoint tracking capability of the controller to within ±0.2˚ of the setpoint. Chattering caused by the control law was reduced by effectively creating a much smaller deadband region, within which the thruster speed input would be 0 rpm.

The controller was tuned to be slightly overdamped and showed consistency across different amplitudes of step inputs. In addition, a closed loop frequency response was conducted at different linearization points. When the frequency response was compared to the time response of the controller to different amplitude sine waves, there was good consistency between the two analyses.

Values in the “Typical Value” column following in Table 50 were derived by taking an average of the data presented in this section. 95% rise time data is derived from Table 48, bandwidth is derived from Figure 151 and gain and phase margins are derived from Figure 149. Table 50 following shows the final characteristics that were derived for the heading controller.

Table 50 - Heading controller characteristics

Characteristic	Typical Value	Worst Case Value	Units
Setpoint Tracking Accuracy	±0.2		deg.
Bandwidth	0.36	0.14	Hz
Rise Time	3.91	4.79	s
Damping Characteristic	Overdamped		
Gain Margin	11.2	6.0	dB
Phase Margin	70.7	47.0	deg.

Finally, Figure 153 following shows the response of the heading controller to a variety of inputs.

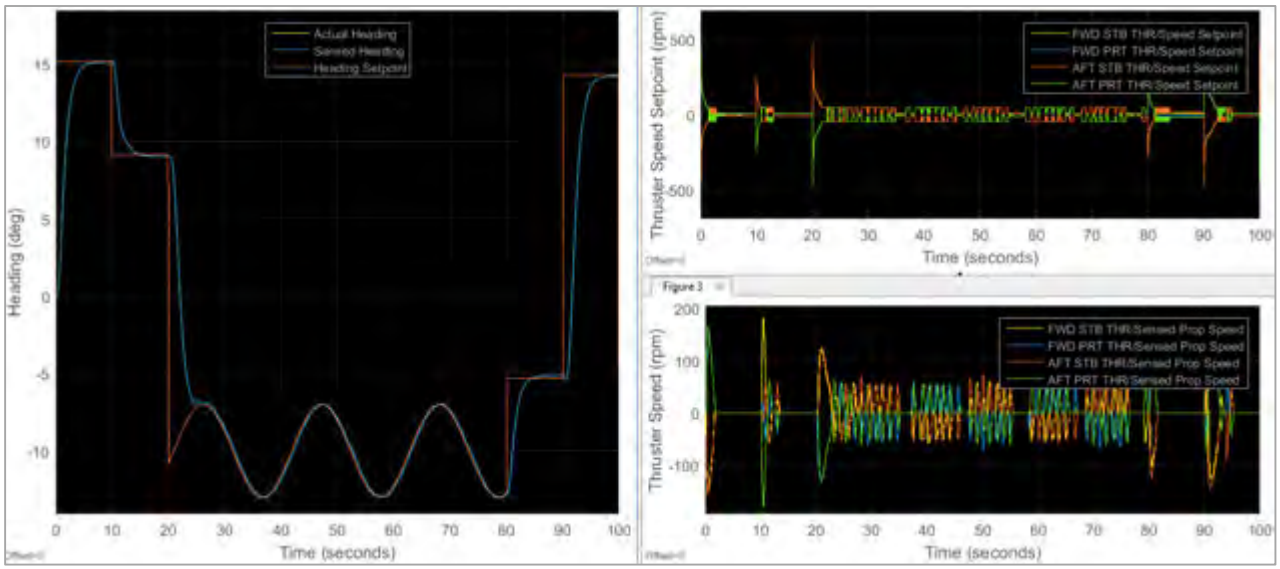

Figure 153 - Response of heading controller to varied inputs

To compare the adaptive controller to a non-adaptive case, the simulation shown in Figure 153 was repeated with a non-adaptive controller. A sensible proportional gain was chosen that corresponded to a tuned 40˚ step response. The gain chosen was 0.0032 and the resulting system response is shown following in Figure 154.

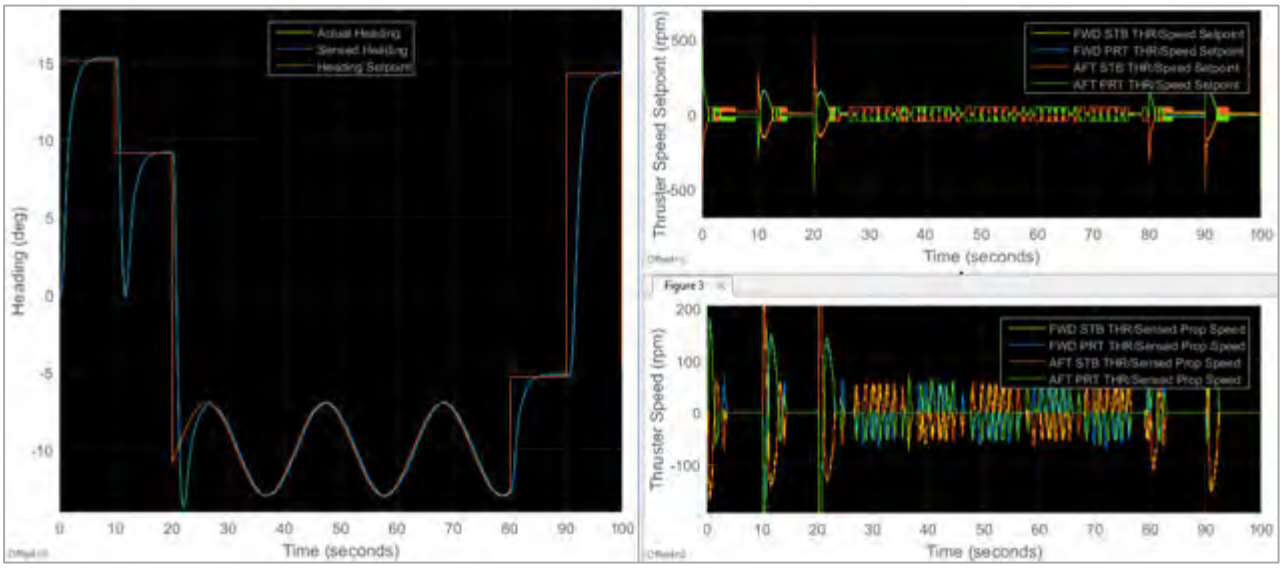

Figure 154 - Response to mixed inputs from standard non-adaptive heading controller

As can be seen in Figure 154, far more overshoot is experienced in some of the transitions between setpoints, demonstrating the necessity of finely tuned gains to warrant a uniform system response. This completes a description of the heading controller and its design. Both the heading and the depth controller have been successfully designed and it is therefore possible to summarise each of their designs in the following section.

8.4 Controller Design Summary

8.4.1 Summary of Controller Designs

Each of the two controllers designed in this chapter used classic linear control methods and were designed to be implemented digitally on a controller executing at 50 Hz. Gain scheduling was employed so as to account somewhat for the nonlinearities in the ROV and thruster dynamic models and provide a consistent response across different operating conditions. Both controllers were designed with broad objectives in mind as opposed to detailed specifications so as to provide a benchmark for future controllers to improve on.

Depth Controller:

An integrator was necessary in the depth controller due to the 20 N bias buoyancy force in the vertical ROV plant. A derivative element was included so as to add phase to the system, as it was not possible to stabilise the system using a controller with proportional and integral elements alone. Controller gain scheduling logic was designed to condition each input as a step that had a previously tuned gain value. The integrator gain was chosen as the scheduled gain due to the structure of the controller: the integrator gain was shown to have the most effect on the overall controller gain, without altering the derivative time constants significantly for a wide range of gains. For continuous inputs, in order to not continually reset the integrator, an adaptation deadband was applied, whereby if two input steps were small compared to each other, the integrator would not be reset. Finally, to account for the buoyancy force, feed forward elements were included in the controller so as to compensate for the additional gain provided by the plant itself in the ascending direction.

The controller was shown to successfully track different step setpoints and continuous setpoints to within ±100 mm as per the resolution of the depth sensor.

Heading Controller:

The heading controller could achieve near-perfect setpoint tracking without an integrator due to the absence of inherent bias forces in the ROV plant such as the buoyancy force for the depth controller. As a result, a proportional gain combined with a derivative element, in the form of a dominant lead compensator, was designed to provide setpoint tracking control. The lack of integrator allowed a large phase margin to be created, and hence the proportional gain could be scheduled to provide a uniform response regardless of step size.

The deadband of the thrusters proved to be a significant factor in the controller because as the error decreased, so did the control signal. Hence, once the control signal reached the thruster speed deadband,

the effective thruster speed output would drop to 0 and there would be no applied thrust. To prevent this and provide setpoint tracking to within a tolerance of ±0.2˚, a discontinuous control law was applied at the deadband, where the minimum propeller speed was applied if the desired control signal fell within the deadband. To lessen the effects of chattering caused by the discontinuous control law, a smaller deadband was created, wherein the control signal would not be modified, resulting in a propeller speed of 0 rpm.

Simulations were conducted, showing that a reasonably uniform response was obtained across all step sizes. In addition, the controller was shown to successfully track continuous input sine waves. The closed-loop frequency characteristics of the system correlated well with time domain simulations, showing that the bandwidth characteristics for the system could be estimated reasonably accurately.

Overall, both controllers showed adequate performance and were concluded to serve as a sufficient baseline on which other future controllers could improve. An aspect that was out of the scope of this project however was the implementation and testing of the controllers on the *SEAHOG* hardware. There are known disadvantages of using classic model-based control techniques in an underwater environment. Therefore, the expected shortcomings of the controllers designed in this report will be discussed in the following section.

8.4.2 Summary of Expected Controller Performance Issues

Typically, model-based controllers in an underwater environment yield disappointingly degraded performance in real life compared to in a simulation environment [17]. This is due to the ill-defined nature of the underwater environment and the abundance of model uncertainties. Classical linear controllers are also ill-suited to the environment due to nonlinearities in the hydrodynamic, thruster and inertial properties of the model and cross coupling effects between motion in different DOFs. In addition, un-modelled environmental disturbances from currents and the tether can have a significant effect on the motion of the body. As a result, the finely tuned controller parameters of PID controllers do not provide robust performance to these factors, causing performance to degrade rapidly.

Some of the issues related to modelled nonlinearities are overcome in the controllers developed in this report, however the controllers are not expected to be robust in the face of external disturbances, motion coupling or model uncertainties. In addition, the controller conditioning logic developed in this report requires fine tuning and may not provide an optimal response in real life and could introduce anomalous behaviour.

As previously stated however, due to the focus on system modelling in this project, it was envisaged for some basic controllers to be designed as a benchmark upon which future work could improve. In order to experimentally verify any designed controllers, it is necessary for the *SEAHOG* to reach a level of development such that it can be tested in a real life environment.

This completes the chapter on controller design, having listed in detail the design of a depth and heading controller for the *SEAHOG* ROV and included expected shortcomings of the chosen design scheme. The full ROV system can now be simulated with the designed controllers, allowing the effectiveness of the controllers to be assessed in a simulation environment.

Chapter 9 - Complete System Simulations

9.1 Introduction

A depth and heading holding controller have been designed for the *SEAHOG* ROV using the decoupled equations of motion for the relevant DOFs. This largely completes the work within the scope of this project. It is necessary however to assess the performance of the designed controllers within the context of the full ROV model and discover how some of the assumptions that were made in the controller design impact the overall system. Subsequently, the performance of the controllers in the complete system will observed, which will serve to inform design decisions in future work.

The ROV model that was developed and used in chapter 6 for open-loop simulations included the following elements:

- Five homogenous thruster models
- *SEAHOG* ROV model
- Depth and attitude sensor models
- Depth sensor mapping from actual to estimated depth

The depth and heading holding controllers were subsequently integrated into the existing Simulink® model, completing the system model within the scope of this report and allowing the heading and depth related thruster inputs to be automatically controlled.

Simulations of the full system with the integrated controllers were conducted so as to assess the controller's expected effectiveness within the system. Specifically, the following scenarios were evaluated:

S_E1. Separate and simultaneous depth and heading setpoint inputs in the absence of any other operator inputs (such as horizontal X and Y thrust).

S_E2. Controllers holding depth and heading setpoints in the presence of short periods of large X and Y operator thrust inputs.

S_E3. Controllers holding heading and depth setpoints in the presence of prolonged, low thrust levels in surge.

S_E4. The effects of control action on the attitude of the ROV body itself.

Each of the above simulations will be described in the following section with their accompanying results and motion analyses.

The complete system Simulink® block diagram is shown following in Figure 155.

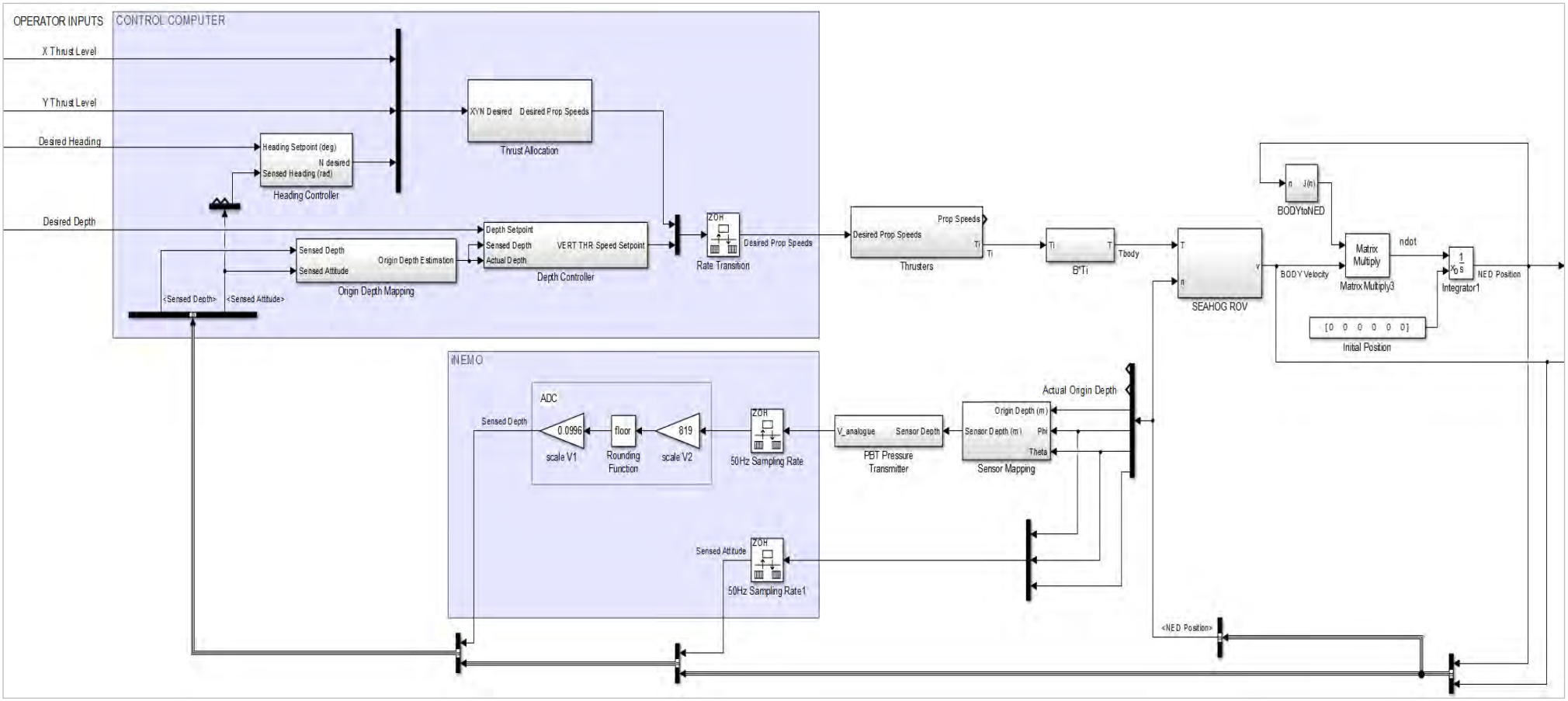

Figure 155 - Simulink® block diagram for complete *SEAHOG* system

9.2 Simulation Scenarios and Results

9.2.1 S_E1 - Heading and Depth Controller Only

The controllers for depth and heading holding developed in this report were designed using a model of the decoupled motion of the ROV in the relevant DOF. As has been previously mentioned, motion cross-coupling can have a detrimental effect on the performance of PID type controllers in an underwater environment. However, due to simulations conducted in chapter 6 of this report, it was established that the separate motion for heave and yaw on the *SEAHOG* was sufficiently decoupled from other motion to be isolated and used as the basis for designing a controller. The controllers are therefore expected to perform as designed in the complete system if there are no other system inputs. It should be noted however, that motion coupling from other ROV manoeuvres (such as surge and sway) are expected to influence the controllers' performances. S_E1 however, is provided to establish that designing the controllers in a decoupled model was in fact a valid basis for the controller designs.

S_E1 simulated heading holding and depth holding manoeuvres in the absence of other operator inputs. The resulting ROV motion therefore was an indication of if cross-coupled drag and inertia had a significant effect on the controllers. A timeline of the simulation is given following in Table 51.

Table 51 - Simulation timeline for separate depth and heading control simulation S_E1

Simulation Time (s)	**0**	**30**	**40**	**55**	**65**	**100**	**110**	**140**
Heading Setpoint (deg.)	0	10	→	-120	→	→	0	END
Depth Setpoint (m)	0	→	0.5	→	-5	0	→	
Other Inputs	None							

Simulation S_E1 was characterised by a small heading and depth step input, separately executed and then repeated with a large step input for each. In Table 51 above, the heading and depth are then set to 0˚ and 0 m at a time of 100 s and 110 s respectively. This final depth and heading manoeuvre is considered to be executed simultaneously since the depth is still being adjusted when the heading setpoint is inputted. The resulting motion from the simulation inputs allowed the performance of the controllers to be assessed separately in the whole ROV system. The motion of the system under the influence of separate and simultaneous controller action could be analysed. The simulation was sufficient to observe all motion that was induced from the controllers in the absence of other inputs and disturbances.

The simulation results from scenario S_E1, as described by Table 51 previously, are shown following in Figure 156.

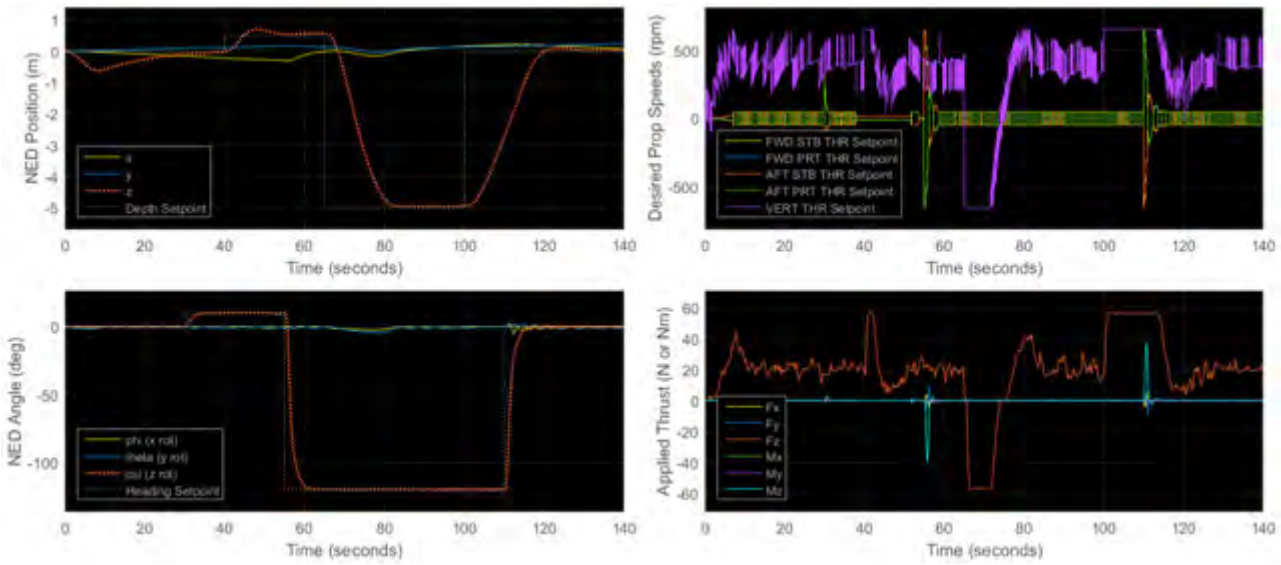

Figure 156 - S_E1 Simulation scenario: resulting motion and control inputs

Figure 156 shows that the controllers performed as designed in the previous chapter. The controller performance was expected to match the performance derived in the previous chapter for the decoupled controller designs, due to how the yaw and depth motion was largely decoupled from the other ROV motion. In addition, due to the orthogonal nature of the vertical and horizontal thrusters, it was expected that both controllers could execute heading and depth holding manoeuvres simultaneously and perform as designed, as shown in Figure 156.

Figure 157 following shows zoomed in views of the depth and heading setpoints, showing that the depth is maintained to within 0.1 m of the setpoint and the heading is maintained to within 0.2˚ of the setpoint, both as specified in chapter 8.

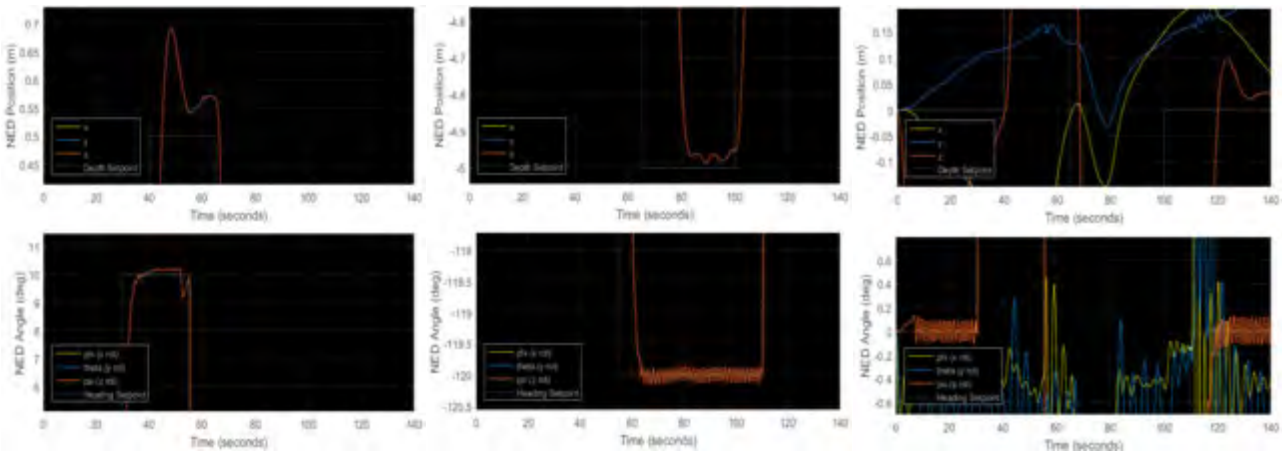

Figure 157 - Detail from S_E1

Comparing the controllers' responses in Figure 156 to simulation results in chapter 8, both the depth and heading controller perform within their designed characteristics throughout the simulation, showing that the decoupled models used to design the controllers were in fact a valid basis upon which to base the designs.

9.2.2 S_E2 - Short Periods of Large Horizontal Thrust Inputs

To assess the influence of high thrust user inputs on the heading and depth controllers, S_E2 was conducted. The influence of X and Y thrusts on the N moment supplied by the heading controller were expected to be observed in this simulation, given that X, Y and N are all supplied by the four horizontal thrusters. Also, the change in vehicle attitude due to the horizontal thrust inputs was expected to allow the performance of the depth controller to be assessed when the ROV was not in a close-to horizontal state.

Thrust inputs with a waveform shown following in Figure 158 were used to simulate the user inputs introduced into the system.

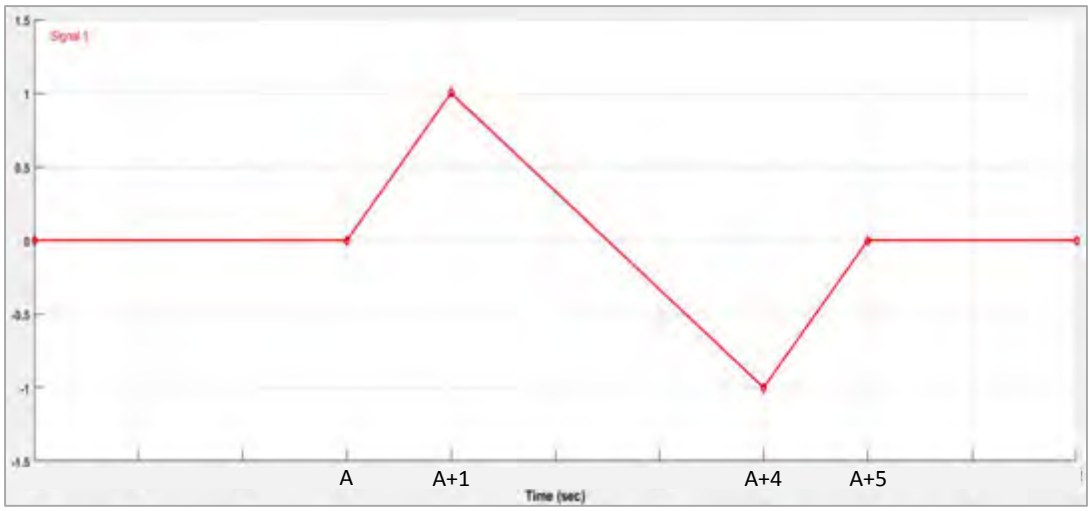

Figure 158 - Operator inputs used to simulate positional adjustments by an operator

The point labelled "A" in Figure 158 was used to denote the beginning of an identical waveform in the simulation timeline following. Figure 158 shows a ramp from zero to full thrust over 1 s, decreasing to full thrust in the opposite direction over 3 s and finally returning to zero thrust over 1 s.

The simulation timeline for S_E2 is shown following in Table 52.

Table 52 - Simulation timeline for short, large horizontal thrust inputs simulation S_E2

Simulation Time (s)	**0**	**40**	**52**	**65**	**90**
Heading Setpoint (deg.)	0	→	→	→	
Depth Setpoint (m)	0	→	→	→	END
Thrust in Surge	0	A	→	A	
Thrust in Sway	0	→	A	A	

S_E2 allowed the performances of the controllers to be assessed first under an operator input in surge, then sway and then both surge and sway simultaneously. This allowed the expected behaviour of the ROV to be observed under slight positional adjustments executed by the operator.

The simulation results from scenario S_E2, as described previously in Table 52 are shown following in Figure 159.

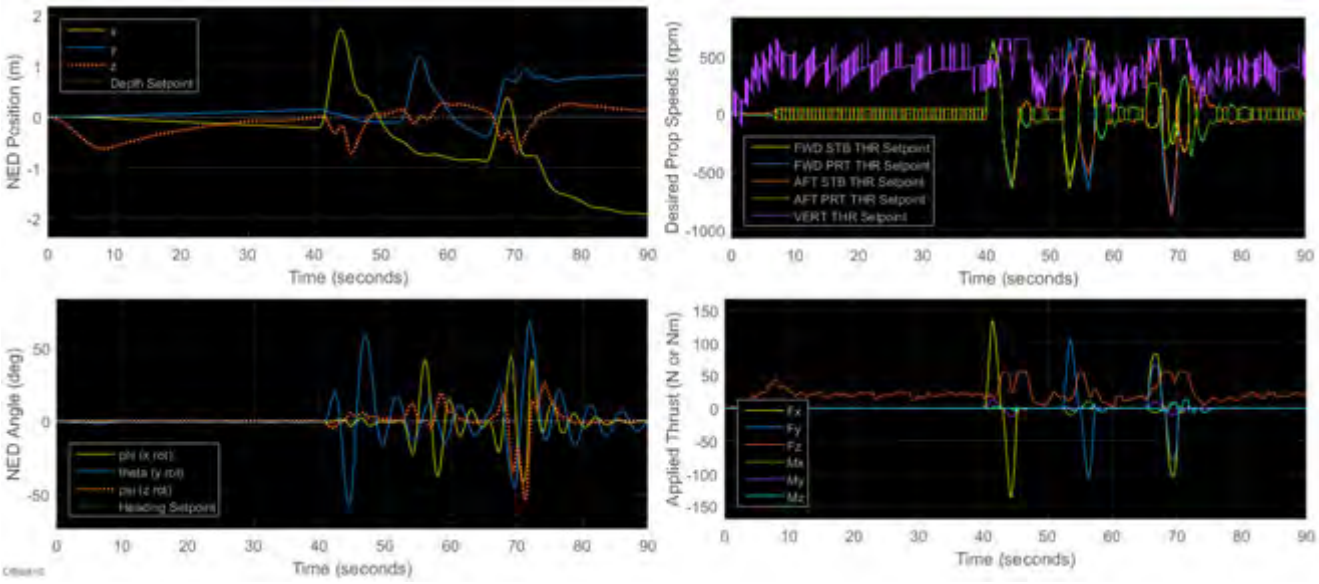

Figure 159 - S_E2 Simulation scenario: resulting motion and control inputs

Figure 159 shows that a large heading disturbance is experienced around 70 s, when a thrust is applied in both the surge and sway directions.

To investigate the controller performance under the influence of separate surge and sway operator inputs, a detailed version of Figure 159 is given following in Figure 160.

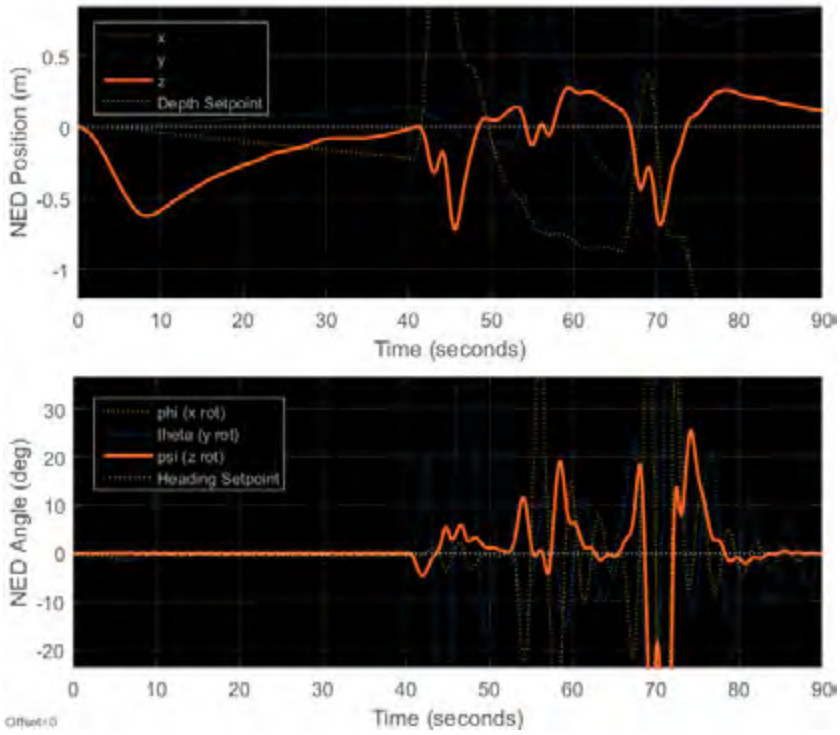

Figure 160 - Detail from S_E2

The results of the controller performance under the influence of the simulated operator inputs is given following in Table 53.

Table 53 - Performance of depth and heading controllers in S_E2

	Disturbance in x	Disturbance in y	Disturbance in x and y
Maximum Departure from Heading Setpoint	6.0˚	19.0˚	54.0˚
Maximum Departure from Depth Setpoint	0.7 m	0.3 m	0.7 m

It can be seen that the performances of the controllers degrade in the presence of other user inputs. However, the following inferences can be drawn from Table 53:

1. The heading controller loses setpoint holding capability under the influence of external torques applied to the ROV hull in the form of cross-coupling drag effects from motion in surge and sway. The torque output N from the controller was tuned without the influences of disturbances as a consideration, therefore the control action is insufficient to maintain the desired heading under the drag torques induced by horizontal translational motion.
2. It is possible that the scaling of thruster inputs applied in the thrust allocation scheme and given previously in equation 6.116 results in the desired yaw moment being attenuated. This could be inferred because there is a larger departure from the heading setpoint during simultaneous x and y operator inputs, as shown previously in Table 53. Applying a maximum X and Y thrust simultaneously will result in the output thrust from the thrust allocation matrix needing to be scaled down so as to lie within the achievable thrust range of the thrusters. Therefore, while the thrust allocation scheme developed in chapter 6 will apportion the thrust inputs in the correct ratio, the absolute value of the applied yaw moment may be smaller than desired by the controller.
3. The effectiveness of the depth holding controller is related to the roll and pitch angles of the ROV. This can be inferred since there isn't a notable increase in departure from the setpoint between the cases when x and y inputs are applied separately and simultaneously. In addition, the orthogonality of the thrust provided by the vertical thruster compared to the horizontal thrusters suggests that the attitude of the ROV alone, excluding other thruster inputs, will influence the performance of the depth controller.

With the investigation into the effectiveness of the controllers in the presence of short periods of large operator inputs complete, insight from the results can be used to investigate the results of the following simulation and confirm or refute the inferences made from this simulation scenario.

9.2.3 S_E3 - Prolonged Low Thrust Levels in Surge

A manual navigation operation for an ROV will typically proceed by moving forwards a particular distance at a certain depth and heading. In order to assess the depth and heading controllers in a navigational type manoeuvre, S_E3 was conducted. From results in chapter 6, it was observed that during a surge manoeuvre the ROV oscillated in the pitch and roll DOFs. These oscillations can be thought of as uncertainties in the decoupled models on which the depth and heading controllers were designed. It is known that classical PID control methods do not perform well in the presence of uncertainties (which are abundant in an underwater environment). While the effects of uncertainties on the controllers' performances were not directly assessed (by varying model parameters), the varying attitude of the ROV body during motion in surge could be thought of as uncertainties in the models that were used to design the controllers. Therefore, in a sense, S_E3 was expected to give insight into the performance of the controllers in the presence of model uncertainties and hence it was expected that the controllers would exhibit degraded performances in the simulation.

A timeline of the simulation inputs of S_E3 is given following in Table 54.

Table 54 - Simulation timeline for prolonged, low thrust in surge simulation S_E3

Simulation Time (s)	**0**	**30-50**	**80**	**110-120**	**160**
Heading Setpoint (deg.)	45	→	-135	→	END
Depth Setpoint (m)	0	→	5	→	
Thrust level in Surge	0	Ramp from 0 to 0.2	0	Ramp from 0 to 0.2	

The ROV was commanded to follow a heading of 45˚ for 80 s before turning 180˚ and returning along its path. The discrepancies in x and y distance travelled could be used as a measure of how accurately the 45˚ heading was maintained.

The simulation results from scenario S_E3, as described previously in Table 54 are shown following in Figure 161.

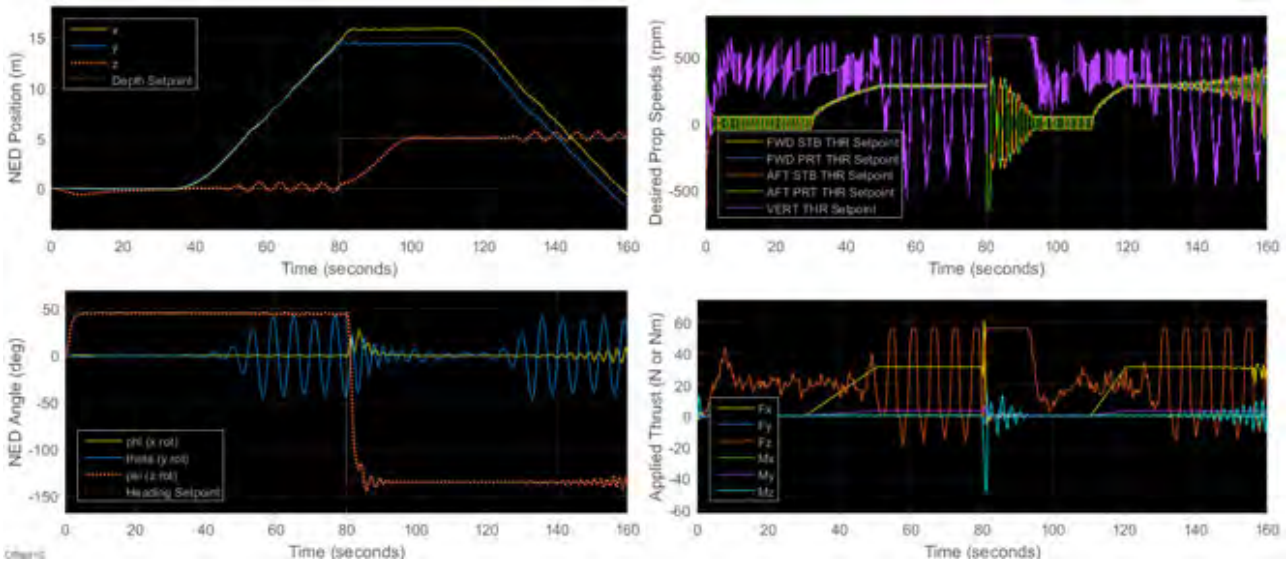

Figure 161 - S_E3 Simulation scenario: resulting motion and control inputs

A detailed view of the results is given following in Figure 162 to show the depth and heading profiles in greater clarity.

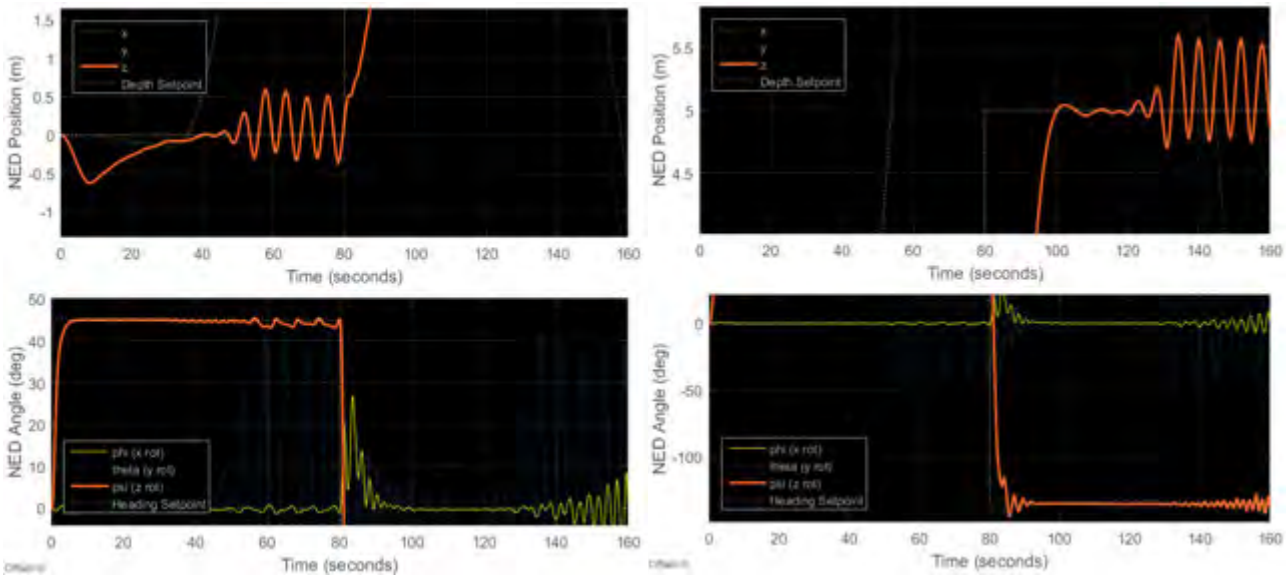

Figure 162 - Detail from S_E3

It can be seen immediately from Figure 161 that the depth of the ROV oscillates in a relative phase to the oscillation of the pitch. This confirms the inference that the attitude of the ROV has the greatest effect on the depth holding capabilities of the depth controller. Once again, the performance of the depth controller is significantly degraded.

The left hand side of Figure 162 shows that the heading controller experiences a small amount of performance degradation as the heading deviates from the setpoint under the influence of motion coupling torques that were induced as a result of the surge thrust operator input. However, the deadband control is seen to periodically correct the heading, resulting in a minor deviation from the desired course.

Figure 161 shows that the small initial deviation in heading in the first 80 s of the simulation was not significant: at a simulation time of 80 s it can be observed that the x and y distance, which should be equal due to the 45˚ heading, are in fact very similar.

Towards the end of the simulation however, the heading is seen to begin to oscillate around the setpoint. This can be attributed to the increased oscillations in roll towards the end of the simulation. As the roll oscillation increased, so did the heading oscillation.

The performances of the controllers were assessed at the worst case deviation from the setpoint in the first and second 80 s of the simulation and the results are presented in Table 55 following.

Table 55 - Performance of depth and heading controllers in S_E3

	Maximum Value		Minimum Value		Value Range	
Simulation Time	1st 80 s	2nd 80 s	1st 80 s	2nd 80 s	1st 80 s	2nd 80 s
Departure from Heading Setpoint	0˚	7˚	-2.8˚	-7.5˚	2.8˚	14.5˚
Departure from Depth Setpoint	0.6 m	0.6 m	-0.3 m	-0.3 m	0.9 m	0.9 m

The data observed in this simulation proves that inference 3 from the previous section is true: that the depth tracking capabilities of the depth controller are influenced primarily by the attitude of the ROV.

Inference 1 from the previous section stated that the heading control design is insufficient to counteract induced torques from drag cross-coupling effects. From the left hand side of Figure 162 previously, it can be seen that the heading controller can in fact hold the heading to some degree under externally induced torques. However, the oscillatory motion experienced by the heading towards the end of the simulation could imply that the nature of the control response will change under the influence of uncertainties present in the real life operating environment.

Inference 2 from the previous section stated that the drop in heading holding capability of the controller could be due to the thrust allocation scheme developed in chapter 6. Due to this simulation's thruster inputs operating far away from propeller speed saturations, it can be assumed that the thrust allocation scheme is not a contributing factor to the drop in performance experienced by the heading controller in this simulation.

As a result of the simulations S_E1 to S_E3, it can be assumed that the decrease in heading and depth tracking performance from the controllers can be reasonably attributed to the varying attitude of the ROV under the influence of horizontal thrusts from an operator. However, the thrust allocation scheme can contribute, depending on open-loop operator inputs, to the desired moment from the heading controller being scaled down and not being as large as desired when applied to the thrusters.

Controller performance degradation was expected, due to the known shortcomings of the chosen controller designs. It should be noted however that effects such as the limit on the thrust that the thrusters can produce could prove to be a significant influence even on more advanced controllers' performances when allocating thrust to thrusters according to desired thrust inputs.

For ease of operation, a final investigation into the effects of the control action on the ROV was conducted and is given in the following section.

9.2.4 Effects of Control Action on ROV Attitude

As found in chapter 6, the current hydrostatic design of the *SEAHOG* results in a fair amount of oscillation in its attitude during manoeuvres in the surge direction. It was important to establish if the control action of the controllers would contribute to decreasing the stability of the ROV during translational manoeuvres.

S_E4.1: A simulation was undertaken to establish the open-loop attitude characteristics of the ROV under the current system setup. An input of 400 rpm was supplied to the vertical thruster, resulting in close-to neutral buoyancy. When the initial vertical motion due to the buoyancy force had been arrested, a full surge input was supplied to the horizontal thrusters. This simulation served to characterise the attitude of the ROV in the absence of control action and to serve as a baseline upon which to compare the ROV attitude under the influence of the controllers. A timeline for the open loop simulation is given following in Table 56.

Table 56 - Simulation timeline for open-loop motion simulation S_E4.1

Simulation Time (s)	0	2	30
Vertical Thruster Input (rpm)	400	→	END
Thrust Level in Surge	0	1	

The results of simulation S_E4.1, shown following in Figure 163, give the characteristics of the *SEAHOG*'s open-loop motion response to a full surge input.

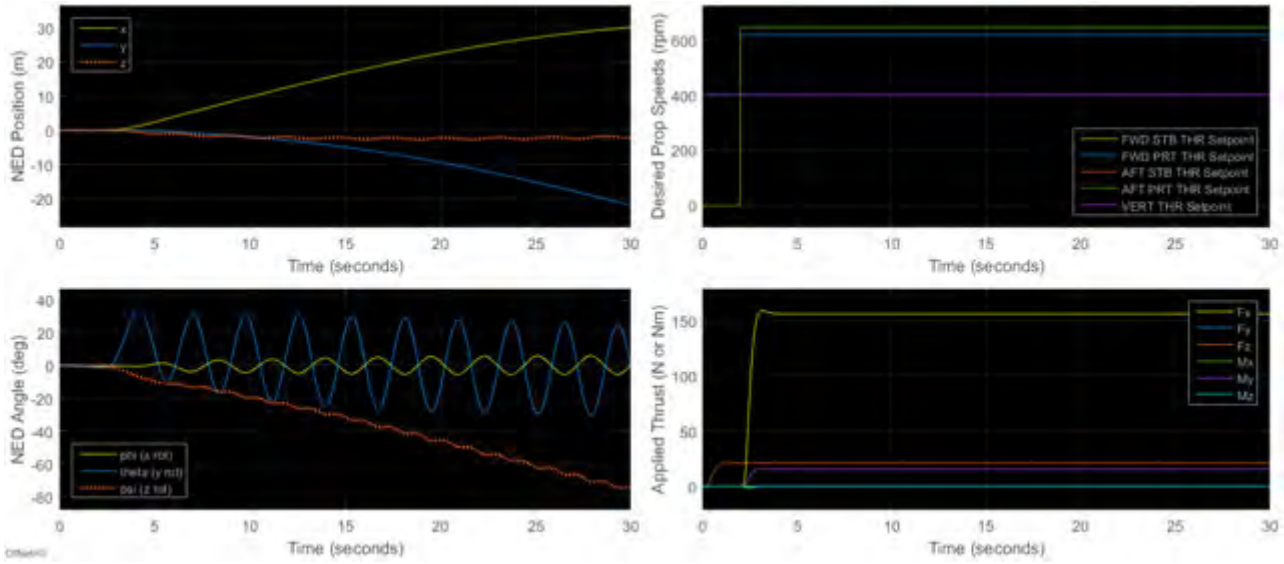

Figure 163 - S_E4.1 Simulation scenario: resulting motion and control inputs

It should be noted, shown by the applied thrust in the bottom right of Figure 163, that before the surge input was applied, the vertical motion of the ROV was arrested by an open-loop heave input from the vertical thruster. The resulting motion from Figure 163 gives a baseline against which simulations S_E4.2 and S_E4.3 can be compared. The resulting oscillation of the pitch and roll in an open-loop configuration is given following in Table 57.

Table 57 - S_E4.1 Open-loop motion characteristics

DOF of Oscillations	Average Amplitude	Average Period	Signal Mean (T ϵ [25;30] s)
Roll	5.5˚	2.9 s	0.25˚
Pitch	28.0˚	2.9 s	-2.5˚

With a baseline established from which simulations S_E4.2 and S_E4.3 could be compared, it was possible to investigate the influence of the depth and heading controllers on the attitude of the ROV.

S_E4.2: A simulation was conducted whereby the depth controller was commanded to hold the ROV at a depth of 0 m. After the ROV had initially stabilised, a full surge thrust input was supplied to the horizontal thrusters. This simulation was compared to S_E4.1 to observe the effect of the controller action on the ROV attitude. A timeline for the simulation is given following in Table 58.

Table 58 - Simulation timeline for depth controller effect on ROV attitude simulation S_E4.2

Simulation Time (s)	0	35	60
Depth Setpoint (m)	0	→	END
Thrust Level in Surge	0	1	

The results of simulation S_E4.2 are shown following in Figure 164.

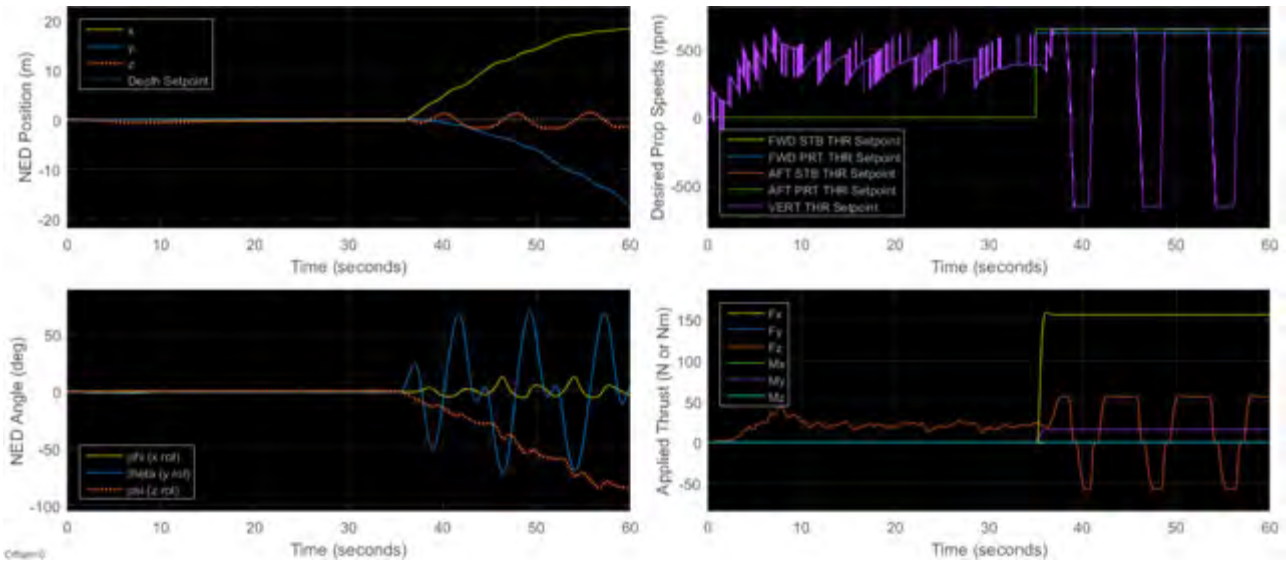

Figure 164 - S_E4.2 Simulation scenario: resulting motion and control inputs

It can be seen that the ROV pitch increases rapidly as the surge input is applied. A limit cycle is observed in the pitch and roll of the ROV with almost double the amplitude oscillations to that of the open-loop motion observed previously in Figure 163. However, the ROV never reaches a greater pitch amplitude than 70˚, avoiding an ill-defined system state at 90˚ pitch.

Initially, the thrust from the depth controller is positive. As the ROV pitches down, the depth controller is seen to correct for the increasing depth and the thrust direction is reversed. As the thrust in the heave direction is reversed, the pitch starts to increase rapidly. From this it can be inferred that the thrust

direction of the vertical thruster has a significant influence on the pitching of the ROV. The more negative the vertical thruster thrust output is, the greater the pitching of the ROV will be.

In summary, it is not recommended to apply full surge inputs under the influence of the depth controller due to the large amount of pitching imparted to the ROV. It is recommended to apply a constant positive thrust in heave until the desired horizontal position is reached. Then the depth controller can be applied.

With the effects of the depth controller on the ROV stability understood, the effects of the heading controller needed to be investigated.

S_E4.3: To investigate the heading controller's effect on the ROV, a similar simulation to S_E4.2 was conducted, except a constant input was supplied to the vertical thruster while the heading was held constant. A timeline for the simulation is given following in Table 59.

Table 59 - Simulation timeline for heading controller effect on ROV attitude simulation S_E4.3

Simulation Time (s)	0	10	40
Heading Setpoint (deg.)	0	→	END
Vertical Thruster Input (rpm)	400	→	
Thrust Level in Surge	0	1	

The results for S_E4.3 are given following in Figure 165.

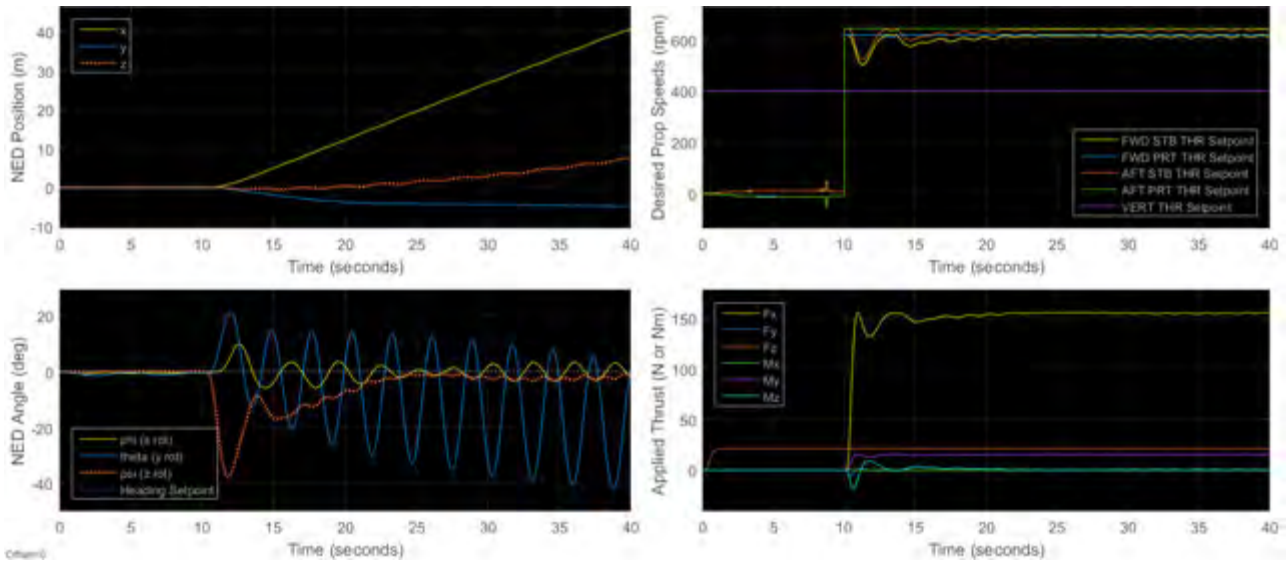

Figure 165 - S_E4.3 Simulation scenario: resulting motion and control inputs

When compared to the open-loop motion in Figure 163 previously, Figure 165 shows that the heading controller does not contribute significantly to increasing the pitching and rolling of the ROV. The simulation shows that the controller is somewhat capable of reaching its desired setpoint after the initial disturbance of the surge input, although a steady state offset of about 2˚ is observed. Table 60 following shows the results for the heading controller's effects on the ROV motion, displayed in the same manner as Table 57 previously.

Table 60 - S_E4.3 Effects of heading controller on motion

DOF of Oscillations	Average Amplitude	Average Period	Mean (T ϵ [25;30] s)
Roll	≈2.5˚	3.0 s	0.0˚
Pitch	23.0˚	3.0 s	-17.0˚

The differences between motion under the influence of the heading controller and in the open-loop case are given following in Table 61. Values were calculated by subtracting Table 57 values from Table 60.

Table 61 - Comparison of motion in S_E4.1 and S_E4.3

DOF of Oscillations	Average Amplitude Difference	Average Period Difference	Difference in Mean (T ϵ [25;30] s)
Roll	-3.0˚	0.1 s	-0.25˚
Pitch	-5.0˚	0.1 s	-14.5˚

Table 61 shows that the heading controller decreased the amplitude of oscillations slightly in the ROV attitude and caused the ROV to pitch down to a greater extent than in the open-loop case.

This completes all of the investigations into the full automatically controlled *SEAHOG* system, allowing for a summary of the results to be given following.

9.3 Summary of Complete System Simulations

With the complete *SEAHOG* system available for simulation, this chapter served to investigate the performance and effectiveness of the designed controllers in a complete system simulation environment. Simulations were conducted for typical ROV manoeuvres such as minor position adjustments and navigation.

Performance of the controllers in the absence disturbances and other horizontal thrust inputs was assessed by conducting depth and heading holding manoeuvres separately and simultaneously. Open-loop simulations in chapter 6 demonstrated how the heave and yaw motion was decoupled sufficiently from the rest of the body's motion so that it could be isolated and used to design controllers. The controllers performed according to their designed characteristics and subsequently it was shown that a decoupled dynamic model was valid grounds on which to design the controllers.

Through simulations where user inputs were applied to the horizontal thrusters, it was established that both the controller performances were reduced significantly in the presence of X and Y applied thrusts. It was found that the effectiveness of the depth holding controller was directly related to how close to horizontal the pitch and roll of the ROV was. The presence of oscillations in the roll and pitch of the ROV resulted in a limit-cycle type response from the depth controller, oscillating about the setpoint.

The heading controller was shown to be reasonably robust to horizontal thrust inputs separately in surge and sway but degraded considerably for simultaneous surge and sway inputs. It was suspected that the thrust allocation scheme developed in chapter 6 could have been a reason for this and that the propeller input scaling function was impacting the performance by scaling down the moment desired by the controller. However, in S_E3 whereby the propellers were not operating close to their speed limits, the performance of the heading controller was still degraded over time. It was therefore clear that the controller scheme was insufficient to correct the heading in the presence of uncertainties and torques induced by the motion of the ROV. It was concluded that the effects of torques applied by motion cross-coupling were in many cases too great to be overcome by the PD controller scheme.

Finally, simulations were conducted to investigate the effect of the controllers on the hydrodynamic stability of the ROV. It was shown that the heading controller does not have a significant impact on the ROV stability. However, it was shown that if thrust was applied in surge, the more negative the vertical thruster thrust was, the more the ROV tended to pitch up. As a result, it was recommended that while the ROV is conducting horizontal motion at high thrust, a constant positive thrust from the vertical thruster should be applied. The depth controller should only be applied once x and y thrust levels do not need to exceed about 20% of maximum thrust.

In summary, under the action of the controllers alone and in an undisturbed environment, the controllers can effectively hold the ROV's heading and depth. At low thrusts the depth controller can maintain the ROV's depth within a band of approximately 1 m, characterised by sinusoidal limit-cycle type behaviour. The heading controller's ability to hold the ROV's heading is largely determined by the amplitude of the roll motion in the ROV.

The results from this chapter provide a large amount of insight into the system design and its capabilities. The following chapter will serve to state conclusions from the insights drawn and propose recommendations for future improvements to the system. It will also provide implications of the current simulation results on the piloting of the *SEAHOG* by an operator.

Chapter 10 - Conclusions and Recommendations

10.1 Introduction

The work that falls within the scope of this dissertation has been completed. This chapter will draw conclusions from the various topics and aspects of the project covered in this report. In addition, recommendations will be made, where applicable, for future work that can draw on results from this dissertation. A trace code will be allocated to each recommendation so that future work on the *SEAHOG* project can be conducted with a clear reference and traceability from previous projects. Recommendations will be given in this chapter that either recommend improving on the work presented in this report, or recommend maintaining certain system configurations. In both cases, whether future work is undertaken as a result of a recommendation, or if the system configuration is changed from the recommended state given in this chapter, the trace code can be used to reference the motivations given for either changing or maintaining a certain system configuration. The trace codes were formulated with the following format:

REC	**16**	**MF**	**THR**	**X**	**XX**
	Year of Publication	Author Initials	Subsystem of Interest: THR = Thruster ROV = *SEAHOG* SNS = Sensors and Hardware CTR = Control Design PIL = Piloting of *SEAHOG*	Designation: H = Hardware S = Software M = Model Improvement V = Verification X = Other	Rec. Number

It should be noted that a literature review is included in Appendix A with its own conclusions and recommendations. The recommendations of Appendix A largely serve to supplement and motivate design decisions made in this dissertation but should be consulted specifically if a holistic picture is desired of possible future work to be carried out on the *SEAHOG*. Appendix B to this report takes the form of a multi-aspect design report, whereby mechanical, electrical and software modifications and improvements were undertaken as part of the scope of this project. The conclusions and recommendations section in

Appendix B should be consulted so as to gain a greater insight into future work that is necessary to further develop the *SEAHOG* ROV towards being an operational platform.

This chapter will provide conclusions and recommendations pertaining to work presented in this dissertation, specifically focussing on the following areas:

- Thruster Model and Hardware improvements
- Mathematical ROV model, including future model inclusions and improvements
- Effect of the mechanical design of the *SEAHOG* on its motion and how the design can be improved
- Comments on the hardware and sensors
- Comments on the ROV heading and depth controller performances

Following this introduction, conclusions and recommendations pertaining to the *SEAHOG* thruster systems will be given.

10.2 Thruster System

10.2.1 Thruster Mathematical Model

The thruster mathematical model was chosen as a single state model that related propeller speed to produced thrust. The thruster system was adequately developed to simulate the propeller speed response according to speed inputs, however, verification of the thrust produced by the thruster in a non-steady-state was not included in the project.

REC16MF-THR-M-01: It is known that the advance speed has a significant effect on the thrust produced and consequently the thrust that is produced from the model in this project is expected to be reduced in real life. Therefore it is recommended that a more advanced thruster model is developed, whereby the thrust output from the thruster is logged in both transient and steady states. Subsequently, a higher state thruster model could be developed, resulting in a greater accuracy in the thrust produced by the *SEAHOG* thrusters and a more accurate depiction of the system's capabilities.

10.2.2 Maxon Motor Controller

The brushless motor controller and power amplifier used in the *SEAHOG* thrusters performed reliably but appeared to give a slightly variable system response between different experimental runs. The software applied control algorithms on the Maxon motor controller proved to be one of the more challenging aspects to model and predict in this project. There was limited information as to the digital algorithms applied within the motor controller to run the motor at a particular speed. Therefore, the model created could only serve as an approximation of the real system.

Advantages of using the Maxon controller's software control algorithms are that the controller applies safety features such as limiting the acceleration of the motor so as to not over-current and damage it. The disadvantage of using the Maxon controller's control algorithms however, is that from a modelling perspective there will always be an element of uncertainty as to the control algorithms themselves.

It is possible to bypass the Maxon controller's control algorithms. While this may risk damage to the motor or amplifier, it can remove a significant uncertainty inherent in the thruster model and may serve to improve the performance of the thruster.

REC16MF-THR-H-01: It is recommended that the current setup is used however, whereby the Maxon controller's speed control algorithms are utilised. The performance of the thruster at this stage was deemed sufficient within the context of the greater ROV system and removing the Maxon's control algorithms should only be considered if there is motivation for improving the thruster performance.

10.2.3 Software Controller Design

The software controller was designed using a classic, non-adaptive PI controller structure. This proved to be robust and effective although the performance of the thruster was somewhat decreased from under the influence of the Maxon speed controller only. The additional custom designed controller was necessary so as to provide perfect speed setpoint tracking, which it drastically improved compared to the case of the Maxon controller only.

REC16MF-THR-S-01: While the performance of the thruster was once again deemed sufficient in the context of the whole ROV system, if thruster performance is prioritised over setpoint tracking capability, the controller could be removed, allowing the thruster to be controlled solely by the Maxon software controller.

One of the greatest drawbacks of the thruster software controller was the limited hardware capabilities of the MSP430 microcontroller. A larger discrepancy between simulation and real life results were observed after the inclusion of the software controller. It was suspected that the fixed-point arithmetic capabilities of the microcontroller were the greatest contributor to the observed discrepancies. A loss of arithmetic precision in the software algorithms of the controller were suspected to negatively impact on the effective speed of the controller in real life compared to the simulation.

REC16MF-THR-H-02: It is recommended that if a more accurate thruster model is required, redesign of the thruster motherboard could be warranted so as to utilise a more sophisticated microcontroller with floating point unit capabilities.

Overall, the performance of the thruster system was sufficient, with the simulation model approximating the real life response of the thruster sufficiently.

10.3 ROV Model

10.3.1 Rigid Body Mass and Inertia Properties

It should be noted that unfortunately, the experimental verification of the actual ROV model was not possible in many cases due to the incomplete state of the ROV. However, advanced CAD techniques were used with high attention to detail so as to approximate the predicted real life case as accurately as possible.

The mass and inertia properties for the *SEAHOG* are predicted to be sufficiently close to the real life values due to the computational power of Solidworks and the attention to detail that was involved in creating the ROV model.

REC16MF-ROV-V-01: Nevertheless, it is recommended that the mass properties of the ROV are verified due to some approximations that were necessary in the determining of the mass and buoyancy of epoxy coatings and subsea cables in the current model formulation.

10.3.2 Added Mass and Inertia Properties

Many assumptions were made in the approximation of the added mass terms for the *SEAHOG*. Specifically, the assumption of three planes of symmetry was enforced so as to obtain a diagonal added mass matrix. This is not the case in real life.

REC16MF-ROV-M-01: It is recommended that the added mass properties of the ROV are determined using a computational tool such as WADAM, that can determine the complete added mass matrix for a body with great accuracy.

Verification of added mass coefficients will require an extensively instrumented and controlled towing rig. It is impractical to facilitate the development of such a vast and extensive rig at UCT.

REC16MF-ROV-V-02: It is therefore recommended that approximate scaled models are used in a smaller scale test environment and dimensional analysis is used to relate the scaled values to the full sized values. It is common practise to only verify some of the diagonal elements in the added mass matrix, due the difficulty in determining the off diagonal elements. Nevertheless, it is recommended that some form of verification is conducted for the added mass terms.

10.3.3 Hydrodynamic Damping

Solidworks Flow Simulation provided an effective and easy to use platform that was employed to determine the hydrodynamic damping properties of the *SEAHOG*. However, there are disadvantages with using the Solidworks Flow Simulation package, such as the automatic meshing function. As a result, there are various levels of improvement that can be applied to determining the hydrodynamic damping properties of the *SEAHOG*. This is an important aspect of the model to address, as it was observed that

small changes to the drag characteristics have a large effect on the attitude of the ROV itself. Improvements to the drag characteristics using Solidworks Flow simulation can be achieved by the following:

REC16MF-ROV-M-02: Due to the limited time that was available for flow simulations, a smaller than recommended computational domain size was used. While it was shown that the smaller domain size did not have a significant effect on the critical values of interest, it is recommended that a domain size is used that has dimensions of 20 times the corresponding body's characteristic length along a side.

REC16MF-ROV-M-03: The full CAD model of the *SEAHOG* was modified slightly and converted to a part file to be analysed by the Flow Simulation software. It is recommended that a simplified CAD model of the *SEAHOG* is created so as to decrease simulation run times and to negate the possibility of anomalous flow conditions influencing the simulation results.

REC16MF-ROV-M-04: The camera tilt tray was fixed in a certain position for all of the ROV flow simulations. It is recommended that the effect of the angle of the tilt tray on the lift and pitch moment of the ROV is investigated.

REC16MF-ROV-M-05: Effects of skin friction due to surface roughness were not accounted for due to the unknown roughness of critical *SEAHOG* components, such as the ROV cover, which was not manufactured at the time of this project. The effects of skin friction will have a significant influence on the drag of the ROV at low speeds. It is therefore recommended that the surface roughness of external *SEAHOG* surfaces is determined and applied to the flow simulations.

REC16MF-ROV-M-06: If more expertise was available for the determination of hydrodynamic properties, it is recommended that a specialist CFD program is used, with a custom mesh and more detailed surface roughness and flow characteristics to obtain damping characteristics for the *SEAHOG*.

REC16MF-ROV-M-07: It is recommended that an investigation is undertaken into how the size of the boss created for the domain of the rotating mesh affects the drag simulation results. According to Solidworks documentation, it is necessary to encompass the entire body that will be rotating within the boss that defines the rotating mesh domain. However, it is unclear how closely the boss must envelope the rotating part, and if extra space between the part and the boss will affect the results significantly.

REC16MF-ROV-V-03: In a similar way to with the added mass, the verification of the hydrodynamic damping properties of the *SEAHOG* will require extensive effort. It is recommended that the hydrodynamic damping properties of the *SEAHOG* are verified by experimental methods.

10.3.4 General ROV Model Improvements

REC16MF-ROV-M-08: The effects of the tether on the ROV are expected to be a significant factor in the control of the system. It is therefore recommended that a model of the tether is created and integrated into the *SEAHOG* model.

REC16MF-ROV-M-09: Advanced thruster modelling aspects were not included in the model developed in this report and are therefore a possibility for future model improvements. It is recommended that advanced thruster effects are considered during future improvement of the *SEAHOG* dynamic model. The effects are listed together here, due to their possibly interlinked nature. Advanced thruster effects that should be considered are: gyroscopically induced torques from the propellers, hydrodynamic drag of the thruster housings, thruster induced drag and rotational flow effects. Thruster induced drag is a phenomenon of damping that occurs as a result of the change in momentum of water that is pulled into the thruster propellers.

10.4 System Design

10.4.1 Mechanical and Structural Elements

It was shown in this project through simulations that the ROV pitch and roll is expected to oscillate considerably under translational motion.

REC16MF-ROV-V-04: It is recommended that experimental verification of the motion of the *SEAHOG* is carried out to verify if the platform is indeed insufficiently stable. This is recommended since there are significant model aspects, such as the tether, that have not been included in the model and may serve to stabilise the vehicle to a greater extent.

REC16MF-ROV-H-01: It is recommended that if experimental verification proves that the ROV does exhibit largely oscillatory behaviour in pitch and roll, through mechanical modifications the distance between the CB and the CG should be increased so as to provide a greater righting moment and hence lead to a more stable platform.

REC16MF-ROV-H-02: The highly oscillatory motion that is observed when the *SEAHOG* executes a surge manoeuvre was shown to be lessened to a small extent if the righting moment arm was increased. It is recommended for aiding in the control of the ROV that pitch control and stabilisation is investigated, since there is no active pitch control in the current design. However, it is only recommended that this is investigated once verification and improvement of the current model has been undertaken. An acceptable level of control may be achievable without pitch control if future improvements to the *SEAHOG* system model result in a more stable system.

REC16MF-ROV-H-03: The *SEAHOG* cover has not yet been manufactured and could readily be modified so as to be more symmetrical and have more favourable drag properties. However, results from this project have shown that motion coupling due to the lack of body symmetry on the *SEAHOG* does not make the vehicle control overwhelmingly cumbersome. It was shown in chapter 6 that the added mass properties of the body can have a huge effect on its behaviour in the water: two examples of which are the effect of the added mass on an ascending heave manoeuvre and the oscillatory behaviour set up by a full surge thrust input. Therefore, it is recommended that the added mass of the body is better defined first by advanced computational methods. Once this has been completed, the body symmetry should be assessed again in a simulation environment before modifications of the shape of the ROV cover are made.

10.4.2 Control Hardware and Sensors

REC16MF-SNS-H-01: As was discussed in chapter 7, the installation of controller computing power onto the ROV will require significant thought and warrants significant planning. It is therefore recommended that a project is undertaken to investigate and specify the exact hardware to be installed on the *SEAHOG* for the purposes of control functions. This includes any possible restructuring of the *SEAHOG* network architecture.

REC16MF-SNS-H-02: It is recommended that investigation into the exact capabilities of the chosen iNEMO AHRS unit and its typical accuracies and reliabilities is undertaken. Some of the available data for the device was presented in this report, but it is necessary to gain a greater understanding of the device and its capabilities.

REC16MF-SNS-V-01: Sensors such as magnetometers are influenced by local magnetic fields. The thrusters use magnetic couplings with powerful neodymium magnets that may disrupt magnetometer readings. It is therefore recommended that an investigation is undertaken into the performance of the chosen navigational sensors on the *SEAHOG* body itself to confirm that the chosen sensors are a valid sensory solution for the *SEAHOG*.

REC16MF-SNS-M-01: It will be necessary and is thus recommended that the ROV Simulink® model is updated for the exact sensor and computing hardware installed.

REC16MF-SNS-S-01: It is possible to use Kalman filtering type algorithms to better predict the ROV depth. It is recommended that obtaining a higher resolution depth estimation by fusing data from the AHRS and the pressure transducer is investigated.

10.5 Controller Design

10.5.1 Depth Controller

The depth controller was designed using an adaptive PID-type structure whereby the controller would supply a propeller speed input to the vertical thruster. By scheduling the integrator gain according to step size and employing a feed-forward compensation element, it was possible to obtain a reasonably uniform response across a wide variety of steps. Successful step and sinusoidal setpoint tracking was obtained from the adaptation laws.

In general, the setpoint tracking accuracy of the controller was limited by the resolution of the depth sensor. The depth controller that was designed showed that reasonable setpoint tracking can be obtained from a PID controller at the available resolution of depth readings. Low speed limit cycle behaviour was not observed to be a significant factor in the depth holding, most probably due to the relatively coarse resolution of the depth sensor.

It was shown that the performance of the depth controller degraded significantly when horizontal X and Y thrusts were applied, causing the ROV to move away from its horizontal orientation. However, the controller did not become unstable and maintained the depth to within a band of approximately 1 m of the desired depth. In general, it is known that PID type controllers are ill-suited to the underwater environment and therefore the depth controller was designed as a preliminary controller to be used as a baseline on which more advanced controllers can be compared. In addition, the assumption in the design of the depth controller that the ROV will remain close-to horizontal during operation, is evidently an assumption that should not be made and that the influence of the ROV's attitude on the depth controller is an aspect that should not be overlooked.

REC16MF-CTR-M-01: The nonlinear thrust to propeller speed relationship may prove that for more precise depth control, using the propeller speed as the control variable is not ideal. If it is desired that linear PID control methods are pursued further on the *SEAHOG*, it is recommended that a depth controller is developed that uses the thrust level as the control variable – such as in the case of the heading controller. The heading controller uses a thrust level as the control variable, which is then approximated as a desired propeller speed using the nonlinear thrust vs. propeller speed equation. This helps to match the nonlinear propeller speed to thrust relationship with the linear PD or PID control action and consequently allows the thrust to be controlled in a linear fashion. The depth controller could be modified to have a thrust level as the control variable and could be compared to the current depth controller's performance.

REC16MF-CTR-M-02: It is recommended however, that adaptive sliding mode control (SMC) is developed for depth holding functions on the *SEAHOG*. SMC offers many advantages over PID control such as being

robust to model uncertainties and disturbances. It has been successfully employed in numerous cases of underwater control.

10.5.2 Heading Controller

The heading controller was designed by using a desired thrust level as the control input. The thrust was balanced between the four horizontal thrusters so as to not induce any translational unbalanced forces and supply a moment only. An adaptive PD controller structure was used with the proportional gain being scheduled according to step size. The speed deadband of the thrusters required a discontinuous control law to be implemented close to the setpoint so that the ROV would settle within 0.2˚ of the setpoint. A uniform response across the entire range of required step sizes was obtained and the tracking of sinusoidal inputs was successfully achieved.

The ability of the controller to track the setpoint was significantly jeopardised by the presence of user inputted X and Y thrusts.

REC16MF-CTR-M-03: During simulations of prolonged low thrust inputs in surge, the controller was seen to be struggling to hold the heading of the ROV and with a greater thrust in surge, it is expected that a steady state heading offset will be observed. The steady state offset has a significant impact on the navigational capabilities of the ROV. It is possible that adding an integrator element to the controller will assist in correcting for torques applied from motion coupling and disturbances and therefore it is recommended that a PID type heading controller is developed.

REC16MF-CTR-M-04: While it is possible that the heading controller designed in this project could be modified to give sufficient real life performance, it is recommended that adaptive SMC structure is utilised for heading holding functions on the *SEAHOG*.

10.6 Practical Considerations for *SEAHOG* Piloting

It was found that in general the *SEAHOG* exhibits largely oscillatory behaviour while travelling in the surge direction. The magnitude of the oscillations are related primarily to the vertical thruster thrust. The more negative the vertical thruster thrust vector is, the greater the magnitude of the oscillations are, to the point of the system reaching an ill-defined state of 90˚ pitch. The practical outworking of this is that it is not recommended that the depth controller is used if a thrust level of greater than approximately 0.2 of the maximum thrust in the surge direction is desired.

REC16MF-PIL-X-01: It is recommended for ROV piloting that a constant vertical thruster thrust is applied while travelling long distances. Once the approximate horizontal position of the ROV is reached, the depth controller can be employed and minor position adjustments can be made at low thrusts.

REC16MF-PIL-X-02: Simulations showed that if the *SEAHOG* is ascending, a continual roll is experienced until the thrust vector from the vertical thruster is in fact orientated in the horizontal direction. This does not seem likely to happen in reality and the added mass properties of the *SEAHOG* must first be better approximated. However, if continuous rolling behaviour is observed, it is recommended that the vertical thrust is decreased or reversed periodically whilst ascending as this serves to stabilise the pitch and roll of the ROV.

REC16MF-PIL-X-03: The depth and heading controllers are expected to operate effectively together in reasonably calm ambient conditions. It is therefore recommended that the depth and heading controllers are used to obtain a particular depth and heading from the *SEAHOG* first. Once the desired heading and depth have been reached, either the horizontal position can be adjusted using low levels of thrust. Or the depth controller can be substituted for a constant, open-loop thrust from the vertical thruster while the horizontal position of the ROV is adjusted.

REC16MF-PIL-S-01: Simulations showed that the motion of the *SEAHOG* was largely oscillatory in pitch and roll when travelling in the surge direction. It was shown in chapter 6 that limiting the rate of change of thrust in surge mitigated the oscillations to some extent. It is therefore recommended that some form of thrust rate limiting is implemented on the ROV control software so as to lessen the oscillatory behaviour during a surge manoeuvre.

10.7 Concluding Remarks

Conclusions from the work conducted in this report have now been drawn and related recommendations have been given. While the list is not exhaustive, some of the most pertinent recommendations were given so as to inform future work that can be conducted on the *SEAHOG*.

This project has provided the basis for an ROV simulation model that can be improved upon, including the following aspects:

- Thruster Model
    - Propeller thrust
    - Motor and drive train
    - Control electronics
    - Software propeller speed controller
- ROV Model
    - Rigid body mass and inertia
    - Added mass and inertia
    - Hydrodynamic damping forces
    - Hydrostatic restoring forces
    - Thrust mapping
    - Provision for externally applied forces such as currents
- Control Electronics and Sensors
    - Proposal of control computation hardware
    - Pressure transducer
        - Sensor model
        - Mapping of sensor position to actual sensed depth
        - Estimation of actual depth according to sensed depth
    - Proposal of AHRS
- Controllers
    - Classical linear PD structure with adaptive elements for heading holding
    - Classical linear PID structure with adaptive elements for depth holding

Recommendations from this chapter provided information for a variety of areas in which the model can be improved and how future work can build upon the results presented in this report. Appendix B to this report contains details of other design work that was conducted as part of this project. It should be consulted so as to gain insight into mechanical, electrical and software development conducted on the *SEAHOG* as part of this project.

Works Cited

[1] Marine Technology Society, “Index,” [Online]. Available: http://www.rov.org/index.cfm. [Accessed 25 June 2012].

[2] R. Christ and R. Wernli, in *The ROV Manual*, Oxford: Elsevier, 2007.

[3] “ROV Categories - Summary,” Marine Technology Society, [Online]. Available: http://www.rov.org/rov_categories.cfm. [Accessed 20 April 2013].

[4] Dredging Today Staff, “UK: Kongsberg Cameras Chosen for SMD Deep Water Trenching Vehicles,” DredgingToday.com, 10 August 2012. [Online]. Available: http://www.dredgingtoday.com/2012/08/10/uk-kongsberg-cameras-chosen-for-smd-deep-water-trenching-vehicles/. [Accessed 16 August 2014].

[5] R. d. Smidt, “Development of the Power and Communications Distribution Systems for an Underwater Remotely Operated Vehicle,” University of Cape Town, Cape Town, 2014.

[6] The Society of Naval Architects and Marine Engineers, “Nomenclature for Treating the Motion of a Submerged Body Through a Fluid,” The Society of Naval Architects and Marine Engineers, New York, 1950.

[7] National Imagery and Mapping Agency, “Department of Defense World Geodetic System 1984,” National Imagery and Mapping Agency, Fairfax, 1984.

[8] T. I. Fossen, Marine Control Systems, Guidance Navigation and Control of Ships, Rigs and Underwater Vehicles, Trondheim: Marine Cybernetics, 2002.

[9] O. M. Faltinsen, Sea Loads on Ships and Offshore Structures, Cambridge: Cambridge University Press, 1990.

[10] M. H. A. Khader, “Effects of wave drag on submerged bodies,” *La Houille Blanche, International*

Water Journal, vol. 8, pp. 465 - 470, 1979.

[11] B. Siciliano and O. Khatib, Springer Handbook of Robotics, Berlin Heidelberg: Springer-Verlag, 2008.

[12] G. Kirchhoff, "Über die Bewegung eines Rotationskorpers in einer Flussigkeit," *Crelle's Journal,* vol. 71, pp. 237-273, 1869.

[13] K. Wendel, "Hydrodynamic Masses and Hydrodynamic Moments of Inertia," David Taylor Model Basin, Maryland, 1956.

[14] F. H. Imlay, "The Complete Expressions for Added Mass of a Rigid Body Moving in an Ideal Fluid," David Taylor Model Basin, Washington D.C., 1961.

[15] O. M. Faltinsen and B. Sortland, "Slow Drift Eddy Making Damping of a Ship," *Applied Ocean Research,* vol. 9, no. 1, pp. 37-46, 1987.

[16] J. Morison and J. Johnson, "The Force Exerted by Surface Waves on Piles," *Journal of Petroleum Technology,* vol. 2, no. 5, pp. 149-154, 1950.

[17] D. R. Yoerger, J. G. Cooke and J. E. Slotine, "The Influence of Thruster Dynamics on Underwater Vehicle Behavior and Their Incorporation Into Control System Design," *IEEE Journal of Oceanic Engineering,* vol. 15, no. 3, pp. 167-178, 1990.

[18] L. Pivano, "Thrust Estimation and Control of Marine Propellers in Four-Quadrant Operations," Norwegian University of Science and Technology, Trondheim, 2008.

[19] T. Fossen, Guidance and Control of Marine Vehicles, Chichester: John Wiley & Sons Ltd., 1994.

[20] M. Blanke, "Ship Propulsion Losses Related to Automated Steering and Prime Mover Control," The Technical University of Denmark, Lyngby, 1981.

[21] A. J. Healey, S. M. Rock, S. Cody, D. Miles and J. P. Brown, "Toward an Improved Understanding of Thruster Dynamics for Underwater Vehicles," *IEEE JOURNAL OF OCEANIC ENGINEERING,* vol. 20, no. 4, pp. 354-361, 1995.

[22] T. I. Fossen and S. Sagatun, "Adaptive control of nonlinear underwater robotic systems," *Modeling, Identification and Control,* vol. 12, no. 2, pp. 95-105, 1991.

[23] M. Blanke, K. Lindegaard and T. I. Fossen, “Dynamic Model for Thrust Generation of Marine Propellers,” *Manoeuvring and control of marine craft,* pp. 363-368, 2000.

[24] T. Hope, “The Characterisation of Magnetic Couplings and the Development of a Thruster Module for an ROV,” University of Cape Town, Cape Town, 2015.

[25] K. Krykowski and J. Hetmańczyk, “Constant Current Models of Brushless DC Motor,” *Electrical, Control and Communication Engineering,* vol. 3, no. 1, pp. 19-24, 2013.

[26] Microchip Technology Inc., “Brushless DC Motor Control Made Easy,” 2002. [Online]. Available: http://ww1.microchip.com/downloads/en/appnotes/00857a.pdf. [Accessed 3 September 2015].

[27] M. I. Gonzalez, “Experiments with eddy currents: the eddy current brake,” *EUROPEAN JOURNAL OF PHYSICS,* vol. 25, no. 4, pp. 463-468, 2004.

[28] J. Baltazar, J. A. C. F. d. Compos and J. Bosschers, “Open-Water Thrust and Torque Predictions of a Ducted Propeller System with a Panel Method,” *International Journal of Rotating Machinery,* vol. 2012, pp. 1-11, 2012.

[29] J. C. G. Pimentel, E. Gad and S. Roy, “Stability analysis of BLDC motor speed controllers under the presence of time delays in the control loop,” *Connected Vehicles and Expo (ICCVE),* pp. 171 - 176, 2013.

[30] O. A. Eidsvik, “Identification of Hydrodynamic Parameters for Remotely Operated Vehicles,” Norwegian University of Science and Technology, Department of Marine Technology, Trondheim, 2015.

[31] W. Wang, “Autonomous Control of a Differential Thrust Micro ROV,” University of Waterloo, Ontario, 2006.

[32] Det Norske Veritas, “Recommended Practice DNV-RP-H103 Modelling and Analysis of Marine Operations,” April 2011. [Online]. Available: http://www2.dnvgl.com/DNV-RP-H103. [Accessed 2 January 2016].

[33] C. E. Brennen, “A Review of Added Mass and Fluid Inertial Forces,” Naval Civil Engineering Laboratory, Port Hueneme, 1982.

[34] COMSOL, “Navier-Stokes Equations,” COMSOL, 2015. [Online]. Available: https://www.comsol.com/multiphysics/navier-stokes-equations. [Accessed 13 December 2015].

[35] C. Chin and M. Lau, “Modeling and Testing of Hydrodynamic Damping Model for a Complex-shaped Remotely-operated Vehicle for Control,” *Journal of Marine Science and Application,* vol. 11, no. 2, pp. 150-163, 2012.

[36] M. James, “The generalised inverse,” *Mathematical Gazette,* vol. 62, no. 420, pp. 109-114, 1978.

[37] STMicroelectrinics, “iNEMO M1,” October 2013. [Online]. Available: http://www.st.com/web/en/resource/technical/document/datasheet/DM00056715.pdf. [Accessed 12 January 2016].

[38] SICK Sensor Intelligence, “PBT Pressure Transmitter,” April 2009. [Online]. Available: https://mysick.com/saqqara/im0032424.pdf. [Accessed 11 January 2016].

[39] R. H. Stewart, Introduction to Physical Oceanography, Texas: Texas A & M University, 2008.

[40] P. J. Craven, R. Sutton and R. S. Burns, “Control Strategies for Unmanned Underwater Vehicles,” *Journal of Navigation,* vol. 51, no. 1, pp. 79-105, 1998.

Appendix A
Literature Survey

Table of Contents

Table of Figures

List of Tables

Glossary

AHRS	Attitude and Heading Reference System
AMR	Anisotropic Magneto Resistance
APRS	Attitude and Position Reference System
ASMC	Adaptive Sliding Mode Control
AUV	Autonomous Underwater Vehicle
Controller	Hardware managing automatic control functions
Control Console	Surface Computer Station with Human Interface
DOF	Degree of Freedom
DSP	Digital Signal Processing
DVL	Doppler Velocity Log
EIA	Electronics Industry Association
FOG	Fibre-Optic Gyroscope
Geodetic	With reference to the Earth
GNC	Guidance, Navigation and Control
GPS	Global Positioning System
IC	Integrated Circuit
IMU	Inertial Measurement Unit
INS	Inertial Navigation System
LBL	Long Baseline
MEMS	Micro Electromechanical System
RARL	Robotics and Agents Research Laboratory
ROV	Remotely Operated Vehicle
RS-485	Recommended Standard 485
Sonar	Sound Navigation Ranging
SMC	Sliding Mode Control
Thruster	ROV actuator – containing a propeller
UCT	University of Cape Town
USBL	Ultra-Short Baseline
UWSN	Underwater Wireless Sensor Network
VRU	Vertical Reference Unit
WSN	Wireless Sensor Network

1. Introduction

The *SEAHOG* Remotely Operated underwater Vehicle (ROV) is a general observation class ROV with a dry mass of approximately 80 kg that is being developed at the Robotics and Agents Research Laboratory (RARL) at the University of Cape Town (UCT). This kind of ROV is typically used for underwater observations and can carry basic manipulator equipment to perform specific tasks at depth.

The *SEAHOG* ROV was commissioned and designed for the purpose of conducting marine research for the Biological Sciences department at UCT. It is thus equipped with fore and aft facing cameras and variable brightness lighting. This will allow the ROV to observe its environment and identify lost equipment or organisms of interest for research purposes. It is envisaged that a gripper module will be developed in the future for the *SEAHOG* for the purpose of retrieving biological samples. Therefore, the necessity for a controller quite large, since a stable platform will be required for observing and manoeuvring the ROV in its environment. In addition, employing a gripper on delicate marine samples will require a high level of operator skill and may not even be achievable without some level of position holding control. Finally, it is foreseeable that multiple trips to the same location under the water will be necessary to conduct successful research and for this reason the ROV will need to be able to have some level of position tracking capability.

The purpose of this literature survey is to supplement the work presented in the main dissertation section of this project by giving background information on the *SEAHOG* ROV project at UCT and describing certain elements of the main report in greater detail.

The scope of this literature survey will present a general overview of ROVs and their uses. It will then introduce the *SEAHOG* specifically. Supplementary information will be given to provide a detailed understanding of the challenges and techniques used in underwater localisation. Finally, an overview of control techniques used to provide particular automatic manoeuvres underwater will be given.

From the knowledge gained in this survey it will be possible to develop control laws with an understanding of their shortcomings and associated challenges. It will therefore be possible to criticise and identify improvements on control strategies developed in the main dissertation section of this project. In addition, since this project's scope does not include the installation of hardware and motion sensors onto the

SEAHOG, it will serve as a valuable starting point for investigations into the real life hardware implementation of control strategies on the vehicle for future projects.

A rendering of the *SEAHOG* is shown below in Figure 1.

Figure 1 - The *SEAHOG* ROV developed at RARL

2. Introduction to ROVs and the *SEAHOG*

2.1. Introduction

To give some context to the project, research is presented in this chapter that outlines the general aspects and principles of an ROV. This is then linked to the *SEAHOG* ROV and its specific features are described and discussed. The purpose of this is to give a clear understanding of the system that is to be controlled in this project. This will help to clarify the scope of this literature review and will allow similar systems to the *SEAHOG* to be identified and analysed.

2.2. What is an ROV?

An ROV or Remotely Operated Vehicle is a tethered underwater robot that allows the vehicle's operator to remain in a comfortable environment while the ROV works in the hazardous environment below [1]. ROVs are able to operate in conditions that are not achievable by human divers, which makes them a valuable tool in marine research. Oil and gas companies use ROVs for collecting data on hydro carbons for mining operations and the military uses ROVs for recovering parts of sunken ships, crashed aircraft parts and weapons. The ability of ROVs to manoeuvre into small areas and to descend into the darkness of our oceans that was previously un-explorable has rendered them highly useful for scientists in this age of discovery [2].

The three basic sub-systems that comprise an ROV system are as follows [3]:

1) Control Console with Human Interface
2) Tether (Chord running between the Control Console and the robot, supplying power and communications)
3) Submersible robot with additional apparatus

Figure 2 alongside shows an illustration of the above subsystems and their interaction in an ROV system.

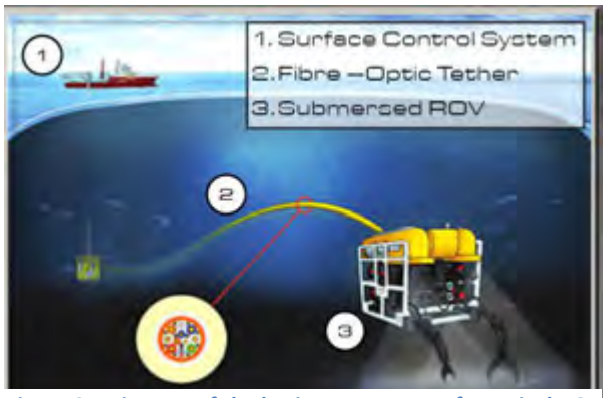

Figure 2 - Diagram of the basic components of a typical ROV system [38]

In an ROV system, the submersible is the actual ROV that will physically manoeuvre in and gather information from the underwater environment. An ROV will typically be equipped with lights and cameras so as to be able to observe its direct environment. End effectors and robotic arms may also be fitted to the ROV to allow it to directly interact with its environment and retrieve samples, for instance. Since the applications of ROVs are incredibly broad however, a range of sensors can be fitted to the submersible depending on its specific application.

The tether is a chord that is connected to the ROV. It runs up to the surface of the water where the control console is situated and serves as a mechanism to supply power to the ROV. In addition, the ROV will receive operator inputs and will send information back via the tether.

The control console is situated on the surface and relays user inputs to the ROV via the tether while displaying relevant information that has been sent from the ROV to the user. The control console should not be confused with the ROV controller that is also referred to in this report. The other controller that is referred to in this report is the hardware on the ROV itself that manages the automatic control functions that will be designed in this project.

Figure 3 below shows the Saab Seaeye Falcon DR which is a commercially available ROV equipped with a gripper arm. This ROV follows a similar design philosophy to that of the *SEAHOG* and contains similar modules and features. This will be discussed later in section 2.5.

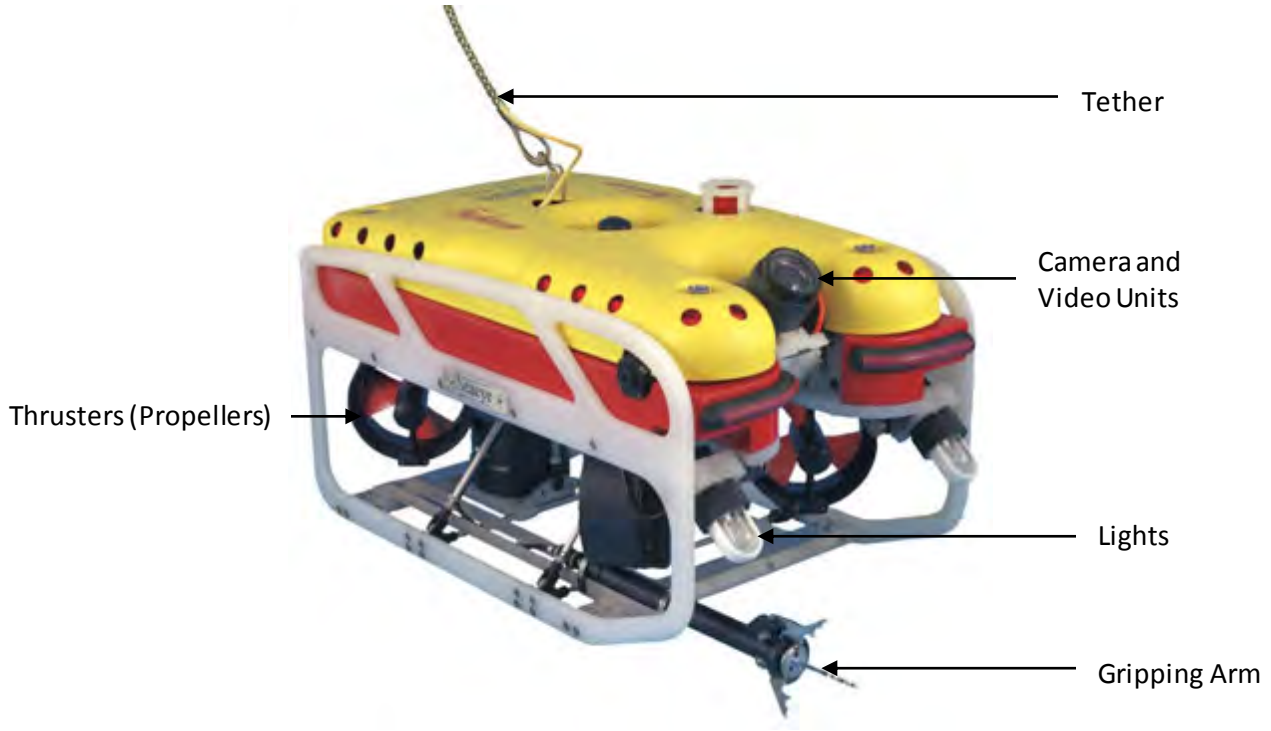

Figure 3 - SAAB Seaeye Falcon ROV [4]

2.3. Applications and Uses of ROVs

While the UCT ROV is a medium-sized general to observation class ROV, there is a wide spectrum of ROV sizes and applications. As technology becomes cheaper and more accessible, ROVs become more and more useful and already fulfil a variety of roles in industry and research institutions. Some applications of ROVs are:

1) Inspections of Hazardous Facilities
2) Underwater Investigation and Exploration
3) Biological Research of Deep Sea Organisms and Equipment Retrieval
4) Oil and Gas Industry Inspections and Maintenance of Sub-sea Equipment
5) Deep Sea Mining and Cable Laying

Figure 4 below shows four different ROVs of varying sizes and classes to illustrate the diverse applications of ROVs.

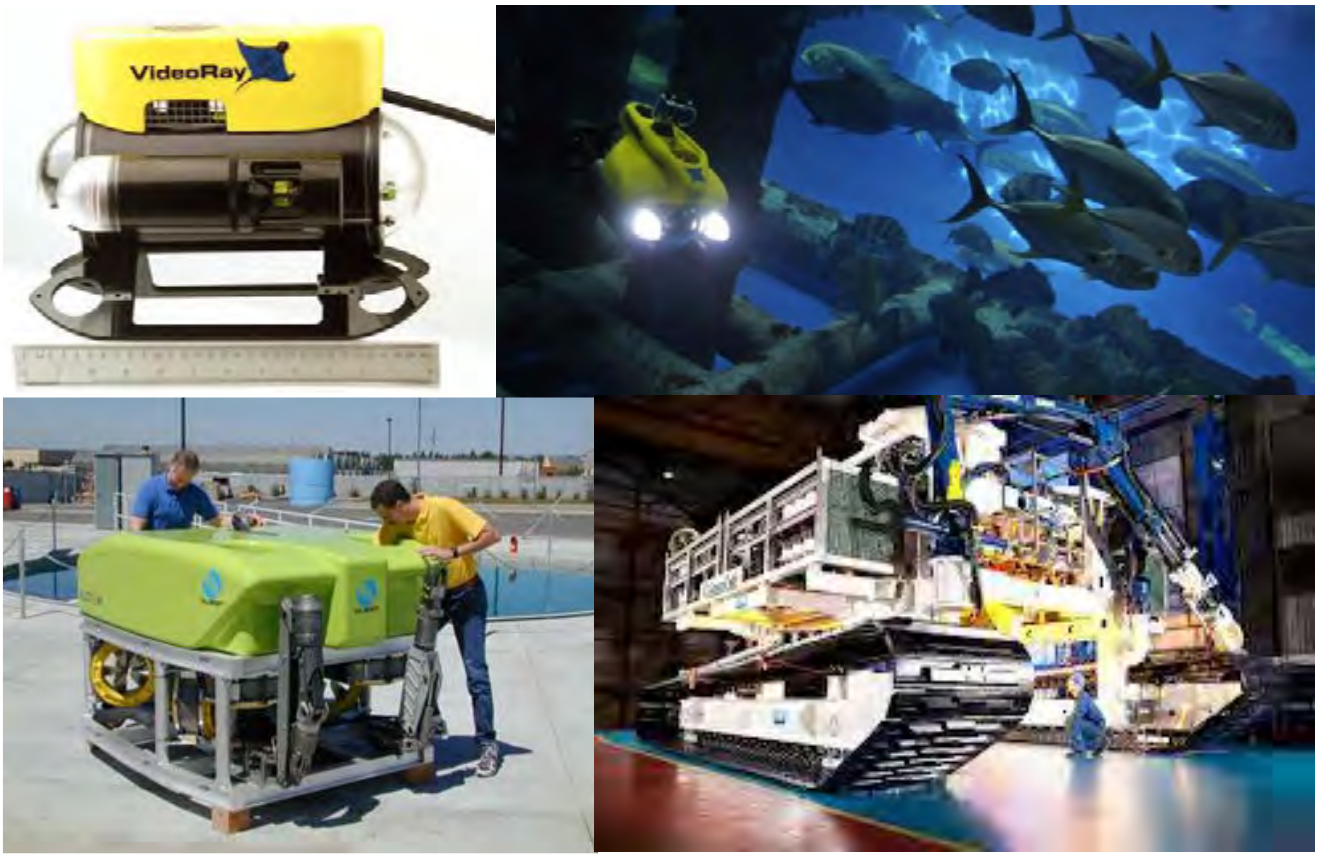

Figure 4 – The VideoRay Scout observation class ROV with a depth rating of 76m [5] [top left]; another VideoRay ROV in action with a GoPro camera mounted on top of it [6][top right]; the Alstorm Quest work class ROV [7] [bottom left]; the CBT800 trencher ROV from SMD designed to dig trenches and bury cables at depths of up to 3000 m [8] [bottom right]

2.4. History of the UCT *SEAHOG*

The *SEAHOG* was commissioned by the department of Biological Sciences at the University of Cape Town in 2009. The department desired an underwater robot to be developed that could assist them in a number of tasks.

A vast portion of the ocean is undocumented due to the inability of human divers to safely reach depths greater than about 50 m in the ocean. For this reason, ROV technology offers huge potential to research institutions that wish to discover more about the depths of our oceans. The Biological Sciences department at UCT is one of these institutions. Therefore, one of the ultimate goals for the *SEAHOG* is to be able to gather marine samples at depths exceeding the reach of human divers and return them to the surface for analysis.

A more immediate goal however, is to be able to assist in the recapturing and deployment of marine research equipment. A need arose when expensive equipment was lost overboard on a research expedition at sea, after which divers were sent down to search for the equipment. This is a dangerous process as the divers cannot spend much time searching for the equipment due to oxygen supply limitations and require a significant amount of decompression time on their ascent to the surface due to the introduction of nitrogen into the body. This makes finding the equipment a time consuming, uncertain and dangerous process.

Thus, a cost effective solution for recovering and deploying research equipment became necessary. An unmanned, remotely operated vehicle that could deliver live video footage and environmental data to the surface perfectly matched this need and resulted in Ms Andrea Plos, of the Biological Sciences Department at UCT, approaching RARL to request the design and manufacture of a low-cost ROV.

Currently the *SEAHOG* is the 3rd generation of ROVs developed at RARL and is a culmination of the experienced gained from two previous ROV iterations. More information on the development of ROVs at RARL can be found in [9].

2.5. Features and Aspects of the UCT *SEAHOG*

The UCT *SEAHOG* follows a similar design philosophy to that of commercially available open frame modular ROVs. One such ROV, the *Falcon* from SAAB, was shown previously in Figure 3. These ROVs and the design philosophy that they follow is very prevalent throughout the range of general observation class ROV models from different developers and manufacturers. One of the key features in the construction of these ROVs is the open frame used as the chassis; onto which all functional modules are fitted. This type of design lends itself to a very modular set of subsystems that can be relatively easily modified and changed with less of an impact on the rest of the vehicle. From a maintenance perspective, each component can also be

easily isolated and swapped out just by unplugging the faulty component and plugging in a spare one. This is an advantage on time-critical missions or when operating from a small and uncomfortable vessel where repairs can sometimes be an arduous and unpleasant task to achieve [9]. Figure 5 below shows the SAAB *Falcon* and the Seatronics *Predator* ROV. The ROVs are shown with their buoyancy covers off to show the modular design with separate sealed units acting as part of a network of modules.

Figure 5 – SAAB *Falcon* ROV with buoyancy cover removed [top] [10]; Seatronics *Predator* ROV with buoyancy cover removed [bottom] [11]

Open frame type designs lead to greater flexibility for future design changes and sensor payload options. Other advantages of open frame modular designs include [9]:

- Greater depth possible, allowing for competition with similar commercially available ROVs
- Options for different thruster configurations possible that could provide greater manoeuvrability
- Simpler to integrate additional sensor payloads and tools
- Modular system reduces risk of damage to entire system if one seal fails
- Modular designs provides scope for standardization, increasing manufacturing efficiency

The *SEAHOG* follows a similar open framed modular design to the two ROVs shown previously in Figure 5. The modular nature of the *SEAHOG* and its open frame design can be seen in Figure 6 below. Labelled modules include the oil compensated junction box that splits the incoming power and communications connections from the tether before connecting to the electronics and power modules. The junction boc, electronics and power pod form the backbone on which the rest of the ROV modules rely.

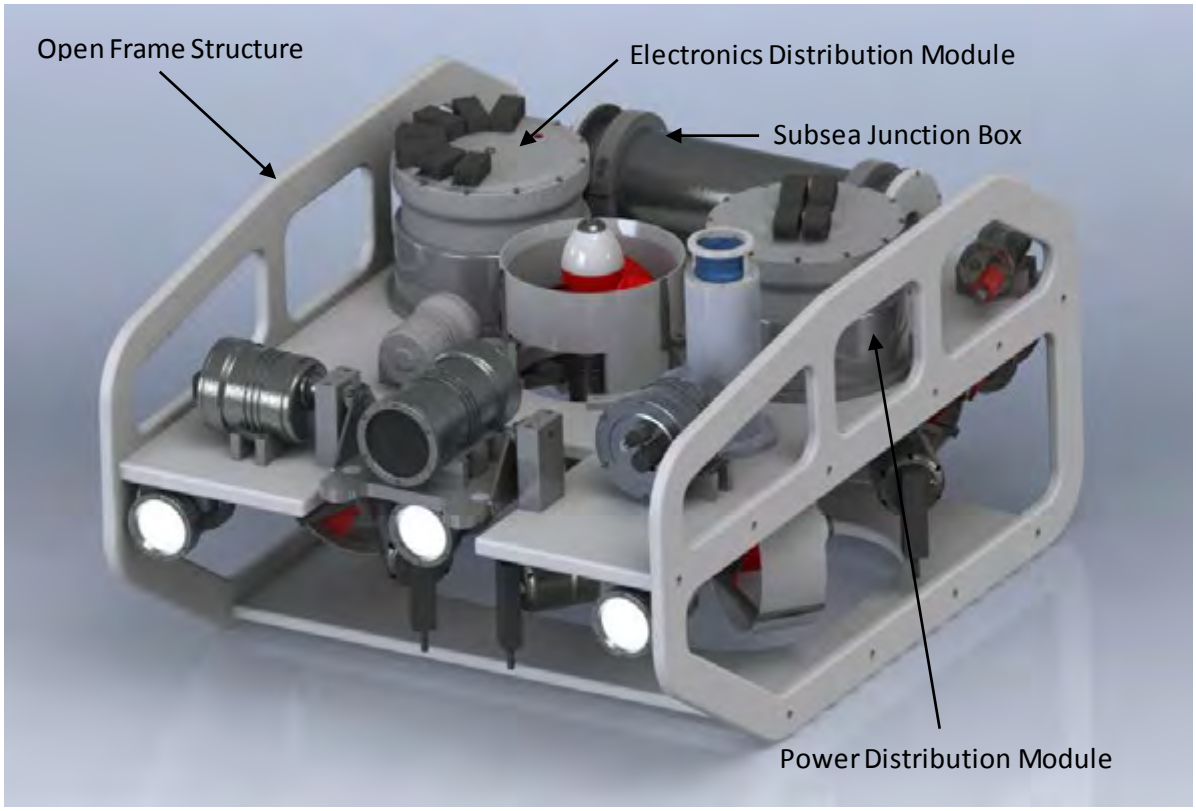

Figure 6 – Rendering of the *SEAHOG* with its buoyancy cover removed, showing the open frame and modular nature of its design

Current features and modules of the *SEAHOG* include:

- 4 Vectored horizontal thrusters (propellers)
- 1 vertical thruster
- Forward facing camera for live video feedback
- Rear facing camera for live video feedback and tether monitoring
- Sonar unit
- Variable brightness led forward and rear lighting
- Available space for environmental and motion sensors
- Basic gripper unit
- 300 m designed operational depth

Renderings of the *SEAHOG* are shown below in Figure 7, depicting its features and modules.

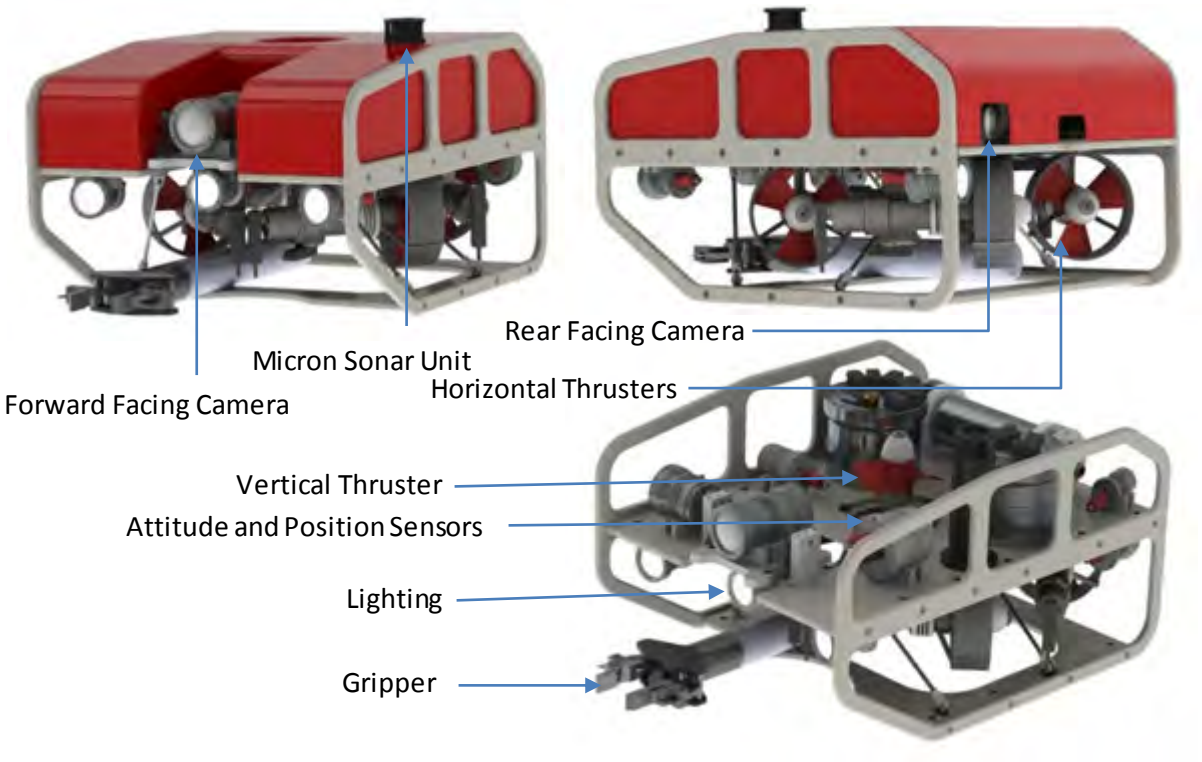

Figure 7 - The *SEAHOG* ROV: Modules and Features

This completes the description of the UCT *SEAHOG*, its features and design philosophy. Now that the system is understood better, aspects of the *SEAHOG* that are related to its controllability can be described.

2.6. The *SEAHOG* as a Controllable System

2.6.1. Actuation

The UCT ROV system represents a six degree of freedom (DOF) rigid-body environment that is under-actuated. The vectored thruster arrangement on the ROV allows for translational motion in the horizontal plane and translational motion in the vertical plane. It also allows the heading or yaw orientation of the ROV to be controlled. The roll and pitch orientations, however, are not independently controllable – this will be described in greater detail in the main report. Figure 8 and Figure 9 below show the ROV firstly in its stable hydrodynamic state and then rotated in the roll and pitch orientations respectively.

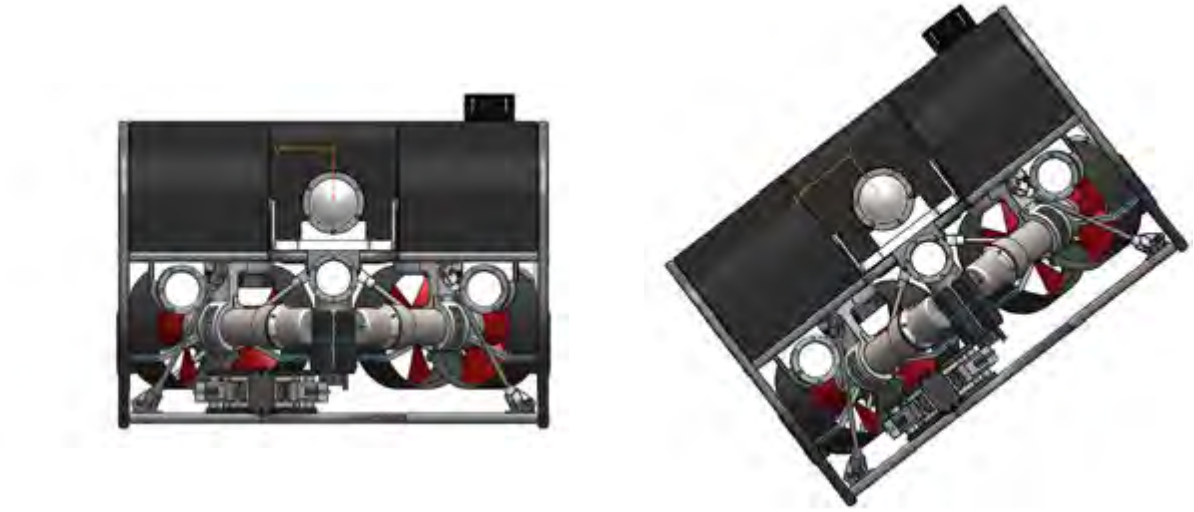

Figure 8 - Front view of the ROV in a stable position [left] and after rotating in the roll direction [right]

Figure 9 - Side view of the ROV in a stable position [left] and after rotating in the pitch direction [right]

Not being able to control the roll and pitch of the ROV is not a problem as long as the ROV maintains a close-to horizontal orientation. The *SEAHOG* has been designed to passively return to a horizontal orientation, however the effectiveness of the passive stabilisation of the robot will be an aspect that is assessed in the main section of this report.

2.6.2. Global Positioning Systems (GPS)

GPS satellites circle the earth twice a day in a very precise orbit and transmit signal information to earth. GPS receivers take this information and use trilateration to calculate the user's exact location [12]. To be able to do this, the GPS receiver must be able to receive signals from three different satellites at any given moment. If the receiver knows how far it is from each satellite and where that satellite is, the ranges will all intersect at a point. This is shown alongside as a two dimensional concept in Figure 10.

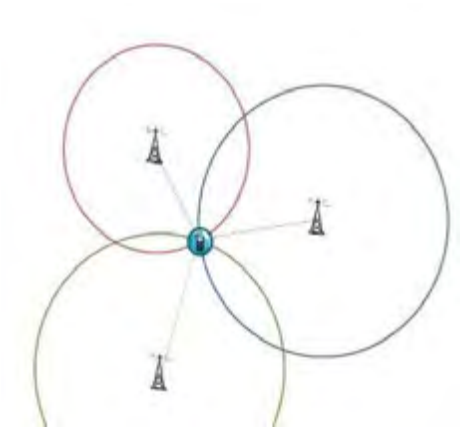

Figure 10 – 2D demonstration of how a device uses trilateration to determine its current position [40]

Trilateration also works in three dimensions and is shown alongside in Figure 11. The yellow and blue spheres intersect along the red circle. All three spheres intersect at the two black dots. Ground based systems know to discard the upper dot. To determine how far the receiver is from each satellite, the GPS receiver compares the time a signal was transmitted by a satellite with the time it was received. The time difference allows the GPS receiver to work out how far away the satellite is [12]. This relies on all GPS devices having very accurate synchronised clocks.

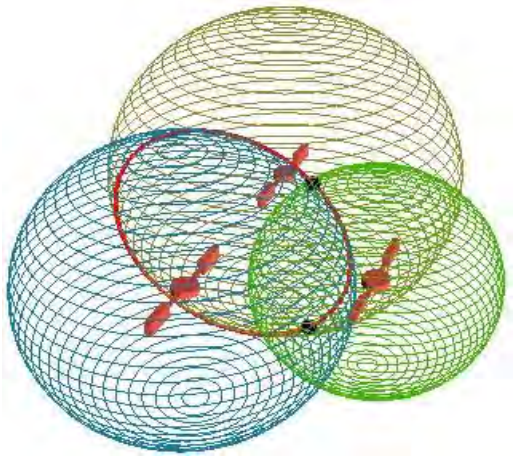

Figure 11 - 3D Trilateration [43]

The miniaturisation of GPS has hugely increased the capability of controlling terrestrial systems. The transport industry utilises GPS extensively in aeroplanes and cars, enabling autopilot and position finding functions to be carried out at any point on the Earth. GPS can achieve a reasonable degree of accuracy at a low cost and can provide a stable absolute position relative to the Earth. It is well known however, that ordinary GPS fails to operate underwater. The reason for this is that the electromagnetic signals from orbiting satellites are heavily damped in water and hence cannot be detected by the GPS receiver in most cases of interest [13].

It is for this reason that the only way in which an ROV can utilise GPS would be to log its global position coordinates on the surface of the water and then track its movement under the surface by other means. Submarines and Autonomous Underwater Vehicles (AUVs) use this technique – tracking their movement underwater by other means and periodically surfacing to correct their predicted position using GPS.

2.6.3. Sensors

Sonar

The *SEAHOG* is equipped with a Micron Sonar unit from Tritech which has already been built into the ROV's communications network. The sonar unit scans in the horizontal plane and is available to be used for the purpose of controlling the ROV. Table 1 below gives a summary of the Micron Sonar unit's capabilities and specifications.

Table 1 - Micron Sonar from Tritech: Features

Feature	Value
Horizontal Beam Width	3˚
Vertical Beam Width	30˚
Horizontal Range	100 m
Communication Protocol	RS232
Acoustic Frequency	700 kHz
Depth Rating	750 m

Attitude and Position Sensors

Figure 7, shown previously on page 9, labels the module that has been manufactured and designated for any kind of attitude and position sensors that are specified for the control system of the ROV. While these have not yet been specified, the module has been designated and manufactured for the purpose of housing these sensors and includes a mounting hole for a pressure transducer. A detailed investigation into commonly used sensors and methods of position finding underwater is undertaken later in Chapter 3.

2.6.4. Control and Communications

Control

The control module that will be designed in this project is expected to be housed in the same housing as the attitude and position sensors mentioned in the previous section. However, at this early stage in the project it is uncertain what control hardware will need to be implemented on the ROV. This means that if it is deemed to be necessary, an extra housing will have to be designed for the control hardware on the ROV. An advantage of the ROV's modular design however is that it will not be a difficult task integrating this extra housing into the ROV's mechanical and communication structure.

Communications Network

The ROV uses a multi-drop RS-485 communications network. The Recommended Standard 485 (RS-485) is a differential serial digital data communication protocol that specifies bi-directional half-duplex data transmission [9]. It is the only Electronics Industry Association (EIA) standard that allows multiple receivers and drivers in "bus" configurations [14]. The RS-485 standard defines the electrical layer that affects the specifications for transceivers but does not specify the structure of the data to be sent. The differential signal voltage range is specified to fall between -7 V and +12 V [9]. Receiver sensitivity is set to

acknowledge differential signals lower than -200 mV and above +200 mV [14]. This means that any difference greater than 400 mV between the differential pair will, depending on its polarity, produce either a high or a low signal. The differential pair provides good immunity to noise and is usually twisted into a "twisted pair" to increase the level of noise reduction. This manifests itself in the ability to transmit data at higher rates and have longer physical distances between modules on an RS-485 network. Typical line signals on the RS485 A and B pair are shown below in Figure 12.

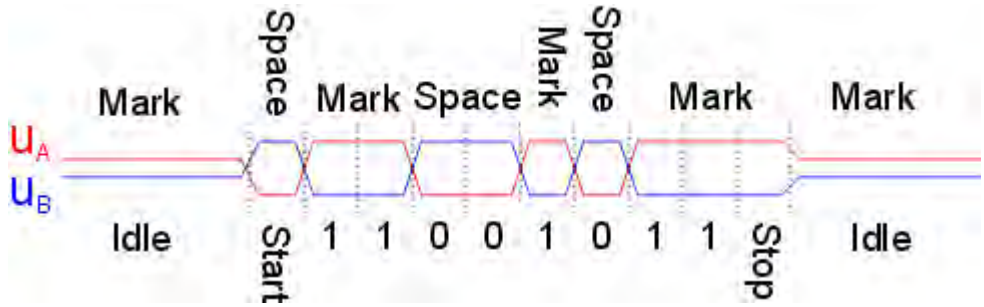

Figure 12 - Typical waveform for data transmission on an RS-485 network [15]

As mentioned before, RS-485 allows for multiple devices to be connected in a "bus" configuration. This allows multiple modules to be connected to the ROV communications network and for extra modules to be added with minimal effort. Each module is assigned an address and only responds if it receives the correct address, otherwise it will not communicate on the network. In this way, a designated "master" module can address each module individually, request information from it and send commands to it.

Figure 13 below shows a typical wiring topography connecting four modules together on a two wire RS-485 multi-drop network.

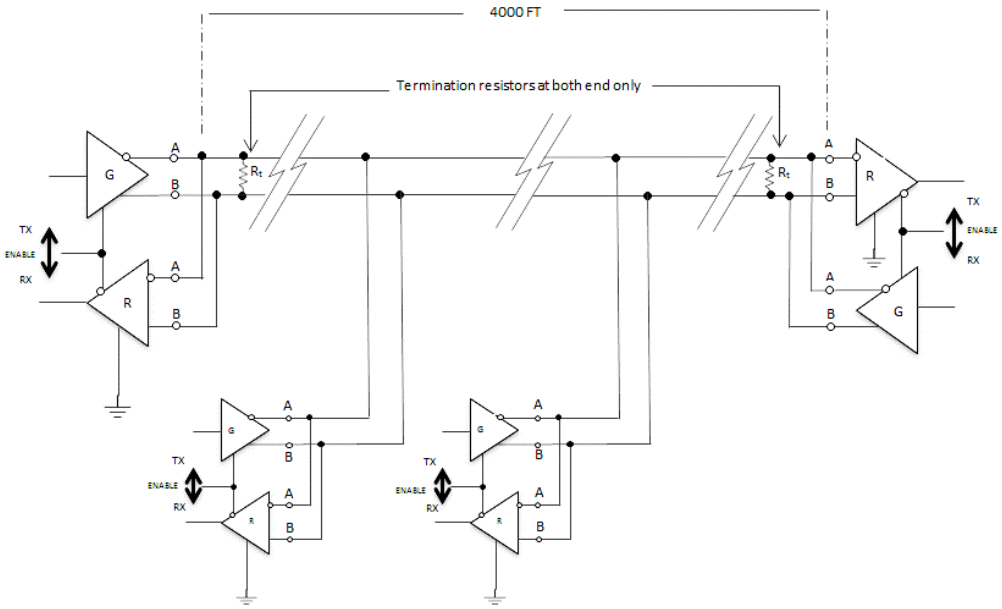

Figure 13 - RS-485 Two wire multi-drop network wiring [16]

2.7. Summary

Remotely operated vehicles or ROVs consist of a surface control console, a tether and a submersible. The control console contains the human interface for the system and transmits user inputs and displays information from the submersible. This exchange of data goes via the tether, which relays power and data from the control console to the submersible.

ROVs range from small observation vehicles to huge deep-water cable laying or mining vehicles. The UCT *SEAHOG* ROV falls into the general observation class ROV. It has a dry mass of about 80 kg. It is equipped with lights, forward and rear facing cameras and a basic gripper. The *SEAHOG* is being developed by RARL as a result of a request from the UCT Biological Sciences department. The purpose of the ROV is to locate, retrieve and deploy marine research equipment and in the long term, to gather marine samples at depths of up to 300 m.

The *SEAHOG* is an under-actuated system with the roll and pitch degrees of freedom not controllable with current thruster arrangements. The *SEAHOG* has a sonar unit and designated housing for position sensors and control hardware. These units will form part of the RS-485 multi-drop communications network on the ROV.

Now that the UCT *SEAHOG* ROV is better understood, an investigation can be undertaken into the necessary aspects needed to successfully control it with reference to the information given in this chapter.

3. Underwater Localisation

3.1. Introduction

To be able to control the position of the ROV it is first necessary to know what the position of the ROV is – whether it is an absolute geodetic position, the position of the ROV relative to the controller console or just the position of the ROV relative to an arbitrary beacon with a fixed position. Each of these positioning strategies has its own challenges, advantages and disadvantages. Each of these strategies will be considered and investigated in this chapter.

This chapter will discuss the limitations and difficulties of position sensing underwater and will then go on to describe some techniques and methods for finding the position of a body underwater. This detailed investigation will give enough insight so as to understand the different methods of position sensing underwater, their limitations and the consequences thereof. From this information, the extent to which the ROV can be controlled will be clearer and any control laws developed in the main part of this report will be done with a clear understanding of how the motion of the ROV will be tracked in the water.

3.2. Limitations of Sensors Underwater

3.2.1. The Underwater Environment

Water as a medium varies hugely from that of air and thus when operating in water, ground based terrestrial sensing techniques may not be effective. It is thus important to know what effect water has on the capability of sensory localisation. In underwater wireless sensor networks (UWSNs), determining the location of every sensor is important and the process of estimating the location of each node in a sensor network is known as localization [17]. While Global Positioning System (GPS) receivers are commonly used for localisation in terrestrial wireless sensor networks (WSNs), they are unfeasible in UWSNs as GPS signals do not propagate through water [18]. Acoustic communications is the most promising mode of communication underwater [18]. However, underwater acoustic channels are characterized by harsh physical layer conditions with low bandwidth, high propagation delay and high bit error rate [18]. Moreover, the variable speed of sound, and the non-negligible node mobility due to water currents pose a unique set of challenges for localization in UWSNs [18].

3.3. Acoustic Positioning

3.3.1. Introduction

As previously mentioned, GPS does not work underwater due to the attenuation of electromagnetic waves in water. This makes the challenge of underwater localisation substantial. Sound Navigation Ranging (Sonar) was invented in the early 1900s and during the World Wars, submarine warfare resulted in the introduction and large scale use of Sonar as a position sensing technique [19]. Sonar uses acoustic pulses to detect and determine the position of an object underwater. This section will describe how Sonar and acoustic positioning works, the different technologies that make use of the principles of acoustic positioning and the capabilities of these technologies.

3.3.2. Sonar

Passive Sonar

There are two types of Sonar: Passive and Active. Passive sonar works on the principles of merely "listening" for acoustic disturbances at specific frequencies in the water. This can give information on how far something is away from the receiver if it is transmitting the calibrated frequency. Figure 14 alongside shows the principle of how passive Sonar works – for example, a hydrophone array that is calibrated to pick up an acoustic pulse from a submarine. The intensity and direction of the received pulses will give an indication of the position of the submarine relative to the sensor.

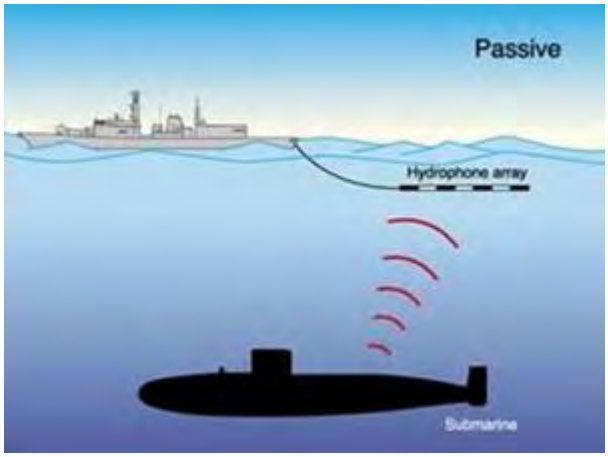

Figure 14 - Principle of Passive Sonar Operation [41]

Active Sonar

Active Sonar is more sophisticated and sends out its own acoustic pulse and "listens" for a return pulse or echo (shown alongside in Figure 15). Sound waves in the water will reflect off of solid objects. The closer the object is, the higher intensity the return pulse will be. Since active Sonar units generate their own acoustic pulse, its direction can be controlled and thus the geography in that direction can be determined. The *SEAHOG* is equipped with a Micron Sonar unit from Tritech. It is an active Sonar unit and scans in a two-dimensional plane, sending pulses, receiving their echoes and hence detecting obstacles in the surrounding environment in a two dimensional plane.

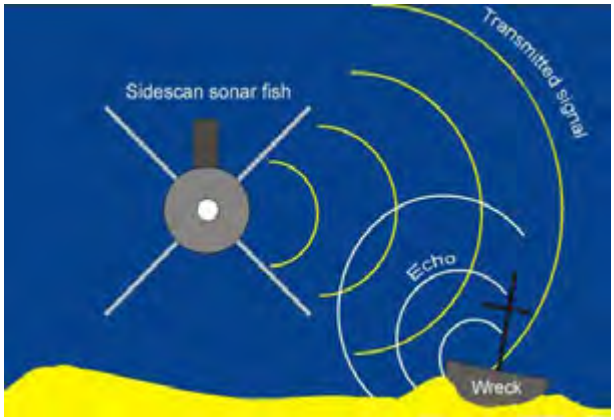

Figure 15 - Principles of Active Sonar Operation [42]

Figure 16 below shows a test of the Micron Sonar unit to be used on the ROV. The physical setup of the test is shown on the right and the Sonar display is shown on the left. It can be seen that the Sonar unit accurately detects the swimming pool walls and other solid features such as the swimming pool steps by scanning 360˚ about its axis. An image is built up by interpreting the data of the echoes received by the sonar unit.

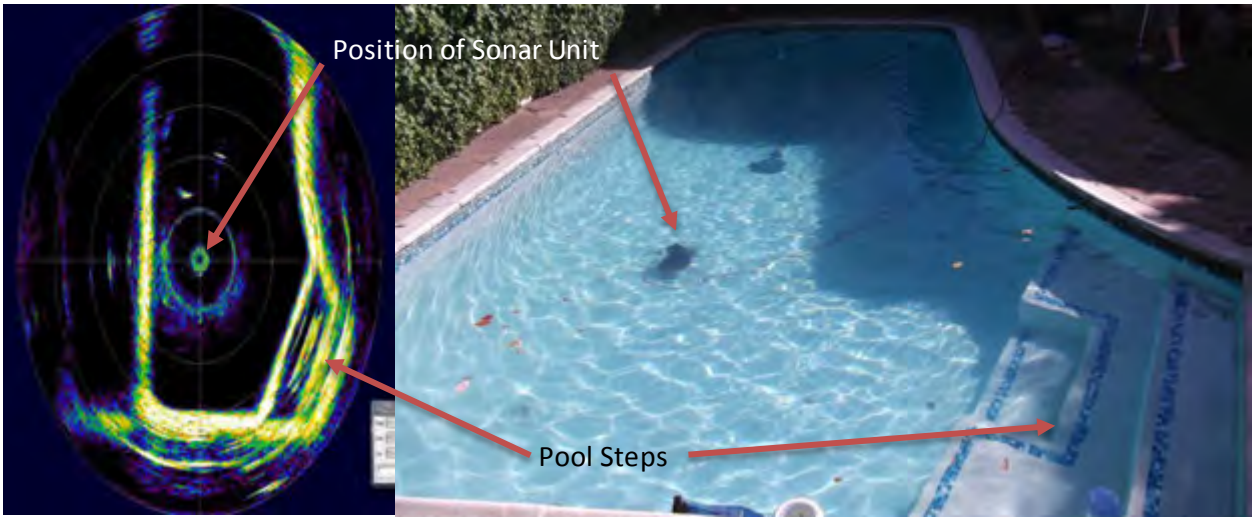

Figure 16 - Micron Sonar pool test and Sonar Image [left]

Automatic Control with Sonar

Now that the principles of Sonar have been investigated, the question of how to use this technology in automatic control remains. While Sonar uses acoustic waves as a sensory mechanism, control by Sonar is achieved by interpreting the received data from the acoustic pulses. This interpretation is done by applying digital signal processing (DSP) methods. For this reason, automatic control using Sonar technology will not be discussed in this section but later in this chapter where vision based control is discussed, since vision based control also relies on DSP.

Factors that Affect Sonar Accuracy and Range

Acoustic sensing relies heavily on the correct velocity of sound in water. If an inaccurate value is used, the determined position will be inaccurate. Thus, factors that affect the velocity of sound will determine the accuracy of the system. Some of these factors are [20]:

- The presence of thermoclines
- Salinity
- Pressure

Thermoclines are temperature gradients in the water, typically a function of depth. In addition, since pressure in a fluid increases with depth, acoustic technology must be able to account for this.

Additional factors that will determine the effectiveness of acoustic technology are [21]:

- The presence of acoustically reflecting surfaces within the operating environment
- Ambient noise
- Volume reverberation
- Surface and seabed reflectivity

Summary

Now that the principles and mechanisms of acoustic positioning have been discussed, using Sonar as an example, and that the challenges of acoustic positioning are known, other acoustic positioning systems can be discussed with more insight.

3.3.3. Baseline Technologies

Principles

Baseline sensing uses acoustic pulses in a similar way to Sonar as previously discussed. In addition, the principles of trilateration, also employed in GPS, are used to determine a position. Baseline technology however is not exactly the same as GPS. It relies on the communication between two devices: transducers and transponders. Due to the nature of baseline positioning, a large amount of computing power is required to interpret all the necessary data required in obtaining a position. Thus, baseline units are often supplied with a dedicated computer for this purpose. An example of the three basic elements of a baseline positioning system are shown below in Figure 17.

Figure 17 - The MicronNav USBL Navigation System from Tritech [22]

Hardware and Types of Baseline Positioning

As shown previously in Figure 17, baseline positioning relies on three separate types of devices:

- Transducers
- Transponders

- Data Processing Computers

A transceiver is a device that can, when commanded, transmit and receive signals. A transducer is similar to a transceiver, but it has the added characteristic of converting one energy form to another (electric to acoustic in this case). A transponder, on the other hand, will receive and transmit signals but only when interrogated by another device to do so. In other words, a transponder has a fixed function and acts independently to user inputs. In the context of an ROV, a transponder on the ROV will be constantly listening for a pulse that it is calibrated to receive. Once it detects or receives that pulse, it will respond in a predetermined way. Different types of baseline technologies exist that work on this principle, each with subtle differences that offer different advantages. Types of baseline positioning include:

- Long Baseline Positioning (LBL)
- Medium Baseline Positioning (MBL)
- Short Baseline Positioning (SBL)
- Ultra-Short Baseline Positioning (USBL)

The differences between the above types of baseline technologies is in fact the length of the "baseline". The baseline is the physical distance between either the transponders or transceivers that will be used to trilaterally determine the position of the object.

How Baseline Positioning Works

Baseline positioning relies on the communication between a transducer and a transponder. In USBL positioning, a transponder will be mounted on the ROV and a transducer will be mounted a few metres under the water surface, usually attached to the vessel on which the control console is stationed.

In this case, as the name suggests, the baseline between transceivers that are used for trilateration is "ultra-short". This is manifested in the transducer – which contains an array of transceivers for picking up signals from the transponder. An example of the transceiver array can be seen previously in Figure 17: the black end of the dunking transducer is where the transceiver array is located. In long baseline positioning however, the baseline can be hundreds of metres [23].

The transducer will scan a three dimensional hemisphere underneath the surface of the boat in a similar way to how Sonar scans in a two dimensional plane. When the acoustic pulse is detected by the transponder on the ROV, it will respond with its own pulse. This pulse is then picked up by the transceiver array mounted on the transducer. Trilateration is performed using the differences in signal intensity sensed by each transceiver (see section 2.6.2 for an explanation of trilateration). In this way, the three dimensional position of the ROV can be found beneath the surface of the water. This makes USBL an incredibly powerful method of position sensing underwater. A depiction of how the devices in a USBL system interact is shown

following in Figure 18. The transceiver can be seen sending out a pulse first and then the transponder responding with its own pulse.

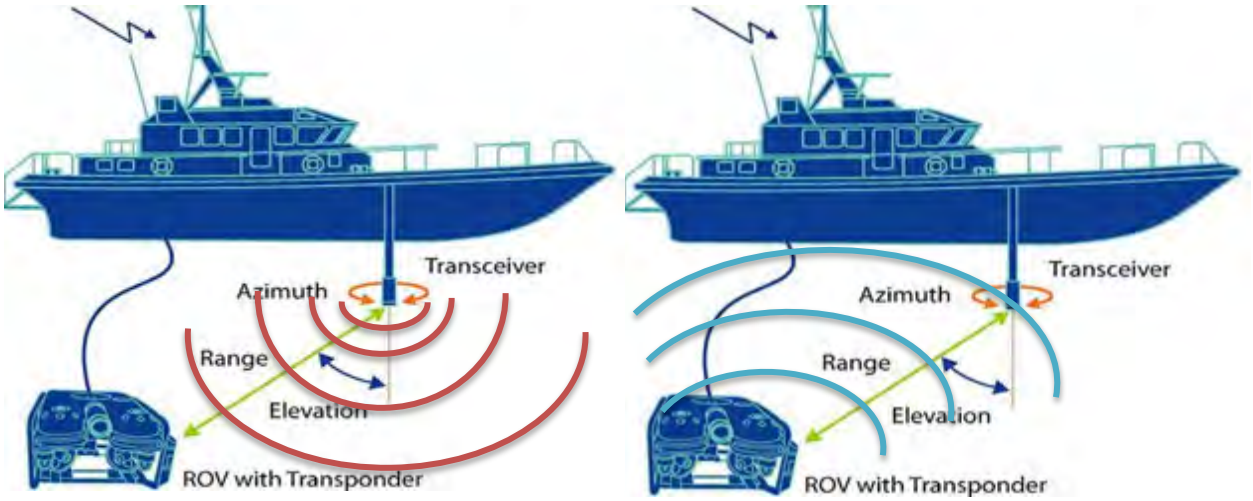

Figure 18 - Depiction of the elements in a USBL system and how they interact [24]

Differences between LBL and USBL

The application of LBL positioning varies from that of USBL. This is because while the technology that is employed is essentially the same in each, there are subtle differences between the two te chniques, which are more suited to different applications. Table 2 below compares some of the main features of these baseline position sensing techniques.

Table 2 - Comparing a typical LBL system with a typical USBL system [23] [21]

Baseline Technology	Transponder Location	Transceiver Location	Baseline Length	Data Processing Location	Advantage of System	Disadvantage of System
LBL	Array - of a known formation on seabed, separate to ROV	ROV Mounted	Hundreds of metres	ROV/Surface	Not Restricted by Depth of Operation	Requires accurately fixing transponders to seabed
USBL	Single unit attached to ROV	Below surface, attached to boat	Tens of millimetres	Surface	Compact, easily deployable system	Limited depth range (150 m)

From the above table it can be seen that LBL is better suited to more permanent, deep sea applications whereas USBL suits rapid deployment but shallower depths. USBL has been depicted previously in Figure 18 and so it is well understood. Figure 19 following shows a typical LBL positioning system. It can be seen that the transponders are fixed to the seabed in a known formation.

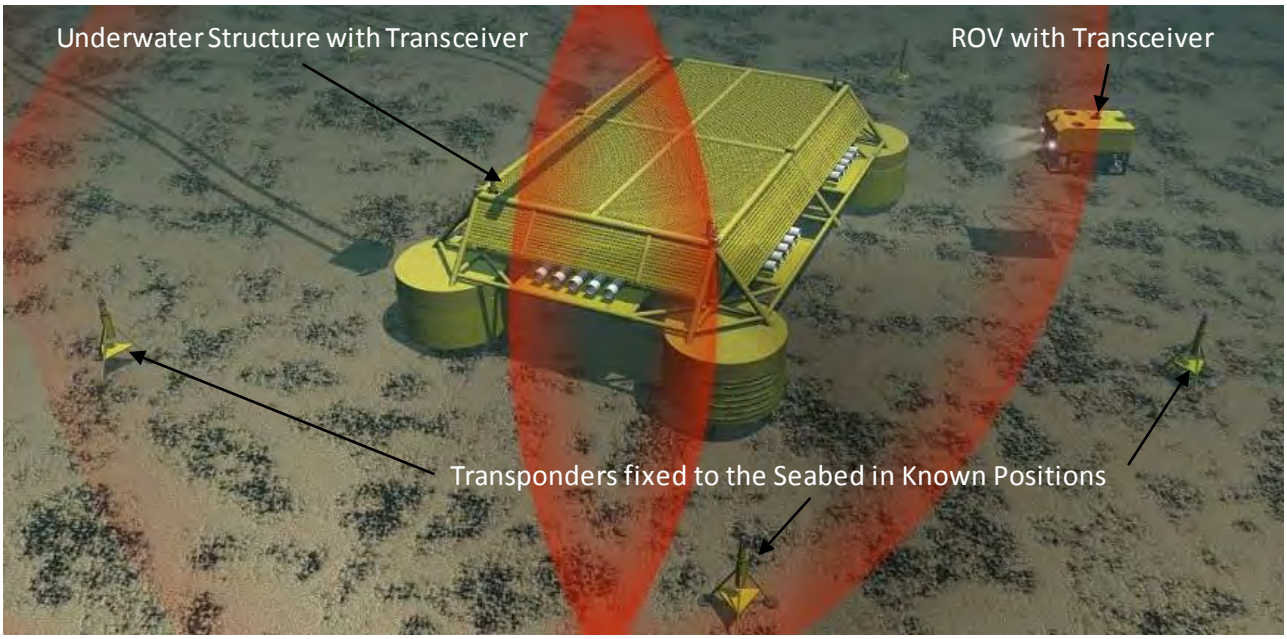

Figure 19 - Typical Long Baseline Positioning System [23]

LBL positioning provides a high accuracy of positioning (within 50 mm range [23]) and is a widely used method for controlling ROVs or even positioning underwater structures.

Capabilities and Complexities of Baseline Sensing

Baseline position sensing is incredibly useful. The level of accuracy that can be achieved is about 50 mm for LBL [23] and about 200 mm for USBL [22]. In addition, GPS receivers can be integrated into the baseline's data processing computer which effectively allows for an absolute geodetic position of the underwater vessel to be found. Baseline technology offers a complete and accurate solution to localise the ROV in its environment and is widely used in any dynamic positioning applications underwater. Dynamic positioning includes automatic control functions such as station keeping or position holding. The ROV needs a three dimensional position reading to be able to retain its three dimensional position – and baseline technology offers a means to position sensing in three dimensional space.

A disadvantage of baseline technology is the high cost. This is an understandable factor however because of the complexity of the system. For instance:

1) A USBL system must account for all the factors that affect the speed of sound in water as listed in section 3.3.2.
2) Because of the close proximity of transceivers on the USBL transducer, they must each be able to sense very subtle differences in signal intensity in the presence of large amounts of noise.
3) The transducer must be able to sense its current orientation, since the boat is not fixed and will sway in the water – which will affect the direction of the acoustic pulse that it sends out. For this reason, USBL

transducers usually include inertial sensors that can determine the orientation of the vessel that they are mounted to. Inertial sensing is discussed later in section 3.4.

4) The data processing computer must be able to interpret all of this data, filter it and supply position updates at a reasonable rate.

This also demonstrates why the construction of one of these systems is too complex to be feasibly included in this project.

Summary

Baseline sensing is highly sophisticated and uses multiple technologies and filtering algorithms to accurately determine the position of a submersed vessel. It uses acoustic pulses in a similar way to Sonar and employs inertial sensing to assist in determining the orientation of the transducer. Baseline systems usually consist of transducers, transponders and a data processing computer. Different configurations of these elements are used depending on what length of baseline is being employed. Long baseline positioning uses an array of transponders with known positions and an ROV mounted transceiver. Ultra-short baseline positioning uses an ROV mounted transponder and a vessel mounted transducer. Both these systems can achieve a positional accuracy of less than 200 mm which can be combined with a GPS to obtain an absolute geodetic position.

3.3.4. Doppler Velocity Logs (DVLs)

Principles

A Doppler velocity Log (DVL) is an acoustic sensing technology that can determine the velocity of a vessel using the Doppler Effect. DVLs are transducers that send acoustic pulses towards the seabed and receive an echo similarly to an active Sonar device. Often a DVL transducer will be combined with other DVLs to form a phased array. By varying the direction and combining more than one DVL transducer, more data can be obtained from the same unit. A phased array DVL is shown below in Figure 20.

Figure 20 - Workhorse Navigator Doppler Velocity Log from Teledyne RD Instruments [25]

How DVLs Work and the Doppler Effect

A DVL will be mounted to a vessel facing downwards so that it can send acoustic pulses towards the seabed. The transducers are angled slightly from the vertical so that if the vehicle is moving, the relative velocity of the returning echo will be different to the velocity of the pulse sent out. This is effectively the principle of the Doppler Effect and allows the velocities of a vessel to be accurately determined.

An acoustic pulse will move at a certain velocity through the water on its own. If the pulse is transmitted from a moving ROV, however, the velocity of the ROV and the velocity of the pulse will combine. In effect, the ROV is "pushing" the pulse along faster than it would usually go (if the pulse is in the direction the ROV is moving). This means that the echo will appear to be moving faster than expected. The DVL then measures how fast the echo pulse is moving and can compare the speed of it to the speed of the generated pulse. This can then be used to determine the velocity of the ROV.

Capabilities and Complexities of a DVL

A DVL will have to compensate for all the factors listed in section 3.3.2 that affect acoustic waves in water. In addition, since acoustic waves in water are a complex area of study, a great deal of testing and investigation to develop a system that delivers a reasonable degree of accuracy will be required. This is not feasible within the scope of this project.

A great advantage of knowing the velocity of the vessel is that it can be simply integrated to determine the distance travelled for that data sample. DVLs can obtain accuracies of up to 0.4% of the total distance travelled by the vessel [26]. This means that if an ROV moves 100 m forwards then the DVL will measure the ROV to have moved within a range of 99.6 – 100.4 m. A phased array DVL can combine its individual transducer readings to determine the velocity in both the horizontal and vertical plane of the ROV. In addition, a DVL can determine what speed the water is moving relative to the ROV and hence determine if there are any currents present.

Similarly to Baseline positioning, a DVL will need to sense its orientation in the water. This makes it a complex system that requires high accuracy hardware and high data processing power. For this reason, the price of DVLs is quite high within the scope of this project.

3.3.5. Summary

GPS does not work underwater due to the attenuation of electromagnetic waves in water. This means that alternative methods must be used to determine the position of an ROV underwater. Acoustic technologies such as Sonar, Baseline Sensing and Doppler Velocity Logs are all a promising alternative to GPS to solve the problem of underwater localisation. The disadvantages of these systems is that they are quite expensive, within the scope of this project, due to their complexity.

Sonar based control relies on the interpretation of digital signals and will be covered in section 3.5 later.

Baseline technology allows for accurate position sensing underwater using the communication between transponders and transducers. Ultra-Short Baseline Positioning is a promising method of localising the ROV underwater due to its compact and easily deployable nature. USBL can obtain accuracies of up to 200 mm and has a depth range of about 150 m.

Doppler velocity logs can give the velocity of the ROV and the surrounding water in the horizontal and vertical planes to within an accuracy of 0.4% of the distance travelled by the ROV. This is achieved with a phased array of transducers that transmit acoustic pulses towards the seabed and measure the Doppler frequency shift in the returning echo. This will give the velocity of the ROV, which can then be integrated to find the change in position of the ROV in that direction.

3.4. Inertial Position and Orientation Sensing

3.4.1. Introduction

Inertial sensing refers to sensors that respond to the movement of an inertial body and it is the most commonly used method to sense physical motion. This is because inertial sensors are relatively simple to make and require no long distance or remote transmission of data. As a result of this, inertial sensors are the cheapest and most accessible solution to sensing motion. In addition, with improvements in manufacturing, inertial sensors have become miniaturised and as many as 9 different sensors can be contained in a 4x4x1 mm integrated circuit (IC) [27]. In general, modern inertial sensing units output data in digital format and thus this section will discuss inertial sensing from a digital electronics viewpoint.

Inertial sensing relies on the use of three different types of sensor, namely:

- Accelerometers
- Gyroscopes
- Magnetometers

Accelerometers sense linear accelerations, gyroscopes sense rotational velocity and magnetometers sense local magnetic field. These sensors are usually combined in the same IC and aligned to three orthogonal axes. This effectively gives a 9 DOF sensor that can sense acceleration, rotation and magnetic field in three axes.

Each of these sensors can be manufactured in different ways and employ different types of technology to obtain a sensory reading. The most common types of accelerometers are micro-electromechanical system (MEMS) accelerometers. The most common type of gyroscopes are MEMS and fibre optic gyroscopes (FOGs). A magnetometer either utilises the interaction of magnetic fields, or relies on quantum phenomena to sense a magnetic field. A magnetometer can either be scalar, and measure the total magnetic field strength in a certain position in space, or vector, and measure the magnetic field strength along a certain axis. The most commonly used magnetometer is one that uses the Hall Effect or Anisotropic Magneto Resistance (AMR). For the sake of context, these commonly used inertial sensors will be explained briefly in the next section.

While inertial sensing offers a highly compact, low cost and easily implementable solution to tracking the motion of a body, it is not without its downfalls and complications. This section will discuss basic and advanced techniques used to navigate with inertial sensors, the disadvantages associated with using them and techniques used to counteract the effects of these disadvantages.

3.4.2. Basic Inertial Sensors

MEMS Accelerometers

A MEMS accelerometer uses a combination of the following elements to determine linear accelerations:

- Moveable Inertial Mass
- Springs
- Energised Plates

The basic setup of a MEMS accelerometer is shown below in Figure 21.

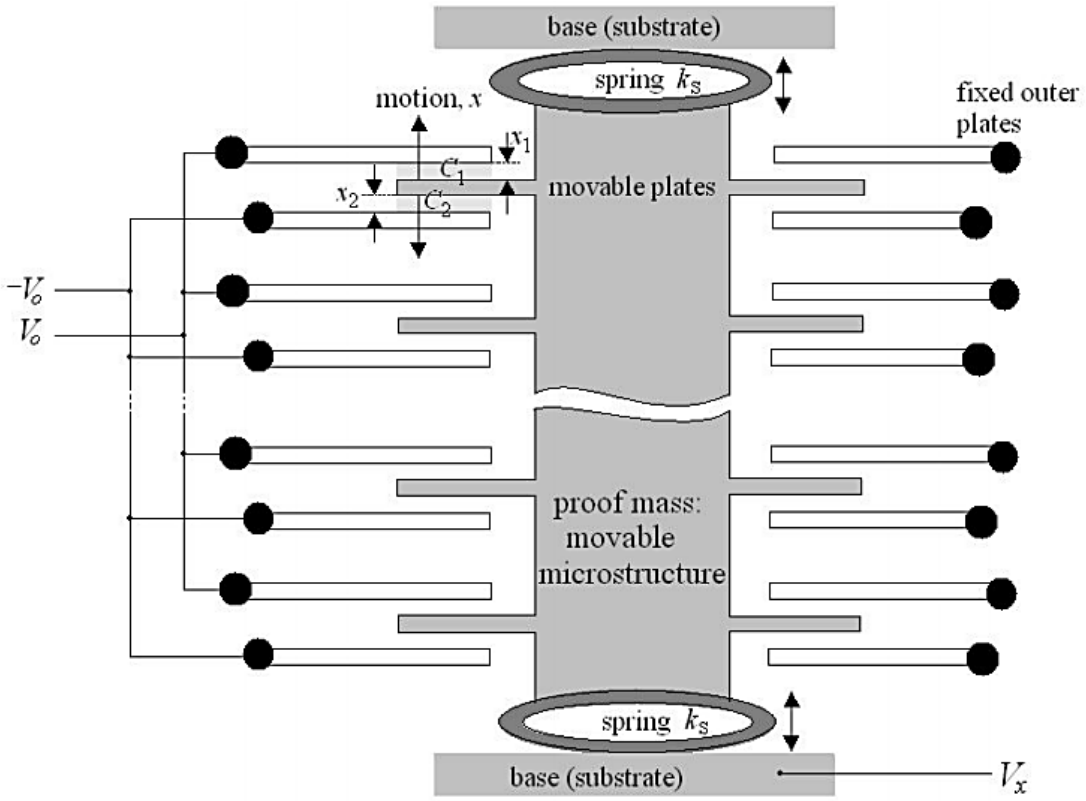

Figure 21 - Elements of a MEMS Accelerometer [28]

To give some scale to the above figure, the distances labelled x_1 and x_2 can be as small as 1.3 µm [28] which is roughly 100 times less than the width of a hair follicle. The voltage supplies V_0, $-V_0$ and V_x in the above figure shows that the movable mass and the plates connected to the black dots form pairs of differential capacitors with air being the dielectric. If the proof mass experiences an acceleration along its axis, it will move and hence change the distances x_1 and x_2. With a known spring constant k_s, known mass m and known distance between the V_0 and $-V_0$ capacitive plates, d, the acceleration is found with [28]:

$$a = \frac{k_s d}{m V_0} V_x \qquad \{3.1\}$$

MEMS Gyroscopes

A MEMS gyroscope uses the effects of Coriolis acceleration to determine an angular rate. These gyroscopes typically consist of two oscillating masses that move in opposite directions. The Coriolis force induced by a rotation and a linear velocity is given by [29]:

$$\overrightarrow{F_{Coriolis}} = -2m\vec{\Omega} \times \vec{v} \qquad \{3.2\}$$

Figure 22 below shows the resultant Coriolis forces when two masses moving in opposite directions experience a rotation Ω.

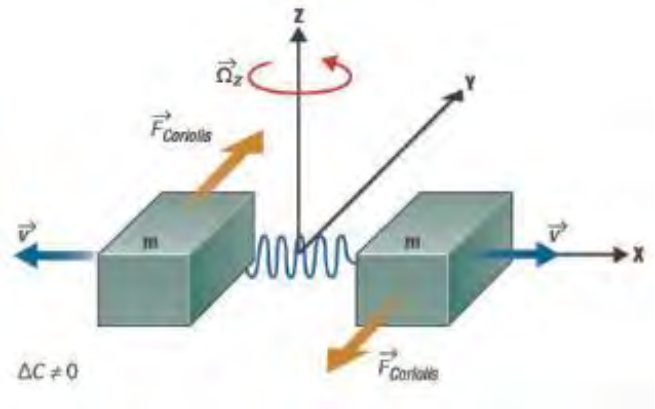

Figure 22 - Resulting Coriolis forces on two anti-oscillatory masses

The resulting physical displacement caused by the Coriolis force is then read from a capacitive sensing structure [29]. When angular velocity is applied, the Coriolis force on each mass acts in opposite directions. This differential value in capacitance is proportional to the angular velocity Ω and is then converted to an output voltage [29].

The reason that a mass pair is used is that when linear acceleration is applied to two masses, they move in the same direction. Therefore, there will be no capacitance difference detected. The gyroscope will output zero-rate level of voltage, which shows that the MEMS gyroscopes are not sensitive to linear acceleration such as shock, or vibration [29].

Fibre-Optic Gyroscopes (FOGs)

A fibre-optic gyroscope uses the relative distance that light travels to determine an angular velocity. These gyroscopes tend to be more accurate than MEMS gyroscopes but are generally much more expensive and take up more space.

A FOG uses a long length of optical fibre (approximately 3km) wound into a small coil [30]. Light is launched into both ends of the fibre coil simultaneously and when this light has travelled along the fibre, it is then split from the fibre into a detector. The two 'paths' of the light that have travelled around the fibre coil (in opposite directions) are compared, and any difference in the time taken for each beam to travel around the coil is measured by interference techniques [30].

If during the passage of the light around the coil, the sensor assembly is rotated, the light travelling in one direction will have to go further than the light travelling in the opposite direction. This will cause a very small difference in the time of the received light beams, but this can be detected and translated into a measurement of how far the sensor has turned [30]. Figure 23 below shows this principle.

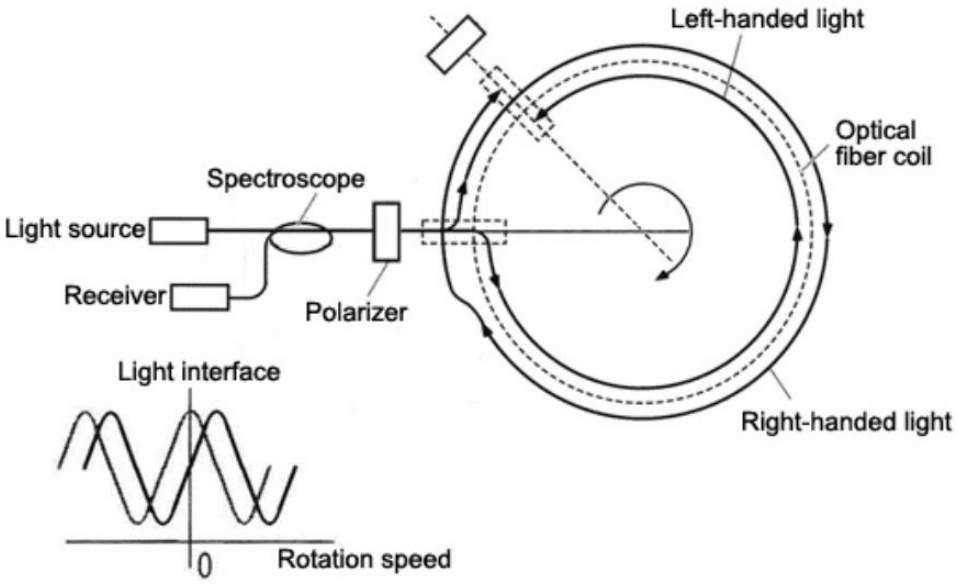

Figure 23 - Principle of a FOG [30]

The number of times the fibre-optic cable is coiled and the diameter of the coil will affect the length of the fibre. The longer the fibre and the more coils that there are, the greater the difference will be for a smaller rotation. This, combined with the sensitivity of the light interferometer unit, is the reason for sizable lengths of fibre being used in FOGs.

Anisotropic Magneto Resistance (AMR) Magnetometers

AMR Magnetometers are slightly less common than Hall Effect magnetometers but are becoming more popular and competitive with them as technology improves [31].

AMR magnetometers make use of a common material, Permalloy, to act as a magnetometer. Permalloy is an alloy containing roughly 80% nickel and 20% iron. The alloy's electrical resistance depends on the angle between the direction of current flow and the alloy's magnetization vector [31]. In an external magnetic field, the magnetization vector rotates toward the direction of the magnetic field and the rotation angle depends on the external field's magnitude [31]. The resistance of the Permalloy strip is minimum when the magnetization vector is perpendicular to the direction of current flow. The effect of an external magnetic field on Permalloy's magnetization vector is shown alongside in Figure 24. To ensure that the Permalloy resistors act in a predictable manner, they are all magnetized in the same orientation by a strong magnetic field during manufacture. The resistor is usually magnetised parallel to its axis. This orientation is known as the "easy axis" as shown alongside in Figure 24.

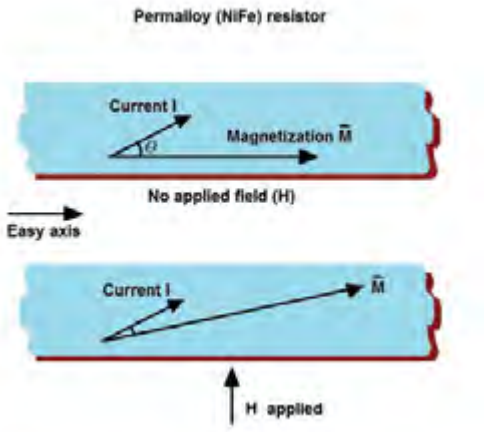

Figure 24 - Effect of an external magnetic field on an anisotropic material

AMR also has better sensitivity than other methods and reasonably good temperature stability. Four AMRs are usually connected in a Wheatstone bridge arrangement to provide better sensitivity [31].

Hall Effect Magnetometers

The most common magnetometer is one that employs the Hall Effect. It works on the principle that a voltage can be detected across a thin metallic element when the element is placed in a strong magnetic field perpendicular to the element's plane. The detected voltage is referred to as the Hall voltage. This effect is demonstrated below in Figure 25, where *B* is the external magnetic field and *I* is the current flowing through the element.

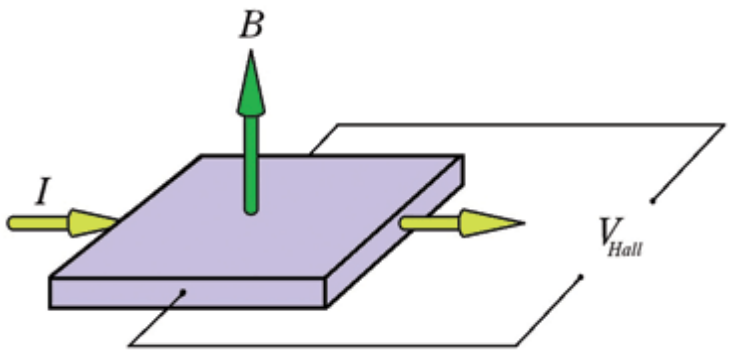

Figure 25 - The Hall Effect

The Hall voltage is given by the relationship:

$$V_{Hall} = \not{k}|I \times B| \quad \{3.3\}$$

Where k is a constant related to the conductor's material properties and dimensions.

Summary

MEMS accelerometers, MEMS gyroscopes and Hall Effect magnetometers are the cheapest most commonly used basic inertial sensors. Now that these sensors are understood on a fundamental level, the way in which these sensors are used can be investigated.

3.4.3. Obtaining Position and Orientation from Inertial Sensors

Introduction

From the previous section, an understanding of basic inertial sensors has been gained. However, each of these sensors only fulfils a specific, limited function. In basic applications such as one DOF tracking, one type of inertial sensor can be adequate for sensing the required motion. However, in order to navigate and track the complete motion of a free body using inertial sensors, a combination of accelerometers, gyroscopes and magnetometers are required – this combination of sensors is called an Inertial Measurement Unit (IMU). This section will briefly describe how inertial sensors are used to find position and orientation and how the motion of the ROV will be tracked using them.

Obtaining Linear and Angular Displacements from Inertial Sensors

This section will describe how displacements of position and orientation are obtained from a single accelerometer, gyroscope and magnetometer respectively.

Accelerometers: On their own, accelerometers provide an acceleration reading, which is the second derivative of position with respect to time. Theoretically the acceleration from the sensor can be integrated twice to obtain a change in position of the body, however, in a digital system the procedure for finding position is subtly different as it is a discrete, iterative process. Since a digital system has a finite sampling period or data output rate, the accelerometer reading can be multiplied by the sampling period to determine the change in velocity of the body. The acceleration can be integrated twice over the sampling period time to find the change in position of the body. Since this change in position is dependent on the velocity reading and the acceleration reading, it is necessary to keep track of the previous velocity and position. A flow chart showing the most basic algorithm for tracking the position of a body using inertial sensors is shown following in Figure 26.

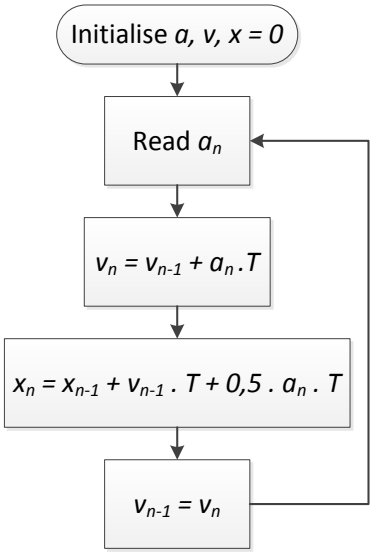

Figure 26 - Algorithm to find change in position from discrete acceleration readings

In the above diagram, T is the sampling period, $v_0 = 0$ and $x_0 = 0$. It is crucial that the initial condition of the vessel is stationary for the calculated position to be accurate. This is because of the dependence of the position reading on previous velocity readings, which cannot be directly determined from inertial sensors.

Gyroscopes: On their own, gyroscopes provide an angular rate. This can be multiplied by the sampling frequency of the gyroscope to obtain a change in orientation. In this way, each time a new change in orientation is available, it can be added to the previous total change to obtain the new total change in orientation from a relative starting point. It is not necessary for the vessel to be stationary for the initial condition of the gyroscope. This is because gyroscopes output a rate of change of orientation, which is only the first derivative of angular position.

Magnetometers: As was previously discussed, magnetometers provide a measure of the local magnetic field. This reading is often calibrated so as to be able to interpret the Earth's own magnetic field. This will be discussed in the next section.

Now that the simple dynamics of inertial sensors is understood, tracking motion in six DOF can be discussed.

Tracking the Motion of a Free Body

A rigid free body has the ability to translate along three orthogonal axes and to rotate about three orthogonal axes. This gives a total of six DOFs. A general depiction of the types of motion that a free body can undergo are shown alongside in Figure 27. The linear motion that the body undergoes will be referred to as a change in position and the rotational motion that the body undergoes will be referred to as a change in orientation.

Figure 27 - Translational and rotational motion for a six DOF system [44]

There are various ways in which these six DOFs can be tracked using inertial sensors. The least number of sensors necessary to completely track the motion is six. The choice of sensors can be either:

1) Three accelerometers (one aligned to each axis) and three gyroscopes (one aligned to each axis).
2) Three accelerometers as above and three magnetometers (one aligned to each axis).

It can be seen that different types of inertial sensors need to be combined to make tracking the complete motion of a six DOF system possible. Now that this is clear, and that the basic dynamics of inertial position tracking are understood, the methods in which these sensors are combined to track the complete motion of a free body can be discussed.

Obtaining Six DOF Position and Orientation from Inertial Sensors

As was mentioned in the previous section, the minimum number of inertial sensors required to determine the complete motion of a free body is six. In addition, there are two combinations of inertial sensors that can achieve this:

1) Three accelerometers (one aligned to each axis) and three gyroscopes (one aligned to each axis).
2) Three accelerometers as above and three magnetometers (one aligned to each axis).

This subsection will discuss how sensor data is used in each of the above cases to determine the complete position and orientation of a free body.

1) The first case is quite simple. Accelerometers are used to measure the linear position of the body as described previously. Gyroscopes track the rotation of the body in three axes – they are typically arranged in a gimbal arrangement. In this way, all six DOFs are accounted for.
2) In the second case, once again the accelerometers are used to determine linear position in three axes. The magnetometers are used to calculate the orientation of the body. An initial calibration will determine the strength and direction of the Earth's local magnetic field. This reading, typically, is then

compensated for so that the compensated magnetic field points in a convenient direction with respect to the other sensors. This principle is shown below in Figure 28, whereby the measured Earth's magnetic field is compensated for in such a way that it aligns with the gravity vector.

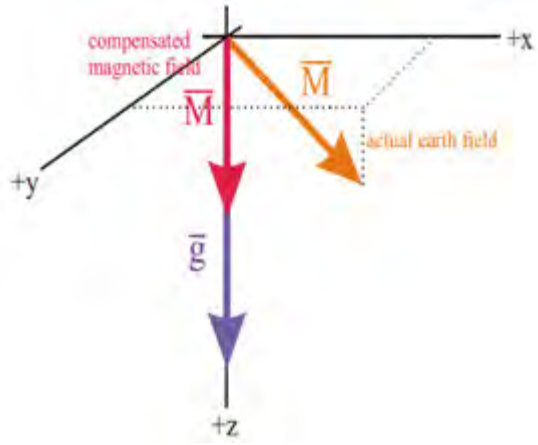

Figure 28 - Measured Earth magnetic field and compensation to align it with the gravity vector

As the x, y and z magnetometer components change, the orientation of the body can be determined using simple geometry. Figure 29 following shows how three magnetometers can be used to determine the orientation of a body. The Earth's magnetic field vector **M** is shown. After calibration and compensation, this vector has known length and orientation. The vector is displayed in a co-ordinate frame that is fixed to the body hosting the magnetometers. Since the length of **M** is known, the components of **M** can be found in the body fixed x, y and z axes and hence the rotations about the x, y and z axes can be determined.

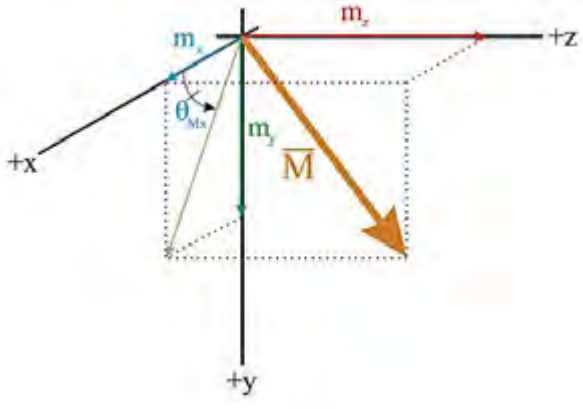

Figure 29 - Earth Magnetic Field Read by Magnetometers [32]

Summary

Position readings can be obtained from accelerometers by integrating the acceleration reading twice with respect to the sensor's sampling time. It is very important that the sensor starts tracking the motion of the body when it is stationary, as accelerometers cannot determine the velocity of a body directly. Gyroscopes provide a rate of rotation and thus a total change in angle can be determined by integrating the gyroscope readings with respect to the sensor's sampling time. The body does not have to be stationary initially to get an accurate change in angle. Magnetometers measure local magnetic fields. The Earth's field is first

calibrated and then compensated for in a magnetometer, so that enough information is known to determine the orientation of a body as the direction of the magnetic vector changes.

The two methods detailed in the previous subsection are the most basic approaches to tracking the position and orientation of a free body. In practice however, it is necessary to combine sensors to achieve more stable and accurate readings. This is due to the weaknesses of the inertial sensors.

Now that inertial sensors and how they are used is understood, common methods used to improve their effectiveness can be discussed. This will also require highlighting the strengths and weaknesses of inertial sensors and some of the challenges faced when using them.

3.4.4. Combining Inertial Sensors: Sensor Fusion and State Estimation

Introduction

Sensor fusion is a huge field of research and is sometimes known as state estimation. Algorithms of how to best combine inertial sensors to give the most accurate estimation of a position or orientation for different applications are constantly being developed. In the scope of this project, it will be necessary to implement this technology rather than develop it from the ground up and for this reason, the information presented in this section will provide a general understanding of how sensor fusion is implemented without going into too much detail.

Sensor fusion is the act of combining different sensors so as to provide more information about the overall motion of a body. In addition, combining more sensors allows the strengths of each type of sensor to be taken advantage of. Certain environments are not suitable for certain sensors, and thus it becomes necessary to have multiple methods of sensing motion. While sensor fusion refers to combining sensors in general, because of the miniaturisation and compactness of inertial sensors, combinations of them are often found on the same IC in an IMU. As a result, extensive sensor fusion research has been carried out on the combining of inertial sensors.

Inertial sensing is not a preferred method of absolute position tracking as the double integration of acceleration leads to rapid error growth – this will be discussed in more detail later. Inertial sensing, however, is often used very effectively to determine the orientation of a body.

Accurate Sensing of a Body's Orientation

The orientation of a body can be determined with three orthogonal inertial sensors. These three sensors can be accelerometers, gyroscopes or magnetometers. The previous section described how gyroscopes and magnetometers are used to find the orientation of a body. Accelerometers use the same procedure as magnetometers – except instead of measuring the Earth's magnetic field, they measure the gravity vector caused by the Earth while assuming that it always points towards the Earth's centre.

In practice, all of these sensors are combined to determine the orientation of a body as they all have strengths and weaknesses. Some examples of these are listed following in Table 3.

Table 3 – Strengths and weaknesses of orientation sensing with different inertial sensors

Sensor	Advantages	Disadvantages
Accelerometer	Impervious to magnetic fields. Determines orientation from a static, stable reference.	Transient linear accelerations cause the resultant sensed acceleration vector to increase in magnitude. It is thus no longer only comprised of gravity, which is a necessity when determining orientation from accelerometers
Gyroscope	Impervious to magnetic fields. Measures rotational states independently of environment.	There is an inherent bias in gyroscopes that results in the zero reading from a gyroscope drifting over time. Navigation via gyroscope is limited due to no North seeking capability.
Magnetometer	Provides North measurement inherently.	External magnetic fields other than the Earth's will be sensed by the magnetometer. This elongates the resultant magnetic vector that is sensed. Orientation can only be sensed from magnetometers when they are only under the influence of the Earth's magnetic field.

From the above, it can be seen that each method alone has some significant flaws that will occur in almost any application. For this reason, inertial sensors are usually combined and the resulting measurements are processed according to data fusion algorithms to allow the sensor that is most likely to have the most accurate reading to have the most impact on the current data point.

This can be achieved by applying a simple weighted average system, whereby each set of sensors gives its own measurement of the orientation, and is then multiplied by a weighting factor and added to the other results for an overall orientation measurement. Table 4 following gives a few examples of the types of weightings that would be given to sensors in certain applications.

Table 4 - Sensor weightings for different applications

Application	Accelerometer	Gyroscope	Magnetometer
Dynamic with high accelerations	Low	High	Medium
Part of machinery amongst ferromagnetic materials	Medium	High	Low
Slow moving marine vessels such as ships	High	Low	Medium
Aerial vehicles such as aircraft	Medium	High	Medium

Techniques of Sensor Fusion

Sensor fusion is linked to the process of state estimation. For this reason, statistical methods are often employed to combine sensor readings in an attempt to determine the orientation of a body as accurately as possible. In essence, these techniques use different algorithms to determine a level of confidence that each sensor is providing a reading that truly reflects the state of the body. Some of the statistical methods that have been implemented in sensor fusion are:

- Maximum Likelihood Estimation and Weighted Least Squares solution [33]
- Bayesian Networks [34], [35]
- Dempster-Shafer Theory [36], [35]
- Kalman Filtering [35]

As previously mentioned, in-depth understanding of the statistical methods used in sensor fusion will not be necessary in the scope of this project, however it is useful to know what the most prevalent methods in industry are. Kalman filtering is used extensively in state estimation in industry and academia. More detailed information on sensor fusion can be found in [35].

Summary

Sensor fusion seeks to combine sensors to give more accurate information about the orientation and position states of a body. Statistical methods such as Bayesian Networks and Maximum Likelihood Estimation are used to determine the probability of a certain sensor's data being accurate and then combining sets of data to give a result that better reflects the true positional states of the body. While these techniques improve the real world accuracy of inertial measurements, there are still other challenges that need to be overcome in inertial sensing. These challenges will be described in the next section.

3.4.5. Aliasing and Data Filtering

Introduction

While sensor fusion helps to significantly improve the reliability and accuracy of an IMU, it does not solve all the problems that are experienced with inertial sensing. In digital systems, the problem of aliasing is well known and is a significant contributor to positional and orientation error in inertial sensing methods. It thus becomes necessary to further process IMU data to improve the stability of the orientation and position measurements obtained from the unit. Simple filtering techniques can be applied, or more advanced techniques that attempt to predict the next IMU reading, in addition to filtering the data. This section will describe the problem of aliasing, and discuss the techniques used to counteract its effects.

Aliasing

Aliasing occurs in digital systems when the sampled signal has a frequency above that of the Nyquist frequency of the sensor sampling it. The Nyquist frequency is half the frequency that a digital system samples at. If the sampling rate of a digital system is too slow, it is possible that the sensor sampling the signal will interpret the data incorrectly and a different waveform to the real one will be observed. This concept is depicted below in Figure 30.

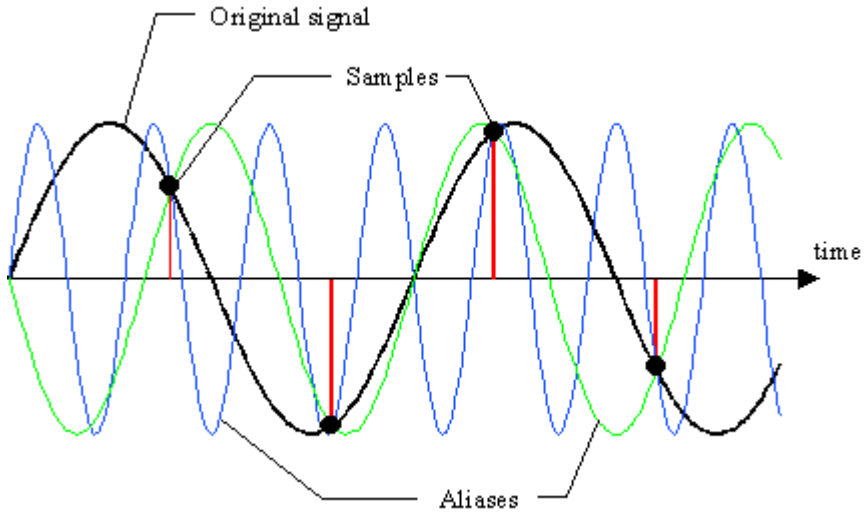

Figure 30 - The effect of aliasing in a digital system [37]

The green and blue signals above (known as aliases) are both possibilities from the given set of sampled data points. It can be seen however that they differ greatly from the original signal. Another way to think of aliasing is that it is a loss of data, which is a more direct description of how aliasing will affect inertial measurements. Now that the concept of aliasing is understood, data loss in the context of inertial sensors can be discussed, and the necessity for data filtering presented.

Data Loss and Integration Error

The real continuous movement of a body can be erratic, with periods of a high frequency of direction change and long periods of being stationary. It is very likely that this movement will not take a regular sinusoidal form. This fact has large implications for the accuracy of position and orientation readings measured by double integrating acceleration and integrating angular rate. This principle is demonstrated following. Consider Figure 31 below:

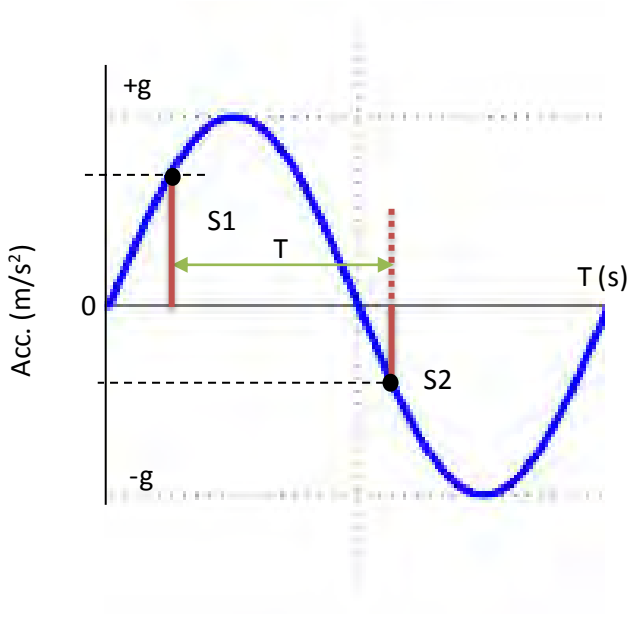

Figure 31 – Sample speed that results in data loss in a digital system

Figure 31 shows a blue sinusoid which we will assume to be the actual acceleration of a body. If we assume the body starts at rest, then at the end of the sinusoid the body will be stationary and in the same position it started. This is because the area above and below the acceleration axis is the same, which effectively means that the velocity of the body will be zero at the end of the sinusoid. The same will be true for position, as the velocity that the body has in one direction is mimicked exactly in the opposite direction, meaning it will have the same displacement in each direction.

However, if we now consider a digital accelerometer with a set sampling rate T, that captures the acceleration data at S1 and S2 above. It can be seen that the magnitude of these values are not the same. Thus, the accelerometer will only "see" part of the actual acceleration of the body. This will result in the sensor showing the body to have accelerated by different amounts in each direction and thus the body will have a non-zero velocity at the end of the sinusoid. This is catastrophic for position sensing because now that the body has a non-zero sensed velocity but a zero actual velocity, the error in position will propagate at a rate of whatever the sensed velocity is. This is known as integration drift.

The above principle can be applied to gyroscopes too, however the error propagation in gyroscopes is less because gyroscopes provide a rate of rotation, meaning that if the above situation was replicated with the

blue sinusoid representing angular velocity rather than linear acceleration, at the end of the sinusoid the body would be stationary but it would not have returned to its starting orientation due to loss of data.

Integration error is the biggest problem of position sensing with inertial sensors and hence they are generally not used for long term position determination. They are often supplemented by sensors such as GPS or LBL sensors so as to have an absolute position update that can correct the inertial reading. However, integration drift can be mitigated to a certain extent. A simple way of doing this is to filter the readings of an accelerometer or gyroscope.

Data Filtering

A factor that affects all electrical sensors is noise, which is inherent in all systems due to ambient and induced electromagnetic radiation. This will cause the zero reading of a sensor to fluctuate around the zero reading. This in itself can cause integration drift in an IMU before the body has even moved. Thus, data filtering forms an important part of successful inertial positioning.

Often, the noise inherent in a sensor will be at a constant frequency that is higher than the frequency of the system's mechanical motion. In general, mechanical systems respond much slower than electrical systems. Thus, the lower frequency readings are desirable, since it is assumed that high frequency changes will not realistically transpire in a mechanical system. The exact types of filters that can be used will depend on the specific type of filtering desired but in principle, a low pass filter is appropriate for this application.

Low pass filtering can be achieved in software or hardware. A low pass filter in its most basic form in hardware consists of a capacitor and a resistor. A passive low pass filter and its transfer function is shown alongside in Figure 32. The values of the resistor and capacitor will determine the frequency above which changes of signal reading will not be observed or "passed". This is known as the "cut-off" frequency and can be found with equation 3.4 below.

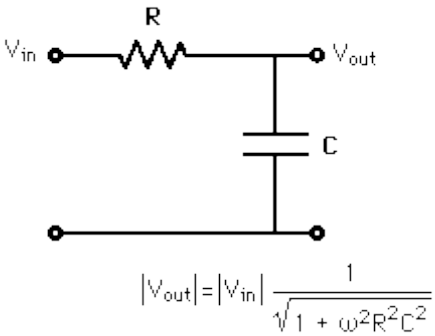

Figure 32 - Passive low pass filter and transfer function

$$f_c = \frac{1}{2\pi RC} \quad \{3.4\}$$

Software filtering is achieved by applying an averaging function to an array of data points that gets updated each time a new reading becomes available. The number of elements in the array will determine how quickly the output signal will respond to a change in the input. The cut-off frequency in software filtering will depend on how fast the array is updated and how quickly an average of the array can be calculated. Software filtering is a crude method of filtering and is only sufficient when an accurate cut-off frequency is not necessary.

Low pass filtering can help to mitigate the previously discussed phenomenon of data loss in digital systems. This would be achieved by setting the cut-off frequency of the filter to be slightly higher than the expected rate of change of acceleration of the body.

Summary

Aliasing in digital systems results in data loss. This is caused by the sampling rate of a digital system and can cause the motion of a body to not be accurately represented. Noise will also contribute to this problem. As soon as the motion of a body is not accurately represented by inertial readings, positional error is introduced. Due to the double integration process from acceleration to position, this error can propagate quickly and is known as integration drift. Orientation error can also be introduced in this manner, but due to gyroscopes providing a rate reading the error does not propagate as quickly.

This error propagation can be mitigated with low pass filtering, which will help the sensor to only reflect readings below a certain cut-off frequency, which can help to improve the accuracy and cancel noise present in the IMU system. There is a chance however that errors will still be introduced into the system even though the system will reject noise better and be more robust against aliasing.

Especially in applications of orientation determination, which uses sensor fusion methods, simple data filtering alone is not always sufficient. If gyroscope readings become inaccurate as a result of integration and bias drift, while orientation readings are still available from magnetometers and accelerometers, it will be necessary to determine that the gyroscope readings are erroneous. This is achieved by employing algorithms that predict the next state that a body will be in and mapping it to the data received from sensors. This will be covered briefly in the next section.

3.4.6. State Prediction and Kalman Filtering

Introduction

Thus far, finding the orientation and position of a body using inertial sensors has been shown to have many associated challenges such as sensor drift, integration drift and aliasing. These challenges make tracking a body's motion over extended periods of time difficult. However, techniques such as sensor fusion and data filtering can be employed to improve the long term stability and accuracy of the inertial measurements.

For long term orientation tracking however, the above techniques might still not be sufficient. The sensor and integration drift of a gyroscope, for instance, may result in the gyroscope readings becoming erroneous over time. When combined with other sensors, it will be important know if this has happened and thus, another stage of data processing is necessary. This is known as state prediction and is used to predict what the next state of a body will be according to previous data.

The Kalman Filter

One of the most commonly used techniques in industrial grade orientation sensors is the Kalman filter. The Kalman filter is a minimum mean-square-error (MMSE) estimator that has the recursive "predict-correct" structure. The Extended Kalman filter (EKF) is just an expansion of the Kalman filter that was developed to handle nonlinear systems. The structure of a basic Kalman filter will be given following to demonstrate its principles.

Kalman filters use knowledge of the process being measured, along with the measurement noise to predict the state of the process. Prediction forms the first step to a Kalman filter algorithm as follows:

$$\begin{aligned} \hat{x}_{t|t-1} &= F_t \hat{x}_{t-1|t-1} + B_t u_t \\ P_{t|t-1} &= F_t P_{t-1|t-1} F_t^T + Q_t \end{aligned} \quad \{3.5\}$$

In the above prediction step, $\hat{x}_{t|t-1}$ represents an estimation of the discrete state x as it transitions from one time step to the next. F represents a model of the process, or what is expected from the real life states. $B_t u_t$ represents the effect of control inputs into the system (u) via a transformation (B) that maps the inputs to the states. P is an estimation of the error between the actual and estimated state. The value of Q represents the process noise, which can be thought of as a measure of how well defined we believe the process model (F) is.

With values obtained for the prediction step of the Kalman filter, update equations are performed to obtain new estimates for the system states as follows:

$$\begin{aligned} K_t &= P_{t|t-1} H_t^T \left(H_t P_{t|t-1} H_t^T + R_t \right)^{-1} \\ P_{t|t} &= (I - K_t H_t) P_{t|t-1} \\ \hat{x}_{t|t} &= \hat{x}_{t|t-1} + K_t \left(y_t - H_t \hat{x}_{t|t-1} \right) \end{aligned} \quad \{3.6\}$$

K is called the Kalman gain and H is a matrix that maps the measurement readings to the states. The measurements themselves are denoted as y and have a noise signal represented by R.

The Kalman filter is a powerful data processing tool, as it allows an accurate estimation of the real state to be gained if the process model and sensor noise are well defined, in which case a small value will be chosen for the process noise, Q. It is important that the process model is well represented however, since if it is not then the Kalman filter can be prone to introducing more error. If the process model is not well defined however, the process noise can be chosen as a larger value, effectively re laxing the range for which the Kalman filter will work. However, as the value of Q increases, the filtering effect of the Kalman filter will decrease, causing the filtered state estimations to mimic the real life noisy data more and more.

The basic principle of a Kalman filter has been described, however Kalman filtering is an extensive field of study and far more advanced Kalman filtering techniques exist. Extended Kalman filters and Unscented Kalman filters are some such techniques and can be found in inertial navigation research in [38] and [39].

It can now be seen that using a Kalman filter, if the noise characteristics of individual inertial sensors is well known, as it often is, long term accuracy of the sensor can be maintained using the predictive nature of the filter. The following section will describe some common inertial navigation systems that are developed as a combination of advanced sensor fusion, filtering and processing techniques.

3.4.7. Advanced Inertial Navigation and Measurement Systems

Now that most of the individual aspects of inertial sensors and the techniques used to process the data supplied from them has been described, it is possible to briefly list common systems that combine inertial sensors and employ advanced sensor fusion and filtering techniques to provide very stable and accurate data.

Table 5 - Types of inertial sensing systems

Type of Inertial System	Description
Inertial Measurement Unit (IMU)	IMU is the generic term given to a combination of inertial sensors. IMUs will often refer to the unprocessed inertial data that is available from various inertial sensors that are combined in the same IC.
Inertial Navigation System (INS)	INS refers to IMUs that form part of a greater navigation system so as to supply positional information of a body. Often, due to the limited positional accuracy of inertial measurements over extended periods of time, an INS will serve to supplement positioning systems such as GPS at a faster rate than GPS, so as to provide interim motion data between GPS position updates. The inertial data is then constantly corrected by the GPS signal to prevent long term inaccuracies. It will include data fusion and processing techniques to give interpreted readings from the raw inertial data.
Attitude and Heading Reference System (AHRS)	AHRS is an inertial system that provides attitude and heading data of a body. Attitude refers to the pitch and roll of a body and heading refers to the horizontal angle of the body with reference to magnetic or geographical North. Fusion and processing such as Kalman filtering is employed on AHRSs to provide long term accurate data.
Attitude and Position Reference System (APRS)	APRS is a less generic term for an INS. In the case of APRS, attitude data is used to supplement low data rate position sensors such as GPS.
Vertical Reference Unit (VRU)	VRUs are often necessary for nautical applications and supplement acoustic sensors that require an accurate vertical reference to determine the orientation of acoustic sensors such as DVLs and Baseline transponders. VRUs will employ data processing and sensor fusion techniques so as to obtain accurate long term vertical orientation information.

This completes a description of some of the commonly used advanced inertial sensors available as industrial products or developed in an academic environment.

3.4.8. Summary

Inertial sensors present one of the most compact and cost efficient way of sensing the motion of a body. MEMS inertial devices offer low cost and sufficiently accurate readings for a huge variety of applications and are found in many devices such as smart phones and cars. Often it is necessary to combine accelerometers, gyroscopes and magnetometers due to the advantages and disadvantages of each sensor. Sensors are usually combined into inertial measurement units such as AHRSs or INSs using advanced methods of sensor fusion and data filtering techniques to obtain long term accurate attitude information.

Inertial sensors are not often used for long term positioning of a body due to the integration drift inherent in the way that position is obtained from acceleration readings. In addition, the effects of aliasing and digital sampling contribute significantly to the integration drift experienced.

Techniques such as Kalman filtering are powerful tools that can predict the long term bias offset of sensors like gyroscopes and hence provide long term orientation accuracy. Often, data will be fused from all three types of inertial sensors and then filtered using low pass and advanced Kalman filtering techniques to provide stable and accurate attitude data of a body.

This completes an in-depth investigation into inertial sensing, allowing the concept of vision based sensing to be briefly described in the following section.

3.5. DSP Based Position and Orientation Sensing

3.5.1. Introduction

As has been described previously, an alternative method to determining position underwater is by using DSP techniques. DSP is a huge field of study and is rather specialised. Therefore, this section will serve only to briefly describe the principle behind localisation using vision and DSP techniques.

3.5.2. General Principles

Feature detection or "Computer Vision" forms the basis of DSP control techniques. Features such as edges and corners provide a well-defined reference by which a body can be localised and therefore the detection of these features in a digital signal forms part of the research field of DSP.

Once a feature has been detected, it can be used as a reference point by which a body can be localised and hence as the position of the feature changes in the captured digital signal, the motion of the body relative to that feature can be determined.

Figure 33 following shows an example of feature detection used on ROV visual data [40].

Figure 33 - Automatic feature detection using a Harris Detector with different threshold levels

3.5.3. Vision Based Localisation

Inspection of subsea structures is often one of the primary applications of general and observation class ROVs. Therefore, almost all ROVs have a camera module. One of the motivations for developing vision based localisation techniques is that it can remove the necessity for IMUs and other navigational sensors while providing adequate station holding control, therefore decreasing the cost of the ROV.

The disadvantage with vision based localisation is that the range depends on ambient visibility and the capabilities of the camera. However, research has been conducted in which systems that are robust to varying visibility and light conditions [40].

3.5.4. Sonar DSP Based Localisation

Sonar sensors are often used in conjunction with other sonar units and inertial sensors to contribute to ROV localisation data. The slow data rate of sonars make them not ideal for dynamic positioning. Another consideration is that sonar devices typically act in a horizontal plane, which limits the operational use of a sonar for localisation to a limited depth range. In addition, since sonar uses reflected acoustic waves to

generate an image, sonar can only be used for localisation if sufficient environmental features are available to detect. However, sonar units have been used successfully to supplement the navigation systems of unmanned underwater vehicles (UUVs) [41].

This completes a brief and general description of how DSP can be used in vision and acoustic sensors to localise an ROV.

3.6. Summary

An in-depth investigation into underwater localisation and its various sensors, techniques and associated challenges has been conducted. It was established that terrestrial based sensing systems such as GPS cannot be employed underwater, making underwater localisation a significant challenge.

It was established that for absolute position sensing, acoustic technologies such as USBL, DVL and sonar present the most reliable and accurate means for determining position underwater. However, the successful development of an acoustic system is highly complicated and is influenced by many factors, making the cost of acoustic systems significant.

A low cost alternative to acoustic sensing is inertial sensing. The disadvantage with inertial localisation however, is that due to integration drift error, long term positioning accuracy is not possible with inertial systems alone. In addition, significant sensor fusion and data processing algorithms are required to provide long term attitude accuracy. However, commercial IMU and AHRS units exist that can provide highly accurate long term attitude readings and are easily integrated into an ROV system.

Finally, a more data intensive and limited sensing technique is that of machine vision and DSP. Due to visibility and light restrictions, vision based localisation is limited to small distances but has been proven to be effective for operations like subsea structure inspection. Vision based localisation, if successfully implemented, offers the lowest cost solution to ROV localisation due to the inclusion of a camera module on almost all ROV systems.

This completes the investigation into underwater localisation. In the following chapters, an investigation will be undertaken into underwater control techniques.

4. Control Techniques for Depth and Heading Holding Underwater

4.1. Introduction

Controlling underwater vehicles is a challenging endeavour due to the following factors [42]:

- Inertial and Hydrodynamic nonlinearities of the ROV plant.
- Nonlinearities of the ROV actuators.
- Motion coupling between DOFs.
- Environmental disturbances and uncertainties.
- Difficulty of determining or measuring vehicle states.

As a result of these factors it has been established that classical linear control techniques are not well suited to underwater control manoeuvres, whereby a large degradation of controller performance is observed in the presence of environmental disturbances. In addition, linear controllers that are not robust to model uncertainties experience degraded real life performance compared to in a simulation environment. Finally, due to the techniques of linearization resulting in a localised approximation of a nonlinear system, sufficient controller performance is not always expected over the entire velocity range of the vehicle under the action of a linear controller [43].

As a result of the obvious insufficiencies of linear controllers for underwater control, various control techniques have been developed to be robust to uncertainties and disturbances and offer consistent performance over the entire operating range of the vehicle and its actuators. Adaptive linear model-based control has been proven to provide sufficient setpoint tracking performance for simple, single axis manoeuvres [44], [45]. Nonlinear control theory such as sliding mode control however, is a very prominently utilised control method for underwater vehicles, due to its stability and robustness to model uncertainties [42], [46].

This chapter will give a brief overview of underwater control methods in general and then describe different control methods whilst keeping in mind their suitability to depth and heading holding operations.

4.2. Guidance Navigation and Control

The field of guidance, navigation and control (GNC) encompasses all automatically assisted robotic manoeuvres and typically refers specifically to autopilot functions. Classically, the GNC design problem involves controlling a vehicle's yaw while moving forward at constant speed so as to coincide with certain waypoints [47]. Figure 34 following shows the typical control structure of a GNC system.

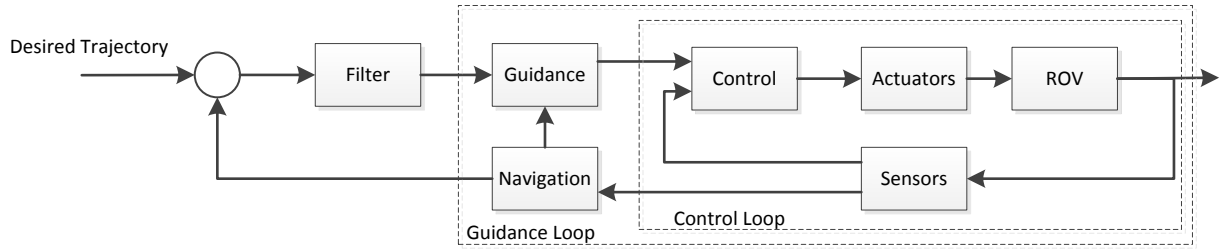

Figure 34 - Typical GNC control system

Since GNC encompasses path following manoeuvres, all the associated challenges of underwater localisation are present in it. This requires advanced techniques of state estimation and algorithms for transitioning between different desired manoeuvres while adapting all the control, guidance and navigation parameters to suit the new manoeuvre, as presented in [48].

GNC systems are of great interest for AUVs and in the case of this project, navigation control tasks do not form part of the scope. Therefore, this section was provided for the sake of completeness and to give an introduction to lower level underwater control manoeuvring techniques that will be given in the following section.

4.3. Overview of ROV Control Methods

4.3.1. Intelligent Control

Neural networks and fuzzy logic have been shown to provide sufficient underwater control efficacy but are reserved mostly for experimental ROV vehicles and not widely in industry [49]. Fuzzy logic intelligence has been shown to be a robust modelling tool in the presence of model uncertainty [50] and has been effectively used for motion control, collision avoidance and sensor fusion [51]. Fuzzy logic controllers however, require an extensive parameter tuning processes, making them difficult to adapt to different systems [49]. In general, intelligent control systems is an advanced control technique and thus is an unlikely candidate for implementation as an initial control structure in this project.

4.3.2. PID Control and Model Based, Linearizing Control

PID controllers form the industry standard for many areas of control, including the control of ROVs [52]. This is due to their ease of tuning and implementation. However, due to the ROV system being characterised by nonlinear dynamics, PID control performance can be degraded and even lead to system instability under certain operating conditions. As a result, a linearizing control law based on model nonlinearities can be used to adapt parameters of the PID controllers so as to provide stable and consistent controller performance throughout the operating range of interest of the ROV. This adaptive linearizing technique has been successfully implemented in [53]. The disadvantage of adaptive linearizing controllers is that they require an accurate mathematical model for the ROV being controlled and will suffer performance degradation in the presence of model uncertainties.

In the cases of PID and linearizing controllers, due to their model based approach, with associated tuned parameters, they are best suited to decoupled simple control manoeuvres such as heading or depth holding.

4.3.3. Sliding Mode Control

Sliding mode control (SMC) is a control technique that is robust to model uncertainties but has the disadvantage of requiring large amounts of switching from actuators. In effect, this high switching action from actuators is the introduction of high frequency noise into the system and is a phenomenon known as chattering. At the expense of wear on actuators, however, sliding mode control has proven to be a superior nonlinear control technique for underwater vehicles, providing consistent performance over the entire operating range of the vehicle. Adaptive sliding mode control (ASMC) techniques have been shown to further enhance the usability of SMC control algorithms by being robust to a change in vehicle parameters, making them usable for ROVs that must be controlled with and without an attached manipulator arm, for example [49].

4.3.4. Model-Free High Order Sliding Mode Control

In general, SMC is a great candidate for underwater control due to its robustness in the face of ROV model changes, uncertainties and disturbances. The disadvantage of SMC however, is the introduction of chattering into the system, which is what model-free high order sliding mode control (MF-HOSMC) seeks to reduce or mitigate. Advantages of MF-HOSMC are [49]:

1. The controller is effective regardless of how accurate the modelled dynamics or parameters are.
2. The control action is smooth and robust, based on second order sliding modes and chattering free.
3. Exponential position and velocity tracking is obtained without acceleration measurements.

MF-HOSMC is one of the most recent techniques developed for ROV control and was published in [49] in 2014. It clearly offers obvious advantages over other methods of control but should be chosen carefully according to the desired control objective.

4.4. Summary

In general, most underwater control techniques are derived based on a dynamic model that can only approximate the real environment with significant uncertainty in the model. Therefore, adaptive controllers that are robust to uncertainties, disturbances and noise are ideal for the underwater environment.

In the context of this project however, limited time is available for developing advanced controllers and therefore suitable candidates for controllers will be simple to design and implement. Since an integral part of the *SEAHOG* project is the modelling of the system, a model-free controller is not critical at this early stage. PID and model-based linearizing controllers are suitable for simple, decoupled motion operations due to the limited permutations of linearization points necessary to provide their adaptive law. SMC controllers provide a robust and simple to implement solution that has a wider range of suitability than PID controllers.

Therefore, suitable candidates for control frameworks in this project are PID linearizing and SMC controllers. This chapter was provided to gain a brief insight into the different control techniques used and some of the issues related to underwater control. Therefore, more detail will be provided in the controller design chapters in the main dissertation report as to the control design process that was undertaken in this report.

5. Conclusions and Recommendations

5.1. Introduction

The *SEAHOG* ROV is an under-actuated system that is passively stabilised in pitch and roll by a static buoyancy system. The ROV is designed for assisting marine research in the form of observations and sample collection. At the time of this project, the control hardware and sensors were not installed or specified for the *SEAHOG* and thus it was decided that this project would encompass the design of controllers for basic control tasks, providing a baseline upon which model verification could be performed and more advanced controllers could be designed. *SEAHOG* motion would be sensed with theoretically modelled hardware.

This literature review provided a more in-depth investigation into some of the sections tackled in the main dissertation part of this report. The purpose of the review was to gain more understanding in certain topics through background research and presentation of basic concepts and main ideas in those topics.

This literature review specifically gave detailed background of the *SEAHOG* ROV and the development of ROVs by RARL at UCT. Underwater localisation, including acoustic, inertial and data fusion techniques were covered, highlighting the challenge of underwater localisation. Finally, a brief overview of underwater control techniques was given.

5.2. Localisation and State Sensing

Work presented in this literature review showed that acoustic sensing techniques such as LBL or USBL present the most accurate and reliable option for position sensing underwater. However, acoustic systems, due their complexity, are expensive.

Inertial sensors offer a low cost and reliable option for at least sensing the orientation of a body. Advanced sensor fusion and Kalman filtering offers accurate long term orientation and attitude information. Typically, 3 axis gyroscopes, magnetometers and accelerometers are combined to form systems such as AHRS, which can aid in navigation by providing a reference to North.

Finally, a data processing intensive but low cost technique for localisation is by using vision or sonar data to identify points of interest in an image and localise the ROV relative to them. This can be the lowest cost technique for localisation, but comes with drawbacks like limited range of use and being influenced by visibility and lighting conditions.

5.3. Control Framework and Techniques

Underwater control is not well suited to classical linear control techniques due to large environmental uncertainties, nonlinear plant and actuator dynamics and motion cross-coupling effects. Therefore, non-linear control techniques such as SMC and MF-HOSMC are reliably and successfully employed in ROVs. Classically, adaptive linearizing PID control was used for underwater control, however this technique suffers from performance degradation and even instability if the ROV operating conditions are not within a close region to the linearization point.

Due to the limited time available in this project for controller development however, it was decided that adaptive linear controllers would be developed for the required heading and depth control operations. It was desired that some of the issues with this technique could be highlighted using the developed dynamic model of the *SEAHOG* and therefore provide a suitable motivation for the development of more robust controllers in future projects.

This completes the literature survey conducted as an appendix to the main dissertation of this project, allowing design decisions to be made with a greater insight into the relevant area.

Works Cited

[1] "What is an ROV?," Marine Technology Society, [Online]. Available: http://www.rov.org/rov_overview.cfm. [Accessed 20 April 2013].

[2] "ROVs- A Brief History," Marine Technology Society, [Online]. Available: http://www.rov.org/rov_history.cfm. [Accessed 21 March 2013].

[3] R. Christ and R. Wernli, in *The ROV Manual*, Oxford: Elsevier, 2007.

[4] SAAB, "Seaeye Falcon & Seaeye Falcon DR," SAAB, 2010. [Online]. Available: http://www.seaeye.com/falcon.html. [Accessed 26 04 2011].

[5] "VideoRay Underwater Video ROV," Tech and Tools for Cruisers, [Online]. Available: http://www.navscratch.dreamhosters.com/category/photography/. [Accessed 20 April 2013].

[6] J. Wetz, "Artificial Reef Project," Harte Research Institute, 2012. [Online]. Available: http://harteresearchinstitute.org/newsletter/winter2012/article2.html. [Accessed 16 August 2014].

[7] "ROV industry getting down to the challenge of deepwater," Oil and Gas Online, 26 March 2001. [Online]. Available: http://www.oilandgasonline.com/doc/ROV-industry-getting-down-to-the-challenge-of-0001. [Accessed 20 April 2013].

[8] Dredging Today Staff, "UK: Kongsberg Cameras Chosen for SMD Deep Water Trenching Vehicles," DredgingToday.com, 10 August 2012. [Online]. Available: http://www.dredgingtoday.com/2012/08/10/uk-kongsberg-cameras-chosen-for-smd-deep-water-trenching-vehicles/. [Accessed 16 August 2014].

[9] R. d. Smidt, "Development of the Power and Communications Distribution Systems for an Underwater Remotely Operated Vehicle," University of Cape Town, Cape Town, 2014.

[10] SAAB Seaeye ltd., "Seaeye Falcon & Seaeye Falcon DR," SAAB Seaeye ltd., [Online]. Available: http://www.seaeye.com/falcon.html. [Accessed 16 August 2014].

[11] Seatronics, "Predator ROV," Seatronics, [Online]. Available: http://www.predator-rov.com/system/.

[Accessed 30 October 2013].

[12] Garmin Ltd., "What is GPS?," Garmin Ltd., 2014. [Online]. Available: http://www8.garmin.com/aboutGPS/. [Accessed 20 August 2014].

[13] G. Taraldsen and T. A. Reinen, "The Underwater GPS Problem," in *OCEANS, 2011 IEEE*, Spain, 2011.

[14] Maxim Integrated Products, Inc., "RS-485 (EIA/TIA-485) Differential Data Transmission System Basics," Maxim Integrated, 2014. [Online]. Available: http://www.maximintegrated.com/en/app-notes/index.mvp/id/736. [Accessed 18 August 2014].

[15] Srugn, "RS-485 (EIA-485)," Electronic Engineering Polytechnic Institute of Surabaya, 11 December 2008. [Online]. Available: http://lecturer.eepis-its.edu/~sragen/index.php?Menu=1&Sub=3&ID=10. [Accessed 18 August 2014].

[16] Optical Systems Design, "SERIAL DATA COMMUNICATIONS," OSD, [Online]. Available: http://osd.com.au/serial-data-communications/. [Accessed 18 August 2014].

[17] V. Chandrasekhar, W. K. Seah, Y. S. Choo and H. V. Ee, "Localization in Underwater Sensor Networks − Survey and Challenges," in *WUWNet*, Los Angeles, 2006.

[18] H. P. Tan, R. Diamant, W. K. Seah and M. Waldmeyer, "A Survey of Techniques and Challenges in Underwater," Institute for Infocomm Research, Singapore, 2009.

[19] W. C. Vergara, "Radar and Sonar," Scholastic, 2014. [Online]. Available: http://teacher.scholastic.com/activities/explorations/bats/libraryarticle.asp?ItemID=234&SubjectID=110&categoryID=3. [Accessed 24 August 2014].

[20] University of Rhode Island, "Speed of Sound," University of Rhode Island, 2013. [Online]. Available: http://www.dosits.org/tutorials/sciencetutorial/speed/. [Accessed 21 August 2014].

[21] Tritech International Ltd., MicronNav System Product Manual, Aberdeen: Tritech International Ltd..

[22] Tritech International Limited, "MicronNav - USBL Tracking System," Tritech International Limited, 2014. [Online]. Available: http://www.tritech.co.uk/product/usbl-tracking-system-micronnav. [Accessed 24 August 2014].

[23] Sonardyne, "LBL All Systems," Sonardyne, 2014. [Online]. Available:

http://www.sonardyne.com/products/positioning/lbl.html. [Accessed 24 August 2014].

[24] Thien Nam Positioning JSC, "Định vị âm(USBL)," Newtab Co., Ltd, 2011. [Online]. Available: http://thiennampositioning.com/services/detail/27-0-dinh-vi-am-usbl-.html. [Accessed 24 August 2014].

[25] Teledyne Technologies Incorporated, "Workhorse Navigator Doppler Velocity Log," Teledyne Technologies Incorporated, 2013. [Online]. Available: http://www.rdinstruments.com/navigator.aspx. [Accessed 25 August 2014].

[26] Teledyne RD Instruments, "Workhorse Navigator," Teledyne RD Instruments, 2006. [Online]. Available: http://www.rdinstruments.com/pdfs/wh_navigator_ds_lr.pdf. [Accessed 25 August 2014].

[27] STMicroelectronics, "LSM9DS0," STMicroelectronics, 2013. [Online]. Available: http://www.st.com/st-web-ui/static/active/en/resource/technical/document/datasheet/DM00087365.pdf. [Accessed 25 August 2014].

[28] M. Andrejašic, "MEMS ACCELEROMETERS," University of Ljubljana, Faculty for mathematics and physics, Ljubljana, 2008.

[29] J. Esfandyari, R. D. Nuccio and G. Xu, "Introduction to MEMS gyroscopes," Extension Media, 15 November 2010. [Online]. Available: http://electroiq.com/blog/2010/11/introduction-to-mems-gyroscopes/. [Accessed 25 August 2014].

[30] Tritech International Ltd., "Intelligent Fibre-Optic Gyro (iFG) Operating Manual," 2014. [Online]. Available: http://www.tritech.co.uk/media/support/manuals/ifg-iintelligent-fibre-optics-gyro-operator-installation-manual.pdf. [Accessed 25 August 2014].

[31] Y. CAI, Y. ZHAO, X. DING and J. FENNELLY, "Magnetometer basics for mobile phone applications," Hearst Business Communications, Inc., 2014. [Online]. Available: http://www.electronicproducts.com/Sensors_and_Transducers/Sensors_and_Transducers/Magnetometer_basics_for_mobile_phone_applications.aspx. [Accessed 25 August 2014].

[32] MEMSense, "Determination of Static Orientation Using IMU Data Revision 1," [Online]. Available: http://memsense.com/docs/TN0003_static_orientation.pdf. [Accessed 31 August 2014].

[33] L. Xiao, S. Boyd and S. Lall, "A Scheme for Robust Distributed Sensor Fusion Based on Average Consensus," IEEE, Stanford, 2005.

[34] J. Hol, "Sensor Fusion and Calibration of Inertial Sensors, Vision, Ultra-Wideband and GPS," Linköping University, Linköping, 2011.

[35] H. Durrant-Whyte and T. C. Henderson, "Multisensor Data Fusion," in *Springer Handbook of Robotics*, Berlin, Springer, 2008, pp. 585-610.

[36] H. Wu, M. Siegel, R. Stiefelhagen and J. Yang, "Sensor Fusion Using Dempster-Shafer Theory," in *IEEE Instrumetation and Measurement*, Anchorage, 2002.

[37] "Avoiding aliasing by Nonuniform sampling," [Online]. Available: http://www.edi.lv/media/uploads/UserFiles/dasp-web/sec-5.htm. [Accessed 6 September 2014].

[38] E. H. Shin, "Estimation Techniques for Low-Cost Inertial Navigation," University of Calgary, Calgary, 2005.

[39] M. Reinštein, "Use of Adaptive Filtering Methods in Inertial Navigation Systems," Czech Technical University, Prague, 2010.

[40] J. Kerdels, J. Albiez and F. Kirchner, "A Robust Vision-Based Hover Control for ROV," *OCEANS 2008 - MTS/IEEE Kobe Techno-Ocean,* pp. 1-7, 2008.

[41] J. Nie, J. Yuh, E. Kardash and T. I. Fossen, "On-Board Sensor-Based Adaptive Control Of Small Uuvs In Very Shallow Water," *International Journal of Adaptive Control and Signal Processing,* vol. 14, no. 4, 1998.

[42] D. R. Yoerger, J. G. Cooke and J. E. Slotine, "The Influence of Thruster Dynamics on Underwater Vehicle Behavior and Their Incorporation Into Control System Design," *IEEE Journal of Oceanic Engineering,* vol. 15, no. 3, pp. 167-178, 1990.

[43] D. R. Yoerger and J. J. Slotine, "Robust Trajectory Control of Underwater Vehicles," *IEEE Journal of Oceanic Engineering,* vol. 10, no. 4, pp. 462-470, 1985.

[44] L. G. Milliken, "Multivariable Control of an Underwater Vehicle," M.I.T. Deprtment of Ocean and Mechanical Engineering, Cambridge, Masachusetts, 1984.

[45] T. H. Koh, M. W. S. Lau and E. L. G. Seet, "A Control Module Scheme for an Underactuated Underwater Robotic Vehicle," *Journal of Intelligent and Robotic Systems,* vol. 46, no. 1, pp. 43-58, 2006.

[46] D. R. Yoerger and J. J. Slotine, "Adaptive Sliding Control of an Experimental Underwater Vehicle," in *International Conference on Robotics and Automation*, Sacramento, California, 1991.

[47] A. Healey and D. Lienard, "Multivariable sliding mode control for autonomous diving and steering of unmanned underwater vehicles," *IEEE Journal on Ocean Engineering,* vol. 18, pp. 327-338, 1993.

[48] M. R. Katebi and M. J. Grimble, "Integrated control, guidance and diagnosis for reconfigurable autonomous underwater vehicle control," *International Journal of Systems Science,* vol. 30, no. 9, 2010.

[49] L. G. García-Valdovinos, T. Salgado-Jiménez, M. Bandala-Sánchez, L. Nava-Balanzar, R. Hernández-Alvarado and J. A. Cruz-Ledesma, "Modelling, Design and Robust Control of a Remotely Operated Underwater Vehicle," *International Journal of Advanced Robotic Systems,* vol. 11, no. 1, 2014.

[50] A. Saffiotti, "The uses of fuzzy logic for autonomous robot navigation," *Soft Computing,* vol. 1, no. 4, pp. 180-197, 1997.

[51] V. KANAKAKIS, K. P. VALAVANIS and N. C. TSOURVELOUDIS, "Fuzzy-Logic Based Navigation of Underwater Vehicles," *Journal of Intelligent and Robotic Systems,* vol. 40, pp. 45-88, 2004.

[52] L. Hsu, R. R. Costa and F. Lizarralde, "Dynamic positioning of remotely operated underwater vehicles," *IEEE Robotics and Automation Magazine,* September 2000.

[53] G. Antonelli, S. Chiaverini, N. Sarkar and M. West, "Adaptive Control of an Autonomous Underwater Vehicle: Experimental Results on ODIN," *IEEE TRANSACTIONS ON CONTROL SYSTEMS TECHNOLOGY,* vol. 9, no. 5, pp. 756-765, 2001.

[54] Nexans, "Nexans Launches New ROV Tether Cable," Kable, 2014. [Online]. Available: http://www.offshore-technology.com/contractors/cables/nexans/press-new-rov-tether-cable.html. [Accessed 24 April 2014].

[55] "RS485 ESSENTIALS APPLIED INTO MDS SYSTEM," Fermax UK, [Online]. Available: http://www.fermaxuk.com/11/290/secciones/boletin2010/index.aspx?idnoticia. [Accessed 29 April

2013].

[56] Doctor Disruption, “Design Methods #19 – Triangulation,” Doctor Disruption, 26 June 2014. [Online]. Available: http://www.doctordisruption.com/design/design-methods-19-triangulation/. [Accessed 20 August 2014].

[57] EXPRO, “Flow Measurement : PassiveSONAR™ Flow Meter and ActiveSONAR™ Flow Meter,” EXPRO, 2014. [Online]. Available: http://www.exprometers.com/SONAR_Technology/Flow_Measurement_PassiveSONAR_and_ActiveSONAR/. [Accessed 21 August 2014].

[58] Metaldec International B.V., “Side-scan sonar in general:,” [Online]. Available: http://www.metaldec.nl/eng/sidescan.html. [Accessed 21 August 2014].

[59] indiagps.in, “3D Triangulation / Trilateration,” indiagps.in, 2014. [Online]. Available: http://indiagps.in/triangulaton-trilateration. [Accessed 24 August 2014].

[60] C. Slaybaugh, “The six axes of translation and rotation,” phpBB, 2013. [Online]. Available: http://photomacrography.net/forum/viewtopic.php?p=134654. [Accessed 28 August 2014].

Appendix B
ROV Upgrades and Maintenance

Table of Contents

Table of Figures

List of Tables

Glossary

ADC	Analogue to Digital Converter
CPU	Central Processing Unit
FEM	Finite Element Method
GUI	Graphical User Interface
HDPE	High Density Polyethylene
PCB	Printed Circuit Board
PVC	Polyvinyl Chloride
ROV	Remotely Operated Vehicle
RS232/ RS485	Recommended Standard 232/485
UART	Universal Asynchronous Receiver/Transmitter

List of Symbols

P	Pressure
d	Internal diameter
t	Wall thickness
σ_H	Hoop stress
σ_L	Longitudinal stress
$P_{collapse}$	Collapse pressure
L	Cylinder length
E	Modulus of elasticity
μ	Poisson's Ration
δ_{max}	Maximum deflection
I	Second moment of area
σ_{max}	Maximum stress

1. Introduction

The *SEAHOG* remotely operated underwater vehicle (ROV) system is extensive and highly integrated, with each aspect of the robot influencing the other. It is a large scale ongoing project that requires continuity between the individual projects that contribute to its development. For these reasons, while the functioning of the ROV as a whole is not the focus of this Master's project, its continual development and successful operation falls inescapably within this project's scope. This appendix serves to detail the mechanical, electrical and communications upgrades and maintenance performed on the ROV systems during the course of this project.

It was necessary to develop the ROV to an operational level in order for testing to be possible on its control systems. While it was the intention of this project and the cumulative effort of three previous Master's projects to have the robot operational and water-ready, this was not quite achieved unfortunately. This made it impossible to carry out tests that evaluated the performance of the ROV underwater under the influence of the designed controller. However, this project brought the ROV significantly closer to being water-ready and developed a simulation to evaluate any installed controller on the robot.

Two Master's students had both worked on the ROV before this project scope was defined. Their work included the development of the lights, cameras, basic frame structure and electrical supply and communication backbone of the ROV. In addition, a basic graphical user interface (GUI) had been developed to communicate with the available modules and monitor various system data. Another Master's student completed the development of some of the remaining subsystems required for the ROV to successfully operate, such as the thrusters and float block. Throughout this development however, some critical tasks had been left out of the ROV development and thus they fell under the scope of this project.

The following tasks were performed as part of the ROV's operational development in this project:

1. Design and fabrication of a new junction box and connection of the fibre-optic tether
2. Modification, implementation and testing of the new Power Pod heat sink
3. Troubleshooting and upgrades to existing camera and light modules
4. Communications overhaul and development of a new ROV GUI

These tasks will be detailed in this appendix, including explanations of their motivations and outcomes. It should be noted however, that some of the upgrades presented in this appendix have been built on directly from previous Master's projects and thus, in these particular cases, previous design decisions will have influenced how these tasks have been completed. Since some of these decisions, such as ones pertaining to the mechanical structure of the ROV, do not accommodate a complete redo under the scope of this project, work presented in this appendix will sometimes serve to mainly document the work carried out in this project for future reference. If it was deemed that a previous design decision was too integrated into the ROV to change it in this project, it will be noted in the relevant section.

Figure 1 following shows the three main systems of interest in this appendix – namely, the Power Pod heatsink, the new Junction Box and the new User GUI.

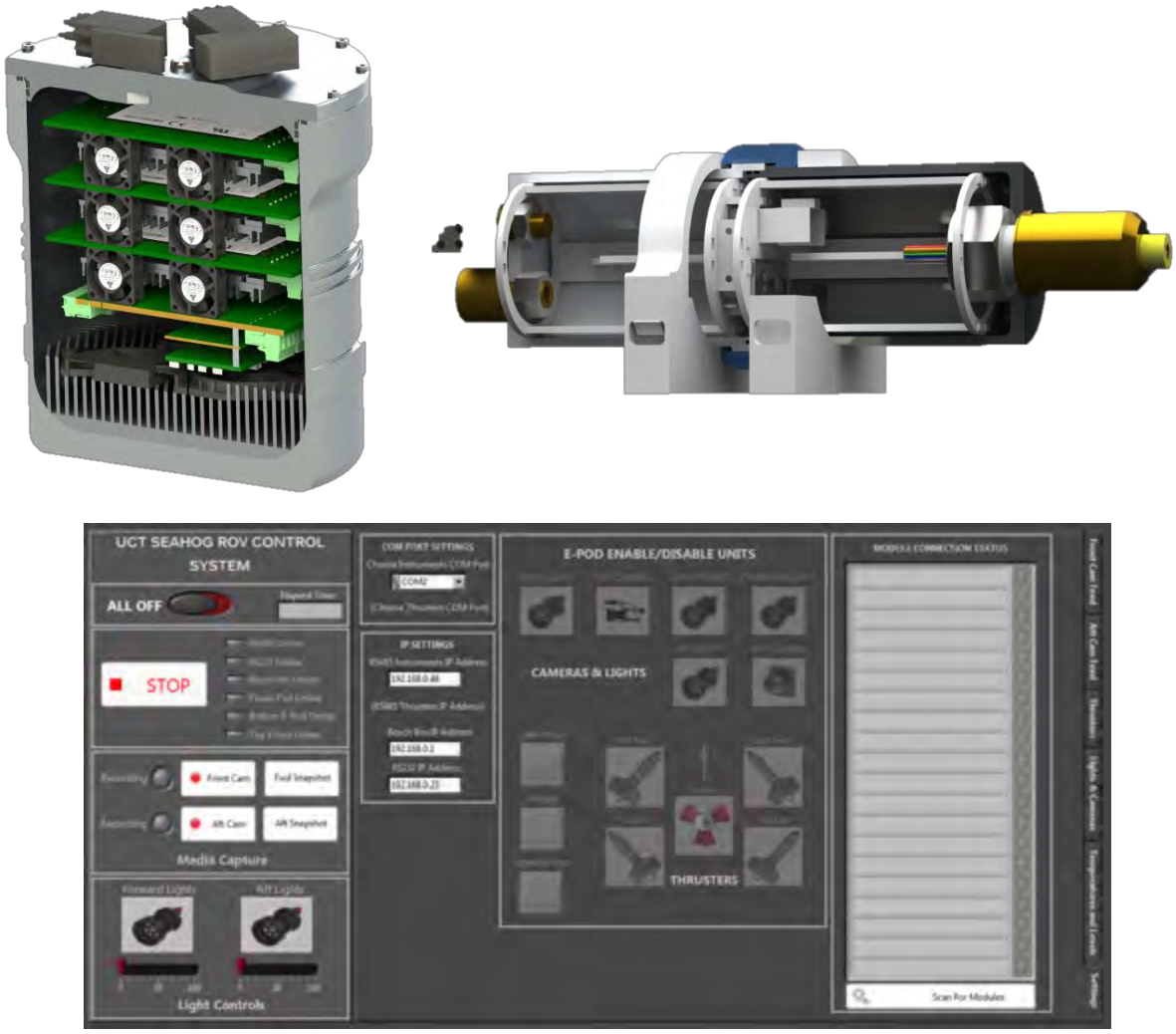

Figure 1 - Summary of systems developed in this appendix - Power Pod heatsink [top left], new Junction Box [top right], new ROV GUI [bottom]

This appendix will detail each of the previously listed tasks and finally, conclusions and recommendations will be drawn from each relevant section for future reference and development.

2. Junction Box

2.1. Introduction

An aspect that had not been addressed by previous projects on the ROV was the connection of the fibre-optic communication lines in the SAAB tether. The tether is neutrally buoyant and contains four copper cores for power transmission, two copper data transmission lines and four shielded fibre-optic cores. As shown following in Figure 2, the SAAB tether is supplying the ROV with power only, with the communication lines taking the form of a short fibre-optic patch-cord.

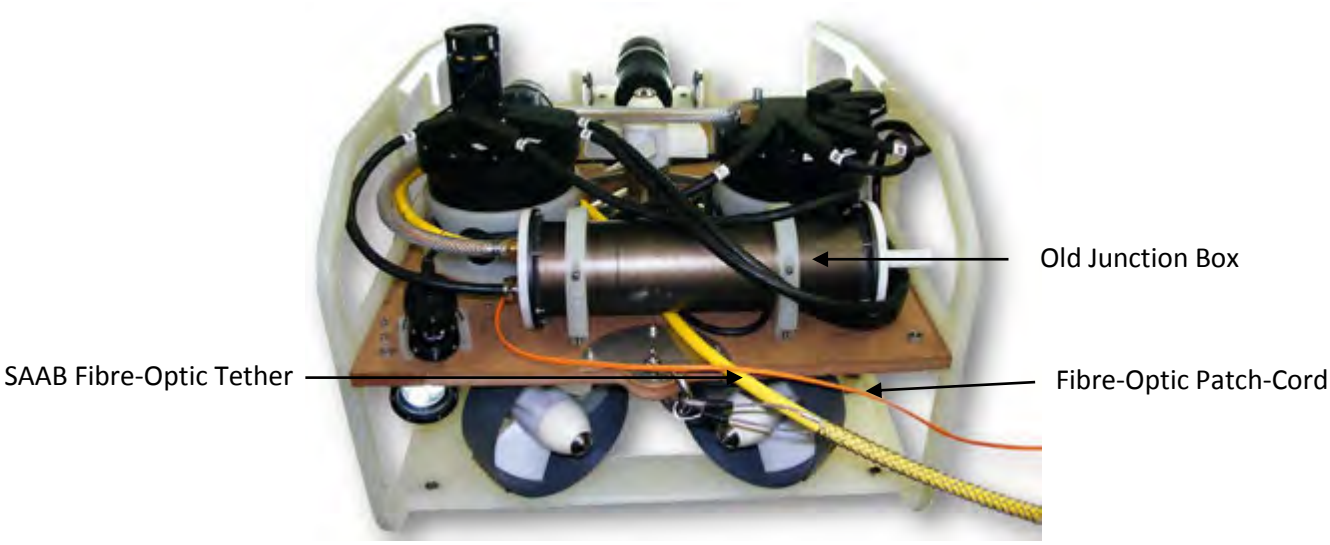

Figure 2 – Rear view of the *SEAHOG* showing the old junction box and corresponding connections

The reason that the patch-cord is being used above in Figure 2 is as follows: the fibre-optic cores in the SAAB tether are shielded in a stainless steel tube. To connect the cores, firstly the protective tube has to be cut without also cutting the fibre-optics. This will expose the bare fibres, which must then be spliced onto their corresponding connectors allowing them to interface with the fibre-optic modems installed on the ROV. The protective tube is 1,5 mm in diameter and thus without specialised tools, a great deal of care must be taken to successfully carry out this task. Once the tube has been cut and the fibres have been exposed, a sharp burr is left on the end of the stainless steel tube. Any relative movement between the fibres and the tube will cause contact between these surfaces and rapidly the fibre will wear down and break off. Thus, a patch-cord was used as a sufficient alternative whilst the ROV was not operational.

However, the task of connecting the tether fibre-optics was not addressed to its full extent, nor was it completed in previous projects.

This chapter will investigate how to connect the fibre-optics in the tether and will detail the process that was performed to achieve this connection. In addition, it will provide an assessment of the previously designed junction box in terms of ease of use and will highlight its issues, providing a motivation for a new solution to connecting the tether in the form of a new junction box.

2.2. Motivation for a New Junction box and Issues with the Old Junction Box

2.2.1.Termination of a Multi-Cored Tether

Introduction: A large amount of background research was carried out on junction boxes in [1]. In addition, the *SEAHOG* ROV project has provided a large amount of insight and experience into the design of air filled pressurised vessels. One remaining aspect of the junction box that has not been well documented however, is the termination of a multi-cored tether; which will be covered in this section so as to give insight into a possible solution for connecting all of the tether cores to the ROV.

Subsea Connector and 'Whip': Tether connection is carried out in different ways depending on the specifications of the ROV. For shallower depth rated ROVs, tethers typically carry signals and data feeds along two copper cores twisted together, known as a twisted pair. In this application, a tether will be connected with what is known as a 'whip'. A whip is a multi-pin subsea connector with a section of tether attached to it. The connector will mate with a connection point on the ROV and the end of the tether whip will be potted to the end of the tether. Figure 3 following shows how this is implemented on the VideoRay Pro ROV.

Figure 3 - Tether connection system on the VideoRay Pro ROV [2]

Figure 4 following shows a typical subsea connector for a tether that is comprised of only copper cores.

Figure 4 - Subsea connector for a 12 cored tether

Using a subsea connector is easy to implement and effective, however the problem with implementing this method with fibre optics is that alignment of the fibres in the connectors can be difficult to achieve. Any misalignments or air gaps in a fibre optic connection creates a large amount of signal attenuation, which negatively impacts bandwidth.

Hard-Wired Fibre-Optics: ROVs that are designed for greater depths usually implement fibre optics for their communication lines, since fibres are lightweight and supply a high enough bandwidth for video and communications, whereas more than one twisted pair is typically implemented for copper cored communications. ROVs that use fibre-optic communications typically have the fibres hard-wired into the system separately as shown following in Figure 5.

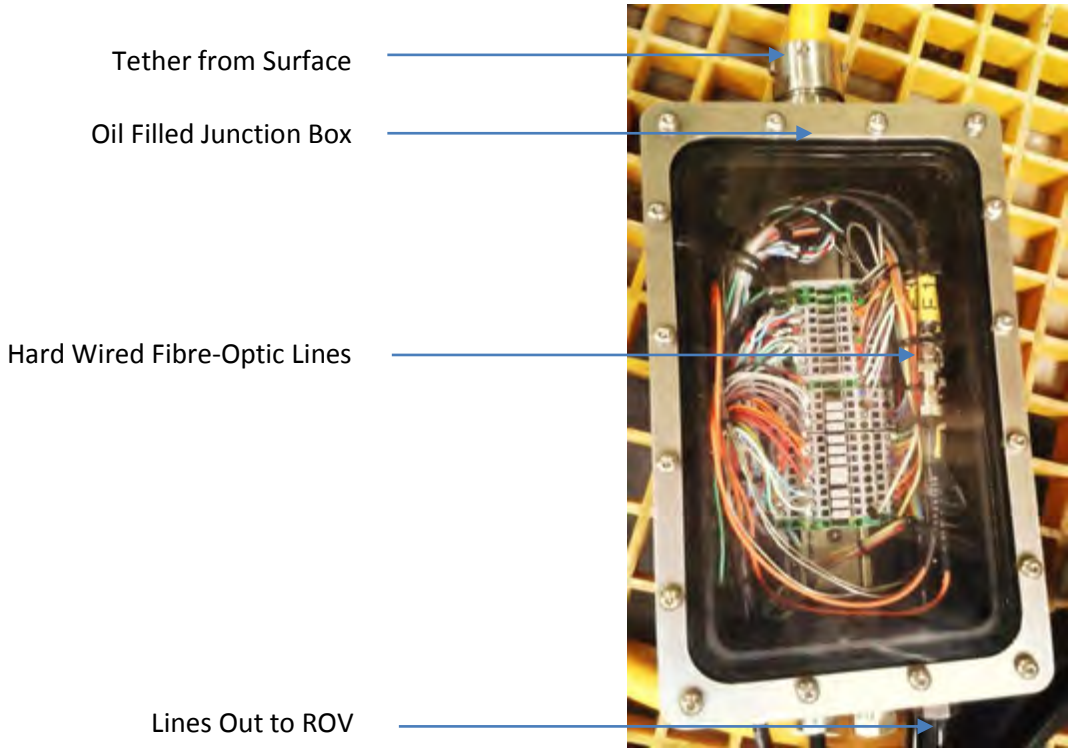

Figure 5 - Oil-Compensated junction box with hard-wired fibre-optic lines

This solution, while being more cumbersome to implement, is the most effective way of ensuring a robust and reliable fibre connection and is implemented widely in industrial ROV applications.

The *SEAHOG* Tether: As previously mentioned in this chapter, the *SEAHOG* ROV includes a tether with six copper cores and four fibre optic cores.

Now that it is understood how tethers are connected in industry, the old junction box design can be analysed.

2.2.2.Oil Compensation

The old junction box was the only oil compensated module on the *SEAHOG*. An oil compensated vessel is filled with oil, making it "incompressible" and can be pressurised with a plunger and springs. For details on the design of this module see [1]. The advantages of oil compensated modules is that they require thinner housing wall thicknesses to survive greater pressures and they prevent water ingress by having a net positive interior pressure. Similar designs have been successfully used in industry and thus oil-compensation was decided upon for the old junction box. A detailed rendering of the old junction box is shown following in Figure 6.

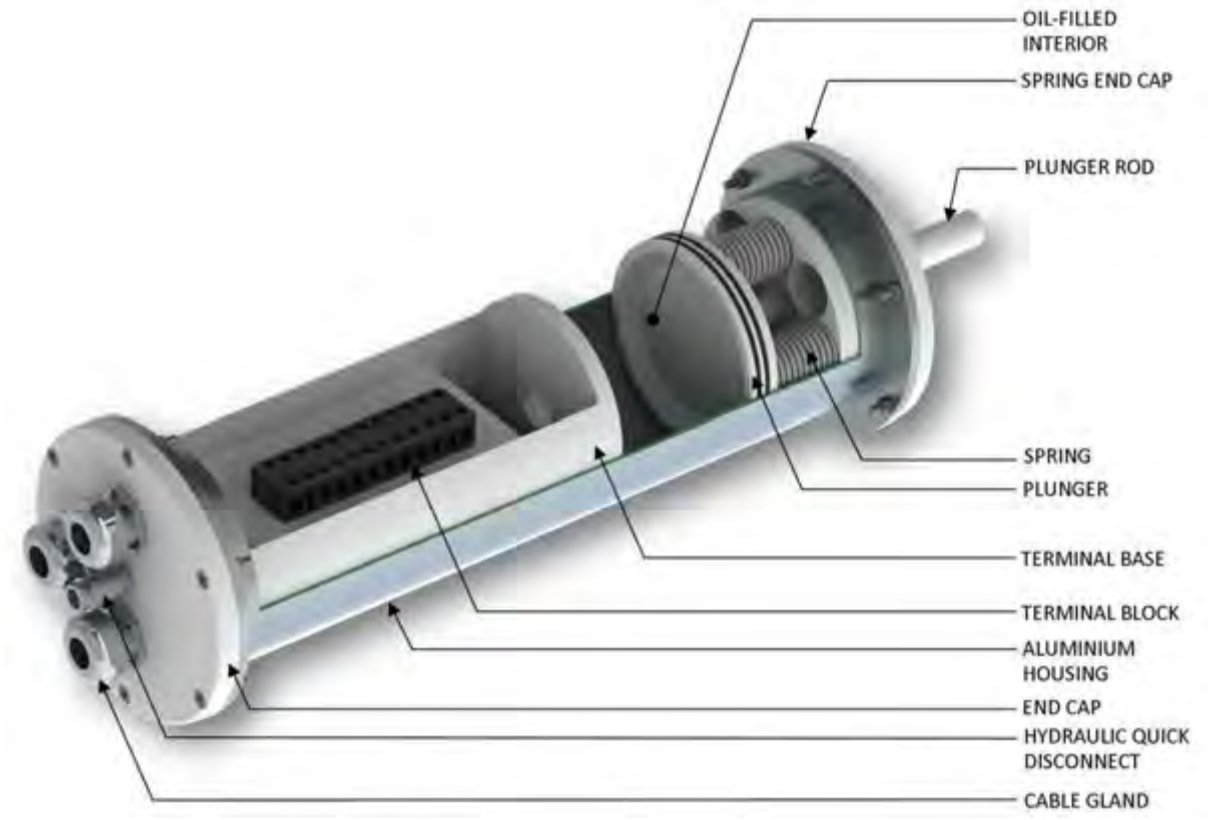

Figure 6 - Rendering of the old junction box with interior details shown [1]

The relatively low differential pressure between the inside and the outside of the junction box allows sealing between the glands and the cables that penetrate the module to be rated to lower pressures than air filled modules. At the time of design and fabrication of the old junction box, less experience had been

gained in module sealing in the form of potting and standard O-ring seals. Therefore it was assumed that the only other option to an oil compensated junction box would be to purchase a specialised subsea tether connector. These connectors are highly expensive and are rated to pressures far in excess of the depth rating of the *SEAHOG* ROV, making it an unnecessary expense. The old *SEAHOG* junction box closely mimics the oil filled and hard wired junction box that can be seen in the previous section. However, as previously mentioned, the oil-filled junction box design is typically used in deeper applications than the *SEAHOG*.

2.2.3.Motivation for New Junction Box

The junction box forms the connection point between the tether and the ROV. The tether must be disconnected from the ROV each time it is transported to and from storage to make the transportation less cumbersome and to prevent damage to components. Thus, the junction box must allow for easy disconnection of the tether. Experience in carrying out this process on the old junction box showed that it was a difficult and time consuming task even when the module was not filled with oil. The addition of oil would make the process messy and even more difficult to carry out.

Results from testing on previous ROV projects showed that only two radial O-ring seals were required to successfully seal a module [3]. In addition, a custom manufactured fibre optic penetrator was designed to feed the fibre optic line from the junction box into the electronics pod and proved to effectively seal the module [1]. The penetrator seals using an O-ring face seal and a polyurethane potting compound. A rendering of the component is shown following in Figure 7. These results are valuable and were considered when deciding how to connect the tether fibre-optics to the ROV without using a patch-cord.

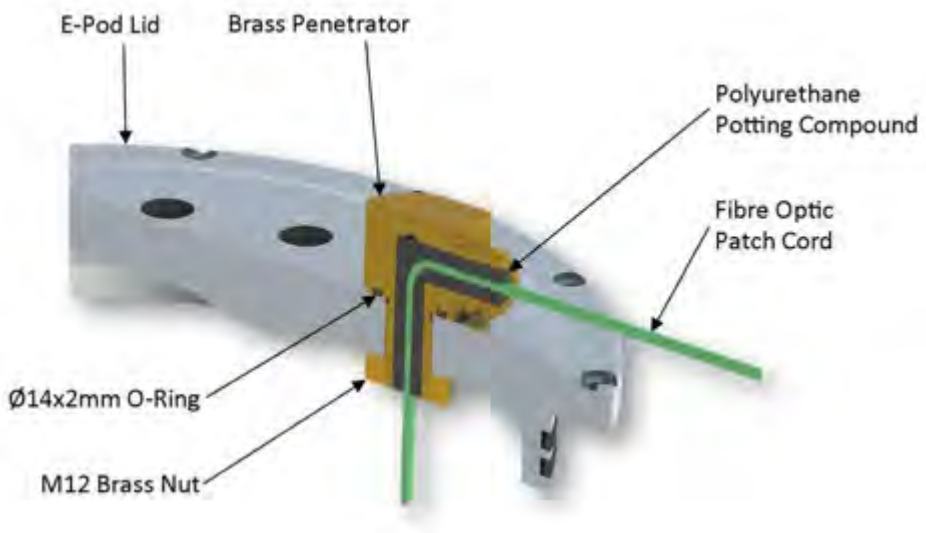

Figure 7 - Rendering of a cross section of the previously designed fibre-optic penetrator fitted to the E-Pod lid [1]

In addition, the *SEAHOG* ROV was commissioned with the intention of carrying out marine research. This may include operations in sensitive marine environments such as fisheries and reefs. Conservation and

preservation of these environments is paramount and thus removing the risk of oil contamination is a compelling reason to remove oil-compensation altogether from the *SEAHOG*.

A summary of the issues with the old junction box is given below:

1. It is not easy to disconnect the tether from the old junction box as six bolts must be undone to open the module and the power lines must then be unscrewed from the chocolate block that they are mounted on.
2. In the above process, all of the components are covered in oil.
3. Due to the springs in the pressure compensation design, the junction box occupies a large amount of space.
4. The risk of oil contamination may prevent ROV operations from being carried out in marine research environments such as reefs and fisheries.

Experience gained from ROV projects since the fabrication of the junction box is summarised below:

1. The relatively low operational depth of the ROV (300 m) allows pressure vessels to be successfully designed without oil compensation and with reasonable housing wall thicknesses.
2. Custom designed penetrators sufficiently seal modules to the rated depth using polyurethane potting compounds and standard O-ring seals.

Therefore, the advantages of oil compensation are not exploited enough on the *SEAHOG* to make them critical. Other ROV modules show that sufficient housing strength and sealing capability can be achieved without oil compensation. Thus, it was decided that a new junction box should be designed in the form of a standard pressure housing. The new design should also improve on the shortcomings of the previous junction box – namely its ease of use and incorporation of the tether fibre-optics. Preferably an operator should be able to disconnect the tether from the ROV without any tools being required.

Now that the motivation for a new junction box has been given, its specifications and design can be formulated.

2.3. Junction Box Specifications

Table 1 following lists the specifications formulated from the previous section that the new junction box should adhere to.

Table 1 - Specifications for the new junction box

Number	Description of Requirement	Target Value
2.3.1	Type of Module	Standard pressure vessel
2.3.2	Depth Rating	300 m
2.3.3	Number of Copper Junction Terminals	6
2.3.4	Number of Optical Fibre Couplings	2
2.3.5	Voltage Rating	470 VDC
2.3.6	Number of Tools Required to Disconnect Tether	0
2.3.7	Design for Underwater Environment	Yes

2.3.1 Type of Module

As previously discussed, oil compensation shall be replaced with a standard pressure module, filled with atmospheric air.

2.3.2 Depth Rating

As previously determined in [1], the depth rating of the ROV is 300 m. Thus this module shall withstand pressures in seawater corresponding to a depth of at least 300 m.

2.3.3 Number of Copper Junction Terminals

The new junction box shall accommodate the connection of four copper cores for power transmission. Provision shall be made for future connection of two data transmission copper cores.

2.3.4 Number of Optical Fibre Junction Terminals

The ROV tether contains four fibre optic cores. Two of these cores are used to communicate from the surface to devices on the RS485 network on the ROV. Thus two fibre-optic junction terminals shall be available to link the ROV to the surface control station.

2.3.5 Voltage Rating

The maximum voltage limit for the ROV is 425 VDC. It was decided in [1] to allow for 10% more than this for transient voltage spikes on the power supply line. Thus insulation between cores in the junction box shall cater for a maximum of 470 VDC.

2.3.6 Number of Tools Required to Disconnect the Tether

Usability is one of the most important design aspects of the junction box. Given that the tether must be disconnected from the ROV each time it is transported, it should be as easy as possible to disconnect the tether from the ROV. Thus the design shall allow for the tether to be disconnected without the assistance of any tools.

2.3.7 Design for Underwater Environment

The junction box forms part of the ROV and will operate in seawater. Thus, design considerations for the underwater environment shall be taken into account, such as corrosion.

Now that the specifications for the new junction box are clearly defined, the new junction box design can be formulated. The final concept for the new junction box is shown in the next section.

2.4. New Junction Box Design

2.4.1. Introduction

Concepts for the new junction box design were derived from industrial designs along with insights drawn from the previous junction box design and experience gained from previous ROV projects. The result of conceptualisation was a mixture of a hard-wired connection solution and a subsea connector.

2.4.2. Overall Design

Figure 8 following shows a rendering of the final junction box design with the housing sectioned and the interior components revealed.

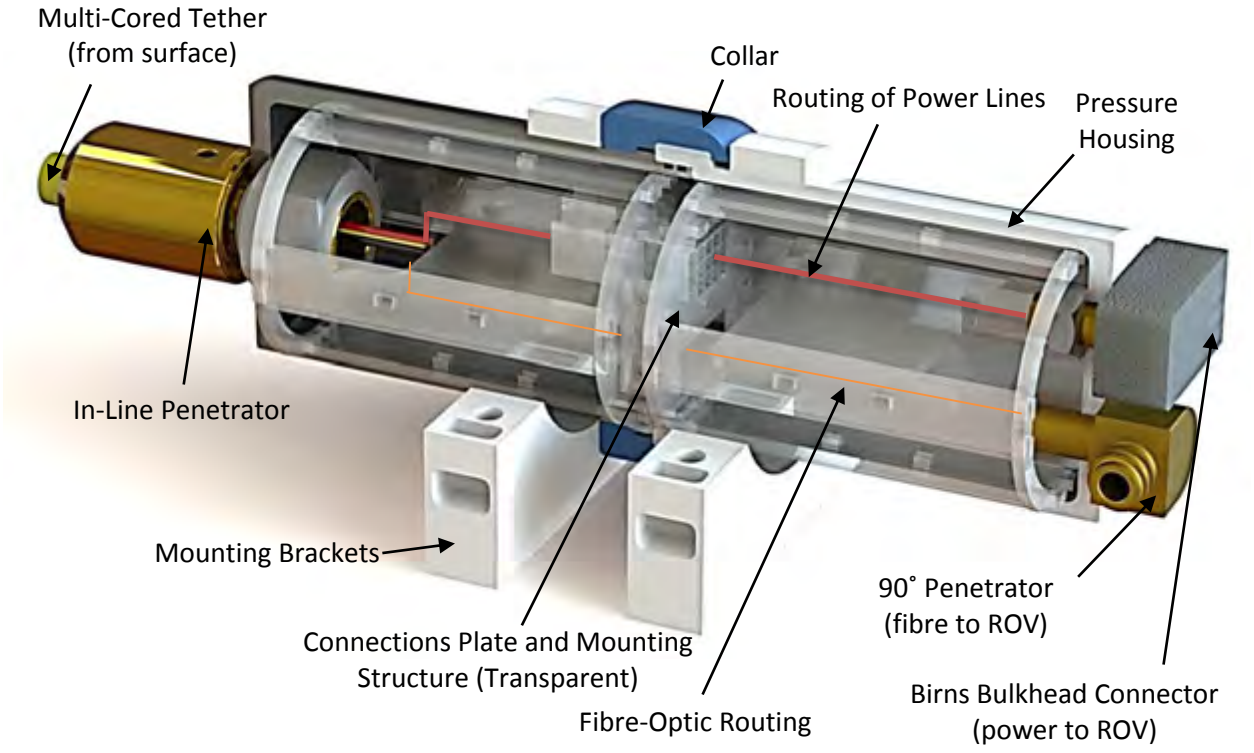

Figure 8 - Rendering of the new Junction Box with sectioned pressure housing and inner detail

Table 2 following lists material choices for selected components in the above design. The material choices will be motivated in the relevant section that describes the components.

Table 2 - Material selections for labelled components

Part Name	Material
Pressure Housings	Aluminium 6082 T6
Collar	Polyvinyl Chloride (PVC)
Penetrators	Brass
Mounting Brackets	High Density Polyethylene (HDPE)

For clarity, an exploded view of the new junction box is given following in Figure 9 to better visualise the new Junction Box design.

Figure 9 - Rendering of an exploded view of the new Junction Box

With an overview of the design given, the following sections detail individual aspects of the design and show how it serves as an appropriate solution for connecting the tether to the ROV.

2.4.3. Structural Elements

Design specification 2.3.6 from section 2.3 previously, required no tools to be necessary on disassembly of the junction box. This resulted in a design that employs novel fastening and connection methods that had not previously been implemented on the ROV.

Many *SEAHOG* ROV modules implement multiple screws to hold vessel lids in place. This is unnecessary because under pressure, the surrounding water will serve to hold the module lid on rather than push it off in general. It is still possible that on resurfacing, a warm module will have a net positive interior pressure which will tend to push the lid off from the inside and thus it is still important to fasten the lid down. However, the extent to which this is achieved is heavily over-designed on other *SEAHOG* modules. Thus,

the junction box implements a PVC 'collar', which is threaded and screws onto the Junction Box housing. A force flow diagram is shown following in Figure 10 to depict how the collar holds the junction box together.

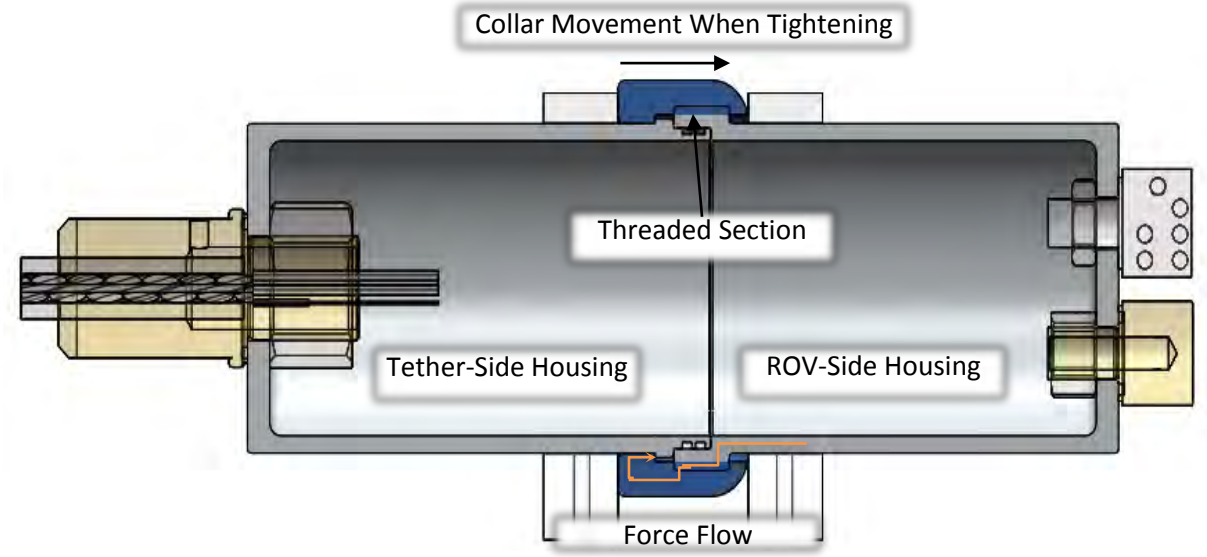

Figure 10 - Junction box sectioned view showing how the collar holds both sides of the junction box housing together

Polyvinyl Chloride (PVC) was chosen for the collar due to its corrosion resistant properties, suitability to seawater and low mass properties. The outer surface of the collar is knurled so that it can be gripped by a hand during its rotation. The cylindrical housings were made from aluminium due to its low mass and resistance to corrosion in seawater when anodised. The housing wall thickness was calculated using theory that can be found in section 2.5 following, in addition to a Solidworks strength simulation analysis.

It should be noted that any loads exerted on the tether are not taken up by the Junction Box itself. The tether is anchored to a point on the ROV with a "Kellem's Grip" which is shown following in Figure 11. Thus, only small loads are expected to be taken up by the connectors on the Junction Box.

Figure 11 - Kellem's grip anchored to ROV base plate to counteract loads on the tether

2.4.4. Sealing Elements

Two radial O-ring seals were implemented to seal the two housing halves. O-ring face seals were used for each of the connectors attached to the housing. Figure 12 following shows the position of the O-rings that were implemented in custom designed parts for the Junction Box.

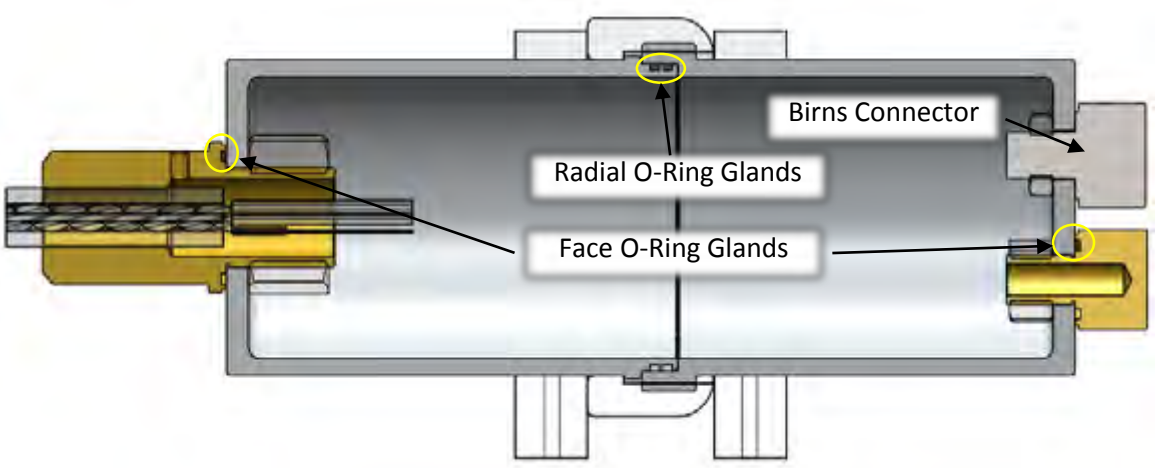

Figure 12 - Position and type of O-ring seals used in the new Junction Box

The two custom designed brass penetrators were filled with a commercial polyurethane potting compound that is widely used in industry to seal components in the subsea environment. Figure 7 previously on page 7 showed a detailed rendering of the previously designed right-angle penetrator and how it is sealed. Figure 13 following shows a detailed view of the new in-line penetrator and the area that is filled with potting compound. It can be seen that the volume of potting compound will prevent water ingress from other openings in the penetrator and will hold the fibre-optics rigid relative to their protective sheath. A detailed potting manual developed at RARL is provided on the accompanying disc to this report.

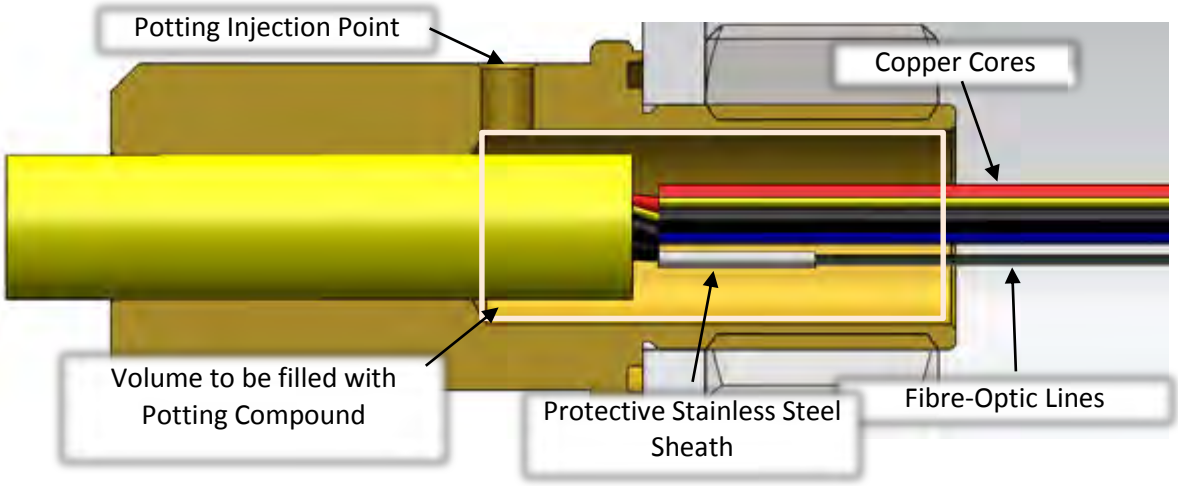

Figure 13 - Detailed view of in-line penetrator and method of sealing

2.4.5. Mounting Elements

Mounting the Junction Box without the use of tools was a challenge in and of itself. A unique approach was taken that used the high elasticity and good fatigue properties of HDPE to create mounting brackets with "teeth" that hold the two bracket sections together. Figure 14 following shows a cross-section of the mounting brackets, where their method of operation and mechanisms to constrain the Junction Box can be seen.

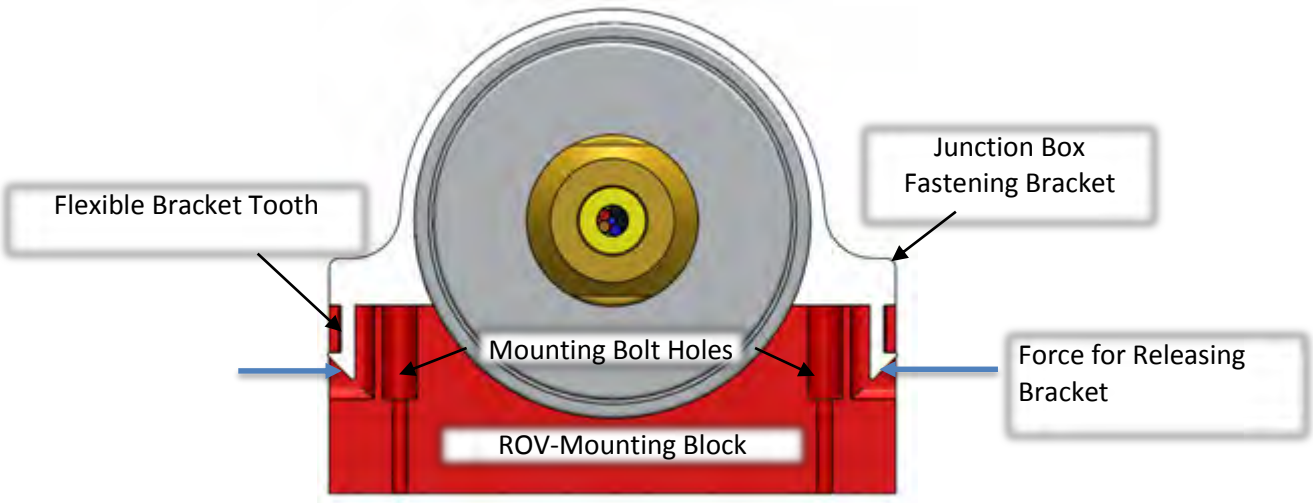

Figure 14 - Cross-section of Junction Box mounting brackets

Two brackets are mounted on either side of the Junction Box collar to constrain the Junction Box in the axial direction. The Junction Box design allows for rotation about its axis, however it was deemed unnecessary to constrain this final degree of freedom as this would help to reduce the twisting torques induced by the tether and other connected cables and hence prevent the mounting nuts of the penetrators inside the junction box from loosening.

2.4.6. Connection Elements for Tether Cores

A Perspex frame holds connectors for both the power and fibre optic lines. The frame holds the fibre and power lines separate to each other, preventing any contact. In addition, the connections can be released by hand after the Junction Box has been opened up. The four copper power lines are connected via a 12 pin Molex connector and the two fibre-optic lines are connected via multi-mode fibre-optic ST mid-couplers. Figure 15 following shows these connectors and their layout in the mounting frame contained within the Junction Box.

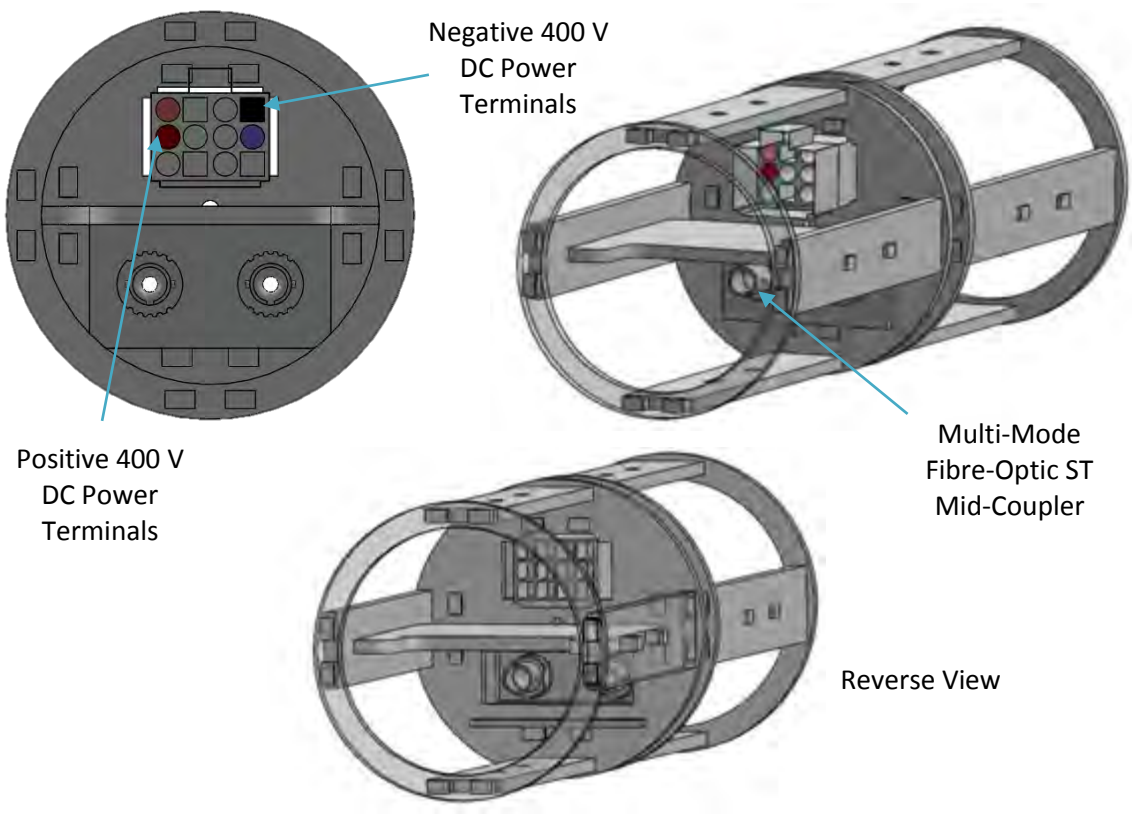

Figure 15 - Junction Box power and fibre-optic wiring terminals and mounting frame

2.4.7. Design for Underwater Environment

All materials chosen for the junction box design are common on the *SEAHOG* due to their suitability to the underwater environment.

Polymers such as PVC and HDPE have good resistance to corrosion in seawater and low water absorption qualities. This is desirable especially in the case of the junction box collar, where material swelling will interfere with the collar thread tolerances.

Aluminium, especially when anodised, has good resistance to corrosion in seawater and is relatively lightweight. In addition, brass is also resistant to corrosion in seawater. A notable factor however, is the galvanic corrosion effect, whereby materials will undergo redox reactions in the presence of an electrolytic medium and corrode. Seawater, with its high salt content, acts as an electrolytic medium and thus brass and aluminium will be subject to galvanic corrosion. Ways to counteract this phenomenon are to include sacrificial anodes in the design with lower galvanic potential than the materials that must be protected, resulting in the sacrificial anode corroding before other materials. This was not implemented in the junction box design due to limited surfaces to mount the anodes on. However, another way to minimise galvanic corrosion is to choose materials that have as close galvanic potentials as possible. As can be seen from Figure 16 following, brass and aluminium have relatively close galvanic potentials and

combined with their individual corrosion resistant properties and the aluminium protective anodised layer, this makes them suitable material choices in the design.

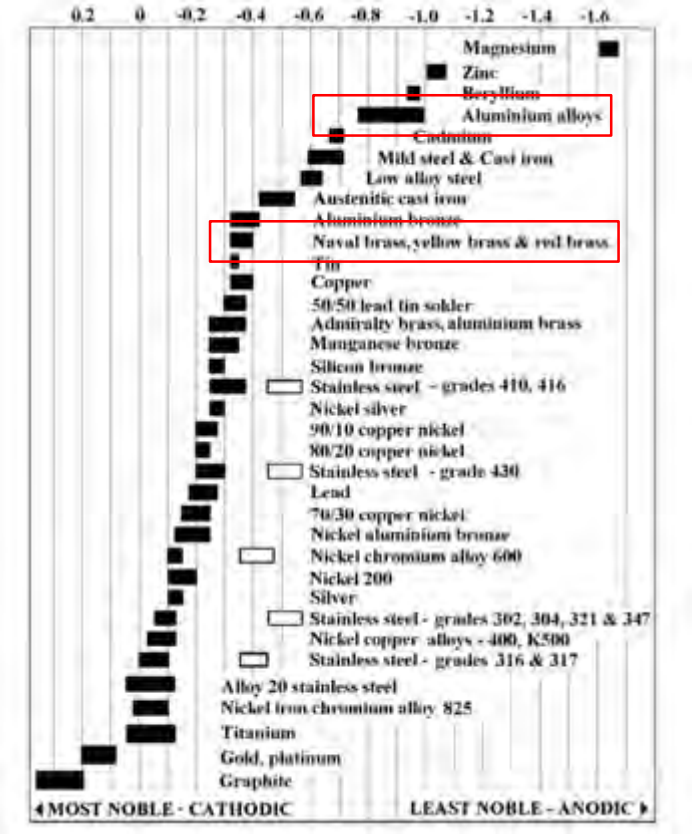

Figure 16 - Galvanic potentials for different materials [4]

2.4.8. Summary

All aspects of the new Junction Box design have now been described. The pressure vessel was designed using theory presented following in section 2.5 and verified with a Solidworks strength simulation analysis. A hand-twistable threaded PVC collar is used to hold both halves of the Junction Box together. This allows the junction box to be opened up and the hard-wired connections to be disconnected inside. A brass in-line penetrator is used to terminate the tether and hard wire the power and fibre optic lines to the rest of the ROV. The penetrator is filled with polyurethane potting compound and holds the fibre optic lines rigidly relative to their stainless steel sheath, preventing them from wearing down and breaking off. Face O-ring seals and radial O-ring seals are used to seal the penetrators and the Junction Box housing respectively from water ingress. Finally, the Junction Box is mounted using HDPE clips with flexible teeth, allowing the junction box to be released without the use of tools.

Mechanical drawings for the different Junction Box components are supplied in appendix C to this report.

Figure 17 following shows the fabricated new junction box before sealing and potting of connectors and anodising of the housing had occurred.

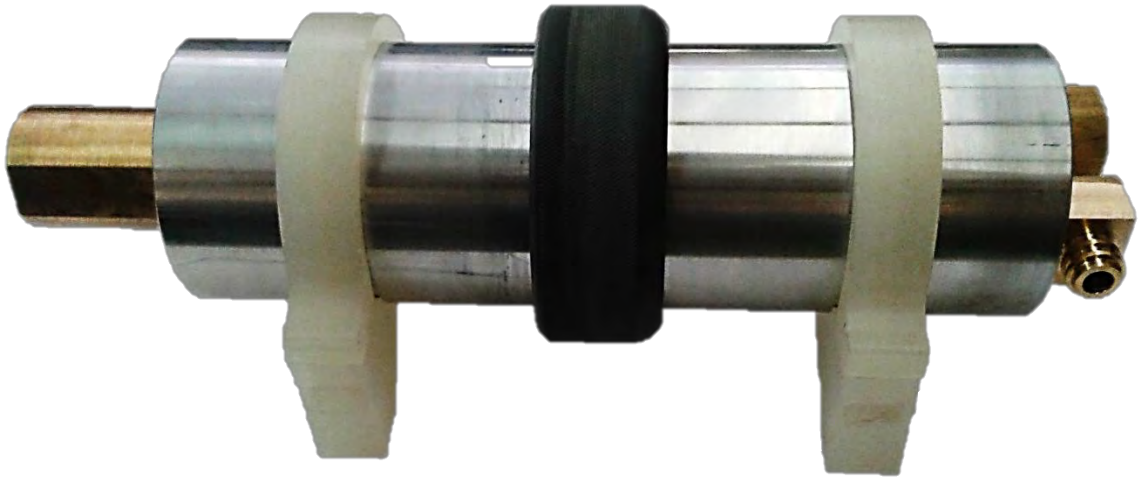

Figure 17 - New Junction Box before potting of connectors

2.5. Pressure Vessel Housing Design

2.5.1. Pressure Vessel Housing Theory

The design of pressure housings on the ROV is comprehensively covered in [3] and [1]. The design theory and principles used for these designs have proved to be successful, with no structural or sealing failures found during testing. Round cylinders and spheres are the two most common shapes used in the design of pressure vessels because, under the influence of an external pressure from a fluid, the stresses induced in the walls of a vessel are almost entirely compressive [5]. Similarly, stresses experienced from internal pressures are almost entirely tensile. Table 3 following lists the symbols that will be used to describe the elements considered in the following pressure calculations.

Table 3 - Description of symbols used in pressure vessel design calculations

Symbol	Description
P	Pressure
d	Internal diameter
t	Wall thickness
σ_H	Hoop stress
σ_L	Longitudinal stress
$P_{collapse}$	Collapse pressure
L	Cylinder length
E	Modulus of elasticity
μ	Poisson's Ration
δ_{max}	Maximum deflection
I	Second moment of area
σ_{max}	Maximum stress

Figure 18 following graphically shows some of the nomenclature presented above in Table 3.

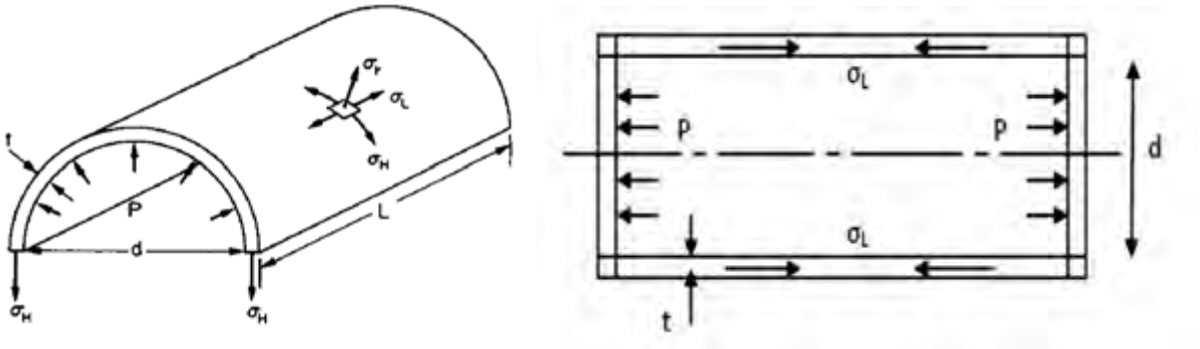

Figure 18 - Stresses on an internally pressurised closed cylinder [5]

The design of vessels under external pressures is not equivalent to the design of vessels under internal pressures due to the possibility of the vessel collapsing under buckling type of failure. A model was developed for the collapse pressure of a thin cylinder by the United States Experimental Model Basin and is presented in Equation 2.1 following [6]. A thin-walled cylinder is typically a cylinder that has a diameter at least 20 times larger than the vessel wall thickness [5].

$$P_{collapse} = \frac{2.42E}{(1-\mu^2)^{\frac{3}{4}}} \cdot \frac{\left(\frac{t}{d}\right)^{\frac{5}{2}}}{\frac{L}{d} - 0.45\left(\frac{t}{d}\right)^{\frac{1}{2}}} \quad \{2.1\}$$

$P_{collapse}$ was treated as the design pressure that the system would experience and was therefore equivalent to the system safety factor multiplied by the working pressure, P. Experience gained from previous ROV projects allowed the design to adopt a lower safety factor in this design than in previous cases. A value of 1.5 was chosen (compared to previous design safety factors of 2.5). Spherical end plates are stronger under pressure than flat ones but due to space requirements on the ROV it was decided to use flat end plates, even though they would be thicker and heavier [5]. In addition, for simplicity of manufacture, it is far easier to mount a successfully sealing connector to a flat surface than a spherical surface. Equations 2.2 and 2.3 following describe the maximum deflection and maximum stress at the centre and circumference of the end plate respectively, as depicted following in Figure 19, where $\alpha = d/2$ and h is the plate thickness [7].

$$\delta_{max} = \frac{P\left(\frac{d}{2}\right)^4}{64E\left(\frac{td^3}{12}\right)} \quad \{2.2\}$$

$$\sigma_{max} = \frac{3P\left(\frac{d}{2}\right)^2}{4h^2} \quad \{2.3\}$$

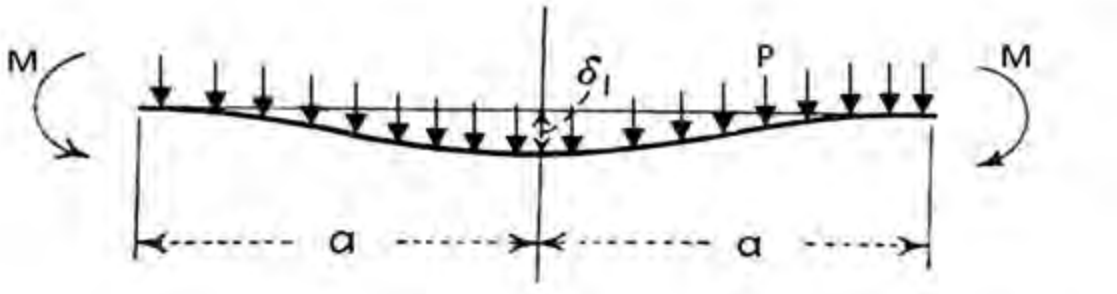

Figure 19 - Loading of a pressurised end plate

2.5.2. Pressure Vessel Design and Results

The material used in the junction box housing design was Aluminium 6082 T6. Its properties are given following in Table 4.

Table 4 - Material properties of Aluminium 6082 T6

Elastic Modulus, E	68.9 GPa
Tensile Strength, S_u	290 MPa
Yield Strength, S_y	250 MPa
Poisson's Ratio, μ	0.33

The two halves of the junction box were treated as a single uniform cylinder. For a set cylinder length and diameter, Table 5 following shows the values that were used while varying the wall thickness until it resulted in a working depth that was close but greater than the minimum working depth of 300 m for the ROV.

Table 5 - Calculation variables and results for wall thickness limit

Fixed Variables		**Result**	
Minimum ROV Working Depth	300 m	Limiting Wall Thickness, t	**1.6 mm**
Internal Diameter, d	68 mm	**Outputs**	
Cylinder Length, L	223 mm	$P_{collapse}$	4.71 MPa
Safety Factor, n	1.5	Working Depth	311.4 m

The thickness of the endplate was varied using a set working depth to produce a maximum stress in the endplate that was below the yield strength of the material.

Table 6 - Calculation variables and results for end-plate thickness limit

Fixed Variables		**Result**	
Set Working Depth	300 m	Limiting Plate Thickness, h	**4 mm**
Internal Diameter, d	68 mm	**Outputs**	
Design Pressure, $P_{collapse}$	4.54 MPa	Maximum Plate Deflection, δ_{max}	0.03 mm
Safety Factor, n	1.5	Maximum Stress In Plate, σ_{max}	246.12 MPa

Table 5 and Table 6 above give the minimum vessel wall thickness to be 1.6 mm and the minimum end-plate thickness to be 4 mm. These values will theoretically lead to a design that can withstand a pressure at 300 m in seawater with a safety factor of 1.5. In practise however, the design required glands for O-ring seals and other elements which resulted in slightly greater wall thicknesses than given. Figure 20 alongside shows the final dimensions used for the purposes of strength design on the new Junction Box.

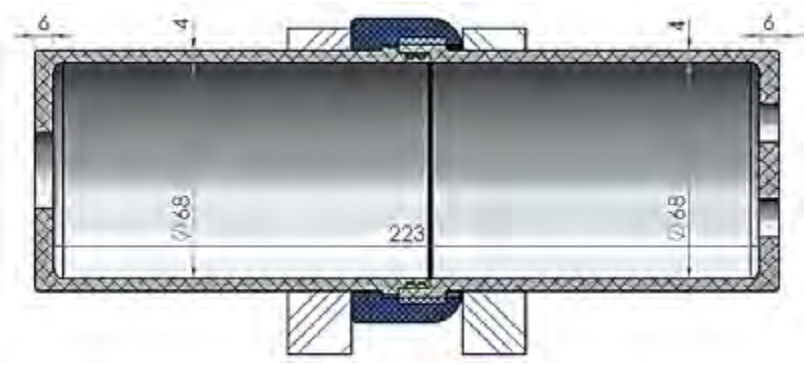

Figure 20 - Final dimensions for new Junction Box housing

It should be noted that the ratio of inner diameter to wall thickness for the Junction Box design is not quite 1:20, as required to use thin cylinder approximation theory [5]. Therefore, to verify the design, a Solidworks strength simulation analysis was carried out on each half of the Junction Box housing. Analysing the housing on its own is a conservative check, since in real life there will be other components in contact with the cylinder adding rigidity to the structure and thus in effect serving to strengthen it. Figure 21 and Figure 22 following show the results of these simulations on each half of the Junction Box housing. The models were quartered due to their symmetry, upon recommendation from a Solidworks simulation specialist, allowing them to be properly constrained in the simulation. The red arrows

represent an applied design pressure of 4.71 MPa and the green arrows represent a fixture whereby the surface can deflect perpendicular to the arrow but not along the axis of the arrow.

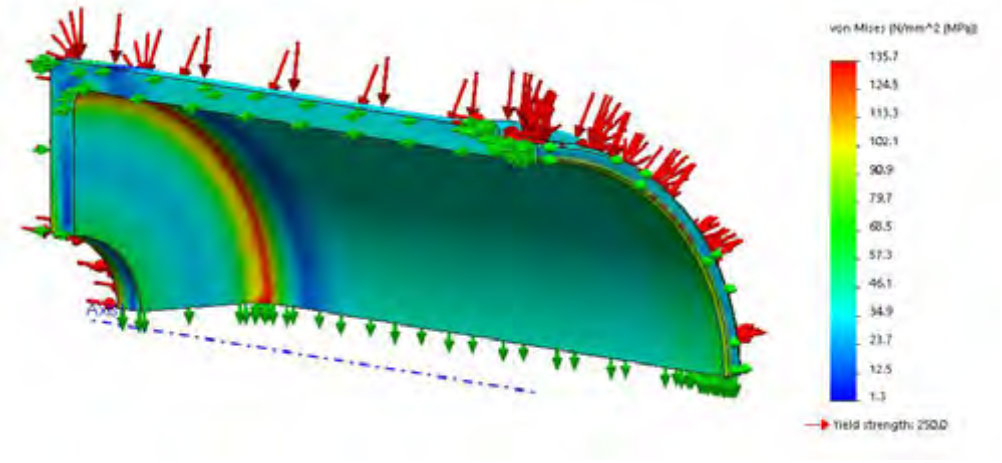

Figure 21 - Solidworks strength simulation analysis on the tether-side Junction Box housing

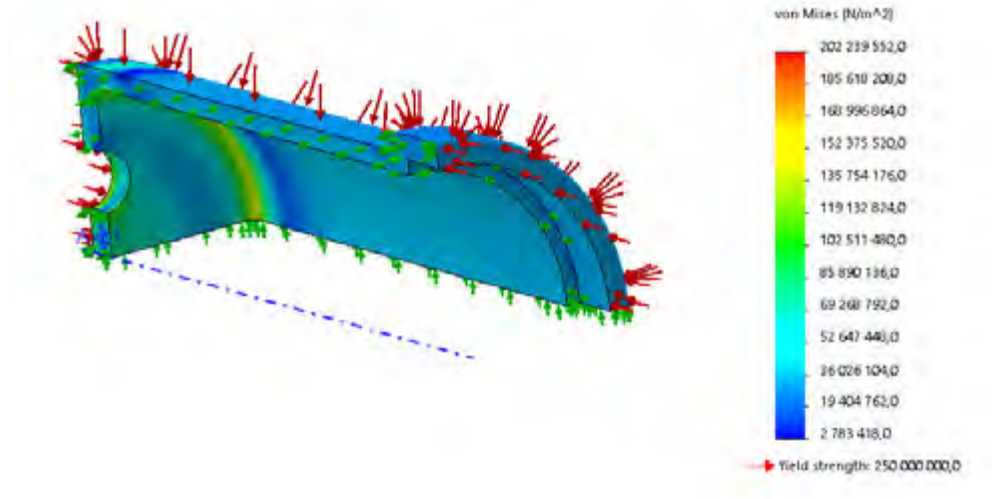

Figure 22 - Solidworks strength simulation analysis on the ROV-side Junction Box housing

The results of the simulations show that the maximum stress experienced in the material is about 170 MPa. This is sufficient as it is only 68% of the material's yield strength. This was expected, as the final wall thickness in the design was 2.5 mm more than the limiting thickness and the end-plate was 2 mm more than the limiting thickness from theoretical calculations.

2.5.3. Summary

It was decided that the resulting wall thickness would be 4 mm and the end plate thickness would be 6mm. This is 2.5 mm and 2 mm more than the design dimensions limits obtained from the United States Experimental Model Basin equations for the wall thickness and end plate thickness respectively. When analysed using the Solidworks simulation, the Maximum stress experienced in the cylinder when loaded with a 1.5 safety factor is only 68% of the material's yield strength. We can thus assume that the cylinder will not fail under the specified loading conditions.

With the final Junction Box design defined and checked for strength using equations developed by the United States Experimental Model Basin and verified using a Solidworks simulation, the Junction Box was ready for manufacture and testing.

2.6. Junction Box Testing and Completion of Design

2.6.1. Introduction

The fibre optic connections were tested along with the strength and sealing of the junction box design. The fibre optic test was to ensure the connections in the tether had been successful and did not attenuate the signal significantly. Pressure testing was carried out as a procedural routine that happens on each ROV module. While it was expected that the O-ring seals and structural integrity of the module would be sufficient, it was important to verify the effectiveness of the brass penetrators at sealing the module.

2.6.2. Pressure Testing

Description and Method:

Pressure testing was conducted following a similar method detailed and prescribed in [1]. The Junction Box was filled with paper towel, sealed and then placed in a water-filled pressure vessel at a company called Marine Solutions. The pressure was increased by five bar with about ten seconds break each time until 45 bar was reached. The module was then left for an hour in the vessel after which the pressure was released and the module retrieved. The pressure vessel testing facility at Marine Solutions is shown following in Figure 23.

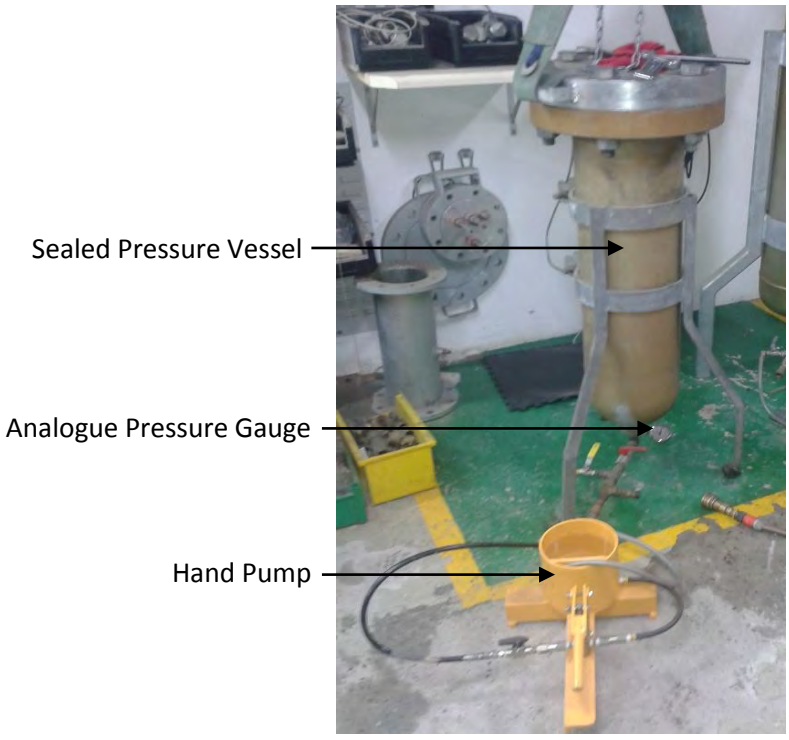

Figure 23 - Pressure testing facility at Marine Solutions

Preliminary Results:

The first attempt at pressure testing resulted in failure of the in-line penetrator at 18 bar. This was due to badly set potting compound. Limited experience and a lack of expertise was the cause of this, as potting at UCT had only been carried out in previous projects. It is suspected that the potting did not set due to either the compound not being mixed well enough with the setting agent or due to the potting being carried out in winter with too low ambient temperatures for the compound to set properly. In addition, the potting compound that was used was purchased a few years previously and is thus also suspected to be expired. Unfortunately there were too many unknowns to identify exactly why the potting did not set.

Design Modification:

The personnel of Marine Solutions were consulted on how to improve the penetrator after the failed pressure test and a solution was formulated. The experts were concerned about the penetrator design even if the potting were to set properly: They argued that the pressure would be enough to push the potted inner section into the junction box as shown following in Figure 24.

Pressure forces water through the interference fit of the tether and penetrator, pushing the potting inwards

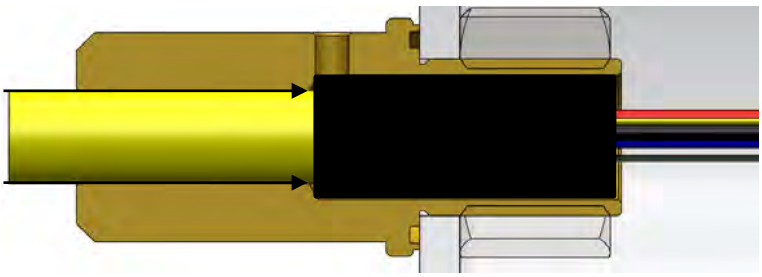

Figure 24 - In-Line Penetrator design concern

To solve this problem, they suggested an “over mould” whereby the outside of the penetrator would be covered in potting compound to seal around the tether itself and prevent any water ingress into the penetrator. The potting was carried out by Marine Solutions using one of their moulds after a small modification to the penetrator so that it would fit into the mould. The new penetrator design is shown superimposed on the old penetrator design following in Figure 25 so that the modifications can be seen clearly.

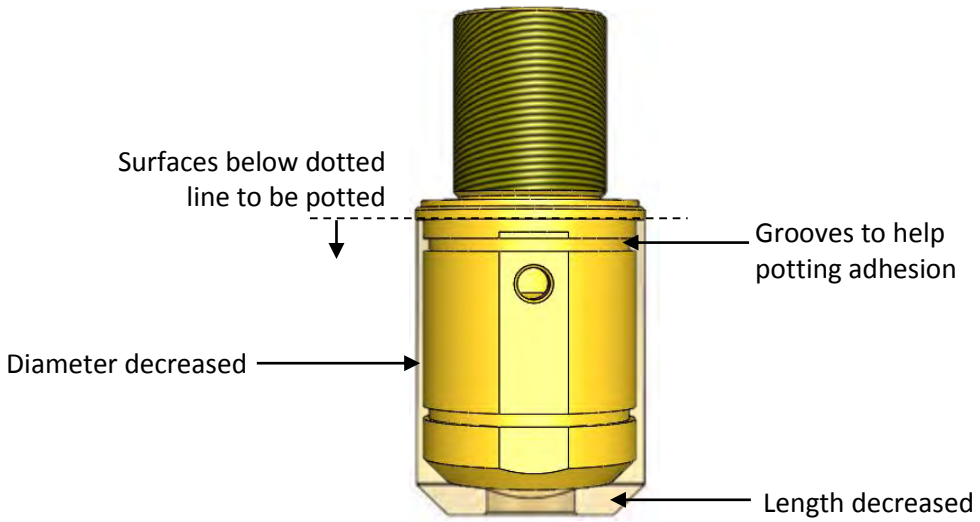

Figure 25 - Modified In-Line Penetrator superimposed on old penetrator

The final potted penetrator is shown following in Figure 26. This was then attached to the Junction Box and pressure tested again. The threaded section of the penetrator can be seen to the left, with the over-moulded section covering the rest of the penetrator and the tether protruding from the right end.

Figure 26 - Final potted In-Line Penetrator attached to tether

Results:

The modified penetrator was tested once again by sealing the Junction Box and increasing the pressure until 45 bar was reached, representing a depth in seawater of approximately 450 m – 1.5 times the design depth of 300 m.

The Junction Box was left for a total of two hours in this pressurised environment before releasing the pressure and removing the module. During the test, no significant pressure drop was observed. On opening the module, the paper towel inside remained completely dry. The Junction Box housing and sealing was thus declared to be sufficient and to have passed the test.

2.6.3. Fibre-Optics Connection

A custom solution was worked out with Netconnect Distribution, who specialise in fibre-optic connections, on how to terminate either end of the tether cable. This section will describe in general the solution to terminate either end of the tether fibre-optics, since termination of the copper cores has never been a problem and is a straight-forward process.

ROV End of Tether:

Recall that one of the main challenges to the termination of the tether fibre-optics was creating a robust solution where the fibres would not rub against the sharp edge of their protective steel tube and break off. This presented a challenge and required a custom solution to be implemented by Netconnect Distribution. Each bare fibre was jacketed with about 10 mm of bare fibre protruding from the stainless steel tube before the jacket started. A tube was inserted over the four jackets, covering the area where the fibres exit the tube and enter their jackets. This tube was then filled with resin and set solid and the whole assembly was covered in heat shrink. The prepared joint is labelled following in Figure 27. The purpose of this preparation was to give the joint strength and protection during transportation and potting.

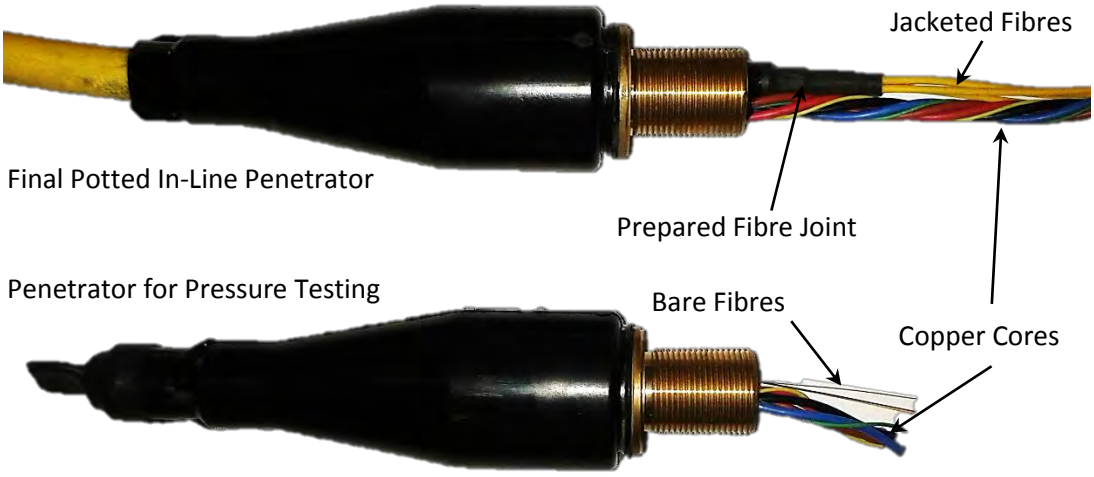

Figure 27 - Final and test in-line penetrator, showing the prepared and unprepared fibre-optics

ST fibre-optic optic connectors were spliced to the end of the grey and orange multi-mode fibres, completing their termination and allowing them to be attached to the mid-coupler mounted within the junction box.

Surface End of Tether:

Termination of the surface end of the tether was performed by breaking the fibre and copper cores out into another junction box. The fibres from the tether were mounted in an SC mid-coupler inside the box, and a fibre patch chord exited the box on the opposite end. The copper cores were mounted in a chocolate block, with a separate power extension cord exiting the box parallel to the fibre patch chord. The inside of the surface junction box is shown following in Figure 28.

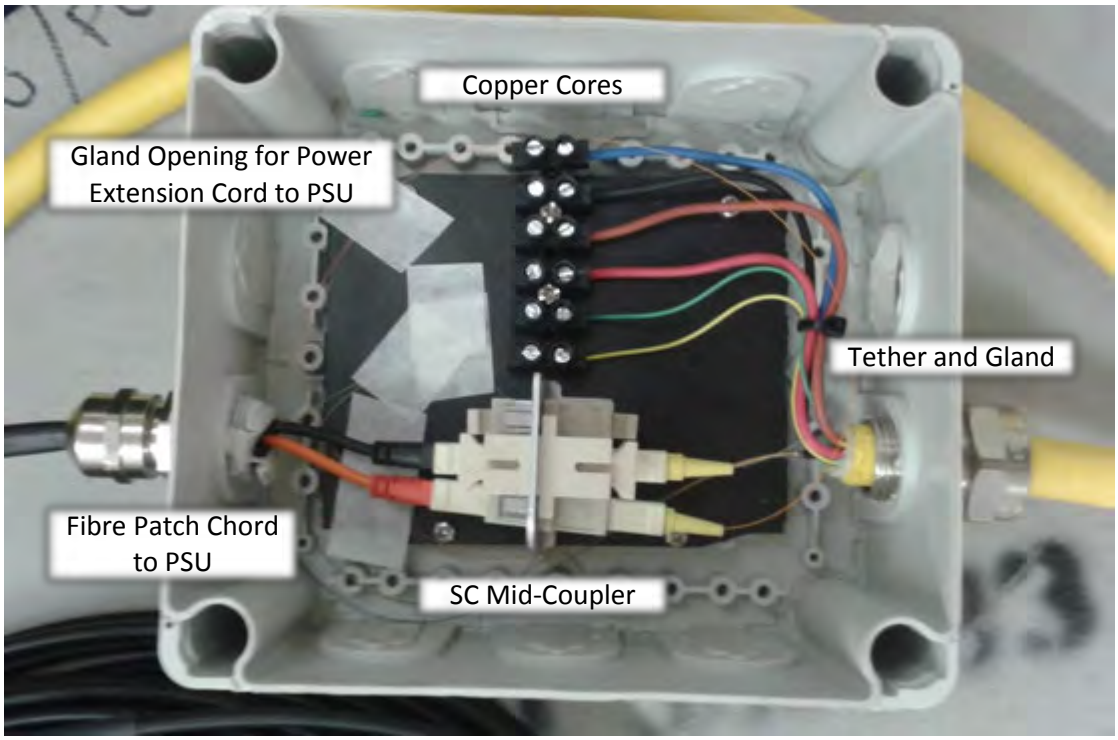

Figure 28 - Surface Junction Box interior

The surface junction box has a requirement of rigidly holding the fibres relative to where they exit their protective tube. The tether gland was employed so as to clamp and rigidly hold the tether relative to the Junction Box. This would ensure that the box does not move relative to the fibres and cause them to wear down and break off.

The surface junction box is specified to IP66 – which certifies it to withstand powerful jets of water and to be dust tight. This is ideal for a marine operating environment.

2.6.4. Fibre-Optics Testing

The fibres were tested by Netconnect Distribution and were concluded to experience a signal attenuation of 0.8 dB and 0.9 dB on either fibre core. This is acceptable and should not significantly negatively impact the signal bandwidth. It was noted however that a bandwidth test should be carried out in the future to evaluate the performance of the fibres.

2.6.5. Conclusion

The new Junction Box design successfully withstood an equivalent of 450 m depth in seawater for two hours, deeming its strength and sealing to be sufficient. The connections of the fibre optics were deemed sufficient, with an acceptable attenuation of 0.8 dB and 0.9 dB on each of the fibre cores.

2.7. Summary

A combination of a pressure vessel design with hard wired power and fibre optic lines was chosen to link the tether to the ROV. A custom in-line penetrator was designed and over-moulded to seal the tether from its surroundings and prevent water ingress into the Junction Box. The fibres and power lines were split inside the Junction Box, mounted on a Perspex frame, and exited the Junction Box on the opposite side. The power lines were wired into a standard Birns bulkhead connector and the fibre optic patch chord was potted into a right angle custom designed penetrator.

The junction box consists of two halves held together by a PVC collar and sealed with two radial O-ring seals. The junction allows the tether to be disconnected from the ROV without the use of tools, improving its ease of use greatly. The Junction Box was pressure tested successfully for two hours at an equivalent depth in seawater of 450 m.

The fibre optics on the ROV end of the tether were set in resin, jacketed and then potted so as to hold them robustly and stationary relative to their protective tube. The multi-mode fibres were terminated with ST connectors on the ROV end and SC on the surface end. A surface junction box was employed to break out the fibre and copper cores into a separate fibre-optic patch chord and power chord. The fibres were tested and experienced an acceptable level of signal attenuation, deeming the connections to be successful.

The surface junction box was envisaged to be mounted within the central tube of the tether reel. This final step however lay beyond the scope of this report and thus the tether was deemed to be sufficiently terminated and prepared for incorporation into the ROV.

3. Power Pod Upgrades

3.1. Introduction

Testing of the initial design of the ROV power pod in [1] proved that the design was insufficient at dumping heat from inside the power pod to the external environment. It was estimated that the power pod could dissipate heat at a rate of 85W in still water. However, it was estimated that at full load and under the same conditions, the pod would have to dissipate heat at a rate of 170 W. Therefore, a new deeper power pod was designed with a large heat sink and four cooling fans. This solution was proposed in [1] and its manufacture had already been undertaken before this project commenced. It was therefore decided that the solution would be implemented from the stage that it was abandoned in the previous project, rather than conceive a completely new solution. This chapter serves merely to document the process undertaken to install the new Power Pod heat sink. It was not within the scope of the project, however, to test and evaluate the cooling capabilities of this new system.

3.2. Mechanical Modifications

A cross-section of the new power pod design is shown following in Figure 29. The deepened housing can be seen, accommodating the heat sink and cooling fans.

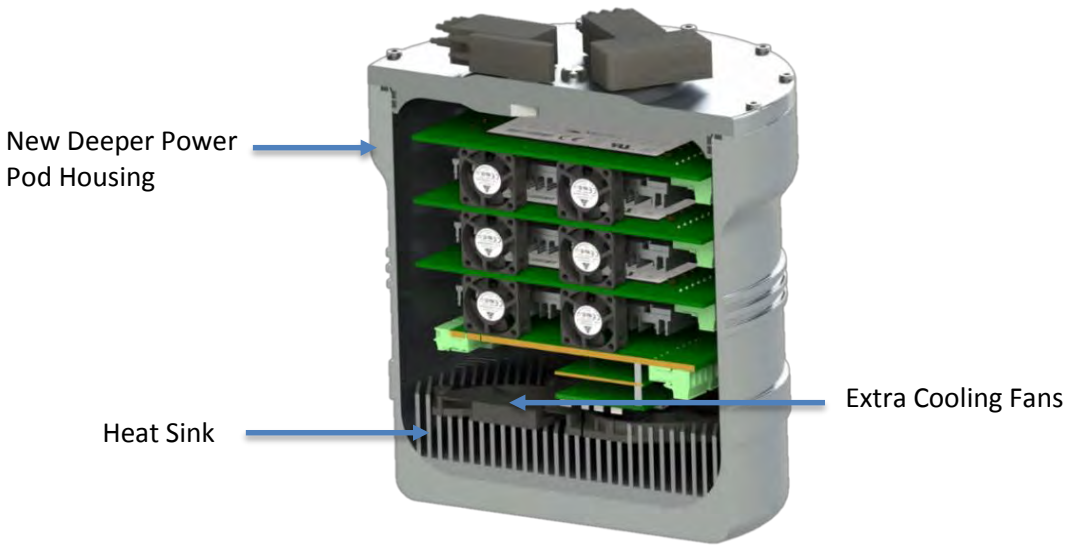

Figure 29 - Cross section of the new power pod

At the time of manufacture, the fans for the heat sink had not been procured. It was later found that the intended fans for the design were very expensive due to their dimensions. The fans were specified to be 70 x 70 x 10 mm but for less than one third of the price, the same fans were available with a height of 15mm rather than 10 mm. Due to the limited space between the power pod circuitry and the cooling fans, the 15mm high fans could not be installed without modification to the heat sink. Thus, as shown following in Figure 30, the slot that the fans are mounted in was milled down by 5 mm to accommodate the taller fans.

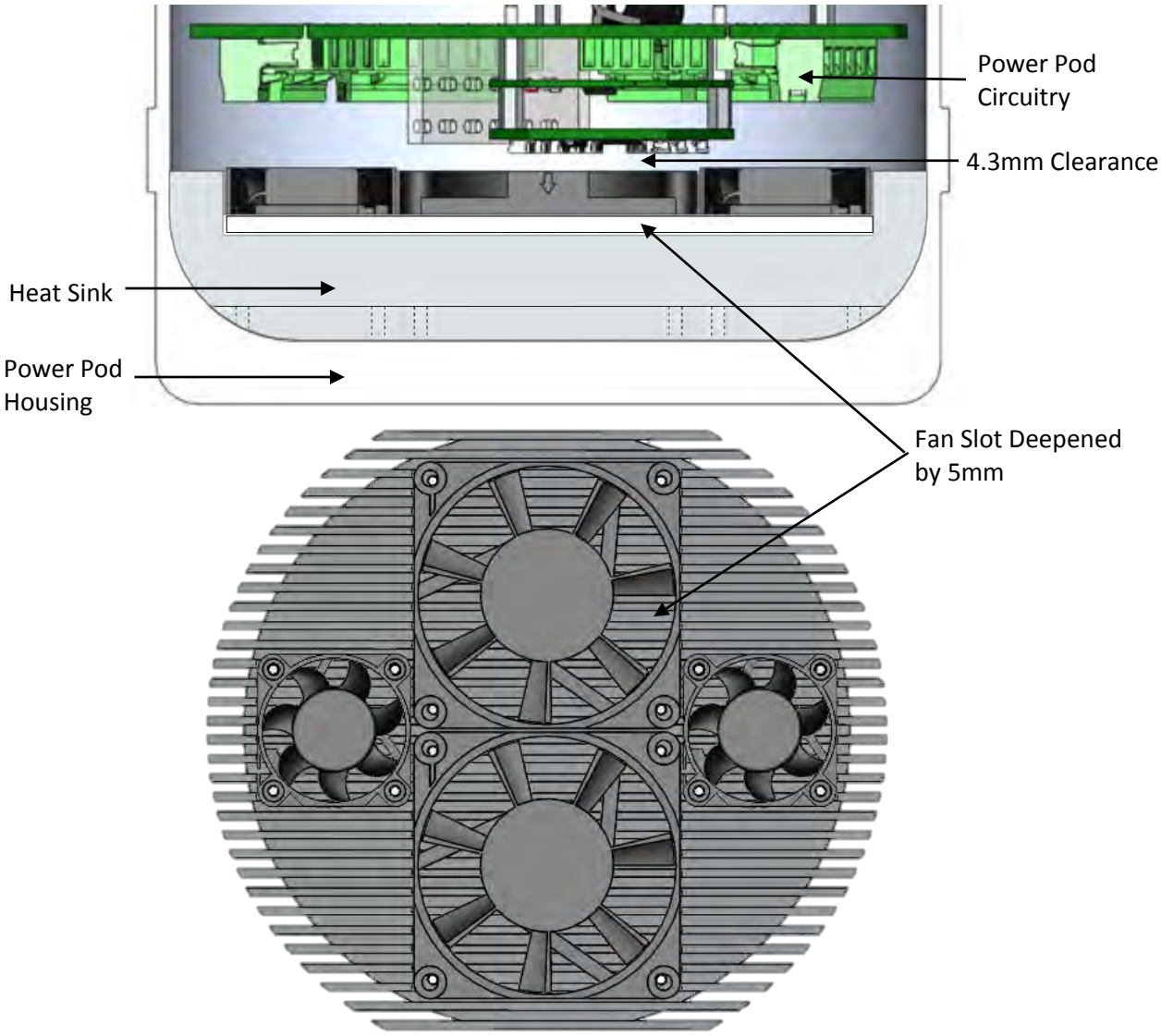

Figure 30 - Heat sink modification with 10 mm high fans displayed

In addition, the fan mounting holes in the heat sink were drilled through and tapped, as this task had not yet been completed. This completed the mechanical modifications to the heat sink and allowed for the task of connecting the fans to be undertaken.

3.3. Electrical Modifications

The heat sink design did not allocate any predetermined wire routing paths or details on how to connect the fans to the power pod. It was decided that instead of connecting each individual fan to the power supply, the fans would be connected to a mutual point on the heat sink in parallel so that only one set of wires had to be routed to the power supply. A basic PCB was designed to accommodate these connectors. It was decided that each fan should have its own connector so that it would be easy to replace in the future if necessary. Molex Pico Clasps were chosen to connect the fans as the available space to connect the fans was limited and cost was not a significant factor in the PCB design. The schematic and printed circuit board (PCB) layout of the connection board are shown alongside in Figure 31.

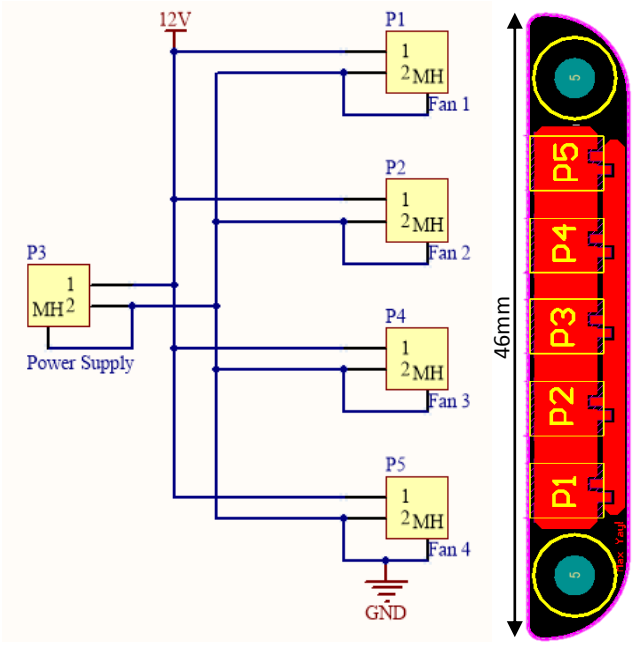

Figure 31 - Heat Sink Fan Connection Schematic and PCB

The connection PCB was mounted on one of the flat ends of the heat sink and the fan power supply line was wired into an available 12 V terminal in the power pod. The completed heat sink with fans connected is shown following in Figure 32.

Figure 32 - Completed heat sink with fans installed and connected

This completes a description of the new heat sink and its components.

3.4. Testing and Conclusions

The task of accurately testing the new cooling solution was deemed to be out of the scope of this project due to it being an extensive and arduous task. Thus the implementation of the heat sink has been documented in this chapter merely to serve as a reference for future related endeavours. It was decided that in the meantime, the new cooling solution would be assessed in the field to determine its effectiveness and gauge whether it is sufficient for general *SEAHOG* operations. Previous testing in [1] showed that the cooling of the power pod without the new heat sink was sufficient to run the ROV at half load indefinitely. Therefore, with the new heat sink it is expected that the heat dissipation is sufficient for low intensity operations such as testing in controlled environments with little or no water currents.

In summary, the new power pod heat sink has been successfully installed but not tested. It implements four extra cooling fans which are each connected to a power distribution PCB. This PCB is then powered from an available 12 V terminal in the power pod.

The power pod upgrades have now been detailed, allowing for the light and camera upgrades to be described in the next chapter.

4. Light and Camera Upgrades

4.1. Introduction

Whilst upgrades were being performed on the ROV GUI, some idiosyncrasies were found in the camera and light modules which required attention for the full operation of the ROV to be possible. These issues were resolved and provided valuable insight into the whole ROV system and the ability to carry out maintenance on it. In fact, it was found to be relatively simple to fault find and perform maintenance on the robot, which endorses the design decision of previous projects to make the ROV consist of modular subsystems.

This chapter will describe the faults found and upgrades carried out on the camera and light subsystems on the ROV. Before maintenance was carried out, the following problems were evident:

1. The front camera module was not turning on and thus the video feed could not be obtained.
2. The aft light module communicated irregularly with the surface controller, and would not respond to commands sent from the surface for a large proportion of the time.
3. The temperature sensing in the light modules was not linked in any way to the temperature sensors in the light modules, but only as a function of the brightness of the light.

4.2. Camera Module Troubleshooting

Tests were performed to ensure that the electronics pod (e-pod) was supplying power to the video camera module; the e-pod terminal to the camera module was probed with a multi-meter. Once this was validated, the camera controller board was investigated. Documentation showed that there was a fuse on the camera control board. After checking for continuity, it was found that the fuse had blown. This fuse was then replaced.

After the fuse was replaced, LEDs on the camera board indicated that it was powered. In addition, commands such as “zoom in” could be seen to be processed by the board and executed by the camera’s optical zoom. However, the camera feed was still not visible at the surface controller. This showed that there was a problem with the video feed line, which is separate to the camera control board. It was initially suspected that the Bosch video encoder had a faulty channel. It was temporarily bypassed and a

new Bosch encoder was used. This did not solve the problem. Using simple continuity tests, the camera feed line was traced back to its connection in the e-pod. Here it was found that the camera feed from the camera module was not plugged into the correct port between the external E-Pod Birns connector and the video connection point on the E-Pod PCB. This mistake was possible because the ROV E-Pod was designed to facilitate four camera feeds. Once this was corrected, the camera feed was visible at the surface control unit and the problem was solved.

4.3. Light Modules Troubleshooting

4.3.1. Irregular Communications Fault

The communication between the surface and most of the light modules performed as expected apart from the aft light module. Communications to this module from the surface would go unanswered frequently and irregularly. It was suspected that noise was creating this irregular communication as the aft light communications lines pass close by the 400 V power pod and tether lines. After moving the light module however, no difference was observed and thus noise was assumed to not be the problem. Since the light module had the ability to process commands correctly intermittently, it was then suspected that the fault lay between the incoming communications lines and the microprocessor. This narrowed the fault down to the MAX3485 converter chip. This chip is used to convert RS485 to RS232 communication protocols. Once the chip was replaced, the aft light started working correctly again.

4.3.2. Disconnected Temperature Sensors

There was no documentation available on the calibration of the light module temperature sensors. Thus it was decided that calibrations should be performed and documented formally. For the calibrations to be performed, the temperature sensors needed to be placed in open air and monitored by a thermal camera. At this point it became apparent that the light modules had not been programmed correctly and were not reading in the temperature sensors at all. The temperature reading was simply a function of the brightness of the lights. It was assumed that was as a result of an outdated version of the code being loaded onto the microprocessors.

Therefore, it was necessary to reprogram the light modules to successfully read the temperature sensors.

4.3.3. Light Module Upgrades

At this stage it was noted that improvements could be made to the individual intelligence of the light modules for overheating scenarios. The overheating handling routine in the light module before upgrades is shown following in Figure 33. It can be seen from the figure that the light has no intelligence preloaded to determine whether or not it is overheating. It must rely on the surface control unit to determine if it is overheating. The disadvantages with this is that there could be a break in communications with the

surface, or the surface controller could be occupied with other processing and the light module would have no indication of if it was overheating and hence it would be damaging itself.

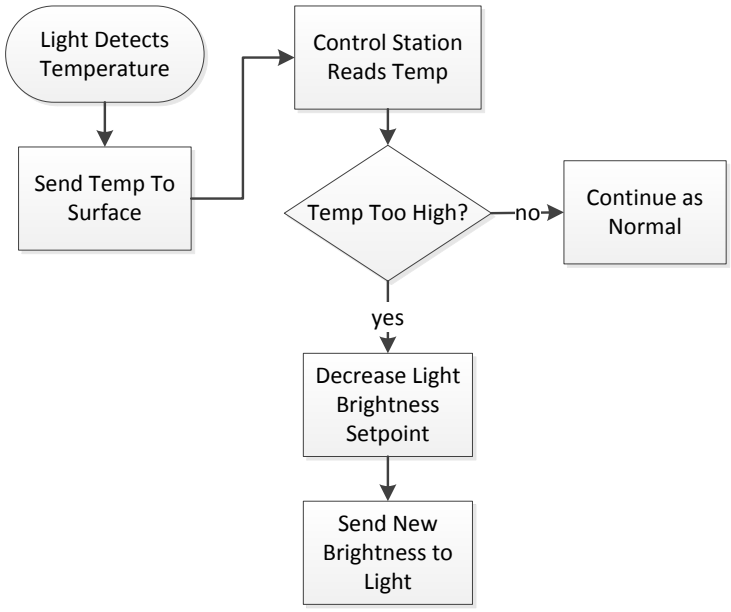

Figure 33 - Flow chart of light module overheating handler routine before upgrades

Since the processing required by the light modules is minimal, and since communication with the light modules happens relatively slowly, it made more sense for the light module to determine itself if it is overheating and take the necessary precautions. This would allow the light to react quicker to overheating and it keeps in line with the distributed intelligence design philosophy behind the ROV.

Therefore, the overheating handler for the light module was upgraded to have on board intelligence; the logic of which is shown following in Figure 34.

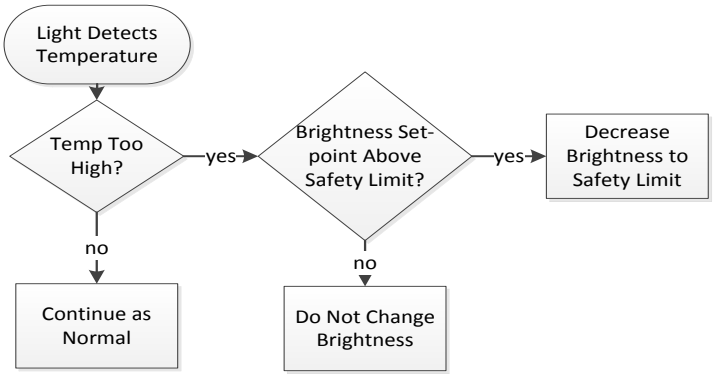

Figure 34 - Upgraded overheating routine for light modules

It can be seen from Figure 34 that no communication is necessary between the light module and the surface controller to determine if the light is overheating. This was successfully implemented and tested with a heat gun to ensure that the light modules responded correctly in all overheating scenarios.

Now that the temperature sensors were connected and successfully reading in temperatures, calibrations could be performed.

4.4. Light Temperature Sensor Calibrations

4.4.1. Calibration of Sensors

Aim:

The purpose of this calibration is to convert raw sensor readings into meaningful real life temperatures.

Background and Theory:

The light modules on the *SEAHOG* ROV use LM35 temperature sensors, which provide a voltage that is linearly related to the centigrade temperature scale [8]. This means that it is expected to only have to apply a gain to the sensor reading to obtain an accurate temperature.

The gain to be applied to the sensor reading will be calculated as an average of the ratio of thermal camera readings to sensor readings, as follows:

$$k_{sensor} = \frac{\sum \frac{Thermal\ Camera\ Reading}{Seansor\ Reading}}{Number\ of\ Readings\ Taken} \quad \{4.4\}$$

The *SEAHOG* control software GUI in LabVIEW was used to capture the temperatures given by the sensors. The temperatures are read once every second. The GUI was modified to populate a spreadsheet with the temperature values on the push of a button.

Apparatus:

- Calibrated Thermal Cameral
- Heat Gun
- Exposed LM35 Temperature Sensors
- ROV Data Logging User Interface

Method:

The four LM35 temperature sensors were secured between two pieces of wood outside their housings. A thermal camera was set up to analyse the temperatures on the four LM35 temperature sensors. The ROV was turned on so that the temperature readings could be monitored and logged. Ten readings were taken at ambient temperature to get an average ambient reading. The temperature sensors were then heated up with the heat gun to around 100˚ C and the temperatures were simultaneously recorded at intervals of 10, 20 and 60 seconds for each sensor and for the thermal camera.

After the calibrations had been implemented, the procedure was repeated to verify the calibration was successful. The calibration set up is shown following in Figure 35 and Figure 36.

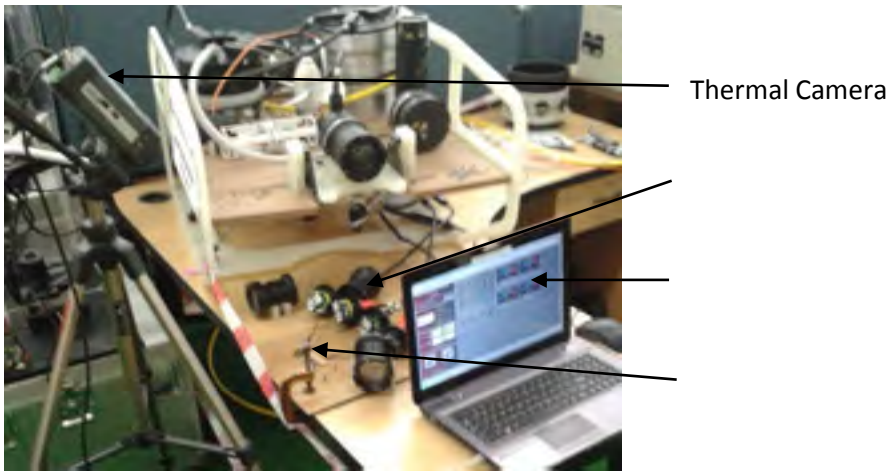

Figure 35 - LM35 light module temperature sensor calibration set up

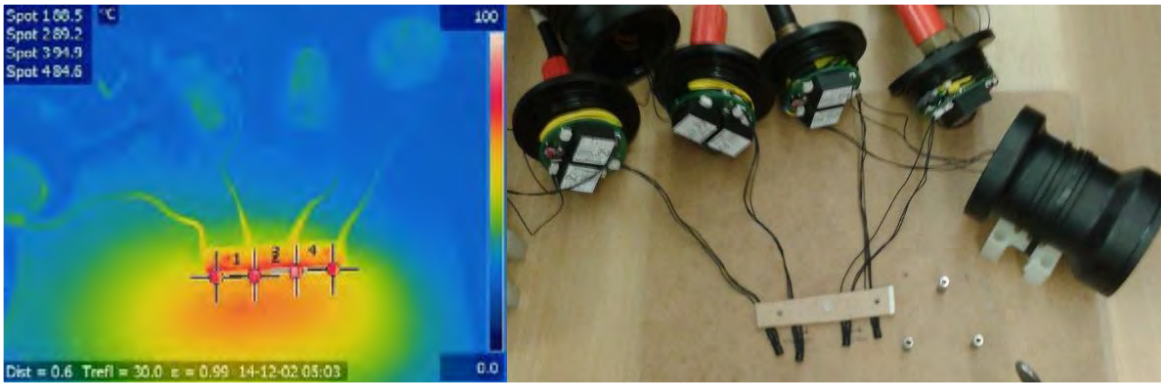

Figure 36 - Thermal image of the LM35 temperature sensors [left] and the corresponding real life image showing secured temperature sensors [right]

Results:

The following graphs in Figure 37 show each respective light module temperature sensor, its thermal camera reading, sensor reading, and theoretical or predicted calibrated reading.

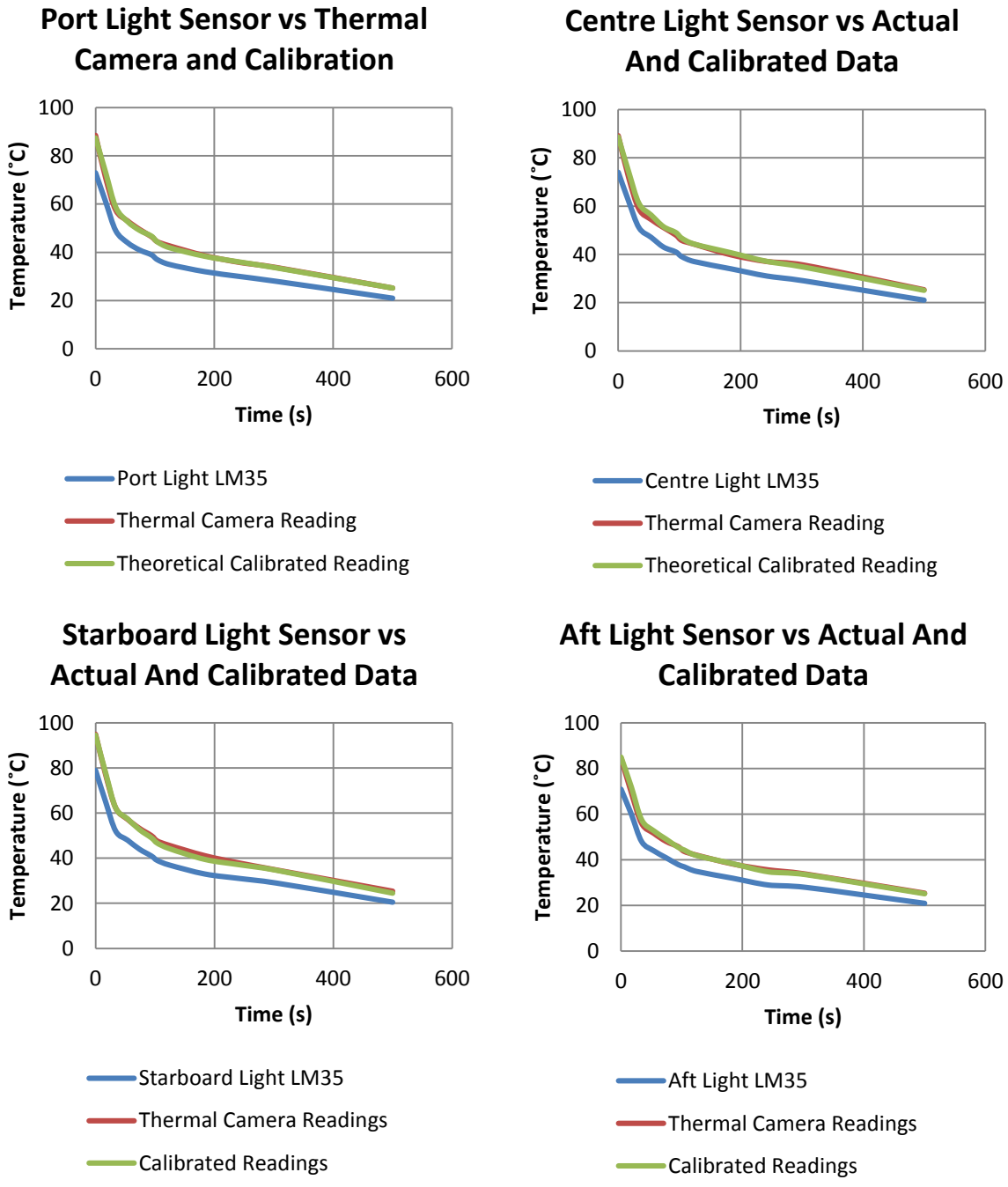

Figure 37 - Graphs showing the thermal camera reading, sensor reading and calibrated reading for each temperature sensor

The calibration gains, maximum and average difference between the calibrated reading and the thermal camera reading for each sensor, represented in the above graphs, are given in Table 7 following. Gains are worked out using equation 4.4 given previously.

Table 7 - Table of Calibration Gains and Predicted Results for Temp Sensors

Sensor	Gain Value	Maximum Temp. Difference Between Calibration and Camera (˚C)	Average Temp. Difference Between Calibration and Camera (˚C)
Port Light	1.20	2.17	0.56
Centre Light	1.18	2.39	0.99
Starboard Light	1.21	1.57	0.69
Aft Light	1.19	2.47	0.77

Using the above gains in Table 7, a verification run was carried out on the sensors to check the performance of the calibration. The results are shown following in Figure 38.

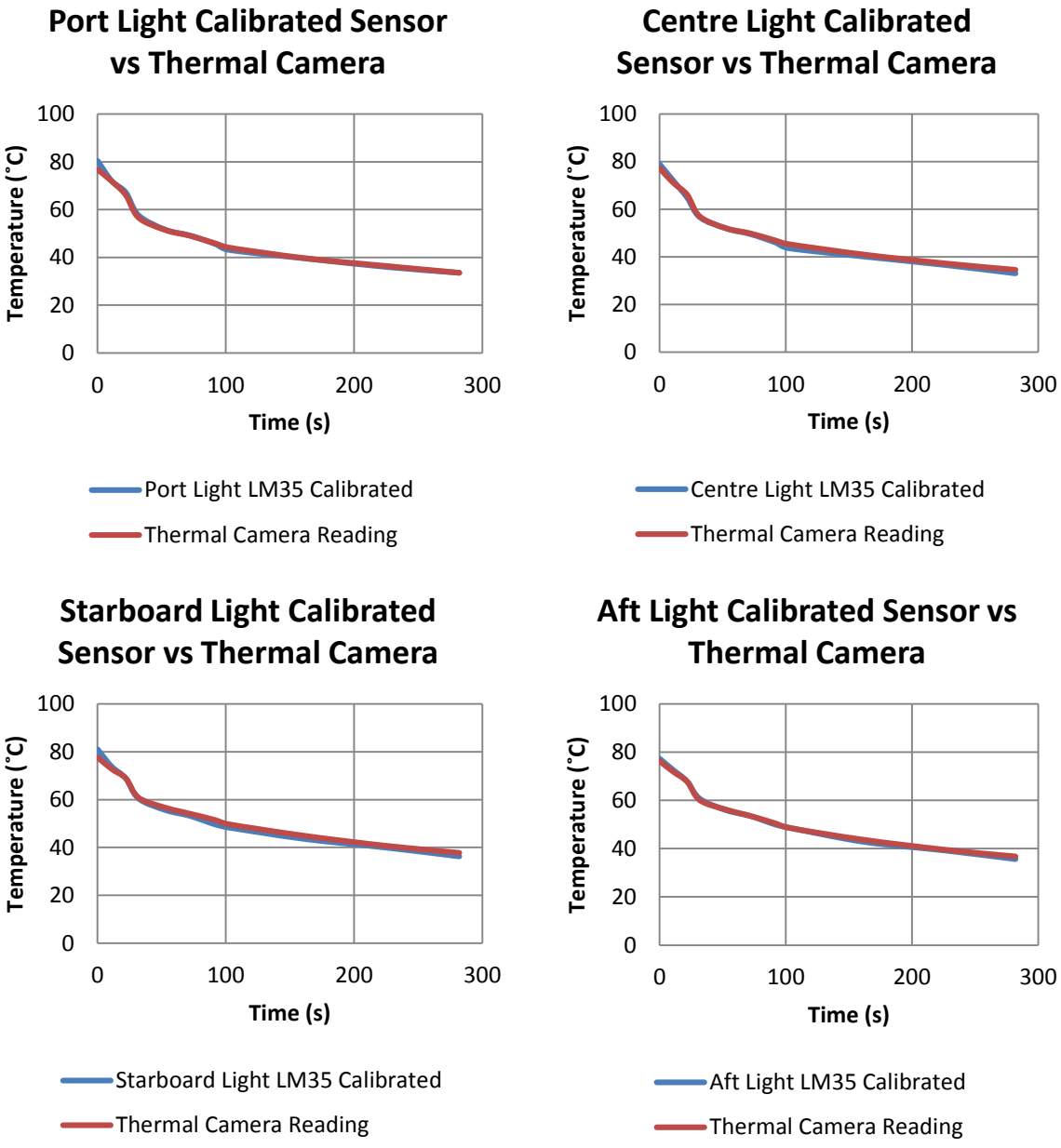

Figure 38 - LM35 sensor readings with applied gains, verified against the thermal camera

The maximum and average error readings between sensors and the thermal camera are shown following in Table 8.

Table 8 - Maximum and average error readings between thermal camera and LM35 sensors during the verification run

Sensor	Maximum Temp. Difference Between Calibration and Camera (˚C)	Mean Temp. Difference Between Calibration and Camera (˚C)	Median of Temp. Difference Between Calibration and Camera (˚C)
Port Light	3.60	0.70	0.2
Centre Light	1.76	0.95	0.88
Starboard Light	3.37	1.18	1.01
Aft Light	1.05	0.50	0.42

Analysis:

The LM35 temperature sensor typically has a ±0.75˚ C accuracy across its full temperature range [8].

Maximum Discrepancy: As can be seen from the results in Table 8, the maximum difference between the actual and sensor temperature readings are far in excess of the sensor accuracy. However, inherent factors in the calibration test setup were present that could have influenced these results. For instance, the ROV GUI is programmed to request temperature readings from the light modules once every second. This means, as can be seen previously in the Starboard and Port lights in Figure 38, that during periods of rapid cooling, such as near to the zero second mark, temperatures can be significantly outdated due to the ROV software.

Mean Discrepancy: Since it is probable that the readings taken at higher temperatures are more likely to be inaccurate, the average discrepancy of the readings should give a more valuable insight into the actual difference between the sensor and camera readings. It can be seen that the port and aft light now lie within the specified tolerance of 0.75˚ C.

Median Discrepancy: However, since the average readings are still influenced by outliers such as high temperature readings, the median was taken to give an even better idea of what the most regular discrepancy was. The median gives more insight into how the data is distributed since it separates the upper and lower halves of the data. It can be seen in Table 8 above that all of the medians lie below the mean, showing that data is mostly clustered slightly below the mean values. At this stage it can be seen that the centre light and starboard light lie closer to the tolerance of 0.75˚ C but are still above it.

Reasons for the tolerances not being reached could still be as a result of the slow update rate of temperatures in the ROV software. In addition, the applied gains for the temperature sensors were rounded off to two decimal places, which can decrease how truthfully the accuracy of the sensor reading is represented.

Conclusion:

Despite the apparent inaccuracy of the starboard and centre light sensor calibrations, it was decided that the calibrations were accurate enough to be sufficient. This is because the light module itself now has built in overheating handling intelligence. The light module itself will retrieve temperature readings much faster than the surface will retrieve its sensor readings, which will negate the danger of outdated temperatures in rapidly changing thermal environments. In addition, testing in [3] showed that the light modules plateau at 30˚ C in water under full load. This means that in predicted operating environments such as the South African coastline, there is little danger of the light module overheating.

With sufficient calibrations carried out for the light sensors, the light control software could be programmed so as to respond to the correct overheating sensor values.

4.4.2. Hardware Implementation

A temperature of 85˚ C was chosen as the safety cut-off temperature for the lights to decrease their brightness. This was then programmed into the GT16 microcontrollers in the light modules using the following formula:

$$ADC_{Cut-off} = \frac{85}{sensor\ gain} \quad \{4.5\}$$

This gave the safety limit as a digital value that would be read from the analogue to digital converter (ADC) on the microcontroller. All the gains shown previously in Table 7, when applied, result in a maximum temperature discrepancy between sensors of 3˚ C. This is quite small and so for standardisation and ease of implementation, a standard ADC safety cut-off value of 70 was chosen for all of the light modules.

4.5. Conclusion

The light and camera modules were overhauled, fixing hardware and software issues and providing valuable insight into the ease of maintenance on the *SEAHOG*. It was found that modular design allows for troubleshooting to be carried out relatively easily, despite the complexity of the ROV.

The light temperature sensors were calibrated sufficiently and the light modules' intelligence was upgraded so that they were able to handle overheating scenarios without instruction from the surface controller.

5. ROV Software and GUI Overhaul

5.1. Introduction

The *SEAHOG* ROV graphical user interface and control software was reasonably basic at the beginning of this project. The software mainly served the purpose of supplying critical information to the user and controlling basic modules like the lights. This was understandable, as the ROV had not quite reached its full development yet; with modules such as the thrusters still undergoing development. Due to the nature of this project, (requiring a functioning ROV to test its control systems) an overhaul of the software was undertaken that had the end goal in mind of being more of a practical user interface rather than a monitoring and debugging interface. This was an in-depth and extensive process and as a result, this chapter will serve to detail the development of the new ROV control software.

So that the software may be better understood, a brief outline of the following will be given:

1. The communications network structure on the ROV
2. The previous GUI and its strengths and weaknesses
3. An explanation of the new GUI, how it works and its features

5.2. *SEAHOG* ROV Communications Network

5.2.1. Network Architecture

Currently, the *SEAHOG* responds to user inputted commands from a surface control console. This takes the form of a laptop PC running a LabVIEW GUI. Commands are sent down to the ROV via a fibre-optic tether. A fibre-optic modem on the ROV splits the tether commands to three different communication networks, each assigned an IP address. One of these channels contains the video feeds from the forward and aft cameras. The remaining two channels are converted to an RS232 and RS485 network. The RS232 is dedicated entirely to the Micron Sonar unit from Tritech, as this was the specification of the unit that was purchased for the ROV. Every other module on the ROV is daisy chained together on an RS485 network and has its own unique address. Figure 39 following shows this communication structure, with each network layer and the protocols used within it.

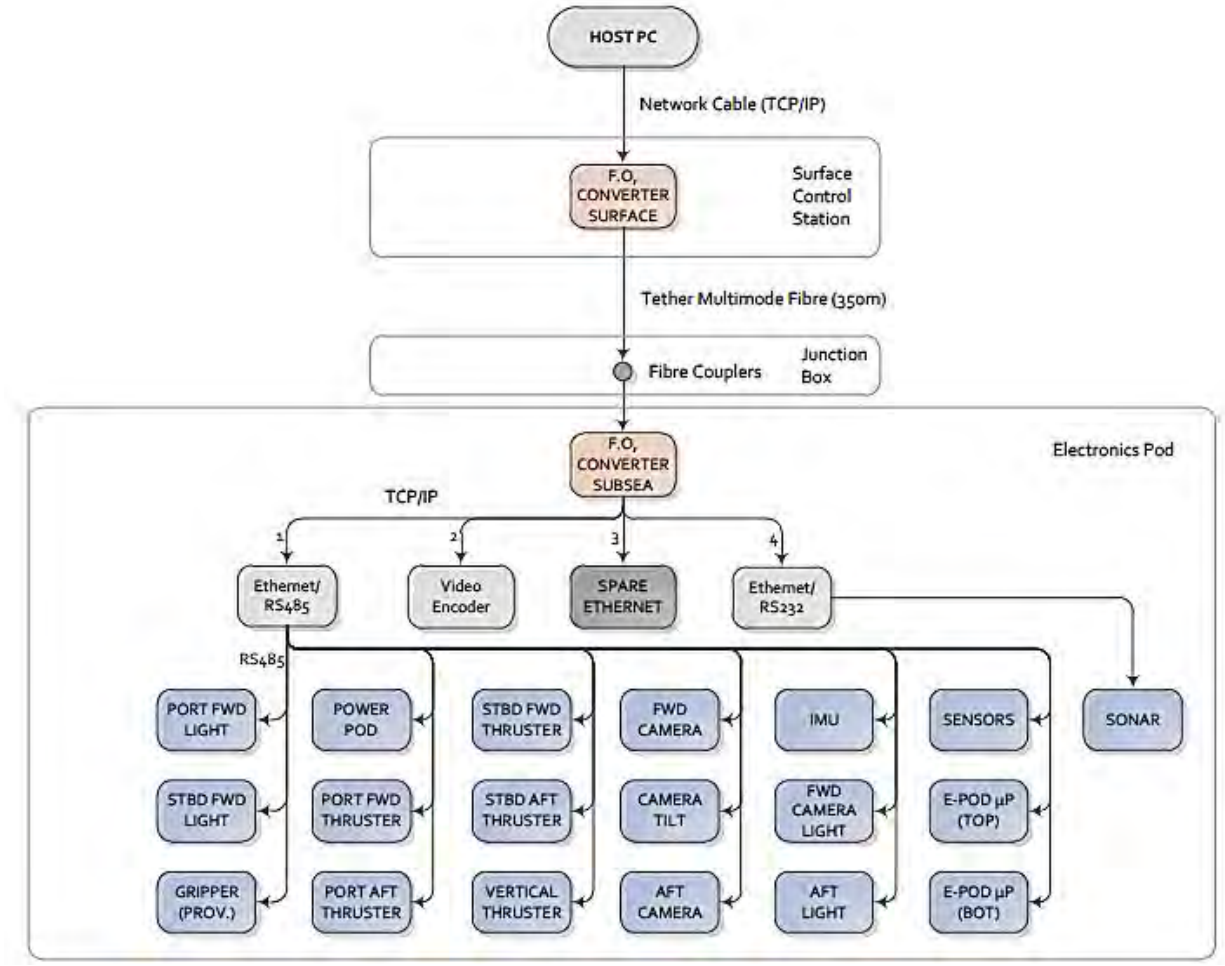

Figure 39 - *SEAHOG* ROV communications network structure [1]

Each individual module on the RS485 network responds to a surface command if it is addressed by the surface control console. Each module is supplied power by the E-Pod, which can be commanded to disable any of its ports to cut power to a specific module.

It should be noted that there is a spare Ethernet channel available to split, if deemed necessary, the RS485 modules over two different networks. In addition, the communications network architecture and decisions to use protocols such as RS485, rather than TCP/IP or CAN throughout the ROV have been made in previous projects and are now fully integrated into the ROV. Thus, it does not fall within the scope of this project to modify the fundamental protocols on which the ROV communicates. Therefore, the new ROV control software will be developed according to the ground work laid out by previous projects and make only minor changes if necessary.

5.2.2. Data Communication Structure

Each TCP/IP device has been configured to act as a virtual serial port apart from the video encoder. Specialised drivers for the Bosch Video encoder handle the communication between the encoder and the LabVIEW software. The other two TCP/IP devices have been configured as virtual serial ports, which

allows LabVIEW to effectively bypass all the media conversion required between the RS485 network and the control console and view it simply as a serial network.

Each RS485 network device receives a packet of ten bytes and sends a packet of ten bytes per communication cycle. The packet structure is shown following in Table 9. It contains two address bytes and eight data bytes.

Table 9 - Generic RS485 serial communications packet used on the *SEAHOG*

Address 1	Address 2	Data 1	Data 2	Data 3	Data 4	Data 5	Data 6	Data 7	Data 8

The address sent by the control console will be checked by each RS485 device against its own address and then either discard the packet, or process it and respond accordingly. The two address bytes were intended to be a form of error checking and each module checks the first and then the second address against its own address to verify if the message is intended for itself.

It should be noted that the above packet structure was a previous design decision that had been made and already extensively implemented on the ROV. To change the communications packet structure would be too radical a change to the ROV to fall within the scope of this project. It is possible that error checking (such as checksum) and diagnostics should be added to the packet structure but those changes do not fall within the scope of this project. Thus, the ROV software was developed using the above packet structure.

Now that the communications network and data structure on the ROV is understood, the previous control software can be described and analysed.

5.3. Previous ROV Control Software

5.3.1. Overview

The previous ROV control GUI was developed by Roger de Smidt so as to aid him in his testing and development of the P-Pod and the E-Pod. Thus, it is a rather rudimental interface that allows for system data to be monitored but is not very user friendly. In addition, the software resulted in large amounts of latency being introduced into the system. It was suspected initially that this latency was due to the TCP/IP to UART (universal asynchronous receiver/transmitter) converter. This was not the case however, as was found during development of the new ROV GUI software.

Features of the previous GUI included:

User Inputs

1. Individual Light Brightness and ON/OFF control
2. Control enable/disable on individual E-Pod power supply terminals
3. Disable/Enable all E-Pod power supply terminals at once

System Monitoring

1. Temperatures in the P-Pod, E-Pod and light modules
2. Voltage levels on the 48, 15, 12 and 5 V lines
3. Current draw on each of the above lines
4. Stable temperature indicator in P-Pod and E-Pod

Warnings

1. Overheating in P-Pod, E-Pod and light modules

In addition, basic checksum data verification was added to the user interface. The checksum routine would simply analyse a received packet and count the number of bytes. If ten bytes were received, it was a valid packet and processed as normal. If not, the packet was discarded. This form of error checking was also implemented in the new control software.

5.3.2. Code Execution Routine and Logic

The code at this stage performed the same routine continuously, regardless of user inputs and system states. The code would simply communicate with each ROV module in turn and process the data received from it. A flow chart showing the logical flow of command executions in the control software is shown following in Figure 40.

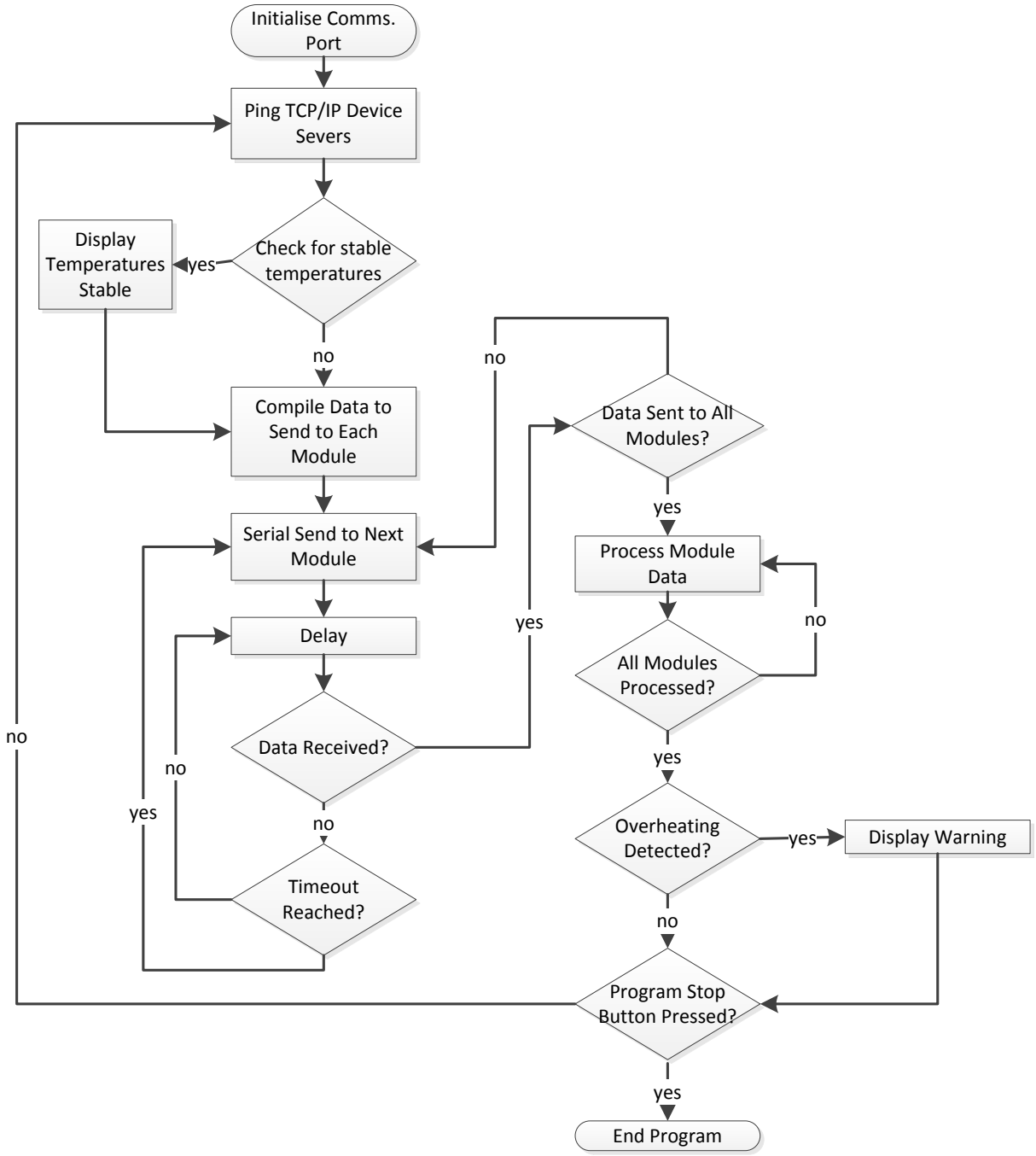

Figure 40 - Flow chart of the ROV control software before upgrades

5.3.3. Analysis of the Old Control Software

Usability:

One of the main problems with the old control software, in terms of usability, was that it was intended mostly for debugging and calibration of the ROV system. As a result, a lot of redundant safety interlocks were present in the software that made it cumbersome to use. For example, to activate a light module, the user had to activate the E-Pod light module port, the light itself and then a master power button. It was found that for ease of use this system required too many user inputs to perform a simple task.

System Latency and Delays:

As was previously stated, the old GUI would communicate with each module per communication cycle regardless of the state of the system. This meant that if a module was not connected, the system would rely on a serial time-out as it waited for a reply from the intended module. This time-out was programmed to take about 0.5 seconds. Therefore, the more modules that were not plugged in, the greater the latency of the system would be. In addition, if the user wanted to communicate with, for instance, a light module, the communication would only take place when the light had reached its turn to be communicated with in the communication cycle. This is because the order in which modules were communicated with was fixed.

It was noted that when all modules were plugged in, the latency in the system decreased drastically but there were still noticeable delays in the system intermittently.

Lack of Functionality:

While there were some useful functions added to the old GUI, such as a master button to disable all E-Pod ports and hence all modules, some functions were omitted that should happen automatically as the ROV enters certain states. A simple example of this is that if the ROV software was stopped or shut down, the ROV itself should also shut down to as much of an extent as possible. Again, this points to the intention of the software not being an end user product, but more of a debugging and analysis platform for the ROV.

Strengths:

Weaknesses aside, the old GUI did offer a basic level of control on the ROV, allowing individual ports to be controlled and analysed. This proved useful while reprogramming the light module control PCBs, as they could be supplied power and left on while the microcontrollers were reprogrammed. Therefore the old GUI still has value in the future during maintenance and analysis functions, where basic control is required of the ROV.

5.3.4. Conclusion

As a result of the previous issues, it was obvious that the ROV software required an overhaul so as to make it more of a user friendly operational interface rather than a debugging and analysis interface. In

addition, the shortcomings of the old GUI proved useful for highlighting issues to be dealt with and functionality to be included in the new platform. This being said, the old GUI serves its purpose of being a debugging and maintenance interface well and offers valuable low level control of certain ROV functions. The previous GUI is shown following in Figure 41.

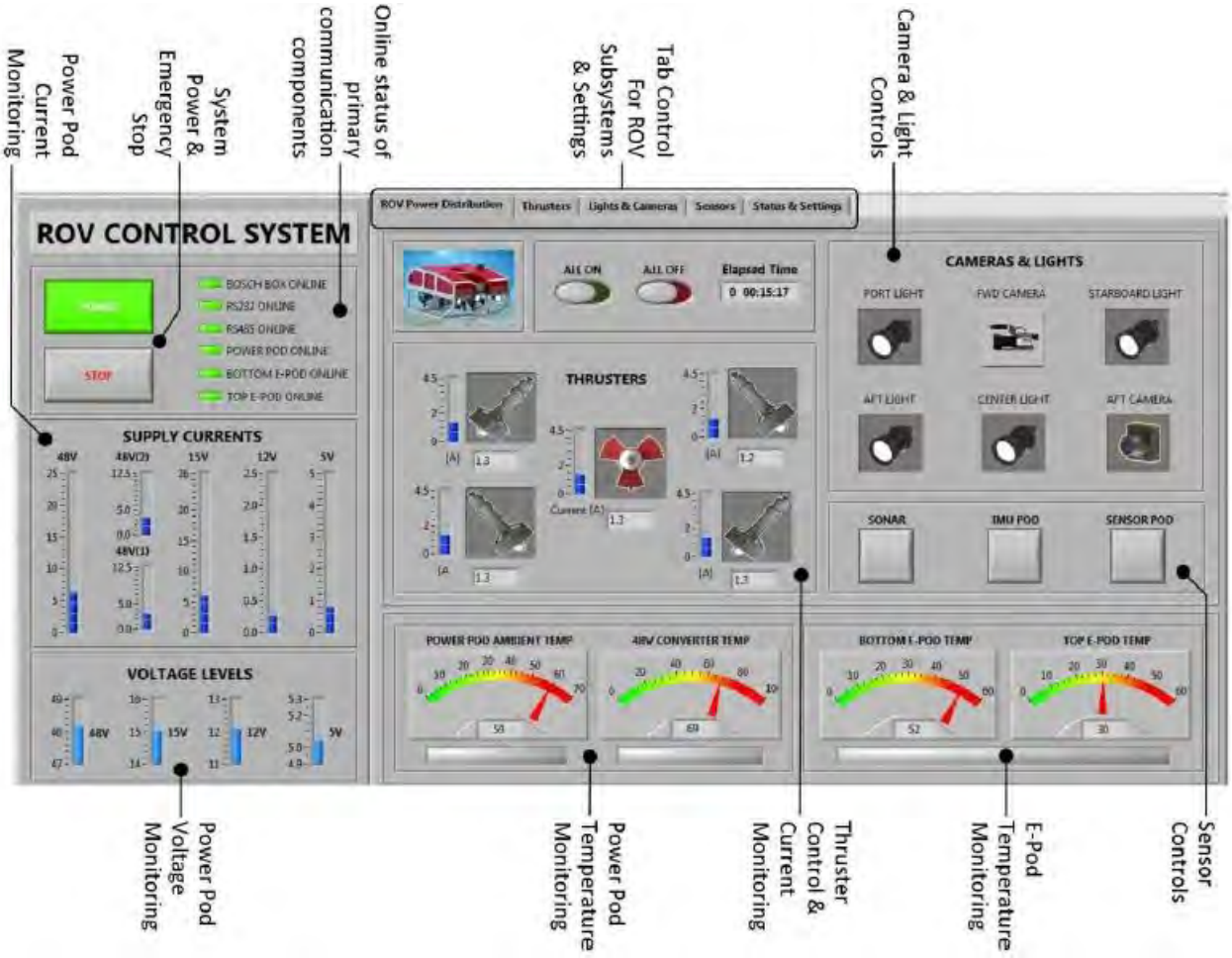

Figure 41 - Previous *SEAHOG* ROV GUI [1]

5.4. Overhauled *SEAHOG* Control Software

5.4.1. Introduction

With the previous ROV GUI software and the *SEAHOG* communications network and data structure understood, enough insight had been gained to tackle the daunting task of overhauling the control software for the ROV. Before any work could be done however, the end goal of the new software had to be clearly understood as well. This included aspects like who the target user and controller of the ROV would be, the features of the new software and the overall purpose of it.

It was decided that the new GUI for the ROV should be the first iteration of software that is capable of controlling all modules on the ROV, can be used by someone that is unfamiliar with the software and has the option, but not the focus, of monitoring all system information. With this in mind, research was carried out so as to highlight the most important points that emphasize the above goals.

5.4.2. Background Research

Considering the goals of the new control software stated in the previous section and as presented in [9], fundamental principles for an effective user interface include the following:

1. Accessibility – The software should be designed to be usable by as many people as possible and transferable without modification, to as many different operating platforms as possible.
2. Compatibility – The needs of the user, the way in which the system is used and the familiarity of a user with similar systems should be kept in focus when designing the interface.
3. Control – A user should be able to exercise control over the system through the software. Simple and consistent user interfaces provide a sense of control to the user. Long delays and unpredictable system responses take away from the sense of control experienced by a user.
4. Directness – Tasks should be executable by directly selecting a command. The outcome of the command should be visible directly after selection.
5. Efficiency – Layout is important, with hand and eye movements being minimised. In addition, relevant sections of the interface should be highlighted when necessary and immediately capture the user's attention.
6. Familiarity – Language and concepts that are familiar to the user should be employed.
7. Safety – To eliminate opportunities for mistakes and confusion to be made during operation, visual cues and reminders should be provided to minimise what the user has to remember during operation.
8. Simplicity – Too much information can be overwhelming to a user and as a result render the interface ineffective. Interfaces should be as simple as possible. Ways to improve the simplicity of user interfaces are as follows:
    a. Present common and necessary functions first

b. Hide unnecessary functions
c. Provide an obvious visual hierarchy, highlighting important elements
d. Make common actions simple to carry out

9. Transparency – The user should be able to operate the software whilst remaining oblivious to its mechanics and inner workings.
10. Trade-Offs – There is no absolute correct solution for a user interface. Design principles and requirements are almost always conflicting and ill-defined, thus trade-offs will have to be decided on with the user's needs in mind, whereby one design principle will take precedent over another.
11. Visibility – The system status and method of use must be clearly visible.

The above principles will be applied when creating the new ROV GUI. They give valuable guidelines that will lead to an effective user interface and will thus be applied wherever possible. Now that the ROV communications system is understood and a clear idea has be gained of what the purpose of the new ROV software will be, including aspects that constitute an effective user interface, requirements and design principles for the new ROV GUI can be formulated.

5.4.3. New ROV Software Design Specifications

The specifications for the new ROV GUI will use the principles presented in the previous section and apply them to the ROV system specifically. In this way, its requirements will be better defined and all of the work carried out on the software will have a clear set of guidelines to follow during its development. The specifications for the ROV GUI are presented following in Table 10.

Table 10 - Specification criteria for new ROV control software

Specification Criteria	Definition for ROV Software
5.4.3.1 Accessibility	Using a Windows operating system, the software shall operate on a range of computers with different capabilities. There shall be standard and automatic data saving protocols that do not require modification over different computers.
5.4.3.2 Compatibility	The ROV will be used for equipment recovery and sample collection. Therefore, the software shall provide a focus on visual feedback from the ROV, with the field of view easily adjustable and the ROV easily manoeuvrable with the defined user inputs.
5.4.3.3 Control	The software shall operate with minimal visible latency between a user input and its execution on the ROV. The system shall include as little as possible arbitrary event triggers (for example, arbitrary hard coded timing delays) to keep the system stability and predictability as good as possible.
5.4.3.4 Directness	User inputs shall be simple and provide a direct outcome in the ROV system. For tasks that require significant portions of time to complete, it shall be possible to observe that the task is busy executing.
5.4.3.5 Efficiency	While this is a largely interpretive criteria, the amount of user

	interactive elements shall be minimised during normal ROV operation and shall be placed in a localised area on the screen. In addition, warnings or safety interlocks shall immediately capture the user's attention.
5.4.3.6 Familiarity	Marine biologists and engineers will both be end users of this product. Thus technical engineering language shall be minimised in the interface.
5.4.3.7 Safety	Important information shall be provided to alert the user if necessary. The software shall not rely on the user to remember large amounts of information to successfully operate the software.
5.4.3.8 Simplicity	Attention shall be drawn to the most important functions on the ROV. Unnecessary system statuses shall not be visible during normal operation unless there is a malfunction, in which case it shall be highlighted immediately. In general, the amount of user inputs shall be minimised and localised.
5.4.3.9 Transparency	The user shall not be aware of software limitations and workings. All functions that are to be carried out by the ROV operator shall be possible from the interface and without any modification to the code.
5.4.3.10 Trade-Offs	Priority shall be given to the responsiveness of the system. After that, system resources shall be minimised and the efficiency of the code shall be optimised to some extent. These principles will override the other principles if a trade-off is required.
5.4.3.11 Visibility	User inputs shall be clearly visible and intuitive. In addition, instructions shall be given if there is possibility for misunderstanding. The system status shall be clear and easily accessible if required.

Now that a clear set of specifications and guidelines for the ROV control software have been formulated, a description of the code can be given.

5.4.4. Description of New Control Software

The overall design architecture of the code can now be described, given the clear set of specifications presented in section 5.4.3 previously. The new design aspects of the code will be presented in this section and motivated with reference to the previously listed specifications.

Parallel Processing:

The new control software runs on a LabVIEW interface and takes advantage of the parallel processing capabilities of this language. LabVIEW is able to process tasks in parallel if there are available cores in the host computer's central processing unit (CPU). It was decided that for accessibility (specification 5.4.3.1) however, parallel processing was to be kept as minimal as possible to allow as wide a range of host computers with different processing capabilities to be able to smoothly run the control software.

The RS485 network was identified as the slowest communication rate in the system, given its baud rate of 115200 bps. The baud rate was extensively implemented on the ROV at the time of this project and thus it would have been beyond the scope of this project to increase it and re-test the communications performance of the subsystems. It was decided that the baud rate would remain at its current rate and would be counted as a previous design decision that could not be modified.

As a result of the relatively slow communication speed on the RS485 network, an entire processing loop was dedicated to sending and receiving data on this network, ensuring that communication between the ROV and the surface could run at maximum speed at all times.

Given that the video feeds require a large data rate and that they are the ROV operator's viewpoint for the operations carried out by the ROV (specification 5.4.3.2), and complying with specification 5.4.3.3 previously in section 5.4.3, any latency experienced on the video feed will jeopardise the effectiveness of the ROV. Thus, a dedicated loop was assigned for processing the video feeds.

Producer and Consumer Loops:

There are a total of four parallel loops used in the control code structure. One is used for RS485 communications as previously mentioned, one compiles data to be sent to the ROV, one processes data received from the ROV and one processes the capturing, displaying and recording of the video feeds. This code structure is arranged in a standard LabVIEW producer-consumer architecture; whereby one loop produces data which is then "consumed" or processed in another loop.

The control software for the ROV consists of a master producer loop, which produces data that is to be sent to the ROV. There is then an intermediate loop for sending and receiving data which is a consumer to the master producer loop and a producer for the data processing loop. Finally, the loop dedicated to

processing data from the ROV is a consumer of the serial send and receive loop. This structure is shown following in Figure 42.

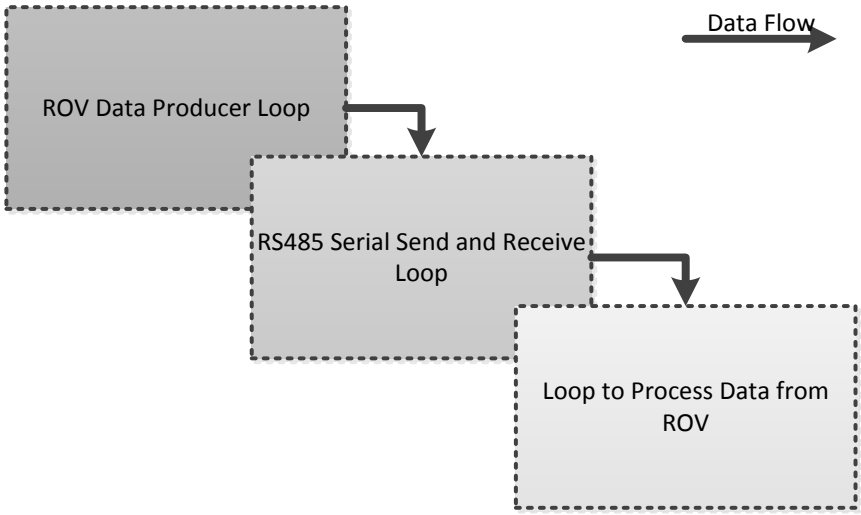

Figure 42 - Producer-Consumer loop structure in the new ROV control software

Data is transferred between loops in LabVIEW using notifiers and queues. Notifiers are typically a single value that can be sent between loops. Queues compile values into an array which is then stored until it is processed by the next loop.

In specification 5.4.3.10 it was stated that a trade-off in the system would favour responsiveness. The queue structure is used to achieve this, with high priority commands being added to the beginning of the queue and low priority commands being added to the end of the queue.

State Machine Structure:

The operation of the ROV was divided into states so as to better define its mode of operation and hence identify tasks that must be carried out by the software in different situations. LabVIEW allows this to be carried out with relative ease by selecting a pre-defined case from a case structure or "if" statement. This complies with specification 5.4.3.7 (safety), as any initialisation or shut down routines should be automatically handled by the software without the user needing to remember to disable or enable system functions manually.

The states of operation of the ROV and their interactions are shown in the following state machine diagram, Figure 43.

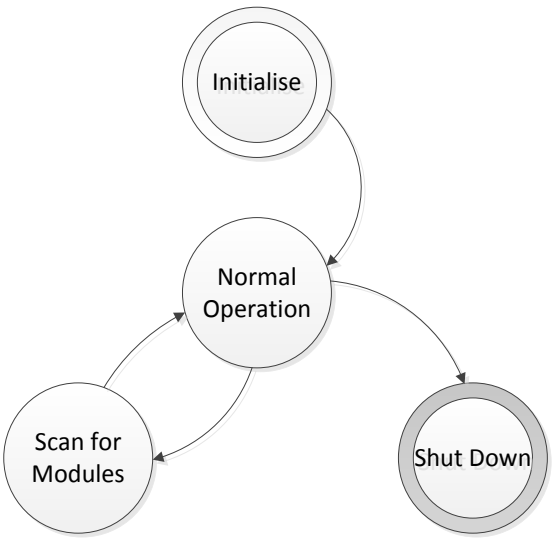

Figure 43 - State diagram for the ROV control software

A description of the control software states is given following:

Initialise: When the code is executed, the ROV enters the "Initialise" state. In this state the code scans for any modules that are connected to the ROV by trying to communicate with them. If the module responds, the software will add the module to a master array of connected modules. Once the array is compiled, the ROV will only communicate to the connected modules, thereby negating any system latency related to serial timeouts. In addition, the camera feeds are initialised in this state.

If there are multiple disconnected modules, the ROV will rely on serial timeouts to move onto communicating with the next module. Thus, there can be significant latency during initialisation. For this reason, in accordance with specification 5.4.3.4 (directness), the user is alerted to the fact that the ROV is busy initialising. Progress of the initialisation is observable as modules become available and are shown as being online. If the ROV is not powered, the software alerts the user with a warning and then closes. The "Settings" GUI tab is displayed during initialisation and is shown following in Figure 44.

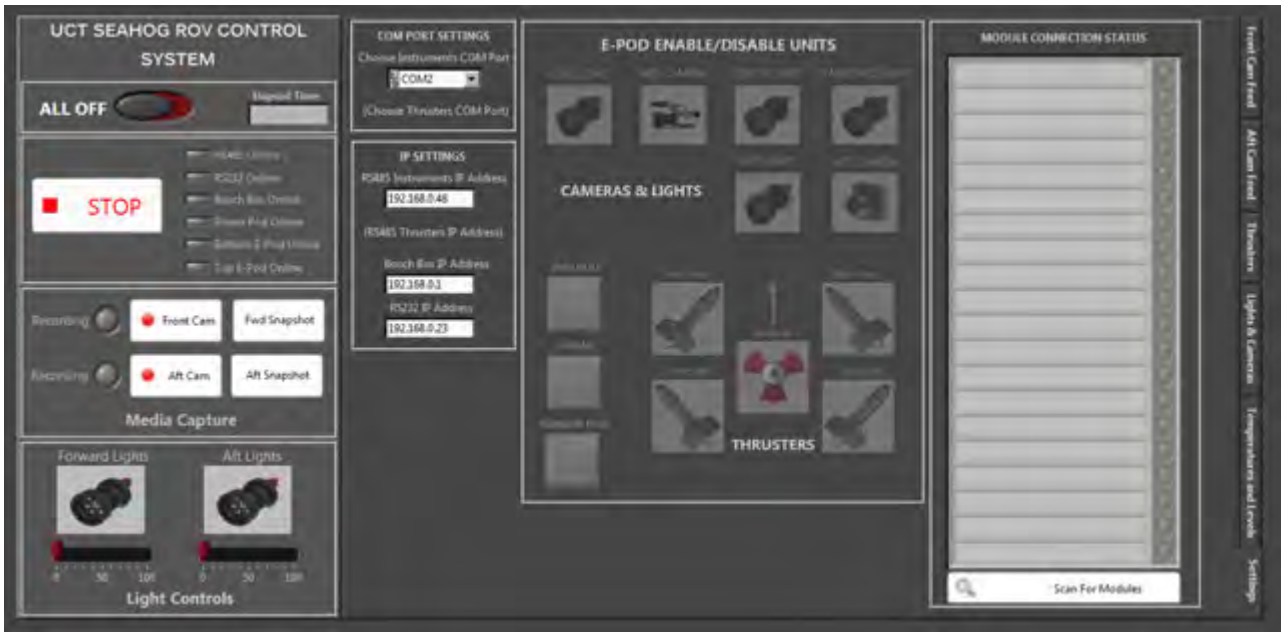

Figure 44 - New ROV GUI "Settings" tab shown during initialisation

After all initialisations are complete, the code automatically enters the “Normal Operation” state and the video feeds and ROV operational interface are automatically displayed. This is in accordance with specification 5.4.3.2 (compatibility) since the video feed will be the ROV operator’s viewpoint throughout all operations.

Normal Operation: This state represents the ROV during all forms of operation under normal circumstances. This state allows the ROV to respond to user commands and carries out routine tasks periodically. A large amount of system data is available from modules such as the power and electronics pods on the ROV. Since there are built in safety mechanisms in these systems for overheating or over current, for example, the information is useful to the operator but not critical during normal operation of the ROV. For this reason, the code will “ping” each connected module every second so as to update system information and check that all modules are still online.

In accordance with specification 5.4.3.8 (simplicity), non-critical system information is hidden in its own tab while the ROV is undergoing normal operation. Figure 45 following shows the GUI during normal operation. The larger and smaller white squares are for the forward and aft camera feeds respectively.

Figure 45 - New ROV GUI "Forward Cam Feed" view during normal operation

In addition to user commands, the interface will respond to triggered events. In accordance with specifications 5.4.3.7 and 5.4.3.8 (safety and simplicity), the user's attention will be drawn immediately to a system warning such as overheating. The relevant fault will be displayed along with a warning. The monitoring interfaces are shown following in Figure 46 and Figure 47. Depending on the fault, the GUI will switch to the relevant tab where the warning is displayed.

Figure 46 - New ROV GUI light and camera module settings and statuses

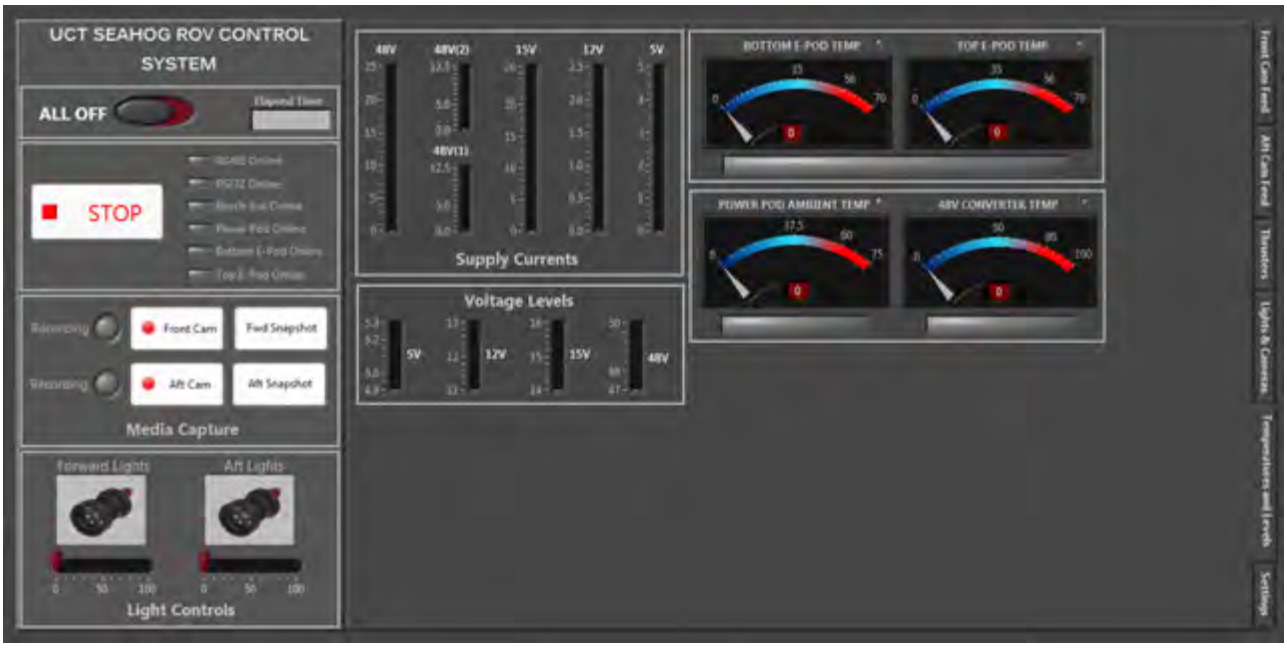

Figure 47 - New ROV GUI P-Pod, E-Pod and overall system statuses

The ROV will remain in the normal operation state unless triggered to leave the state by the user. The two other states that the ROV can enter from normal operation are “Scan for Modules” or “Shut Down”. If the program is stopped, the code will enter the “Shut Down” state. If the user presses the “Scan for Modules” button, then the “Scan for Modules” state is entered.

Scan for Modules: During testing, it may be necessary to plug in and unplug certain modules of the ROV. In addition, if a failure occurs during operation and a module becomes unresponsive, serial timeouts will be introduced and thus the system latency will increase. Finally, there is a possibility that ROV does not communicate with a connected module, for whatever reason, successfully while initialising. For the previous three reasons, it would be advantageous if a user input could command the ROV to re-initialise and hence refresh the master array of connected modules.

In effect, the “Scan for Modules” state follows the same routine as for the initialise state, but does not reset all values to zero, thus maintaining previous system values upon completion. Once the re-initialisation procedure is complete, the ROV automatically returns to the “Normal Operation” state. The “Scan for Modules” button can be seen previously in the lower right corner of Figure 44.

Shut Down: As previously defined in section 5.4.1, the new control software will move towards being an end user product and less of a debugging and maintenance interface. Therefore, when the code execution is terminated, the ROV should shut down to as much of an extent as possible automatically, without the user having to remember to manually switch off each module. This is in accordance with requirement 5.4.3.7 (safety) as previously defined in section 5.4.3.

When the ROV code is stopped, a command is sent to the electronics pod to disable all its modules. The software then waits for a response from the E-Pod to say that it has received the shutdown command. After this, the code terminates. This leaves all the ROV subsystems unpowered, preventing uncontrollable and dangerous actions to occur, such as the thrusters turning on. This leaves the ROV in a state to be turned off at the power supply unit.

Event Driven Processing:

LabVIEW includes event structures which respond to certain events such as user inputs or timed triggers. This coding structure decreases the power consumption of the host computer as it allows the code to remain idle until an event must be processed. The "Normal Operation" state makes use of an event structure to compartmentalise code execution routines according to the specific user input or timed event. LabVIEW adds each event to a queue so that events are not missed and every command is processed.

Summary:

The new control software for the ROV will make use of LabVIEW's parallel processing capabilities, using four while loops that are executed simultaneously. One of these is for generating commands to send to the ROV, one is for sending and receiving data from the ROV, one is for processing data received from the ROV and one is for capturing, displaying and recording video data from the ROV.

The code follows a state machine structure whereby the code that is executed depends on the state of the system. There are four states in the system: Initialise, Normal Operation, Scan for Modules and Shut Down. "Initialise" is entered as the code is executed and upon completion, the code automatically enters the "Normal Operation" state. "Scan for Modules" is entered if the "Scan for Modules" button is pressed, which effectively re-initialises the ROV without changing any system values. If the code is terminated using the "Stop" button, the ROV enters the "Shut Down" state, disabling all modules.

Finally, the code makes use of an event structure, which improves the power consumption of the host computer by allowing the code to idle until a user input or timed event must be processed. This makes the system very responsive, as commands are executed immediately as they are requested.

A summary of how requirements from section 5.4.3 are achieved is given following in Table 11.

Table 11 - Summary of how specifications are implemented in the code

Specification Criteria	Definition for ROV Software
5.4.3.1 Accessibility	Parallel processing is kept to a minimum, allowing as many host computer systems with a wide range of processing capabilities to smoothly run the control software. Media such as pictures and videos is saved in a folder on the desktop. The software will automatically search for this folder and if it does not exist, it will be created.
5.4.3.2 Compatibility	Complete control of the ROV is possible from the main control window that displays the video feed. Initialisation automatically displays the video feed so that visual feedback from the robot is available immediately.
5.4.3.3 Control	Parallel processing, with a dedicated communication loop for the RS485 network allows for data to be sent to and processed from the ROV at a maximum rate. Event structures allow commands to be executed immediately. State machine structure allows the ROV to initialise and determine which modules are connected to it. The ROV will then not communicate with any modules that are not connected and hence not introduce latency through serial timeouts. Notifiers are used between loops to determine when data has been processed, thereby reducing arbitrary timing delays required to allow the system to process certain commands before moving onto other commands.
5.4.3.4 Directness	Initialisation alerts the operator that the ROV is busy thereby allowing the operator knowledge of the system state. Simple push buttons are used in most cases to provide a visible direct outcome after the command has been executed.
5.4.3.5 Efficiency	Controls are placed in a way that minimises eye and hand movement of the operator. Safety interlocks such as the “disable all modules” command will flash while active to alert the operator that the program has disabled the modules. Warnings will take the operator to the relevant information immediately and display a warning message.
5.4.3.6 Familiarity	Marine biologists and engineers will both be end users of this product. Thus technical engineering language is minimised in the interface.
5.4.3.7 Safety	Initialisation and shut down routines automatically enable or disable modules so that the operator does not have to remember to do this. This means that dangerous situations whereby a module turns on in an uncontrolled fashion are negated. Any warning or important system information is displayed in a message to the user.
5.4.3.8 Simplicity	The most important function of the ROV is to provide visual feedback to the operator. Attention is drawn to this with a large video feed window and automatic navigation to this window. System information that is not critical is hidden in tabs so as to not draw attention away from visuals during operation. User inputs are minimised, with simple direct inputs directly resulting in an outcome on the ROV.

5.4.3.9 Transparency	The operator is not aware of software limitations and workings. All functions that are to be carried out by the ROV operator are possible from the interface and without any modification to the code.
5.4.3.10 Trade-Offs	Priority is given to system responsiveness using queue data structures between processing loops. High priority commands are added to the front of the queue and low priority commands are added to the end. Code is optimised and power consumption is kept minimal by using event structures; allowing the code to idle if no commands need to be processed. In addition, the rate of loops that execute multiple times is limited.
5.4.3.11 Visibility	User inputs are clearly visible and intuitive. Important system statuses are displayed constantly, allowing them to be monitored at all times and thereby giving a clear indication of the system status.

Now that the code is clearly understood, along with how it achieves its specifications, features of the new control software can be listed.

5.4.5. New Control Software Features

Features of the new control software are given in Table 12 following.

Table 12 - Feature of the new control software

Module	Feature Description	Present in Old Software?
	User Inputs	
Forward and Aft Lights	ON/OFF Brightness	Yes
Forward Camera	ON/OFF Zoom In/Out Record Video Capture Image Zoom Rate Focus Type Recording Frame Rate	No
Aft Camera	Record Video Capture Image Recording Frame Rate (same as forward cam.)	No
Electronics Pod	Disable Individual Modules Disable All Modules Scan for Modules	Yes Yes No
	System Monitoring	
Power Pod	Temperatures Currents (5V, 12V, 15V, 48V lines) Voltages (5V, 12V, 15V, 48V lines) Stable Temperatures Overheating Indicator	Yes

Electronics Pod	Temperatures Stable Temperatures Overheating Indicator	Yes
Light Modules	Temperatures Overheating Indicator	Yes
Camera Modules	Frame Rate Too High Indicator	No
All Modules	Connection Status	Yes
System	Elapsed Time	Yes
	Warnings	
Power Pod	Overheating Notification	No
Electronics Pod	Overheating Notification	No
Light Modules	Overheating Indicator	Yes
System	ROV Not Powered	No
	Automatic Functions	
System	Disable All Modules on Shut Down	No
All Modules	Ping (retrieve data) at 1Hz	No
Camera Modules	Create or Find Media Storage Folder	No

With the features of the new control software listed and a description of it given, the code execution logic and state structures can now be detailed.

5.4.6. Code Execution Logic and State Structures

An extensive knowledge has been gained of the new control software form the previous sections. The general principles, features and operations of the software have been outlined but the logic behind it still remains to be detailed. This section will describe in some level of detail the execution of the code and the interactions between different processing loops.

Before the code enters the “Initialise” state and the parallel processing loops are entered, some general functions are performed. These functions are shown in Figure 48 following. In addition, Figure 48 following shows the data busses that carry information between different loops and which loops receive data from which bus. These data busses, as previously described, take the form of notifiers or queues in LabVIEW.

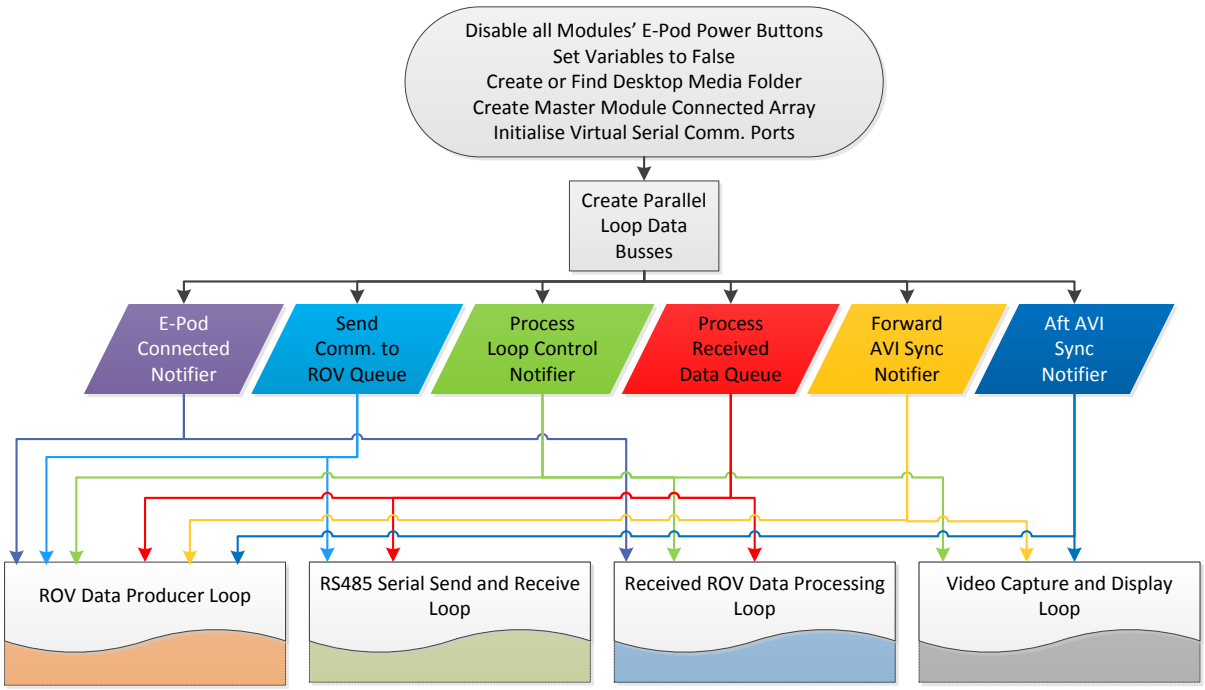

Figure 48 - Initialisation of code and detail of data busses between parallel loops

Colour schemes in Figure 48 will be used to describe the mechanisms by which data is sent from one loop to another in the following flow diagrams that describe the code execution logic.

Apart from the RS485 communications loop, once the initialisations shown previously in Figure 48 have been completed, the loops enter the state machine execution structure as shown in Figure 43 on page 53. Namely, each loop enters the "Initialisation" state.

Figure 49 following describes the notation used to indicate how parallel loop busses will be shown in the following descriptive flow diagrams.

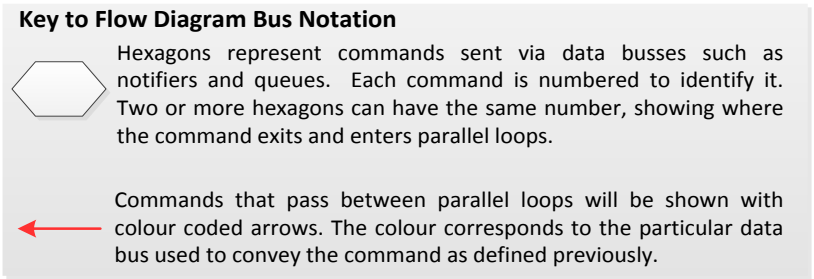

Figure 49 - Key to flow diagram bus notation

Shown following are detailed flow diagrams that describe the execution logic of the four parallel processing loops used in the ROV control software. These loops are namely: Master Producer Loop, Serial Communications Loop, Data Processing Loop and Video Loop.

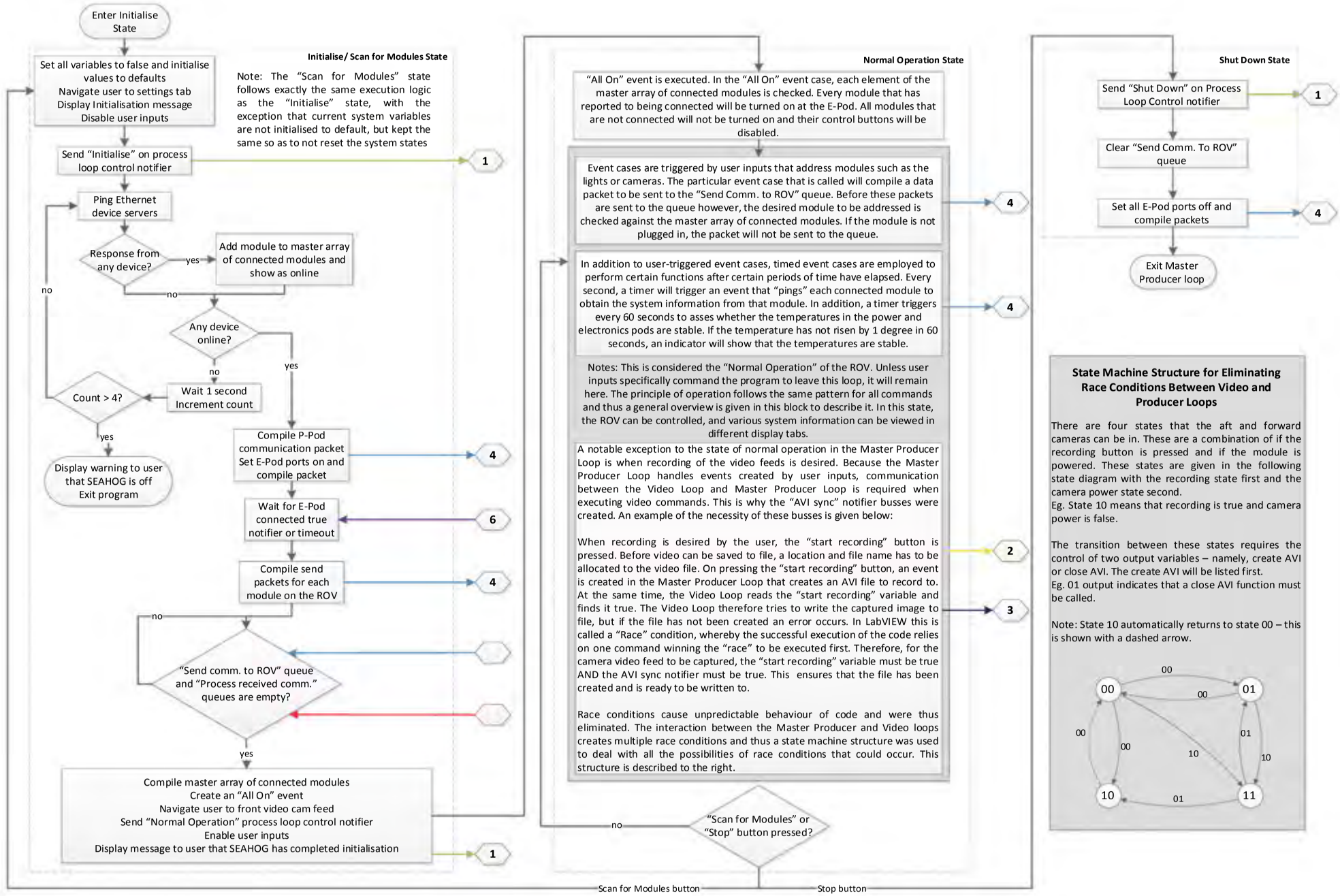

Figure 50 - Flow diagram showing execution logic for the Master Producer Loop

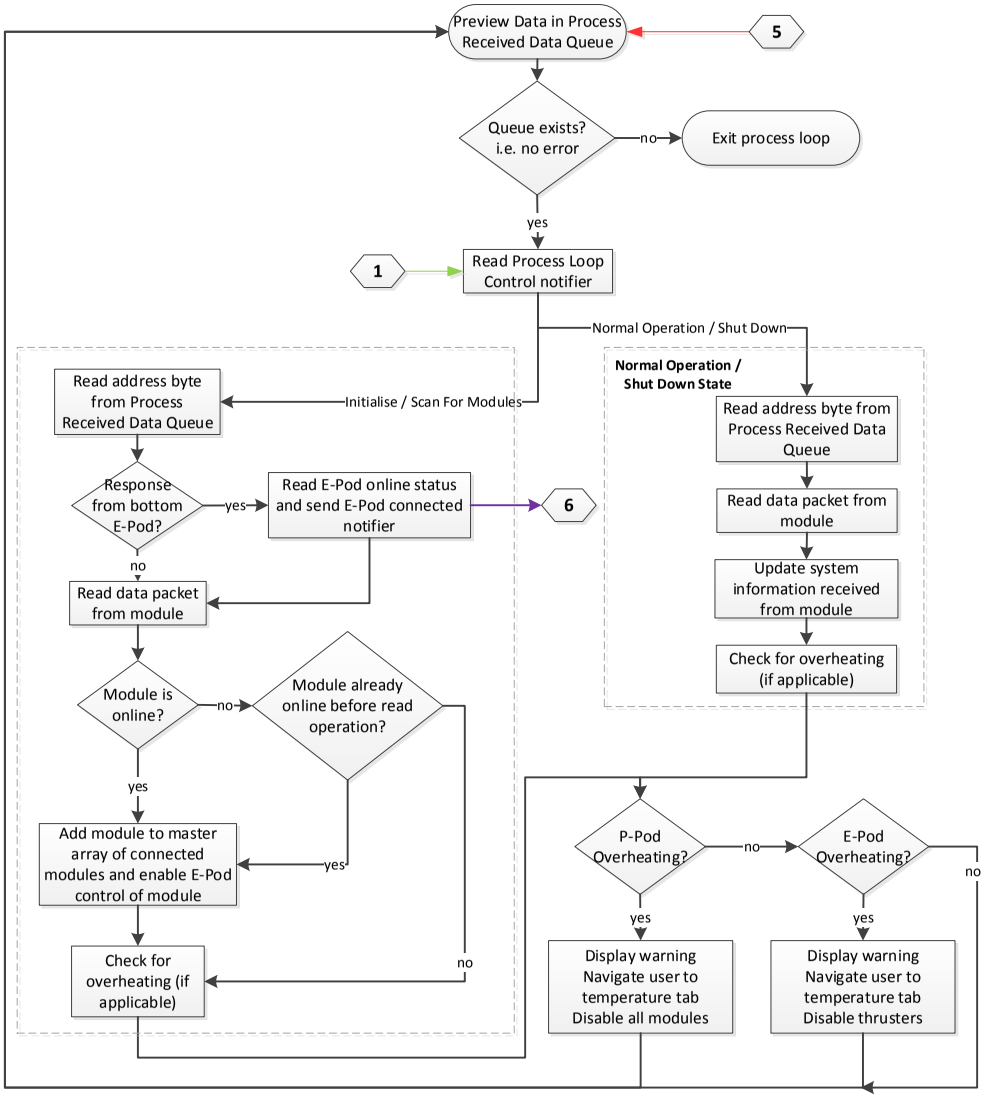

Figure 51 - Flow diagram showing the execution logic for the Processing Loop

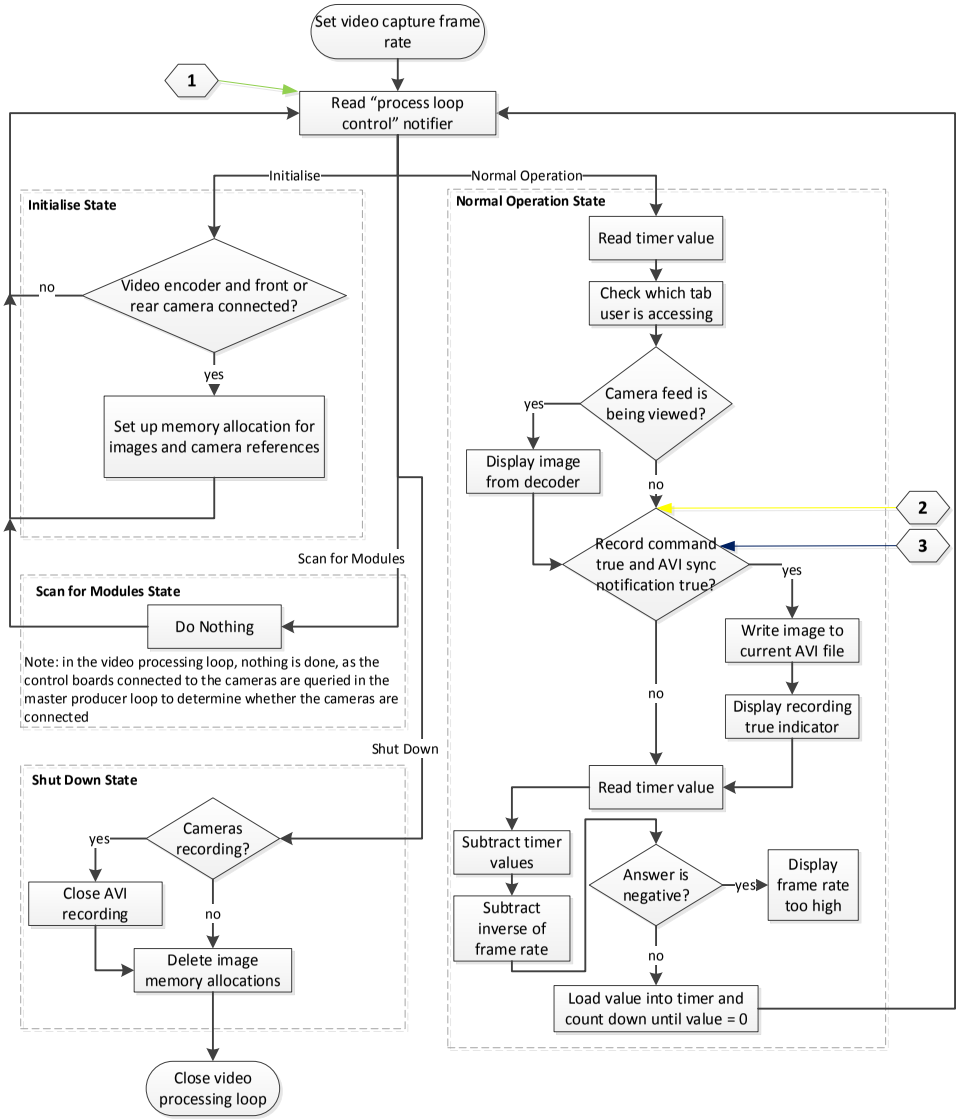

Figure 52 - Flow diagram showing the execution logic of the Video Processing Loop

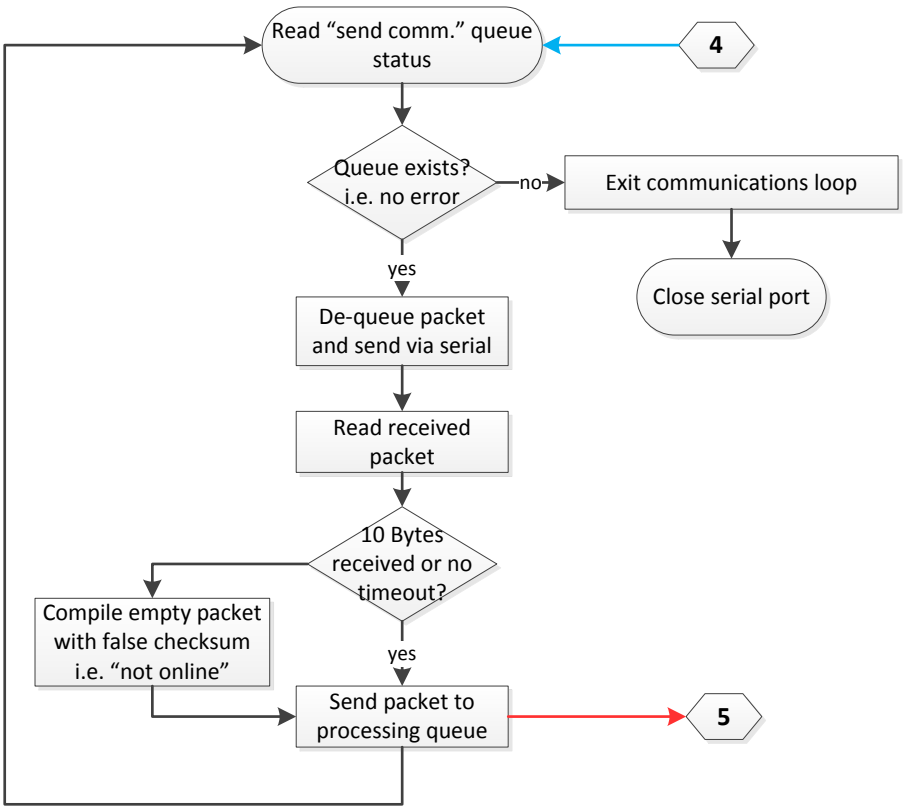

Figure 53 - Flow diagram showing the execution logic of the Serial Communications Loop

This completes the detailed description of the new ROV control software. Execution routines have been provided in the form of flow charts and the interaction of parallel loops using data busses has been shown. The new control software is now described in sufficient detail to understand every aspect of it. Even more detailed insight, if required, can be gained from the control interface’s LabVIEW block diagram, which is fully commented. This report was compiled according to ROV GUI version 16.42.

Now that the new control software is fully understood, some insights can be drawn from using it in operation of the ROV and conclusions of the code overhaul can be drawn.

5.4.7. Testing of the New Control Software

While no “formal” testing was carried out on the software, the code was debugged in as many operating scenarios as possible to ensure predictable operation. This included the modification of system states, such as controlling lights and their brightness and simulating overheating scenarios by heating up module temperature sensors with a heat gun. In this section, comments will be made on how the code fulfils its requirements and its performance in the specification category as given previously in Table 10 if appropriate.

Accessibility: It was important to assess how the code would perform on a platform with less than four processing cores, since the software makes use of four parallel loops. Unfortunately however, the ROV was not available for enough time to conduct all the desired software tests. This was due to manufacturing

processes of other critical systems (such as the Junction Box) on the ROV, rendering it impossible to operate. The code was therefore only tested on the laptop on which it was developed, with an Intel i7 processor and 8 GB RAM.

Control: System latency was reduced so that no perceivable delays existed between the execution and the result of a command on the ROV. This was tested by changing light brightness and controlling the zoom of the front camera. It should be noted that errors were sporadically present in the communications, which was apparent while changing light brightness. However, due to the "ping" function of the code, whereby correct system values are sent every second to modules, error values would be corrected after the next "ping" cycle. This was deemed sufficient, as it is used on non-critical system variables, such as light brightness's – where it does not matter if the light dims slightly for a brief period in time.

Safety: The system Initialisation, the "Scan for Modules" and the "Shut Down" functions worked reliably with all connected modules being found 100% of the time during initialise and disconnected from power 100% of the time during shut down, successfully decreasing the amount of procedures the user must remember to carry out during operation of the ROV.

Trade-Offs: The code was optimised to some extent by monitoring the system performance in Windows Task Manager. This allowed parts of the code that use unnecessary amounts of system resources to be identified. An example of one of these optimisations was to limit the rate that some of the loops could run at, so that the loop was not executed at the maximum rate possible, as this was deemed unnecessary.

This completes a description of the testing procedures carried out on the new user GUI for the *SEAHOG*. A summary can now be given of the architecture of the code in the following subsection.

5.4.8. Summary of New Code Architecture, Features and Results

The new GUI developed for the *SEAHOG* has the functionality of controlling the lights and cameras of the ROV in addition to monitoring all vehicle system data. It includes safety warnings for overheating and it detects automatically which modules are connected. System data and sensory information is updated once per second.

The code runs in LabVIEW using four parallel loops – two in a producer consumer arrangement, with one loop dedicated to generating serial commands to be sent to the ROV. One loop is dedicated solely to processing serial data as this is the slowest rate of data processing in the software. Commands received from the *SEAHOG* are processed in another parallel loop. Finally, one loop is dedicated to processing video data due to its data intensive nature.

The software is designed to be transferrable and work on any computer running a Windows operating system. Any recorded or captured data is stored in an automatically created desktop folder.

The producer loop takes the form of a state machine, whereby it will automatically handle initialise and shutdown functions, with its default state being for normal operation of the *SEAHOG*. The code uses an event based data processing structure, where the code does not continuously execute a given routine, but listens for user and timed events and then executes subroutines called by the event.

The result is a reliable and far more responsive GUI, in which all system data can be monitored but is stored in tabs so that the operator can focus on the control of the ROV if there are no anomalies in the system.

The final developed GUI is given following in Figure 54.

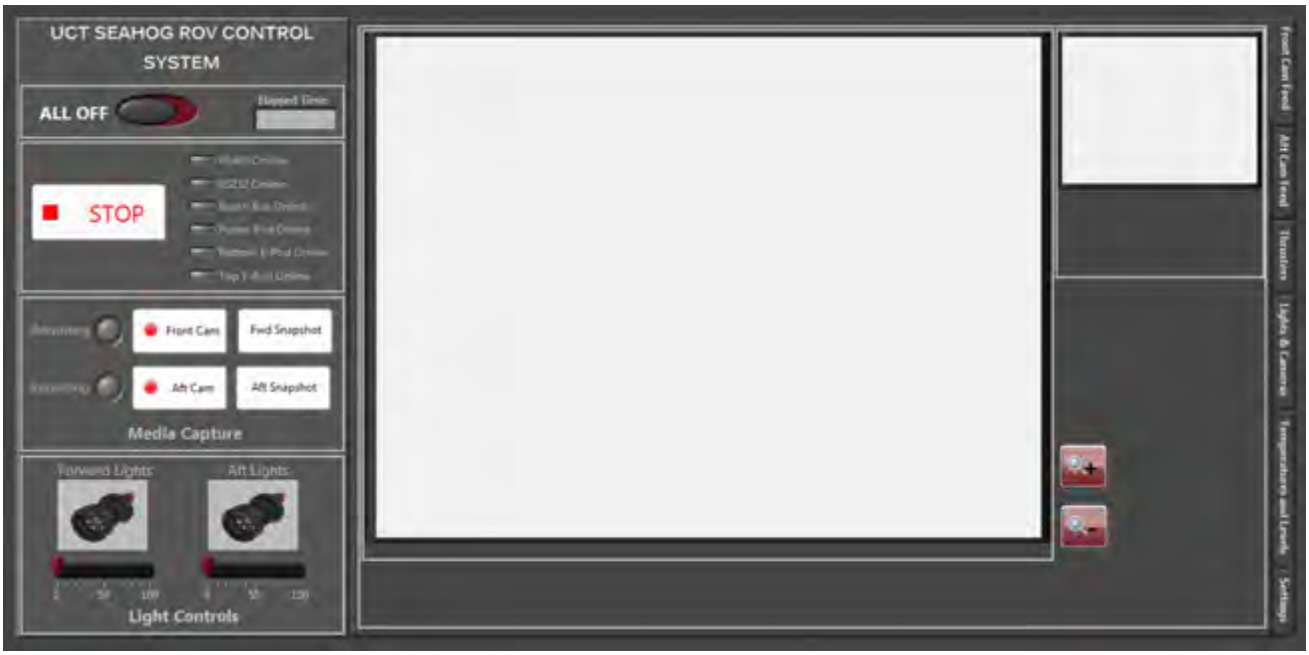

Figure 54 - New ROV GUI control interface

5.5. Summary of GUI Overhaul Process

The previous GUI has been overhauled in this chapter, resulting in a more user-friendly control interface for the *SEAHOG*. The previous GUI has a focus of maintenance and testing and should thus be used when it more basic commands are required to be sent to individual modules – specifically, the old GUI does not have automatic detection of which modules are connected, and thus if it is desired to power a specific module on and off to debug code, for example, while keeping the rest of the ROV powered, it is recommended that the old GUI is used.

Due to the user focussed overhaul of the operator software, the *SEAHOG* system is very responsive and all completed modules at this point in time are integrated into the software. Additional safety warning features have been added to the code, including automatic functions such as initialise and shut down, whereby all modules are powered off before the code is halted.

This completes the in depth investigation and process conducted to overhaul the user software for the *SEAHOG* and allows conclusions and recommendations for each chapter of this appendix to be given in the following chapter.

6. Conclusions and Recommendations

6.1. Junction Box

The Junction Box was successfully pressure tested for 2 hours at a pressure equivalent to a depth of 450 m in the ocean. The custom designed brass penetrators performed adequately, after a design modification was made to the tether in-line penetrator, whereby a polyurethane over-mould was conducted on the external faces of the penetrator.

It is recommended that the surface junction box is rigidly mounted inside the tether reel. This design will prevent relative movement between the tether and the surface junction box, preventing wear of the delicate fibres mounted inside the box. It is then recommended that the extension power and fibre chords are coiled on brackets outside the drum. The concept is shown following in Figure 55.

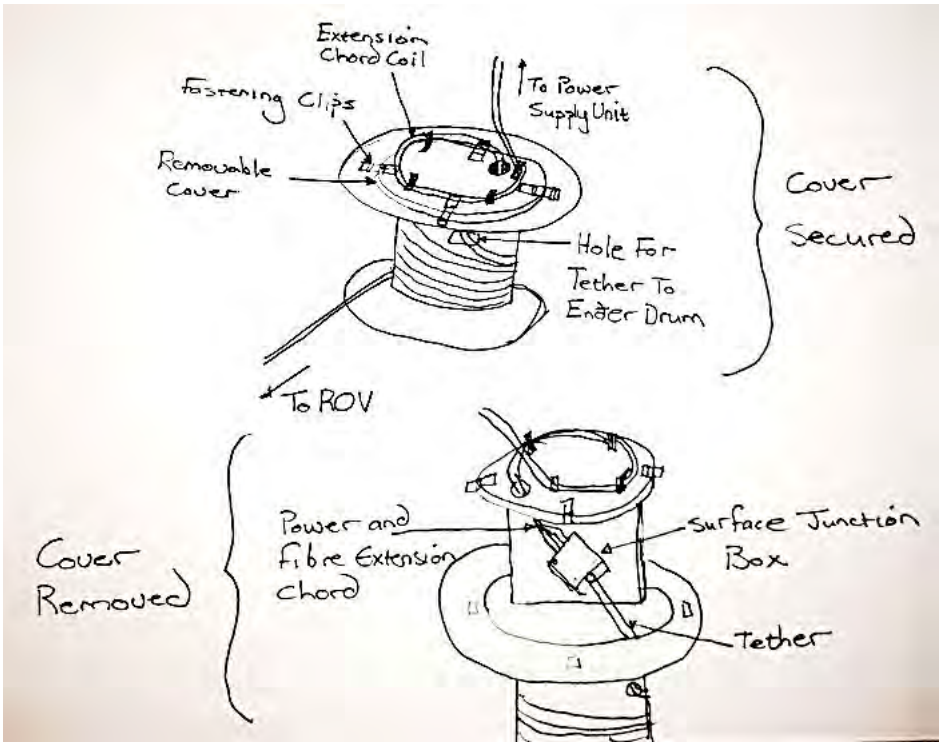

Figure 55 - Tether reel and surface Junction Box mounting concept

It is recommended for ease of use that the PVC collar is redesigned to be thinner and made of aluminium. Aluminium is recommended because it was observed that the PVC would stick to the aluminium Junction Box housing, making removal of the collar difficult.

Finally, the clip mechanism for the mounting bracket worked adequately, however the dimensions of the HDPE "teeth" resulted in the tooth being quite stiff and hence it was difficult to unclip the bracket. It is recommended in the future that the teeth are longer, reducing the force required to bend the tooth and unclip the mechanism.

6.2. Power Pod

The Power Pod heat sink and four cooling fans were successfully installed. The fans are powered by a 12 V port in the Power Pod and individually connect to a small power distribution PCB.

It was observed during testing and system development that the Power Pod would exhibit higher temperatures than before on external surfaces in the region of the heat sink after the heat sink was installed. It was therefore assumed that the heat sink was indeed contributing positively to the heat sinking capabilities of the Power Pod. However, no formal assessment or testing was carried out in this project to determine the extent of this improvement. It is thus recommended that a future project assesses the heat sinking capabilities of the installed cooling systems formally so that the operational capabilities of the ROV can be better determined.

A proposed procedure to test the heat sinking capabilities of the Power Pod to some extent without running the entire ROV system in the water is as follows:

1. Immerse the Power Pod in a vessel of water while connected to all ROV modules.
2. Remove the propellers from all the thrusters and mount aluminium tubes statically over the thruster membranes. The rotation of the inner magnetic motor will cause an eddy braking effect in the aluminium tubes and hence apply a load to the motor.
3. Run the thrusters such that a significant current is drawn from each motor. This will apply a load to the entire ROV system and cause an increase in temperature in the Power Pod, allowing its heat sinking capabilities to be further assessed.

In addition, standard procedures that are carried out on every ROV module must still be completed for the new Power Pod housing. This includes anodising the housing and pressure testing it.

6.3. Light and Camera Modules

The light and camera modules were successfully connected to the main ROV communication network, with all communication issues being resolved. This showed how a modular subsystem structure allows for ease of debugging and maintenance. On-board intelligence was added to the light modules, allowing them to detect overheating scenarios independently of the main surface control console. In addition, the temperature sensors for the light modules were calibrated and verified to ±1˚ C of accuracy. This was deemed sufficient, as the light modules were programmed to indicate overheating at 85˚ C, which is far enough below the critical temperatures for the system of 100˚C.

The camera and light subsystems are fairly rudimentary and display robust operation for their possible functions. Therefore, recommendations for these subsystems are fairly limited. It is recommended however, that some kind of diagnostic reporting is implemented on the ROV to aid in error checking and accurately identify faults for maintenance and debugging purposes. This would be a time consuming endeavour however, so it is envisaged only for future work.

6.4. ROV Control Software

The overhaul of the user software for controlling the ROV was very successful, providing a responsive and user-friendly interface through which all systems that were not undergoing development could be controlled and monitored. Multi-core processing was taken advantage of in LabVIEW to handle separate tasks independently. The result was a highly responsive low latency interface.

An obvious recommendation is the incorporation of the remaining systems into the user software such as the thrusters and camera tilt unit. However, it is recommended that an in-depth assessment of the future control requirements of the ROV is made before the thrusters and motion sensors are incorporated into the user software. Possible restructuring of the network architecture will be required and is expanded upon more in the main dissertation part of this project.

Features that should be added to the software to bring the ROV closer to an industrial grade system include:

- Data logging of all telemetry and sensory data.
- Embedded diagnostics for error checking and maintenance.
- Investigation and implementation of where self-healing techniques can be implemented in the software.

Some of the above tasks will be simple to implement but are probably more easily incorporated when all ROV subsystems are available to be incorporated into the system. Diagnostics and self-healing however,

might be a more extensive task, due to the necessity of modification to embedded code on individual subsystems.

Some areas exist for optimisation of the current GUI code, as given following:

- E-Pod and P-Pod data processing routines update all global variables associated with them even if the particular data hasn't been read in the preceding communication cycle. A more discerning structure could be created so that only variables from data that has been read are updated.
- Rarely, an anomaly occurs in the camera feed whereby the camera feed goes blank. Restarting the code and re-establishing connection with the camera video encoder is required to regain the video feed. This issue happens rarely but could be the source of some investigation.
- There is a small latency between real motion and the motion being captured in the video feed. The latency is not very noticeable unless rapid motion is observed by the camera, however, this would be an area of investigation if vision based control research is desired of the *SEAHOG* system.

6.5. Final Comments

This appendix served to detail some of the aspects undertaken in this project that did not form part of the main focus. A successful redesign of the Junction Box resulted in a space and mass saving that turned out to be critical for the buoyancy of the ROV to be balanced correctly. Maintenance was conducted on the system to ensure that existing subsystems were fully operational. Additional heat sinking capacity was installed in the Power Pod, which was shown in a previous project to be incapable of successfully dumping heat to the surroundings at a rate that would allow for full power operation of the ROV. Finally, an in-depth overhaul of the user control software was conducted so as to remove the latency experienced in the old software and incorporate all available modules into the new software.

This appendix serves partly as a reference for future work that will be carried out on the *SEAHOG* systems but also, where applicable, demonstrates the holistic nature of tasks carried out in this project.

Works Cited

[1] R. d. Smidt, “Development of the Power and Communications Distribution Systems for an Underwater Remotely Operated Vehicle,” University of Cape Town, Cape Town, 2014.

[2] KCF Technologies, Inc., “Smart Tether™ for ROVs,” KCF Technologies, Inc., 2014. [Online]. Available: https://kcftech.com/smarttether/rovs.html. [Accessed 17 May 2015].

[3] T. E. Knight, “Development of the Steering and Propulsion and the Camera and Lighting Systems for an Observation Class Remotely Operated Vehicle,” University of Cape Town, Cape Town, 2012.

[4] Speciality Steel Industry of North America, “CORROSION: GALVANIC CORROSION,” [Online]. Available: http://www.ssina.com/corrosion/galvanic.html. [Accessed 2 June 2015].

[5] E. Hearn, Mechanics of Materials: Volumes 1 & 2, 3 ed., Butterworth-Heinemann, 1997.

[6] K. Siemon, in *Manual for the Design of Ferrous and Non-Ferrous Pressure Vessels and Tanks*, Michigan, Edwards Brothers, Inc., 1948, p. 94.

[7] S. Timoshenko and S. Woinowsky-Kreiger, Theory of Plates and Shells, New York: McGraw-Hill Book Company, Inc., 1959.

[8] Texas Instruments Incorporated, “LM35 Precision Centigrade Temperature Sensors,” October 2013. [Online]. Available: http://www.ti.com/lit/ds/symlink/lm35.pdf. [Accessed 21 December 2014].

[9] W. O. Galitz, “General Principles,” in *The Essential Guide to User Interface Design*, Indianapolis, Wiley Publishing Inc., 2007, pp. 45-58.

Appendix C
Mechanical Drawings

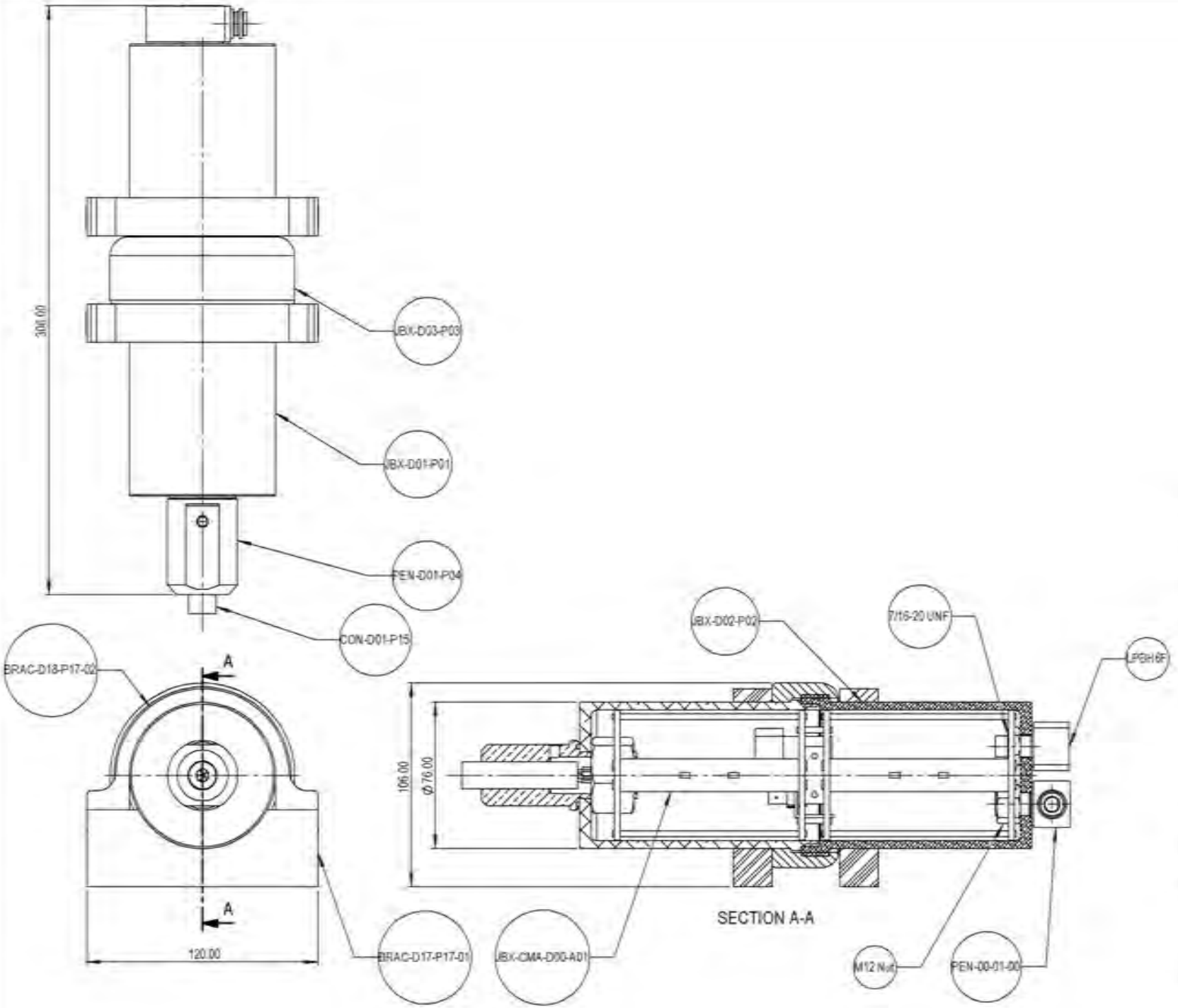

PartNo	PART NUMBER	QTY.
JBX-D02-P02	JBX-P02-ROV Side Housing	1
JBX-D01-P01	JBX-P01-Tether Side Unit	1
NA	CON-P01-LPBH6F	1
PEN-00-01-00	PEN-P00 Fiber Optic Penetrator	1
JBX-CMA-D00-A01	JBX-CMA-A01-Connector Mounting Assembly	1
	7/16 - 20 UNF-NUT	1
	M12 NUT	1
	M24 NUT	1
JBX-D03-P03	JBX-P03-Collar	1
PEN-D01-P04	PEN-P04-In Line Tether Penetrator	1
CON-D01-P15	CON-P15-Tether Cable	1
BRAC-D17-P17-01	BRAC-P17-Chock Block Junction Box REV1.0	2
BRAC-D18-P17-02	BRAC-P17-03-Chock Block Junction Box REV1.0 Clip	2

A3 Landscape	University of Cape Town Department of Mechanical Engineering			
	Title: JBX-A01-Junction Box Assembly REV1.0			
Assembly Drawing	Scale: 1:2	Date: 2016-03-24	Sheet 1	of: 8
	Drawn By: Max Finbow FNBMAX001		Drawing Number: JBX-D00-A01	

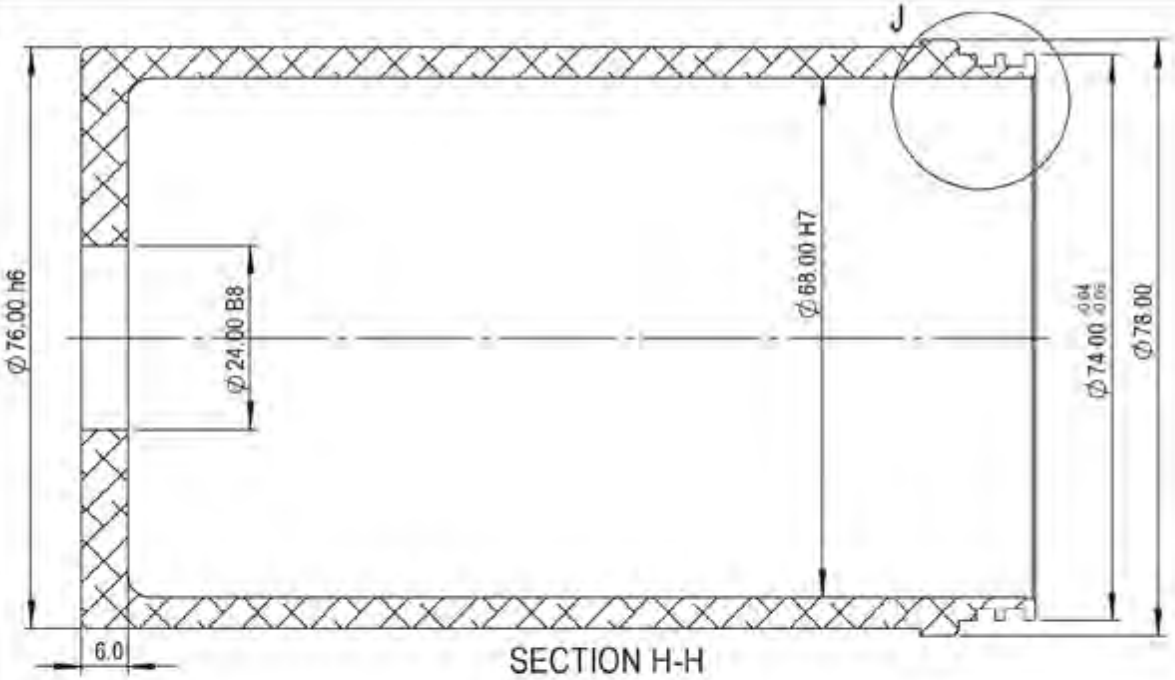

SECTION H-H

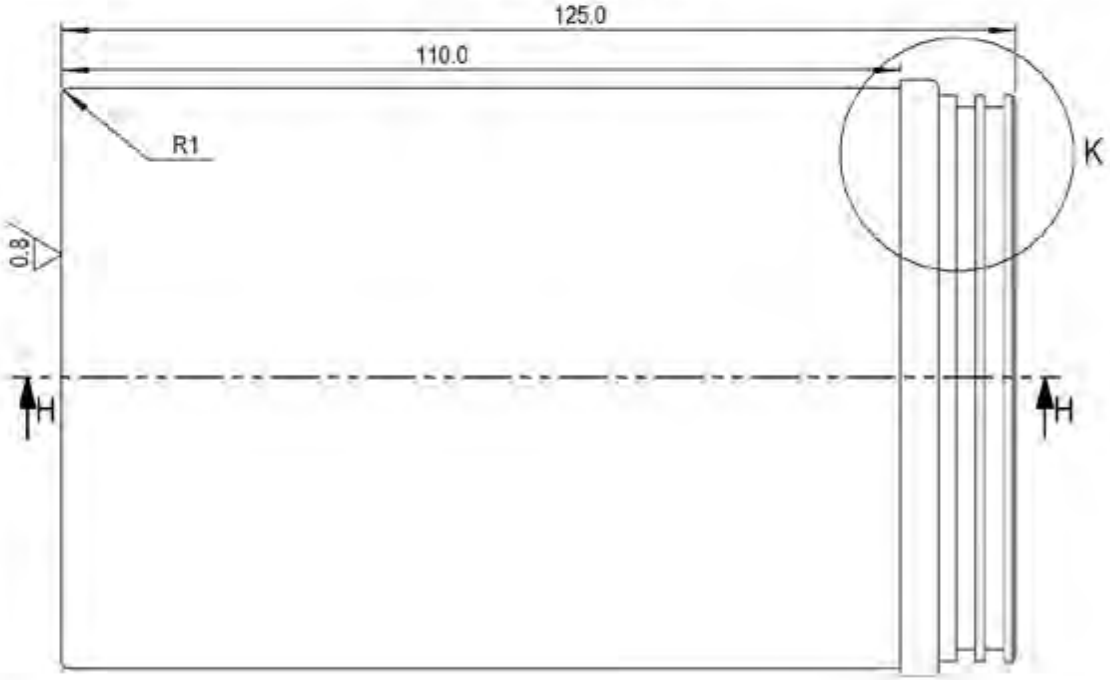

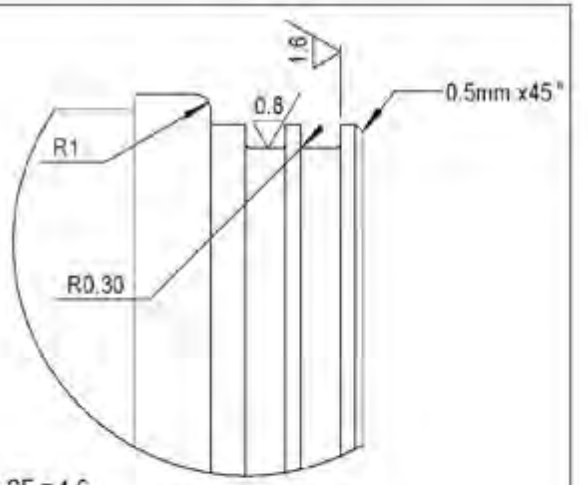

GLAND SIDE WALLS SF = 1.6
GLAND FACES SF = 0.8
GLAND FILLETS = 0.3mm

DETAIL K
SCALE 2 : 1

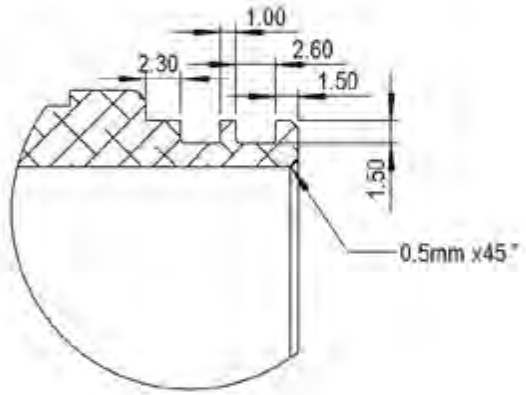

DETAIL J
SCALE 2 : 1

A4 Landscape	University of Cape Town Department of Mechanical Engineering			
	Title: JBX-P01-Tether Side Lid			
Qty: 1	Scale: 1:1	Date: 2016-03-24	Sheet2	of 8
Material: AL 6082 T6	Drawn By: Max Finbow FNBMAX001		Drawing Number JBX-D01-P01	

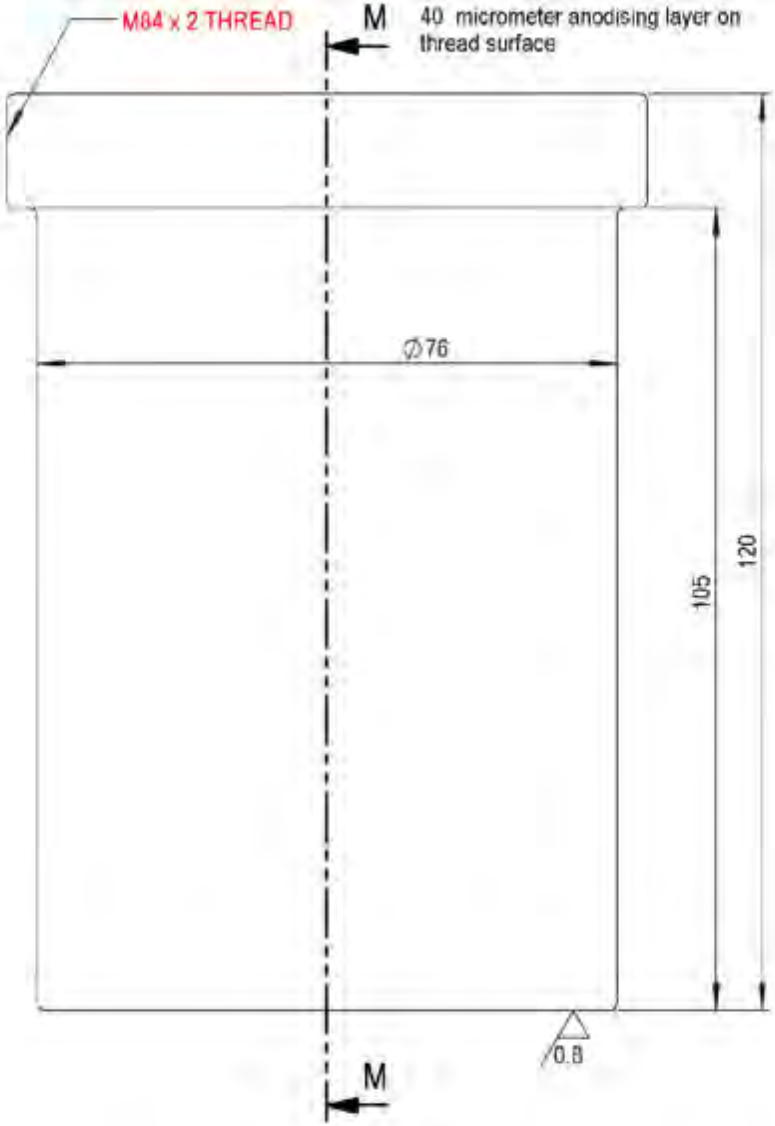

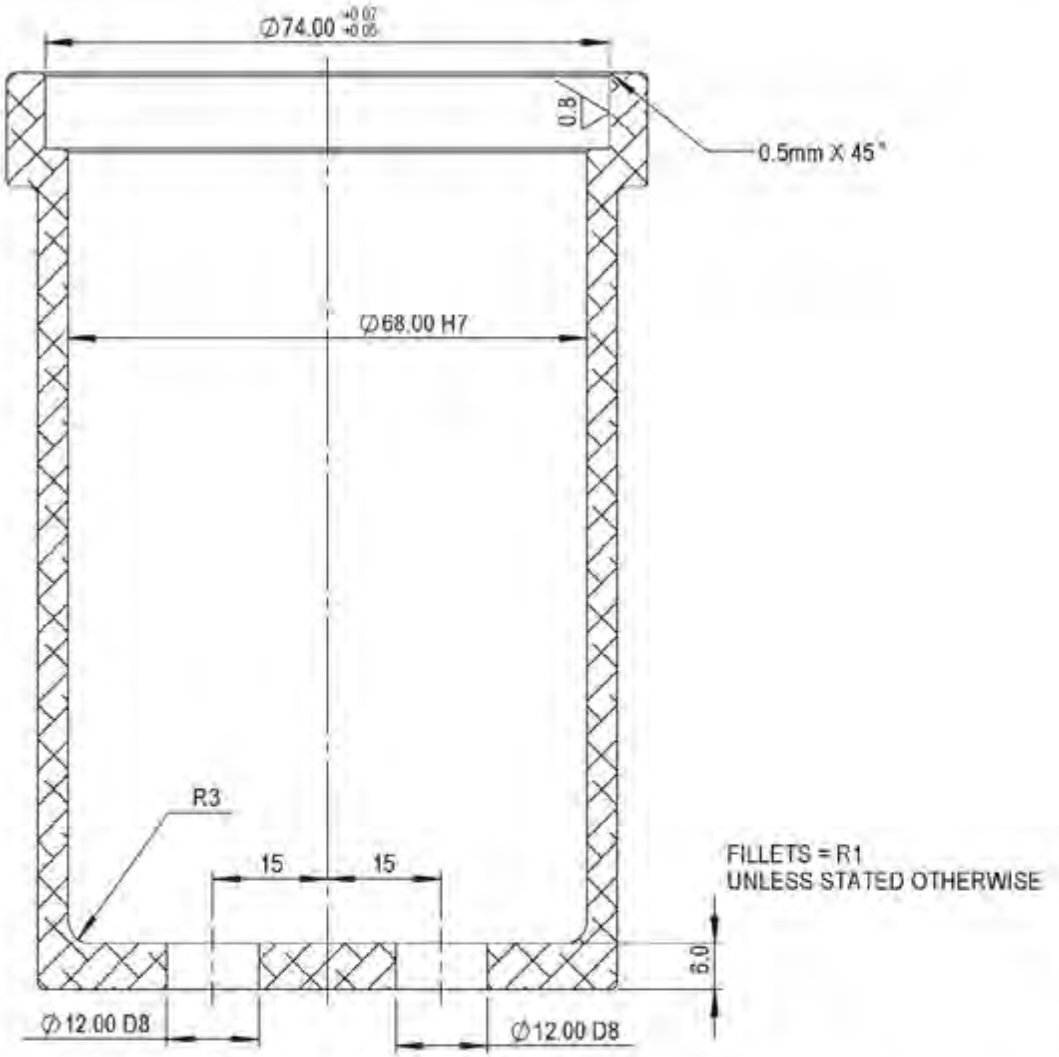

SECTION M-M

A4 Landscape	University of Cape Town Department of Mechanical Engineering			
	Title: JBX-P02-ROV Side Housing			
Qty: 1	Scale: 1:1	Date: 2016-03-24	Sheet3	of 8
Material: AL 6082 T6	Drawn By: Max Finbow FNBMAX001		Drawing Number JBX-D02-P02	

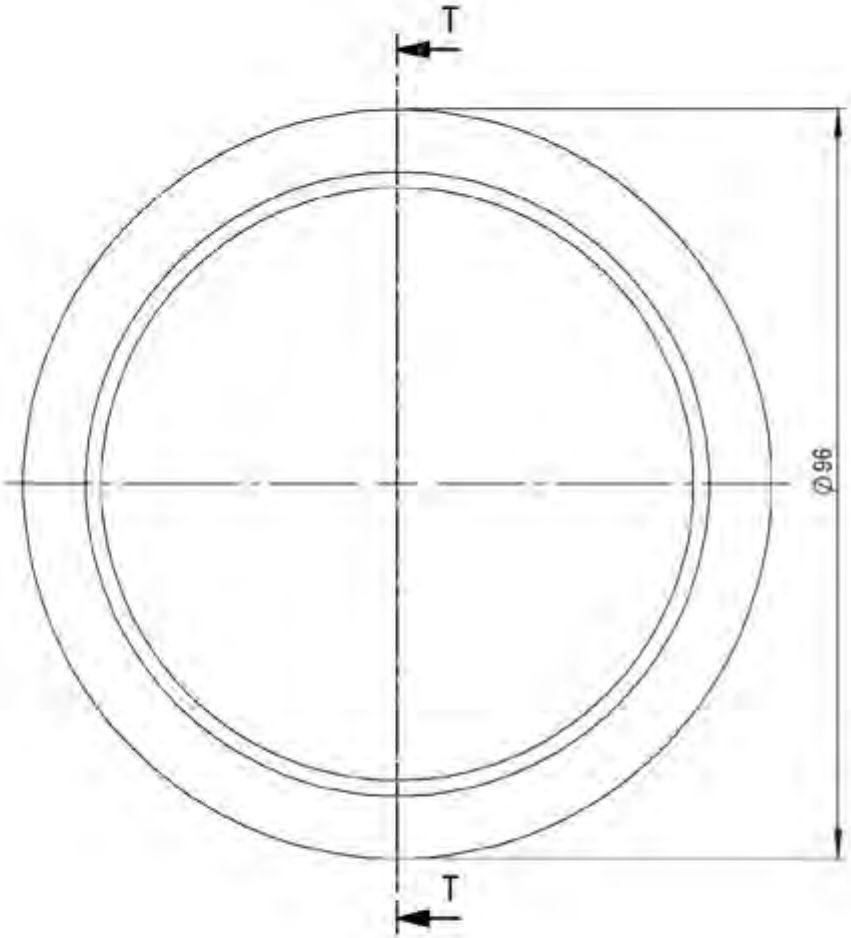

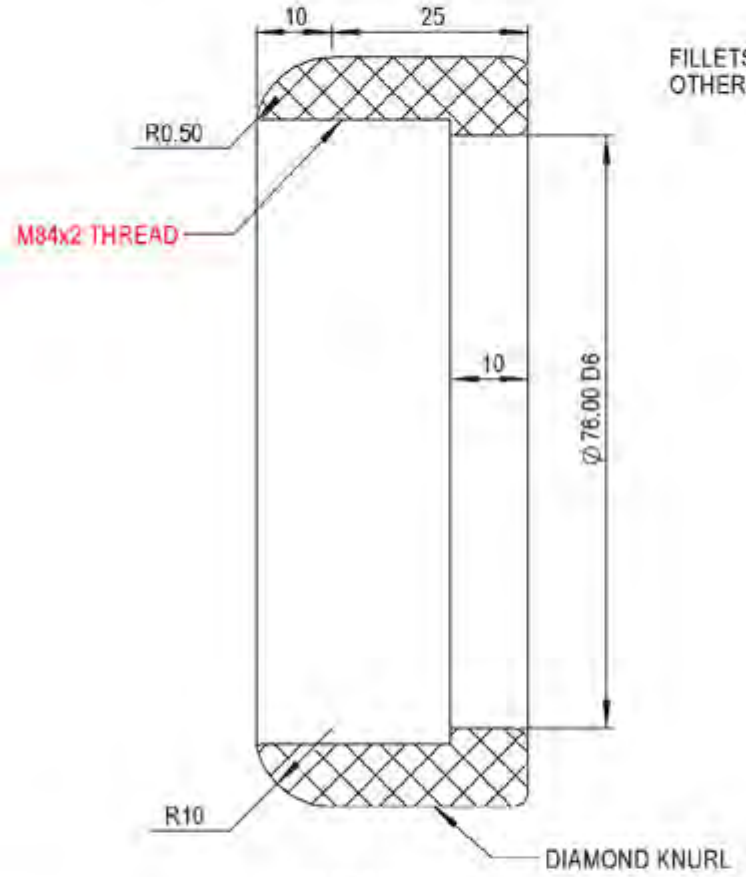

SECTION T-T

A4 Landscape	University of Cape Town Department of Mechanical Engineering			
	Title: JBX-P03-Collar			
Qty: 1	Scale: 1:1	Date: 2016-03-24	Sheet4	of 8
Material: PVC Rigid	Drawn By: Max Finbow FNBMAX001		Drawing Number: JBX-D03-P03	

GLAND SIDE WALLS SF = 1.6
GLAND FACES SF = 0.8
GLAND FILLETS = 0.3mm

ALL CHAMFERS 0.5mm X 45°
UNLESS OTHERWISE STATED
ALL FILLETS R=1mm
UNLESS OTHERWISE STATED

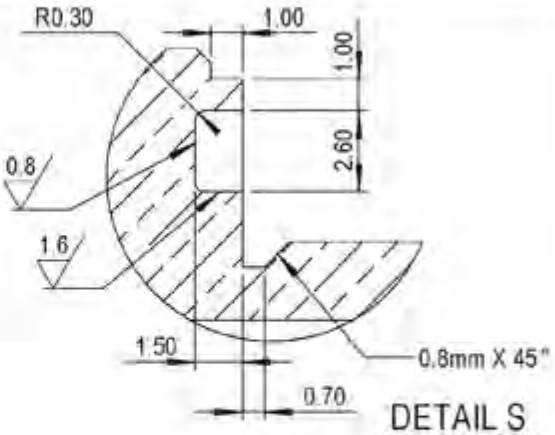

DETAIL S
SCALE 4 : 1

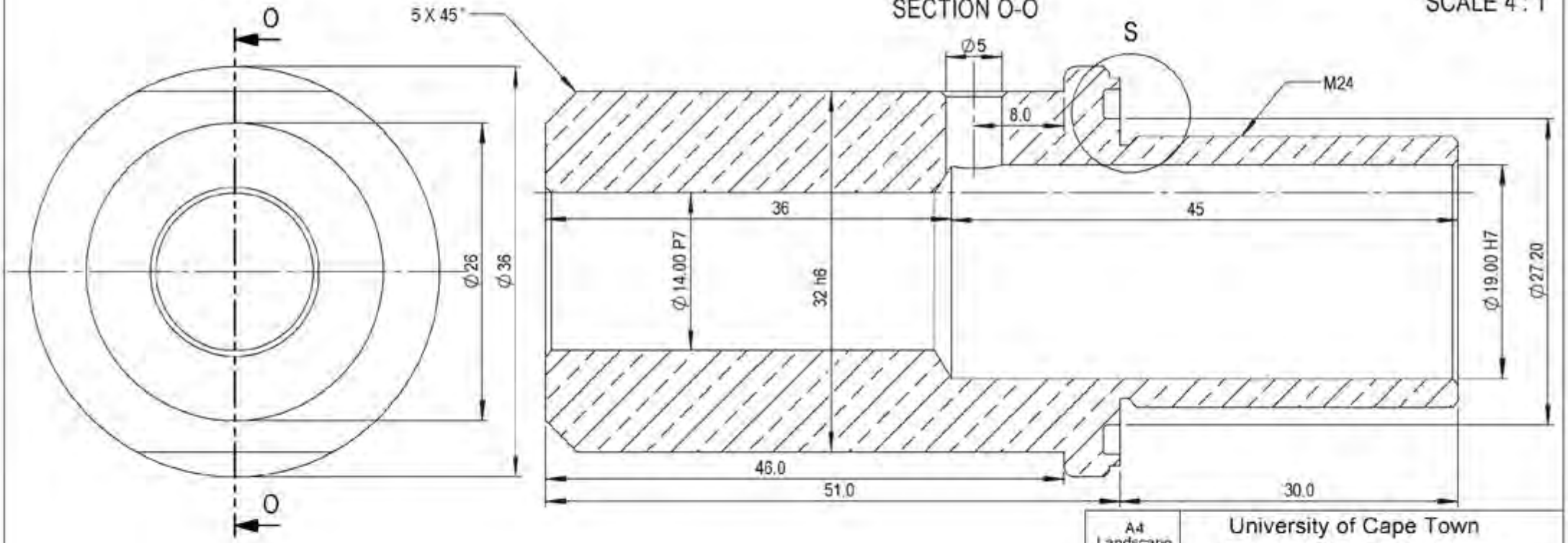

A4 Landscape	University of Cape Town Department of Mechanical Engineering			
	Title: PEN-P04-In Line Tether Penetrator			
Qty: 3	Scale: 2:1	Date: 2016-03-24	Sheet5	of 8
Material: Brass	Drawn By: Max Finbow FNBMAX001		Drawing Number PEN-D01-P04	

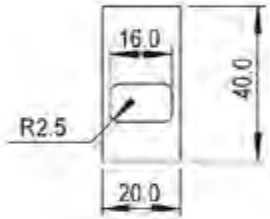

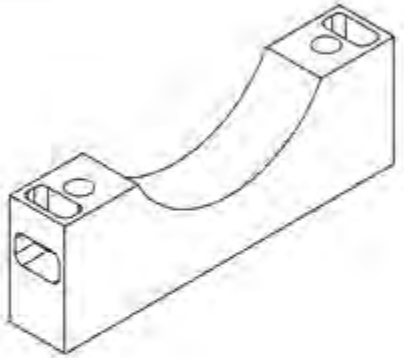

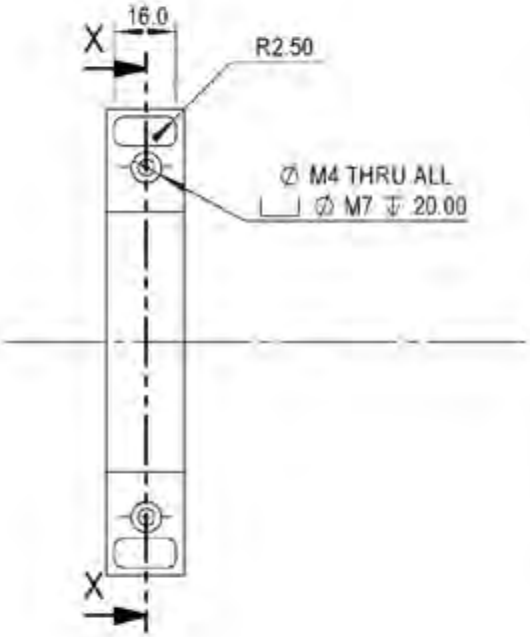

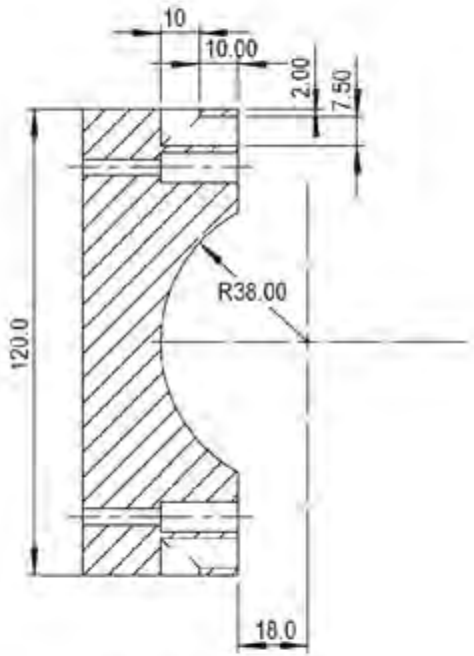

SECTION X-X

A4 Landscape	University of Cape Town Department of Mechanical Engineering			
	Title: BRAC-P17-Chock Block Junction Box REV1.0			
Qty 2	Scale: 1:2	Date: 2016-03-24	Sheet6	of 8
Material: PP Homopolymer	Drawn By: Max Finbow FNBMAX001		Drawing Number BRAC-D17-P17-01	

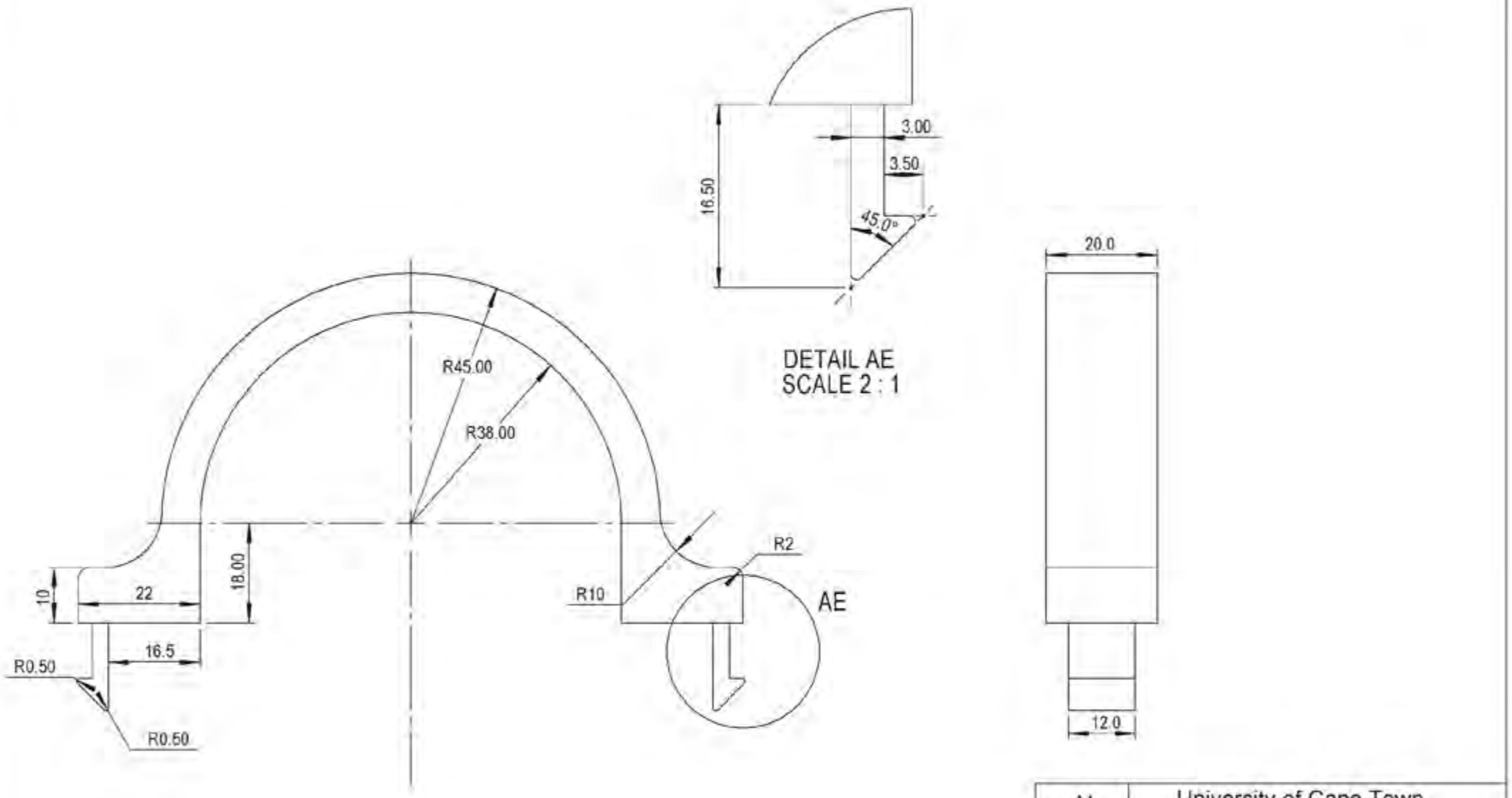

A4 Landscape	University of Cape Town Department of Mechanical Engineering			
	Title: BRAC-P17-02-Chock Block Junction Box REV1.0 Clip			
Qty. 2	Scale 1:1	Date: 2016-03-24	Sheet7	of 8
Material: PP Homopolymer	Drawn By: Max Finbow FNBMAX001		Drawing Number BRAC-D18-P17-02	

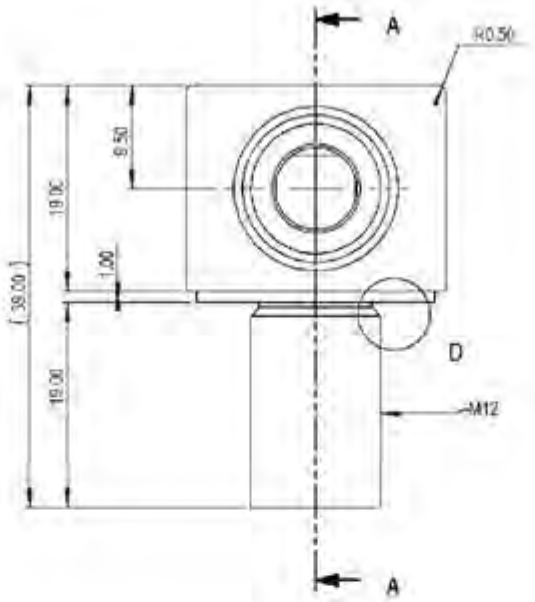

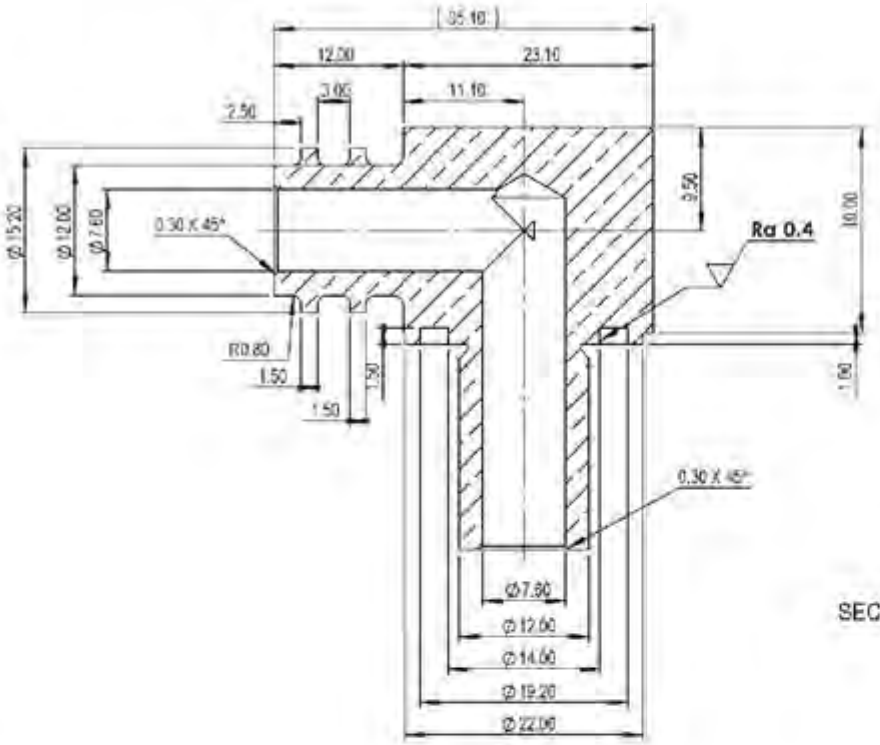

SECTION A-A

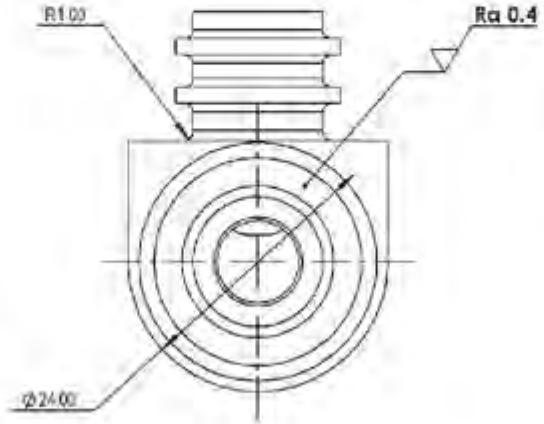

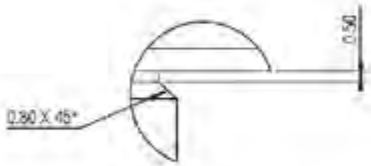

DETAIL D
SCALE 4 : 1

A3 Landscape	University of Cape Town Department of Mechanical Engineering				
	Title: PEN-P01 Fibre Optic Penetrator				
Quantity: 1	Part Finish:	Date: 2016-09-24	Scale: 2:1	Sheet 8	of 8
Material: Brass	Drawn By: Roger de Smidt DSMROG001			Drawing Number: PEN-00-01-08	

Appendix D
Ethics Form

EBE Faculty: Assessment of Ethics in Research Projects

Any person planning to undertake research in the Faculty of Engineering and the Built Environment at the University of Cape Town is required to complete this form before collecting or analysing data. When completed it should be submitted to the supervisor (where applicable) and from there to the Head of Department. If any of the questions below have been answered YES, and the applicant is NOT a fourth year student, the Head should forward this form for approval by the Faculty EIR committee: submit to Ms Zulpha Geyer (Zulpha.Geyer@uct.ac.za; Chem Eng Building, Ph 021 650 4791). Students must include a copy of the completed form with the thesis when it is submitted for examination.

Name of Principal Researcher/Student: Maximillian Finbow Department: Mechanical Engineering

If a Student: Yes Degree: MSc. Eng Supervisor: Hennie Mouton

If a Research Contract indicate source of funding/sponsorship:

Research Project Title: The Dynamic Modelling and Development of a Controller for a general purpose underwater ROV

Overview of ethics issues in your research project:

Question 1: Is there a possibility that your research could cause harm to a third party (i.e. a person not involved in your project)?	YES	NO X
Question 2: Is your research making use of human subjects as sources of data? If your answer is YES, please complete Addendum 2.	YES	NO X
Question 3: Does your research involve the participation of or provision of services to communities? If your answer is YES, please complete Addendum 3.	YES	NO X
Question 4: If your research is sponsored, is there any potential for conflicts of interest? If your answer is YES, please complete Addendum 4.	YES	NO X

If you have answered YES to any of the above questions, please append a copy of your research proposal, as well as any interview schedules or questionnaires (Addendum 1) and please complete further addenda as appropriate.

I hereby undertake to carry out my research in such a way that

- there is no apparent legal objection to the nature or the method of research; and
- the research will not compromise staff or students or the other responsibilities of the University;
- the stated objective will be achieved, and the findings will have a high degree of validity;
- limitations and alternative interpretations will be considered;
- the findings could be subject to peer review and publicly available; and
- I will comply with the conventions of copyright and avoid any practice that would constitute plagiarism.

Signed by:

	Full name and signature	Date
Principal Researcher/Student: Maximillian Finbow	Signed	26/01/15

This application is approved by:

Supervisor (if applicable):	HENDRIK DANIEL MOUTON Signed	29/01/2015
HOD (or delegated nominee): Final authority for all assessments with NO to all questions and for all undergraduate research.	Signed R.D. Knutsen	06/02/2015
Chair : Faculty EIR Committee For applicants other than undergraduate students who have answered YES to any of the above questions.		